

# **EFFECT OF SURFACE FINISH ON FATIGUE OF AUSTENITIC STAINLESS STEELS**

A thesis submitted to The University of Manchester for the degree of Doctor of  
Philosophy in the Faculty of engineering and physical science

**2010**

**Saeed Al-Shahrani**

**School of Materials**

## **Table of Contents**

<b>Abstract</b> .....	24
<b>Declaration</b> .....	25
<b>Copyright</b> .....	26
<b>Acknowledgements</b> .....	27
<b>Chapter 1</b> .....	28
<b>Introduction</b> .....	28
<b>Chapter 2</b> .....	31
<b>Literature Review</b> .....	31
2.1. <b>A Brief Overview of Stainless Steel</b> .....	31
2.1.1. <b>History of Stainless Steel</b> .....	31
2.1.2. <b>Applications of Stainless Steels</b> .....	32
2.1.3. <b>Stainless Steel Types and Grades</b> .....	32
2.1.4. <b>Austenitic Stainless Steels</b> .....	34
2.1.4.1. <b>Composition and constituents</b> .....	34
2.1.4.2. <b>The Iron-Chromium-Nickel System</b> .....	37
2.1.4.3. <b>Grades of Austenitic Stainless Steels</b> .....	38
2.1.4.4. <b>Mechanical Properties of Austenitic Stainless Steels</b> .....	39
2.1.4.5. <b>Physical Properties</b> .....	41
2.1.4.6. <b>Fatigue Properties</b> .....	41
2.2. <b>Fatigue of Materials</b> .....	42
2.2.1. <b>Introduction</b> .....	42
2.2.2. <b>Fatigue Design Methodology</b> .....	43
2.2.2.1. <b>Total –Life Approach</b> .....	43
2.2.2.2. <b>Damage-Tolerance Approach</b> .....	45
2.2.2.3. <b>Safe-Life and Fail-Safe Approach</b> .....	45
2.2.3. <b>Stress-Life (S-N) Approach</b> .....	46
2.2.3.1. <b>Cyclic Stress [17-19]</b> .....	46
2.2.3.2. <b>The S-N Curve</b> .....	48
2.2.3.3. <b>Fatigue Limit</b> .....	48
2.2.3.4. <b>The Effect of Mean Stress on Fatigue life Under Stress-Life Approach</b> .....	49
2.2.3.5. <b>Effect of Surface Treatments under Stress-Life Approach</b> .....	49
2.2.4. <b>Strain-Life (E-N) Approach</b> .....	50
2.2.4.1. <b>Strain Controlled Test Method</b> .....	50
2.2.4.2. <b>Cyclic Material Behaviour Under strain controlled Loading</b> .....	51
2.2.4.3. <b>Strain Based Approach to Total Life</b> .....	52



2.2.5.	<i>Fatigue damage and crack initiation mechanism</i> .....	54
2.2.6.	<i>Crack Propagation</i> .....	59
2.2.7.	<i>Fatigue Fracture Surface and Macro/Micro Features</i> .....	61
2.2.8.	<i>Statistical analysis of Fatigue Data</i> .....	62
2.2.8.1.	<i>Two-Point Strategy</i> .....	62
2.2.8.2.	<i>Boundary Method</i> .....	62
2.2.8.3.	<i>Staircase Testing</i> .....	63
2.2.8.4.	<i>Analysis for staircase method</i> .....	64
2.2.9.	<i>Effect of Cyclic Deformation on near surface microstructures of austenitic stainless steels</i> .....	65
2.3.	<i>Short Fatigue Cracks</i> .....	67
2.3.1.	<i>Short Crack Regimes</i> .....	70
2.3.2.	<i>Short Crack Growth</i> .....	72
2.3.3.	<i>Microstructural Barriers</i> .....	73
2.3.4.	<i>Crack Closure Effect</i> .....	77
2.4.	<i>Short Fatigue Crack Models</i> .....	80
2.4.1.	<i>The N-R Model</i> .....	82
2.4.2.	<i>N-R Model Developments</i> .....	85
2.4.2.1.	<i>Residual Stresses</i> .....	85
2.4.2.2.	<i>Notches</i> .....	86
2.4.2.3.	<i>Surface Finish and Residual Stress</i> .....	89
2.4.2.4.	<i>Grain Orientation Factor</i> .....	91
2.5.	<i>Surfaces and Machining</i> .....	94
2.5.1.	<i>Characterization of Machined Surfaces</i> .....	95
2.5.2.	<i>Turning Process</i> .....	96
2.5.3.	<i>Effect of Machining Parameters on Surface integrity and Fatigue Life</i> .....	98
2.5.3.1.	<i>Effects of Machining on Surface Roughness</i> .....	98
2.5.3.2.	<i>Effects of Machining on Residual Stress</i> .....	105
2.5.3.3.	<i>Effects of Machining on Fatigue Resistance</i> .....	113
2.5.4.	<i>Effect of Machining on near surface Microstructure of Austenitic stainless steels</i> .116	
<b>Chapter 3</b> .....		121
<b>Experimental Techniques and Methods</b> .....		121
3.1.	<i>Introduction</i> .....	121
3.2.	<i>Materials and Specimen Preparation</i> .....	121
3.3.	<i>Mechanical Properties</i> .....	121
3.4.	<i>Metallographic Specimen Preparation</i> .....	122
3.5.	<i>Measurement of Grain Size of As-Received Materials</i> .....	123
3.6.	<i>Preliminary Sample Preparation and Selection of Machining Parameters</i> .....	123

3.7.	<i>Fatigue Specimens Preparation</i> .....	125
3.8.	<i>Annealing Following Machining</i> .....	127
3.9.	<i>Electropolishing Following Annealing</i> .....	127
3.10.	<i>Fatigue Limit Determination</i> .....	128
3.11.	<i>Calculation of Applied Load</i> .....	129
3.12.	<i>Staircase Method Procedure</i> .....	130
3.13.	<i>X-ray Diffraction Technique to assess martensitic phase</i> .....	130
3.14.	<i>X-ray Diffraction Technique to measure Residual Stress</i> .....	131
3.15.	<i>Full Width at Half the Maximum Peak (FWHM) of Machined Surface</i> .....	131
3.16.	<i>Surface Roughness</i> .....	132
3.16.1.	<i>Stylus Profilometry</i> .....	132
3.16.2.	<i>Optical profilometry</i> .....	132
3.17.	<i>Surface Hardness</i> .....	133
3.18.	<i>Nano-Indentation</i> .....	133
3.19.	<i>Electron Microscopy for Fracture surfaces and Fatigue Cracks</i> .....	134
3.20.	<i>Scanning Electron Microscopy (SEM)</i> .....	134
3.20.1.	<i>Electron Backscatter Diffraction (EBSD)</i> .....	134
3.20.2.	<i>Transmission Electron Microscopy (TEM)</i> .....	137
3.20.3.	<i>Sample preparation for TEM using Focused Ion Beam (FIB)</i> .....	138
3.21.	<i>Ni Plating of specimens</i> .....	141
<b>Chapter 4</b>	.....	142
<b>Results</b>	.....	142
4.1.	<i>Materials and Specimen Preparation</i> .....	142
4.1.1.	<i>Materials</i> .....	142
4.1.2.	<i>Grain Size</i> .....	143
4.1.3.	<i>Specimen Preparation</i> .....	146
4.1.3.1.	<i>Selection of Machining Parameters</i> .....	146
4.2.	<i>Surface Characterisation</i> .....	147
4.2.1.	<i>Surface Roughness using Stylus Profilometry</i> .....	147
4.2.2.	<i>Surface Roughness using Optical profilometry</i> .....	148
4.2.3.	<i>Hardness</i> .....	149
4.2.4.	<i>Residual Stress</i> .....	150
4.2.5.	<i>Plastic Strain</i> .....	156
4.2.6.	<i>Surfaces of Machined Specimens before Fatigue Test</i> .....	158
4.3.	<i>Fatigue Limit</i> .....	160
4.3.1.	<i>Fatigue Limit of AISI 304L</i> .....	160
4.3.2.	<i>Fatigue Limit of AISI 316L</i> .....	160

4.4.	<i>Surface Characterization of run-out specimens</i> .....	162
4.5.	<i>Fracture Morphology in failed specimens</i> .....	165
4.6.	<i>EBSD of near surface of fatigued run-out specimens</i> .....	169
4.6.1.	<i>EBSD of AISI 304L</i> .....	170
4.6.1.1.	<i>Machined Samples</i> .....	170
4.6.1.2.	<i>Electropolished Samples</i> .....	172
4.6.1.3.	<i>Annealed Samples</i> .....	173
4.6.2.	<i>EBSD of AISI 316L</i> .....	175
4.6.2.1.	<i>Machined Samples</i> .....	175
4.6.2.2.	<i>Electropolished Samples</i> .....	177
4.6.2.3.	<i>Annealed Samples</i> .....	178
4.7.	<i>Microstructural Damage Characterisation</i> .....	180
4.7.1.1.	<i>Stable Cracks in AISI 304L</i> .....	180
4.7.1.2.	<i>Stable Cracks in AISI 316L</i> .....	182
4.8.	<i>Characterisation of Surface Damage after fatigue using X-Ray Diffraction</i> .....	184
4.8.1.	<i>AISI 304L</i> .....	184
4.8.2.	<i>AISI 316L</i> .....	187
4.9.	<i>Characterisation of Surface Damage after fatigue using Nano-indentation</i> .....	190
4.9.1.	<i>Nano-indentation of AISI 304L</i> .....	190
4.9.2.	<i>Nano-indentation of AISI 316L</i> .....	192
4.10.	<i>X-Ray Diffraction for fatigue samples before and after fatigue test</i> .....	194
4.10.1.	<i>AISI 304L</i> .....	194
4.10.2.	<i>AISI 316L</i> .....	199
4.11.	<i>Interactions of Cracks with Microstructure</i> .....	202
4.11.1.	<i>Interactions of Cracks with Microstructure of AISI 304L</i> .....	202
4.11.2.	<i>Interactions of Cracks with Microstructure of AISI 316L</i> .....	202
4.12.	<i>Characterisation of Surface Damage after fatigue using TEM</i> .....	208
4.12.1.	<i>Fine machined sample</i> .....	208
4.12.2.	<i>Electropolished Sample</i> .....	210
<b>Chapter 5</b>	.....	216
<b>Discussion</b>	.....	216
5.1.	<i>Materials and Microstructures</i> .....	216
5.2.	<i>Selection of Machining Parameters</i> .....	217
5.3.	<i>Observed Fatigue Limit and Surface Residual Stress</i> .....	217
5.4.	<i>Near Surface and Microstructure of AISI 304L</i> .....	220
5.5.	<i>Surface Cracks and Fracture Surface in AISI 304L</i> .....	221
5.6.	<i>Near Surface and Microstructure of AISI 316L</i> .....	222

5.7.	<i>Surface Cracks and Fracture Surface in AISI 316L</i> .....	223
5.8.	<i>Analysis of the crack path</i> .....	224
5.8.1.	<i>The Crack Path in AISI 304L</i> .....	225
5.8.2.	<i>The Crack Path in AISI 316</i> .....	232
5.8.3.	<i>The Crack Path in AISI 304L (Interaction with Martensite)</i> .....	237
5.9.	<i>Reproducibility of N-R model</i> .....	240
5.9.1.	<i>N-R model for fatigue crack growth in shot-peened Aluminium</i> .....	240
5.9.2.	<i>N-R Model to predict notches effect on Fatigue Crack Growth in Mild Steel</i> .....	242
5.10.	<i>Fatigue Limit Prediction for Machined Surfaces</i> .....	243
5.11.	<i>Validity of the N-R Model for austenitic stainless steels</i> .....	250
5.12.	<i>Development of N-R Model for the Fatigue Limit of Austenitic Stainless Steels</i> ..	253
5.12.1.	<i>Refined Barrier Spacing</i> .....	253
5.12.2.	<i>Surface Roughness Effect</i> .....	255
5.12.3.	<i>Relaxation of Residual stress</i> .....	256
5.12.4.	<i>Other Factors</i> .....	263
5.13.	<i>Annealed Microstructure</i> .....	266
	<b>Chapter 6</b> .....	270
	<b>Conclusion and Further Work</b> .....	270
6.1.	<i>Summary of experimental work</i> .....	270
6.2.	<i>Summary of research Observations</i> .....	271
6.2.1.	<i>Surface and Microstructure Characterisation</i> .....	271
6.2.2.	<i>Fatigue Test -Results</i> .....	272
6.2.3.	<i>Short Fatigue Crack Model of Austenitic Stainless Steels</i> .....	273
6.3.	<i>Conclusions</i> .....	274
6.4.	<i>Further Work</i> .....	274
	<b>Appendix-A</b> .....	283
	<b>Appendix-B</b> .....	296

## **List of Figures**

<b>Figure 1-1:</b> overview of the experimental work in this PhD. ....	30
<b>Figure 2-1:</b> Tensile stress and proof stress of austenitic stainless steels and other materials [13]. ....	34
<b>Figure 2-2:</b> Schaeffler-Delong diagram [10].....	36
<b>Figure 2-3:</b> The Fe-Cr equilibrium diagram[2].....	38
<b>Figure 2-4:</b> Modification of austenitic stainless steels with the addition of other elements to obtain particular properties [9].....	39
<b>Figure 2-5:</b> Stress-strain curves for stainless steels [9].....	40
<b>Figure 2-6:</b> Effects of cold working on mechanical properties of austenitic stainless steels [9].....	40
<b>Figure 2-7:</b> Effect of environment on fatigue strength for some stainless steels (Fatigue strength at 40 Co and rotating bending stress at 100Hz. Tested in air and 3% NaCl at various pH) [9]. ....	42
<b>Figure 2-8:</b> Wöhler diagram [17]. ....	44
<b>Figure 2-9:</b> Typical fatigue stress cycles. (a) Reversed stress; (b) repeated stress; (c) irregular or random stress cycle [19].....	47
<b>Figure 2-10:</b> Effect of mean stress on fatigue life [16]. ....	49
<b>Figure 2-11:</b> Transient behaviour-cyclic hardening [20]. ....	51
<b>Figure 2-12:</b> Transient behaviour-cyclic softening[20].....	52
<b>Figure 2-13:</b> Schematic of a total strain-life curve[17]. ....	53
<b>Figure 2-14:</b> Mechanism of crack nucleation from a row of intrusions [21]. ....	55
<b>Figure 2-15:</b> Crack initiation due to environmentally assisted slip irreversibility: (a) exposure of fresh surface; (b) absorption of fresh metal surface; (c) local decohesion [22].....	56
<b>Figure 2-16:</b> Early evolution of the surface relief of 316L steel as detected by AFM on the surface replica:(a), N=350; (b), N=500; (c), N=1000; (d), N=2000 [24]. ....	57
<b>Figure 2-17:</b> Specimen surface with a rectangular crater at different stages of the fatigue life ( $\epsilon_{ap} = 1 \times 10^{-3}$ ), (a) N= 300 cycles, crater was produced using FIB, (b) N=300+300 cycles, (c) and (d) N= 300 + 1500 cycles. ....	58
<b>Figure 2-18:</b> Schematic representation showing stages I and II of fatigue crack propagation in polycrystalline metal [33]. ....	60

<b>Figure 2-19:</b> Schematic representation showing fatigue crack propagation mechanism (stage II)[18].	60
<b>Figure 2-20:</b> a) Typical fatigue fracture surface; b) Striations [17].	62
<b>Figure 2-21:</b> The way of running two tests using the boundary technique [34].	63
<b>Figure 2-22:</b> Schematic show staircase method [11].	65
<b>Figure 2-23:</b> Typical fatigue crack growth rates ( $da/dN$ ) for long and short cracks as function of stress intensity factor range $\Delta K$ [4].	68
<b>Figure 2-24:</b> Schematic showing the period of total cycle fatigue life [44].	69
<b>Figure 2-25:</b> A schematic shows small crack behaviour as a function of applied cyclic stress [46].	70
<b>Figure 2-26:</b> A schematic illustration of small crack growth and transition to long crack. (a) relative life ratio spent at each stage; (b) Crack growth rate versus crack depth; (c) transition from a microstructurally small crack to a physically small crack and eventually a long crack [46].	71
<b>Figure 2-27:</b> Three regimes of short crack behaviour [5].	72
<b>Figure 2-28:</b> Crack growth development for constant stress ranges [5].	73
<b>Figure 2-29:</b> a) Transition electron micrograph of dislocation pileup at a ) phase boundary in AISI F51 duplex steel after cyclic deformation; b) Schematic shows the relationship between the barrier strength of a grain boundary and misorientation between neighbour [22].	74
<b>Figure 2-30:</b> Oscillation in the crack propagation rate (2024 T3 aluminium alloy); minima are due to the barrier effect of grain boundaries [22, 49].	75
<b>Figure 2-31:</b> Slip-band cracks in the $\beta$ -titanium alloy (loading direction: $\leftrightarrow$ ) and crack length vs. number of cycles for the crack marked by arrows [49].	75
<b>Figure 2-32:</b> crack propagation along slip bands and across a grain boundary [51].	76
<b>Figure 2-33:</b> General crack closure mechanisms: (a) plasticity-induced crack closure, (b) Oxide-induced closure, (c) Roughness-induced closure, (d) Viscous fluid-induced closure, (e) Phase transformation-induced closure [18].	77
<b>Figure 2-34:</b> illustrates the effect schematically, comparing load and crack opening displacement during a typical cycle [22].	78
<b>Figure 2-35:</b> Schematic representation of the mechanism of fatigue crack closure; (a-c) development of a plastic wake [22].	79
<b>Figure 2-36:</b> Mechanism and material flow of plasticity-induced crack closure [22].	79
<b>Figure 2-37:</b> Schematic diagram of Kitagawa–Takahashi diagram[65].	80

<b>Figure 2-38:</b> Configuration of the three zones of the N-R model in which the equilibrium of forces are considered [71].	83
<b>Figure 2-39:</b> Surface stress characteristics. (a) Residual stress profile; (b) $\sigma_1$ stress distribution; Kitagawa–Takahashi type diagram for unpeened and shot peened specimens of Al 2024-T351, four-point bending, $R=0.1, D=\text{grain diameter}$ [73].	85
<b>Figure 2-40:</b> Comparison of predicted non-propagating crack lengths and experimental results (centre circular-notch plate, $R=-1$ ) [76].	88
<b>Figure 2-41:</b> a) Depth profiles of axial residual stress, b) Closure stress profiles; c) Predicted threshold stress profiles for machined samples; d) Predicted threshold stress profiles for annealed samples.	91
<b>Figure 2-42:</b> Schematic evolution of a crack through the material microstructure: expected trend of the crystallographic orientation factor $m^*_i$ as the crack grows [79].	92
<b>Figure 2-43:</b> Courses of characteristic properties of surface layers after [85].	96
<b>Figure 2-44:</b> Schematic of turning operation [86].	97
<b>Figure 2-45:</b> Turning Tool [87].	97
<b>Figure 2-46:</b> Response surface diagram obtained for the tool R0.4 Feed rate (mm/rev) and cutting depth (mm)[88].	99
<b>Figure 2-47:</b> a) Influence of feed rate on surface roughness; b) Influence of depth of cut on surface roughness; c) Influence of cutting speed on surface roughness; d) Effect of nose radius on surface roughness( feed rate = 0.21 mm/rev., cutting depth= 1.3 mm, cutting speed = 1700 rpm).	100
<b>Figure 2-48:</b> Surface roughness at cutting speeds from 50 to 999 m/ min [89]	101
<b>Figure 2-49:</b> Effect of nose radius on $R_{max}$ , feed rate = 0.2 mm/rev [90].	102
<b>Figure 2-50:</b> Roughness evolution with feed and cutting speed [91].	103
<b>Figure 2-51:</b> a) Influence of depth of cut on surface roughness parameters; b) Influence of feed rate on surface roughness parameters; c) Influence of cutting speed on surface roughness parameters [92].	104
<b>Figure 2-52:</b> a) Residual stress at cutting speeds from 50 to 230 m/min [89].	105
<b>Figure 2-53:</b> b) Axial residual stress $\sigma_3$ versus feed rate; c) Circumferential residual stress $\sigma_1$ versus feed rate [89].	106
<b>Figure 2-54:</b> a) Parallel residual stress evolution for the carbon steel material; b) Perpendicular residual stress evolution for the carbon steel material [91].	107

<b>Figure 2-55:</b> a) Influence of feed rate on residual stress; b) Influence of depth of cut on residual stress; c) Influence of cutting speed on residual stress; d) Effect of nose radius on surface stress( feed rate = 0.21 mm/rev., cutting depth= 1.3 mm, cutting speed = 1700 rpm).....	108
<b>Figure 2-56:</b> a) variation in residual stress with machining feed rate, b) variation in residual stress with machining cut depth [93].....	109
<b>Figure 2-57:</b> a) Evolution of the superficial residual stresses with the cutting speed; b) with the feed; c) with the depth of cut; d) Typical shape of residual stress and peak half-width profile for the AISI 316L steel [94].....	111
<b>Figure 2-58:</b> Fatigue life of turned specimens with different nose radius[90].....	114
<b>Figure 2-59:</b> Interaction of axial residual stress and hardness on fatigue life [97]....	115
<b>Figure 2-60:</b> Influence of surface roughness on fatigue limits of all analyzed specimens [92].....	116
<b>Figure 2-61:</b> TEM-cross-section of the direct surface regions of deep rolled AISI 304 (scale bar is 400 nm) [36].....	118
<b>Figure 2-62:</b> Dark field TEM of the direct surface regions of shot peened of AISI 304, showing nanocrystalline fcc-bcc layer [36].....	118
<b>Figure 2-63:</b> Variation of martensite content with depth below the surface for peened and deep rolled 304 [36]. .....	119
<b>Figure 2-64:</b> Schematic illustrations of (A) the SMAT technique and (B) the localized plastic deformation zone induced by the vibrating [100].....	119
<b>Figure 2-65:</b> Typical plane-view TEM observations of the top surface of SMATed AISI 304 stainless steel [99]. .....	120



<b>Figure 3- 1:</b> Sketch of a tensile test specimen. ....	122
<b>Figure 3- 2:</b> Schematic view of sectioning of as-received material. ....	123
<b>Figure 3- 3:</b> Configuration of cylindrical specimen used in this Project.....	124
<b>Figure 3- 4:</b> geometry of fatigue specimens. ....	126
<b>Figure 3- 5:</b> As-Machined, Annealed and As-Electropolished Samples. ....	127
<b>Figure 3- 6:</b> Schematic image and photo of the electro-polishing cell. ....	128
<b>Figure 3- 7:</b> R.R Moore rotating-bending machine [107]. ....	129
<b>Figure 3- 8:</b> X-Ray diffractometer (proto i-XRD) [108]. ....	131
<b>Figure 3- 9:</b> Fixing of microhardness specimens. ....	133
<b>Figure 3- 10:</b> Schematic of the components of an EBSD system [111].....	136
<b>Figure 3- 11:</b> The formation of the Kikuchi diffraction pattern [112].....	137
<b>Figure 3- 12:</b> An Overview of the TEM. ....	138
<b>Figure 3- 13:</b> Lift-out TEM sample preparation. a) Area of interest on the sample surface; b) Platinum protective layer over the interest area; c) U-shaped profile of the sample before left out; d) Left out of the sample; e) Connecting the TEM sample to the grid; f) TEM sample fixed on the grid before thinning; g) Final shape of the sample after thinning.....	139
<b>Figure 3- 14:</b> Lift-out TEM sample preparation. a) Area of interest on the sample surface; b) Platinum protective layer over the interest area; c) U-shaped profile of the sample before left out; d) Left out of the sample; e) Connecting the TEM sample to the grid; f) TEM sample fixed on the grid before thinning; g) Final shape of the sample after thinning.....	140
<b>Figure 3- 15:</b> Schematic image and photo of the Electroplating setup.....	141

<b>Figure 4- 1:</b> the microstructure of AISI 304L and AISI 316L as received, observed by optical microscopy; a) AISI 304L As-Received (Etched with Oxalic Acid), b) AISI 304L As-Received (Etched with 50% of HNO <sub>3</sub> and 50% of H <sub>2</sub> O), c) AISI 316L As-Received (Etched with Oxalic Acid), d) AISI 316L As-Received (Etched with 50% of HNO <sub>3</sub> and 50% of H <sub>2</sub> O).....	144
<b>Figure 4- 2:</b> EBSD microstructure map of the as-received microstructure of AISI304L; a) band contrast map; b) Euler map.....	145
<b>Figure 4- 3:</b> EBSD microstructure map of fine machined and annealed sample of AISI304L. ....	145
<b>Figure 4- 4:</b> Effect of machining parameter on residual stress.....	147
<b>Figure 4- 5:</b> Effect of machining parameter on roughness Ry. ....	147
<b>Figure 4- 6:</b> Line segment profile of fine condition-C (Optical profilometry data). S: the spacing of adjacent local peaks; Ry: the high peak-to-valley.....	149
<b>Figure 4- 7:</b> Line segment profile of Rough condition-A (Low cutting depth, high feed rate), (Optical profilometry data). ). S: the spacing of adjacent local peaks; Ry: the high peak-to-valley.....	149
<b>Figure 4- 8:</b> Comparison of the surface hardness (Vickers) of the machined, electropolished, Annealed and as received (AISI 304L/AISI 316L). ....	150
<b>Figure 4- 9:</b> Residual Stress of AISI 304L; a) Depth profiles of axial residual stress, b) Depth profiles of circumferential residual stress.....	152
<b>Figure 4- 10:</b> Effect of annealing on the depth profiles (AISI 304L); a) axial residual stress, b) circumferential residual stress. ....	153
<b>Figure 4- 11:</b> Residual Stress of AISI 316L; a) Depth profiles of axial residual stress, b) Depth profiles of circumferential residual stress.....	154
<b>Figure 4- 12:</b> Effect of annealing on the depth profiles (AISI 316L); a) axial residual stress, b) circumferential residual stress. ....	155
<b>Figure 4- 13:</b> Variation of diffraction peak width (FWHM) with depth below surface (AISI 304L); a) axial residual stress, b) circumferential residual stress.....	157
<b>Figure 4- 14:</b> Variation of diffraction peak width (FWHM) with depth below surface (AISI 316L); a) axial residual stress, b) circumferential residual stress.....	158
<b>Figure 4- 15:</b> Machined surfaces before fatigue test of AISI 304L; a) Fine machined (C); b) Rough Machined (A); c) Electropolished (annealed). ....	159

<b>Figure 4- 16:</b> Fatigue data of AISI 304L/AISI 316L (electropolished & annealed (3), electropolished (not annealed) specimens). Open symbols are run-outs and closed symbols are failures. ....	161
<b>Figure 4- 17:</b> Fatigue data of AISI 304L/AISI 316L (fine machined (1), rough machined (4) specimens). Open symbols are run-outs and closed symbols are failures. ....	161
<b>Figure 4- 18:</b> Fatigue data of AISI 304L/AISI 316L (fine machined & annealed, rough machined & annealed specimens). Open symbols are run-outs and closed symbols are failures. ....	162
<b>Figure 4- 19:</b> Surface cracks in run-out fatigued samples for AISI 304L: a) Electropolished (3) (336 MPa); b) Fine machined(1) run-out fatigued samples (328 MPa); c) Rough machined(4) run-out fatigued samples (294 MPa).( $\leftrightarrow$ stress axis)...	163
<b>Figure 4- 20:</b> Surface cracks in run-out fatigued samples for AISI 316L: a) Electropolished (3) run-out fatigued samples (304 MPa); b) Fine machined (1) run-out fatigued samples (320MPa) ( $\leftrightarrow$ stress direction). ....	164
<b>Figure 4- 21:</b> Fracture surfaces of AISI 304L, fine machined (1) and fatigue tested at 330 MPa. ....	166
<b>Figure 4- 22:</b> Fracture surfaces of AISI 304L, Electropolished (3) and fatigue tested at 336 MPa. ....	167
<b>Figure 4- 23:</b> Fracture surfaces of AISI 316L, fine machined (1) and fatigue tested at 322 MPa. ....	168
<b>Figure 4- 24:</b> Fracture surfaces of AISI 316L, Electropolished (3) and fatigue tested at 298 MPa. ....	169
<b>Figure 4- 25:</b> AISI 304L a) Band contrast map of fine machined(C) specimens <b>before</b> ; b) Euler map of fine machined (C) specimens <b>before</b> ; c) Band contrast map of fine machined(1) specimens <b>after</b> fatigue test (328 MPa); d) Euler map of fine machined (1) specimens <b>after</b> fatigue test. Small angle grain boundaries are indicated by the white lines in (b and d). ....	171
<b>Figure 4- 26:</b> AISI 304L a) Band contrast map of rough machined (A) specimens <b>before</b> ; b) Euler map of rough machined (A) specimens <b>before</b> ; c) Band contrast map of rough machined (4) specimens <b>after</b> fatigue test (286 MPa); d) Euler map of rough machined (4) specimens <b>after</b> fatigue test. ....	172

- Figure 4- 27:** AISI 304L a) Band contrast map of electropolished (annealed) specimens **before**; b) Euler map of electropolished (annealed) specimens **before**; c) Band contrast map of electropolished (3) specimens **after** fatigue test (338 MPa); d) Euler map of electropolished (3) specimens **after** fatigue test. .... 173
- Figure 4- 28:** Figure 4- 26: AISI 304L a) Band contrast map of fine machined & annealed(C) specimens **before**; b) Euler map of fine machined & annealed(C) specimens **before**; c) Band contrast map of fine machined & annealed(2) specimens **after** fatigue test (352 MPa); d) Euler map of fine machined & annealed(2) specimens **after** fatigue test. .... 174
- Figure 4- 29:** AISI 304L a) Band contrast map of rough machined & annealed (A) specimens **before**; b) Euler map of rough machined & annealed (A) specimens **before**; c) Band contrast map of rough machined & annealed (5) specimens **after** fatigue test (338 MPa); d) Euler map of rough machined & annealed (5) specimens **after** fatigue test. .... 175
- Figure 4- 30:** AISI 316L a) Band contrast map of fine machined (C) specimens **before**; b) Euler map of fine machined (C) specimens **before**; c) Band contrast map of fine machined (1) specimens **after** fatigue test (304 MPa); d) Euler map of fine machined (1) specimens **after** fatigue test. .... 176
- Figure 4- 31:** AISI 316L a) Band contrast map of rough machined (A) specimens **before**; b) Euler map of rough machined (A) specimens **before**; c) Band contrast map of rough machined (4) specimens **after** fatigue test (290 MPa); d) Euler map of rough machined (4) specimens **after** fatigue test. .... 177
- Figure 4- 32:** AISI 316L a) Band contrast map of electropolished specimens **before**; b) Euler map of electropolished specimens **before**; c) Band contrast map of electropolished (3) specimens **after** fatigue test (306 MPa); d) Euler map of electropolished (3) specimens **after** fatigue test. .... 178
- Figure 4- 33:** AISI 316L a) Band contrast map of fine annealed specimens **before**; b) Euler map of fine annealed specimens **before**; c) Band contrast map of fine machined & annealed (2) specimens **after** fatigue test (294 MPa); d) Euler map of fine machined & annealed (2) specimens **after** fatigue test. .... 179
- Figure 4- 34:** AISI 316L a) Band contrast map of rough annealed specimens **before**; b) Euler map of rough annealed specimens **before**; c) Band contrast map of rough machined & annealed(5) specimens **after** fatigue test (264 MPa); d) Euler map of rough machined & annealed(5) specimens **after** fatigue test. .... 180

- Figure 4- 35:** Crack-like features in fatigued (run-out) specimens of AISI 304L: a) Fine machined (1) sample (tested at 324 MPa); b) Rough machined (4) sample (tested at 288 MPa); c) Fine machined & Annealed (2) sample (tested at 350 MPa); d) Rough machined & Annealed (5) sample (tested at 336 MPa); e) Electropolished (3) sample (tested at 338 MPa) ( $\leftrightarrow$  stress axis)..... 181
- Figure 4- 36:** Crack-like features in fatigued (run-out) specimens of AISI 316: a) Fine machined (1) sample (tested at 316 MPa); b) Rough machined (4) sample (tested at 292 MPa); c) Fine machined & Annealed (2) sample (tested at 310 MPa); d) Rough machined & Annealed (5) sample (tested at 260 MPa); e) Electropolished (3) sample (tested at 298 MPa), ( $\leftrightarrow$  stress axis)..... 183
- Figure 4- 37:** a) Depth profiles of axial residual stress for AISI 304L fine machined before and after fatigue; b) FWHM profile with depth below surface for AISI 304L fine machined before and after fatigue. .... 185
- Figure 4- 38:** a) Depth profiles of axial residual stress for AISI 304L rough machined before and after fatigue; b) FWHM profile with depth below surface for AISI 304L rough machined before and after fatigue..... 186
- Figure 4- 39:** a) Depth profiles of axial residual stress for AISI 316L fine machined before and after fatigue; b) FWHM profile with depth below surface for AISI 316L fine machined before and after fatigue. .... 188
- Figure 4- 40:** a) Depth profiles of axial residual stress for AISI 316L rough machined before and after fatigue; b) FWHM profile with depth below surface for AISI 316L rough machined before and after fatigue..... 189
- Figure 4- 41:** Subsurface nanohardness profile of (AISI 304L); a) fine machined before and after fatigue test; b) rough machined before and after fatigue test. .... 191
- Figure 4- 42:** Subsurface nanohardness profile of (AISI 316L).: a) fine machined before and after fatigue test; b) rough machined before and after fatigue test. .... 193
- Figure 4- 43:** X-ray spectrum of AISI 304L a) Fine machined (C) (not fatigued); b) Fine machined (1) fatigue (run-out) at 324 MPa..... 195
- Figure 4- 44:** X-ray pattern of AISI 304L a) Rough machined (A) ( not fatigued); b) Rough machined ( 4) fatigue test (run-out) at 292 MPa..... 196
- Figure 4- 45:** X-ray pattern of AISI 304L run-out Electropolished (3) tested at at 336 MPa ..... 197
- Figure 4- 46:** X-ray spectrum of AISI 304L a) Fine machined & annealed (2) fatigue test (run-out) at 342 MPa..... 197

<b>Figure 4- 47:</b> X-ray spectrum of AISI 304L a) Rough machined & annealed (5) fatigue test (run-out) at 336 MPa.....	198
<b>Figure 4- 48:</b> X-ray diffraction patterns of AISI 304L for fine machined (1), rough machined (4) and electropolished (3) fatigued specimens (the vertical axis represents the intensity for electropolished specimen).....	199
<b>Figure 4- 49:</b> X-ray pattern of AISI 316 a) Fine machined (C) (not fatigued); b) Fine machined (1) fatigued (run-out) at 320 MPa.....	200
<b>Figure 4- 50:</b> X-ray pattern of AISI 316, Rough machined (4) fatigued (run-out) at 286 MPa.....	201
<b>Figure 4- 51:</b> X-ray pattern of AISI 316 Electropolished (3) and fatigued (run-out) at 300 MPa.....	201
<b>Figure 4- 52:</b> a) Band contrast map of AISI 304L Electropolished (3) specimen (fatigued test at 338 MP); b) and c) the misorientation profile of twins in a), (white line represent the location of the misorientation profile). ....	203
<b>Figure 4- 53:</b> a) Band contrast map of AISI304L rough machined (4) specimen (fatigued test at 288 MP); b) and c) the misorientation profile of twins in a), (white line represent the location of the misorientation profile). ....	204
<b>Figure 4- 54:</b> EBSD of Crack features in rough annealed specimen which broken at 262 MPa (position of this crack is located at a distance about 6 mm from the fracture surface) in AISI 316L: a) Band contrast map; b) Euler map (M: Matrix and T: Twin). c) and d) the misorientation profile of twins in a), (white line represent the location of the misorientation profile.), e) {111} pole figure shows the orientations of the lamellar features and matrix in b). ....	205
<b>Figure 4- 55:</b> a) Arrested cracks by twins in fatigued specimen AISI 304L(Rough machined & annealed specimen fatigued at 340 MPa) Euler map of the crack; b) {111} pole figure shows the orientations of the lamellar features and matrix in a; c and d) the misorientation profile of twins in a). ....	206
<b>Figure 4- 56:</b> In AISI 316L; a) Arrested cracks by twins [GB: Grain Boundary] in fatigued specimen (Electropolished (3) specimen fatigued at 306 MPa); b) Euler map of a. c) the misorientation profile of twins in a), (white line represent the location of the misorientation profile.). d) {111} pole figure shows the orientations of the lamellar features and matrix in b). ....	207

- Figure 4- 57:** a) The position selected to extract TEM sample from the surface of run-out fine machined-1 sample of AISI 304L (fatigued at 336 MPa); b) Final shape of TEM sample fixed on TEM grid after thinning using FIB. ....208
- Figure 4- 58:** a,b) A bright field image from different regions near the surface, illustrating the deformed microstructure and nanocrystalline regions of run-out fine machined-1 sample of AISI 304L (fatigued at 336 MPa). ....209
- Figure 4- 59:** a) The position selected to extract TEM sample from the surface of run-out fine machined-1 sample of AISI 304L (fatigued at 336 MPa); b) Final shape of TEM sample fixed on TEM grid after thinning using FIB (white layer is Platinum (Pt)). ....210
- Figure 4- 60:** A bright field image near the surface, illustrating the deformed microstructure and fatigue crack of run-out electropolished specimen of AISI 304L (fatigued at 336 MPa).....211
- Figure 4- 61:** a) EDX analysis of Pt layer on the surface, b) EDX analysis of the material filled the crack (bottom of the crack), c) EDX analysis of the matrix. ....212
- Figure 4- 62:** The cross-sectional TEM observations of run-out electropolished specimen of AISI 304 (fatigued at 336 MPa), a) bright field, b) SAED patterns, C) Indexed diagram for FCC crystal structure and (d and e) dark field images.....215

<b>Figure 5- 1:</b> The effect of surface residual stress on the fatigue limit , a) measured fatigue limit as a function of the surface residual stress; b) change in fatigue limit relative to the intrinsic fatigue limit for electropolished samples (type 304); c) change in fatigue limit relative to the intrinsic fatigue limit for electropolished samples (type 316); d) change in fatigue limit relative to the intrinsic fatigue limit for electropolished samples (type 304/type 316). Gs: Grain Size; Hv: Hardness; FL: Fatigue Limit of electropolished and annealed. ....	219
<b>Figure 5- 2:</b> Relationship between the specimen coordinate system XYZ (or RD, TD, ND for a rolled product) and the crystal coordinate system [100], [010], [001] [119]. ....	224
<b>Figure 5- 3:</b> a) Test sample section showing the region of the EBSD map; b) the corresponding map showing the interaction between the crack and the twin (T) in grain (G1). ....	226
<b>Figure 5- 4:</b> a) the corresponding map showing the interaction between the crack and the twin, b) stereographic projection {111} pole figure for grain surrounding the arrested crack with the plane system of the highest Schmid factor trace, c) stereographic projection {111} pole figure for the twin with the plane system of the highest Schmid factor trace.....	229
<b>Figure 5- 5:</b> Schematic describing the crack plane misorientation across a grain boundary in terms of the tilt angle (a), and the twist angle (b.) [121]. ....	230
<b>Figure 5- 6:</b> Determination of cracked plane and angles of twist and tilt components; (a) {111} pole figure (Sold black circles represent pole figure of {111} for G1 and the open black circles for the twin). ....	231
<b>Figure 5- 7:</b> a) Test sample section showing the region of the EBSD map; b) the corresponding map showing the interaction between the cracks and the twins. ....	232
<b>Figure 5- 8:</b> a,b) the corresponding map showing the interaction between the crack and the twin, c) stereographic projection {111} pole figure for grain surrounding the arrested crack with the plane system of the highest Schmid factor trace, d) stereographic projection {111} pole figure for the twin with the plane system of the highest Schmid factor trace.....	235
<b>Figure 5- 9:</b> Determination of cracked plane and angles of twist and tilt components; (a) {111} pole figure (Sold black circles represent pole figure of {111} for matrix and the open black circles for the twin). ....	236



<b>Figure 5- 10:</b> a) bright field image of the crack in AISI304L as electropolished sample; b) Diffraction pattern; c) Dark field image, which shows the crack arrested at a martensite packet interface. The (110) martensite diffraction spot used is circled in (b) and labelled.....	237
<b>Figure 5- 11:</b> Pole figure show the traces of slip planes in figure 1-b and the crack traces in figure 1-a. ....	238
<b>Figure 5- 12:</b> Crack interaction with martensite in AISI304L as electropolished sample; a) Bright field image; b) Dark field image; c) Zoom in of the martensite region in a); d) Zoom in of the crack tip show the martensite stop the crack. ....	239
<b>Figure 5- 13:</b> Residual stress profile used in the implementation of the model [73]...	240
<b>Figure 5- 14:</b> Threshold stress profile using N-R model for unpeened and shot peened specimens to check the model used in this work. ....	241
<b>Figure 5- 15:</b> Kitagawa-Takahashi type diagram for unpeened and shot peened specimens of AL 2024-T351, four-point bending, $R=0.1$ , $D$ =grain diameter [73]. ....	241
<b>Figure 5- 16:</b> Threshold stress as a function of the crack length for different notches size to check the model used in this work.....	242
<b>Figure 5- 17:</b> Threshold stress as a function of the crack length for different notches size reported in[76].....	243
<b>Figure 5- 18:</b> AISI 304L, a) Residual stress of fine and rough conditions; b) Estimated closure stress of fine and rough conditions. ....	245
<b>Figure 5- 19:</b> AISI 316L, a) Residual stress of fine and rough conditions; b) Estimated closure stress of fine and rough conditions. ....	246
<b>Figure 5- 20:</b> AISI 304L, a) Threshold stress profiles predicted for; as machined specimens, annealed specimens and electropolished specimens (TS: Threshold stress). ....	248
<b>Figure 5- 21:</b> AISI 316L, a) Threshold stress profiles predicted for; as machined specimens, annealed specimens and electropolished specimens (TS: Threshold stress). ....	249
<b>Figure 5- 22:</b> Predicted fatigue limit in comparison with the measured fatigue limit (N-R Model) for all conditions for AISI 304L and AISI 316L.....	249
<b>Figure 5- 23:</b> Effect of refined barrier spacing ( $0.5 \mu\text{m}$ for AISI 304L and $3 \mu\text{m}$ for AISI 316L) on the threshold stress in machined samples for AISI 304L and AISI 316L. ....	254

<b>Figure 5- 24:</b> Effect of refined barrier spacing (0.5 $\mu\text{m}$ for AISI 304L and 2 $\mu\text{m}$ for AISI 316L) on the threshold stress in electropolished annealed-3 samples for AISI 304L and AISI 316L. ....	255
<b>Figure 5- 25:</b> Effect of neglecting surface roughness effect on the threshold stress in machined samples for AISI 304L and AISI 316L. ....	256
<b>Figure 5- 26:</b> Closure stress profiles of the fine-1 and rough-4 machined samples for AISI 304L before and after fatigue test. ....	257
<b>Figure 5- 27:</b> Closure stress profiles of the fine and rough machined samples for AISI 316L before and after fatigue test. ....	258
<b>Figure 5- 28:</b> Effect of stress relaxation using measured residual stresses after fatigue test on the threshold stress in machined samples for AISI 304L and AISI 316L. ....	258
<b>Figure 5- 29:</b> Stress ratio between the residual stress before and after fatigue test for AISI 304L. ....	260
<b>Figure 5- 30:</b> Stress ratio between the residual stress before and after fatigue test for AISI 316L. ....	261
<b>Figure 5- 31:</b> Effect of residual stress relaxation on the threshold stress in machined samples for AISI 304L and AISI 316L using relaxation factor of 0.5. ....	262
<b>Figure 5- 32:</b> Predicted fatigue limit in comparison with the measured fatigue limit (new model) for machining conditions for AISI 304L and AISI 316L. ....	262
<b>Figure 5- 33:</b> Effect of residual stress relaxation for machining conditions using relaxation factor of 0.5, intrinsic fatigue limit (increased by 5% for fine-1 machined and by 30% for rough-4 machined condition), refined barrier spacing (0.5 $\mu\text{m}$ ). ....	265
<b>Figure 5- 34:</b> Predicted fatigue limit in comparison with the measured fatigue limit (new model) for machining conditions for AISI 304L and AISI 316L. ....	265
<b>Figure 5- 35:</b> Effect of annealed microstructure on the threshold stress in AISI 304L and AISI 316L (neglecting surface roughness effect and using barrier spacing of observed grain size (3 $\mu\text{m}$ )). ....	268
<b>Figure 5- 36:</b> Effect of annealed microstructure on the threshold stress in AISI 304L and AISI 316L (neglecting surface roughness effect and using barrier spacing of observed martensite packet size (0.5 $\mu\text{m}$ ) for AISI 304L and observed twin spacing (3 $\mu\text{m}$ ) for AISI 316L. ....	268
<b>Figure 5- 37:</b> Predicted fatigue limit in comparison with the measured fatigue limit (new model) for annealed microstructure for AISI 304L and AISI 316L. ....	269

---

<b>Figure A- 1:</b> Surface map and line profile for fine sample show the high peak-to-valley. .....	290
<b>Figure A- 2:</b> Surface map and line profile for fine sample show the spacing of adjacent local peaks.....	291
<b>Figure A- 3:</b> Surface map and line profile for rough sample show the high peak-to-valley. ....	292
<b>Figure A- 4:</b> Surface map and line profile for rough sample show the spacing of adjacent local peaks.....	293
<b>Figure A- 5:</b> Chemical composition analysis for AISI 304L/ AISI 316L.....	294

### **List of Tables**

<b>Table 2- 1:</b> <i>The AISI 300 series of austenitic stainless steels [10].</i> .....	39
<b>Table 2- 2:</b> <i>Typical physical properties for various stainless steel categories [9].</i> .....	41
<b>Table 2- 3:</b> <i>Values <math>d</math> and <math>m</math> for use with the boundary method [34].</i> .....	63
<b>Table 2- 4:</b> <i>Mechanical properties of a mild steel 0.22%C [76].</i> .....	87
<b>Table 2- 5:</b> <i>Data of notched specimens<sup>10</sup> and their observed and predicted fatigue limits (<math>R=-1</math>) [76].</i> .....	87
<b>Table 2- 6:</b> <i>Comparison of fatigue limits obtained by model prediction and experiments [35].</i> .....	89
<b>Table 3- 1:</b> <i>Cutting conditions for cylindrical specimens.</i> .....	
<b>Table 3- 2:</b> <i>Cutting conditions for fatigue specimens.</i> .....	126
<b>Table 3- 3:</b> <i>Fatigue specimen conditions for AISI 304L and AISI 316L (RS: residual stress). Note, conditions 3 and 6 were prepared by electropolishing a fine machined specimen (C).</i> .....	126
<b>Table 3- 4:</b> <i>Composition of Nickel Bath.</i> .....	141
<b>Table 4- 1:</b> <i>Chemical composition of the stainless steels employed, and comparable higher carbon steels (wt %).</i> .....	
<b>Table 4- 2:</b> <i>Mechanical properties of as-received materials. (<math>R_{p0.2\%}</math> = Yield strength at 0.2% strain / UTS = Ultimate Tensile Strength).</i> .....	142
<b>Table 4- 3:</b> <i>Values of <math>M_s</math> and <math>M_d</math> values for AISI 304L and AISI 316L.</i> .....	142
<b>Table 4- 4:</b> <i>Grain sizes of as-received and as-annealed materials.</i> .....	143
<b>Table 4- 5:</b> <i>Roughness measurements of machined specimens with different machining conditions.</i> .....	148
<b>Table 4- 6:</b> <i>Roughness measurements of machined specimens by stylus profilometry and optical profilometry.</i> .....	148
<b>Table 4- 7:</b> <i>Surface hardness (Vickers) of the machined, electropolished, Annealed (AISI 304L/AISI 316L).</i> .....	150

<b>Table 4- 8:</b> Fatigue limits obtained by staircase method ( $\pm$ one standard deviation), (RS: residual stress).....	162
<b>Table 4- 9:</b> Ratios between BCC peaks and austenite peaks for run-out samples. ....	199
<b>Table A- 1:</b> Fatigue test data of AISI 304L Fine machined (1).....	283
<b>Table A- 2:</b> Fatigue test data of AISI 304L Fine machined & annealed (2).....	284
<b>Table A-3:</b> Fatigue test data of AISI 304L Fine machined & annealed Electropolished(3).....	285
<b>Table A- 4:</b> Fatigue test data of AISI 304L Fine machined & Electropolished(6).....	285
<b>Table A- 5:</b> Fatigue test data of AISI 304L rough machined (4).....	286
<b>Table A- 6:</b> Fatigue test data of AISI 304L rough machined & annealed (5).....	286
<b>Table A- 7:</b> Fatigue test data of AISI 316L Fine machined (1).....	287
<b>Table A- 8:</b> Fatigue test data of AISI 316L Fine machined & annealed (2).....	287
<b>Table A- 9:</b> Fatigue test data of AISI 316L Fine machined & annealed Electropolished (3).....	288
<b>Table A- 10:</b> Fatigue test data of AISI 316L rough machined (4).....	288
<b>Table A- 11:</b> Fatigue test data of AISI 316L rough machined & annealed (5).....	289

***Abstract***

The effect of surface finish on fatigue limit of two types of austenitic stainless steels (AISI 304L and AISI 316L) has been investigated. Fatigue specimens having two different surface conditions were obtained by changing the final cutting condition; annealing was performed to separate the residual stress effects from surface roughness. Electropolished samples were tested as a reference for each material.

A generic mechanistic model for short fatigue crack propagation proposed by Navarro and Rios (N-R model) was implemented to assess its suitability for predicting the fatigue behaviour of specimens with various controlled surface conditions, obtained by machining. The surface/material properties required to implement this model were obtained by electron backscatter diffraction (EBSD), surface profilometry, hardness testing and X-ray diffraction residual stress measurement. The fatigue limits were determined using rotating-bending by means of the staircase method.

The fatigue limits predicted by the N-R fatigue model were compared with the results of the fatigue tests. There was no agreement between the prediction and observations, indicating that the original form of the N-R model is not appropriate for austenitic stainless steels.

In AISI 304L, the surface residual stresses are the dominant parameter, allowing prediction of the effects of machining on fatigue resistance while, the surface roughness developed by machining has no significant effect. In AISI 316L, the effect of surface roughness is found to be negligible, with a weaker effect of surface residual stress than has been observed for AISI 304L.

Crack nuclei in run-out ( $>10^7$  cycles) fatigue tests were observed to arrest at twins and martensite packets, developed by fatigue in AISI 316L and AISI 304L, respectively.

Good agreement with experiments was achieved by using a modification to the fatigue model, which takes account of the observed effect of the plastic deformation on the microstructure.

***Declaration***

No portion of the work referred to in the thesis has been submitted in support of an application for another degree or qualification of this or any other university or other institute of learning

## **Copyright**

- i.* The author of this thesis (including any appendices and/or schedules to this thesis) owns certain copyright or related rights in it (the “Copyright”) and he has given The University of Manchester certain rights to use such Copyright, including for administrative purposes.
- ii.* Copies of this thesis, either in full or in extracts and whether in hard or electronic copy, may be made **only** in accordance with the Copyright, Designs and Patents Act 1988 (as amended) and regulations issued under it or, where appropriate, in accordance with licensing agreements which the University has from time to time. This page must form part of any such copies made.
- iii.* The ownership of certain Copyright, patents, designs, trade marks and other intellectual property (the “Intellectual Property”) and any reproductions of copyright works in the thesis, for example graphs and tables (“Reproductions”), which may be described in this thesis, may not be owned by the author and may be owned by third parties. Such Intellectual Property and Reproductions cannot and must not be made available for use without the prior written permission of the owner(s) of the relevant Intellectual Property and/or Reproductions.
- iv.* Further information on the conditions under which disclosure, publication and commercialisation of this thesis, the Copyright and any Intellectual Property and/or Reproductions described in it may take place is available in the University IP Policy (see <http://www.campus.manchester.ac.uk/medialibrary/policies/intellectual-property.pdf>), in any relevant Thesis restriction declarations deposited in the University Library, The University Library’s regulations (see <http://www.manchester.ac.uk/library/aboutus/regulations>) and in The University’s policy on presentation of Theses



## ***Acknowledgements***

*I am most grateful to all people at the University of Manchester who have helped me through this work.*

*I am particularly grateful to my supervisor Dr. James Marrow, for his advice, suggestions and continuous support. I am really happy to work under his supervision.*

*I would like to express my deepest gratitude to my management in Saudi Basic Industries Corporation (SABIC) who have supported me to do this PhD's degree. Especially thanks to previous SABIC Technology Centre General Managers Eng. Abdullah Al-Enzyan and Eng. Musad Al-Garni and current General Manager Dr. Waleed Al-Shalfan and my section manager Mr. Mahmoud Al-Manee, for their advice, encouragement and support.*

*Finally, I would like to acknowledge the sacrifices made by my family over these years. Although I have enjoyed my graduate school experience, I regret spending so much time away from family (and friends). The love and encouragement from my wife, Om Abdulaziz, promoted the accomplishment of this dissertation. Big hugs to my son Abdulaziz and my daughter Aseel for bringing a great joy to my family. Finally, utmost appreciation to my parents, the forever supporter in my life, which I could not express in words and can not repay them by any means. Without their lasting love and their prayers none of this would have been possible.*

# *Chapter 1*

## *Introduction*

The stainless steels have led to a wide range of successful applications which demand high levels of reliable performance in aerospace, automotive, petrochemical plant, power generation, oil and gas extraction, construction industry and household appliances and other major industries [1, 2].

The fatigue resistance of austenitic stainless steels is critical to the performance of pipework and cladding in heat exchangers and cooling systems. Surface machining is common in such components, and it is important to be able to assess the likely effects of surface treatments. The fatigue limit is known to be sensitive to surface roughness, work hardening, microstructure and residual stress induced by surface working [3, 4]. Due to the difficulty in obtaining a fundamental understanding of the influence of these factors on the fatigue limit obtained by experiments a fatigue model which can elucidate the contribution of each surface effect to the fatigue limit is required.

The fatigue limit is defined as the condition for which initiated fatigue cracks do not propagate under mechanical loading due to their interaction with microstructure. The loading and the microstructure with which the crack interacts are factors that are sensitive to surface preparation. This interaction occurs over a length scale that is comparable to the microstructural scale. So the model required to elucidate this interaction should be one of the short fatigue crack models [5-7].

A generic mechanistic model for short fatigue crack propagation proposed by Navarro and Rios (N-R model) has been implemented to predict the fatigue behaviour of specimens with various controlled surface conditions, obtained by machining. So far this model has only been applied to mild steels and aluminium alloys, but has not been applied previously to stainless steels. The aim of this study is to understand how the propagation of short cracks, which can determine the lifetime of components, is affected by the residual stresses and surface roughness that arise from surface machining and to evaluate and to validate the applicability of the N-R model to austenitic stainless steels by comparing the model predictions with experimental observations.

In this study two types of austenitic stainless steels (AISI 304L and AISI 316L) were employed. Fatigue specimens having different surface conditions were produced by changing the final cutting conditions of lathe. A response surface, which gave an empirical description of the effects of machining parameters on roughness and surface residual stress [8], was used to design the test specimens.

Scanning Electron microscope (SEM), Focused Ion Beam (FIB), Electron backscatter diffraction (EBSD), surface profilometry, optical profilometry, hardness testing and X-ray diffraction residual stress measurement were employed to characterise the surface/material properties. The fatigue limits were determined using a rotating-bending machine by means of the staircase method.

This PhD thesis can be classified into the following subjects:

- Design and preparation of fatigue specimens with controlled surface characteristics.
- Characterisation of surface/material properties of machined specimens before and after fatigue testing.
- Demonstration of how the microstructure of austenitic stainless steels interacts with fatigue cracks.
- Implementation of the fatigue model (N-R) using the observed surface/material properties to predict fatigue behaviour.
- Comparison of the fatigue limit, observed by staircase method, with the model prediction.

The overview of this project is presented in Figure 1- 1.

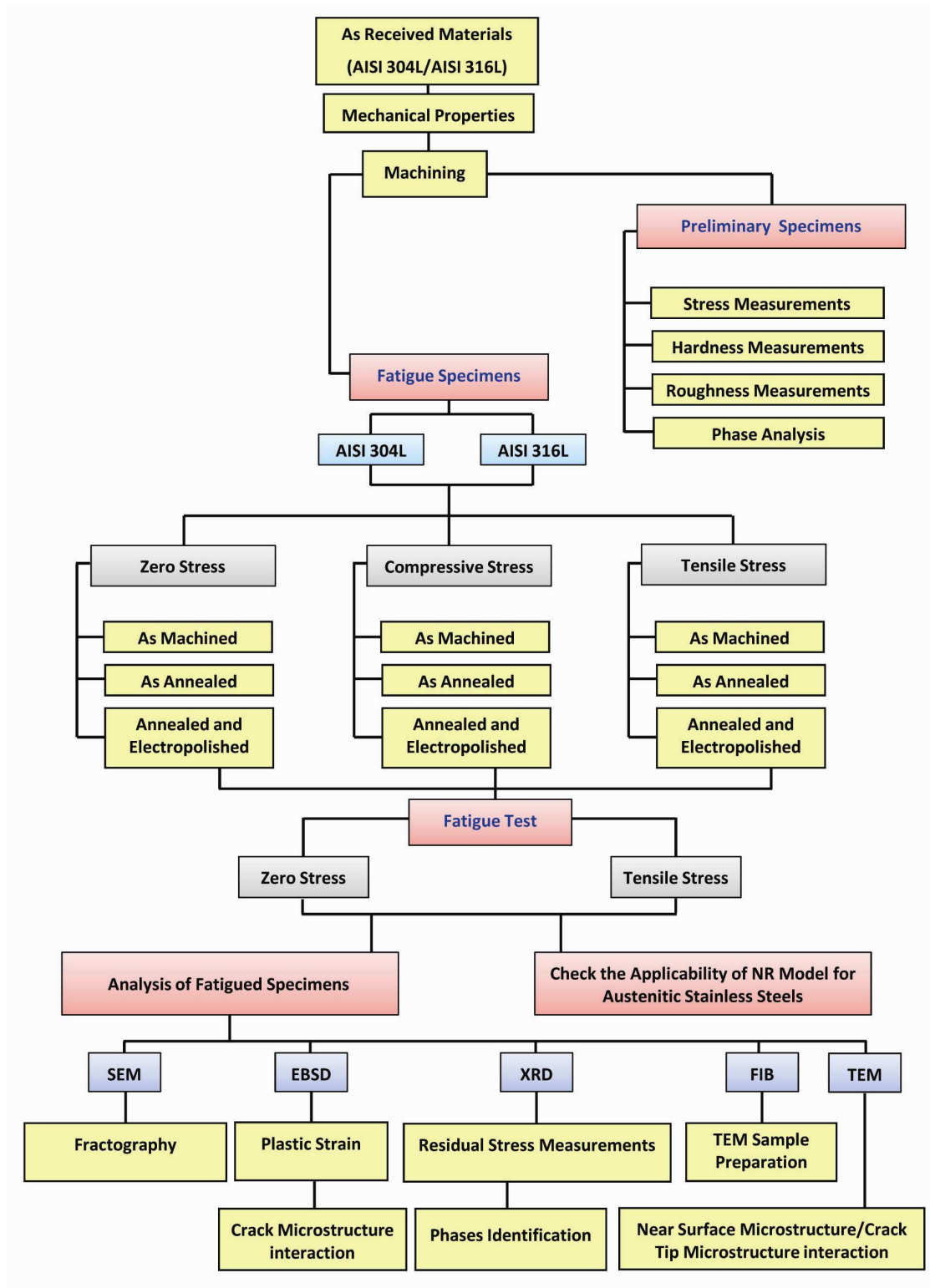


Figure 1- 1: overview of the experimental work in this PhD.

# Chapter 2

## *Literature Review*

*A brief literature review is presented to outline previous research efforts of interest to this research. This literature review is divided into three sections. First, Austenitic stainless steels (e.g. history, applications, and types). The other two sections discuss fatigue of materials, short fatigue cracks, short fatigue cracks models and machining and their effects on fatigue limit.*

### **2.1. A Brief Overview of Stainless Steel**

The stainless steels are characterised as iron base alloys which contain at least 10.5% chromium (Cr). Stainless Steel is a common name for metal alloys that consist of 10.5% or more Chromium (Cr) and more than 50% Iron (Fe) [9, 10].

A thin passive layer of chromium oxide is formed on the surface as a result of Cr reaction with oxygen in the air. Hence, the passive layer generates a high oxidation resistance in an oxidizing atmosphere. The passive layer has the ability to self heal, which means that if the surface is scratched new chromium oxide will form in the scratch, and protect the steel from corrosion. This layer affords corrosion resistance and prevents further oxidation [9]. For these advantages the stainless steels are used in the harsh environments of the chemical, oil production and power generation industries, and in utility goods such as furniture, automotive parts and cutlery.

Several important sub-categories of stainless steels have been developed. The sub-categories are austenitic, martensitic, ferritic, duplex, precipitation hardening and super alloys [2, 9-12].

#### **2.1.1. History of Stainless Steel**

In around 1910, stainless steel was discovered separately by researchers in Britain and Germany. The English metallurgist Harry Brearley was trying to develop a new material to protect cannon barrels from erosion. He discovered that the addition of chromium to iron created an alloy that resisted corrosion (rusting). This discovery led to the patent of steel with 9-16% chromium and less than 0.70% carbon [9].

In Essen, Germany, B. Strauss was working to find a suitable material for protective tubing for thermocouples and pyrometers. He found that the specimens of alloys with more than 20% Cr did not rust even after having been left lying in the laboratory for quite some time. As a result of this discovery steel with 0.25% carbon, 20% chromium and 7% nickel was developed (first austenitic stainless steel).

In the same time as the work in England and Germany, heat-resistant steels were developed when F.M. Becket in Niagara Falls, USA, was trying to find a cheap and scaling-resistant material for furnaces that were run at temperatures up to 1200°C. He discovered that at least 20% chromium was necessary to achieve resistance to oxidation or scaling [1, 9].

### 2.1.2. *Applications of Stainless Steels*

Shortly after the discovery of stainless steels, it was comprehended that this material had many more valuable properties, which make it appropriate for a huge range of miscellaneous uses.

The first application of stainless steels was in cutlery in Sheffield [9]. The attractive appearance, corrosion resistance, low maintenance, strength and stop painting or other protective coatings dominated by stainless steel have led to a wide range of successful applications which demand high levels of reliable performance in surgery, aerospace, automotive, chemical plant, power generation, oil and gas extraction, sports, construction industry and household appliances and other major industries. A major field of application for the stainless steels is the oil and gas industry [2, 9, 10, 12].

### 2.1.3. *Stainless Steel Types and Grades*

Changing the mechanical, physical and corrosion properties of the steel required changing the Chromium content and adding other elements like Nickel, Molybdenum, Titanium and Niobium. Subsequently this led to the development of several important subcategories of stainless. The sub-categories are ferritic, martensitic, austenitic, duplex, precipitation hardening. Each one of the grades is grouped into one of five stainless steel families [2, 9-12].

These families are named based on their metallurgical microstructure. The microstructure may be composed of the stable phases austenite or ferrite, a mix of these

two (duplex), martensite or a hardened structure containing precipitated micro-constituents [10].

Ferritic stainless steels have the same structure as pure iron at room temperature (ferrite). The corrosion resistance and toughness of this material is moderate. A typical application of ferritic stainless steels is exhaust pipes in the automotive industry [2, 9, 10, 12].

The martensitic stainless steels have relatively high carbon content and are hardenable through heat treatment (forming martensite). Their corrosion resistance is moderate, but the hardness and strength is high. This material is typically used in knife blades, surgical instruments and shafts [2, 9, 10, 12].

The austenitic stainless steels have superior corrosion resistance and toughness. They are the most common stainless steels. Figure 2-1 shows the tensile properties of austenitic stainless steels compared with other materials. This material is used in many applications such as, kitchen sinks, food processing and chemical industry for pipe, heat exchange tubes, and boilers. Also, austenitic stainless steel is one of the important structural materials used for the in-core components and pressure boundaries of light water reactors (LWR) [2, 9, 10, 12]. In these applications, the components of the structure are often subjected to repeated stresses as a result of mechanical vibration start up and shutdown process. Therefore resistance to fatigue is an essential requirement in the design of the structures and components against failure under dynamic load.

The duplex stainless steels containing relatively high chromium (between 18 and 28%) and moderate amounts of nickel (between 4.5 and 8%). The nickel content is insufficient to generate a fully austenitic structure and the resulting combination of ferritic and austenitic structures. Most duplex steels contain molybdenum in a range of 2.5 - 4%. Due to high resistance to stress corrosion cracking, increased resistance to chloride ion attack, higher tensile and yield strength than austenitic or ferritic steels and good weldability and formability the duplex stainless steels are used in many applications. The duplex grades are used frequently in heat exchangers, Marine applications, Desalination plants, Food pickling plants, Off-shore oil & gas installations and Chemical & petrochemical plant [2, 9, 10, 12].

Precipitation hardening stainless steels are characterized by high strength and middling corrosion resistance. They are divided into three types based on the structure (austenitic, semi austenitic and martensitic (maraging)). Due to their high strength,

these materials are used in the aerospace industry and other high-technology industries[2, 9, 10, 12].

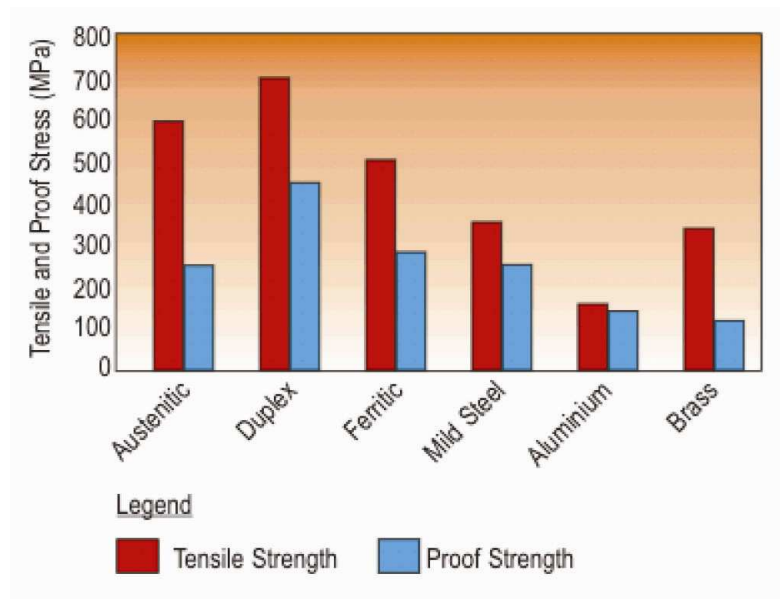


Figure 2-1: Tensile stress and proof stress of austenitic stainless steels and other materials [13].

#### 2.1.4. Austenitic Stainless Steels

##### 2.1.4.1. Composition and constituents

Fe, Cr and Ni are the essential alloying elements of Austenitic Stainless Steel. Chromium provides the stainless steels with corrosion resistance. Chromium is also added to promote a ferritic structure (ferrite stabiliser). As the chromium content increases the corrosion resistance increases.

The nickel is added to stabilise austenite. Nickel generally increases ductility and toughness. It is also added to improve the strength by forming the intermetallic compounds in precipitation hardening steels [2, 9, 10, 12].

Alloying elements such as C, N, Mo, Mn, Ti, Nb, V, W, Cu, Al, ... can be classified as ferrite-stabilisers or austenite-stabilisers. One commonly used tool to predict the structure at room temperature from the chemical composition is the Schaeffler-DeLong diagram, Figure 2-2. It was originally developed for welding, but it can be used for heat treatments as well. It plots the compositional limits at room temperature of austenite, ferrite and martensite, in terms of nickel and chromium equivalents. The diagram is



based on the fact that the alloying elements can be divided into ferrite stabilisers and austenite-stabilisers. It is known that Chromium and Nickel are added to promote a ferritic structure and austenitic structure respectively. Therefore the total ferrite and austenite stabilising effect of the alloying elements in the steel is possible to be calculated using the Schaeffler-Delong diagram. This gives the expected final microstructure for a given chemistry after cooling from a high temperature, such as in the welding process, by inspecting nickel and chromium equivalents. The chromium equivalent has been empirically determined using the most common ferrite-forming elements (Concentrations in wt %) [2, 9, 10]:

$$Cr_{eq} = (Cr) + 2(Si) + 1.5(Mo) + 5(V) + 5.5(Al) + 1.75(Nb) + 1.5(Ti) + 0.75(W) \quad (2-1)$$

In the same way the nickel equivalent has been empirically determined using the austenite-forming elements (Concentrations in wt %):

$$Ni_{eq} = (Ni) + (Co) + 0.5(Mn) + 0.3(Cu) + 25(N) + 30(C) \quad (2-2)$$

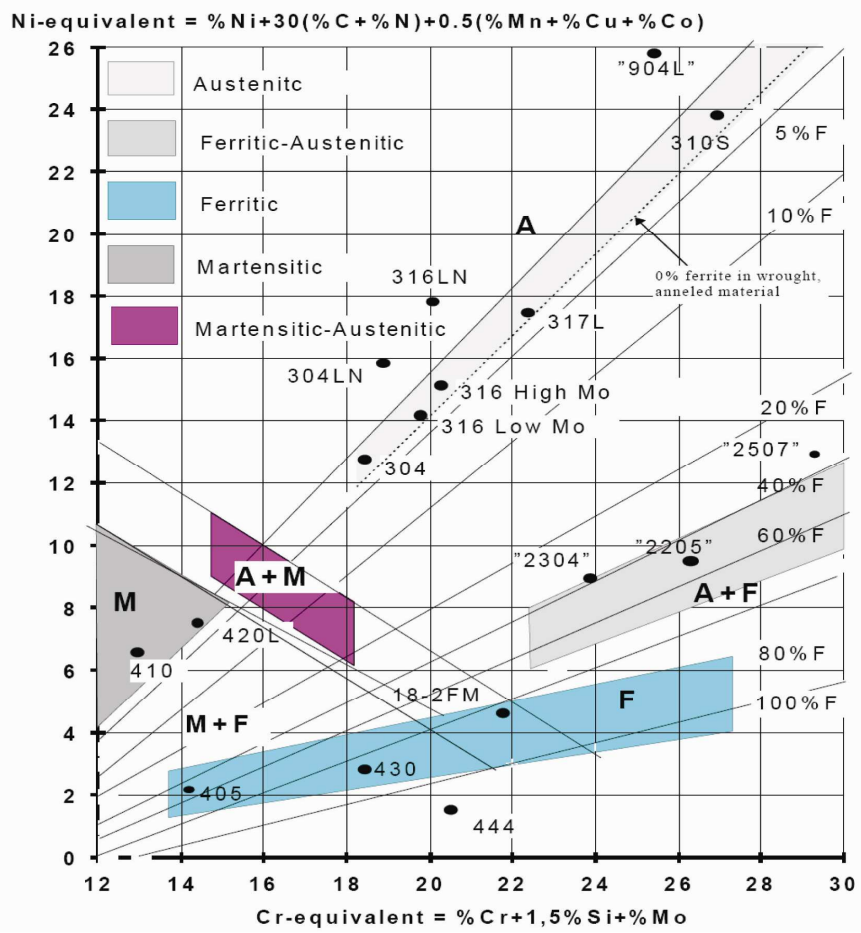


Figure 2-2: Schaeffler-Delongs diagram [10].

Austenitic stainless steels are often in a metastable austenitic state at room temperature. Most grades have an  $M_s$  (martensite-start) temperature below  $0^\circ\text{C}$ . However, plastic deformation can induce martensite at temperatures higher than  $M_s$  (martensite-start). Chromium is a ferrite stabiliser and nickel is added as an austenite stabiliser, so that the microstructure at ambient temperature is austenitic. These alloys are called austenitic since their structure remains austenitic (FCC) at room temperature.

$M_s$  is the temperature where spontaneous transformation starts. Eq. (2-3), describes the effect of chemical composition on  $M_s$ .

$$M_s (^\circ\text{C}) = 502 - 810 (C) - 1230 (N) - 13 (Mn) - 30 (Ni) - 12 (Cr) - 54 (Cu) - 6 (Mo) \quad (2-3)$$

*wt%*

The composition plays an important role in the stability of austenite.  $M_{d30}$  is the temperature at which martensite will form at a strain of 30%. Eq. (2-4) has been derived to describe the effect of alloying elements.

$$M_{d30} = 551 - 462(C+N) - 9.2Si - 8.1Mn - 13.7Cr - 29(Ni+Cu) - 18.5Mo - 68Nb - 1.42(GS - 8.0) \quad (2-4)$$

( $^{\circ}C$ )

Where  $GS$  = grain size, ASTM grain size number.

Steels that present higher values of  $M_d$ , for example AISI 304, are more susceptible to form induced martensite when deformed at room temperature. Steels like AISI 316, that present low values for temperature  $M_d$ , generally do not present strong martensite formation when deformed at room temperature [14].

#### 2.1.4.2. *The Iron-Chromium-Nickel System*

The phases (crystal structures) that may be observed in a simple iron, nickel, chromium ternary alloy at ambient temperature are  $\alpha$ ,  $\delta$ ,  $\gamma$ ,  $\sigma$  and  $\alpha'$ .  $\alpha$  and  $\delta$  are both referred to as ferrite and are structurally identical i.e. body-centred cubic.  $\gamma$  is commonly referred to as austenite and is face-centred cubic.  $\sigma$  is an intermetallic compound (Known as Sigma Phase) of iron and chromium and is body-centred tetragonal. Sigma phase is hard and brittle and can be produced in alloys containing substantially less than 50 % Cr. It takes place in the temperature range 750  $^{\circ}C$  to 820  $^{\circ}C$ .  $\alpha'$  is either body-centred cubic or tetragonal (depending on the exact composition) [10].

The binary iron-chromium equilibrium diagram is illustrated in Figure 2-3. This diagram shows that the stable structures of binary alloys are ferritic over the whole temperature range. Since chromium has the same BCC crystal structure as  $\alpha$  ferrite, it extends the  $\alpha$  phase region and suppresses the  $\gamma$  phase region ( $\gamma$ -loop). As a result, the  $\gamma$ -loop is formed in the Fe-Cr phase diagram and divides it into FCC and BCC regions. There is a narrow two-phase alloy ( $\alpha + \gamma$ ) range between 12 and 13 wt% Cr in the binary alloy system [2, 10].

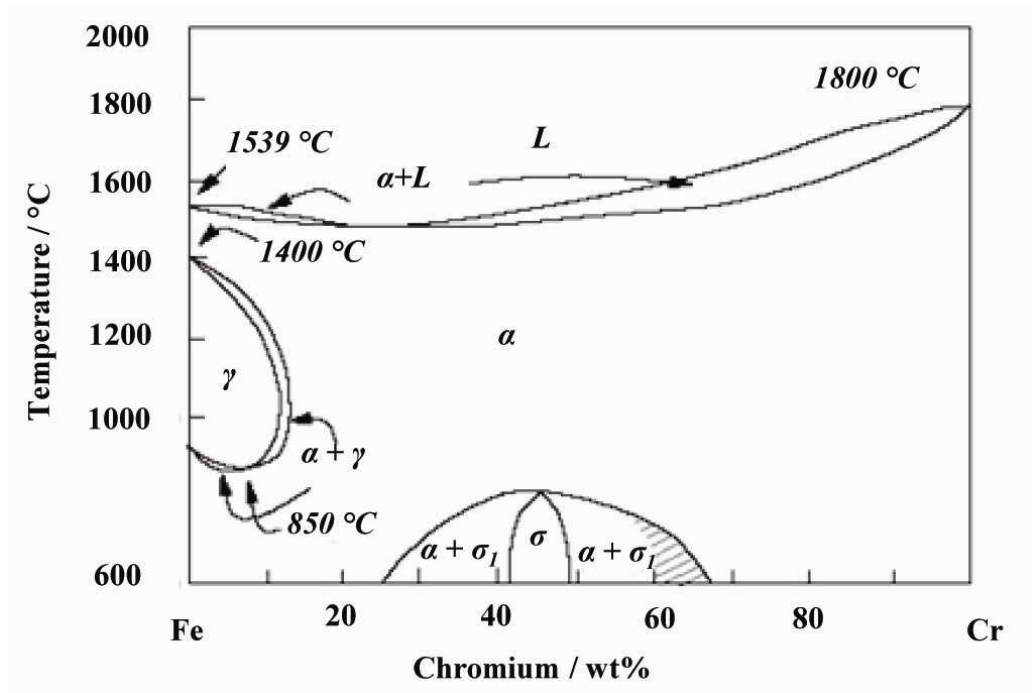


Figure 2-3: The Fe-Cr equilibrium diagram[2].

#### 2.1.4.3. Grades of Austenitic Stainless Steels

Type 304 is the basic 18Cr8Ni (18/8) austenitic stainless steel. It is used for chemical processing equipment, for food, dairy, and beverage industries, for heat exchangers. Type 316, which contains up to 3 wt% Mo, offers much better resistance to pitting, sulphuric acid, and hot organic acids. Hence, it is used widely in marine applications and coastal environments (Figure 2-4) [12]. The AISI 300 specifications for the compositions of different austenitic stainless steels (wt %) are shown in Table 2- 1. The letter “L” after a stainless steel type indicates low carbon (<0.03 wt %) and “N” contain nitrogen (as in 316LN). The “H” grades contain a minimum of 0.04% carbon and a maximum of 0.10% carbon and are designated by the letter “H” after the alloy [1, 2, 9-12]. 304L and 316L are investigated in this project.

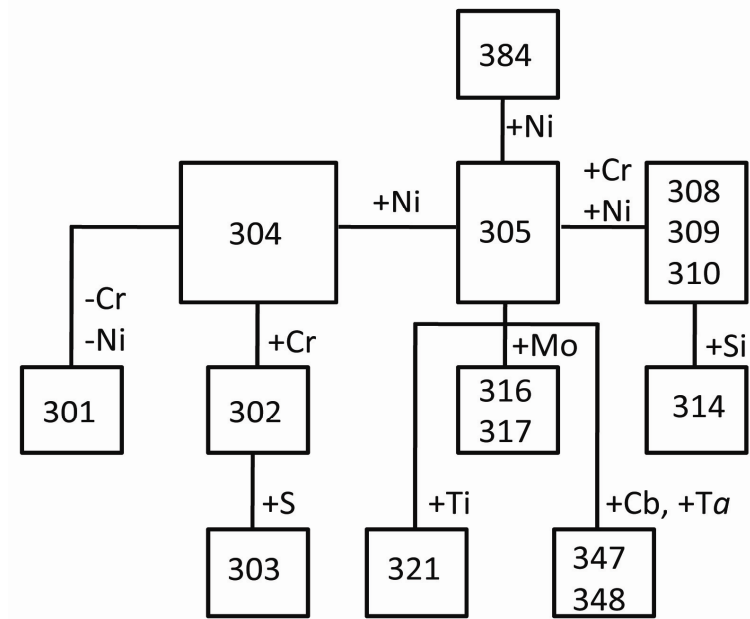


Figure 2-4: Modification of austenitic stainless steels with the addition of other elements to obtain particular properties [9].

Table 2- 1: The AISI 300 series of austenitic stainless steels [10].

	<b>C max</b>	<b>Si max</b>	<b>Mn max</b>	<b>Cr</b>	<b>Ni</b>	<b>Mo</b>	<b>Ti</b>	<b>Nb</b>
<b>301</b>	0.15	1.00	2.00	16-18	6-8			
<b>302</b>	0.15	1.00	2.00	17-19	8-10			
<b>304</b>	0.08	1.00	2.00	17.5-20	8-10.5			
<b>310</b>	0.25	1.50	2.00	24-26	19-22			
<b>316</b>	0.08	1.00	2.00	16-18	10-14	2.0-3.0		
<b>321</b>	0.08	1.00	2.00	17-19	9-12		5 x %C min.	
<b>347</b>	0.08	1.00	2.00	17-19	9-13			10 x %C min.

#### 2.1.4.4. Mechanical Properties of Austenitic Stainless Steels

As shown in Figure 2-5 austenitic steels have a relatively low yield stress. The strength of the austenitic steels is improved by adding carbon, nitrogen and, also molybdenum. But carbon addition to austenitic can be detrimental to corrosion resistance via sensitization (Sensitization refers to the intergranular precipitation of chromium carbides and the concomitant depletion of chromium in the regions adjacent to the grain boundaries, when austenitic stainless steels are extensively heated or slowly cooled

through the temperature range 1123 K to 723 K). So, this element cannot be used for increasing strength. As shown in this Figure austenitic steels show very high ductility. Martensite can be induced by plastic deformation. Mechanical properties of austenitic stainless steels change as a result of cold working. Figure 2-6 illustrates the effects of cold working on the mechanical properties of austenitic stainless steels.

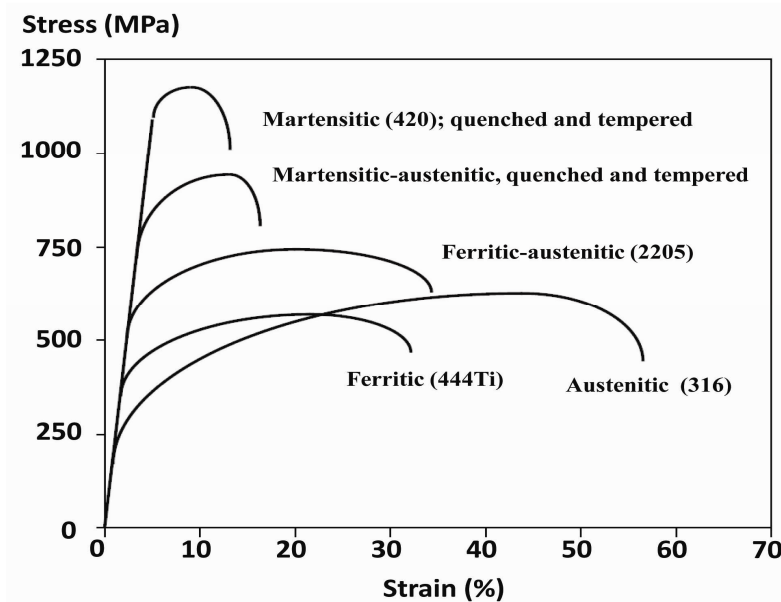


Figure 2-5: Stress-strain curves for stainless steels [9].

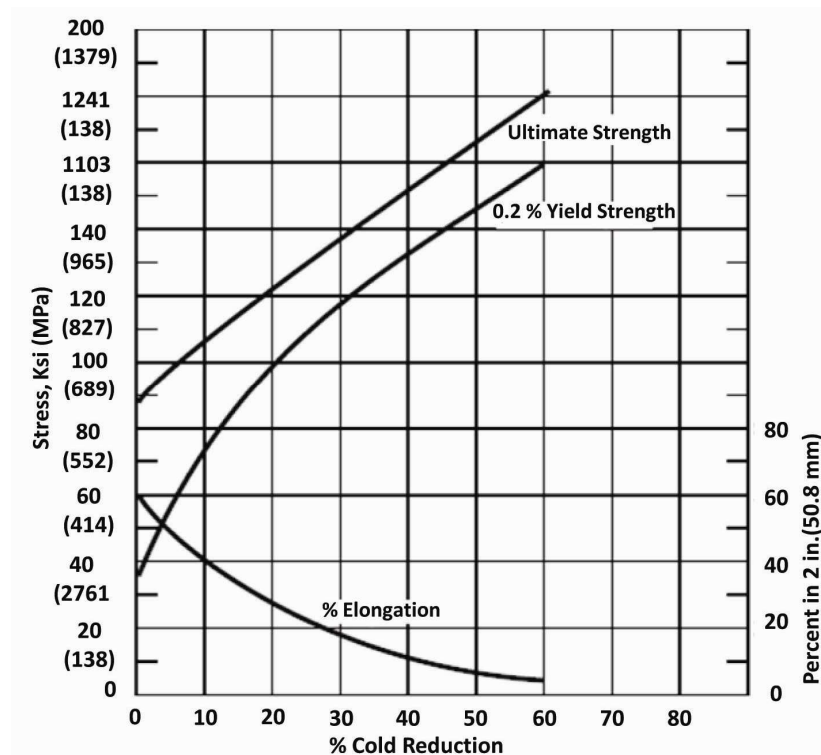


Figure 2-6: Effects of cold working on mechanical properties of austenitic stainless steels [9].

#### 2.1.4.5. *Physical Properties*

Table 2- 2 illustrates the typical values for some physical properties of stainless steels. It can be seen from the data that there are quite different physical properties across stainless steels [9].

*Table 2- 2: Typical physical properties for various stainless steel categories [9].*

Property	Type of stainless steel			
	Martensitic*	Ferritic	Austenitic	Ferritic austenitic
Density (g/cm <sup>3</sup> )	7.6-7.7	7.6-7.8	7.9-8.2	8
Young's modulus (N/mm <sup>2</sup> ) or (MPa)	220,000	220,000	195,000	200,000
Thermal expansion (x 10 <sup>-6</sup> /°C) 200-600 °C	12-13	12-13	17-19	13
Thermal conductivity (W/m °C) 20 °C	22-24	20-23	12-15	20
Heat capacity (J/kg °C) 20 °C	460	460	440	400
Resistivity (10 <sup>-9</sup> Ω-m) 20 °C	600	600-750	850	700-850
Ferromagnetism	Yes	Yes	No	Yes

\* in the hardened and tempered condition.

#### 2.1.4.6. *Fatigue Properties*

As load amplitude decreases the number of cycles to failure will increase. Below a specific amplitude stress no failure occurs within the test period (typically 10<sup>7</sup> cycles). This stress level is known as the fatigue endurance limit, or more commonly as the fatigue limit.

An effect of environment on the fatigue mechanism itself can take place such as corrosion fatigue, or where corrosion pits can act as stress concentrations and also aid initiation. Therefore, if equipment is exposed to corrosion attack, the life of this equipment will be affected. Figure 2-7 shows the effect of an aggressive environment on fatigue strength for some stainless steels. It can be seen from this Figure that a lower pH, i.e. a more aggressive condition, gives lower fatigue strength. Comparison of the two austenitic steels shows that the higher alloyed grade, 316LN, that has the higher corrosion resistance also has a higher corrosion fatigue strength [9].

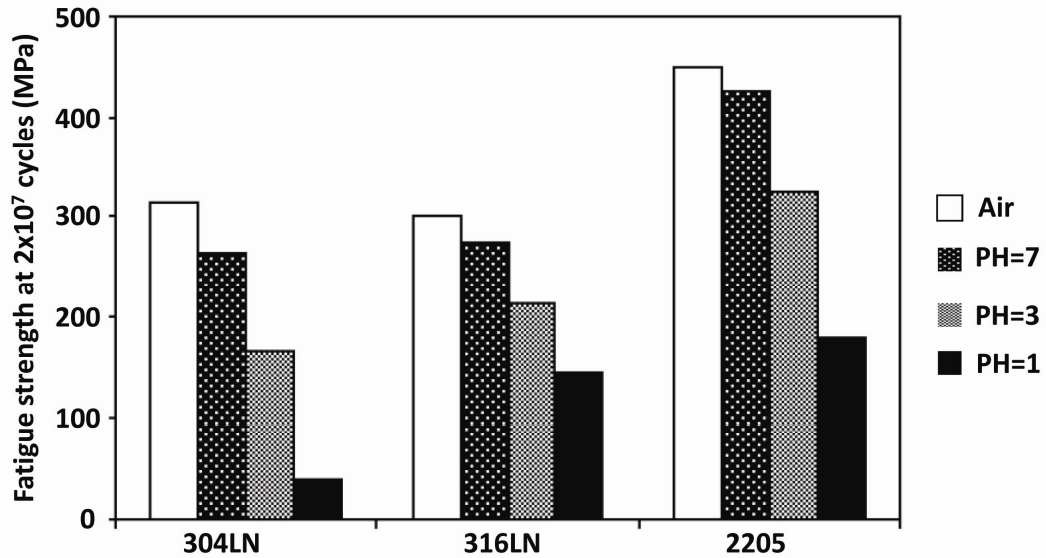


Figure 2-7: Effect of environment on fatigue strength for some stainless steels (Fatigue strength at  $40\text{ Co}$  and rotating bending stress at  $100\text{ Hz}$ . Tested in air and 3% NaCl at various pH) [9].

## 2.2. Fatigue of Materials

### 2.2.1. Introduction

Fatigue occurs when the component or structure is subjected to repeated stress cycles and subsequently fails at stresses below the tensile strength,  $\sigma_{ts}$ , and often below the yield strength,  $\sigma_y$ , of the material. Due to global competition and higher customer demands for safety, durability and reliability of products in industrial field, all products should be designed and tested for sufficient fatigue resistance. Many different failure modes exist in all fields of engineering. These failures can occur in simple, complex, inexpensive, or expensive components or structures. Mechanical failures have caused many injuries and much financial loss. The loss of a wing, propeller or wheel, or a steering failure leads to a serious threat to life or property or the disruption of essential services [15-19]. According to studies carried out by S. Nishuda et al., between 80-90% of all structural failures occur through a fatigue mechanism [15].

Austenitic stainless steels are currently used in industrial installations, such as petrochemical plants, electric-power generating stations and process plants as piping, shafts and structural materials. In these applications, the components of the structures are subjected to repeated stresses as a result of vibration or pressurisation cycles. Therefore, it is of both academic and industrial interest to study the fatigue behaviour of Austenitic stainless steels.



Low-cycle fatigue, high-cycle fatigue and thermal fatigue are types of metal fatigue. Low-cycle fatigue is related to macro-plastic deformation in every load cycle, due to the high stress amplitudes, typically over the yield strength. High-cycle fatigue is more associated with elastic behaviour of the material on a macro scale and plastic behaviour at the microscale. Thermal fatigue is combination of thermal and mechanical fatigue [15, 16, 18, 19]. The current study is mainly focused on high-cycle fatigue, especially on fatigue crack initiation and early growth (short crack).

### 2.2.2. *Fatigue Design Methodology*

In prevention of fatigue failure, design criteria have evolved from the concept of infinite life to a damage tolerance philosophy. In the indefinite life design methodology, the maximum stress is kept below the material's fatigue stress limit.

#### 2.2.2.1. *Total –Life Approach*

Stress or strain based Wöhler diagrams can be used to predict the approximate number of cycles to failure,  $N_f$  for the components (Figure 2-8). In this method, the number of stress or strain cycles necessary to induce fatigue failure in un-cracked (smooth surface) laboratory specimens is estimated under controlled amplitudes of cyclic stresses or strains.

High-cycle fatigue (HCF) is characterized in terms of the stress range, as the material is subject to low stress and this leads to elastic deformation. While the stresses associated with low-cycle fatigue (LCF) are generally high enough to cause appreciable plastic deformation prior to failure. Consequently, the fatigue life is characterized in terms of strain range.

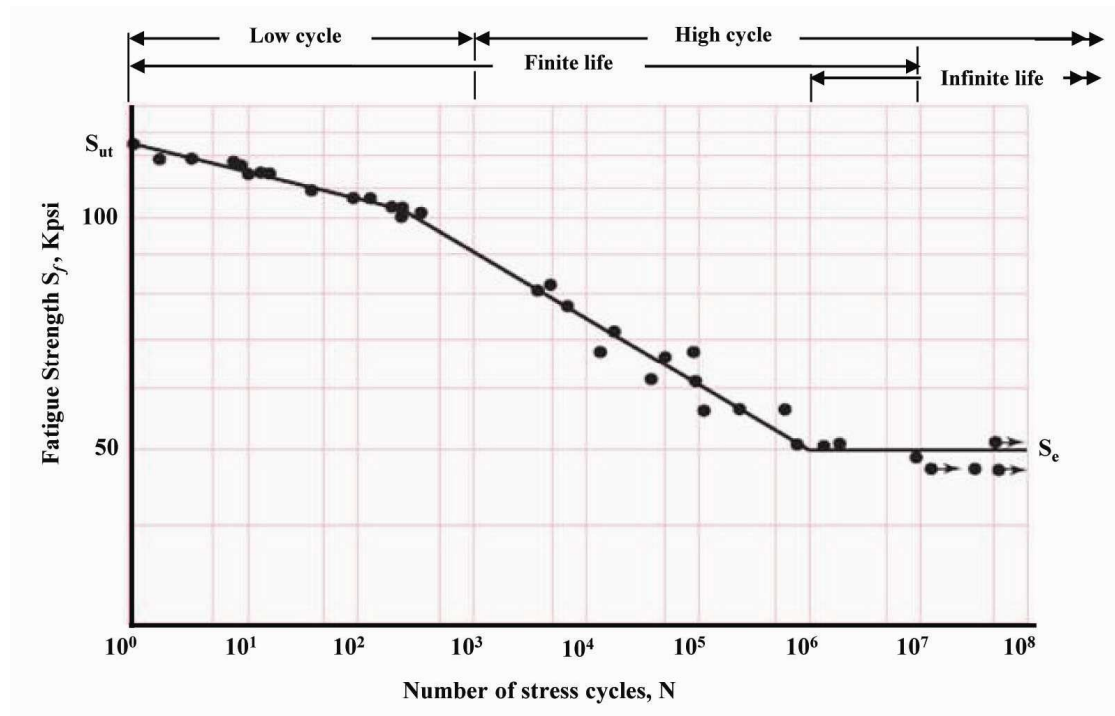


Figure 2-8: Wöhler diagram [17].

The strain-based Wohler diagram can be described by combining Basquin's equation (Eq.2-5) for the high cycle fatigue regime ( $N_f > 10^4$  cycles) and Manson's and Coffin's equation (Eq.2-6) for the low cycle fatigue regime ( $N_f \leq 10^4$  cycles).

$$\frac{\Delta\sigma}{2} = \sigma'_f (2N_f)^b \quad (2-5)$$

$N_f$ : Number of cycles to fracture (corresponding to  $2N'_f$  load reversal).

$\Delta\sigma/2$ : Stress Amplitude.

$\sigma'_f$ : Fatigue strength coefficient.

$b$ : Fatigue strength exponent.

$$\frac{\Delta\varepsilon_{pl}}{2} = \varepsilon'_f (2N_f)^c \quad (2-6)$$

$\Delta\varepsilon/2$ : Plastic strain Amplitude.

$\varepsilon'_f$ : Fatigue ductility coefficient.

$c$ : Fatigue ductility exponent.

More details about this approach are discussed in the next sections (2.2.4.3).

#### 2.2.2.2. *Damage-Tolerance Approach*

The basic hypothesis of the damage-tolerance approach is that each engineering component contains imperfections in the form of cracks.

Non-destructive techniques (NDT), such as, visual, dye-penetrant, x-ray technique or ultrasonic method are used to detect and determine the size of pre-existing flaws. The number of fatigue cycles or time to propagate the dominant crack from the pre-existing flaw size to some critical dimension represents the useful fatigue life. The damage-tolerant approach can be used most readily under conditions of small scale yielding (i.e. neglecting the plastic strain field of any stress concentration), where the crack tip plastic zone is small compared to the characteristic dimensions of the cracked component (including the crack size) and where elastic loading conditions prevail. So, under these circumstances, linear elastic fracture mechanics is applicable.

It will be seen that the application of a damage-tolerant approach based on LEFM to short cracks may lead to nonconservative design.

#### 2.2.2.3. *Safe-Life and Fail-Safe Approach*

In safe-life design approach, the typical cyclic load spectra are determined from the structural component in service. Using this information, the components are tested in the laboratory under identical load conditions to those typical of service spectra. From this test a useful fatigue life is estimated. The estimated fatigue life is modified with a factor of safety to predict the safe life for this component. When the expected safe operation life is expired, the component is retired from service.

Fail-safe design requires that if one part fails, the system does not fail. To achieve fail-safe design, some techniques are used such as multiple load paths, load transfer between members, crack stoppers built at intervals into the structure, and periodic inspections. The periodic inspection is essential in some safety-critical situations (e.g. aircraft and nuclear industries) to enable quick repair or replacements.

### 2.2.3. *Stress-Life (S-N) Approach*

The stress-life approach to fatigue was first introduced by Wöhler. In this approach, the total number of cycles or time to induce fatigue damage and to initiate a dominant fatigue flaw that propagates to final failure represents the fatigue life of a component.

In high cycle fatigue (HCF) applications, where low amplitude cyclic stresses induce primarily elastic deformation in a component which is designed for long life, the stress-life approach can be used.

In low cycle fatigue (LCF), where plastic deformation prevails during cyclic loading, as a result of high stress amplitudes or stress concentrations, a strain based approach can be applied as considered in the next section [2.2.4].

#### 2.2.3.1. *Cyclic Stress [17-19]*

It is necessary here to define briefly the general types of fluctuating stresses that can cause fatigue. Figure 2-9-a illustrates typical fatigue stress cycles. The maximum and minimum stresses in this type of stress cycle are equal. This is referred to as a reversed stress cycle. Tensile stress is considered positive, and compressive stress is negative. In high cycle fatigue, below the yield stress, the conditions are essentially elastic so the applied strain is proportional to the applied stress.

Figure 2-9-b shows a repeated stress cycle in which the maximum stress  $\sigma_{max}$  and minimum stress  $\sigma_{min}$  are not equal. This figure shows sinusoidal loading with the minimum and maximum stresses both in the tensile region. In this illustration they are both tensile, but a repeated stress cycle could just as well contain maximum and minimum stresses of opposite signs or both in compression. The stress level may vary randomly in amplitude and frequency as shown in Figure 2-9-d. This might occur in a part such as an aircraft wing, which is subjected to periodic unpredictable overloads due to gusts or manoeuvres.

There are several parameters used to characterize the fluctuating stress cycle, namely, mean stress, stress range, stress amplitude, stress ratio R, and the alternating stress ratio A. The mean stress is defined as the average of the maximum and minimum stress in the cycle (Eq. 2-7) [15-19].

$$\sigma_m = \frac{\sigma_{max} + \sigma_{min}}{2} \quad (2-7)$$

The stress range  $\sigma_r$  is twice the alternating stress or the difference between  $\sigma_{max}$  and  $\sigma_{min}$ .

$$\sigma_r = \sigma_{max} - \sigma_{min} \quad (2-8)$$

Stress amplitude  $\sigma_a$  is one half of the stress range:

$$\sigma_a = \frac{\sigma_r}{2} = \frac{\sigma_{max} - \sigma_{min}}{2} \quad (2-9)$$

The stress ratio  $R$  and the alternating stress ratio  $A$  are the ratio of minimum and maximum stress and the ratio of the stress amplitude and the mean stress respectively.

$$R = \frac{\sigma_{min}}{\sigma_{max}} \quad \text{and} \quad A = \frac{\sigma_a}{\sigma_m} \quad (2-10)$$

$R = -1$  and  $R = 0$  are two common test conditions used for obtaining fatigue properties. Due to  $\sigma_{min}$  being equal to  $-\sigma_{max}$  the stress ratio  $R = -1$  is called the fully reversed condition while it is called pulsating tension if  $R = 0$  where  $\sigma_{min} = 0$ .

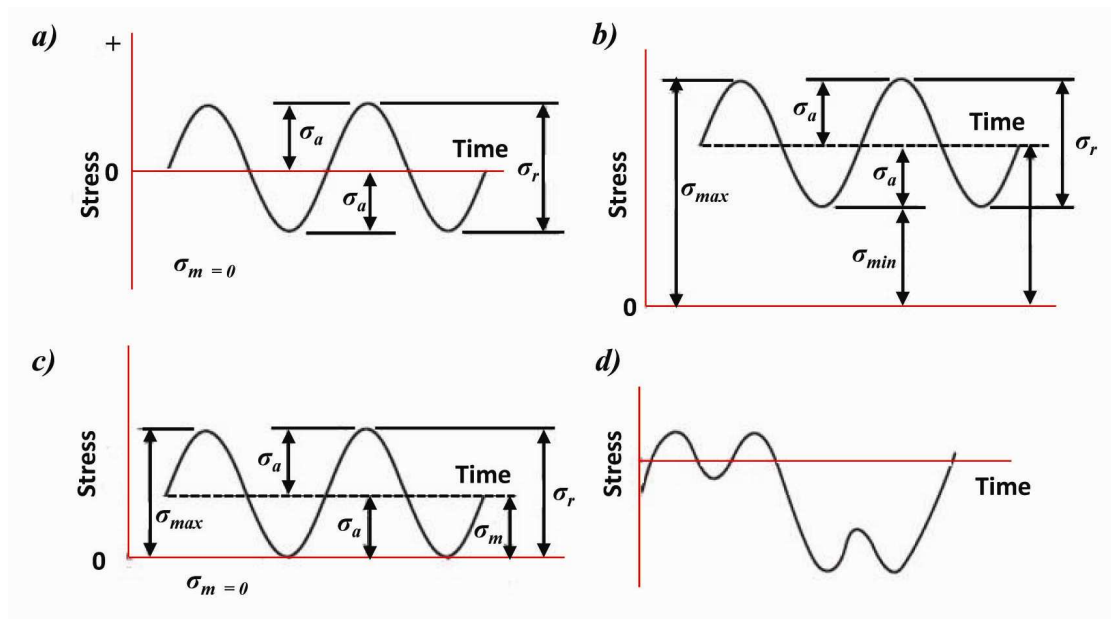


Figure 2-9: Typical fatigue stress cycles. (a) Reversed stress; (b) repeated stress; (c) Pulsating tension (d) irregular or random stress cycle [19].

### 2.2.3.2. *The S-N Curve*

A common method of presenting engineering fatigue data is by means of the S-N curve, a plot of stress  $S$  against the number of cycles to failure  $N$ . A log scale is almost always used for  $N$  (Figure 2-8) [15-19]. Laboratory simulation tests can be carried out to determine the fatigue properties of materials. In this, a series of tests is carried out by subjecting a specimen to stress cycling at relatively large maximum stress amplitude ( $\sigma_{max}$ ). The number of cycles to failure is counted. This procedure is repeated on other specimens at progressively decreasing maximum stress amplitudes. The test stress is decreased for each succeeding specimen until one or two specimens do not fail in the specified numbers of cycles, which is usually at least  $10^7$  cycles. Data are plotted as stress  $\sigma$  versus the logarithm of the number  $N$  of cycles to failure for each of the specimens [15-19].

For some ferrous (iron base), the S-N curve becomes horizontal at low stress amplitude values below a limiting stress level called fatigue limit. Life of  $1 \leq N \leq 10^3$  cycles is generally classified as low-cycle fatigue, whereas high-cycle fatigue is considered to be  $N > 10^3$  cycles (Figure 2-8) [16-19].

### 2.2.3.3. *Fatigue Limit*

The characterisation of the fatigue life in terms of nominal stress amplitude using experimental data obtained from rotating bend tests on smooth specimens was done by Wöhler on fatigue of alloys used for railroad axles. In these tests smooth (un-notched) specimens, hour-glass in shape are fatigue tested in plane bending, rotating bending, uniaxial compression-tension (Push-Pull) or tension-tension cyclic loading.

The data obtained from such an experiment are used to create a stress-life plot (S-N curve). Where the stress amplitude  $\sigma_a$  for fully reversed loading (equal to one half of the stress range from the maximum tension to maximum compression), is plotted versus fatigue cycles to failure,  $N_f$  (Figure 2-8).

In the S-N curve, when the material under a constant amplitude loading conditions exhibits a plateau stress level, typically beyond about  $10^6$  fatigue cycles, the specimen below this stress level could be cycled indefinitely without failure. This stress amplitude is known as the fatigue limit. The endurance limit is defined as the fatigue strength at a given (long) life.

#### 2.2.3.4. *The Effect of Mean Stress on Fatigue life Under Stress-Life Approach*

The mean stress plays an important role in influencing the fatigue behaviour of engineering materials. This can be seen in Figure 2-10, where alternating stress  $S_a$  is plotted versus the number of cycles to failure  $N_f$  for different mean stresses. It can be seen that the fatigue life decreases as mean stress increases. Also, this plot shows that tensile mean stresses are detrimental and compressive mean stresses are beneficial. The three vertical lines indicating fatigue life:  $N_{ft}$ ,  $N_{f0}$ , and  $N_{fc}$ , representing fatigue life for tensile, zero, and compressive mean stress, respectively.

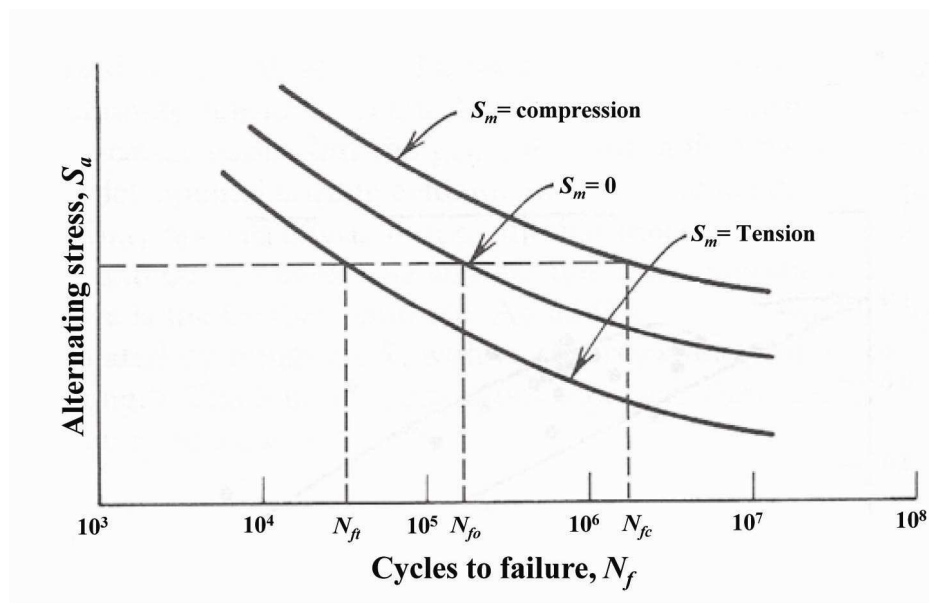


Figure 2-10: Effect of mean stress on fatigue life [16].

#### 2.2.3.5. *Effect of Surface Treatments under Stress-Life Approach*

The surface has a substantial influence on fatigue behaviour because most fatigue cracks nucleate at the surface [18]. Differences in surface roughness, microstructure, chemical composition, and residual stress act as surface effects which may lead to initiation of fatigue cracks. The effects of these factors will be discussed in the section on surfaces and machining (2.5). In the near surface regions of the materials, surface treatment processes, such as carburizing, nitriding, flame hardening, induction hardening and shot peening are designed to give high strength, wear resistance or corrosion resistance. When the material is subjected to machining operations such as grinding, polishing, turning and milling, different degrees of surface roughness will be developed. The valleys of a rough surface act as stress concentrations and create suitable sites to nucleate fatigue cracks.

The residual stresses developed by the surface treatments can have an important effect on the fatigue life. These residual stresses change the mean level of the fatigue cycle for crack nucleation. Therefore, the residual stresses can be beneficial if they are compressive and detrimental if they are tensile especially for high strength materials. In soft materials, this beneficial effect becomes less significant at large applied stress due to a large amplitude of the pulsating stress relaxing the residual stress. This effect can be emerged from the studies which investigate the effect of shot peening on fatigue life for different materials [18].

#### 2.2.4. *Strain-Life ( $\epsilon$ -N) Approach*

The fatigue failure curve can be divided into low cycle and high cycle regimes. In the low cycle fatigue regime, the plastic deformation is macroscopic and microscopic localized plastic deformation occurs in the high cycle regime. For cycles above the yield stress, the bulk of the metal is plastically deformed. In both regimes (HCF and LCF), the presence of stress concentration such as, sharp corners, holes or notches, can make the material response to cyclic loading strain controlled. So, cyclic strain controlled tests can characterize the fatigue behaviour of material better than cyclic stress controlled tests, especially, in the low cycle fatigue regime and notched components.

The strain life approach is based on the assumption that the life spent on crack nucleation and small crack growth of a notched component can be approximated by a smooth laboratory specimen under the same cyclic deformation at the crack initiation site.

##### 2.2.4.1. *Strain Controlled Test Method*

Strain life is typically represented as a curve of strain versus fatigue life. To obtain such a data strain-controlled axial fatigue tests are conducted by using smooth, polished specimens. An extensometer is allocated to the gage length to control and measure strain over the gage section. Stress and plastic strain variation are recorded periodically throughout the test and the test is continued until fatigue failure occurs. The surface finish condition of the component may be simulated on testing laboratory specimens to include the effect of surface finish.



#### 2.2.4.2. Cyclic Material Behaviour Under strain controlled Loading

When the material is subjected to fully reversed strain-controlled loading, the material may behave in one of the following ways: cyclic hardening, cyclic softening, remaining stable or some combination of these behaviours.

As shown in Figure 2-11, in cyclic hardening, the stress developed in each successive strain reversal increases as the number of cycles increase. In cyclic softening (Figure 2-12), the stress decreases as the number of cycles increases. In cyclic hardening or cyclic softening, the rate of change of the stress will gradually decrease and the stress magnitude will reach a stable level and remain stable up to the end of fatigue life where the first fatigue crack is detected.

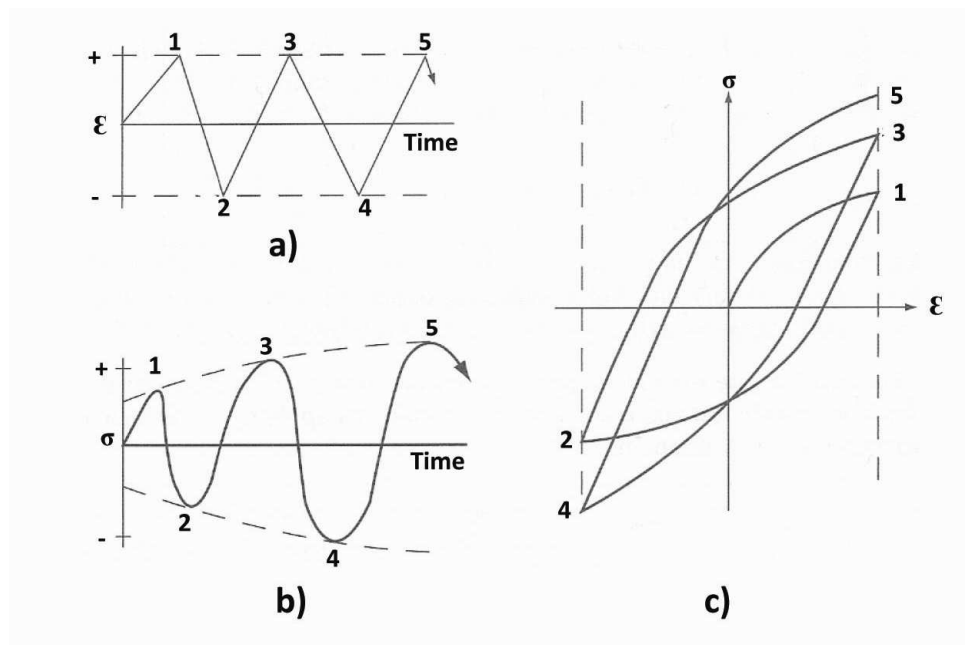


Figure 2-11: Transient behaviour-cyclic hardening [20].

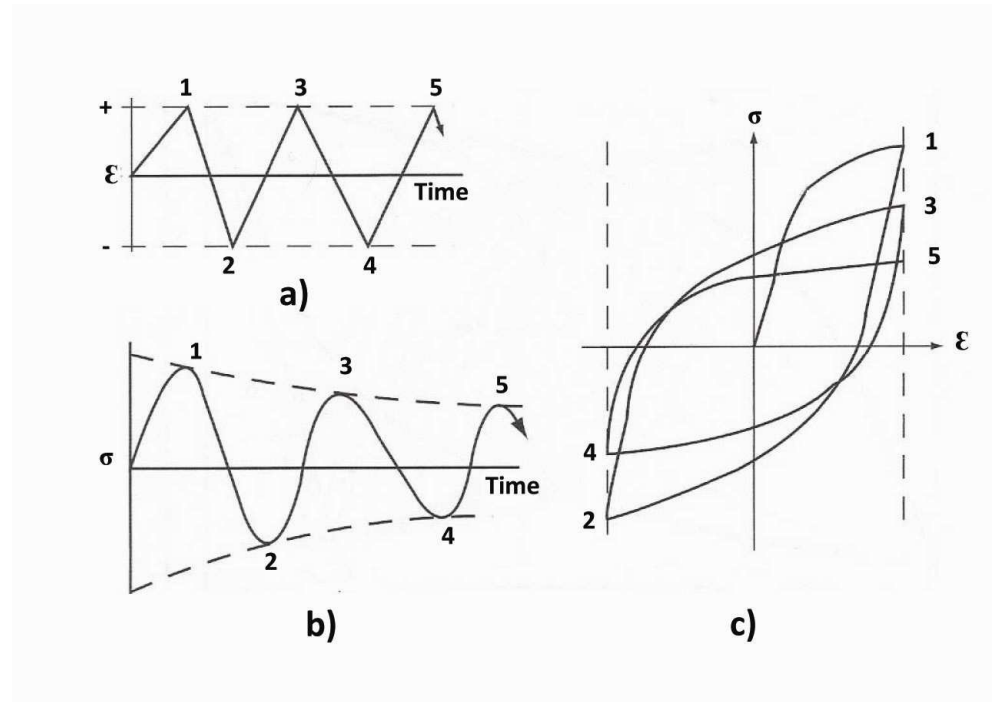


Figure 2-12: Transient behaviour-cyclic softening[20].

#### 2.2.4.3. Strain Based Approach to Total Life

The relation of the total strain amplitude ( $\mathcal{E}_a$ ) and the fatigue life in reversals to failure ( $2N_f$ ) can be expressed in the following form:

$$\varepsilon_a = \varepsilon_a^e + \varepsilon_a^p = \frac{\sigma_f'}{E} (2N_f)^b + \varepsilon_f' (2N_f)^c \quad (2-11)$$

Where:  $E$ : The modulus elasticity.

$\sigma_f'$ : Fatigue strength coefficient.

$b$ : Fatigue strength exponent.

$\varepsilon_f'$ : Fatigue ductility coefficient.

$c$ : Fatigue ductility exponent.

Eq. (2-11) is called the strain life equation. This equation is a combination of two curves; the elastic strain amplitude-life and plastic strain amplitude-life. In eq. (2-11), the left part  $(\frac{\sigma_f'}{E} (2N_f)^b)$  is Basquin's equation (Eq. 2-5) divided by the modulus of elasticity. The right part  $(\varepsilon_f' (2N_f)^c)$  is the equation proposed by Manson and Coffin (Eq. 2-6). It represents the relation between plastic strain and life.

As shown in Figure 2-13, both curves become straight lines where plotted on log-log scales. The intersection of the elastic and plastic strain life curves is transition fatigue ( $2N_T$ ), where the magnitude of elastic strain and plastic strain amplitude are equal. In Figure 2-13, the left side of  $2N_T$  represents the plastic strain region (LCF) and the right side represents the elastic strain region (HCF).

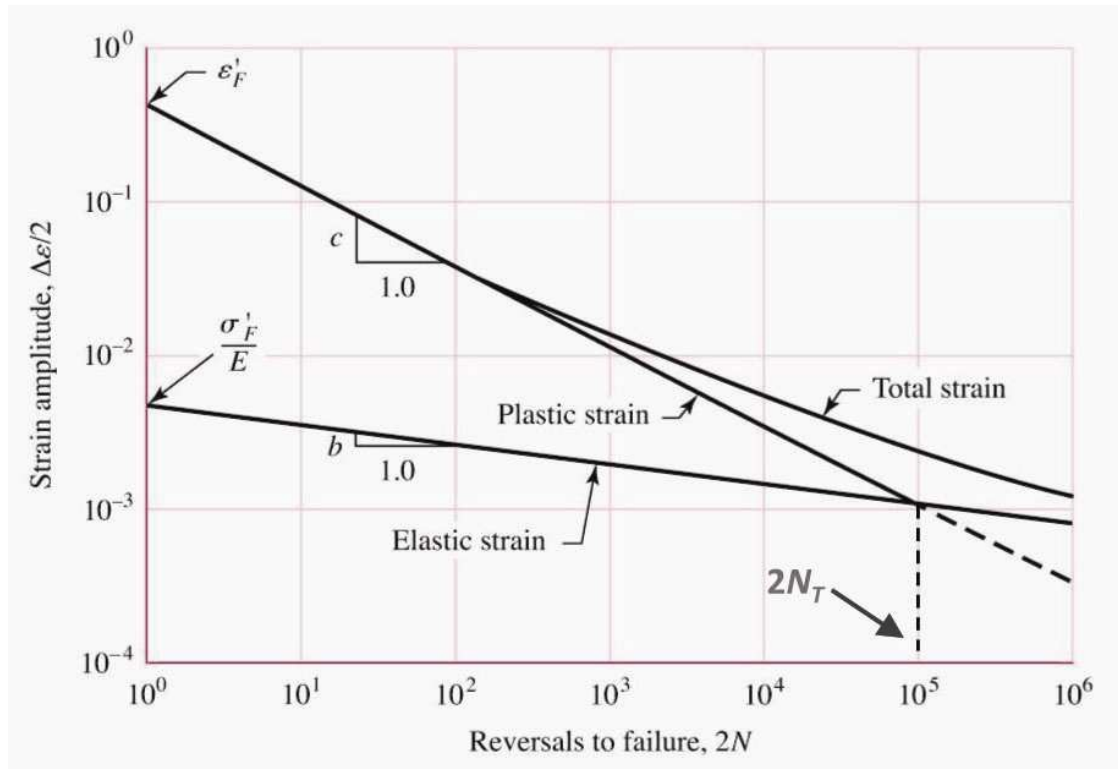


Figure 2-13: Schematic of a total strain-life curve[17].

In strain controlled cycling a mean stress leads to mean strain. The mean stress usually relaxes at large strain amplitudes as a result of plastic deformation. When the mean stress is not relaxed, it can significantly affect the fatigue life. Mean stress leads to a detrimental effect when it is tensile and a beneficial effect when it is a compressive mean stress as discussed before. The effect of residual stress on fatigue life is generally similar to the mean stress effect [16, 18].

The effect of mean stresses from the surface finish can emerge as significantly influences is the high cycle fatigue regime where elastic strain is dominant and there is little influence is the low cycle fatigue regime.

### 2.2.5. *Fatigue damage and crack initiation mechanism*

Cyclic loading leads to modification of the internal dislocation arrangement and formation of the typical structures. Cyclic strain is localized to thin deformation bands-persistent slip bands (PSBs). PSBs have structure that differs from the structure of the matrix. Surface relief takes place in the sites where PSBs intersect the surface as a result of localization of the cyclic plastic strain to the PSBs. Subsequently, persistent slip markings (PSMs) consisting of extrusions and intrusions are formed on the surface [18, 21].

Localized cyclic plastic straining on flat surface represent the first step in the nucleation of a fatigue crack. As a result of very small radius of the intrusions, the sharp tip of the intrusions act as an effective stress raiser. Slip-unslip mechanism takes place along the primary plane because of the high stress concentration in the tip of the intrusion.

Figure 2-14 shows schematically the nucleation of surface cracks from a row of intrusions. Along the PSM the semi-elliptical intrusions are nucleated and alternate with the extrusions. Anti-plane shear deformation is developed in the material between the neighbouring intrusions. Subsequently new surface are formed and lead to nucleation of semi elliptical cracks at the tip of the intrusions. Finally, the linkage of the half-elliptical cracks leads to the formation of a shallow crack along the whole PSM [21].

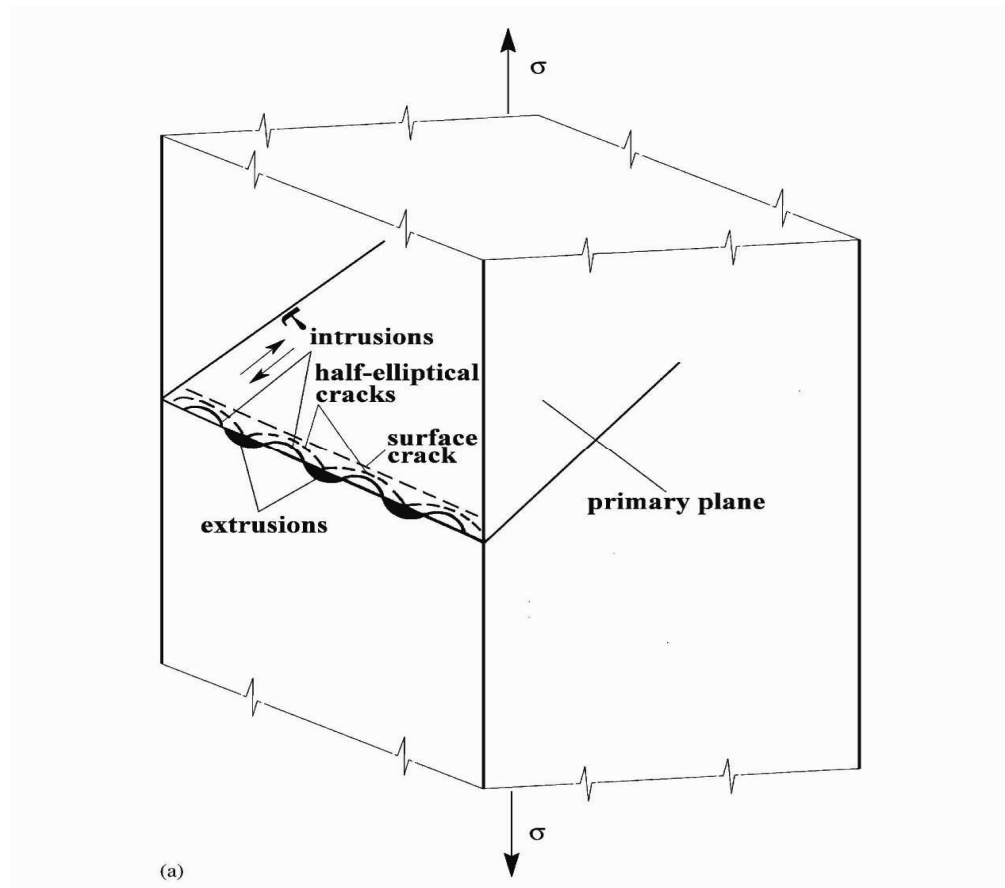


Figure 2-14: Mechanism of crack nucleation from a row of intrusions [21].

Generally, intrusions represent sharp defects equivalent to incipient cracks. The crack emanates from the tip of the intrusions and grows under the effect of cyclic loading.

Figure 2-15 shows schematically crack initiation due to environmentally assisted slip irreversibility. Shallow microcracks nucleate from the tip of the intrusion as a result of an irreversible slip along the primary slip plane. In tensile loading a new surface is formed, where fresh metal surface is exposed to oxygen from the environment (Figure 2-15). Absorption of the oxygen prevents complete re-welding of the new surface in the compression load (Figure 2-15-b). Subsequently, local decohesion along the slip band generates crack-initiation sites (Figure 2-15-c) [22].

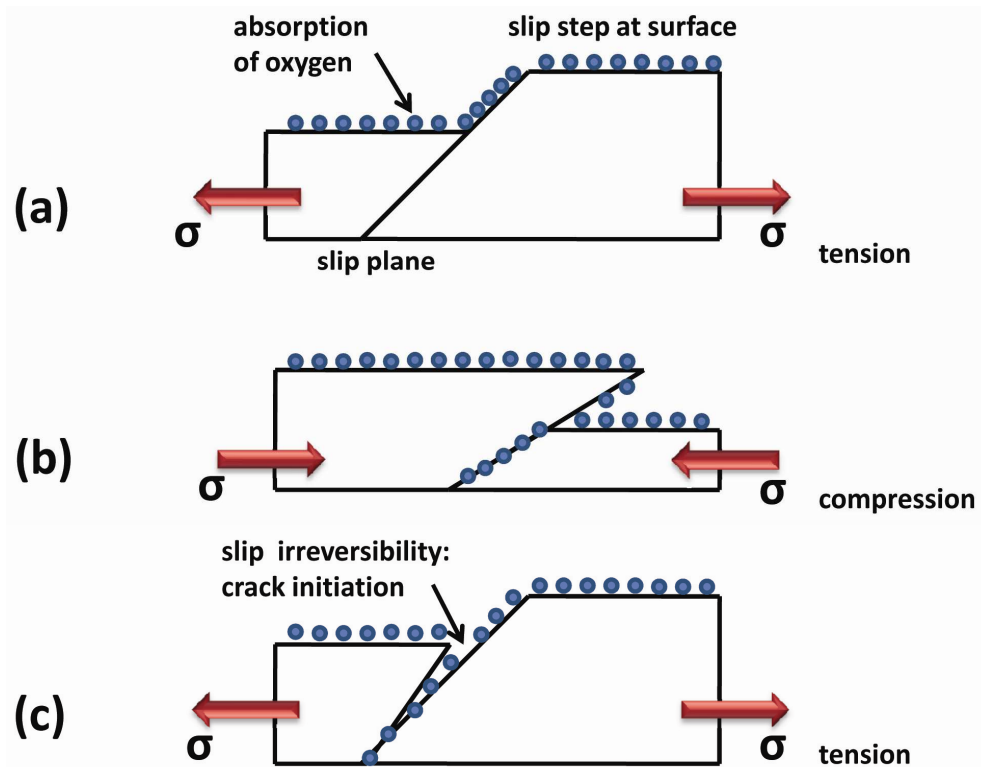


Figure 2-15: Crack initiation due to environmentally assisted slip irreversibility: (a) exposure of fresh surface; (b) absorption of fresh metal surface; (c) local decohesion [22].

Crack initiation has been confirmed in austenitic steels to initiate in slip bands (Figure 2-16) [23]. Recent studies by Polack [23-25] on austenitic stainless steels using scanning electron microscopy (SEM) and atomic force microscopy (AFM) suggest the original role of intrusions in fatigue crack initiation. He used scanning electron microscopy (SEM) combined with focused ion beam (FIB) machining to study the initiation of a stage I fatigue crack on the surface of 316L steel. The specimens were cycled in an electro hydraulic testing system with a constant strain rate  $1.5 \times 10^{-3} \text{ s}^{-1}$  and constant plastic strain amplitude of  $1 \times 10^{-3}$ . After 300 cycles a cross-sectional surface perpendicular to the direction of parallel PSMs was prepared using FIB as shown in Figure 2-17 [26]. The specimen was returned to the fatigue test for more cycles. The test was interrupted periodically to observe the exposed surface. He concluded that cyclic strain is localized early in fatigue life to individual PSBs and strain localization results in the formation and growth of PSMs in locations where PSBs emerge on the crystal surface.

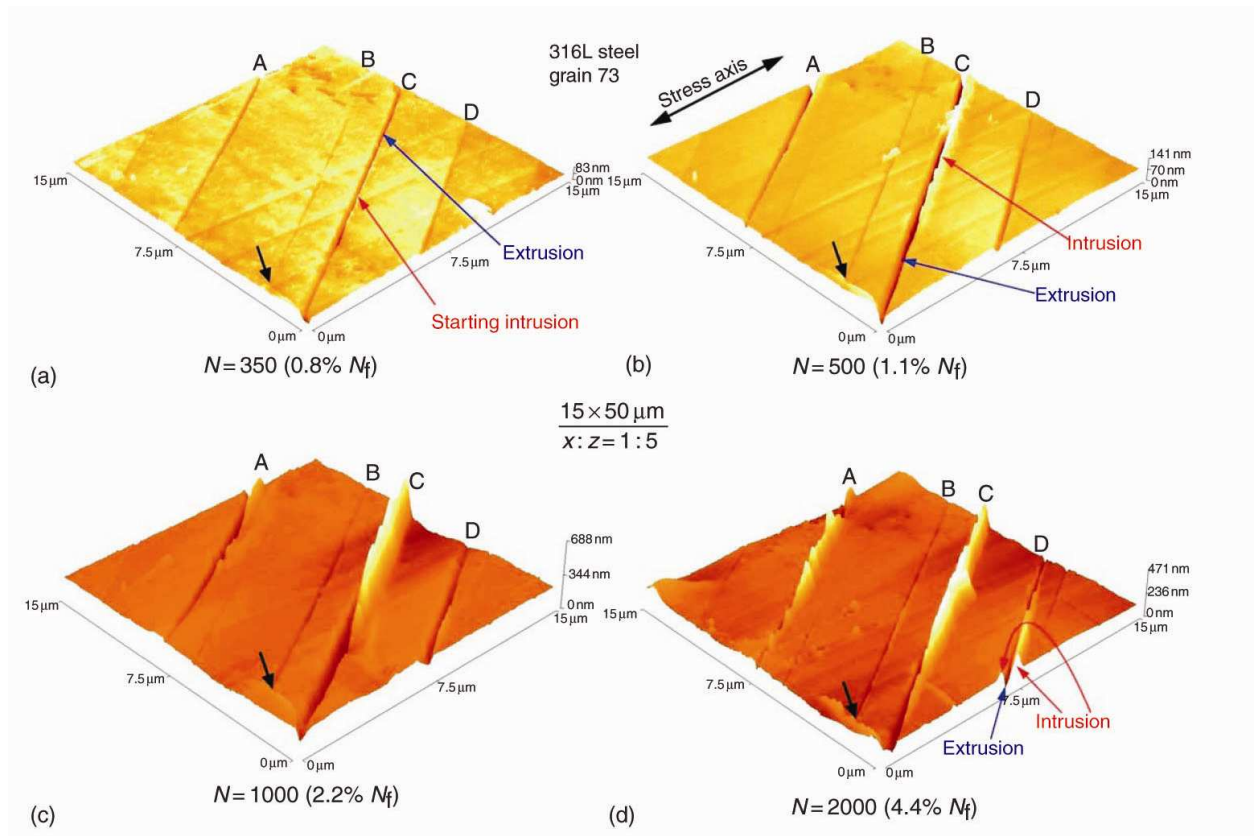


Figure 2-16: Early evolution of the surface relief of 316L steel as detected by AFM on the surface replica:(a),  $N=350$ ; (b),  $N=500$ ; (c),  $N=1000$ ; (d),  $N=2000$  [24].

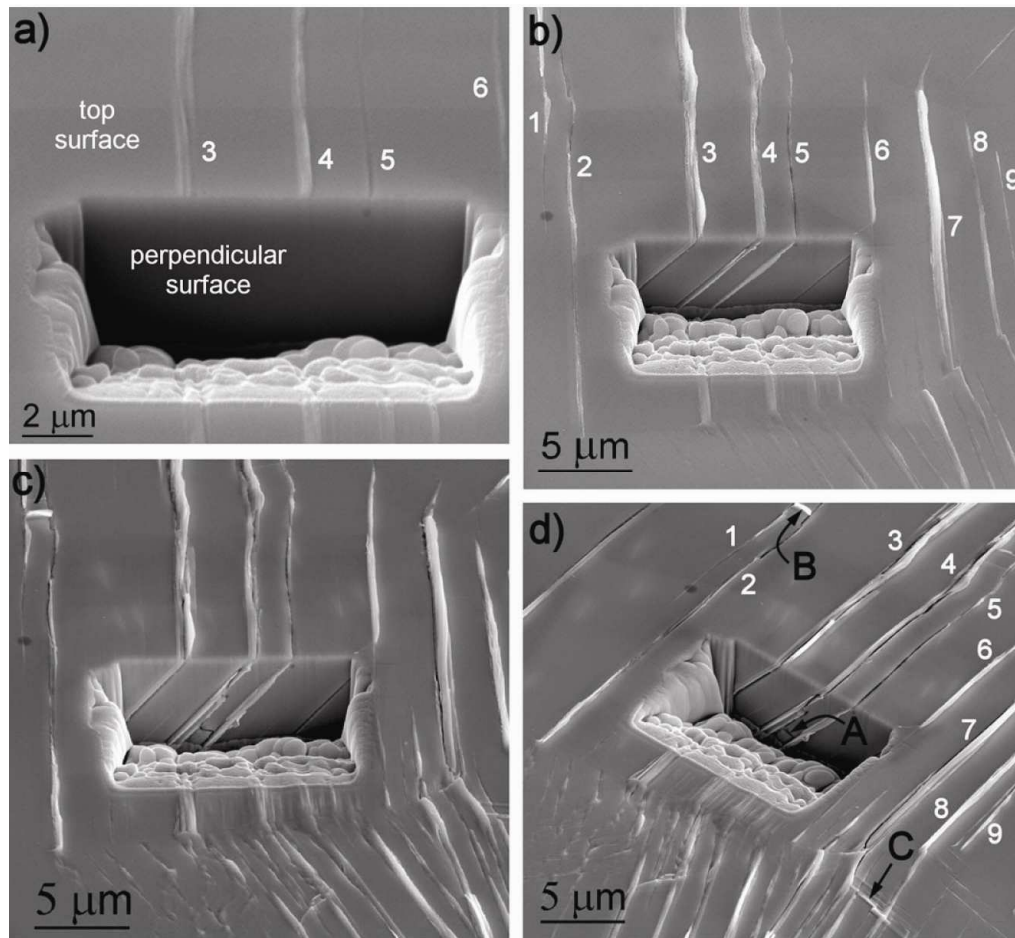


Figure 2-17: Specimen surface with a rectangular crater at different stages of the fatigue life ( $\epsilon_{ap} = 1 \times 10^{-3}$ ), (a)  $N = 300$  cycles, crater was produced using FIB, (b)  $N = 300 + 300$  cycles, (c) and (d)  $N = 300 + 1500$  cycles [26].

Man et al. [27-29] and Villechaise et al. [30] used field emission scanning electron microscopy (FESEM) and atomic force microscopy (AFM) in combination with electron back-scattering diffraction (EBSD) to study the persistent slip markings (PSMs), which mark locations where PSBs emerge on the surface of the material.

However, fatigue crack nucleation does not always occur only at slip bands. Non-metallic inclusions and second phase particles are considered as crack initiation sites, particularly in high-strength alloys where particles might be broken as consequence of prior deformation processing [31]. The fatigue cracks were also observed to initiate due to the porosity on or just beneath the surface as in udimet 720Li Ni-base alloy [32]. Surface roughness (due to the manufacturing process and machining) could also encourage crack initiation on the material surface [33]. Even the best-prepared engineering surfaces contain micronotches such as triple point of grain boundaries, inclusions and machining marks.



### 2.2.6. *Crack Propagation*

As discussed above, the initiation of one or more microcracks due to cyclic plastic deformation followed by crystallographic propagation is termed by Stage I. In stage II, microcracks join together and begin to propagate through the material in a zigzag manner essentially perpendicular to the applied tensile stress as shown in Figure 2-18. During this stage of propagation, repetitive plastic blunting and sharpening process at the crack tip, leads to drive the crack growth. At the beginning of the stress cycle (zero or maximum compressive load), the crack tip has the shape of the sharp double-notch (Figure 2-19-a). As the tensile stress is applied (Figure 2-19-b), localized deformation occurs at each of these tip notches along slip planes that are oriented at  $45^\circ$  angle relative to the plane of the crack. As a result of crack widening, shear deformation drives the tip forward (Figure 2-19-c). The applied compressive load reverses the direction of shear deformation at the crack tip (Figure 2-19-d) until, the end of the cycle; a new sharp double-notch tip will be formed (Figure 2-19-e). Subsequently, the crack tip has advanced a one-notch distance during the course of a complete cycle. This process is repeated with each subsequent cycle until some critical crack dimension is achieved. Eventually, the third stage is commenced. When the fracture toughness is exceeded, the remaining cross-section of the material will experience rapid fracture, called the third stage [16, 18, 19].

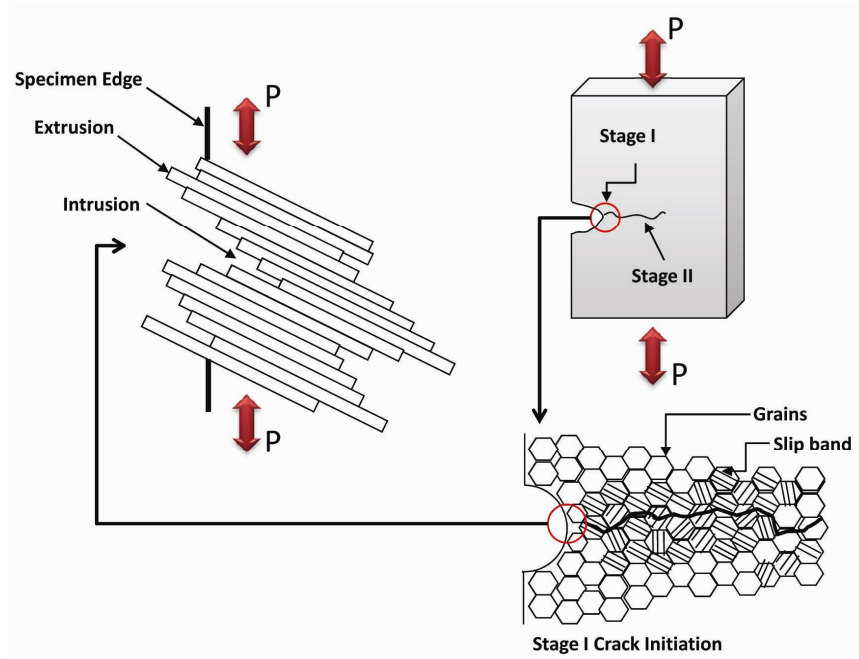


Figure 2-18: Schematic representation showing stages I and II of fatigue crack propagation in polycrystalline metal [34].

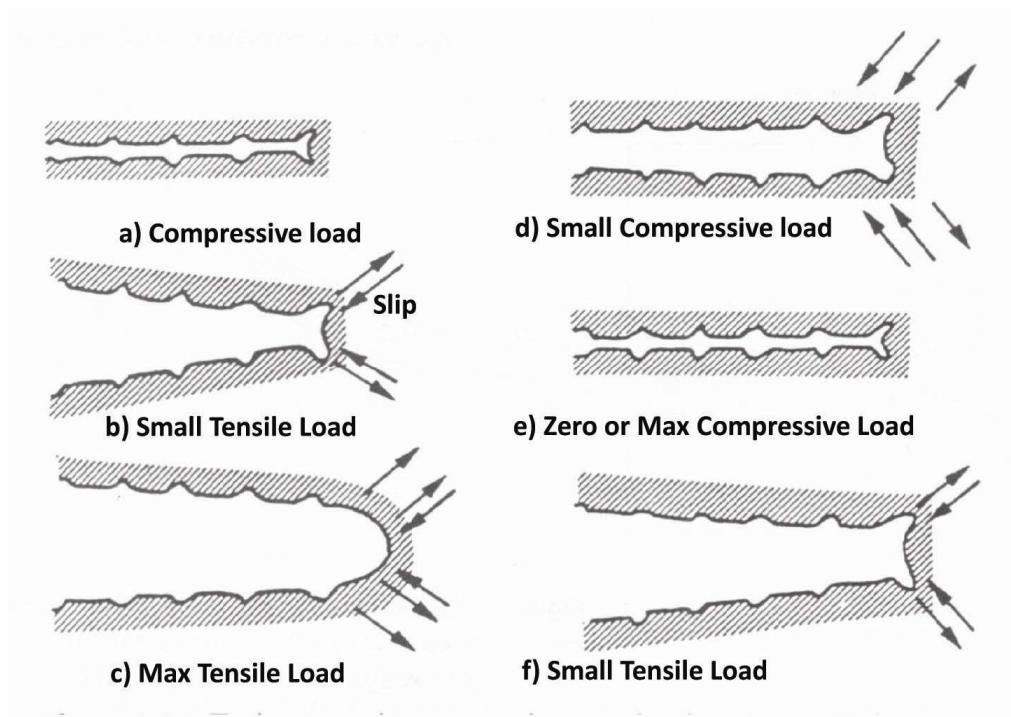


Figure 2-19: Schematic representation showing fatigue crack propagation mechanism (stage II)[18].

### 2.2.7. *Fatigue Fracture Surface and Macro/Micro Features*

A fatigue failure has a manifestation similar to a brittle fracture, as the fracture surfaces are flat and mostly perpendicular to the stress axis with the absence of necking. The detailed fracture features of a fatigue failure are different, however, from a static brittle fracture as a result of the three stages of development (Figure 2-20-a) [15, 18].

Stage I is the initiation of one or more microcracks due to cyclic plastic deformation followed by crystallographic propagation. These initial microcracks grow and join together. Stage I cracks are not normally visible to the naked eye. Progress from microcracks to macrocracks represents Stage II. In this stage a parallel wave-like fracture surface is formed. This surface can have wavy dark and light bands. These bands are called beach marks, clamshell marks, arrest lines, or conchoidal marks the term “Beach marks” is the most widely used. During cyclic loading, opening and closing of the cracked surfaces, rubbing together, changes in the level or frequency of loading and the corrosive or oxidative nature of the environment all lead to the beach mark appearance. One beach mark can contain thousands of striations (Figure 2-20b). These striations can't be seen by naked eye. So, microscopic magnifications between 1000X and 50,000X must be used to view the striations. The striations are formed by a plastic crack tip blunting mechanism during the loading and unloading portion of the fatigue cycle as will be discussed later. Materials that exhibit ductile behaviour often display appreciable striations while they are difficult to observe in high strength materials.

When the remaining material cannot sustain the loads, fast fracture occurs (stage III). Stage III is final fast fracture. The propagation of stage III or unsteady cracks represents a small portion of the overall fatigue life of components. Stage III is related to unstable crack growth as  $K_{max}$  approaches  $K_{IC}$ . At this stage, crack growth is controlled by static modes of failure and is very sensitive to the microstructure, load ratio, and stress state (plane stress or plane strain loading).

A stage III fracture can be brittle, ductile, or a combination of both. A flat and featureless appearance dominates on this stage because of the failed parts tend to rub and slid against each other. Stage III may also develop a fibrous appearance called chevron lines; these point toward the origins of the initial cracks [15-19].

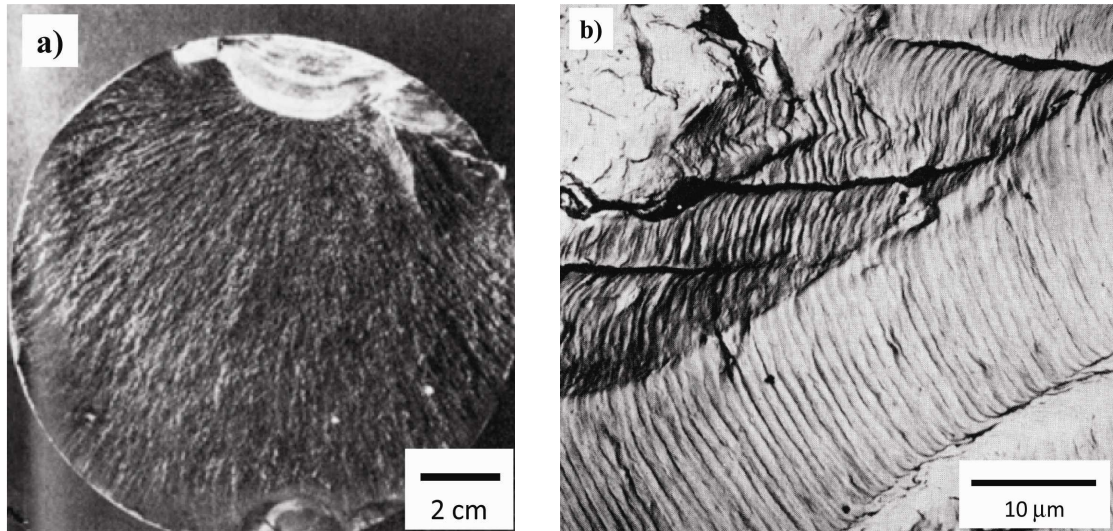


Figure 2-20: a) Typical fatigue fracture surface;, b) Striations [17].

### 2.2.8. Statistical analysis of Fatigue Data

To obtain meaningful engineering data a large numbers of specimens must be tested. Statistical treatment of collected data should follow the fatigue tests.

The two point strategy, the boundary method and the staircase method are methods to obtain the fatigue limit.

#### 2.2.8.1. Two-Point Strategy

In the two-point strategy, the first specimen is tested at a randomly stress level, If the specimen fail then the next specimen is tested at one increment below the first stress level until a stress level that has produces a run-out. At a stress level that produce run-out another specimen tested at a stress level above until the stress level produce failure is reached. After this point is reached, all further testing is concentrated at these two levels[35].

#### 2.2.8.2. Boundary Method

The boundary method starts by testing one randomly chosen specimen at any level of alternating load (Figure 2-21) [35]. If the specimen not fail (i.e. run-out) for  $10^7$  cycles, the next specimen will be tested at higher levels raised stepwise until the specimen fractured before  $10^7$  cycles (or whatever lifetime is chosen). This level, where the specimen fractures, becomes the first tested level. If the first tested specimen fails before  $10^7$  cycles (or whatever lifetime is chosen), the next specimens will be tested

stepwise on lower levels of alternating load, until the opposite event (no fracture). For the next level of alternating load, the distance  $D$  (Figure 2-21) has to be estimated. It is given by:

$$\text{If } r \leq 0.5n \quad D = \left(1 - \frac{r}{n}\right) \cdot d \cdot S_a \quad (2-12)$$

$$\text{If } r \geq 0.5n \quad D = \left(-\frac{r}{n}\right) \cdot d \cdot S_a \quad (2-13)$$

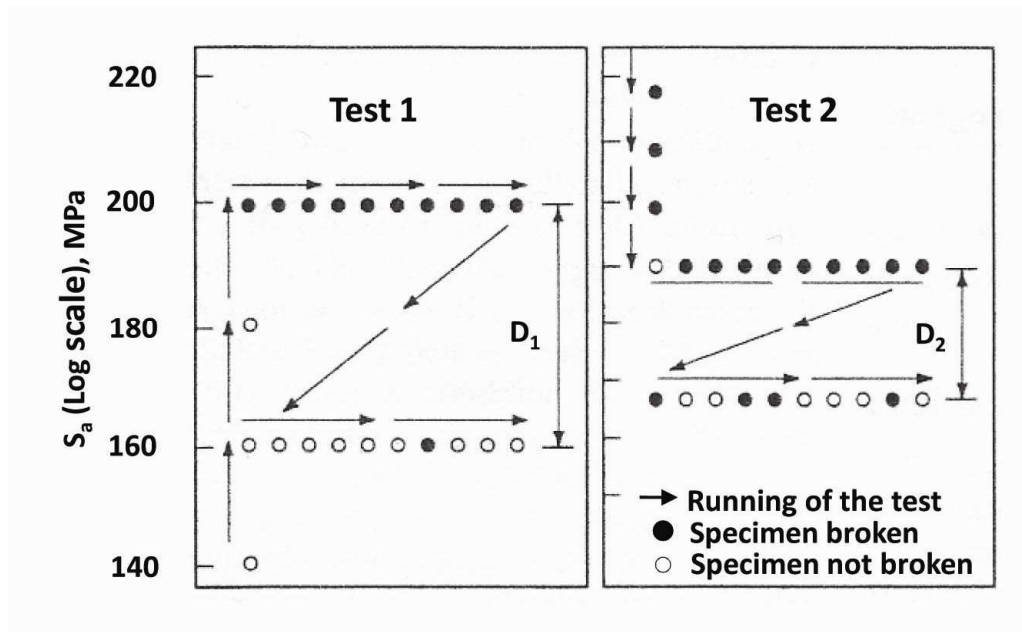


Figure 2-21: The way of running two tests using the boundary technique [35].

Where  $r$  is number of broken specimens,  $n$  is number of tested specimens,  $S_a$  is the alternating load of the first tested level and  $d$  is the estimated size of the transition region according to Table 2- 3. The boundary method was used in the previous work and it was not suitable method for determining the bounds of cyclic stress amplitude for 10% and 90% probability of failure. It showed that the scatter in fatigue limit was insignificant due to the reproducibility of surface finish [36].

Table 2- 3: Values  $d$  and  $m$  for use with the boundary method [35].

Factor	Notched specimen	Smooth specimen	Simple parts	Parts like bolts
$d$	0.05 – 0.15	0.1 – 0.3	0.2 – 0.4	0.4 – 1.2
$m$	1 – 1.2	1 – 1.2	1.4 - 2	2-3.2 - ?

### 2.2.8.3. Staircase Testing

Staircase testing is used widely. It is defined in British standard (BS 3518-5) [11]. In a series of tests, an initial estimate of the fatigue limit and a stress step size (increment)

are selected. The first specimen is tested at a stress level equal to the estimated mean value of the fatigue strength. If failure occurs before the selected lifetime (typically  $10^7$  cycles), the next specimen is tested at one increment below the first stress level. If there is no failure (run-out) at the first stress level, then the next test is at the stress one increment above the first level. This procedure is continued for all the test specimens to be tested, the stress level for each test dependent on the previous result. Statistical methods, described below, are then used to determine the average endurance limit as well as the standard deviation [11]. The staircase method was used in this project, so its analysis is presented in more detail in the next section.

#### 2.2.8.4. Analysis for the staircase method

The analysis the for staircase method is as follows [11]. The analysis uses the less frequent occurrence in the test results, i.e. if there are more failures than run-out, and then the number of run-out is used. The mean fatigue strength is given by:

$$m = S_o + d \left( \frac{A}{n} \pm \frac{1}{2} \right) \quad (2-14)$$

Where  $S_o$  is lowest stress;  $d$  is stress increment;  $n$  is total of less frequent events ( $n = \sum_{i=0}^Z ni$ );  $A = \sum_{i=0}^Z in_i$ ;  $ni$  is number of the less frequent events at  $i$ -th stress above  $S_o$ ;  $i$  is coded stress level ( $i = 0$  for  $S_o$ );  $z$  is number of stress levels above  $S_o$ . If the less frequent event is a run-out,  $+ 1/2$  is used and  $-1/2$ , if the less frequent event is failure (Figure 2-22).

The standard deviation is given by:

$$S = 1.62d \left\{ \frac{B \sum_{i=0}^Z n_i - A^2}{n^2} + 0.029 \right\} \quad (2-15)$$

But only when

$$\frac{B \sum_{i=0}^Z n_i - A^2}{n^2} \text{ is greater than } 0.3. \quad \text{or } S = 0.53d \quad (2-16)$$

$$B = \sum i^2 n_i \quad (2-17)$$

The standard error of the mean estimated from experimental results is:

$$S_x = \frac{GS}{\sqrt{n_r}} \quad (2-18)$$

Where  $n_r$  is the number of test specimens tested;  $G = 1$  approximate.

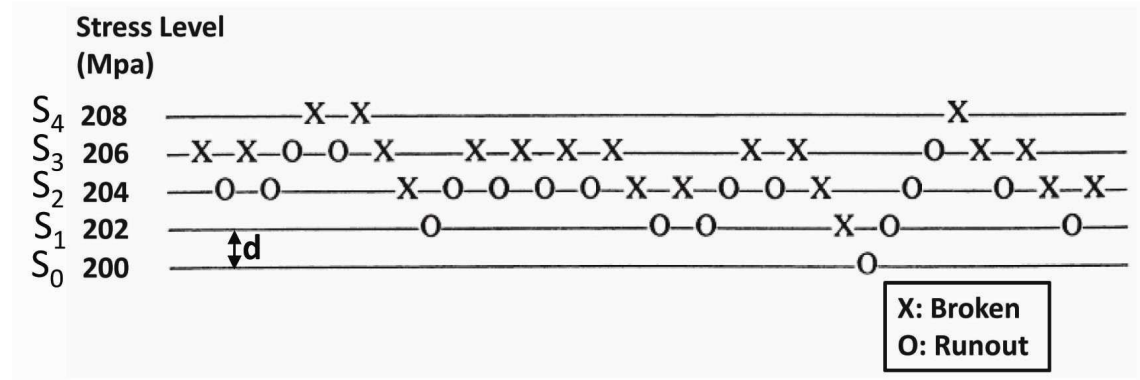


Figure 2-22: Schematic to show the staircase method [11].

### 2.2.9. Effect of Cyclic Deformation on near surface microstructures of austenitic stainless steels

This research is concerned directly with the effects of surface machining on the high cycle fatigue resistance of austenitic stainless steels. There is a limited literature in this field.

Altenberger et al. [37] conducted Tension/compression fatigue tests under stress control without mean stresses ( $R = -1$ ) on cylindrical specimens of the austenitic stainless steel AISI 304 that were shot peened or deep rolled with different peening intensities, and rolling pressures, respectively.

They found that a complex near surface microstructure, consisting of nanocrystalline regions, deformation bands and strain induced martensitic twin lamellae with high dislocation densities in the austenitic matrix of a surface-rolled type 304 austenitic stainless steel. The quantity and depth of martensite varied with surface processing, and extended throughout the plastically strained region. Low cycle fatigue was shown to increase the martensite content [37].

M. Topic and et al. [38], investigated the fatigue behaviour of AISI 304 stainless steel as a function of drawing strain. The specimens were all annealed at 1050 °C for 15 min and afterwards water cooled. They were then repeatedly drawn through different lubricated tungsten-carbide dies at a speed of 50 mm min<sup>-1</sup> without intermediate annealing. All specimens were drawn strains which ranged from 0.09 to 0.585 and the volume percentage of strain-induced martensite for each case were obtained by X-ray diffraction analysis which ranged from 8 to 36 % respectively. All different strained

specimens were subjected to three-point fatigue testing carried out under load control at room temperature.

In the specimens with a previously developed amount of martensite of less than 20%, the fatigue limit was higher than that with a martensite content of more than 20%. Above the fatigue limit, crack initiation became easier with increasing amounts of martensite above 20%, crack propagation rates also increased due to decreasing ductility and the fatigue life of the material decreased.

C. Muller-Bollenhagen [39], studied the very high cycle fatigue behaviour of AISI 304 austenitic stainless steel and the effect of strain-induced martensite for both shot peening and deep rolling. The fatigue tests were conducted under axial tension-compression loading with a stress ratio of  $R = -1$  in ambient air. In the case of deep rolled surfaces, the martensitic layer was increased by fatigue-induced martensite formation. He found that more than 50% of the initial compressive residual stress was relaxed after LCF loading. He concluded that martensite, whether formed through cyclic or monotonic plastic deformation, strongly influences the fatigue limit and causes a strong sensitivity of the fatigue limit to the test conditions. It was found that increased fatigue limit. The fatigue limit below 19% was higher than that above. He attributed this to the compressive residual stresses which develop after phase transformation at the plastic zone of the crack tip.

K. Masaki [40], investigated crack initiation and propagation behaviour during the rotating bending fatigue test of hard shot peened type 316L austenitic stainless steel in high cycle fatigue. The compressive residual stress decreased generally under repeated loading but was not fully relaxed. The crack was developed in the axial direction and continued to propagate. Circumferential cracks formed from axial cracks and the propagated rapidly to fracture.

Duyi Ye et al. [41] studied the low-cycle fatigue (LCF) behaviour of SUS304-HP austenitic stainless steel systematically using tension-compression cycling under fully reversed total strain amplitude control conditions at room temperature. SUS304-HP is an improved version of type 304 austenitic stainless steel. They found that with increasing total strain amplitudes the slip band density increased and the dislocation structure changed from a planar array to a more cellular-like structure. Cyclic deformation-induced austenite/martensite transformation was observed at higher cyclic strain amplitudes.



S. Ganesh [42] studied the effect of prior cold work on the room temperature low-cycle fatigue behaviour of austenitic stainless steel. Strain-controlled low-cycle fatigue tests were carried out on AISI 304LN austenitic stainless steel specimens that were cold worked by swaging to different levels (10 to 30% reduction in area) prior to testing. He found that with an increase in the percentage of prior cold work, there was a reduction in the transition fatigue life (the life at which elastic and plastic components of strain are equal), i.e., the stronger prior cold-worked material exhibited enhanced lives at lower total strain amplitudes, as crack initiation occupies a significant portion of the fatigue life at these (low) total strain amplitudes. A decreasing transition fatigue life can be associated with increasing crack initiation resistance. The stronger 30% prior cold-worked material resisted the imposed strain elastically on the basis of its strength, while the ductile 10% prior cold-worked material resisted the strain plastically on the basis of its greater ductility.

In summary, in both regimes (HCF and LCF), the presence of stress concentrations such as, sharp corners, holes or notches, make the material response to cyclic loading strain controlled. In high cycle fatigue regime, the residual stresses show little relaxation due to the low stress amplitude.

It can be seen from the previous discussion that low cycle fatigue resistance increases the martensite amount. In the low cycle fatigue regime, there is an optimum volume fraction of deformation induced martensite in austenitic stainless steels of about 20%. In the case of low cycle fatigue plastic deformation takes place in each cycle.

### **2.3. Short Fatigue Cracks**

Small fatigue flaws (of size range from a fraction of a millimetre to several millimetres) have attracted the attention of material scientists and researchers since the growth rates of such cracks can be significantly greater than the corresponding rate of long flaws for the same value of applied stress intensity factor range,  $\Delta K$ , and they also grow at values of  $\Delta K$ , below that of the threshold values,  $\Delta K_{th}$  of the long cracks (Figure 2-23). This abnormal behaviour was first shown by Pearson [43].

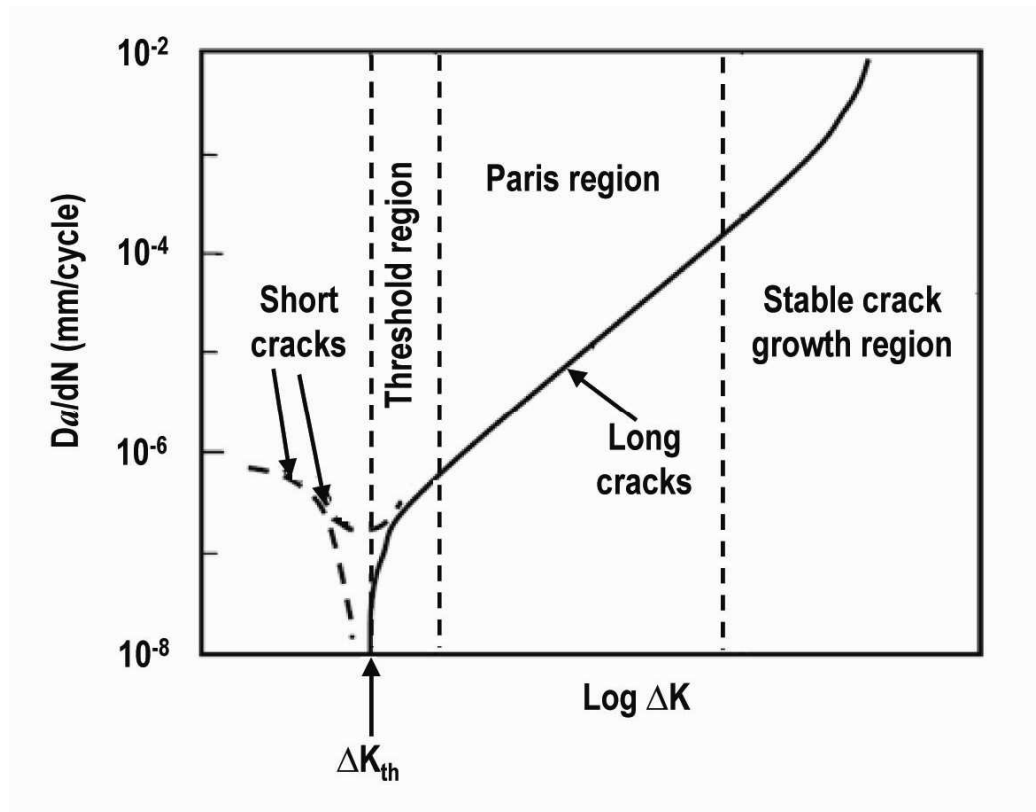


Figure 2-23: Typical fatigue crack growth rates ( $da/dN$ ) for long and short cracks as function of stress intensity factor range  $\Delta K$  [4].

Stolarz, J [44] reported that the regime of microcrack propagation prevails during 65-90% of the fatigue life, while only the last 5-10% of the fatigue life can be considered as to be determined by long cracks and treated by linear elastic fracture mechanics (LEFM). The remaining 5-25% is determined by the mechanisms of crack initiation. Hence, using the data of long cracks in fatigue lifetime calculations of engineering components, can lead to considerable overestimates in the fatigue lives (Figure 2-24) [45].

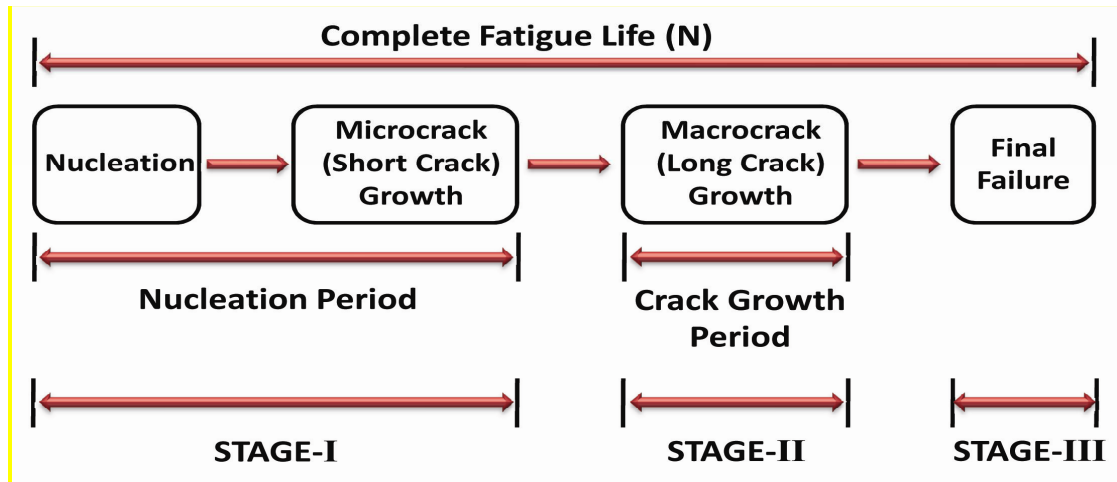


Figure 2-24: Schematic showing the period of total cycle fatigue life [45].

Suresh and Ritchie [18, 46] defined regimes of microstructurally short cracks, mechanically short cracks, physically short crack and long cracks. Microstructurally short cracks are the cracks that interact with local microstructural features (grain, phase boundaries, precipitates and pores). Once the crack length exceeds several grain diameters, the strong influence of microstructure disappears, and crack propagation is driven by the plastic zone ahead of the crack tip. These cracks are termed mechanically short cracks. A crack of the order of 1 mm in length is termed a physically short crack when the size of the plastic zone at the crack tip is negligibly small as compared to the crack length, and hence the concept of LEFM is applicable. Fatigue cracks exhibit apparent anomalies in propagation rate below a certain crack size as a result of the dependence of environmental stress corrosion fatigue effects on crack dimensions; these flaws are referred to as chemically small cracks.

In small cracks, the crack tip driving force is different from that of a long crack. So, linear elastic fracture mechanics (LEFM) is inadequate to describe the short crack driving force. This limitation of LEFM is due to the fact that the elastic stress field can not accurately describe the high strain fields at the tip of small cracks in highly stressed materials [5]. The ratio of the plastic zone size, to the crack length is different for the two cases. For long crack under  $\Delta\sigma < \Delta\sigma_{FL}$  loading, the plastic zone size is less than the crack length, whereas for small cracks the plastic zone size and crack length are comparable. To use LEFM accurately the plastic zone should be small, typically less than one-fiftieth of the crack length [6].

### 2.3.1. *Short Crack Regimes*

Figure 2-25 shows how crack growth behaviour is affected by crack size  $a$  and applied load. Figure 2-26 shows the typical behaviour of small initiated surface crack,  $a > 3 \mu\text{m}$ , at a nominal stress slightly above the fatigue limit of material in fully reversed condition [47]. The initiated crack propagates through several surface grains in a shear mode at an angle of about 45 degrees with respect to the applied stress axis (stage I).

With increasing crack length or increasing  $\Delta K$ , the effect of normal stress becomes more significant and force the crack to propagate in a direction perpendicular to the applied stress by operating various slip systems (stage II) [5].

The crystallographic slip system and constraint of adjacent grains play important roles in the growth of a stage I crack and its transition from stage I to stage II cracking. In stage I, crack growth is influenced by the microstructure, the grain boundaries and other microstructure features. The cracks in this stage are termed microstructural or crystallographic small cracks [5].

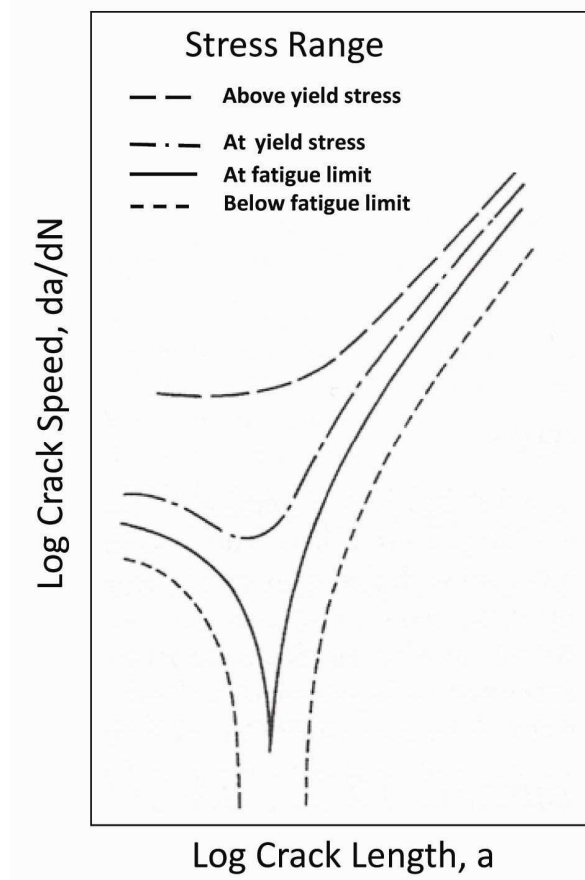


Figure 2-25: A schematic shows small crack behaviour as a function of applied cyclic stress [47].

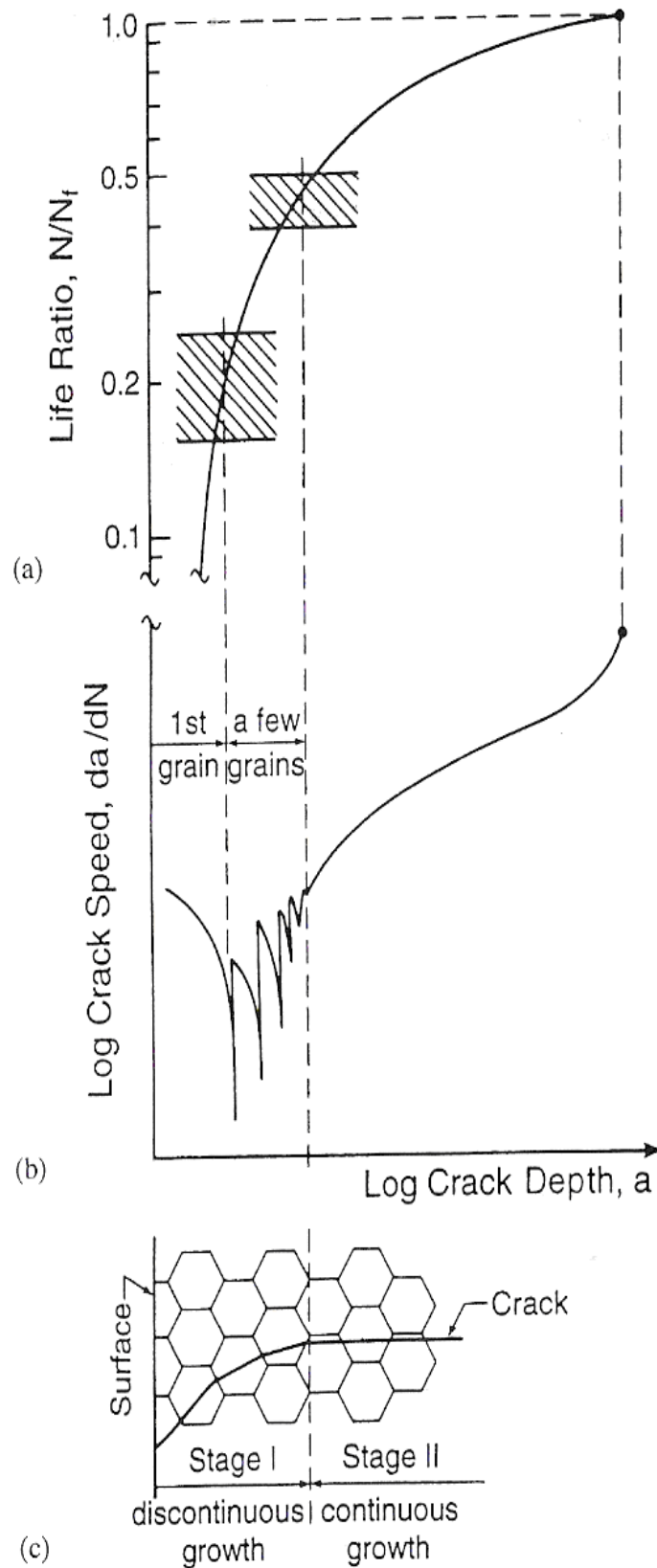


Figure 2-26: A schematic illustration of small crack growth and transition to long crack. (a) relative life ratio spent at each stage; (b) Crack growth rate versus crack depth; (c) transition from a microstructurally small crack to a physically small crack and eventually a long crack [47].

### 2.3.2. Short Crack Growth

As shown in Figure 2-27 several different microstructural barriers to crack growth, of spacing  $d_1$ ,  $d_2$  and  $d_3$ , can exist in a single material such as ferritic-pearlitic banded structure or as several grain diameters [5]. Also, it can be seen in both figures that as the crack length increases in the range  $0 < a < d$  for a constant stress or strain range, the crack growth rate decreases and become zero as the crack arrests (fatigue limit condition). In Figure 2-28, the cyclic interval x-y, represents the period of arrest. Just above the fatigue limit the period x-y will gradually decrease as the stress range level increases.

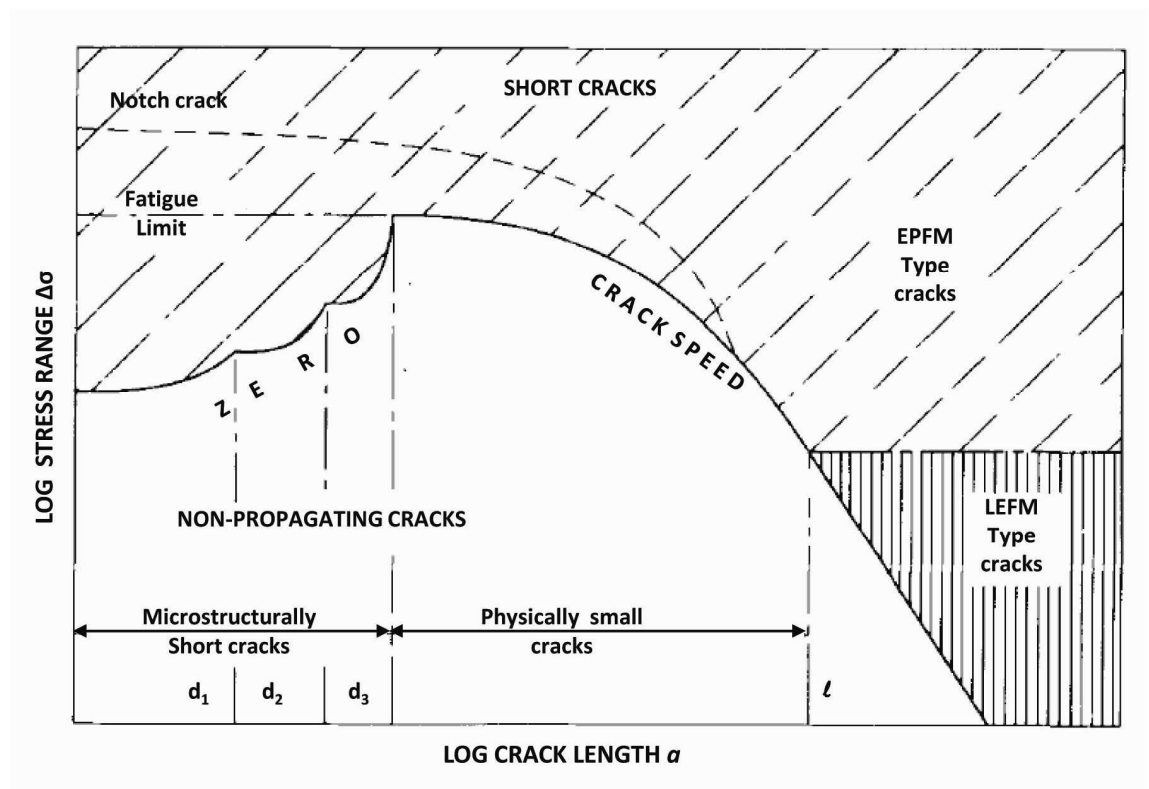


Figure 2-27: Three regimes of short crack behaviour (cross wide range of materials)[5].

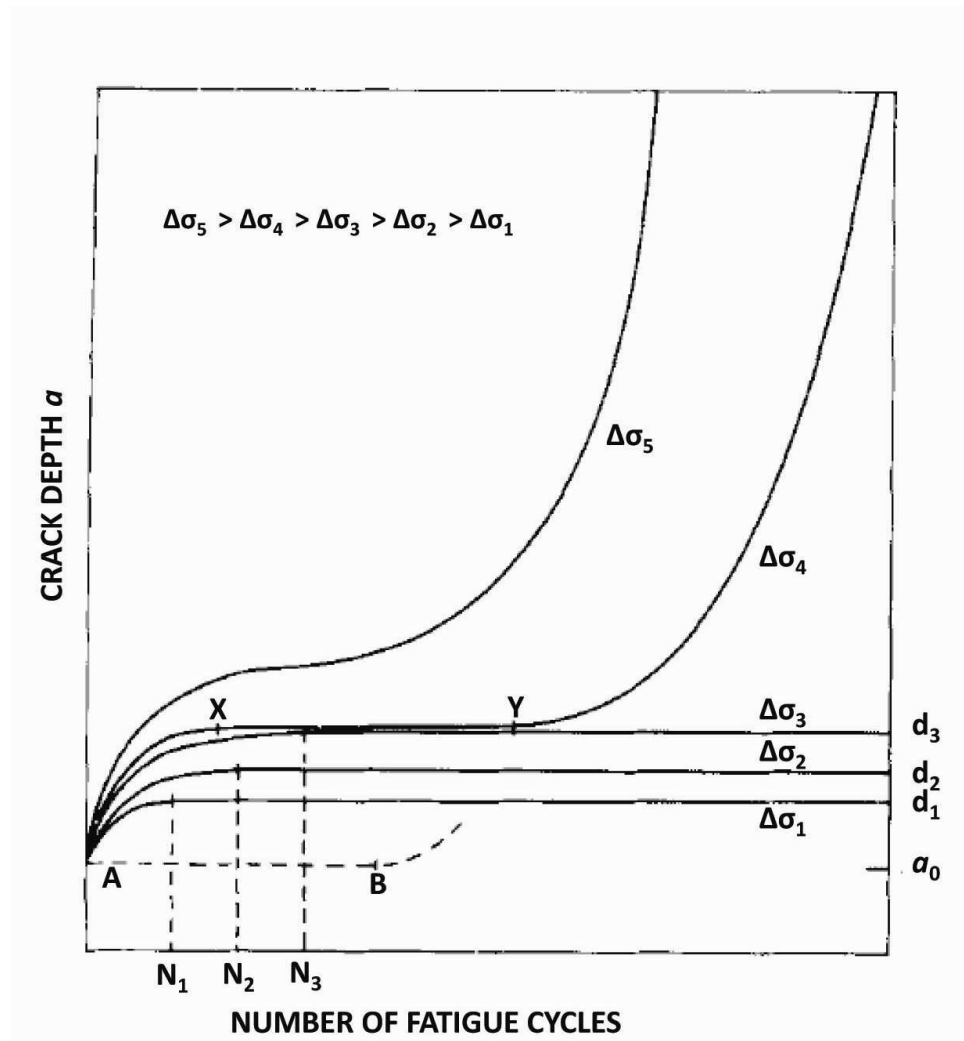


Figure 2-28: Crack growth development for constant stress ranges [5].

### 2.3.3. Microstructural Barriers

Detailed understanding of how an advancing crack interacts with the microstructure at multiple length scales is required to design microstructures for damage tolerance. It has been proposed that the arrest of cracks takes place when the dislocation pile-up (representing the crack plastic zone) is unable to overcome the constraint provided by dominant microstructural barriers, such as grain boundaries, twin boundary, or pearlite zone [5].

Plastic deformation at the crack tip occurs during the advance of crack propagation in metals and alloys. Plastic deformation by dislocation motion takes place when the critical resolved shear stress on a slip plane in a favourably oriented grain is exceeded. The dislocations pile up along the slip band as a result of hindrance of transition of plasticity. This hindrance might occur because of a large misorientation between the neighbouring slip systems. This mechanism is shown in (Figure 2-29). In the adjacent

grain, the stress increases at dislocation source due to pile up of dislocations along a slip band. Subsequently, when the critical stress is exceeded, slip is activated in the neighbouring grain.

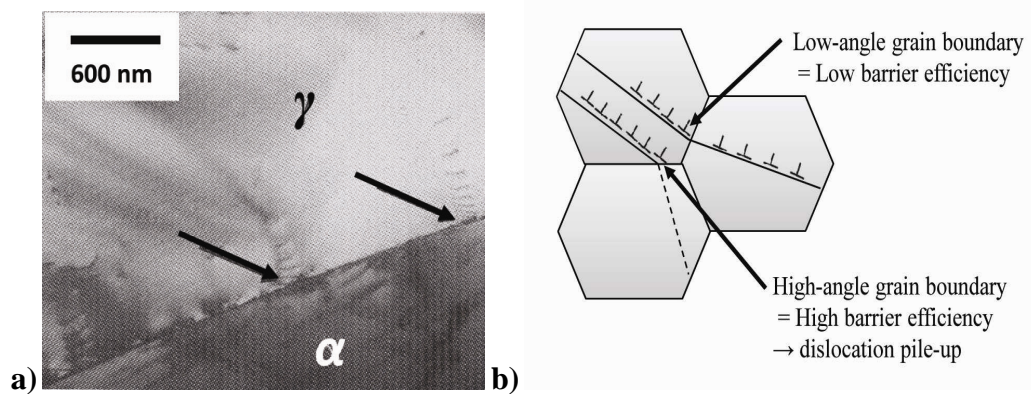


Figure 2-29: a) Transition electron micrograph of dislocation pileup at a ) phase boundary in AISI F51 duplex steel after cyclic deformation; b) Schematic shows the relationship between the barrier strength of a grain boundary and misorientation between neighbour [22].

As the distance between crack tip and adjacent grain boundary decreases, the dislocation density along the slip band increases and the dislocations become less mobile. This leads to a higher resistance to the crack advance (i.e. crack propagation rate decreases). When the neighbouring grain becomes plastically deformed and the slip is activated, cyclic slip displacement on the respective slip planes is promoted and leading to increase in the crack propagation. The consequence of this mechanism is an oscillation in the crack propagation rate (Figure 2-30). This behaviour has been observed for microstructurally short fatigue cracks in several studies [48] and this represents the basis of the short crack model of Navarro and de los Rios [49].



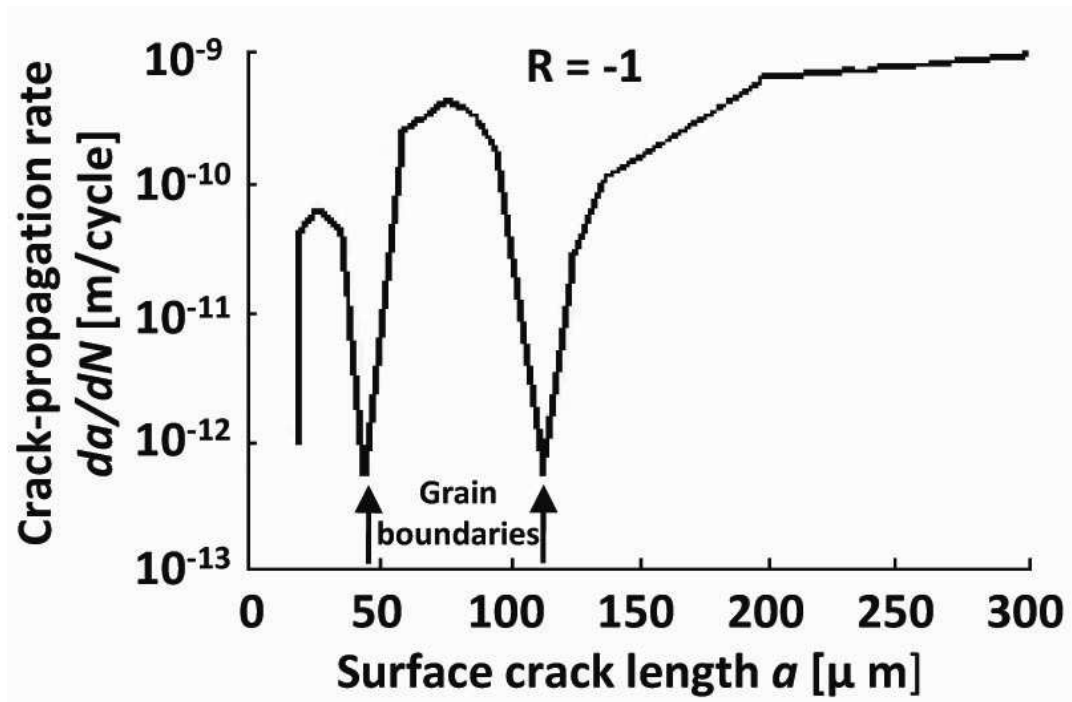


Figure 2-30: Oscillation in the crack propagation rate (2024 T3 aluminium alloy); minima are due to the barrier effect of grain boundaries [22, 50].

The grain boundary forms an effective barrier against fatigue crack propagation when the angle between the slip systems of neighbouring grains is large. If adjacent slip systems are lying in the same plane (low angle grain boundaries) direct slip transmission is possible [51] and crack propagation rate remains constant (Figure 2-31) [50].

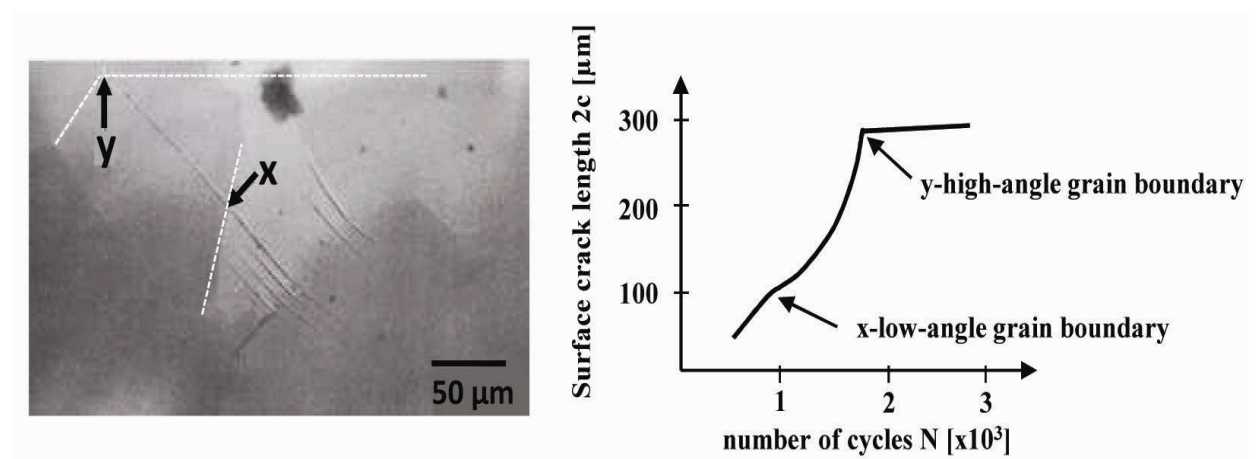


Figure 2-31: Slip-band cracks in the  $\beta$ -titanium alloy (loading direction:  $\leftrightarrow$ ) and crack length vs. number of cycles for the crack marked by arrows [50].

Zhai et al. [52, 53], in a study on fatigue crack propagation in the Al alloy, investigated the effect of the twist and tilt angles of the crack plane deflection at a grain boundary on

the path and the growth of a short crack. They concluded that twist misorientation has a more profound influence on crack resistance than the tilt misorientation. Figure 2-32 illustrates the tilt and twist misorientation relationship between two neighbouring grains containing a slip band crack and two activated slip planes.

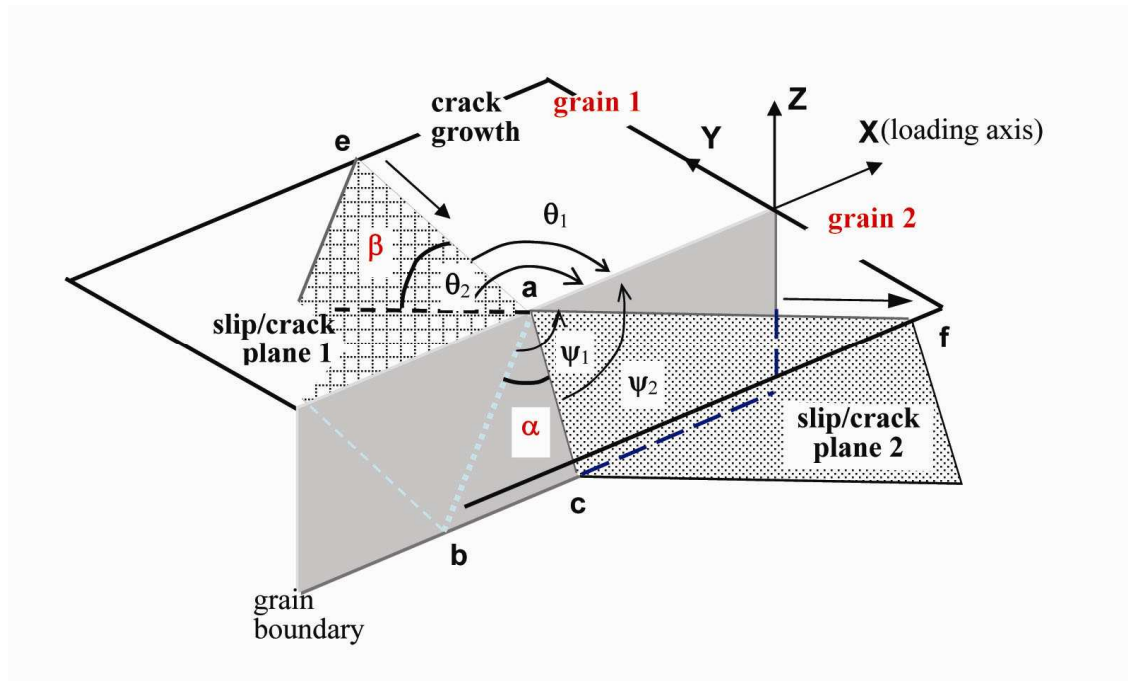


Figure 2-32: crack propagation along slip bands and across a grain boundary [52].

Several studies investigated the influence of the grain size on the early crystallographic crack propagation (microstructurally short stage I cracks) [54, 55]. According to these studies, large slip length in coarse grained materials makes the transition of the plastic zone from the cracked grain to the neighbouring un-cracked grain easy. The barrier effect of the grain boundaries decreases even for high crystallographic misorientation. The consequence is a lower fatigue limit while the decreases and arrests in growth rate due to the grain boundaries and crack deflections were more remarkable in fine grained materials [54, 56].

Zhong et al. [57] examine the effect of martensite/retained austenite (M/A) at low-angle grain boundaries (*LAGB*) on the resistance to crack growth in high strength pipeline steel. Whereas a *LAGB* alone is insufficient to hinder crack growth, the existence of the M/A acts as an effective barrier to dislocation motion and resistance to crack growth.

In the presence of multiple phases, the behaviour of the crack will be different in the two phases. Tang et al. [58] showed this by studying the development of dislocation

structure in the plastic zone ahead of a crack tip in a duplex stainless steel deformed in the TEM. They found that the cracks grow in straight manner and the plastic zone is broad because of the ability of the dislocations emitted from the crack tip to cross slip, in the austenite phase, the crack grows in a zigzag manner as that dislocations are confined to narrow strips and form inverse pile ups.

#### 2.3.4. Crack Closure Effect

The premature contact of the crack faces during unloading from tension is known as crack closure. Only the part of the fatigue cycle when the crack is open contributes to crack propagation. The crack closure effect was first proposed by Elber [18]. If the crack is perfectly sharp and behaves completely elastically, the crack will be closed when unloading from tension is complete, i.e.,  $\sigma = \sigma_{min}$ .

Taylor (1988) [59] reported five types of crack closure, namely, plasticity induced closure, oxide-induced closure, roughness-induced closure, viscous fluid-induced closure and phase transformation-induced closure. The basic idea of these mechanisms is presented schematically in Figure 2-33.

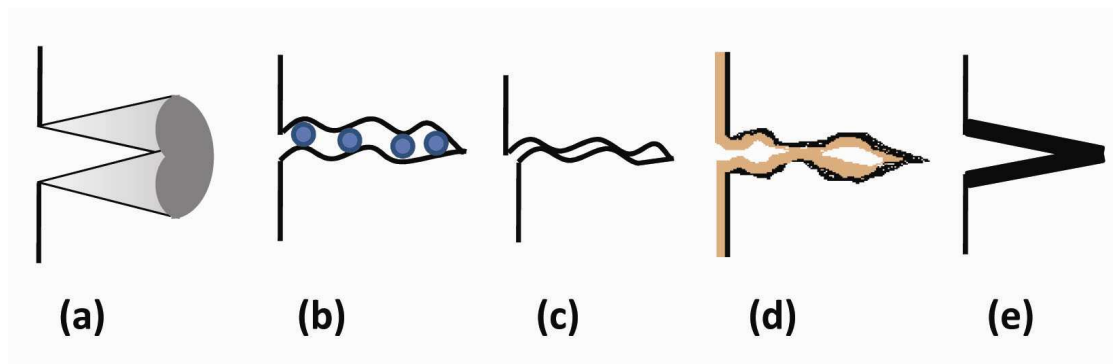


Figure 2-33: General crack closure mechanisms: (a) plasticity-induced crack closure, (b) Oxide-induced closure, (c) Roughness-induced closure, (d) Viscous fluid-induced closure, (e) Phase transformation-induced closure [18].

When the crack closed ( $\Delta K_{cl}$ ), the range of stress intensity factor  $\Delta K$  is reduced from  $(K_{min} - K_{max})$  to  $\Delta K_{eff} (K_{cl} - K_{max})$ . The plastic deformation helps to partially close the crack surfaces such that the crack will close and open at a stress level higher than  $\sigma_{min}$ . This effect results in a smaller effective stress intensity factor range,  $\Delta K$ , value and consequently, a smaller crack growth rate. Figure 2-34 shows the effective stress intensity factor  $\Delta K_{eff}$  for small and negative stress ratio R. The effect of crack closure

becomes obvious at the instance that the fatigue cracks can grow only when they are completely open. Cracks with short dimensions are less affected by closure phenomenon and will grow faster than corresponding long cracks subjected to the same stress intensity factor,  $\Delta K$ . In general, crack closure effects increase with crack length.

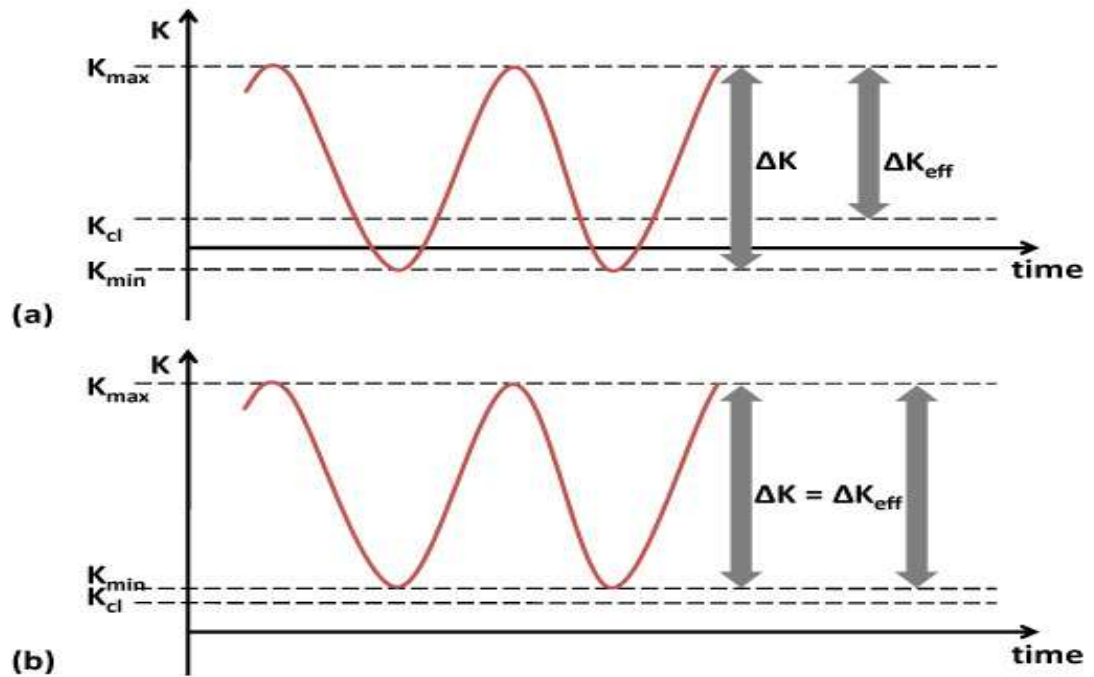


Figure 2-34: illustrates the effect schematically, comparing load and crack opening displacement during a typical cycle [22].

Plastic deformation at the crack tip takes place during the advance of crack propagation in metals and alloys. The size of the plastic zone ahead of the crack tip increases, as a result of increase in the range of the stress intensity factor  $\Delta K$  with increasing crack length and a constant stress amplitude (i.e.  $\Delta\sigma/2 = \text{constant}$ ). The crack tip plastic zone at all stages of advancing fatigue crack forms an envelope that contains all the previous plastic zone sizes and its presence in the crack wake is a cause of crack closure behaviour (Figure 2-35).

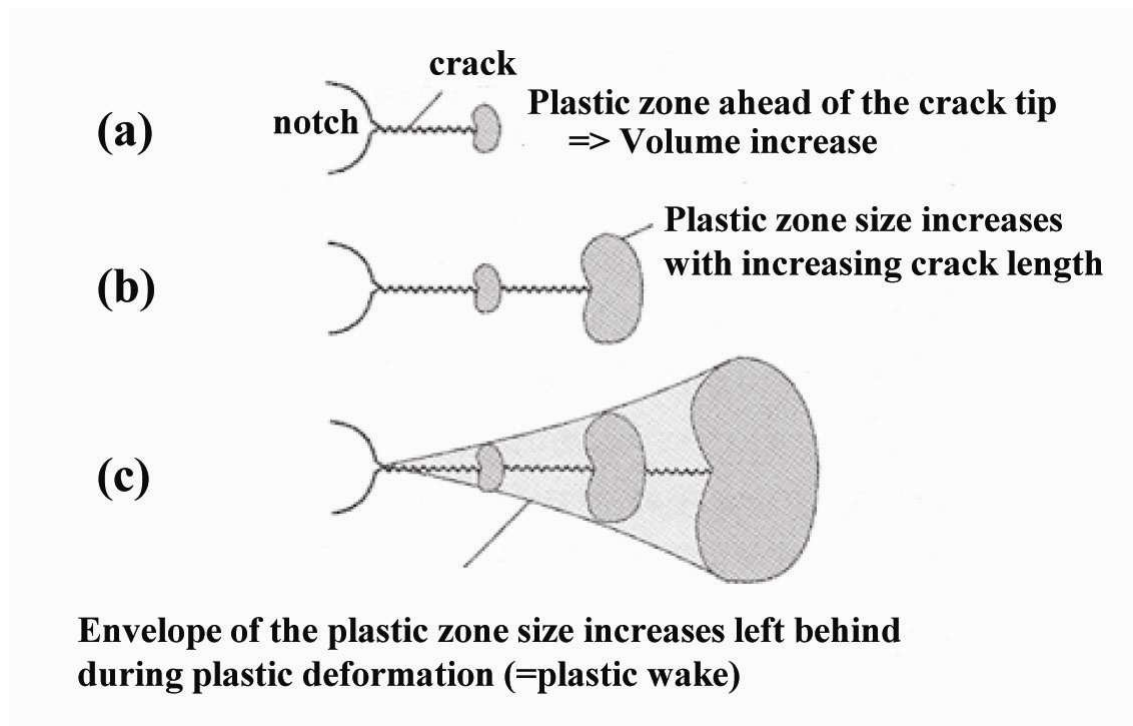


Figure 2-35: Schematic representation of the mechanism of fatigue crack closure; (a-c) development of a plastic wake [22].

Under plane stress conditions, local necking of the component takes place as a result of stretching in the plasticity zone at the crack tip. This leads to formation of a wedge along the both sides of the crack when the crack propagates (Figure 2-36). Consequently, premature contact of the crack faces will occur. This mechanism is known by plasticity-induced crack closure [22].

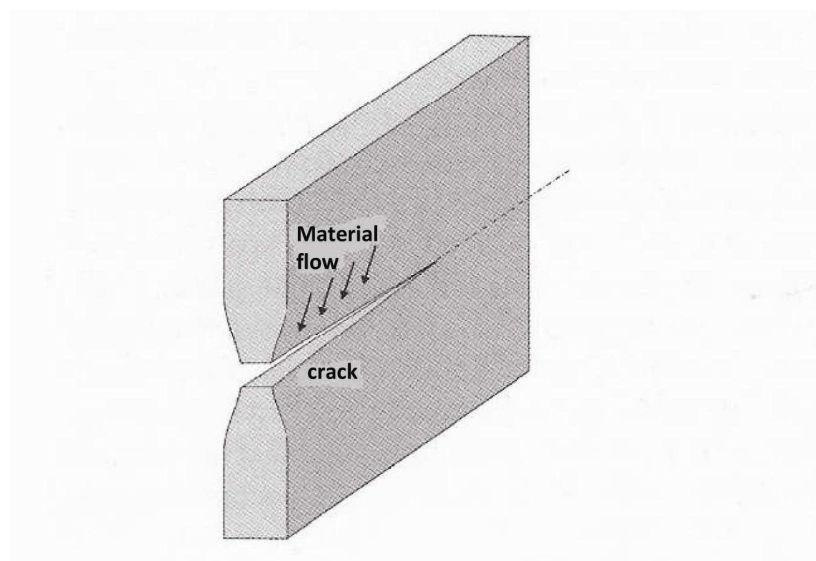


Figure 2-36: Mechanism and material flow of plasticity-induced crack closure [22].

#### 2.4. Short Fatigue Crack Models

As discussed in the previous sections, short fatigue cracks have unique characteristics compared with long fatigue cracks in terms of their crack growth and threshold behaviour. Many studies have been carried out to model short crack growth rate behaviour (e.g. [5, 7, 60-65])

The Kitagawa-diagram was one of the first ways to characterize the threshold behaviour of the short fatigue cracks quantitatively [66]. As shown in Figure 2-37, the threshold stress is plotted versus the crack length ( $a$ ). As crack length changes, the threshold stress profile changes. The Kitagawa-diagram assumes that below a certain crack length  $a_1$  the non-propagation criterion is defined by the fatigue limit.

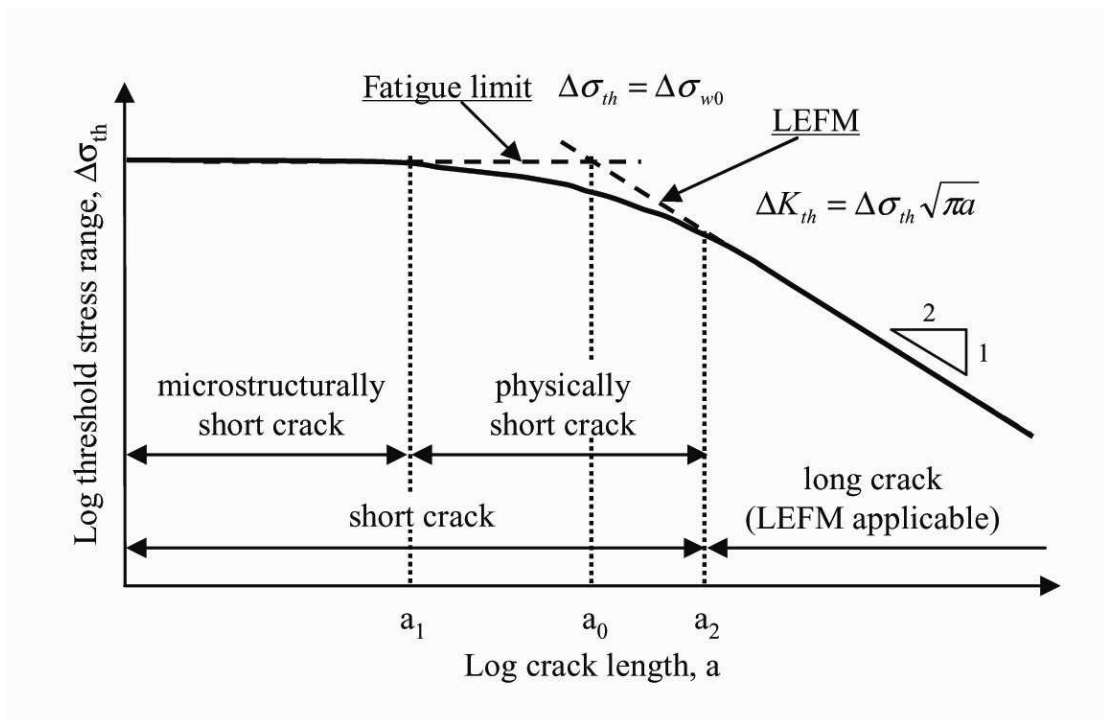


Figure 2-37: Schematic diagram of Kitagawa–Takahashi diagram[66].

Crack lengths over  $a_2$  represent the long crack region. In this region, the threshold stress profile shows a smooth decrease to straight line of slope  $-0.5$  on the logarithm plot. The linear elastic fracture mechanics (LEFM) approach is applicable as follows:

$$\Delta\sigma_{th} = \frac{\Delta K_{th}}{Y\sqrt{\pi a}} \quad (2-19)$$

Where:  $\Delta K_{th}$  : Threshold stress intensity for long crack.

$Y$  : Dimensionless (depends on geometry and mode of loading).

The region between  $a_1$  and  $a_2$  represents physically short crack fatigue cracks. A continuum elastic-plastic mechanics approach is applicable.

A simple equation for the smooth transition from the fatigue limit controlled regime to the  $\Delta K_{th}$  controlled regime of the Kitagawa diagram, depending on  $a_0$ , was proposed by Elhaddad [18]:

$$\Delta K = \Delta\sigma_{th}\sqrt{\pi(a + a_0)} \quad (2-20)$$

The crack of length  $a$  behaves as if it had a length  $a+a_0$ , which has the long crack threshold value.

As the crack length goes to zero, the threshold stress goes to the fatigue limit of the material.

$$\Delta K_{th} = \Delta\sigma_{wo}\sqrt{\pi a_0} \quad (2-21)$$

At any effective crack length  $(a+a_0)$ , the threshold stress range become:

$$\Delta K_{th} = \Delta\sigma_{th}\sqrt{\pi(a + a_0)} \quad (2-22)$$

This model can give the threshold stress profiles in the physically short fatigue crack regime in the Kitagawa-diagram.

Several crack growth models have been proposed to describe the short fatigue crack propagation, taking into account the microstructural effect on the growth behaviour.

Tanaka and Mura [67] modelled fatigue crack initiation due to planar-slip irreversibility on the basis of continuously distributed dislocations. They assumed that dislocations

pileup at grain boundaries and consider crack initiation to occur when the stored strain energy of the accumulated dislocations exceeds a certain critical value.

Taira et al. [68] modified the general concept of describing a crack and its plastic zone by any array of distributed dislocations suggested by Bilby, Cottrell, and Swinden (BCS) to quantify the barrier efficiency of grain boundaries.

Tanaka et al. [69], modelled the interacting of the slip band at the tip of a small fatigue crack with grain boundaries for four cases: a slip band not reaching the grain boundary, a slip band blocked by the grain boundary, a slip band propagated into an adjacent grain, and a slip band propagated through one and then blocked by the second grain boundary. The theory for continuously distributed dislocations is used to calculate the crack tip sliding or opening displacement and microscopic stress intensity factor under tensile and shear loading.

Grabowski et al. [70] showed that the oscillating crack propagation in nickel-based superalloys was caused by a sequence of weak and hard barriers. Subsequently, the crack deflects at grain boundaries and within the grain. Their model showed the effects of microstructure on short crack growth rate.

These all consider that the plastic zone is restricted by grain boundaries. All these models are originally based on the Dugdale-BCS models [71].

#### 2.4.1. *The N-R Model*

Navarro and de los Rios [72] developed the so called N-R model of short fatigue crack growth which accounts for the interaction between the crack and the microstructural barriers. In this model the threshold condition is determined by whether or not the friction stress exceeds the strength of the barrier at grain boundary under mode-II loading.

N-R model is based on the concept proposed by Bilby [71] of simulating the crack and the plastic zone by a distribution of dislocations.

The basic concept of the model is that the crack tip plastic zone is blocked at a barrier and remains blocked until slip is activated beyond that barrier. The process of overcoming the microstructural barrier may happen by pushing dislocations through the barrier zone or by unpinning the dislocation source within that zone. Once the plastic



slip is re-activated, the plastic zone spreads to the next barrier, where it is blocked again and the process repeats itself.

Figure 2-38 shows a crack of length  $2a$  crossing a number of grains in a polycrystalline material and having its plastic zone blocked at the  $i$ th microstructural barrier.  $D$  corresponds to the grain size, and the grain boundaries are the only microstructural barriers considered in the material. Therefore,  $D$  represents the mean distance between barriers. The crack itself, its plastic zone, and the barrier zone are modelled by means of a continuous distribution of dislocations, sustaining different frictional stresses. A frictional stress  $\sigma_1^i$  in the crack represents a possible resistance to opening. The plastic zone, which spans from the crack front to the barrier where it is stopped, is subjected to a frictional stress  $\sigma_2^i$ , which represents the resistance to movement of dislocations in such a zone. Finally,  $r_o^i (< D)$  represents the small additional zone of length (i.e. the barrier which represents the mismatch zone between adjacent grains). The frictional stress  $\sigma_3^i$  is the stress acting upon the barrier.

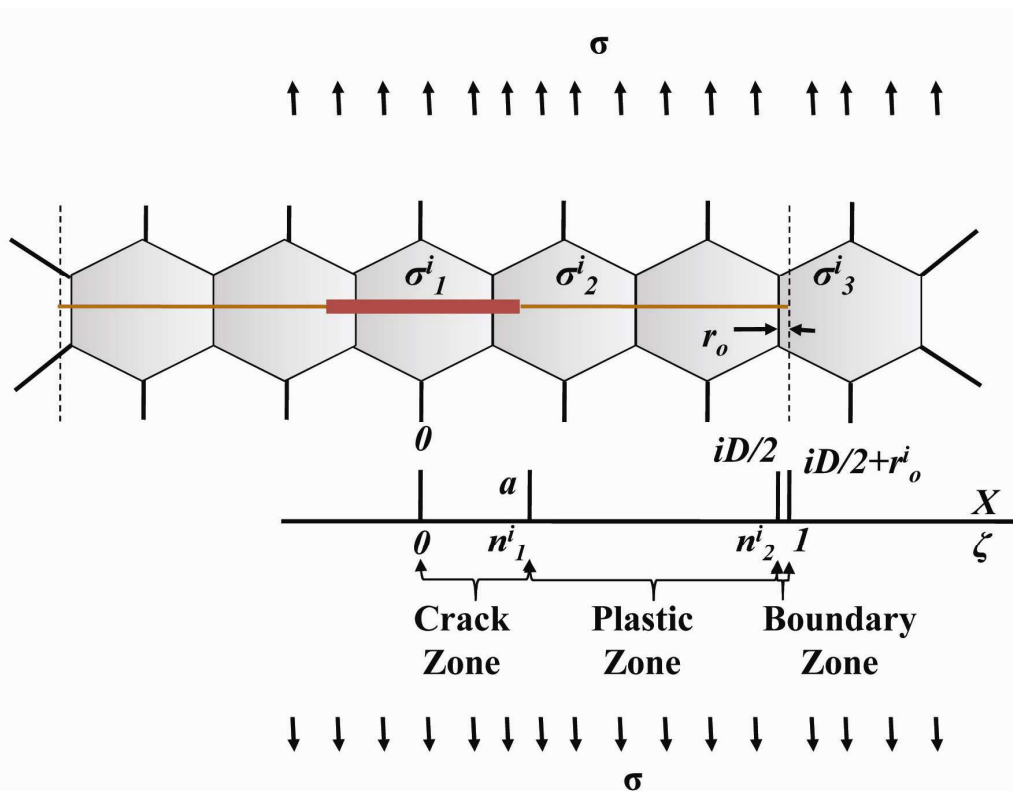


Figure 2-38: Configuration of the three zones of the N-R model in which the equilibrium of forces are considered [72].

As the crack propagates the stress  $\sigma_3^i$  in the barrier zone increases gradually as a result of dislocation pileup. If the stress  $\sigma_3^i$  reaches a value high enough to activate the dislocation sources or to inject dislocations through the mismatch zone, the plastic zone will expand to cover a new whole grain and will be stopped at the next barrier. When this happens, it is said the crack has overcome the microstructural. This can be written as:

$$\sigma_3^i = m_i^* \tau_c^i \quad (2-23)$$

Where  $m_i^*$  is the effective orientation factor at the  $i_{th}$  barrier and  $\tau_c^i$  is the critical stress required to trigger plastic slip in the material.

The minimum applied stress required to overcome the  $i_{th}$  microstructural barrier occurs when the crack front is exactly at a grain boundary ( $a = iD/2$ ), since at this point the stress  $\sigma_3^i$  reaches its maximum value. Such a threshold applied stress can be expressed as [72, 73]

$$\sigma_{Li} = \frac{4}{\pi} m_i^* \tau_c^i \left( \frac{r_0^i}{iD} \right)^{1/2} \quad (2-24)$$

Within the framework of the model described here, the fatigue limit is defined as a stress under which a crack growing within the first grain is unable to propagate into the next grain, and thus it can be calculated by setting  $i = 1$  in eq.(2-24) to give

$$\sigma_{FL} = \frac{4}{\pi} m_1^* \tau_c^1 \left( \frac{r_0^1}{D} \right)^{1/2} \quad (2-25)$$

If the parameters  $r_0^i$  and  $\tau_c^i$  are considered material constants, then eq.(2-24) and (2-25) can be used to obtain the relationship between the threshold stress  $\sigma_{Li}$  and the fatigue limit  $\sigma_{FL}$  of the material. This relationship is a function of the crack length, expressed in a non-dimensional form ( $i= a/(D/2)$ ) and the ratio of the effective crystallographic orientation coefficient  $m_i^*$  for the current barrier and to the effective crystallographic orientation coefficient for the first barrier, according to  $m_1^*$ .

$$\frac{\sigma_{Li}}{\sigma_{FL}} = \frac{m_i^*}{m_1^*} \frac{1}{\sqrt{i}} \quad (2-26)$$

## 2.4.2. N-R Model Developments

### 2.4.2.1. Residual Stresses

N-R model has been applied to engineering problems including notches and shot peening in aluminium alloys. It has been developed further to accommodate these problems. De los Rios [74] studied the effect of shot-peening on crack propagation and fatigue life prediction in AL2024-T351. He used Eq. (2-27) to describe the crack propagation limit conditions for peened and un peened ( $\sigma_I=0$ ) material.

$$\sigma_{arrest} = \frac{m_i}{m_1} \frac{\sigma_{FL} - \sigma_1}{\sqrt{i}} + \sigma_1 \quad (2-27)$$

$$\frac{m_i}{m_1} = 1 + 0.5 \ln(i) \quad (2-28)$$

$m_i/m_1$ : Grain orientation factor.

$\sigma_{FL}$ : Fatigue limit.

$\sigma_I$ : Closure stress.

$i$ : the number of half grains within the crack system ( $i=2a/D$ ).

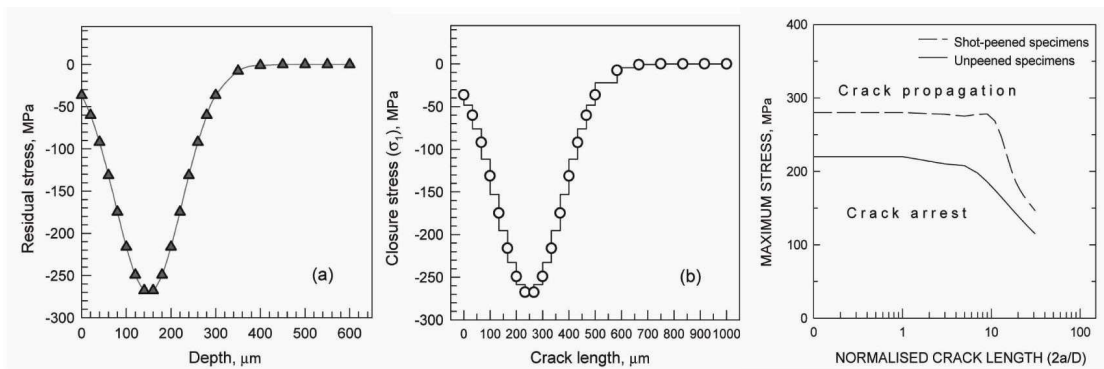


Figure 2-39: Surface stress characteristics. (a) Residual stress profile; (b)  $\sigma_I$  stress distribution; Kitagawa–Takahashi type diagram for unpeened and shot peened specimens of Al 2024-T351, four-point bending,  $R=0.1, D=\text{grain diameter}$  [74].

Figure 2-39 a, b, showed the profile residual stress and closure residual stress for peened material. Figure 2-39-c, demonstrates the crack propagation limit conditions for peened and unpeened materials. The dashed curve describes the crack arrest conditions for peened material. From this curve the effect of residual stress can be seen by an increase in the fatigue limit and an extension of the crack arrest field. Also, both curves

tend to meet at long crack lengths. This can take place when the effect of the residual stress vanishes.

The effect of surface roughness is neglected temporarily and considers only the effect of the closure stress, the smooth specimen fatigue limit,  $\sigma_{FL}^{CL}$ , is obtained by considering that the closure stress is exerted within the first half grain [75].

$$\sigma_{FL}^{cl} = \sigma_{FL} + \sigma_1^1 \quad (2-29)$$

The threshold stress under the closure stress ( $\sigma_{Li}^{CL}$ ) can then be given by substituting  $\sigma_{FL}$  with  $\sigma_{FL}^{CL}$  in Eq. (2-27), thus

$$\sigma_{Li}^{CL} = \sigma_1^i + \frac{m^i \sigma_{FL}^{CL} - \sigma_1^1}{m^1 \sqrt{i}} \quad (2-30)$$

Substituting eq. (2-29) into eq. (2-30) results in

$$\sigma_{Li}^{cl} = \sigma_1^i + \frac{m^i \sigma_{FL}}{m^1 \sqrt{i}} \quad (2-31)$$

The closure stress,  $\sigma_i$ , can be obtained by integrating the residual stress,  $f(RS)$ , over the crack length [76],

$$\sigma_1^i = \frac{1}{i} \int_0^i f(RS) di \quad (2-32)$$

This expression considers only the mode-I component of the residual stress. For crystallographic stage I cracking, its effect may be interpreted in terms of the shear component of this stress in the crack plane. So, this expression is an approximation.

#### 2.4.2.2. Notches

C.Vallellano [77-79] used the microstructural fracture mechanics techniques to study fatigue crack growth threshold conditions at notches. He obtained the Kitagawa diagram for the notched case by combining the plane case with a notch influence factor (Z).

$$Z_i = \frac{\sqrt{i}}{\bar{\alpha} + \bar{\beta}} \left[ \frac{\bar{\beta}}{\lambda_i} + \frac{\bar{\alpha}}{\sqrt{1 + \lambda_i^2}} \right]^{\frac{1}{2}} \quad (2-33)$$

$$\lambda_i = \frac{1}{\alpha^2 + \beta^2} \left[ \alpha \sqrt{\left( \alpha + \frac{iD^2}{2} \right)^2 - \alpha^2 + \beta^2} - \beta \left( \alpha + \frac{iD}{2} \right) \right] \quad (2-34)$$

$\bar{\alpha}$  and  $\bar{\beta}$  are dimensionless forms of the notch depth and half width respectively.

$$\bar{\alpha} = \frac{2\alpha}{D} \quad (2-35)$$

$$\bar{\beta} = \frac{2\beta}{D} \quad (2-36)$$

$D$ : Average grain size.

So, the N-R model [72] for microstructural crack growth becomes in this expression:

$$\sigma_{\text{arrest}} = Z_i \left[ \frac{m_i \sigma_{FL}}{m_1 \sqrt{i}} \right] \quad (2-37)$$

They compared the predictions of their model with results from the literature to check the predictive capability of their model.

Table 2- 4, show data of CSA G40.11 steel. Table 2.5 shows the data of notched specimens and the experimental and predicted values for fatigue limit of each specimen. Figure 2-40 shows the variation of the threshold stress as a function of crack length in the notch with the smallest radius.

From Table 2- 5 and Figure 2-40, it can be seen, the predictions are highly consistent with the experimental data.

Table 2- 4: Mechanical properties of CSA G40 steel [78].

Material	R	$\sigma_y$ (MPa)	$\sigma_{FL}$ (MPa)	$K_{th\infty}$ (MPa $\sqrt{m}$ )	D ( $\mu m$ )
CSA G40.11	-1	376	280	8	30

Table 2- 5: Data of notched specimens and their observed and predicted fatigue limits ( $R=-1$ ) [78].

$\alpha=\rho$ (mm)	$K_t$	$\sigma_{FL}^N$ (Exp.) (MPa)	$\sigma_{FL}^N$ (Pred.) (MPa)	Error (%)
0.20	2.98	168	156.7	6.7
0.48	2.96	124	123.5	0.4
4.80	2.62	104	107.4	-3.3

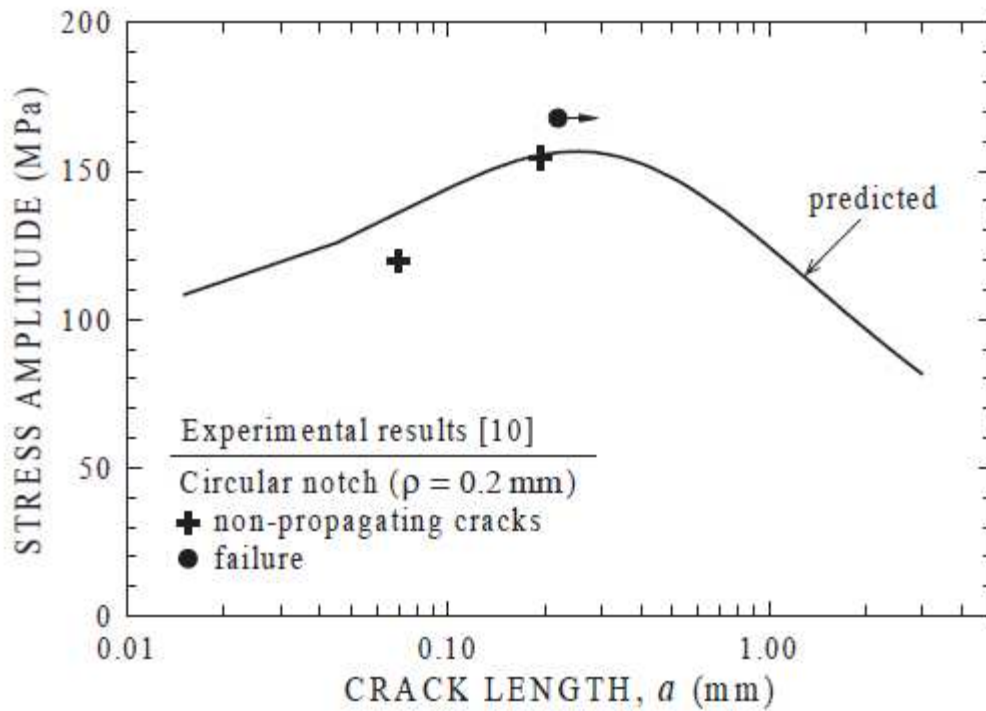


Figure 2-40: Comparison of predicted non-propagating crack lengths and experimental results (centre circular-notch plate,  $R=-1$ ) [78].

Curtis et al. [80] proposed that the necessary closure stress (representing the effect of the residual stress profile on the crack wake) could be neutralized by the effect of surface roughness. So, they used micromechanical notch sensitivity model and the N-R model for crack propagation Eq. (2-33).

$$\sigma_{arrest} = Z_i \left[ \sigma_1^i + \frac{m_i}{m_1} \frac{\sigma_{FL} - \sigma_1^i}{\sqrt{i}} \right] \quad (2-38)$$

$\sigma_1^i$  : Closure stress.

The relationship between the closure stress and the residual stress was given by [74, 76, 80]:

$$\sigma_1 = \frac{1}{a} \int_0^a f(\text{Residual stress}) da \quad (2-39)$$

C.A. Rodopoulos [76] used N-R model combined with micromechanical notch sensitivity model and closure stress to optimize the fatigue properties of aluminium alloys by controlled shot peening.

### 2.4.2.3. Surface Finish and Residual Stress

M. Kuroda and T. J. Marrow [3, 4, 36] studied the effect of the surface finish on the fatigue limit of two types of Type 304 stainless steels with different grain size. Material 1 had a grain size of  $\sim 8\mu\text{m}$  and a bulk hardness in the annealed, electropolished condition of 240 Hv; material 2 had a grain size of  $\sim 40\mu\text{m}$  and a bulk hardness of 200 Hv.

The effect of the surface finish on the fatigue limit was simulated using the N-R model Eq. (2-31). Fatigue specimens having two different surface conditions were obtained by changing the final cutting condition; annealing was performed to separate the residual stress effects from surface roughness.

They used the N-R model to predict the effect of roughness and the residual stress of machined samples.

The closure stress (Figure 2- 41-c) was obtained by integrating the depth profile of the residual stress (Figure 2- 41-a & b) using Eq. (2-39).

The profile of roughness on the specimen surfaces was considered as a sequence of micronotches and the influence factor ( $Z$ ) was calculated using Eq. (2-33).

Table 2- 6: Comparison of fatigue limits obtained by model prediction and experiments [36].

Material	Condition	Model Prediction (MPa)	Experiments (MPa)
Material 1	Fine Machined	521	$295 \pm 2$
	Fine Machined & Annealed	270	$295 \pm 4$
Material 2	Rough Machined	510	$323 \pm 7$
	Rough Machined & Annealed	285	$375 \pm 3$

The predicted effect of the surface roughness on the fatigue limit analyzed by comparing the threshold stress profiles of the annealed samples as shown in Figure 2-41-e. It can be seen that the predictions are insensitive to the surface roughness. By comparing the threshold stress profiles for machined and annealed samples in Figure 2-41-e & d, the predictions is sensitive to the residual stress effect. There is no agreement between the prediction and observations as shown in Table 2- 6.

They concluded that the model did not predict the observed fatigue behaviour. A development of the model would be required for proper prediction to study the surface effects on fatigue in austenitic stainless steels.

They suggested that modifications to the model to take better account of near-surface microstructural parameters (including local plasticity and grain structure) are important factors in improving model predictions.



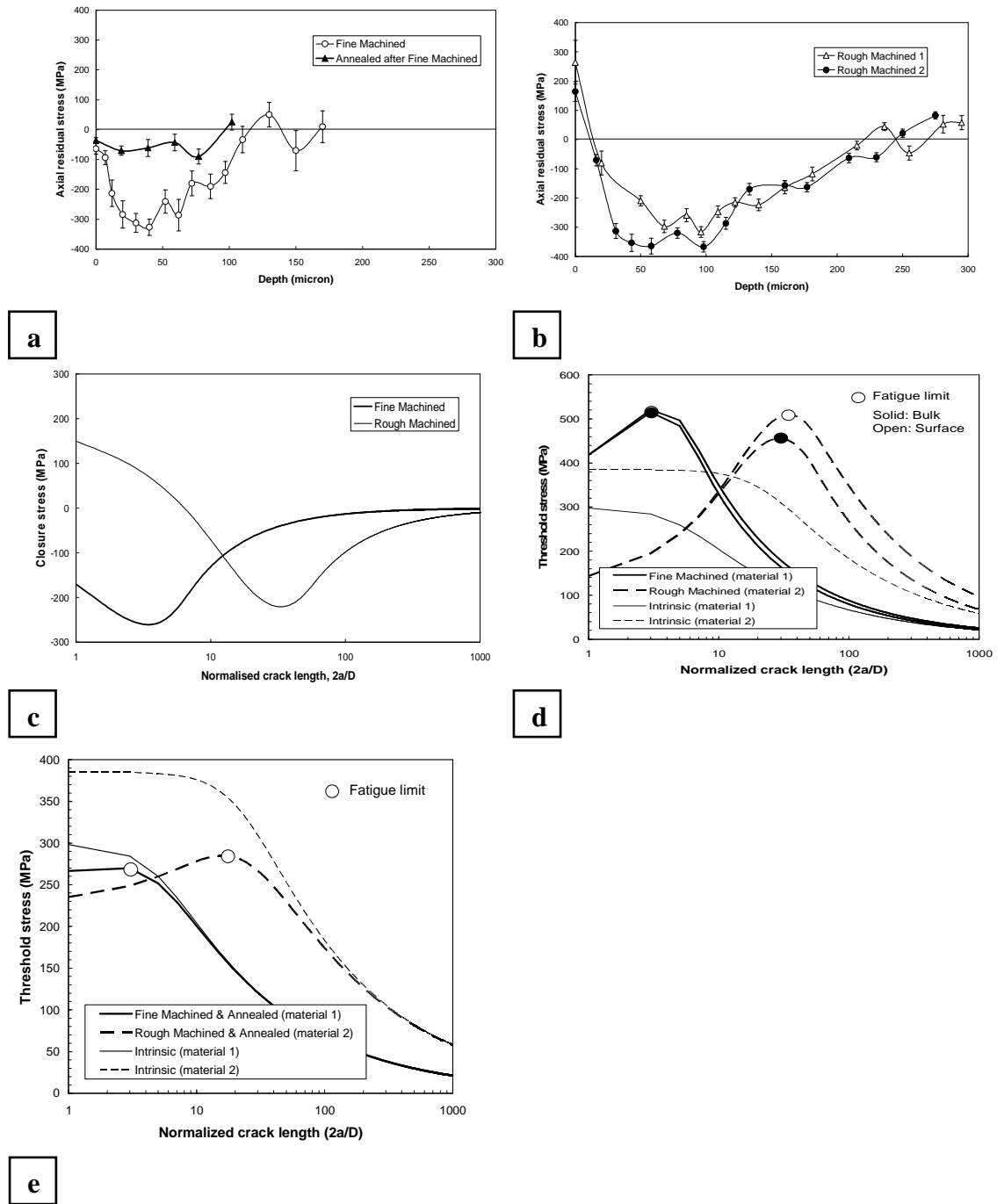


Figure 2- 41: a) Depth profiles of axial residual stress, b) Closure stress profiles; c) Predicted threshold stress profiles for machined samples; d) Predicted threshold stress profiles for annealed samples.

#### 2.4.2.4. Grain Orientation Factor

Orientation factor ( $m_i$ ) measures the mismatch between the current crack plane and the subsequent slip direction in the neighbouring grains. When the crack length is much smaller than the size of a grain just after nucleation, the crack will grow on the most favourable orientation and the orientation factor should be close to the average which is

around 2 for cubic (f.c.c. and b.c.c.) materials [81]. When the crack propagates past the microstructural barrier represented by the grain boundaries (Figure 2-42), the crack tip will confront a number of different grains and its plastic zone will expand, therefore, over several grains with widely different orientations.

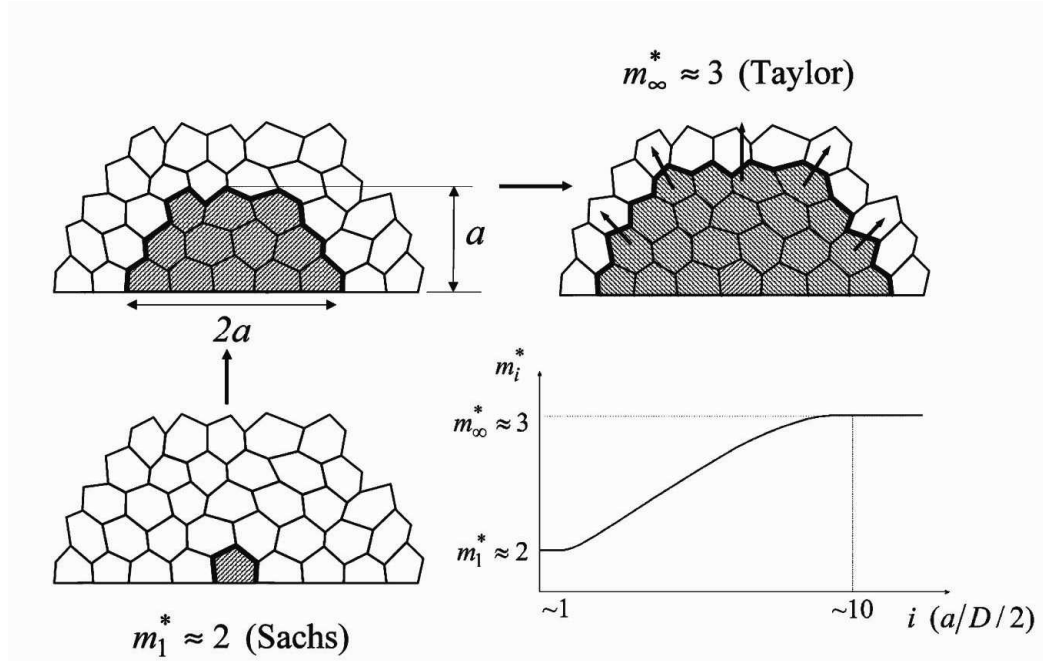


Figure 2-42: Schematic evolution of a crack through the material microstructure: expected trend of the crystallographic orientation factor  $m_i^*$  as the crack grows [81].

Several attempts have been described for the grain orientation factor,  $m^i/m^1$  for mild steels and aluminium alloys but not for austenitic stainless steels [4, 79, 82]:

$$\frac{m^i}{m^1} = 1 + 0.5 \ln i \quad \text{For mild steel (I)} \quad (2-40)$$

$$\frac{m^i}{m^1} = 1 + 0.35 \ln i \quad \text{For Aluminium alloy (I)} \quad (2-41)$$

$$\frac{m^i}{m^1} = 1 + 2.07 \left[ \frac{2}{\pi} \arctan 0.522(i-1) \right]^{1.86} \quad \text{For mild steel (II)} \quad (2-42)$$

The relationship of the grain orientation factor has been suggested, in the absence of experimental data [77-79].

$$\frac{m^i}{m^1} = \frac{\sqrt{\bar{a}_0}}{(if + \bar{a}_0^f - 1)^{\frac{1}{2f}}} \quad \text{No experimental data (III)} \quad (2-43)$$

$$\bar{a}_0 = \frac{a_0}{D/2} \quad (2-44)$$

$$a_0 = \frac{1}{\pi} \left( \frac{K_{t/\infty}}{Y \cdot \sigma_{FL}} \right)^2 \quad (2-45)$$

where  $a_0$  and  $\bar{a}_0$  are the intrinsic crack length and its dimensional value, respectively;  $f$  is the fitting parameter, the values of which are reported to be 2.5 and 1.65 for ferritic steel and copper, respectively;  $Y$  is the dimensionless constant that depends on geometry and mode of loading (generally  $Y=1$ );  $K_{t/\infty}$  is the threshold stress intensity factor for long cracks.

Murakami et al. [83] estimated the threshold stress intensity factor ( $K_{t/\infty}$ ) for long cracks using the following empirical relationship.

$$K_{t/\infty} = 1.65 \times 10^{-3} (H_V + 120) (\sqrt{area})^{\frac{1}{3}} \quad (2-46)$$

Where the  $K_{t/\infty}$  is in  $MPa\sqrt{m}$ ; the  $\sqrt{area}$  in  $\sqrt{m}$ .  $\sqrt{area}$  represents crack length, defined as the square root of the area of the defect projected in the direction of the maximum tensile stress.  $\sqrt{area}$  has been assumed to be 1000  $\mu m$  [77].  $H_V$  is the Vickers hardness.

## 2.5. Surfaces and Machining

In the finishing process, surface integrity is very important because of its impact on the products performance. Surface integrity is defined as the relationship between the surface geometry (surface roughness) and physical properties such as residual stress, hardness and microstructure of the surface layers. Surface integrity influences the quality of the machined surface and subsurface of components that have to withstand high static and dynamic stress. When a metallic material is machined using operations such as milling, turning, or grinding, a combination of macroscopic and microscopic inhomogeneous plastic deformation are produced in addition to the local production of thermal energy in the area of the near surface material [84, 85].

Surface working conditions of machined components have attracted the attention of scientists and researchers to study and investigate the effect of machining parameters on these surfaces and how to produce optimized surfaces, which can prolong the fatigue life of the components.

Before going deeply into the effects of machining parameters on the machined surfaces, we should know what these parameters are and how their effects are measured and evaluated. This will be outlined in the following discussion.

Machining is the broad term used to describe removal of material from a workpiece in the form of chips, using very hard cutting tools and powerful, rigid machine tools. Machining is necessary where tight tolerances on dimensions and finishes are required. Machining processes can be divided into three categories:

- ❖ Cutting, generally involving single-point or multipoint cutting tools (Traditional machining processes).
- ❖ Abrasive processes, such as grinding.
- ❖ Nontraditional machining processes, utilizing electrical, chemical, and optimal sources of energy.

Traditional machining processes include several processes such as turning, milling, drilling, grinding. There are a number of non-traditional machining processes such as Electrodischarge machining (EDM), Electrochemical machining (ECM), Electrolytic grinding (ELG), Laser Machining, Ultrasonic Machining, Water jet machining, Electron beam machining (EBM), Plasma cutting [86, 87].

The turning process is replacing grinding as a method in the production of precision steel products such as, bearing, gears, cams, shafts and axels due to its operational flexibility, economic benefit, higher surface quality and production time.

In grinding, the effect of the rake angles vary over a large area of machined surface due to the multiple edges which are randomly scattered on the grinding wheel. While in a turning operation, it is possible to precisely modify the rake angle because of the single point tool [85].

### 2.5.1. *Characterization of Machined Surfaces*

In several studies, different testing methods and their properties were used to describe adequately the condition of machined, shot peened or rolled surfaces. Microhardness HV, the residual stresses  $\sigma_{rs}$  (usually determined by x-ray diffraction or mechanical methods), the surface roughness  $R_t$  (depth of roughness) and  $Ra$  (roughness average), and the half-width values HW of the x-ray interference lines are the properties which can describe the surface and sub surface after mechanical treatments.

Figure 2-43 shows schematically an example of the depth distributions of a mechanically treated surface for the properties HV, HW, and the residual stresses  $\sigma_{rs}$  in longitudinal and transversal directions obtained by x-ray diffraction and successive electrolytic surface removal as well as a near-surface abnormal microstructure [88].

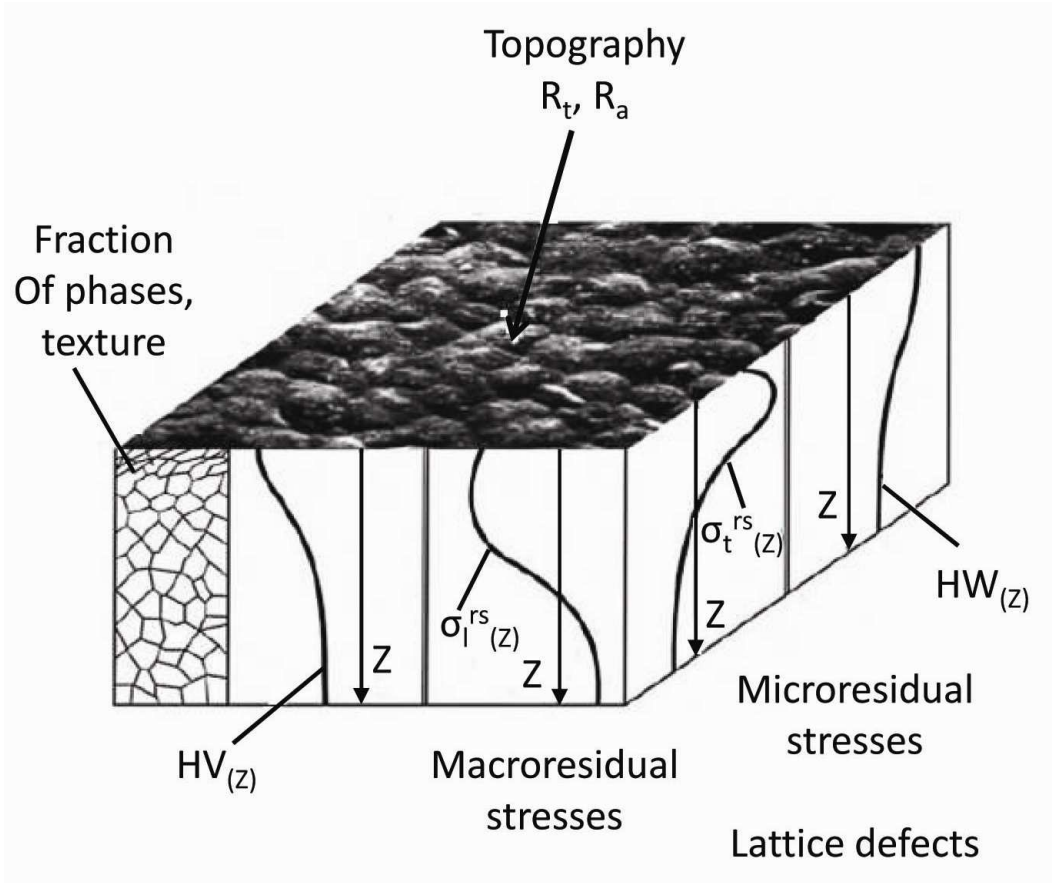


Figure 2-43: Courses of characteristic properties of surface layers after mechanical treatment [88].

### 2.5.2. Turning Process

Turning is the machining operation that produces cylindrical parts. Turning is performed on a lathe. In a lathe the tool is stationary and the workpiece is rotated. The workpiece is mounted on the chuck which rotates relative to the stationary tool.

There are three primary parameters, namely, cutting speed, feed rate and depth of cut (DOC). These three parameters are controllable where the operator can adjust them to produce the desired surface [86, 87]. The cutting speed, feed rate and depth of cut are shown in Figure 2-44 [86, 87].

*Cutting speed* is the rate at which the workpiece moves relative to the tool. Most machine tools have rotating spindles. The speed here is called spindle speed, commonly measured in revolutions per minutes (rpm) (spindle speed). The metric unit of cutting speed is metre per minutes (m/min.) and the English unit is feet per minute (fpm). The surface speed is sometimes reported in surface feet per minute (sfpm), and it refers only to the workpiece [86, 87].

*Feed rate* is the speed a cutting tool travels along the workpiece, and is commonly measured in millimetres per revolution.

*Depth of cut* (DOC) is the thickness of layer being removed from the workpiece or the distance from the original surface of the workpiece to the cut surface in a single pass. It is commonly expressed in millimetres.

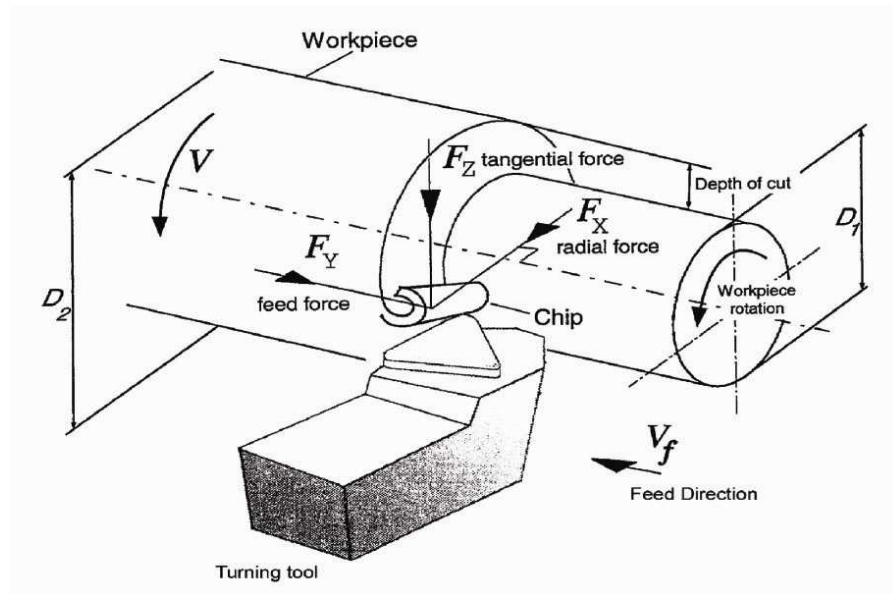


Figure 2-44: Schematic of turning operation [84].

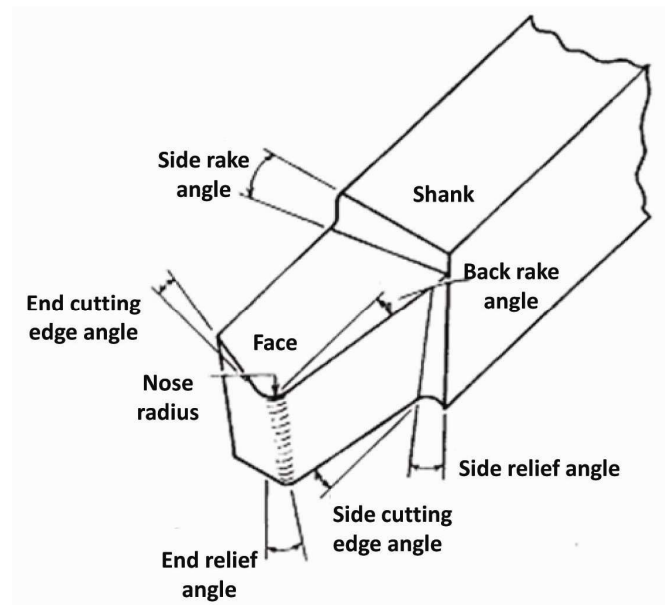


Figure 2-45: Turning Tool [89].

Figure 2-45 shows the standard terminology for cutting tool. In single point tool (e.g. turning operation), rake angle and the end and side relief angle are the most important angle.

The back rake angle affects the ability of the tool to shear the work material and form the chip. This angle can be positive or negative. The cutting force is reduced when the back rake angle is positive leading to small deflection of the workpiece, tool holder and machine. The strength of the tool is reduced as well as its capacity to conduct heat as the back rake angle is too large.

### 2.5.3. *Effect of Machining Parameters on Surface integrity and Fatigue Life*

#### 2.5.3.1. *Effects of Machining on Surface Roughness*

Kuroda et al [90] developed a model to prepare fatigue specimens of austenitic stainless steel with designed surface characteristics (response surface Model). They found that the response surface model adequately represented the largest peak to valley height (roughness  $R_y$ ) and the axial residual stress, but a good fit was not always achieved for the mean spacing of adjacent local peaks (roughness  $S$ ) and the microhardness. The response surface model obtained was used to successfully select machining conditions to design fatigue specimens with controlled combinations of roughness and surface residual stress.

Figure 2-46 is the response surface diagram of  $R_{0.4}$  (cutting nose radius of 0.4) analysed at the constant spindle speed of 1700 r/m. This Figure shows the effects of feed rate and cutting depth on the roughness  $R_y$  ( $\mu\text{m}$ ) and residual stress (MPa). This response surface was then used to identify combinations of feed rate and cutting depth which gave significant and controlled variations in roughness and residual stress.



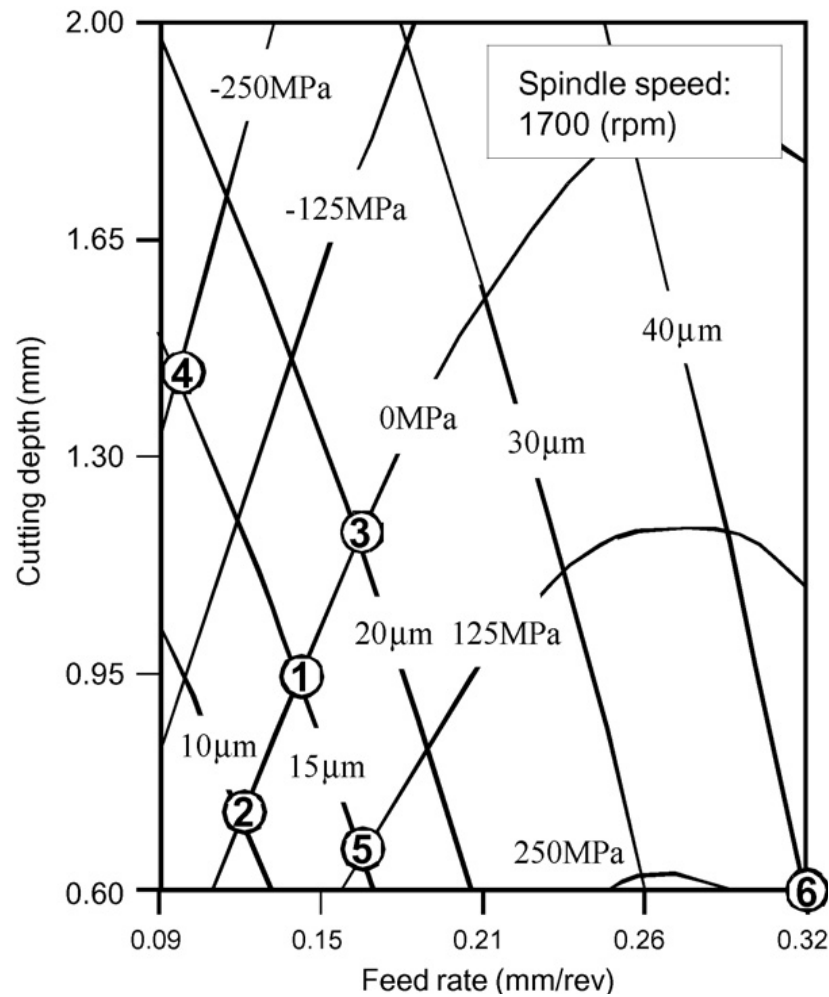


Figure 2-46: Response surface diagram obtained for the tool R0.4 Feed rate (mm/rev) and cutting depth (mm)[90].

Equations (2-47) and (2-49) describe the response surface in Figure 2-46. Where A, B and C are the variables of the spindle speed (rpm), the feed rate (mm/rev.) and cutting depth (mm), respectively.

$$R_y = -1.03 - 1.90 \times 10^{-3}A + 57.2B + 5.45C - 2.48 \times 10^{-6}A^2 + 149B^2 - 0.239C^2 + 0.0235AB + 4.06 \times 10^{-3}AC - 11.3BC \quad (2-47)$$

$$S = +82.8 - 0.0963A + 414B - 22.1C + 9.41 \times 10^{-6}A^2 - 491B^2 - 4.41C^2 + 0.165AB + 0.0349AC - 74.5BC \quad (2-48)$$

$$RS = -715 + 0.365A + 5370B - 218C - 6.65 \times 10^{-5}A^2 - 9960B^2 + 27.4C^2 - 0.0618AB - 0.0594AC + 177BC \quad (2-49)$$

In this work, several simple cylindrical specimens of type 304 having various surface characteristics were first produced by changing the final cutting conditions (spindle speed, feed rate and cutting depth) of the lathe. Spindle speed between 440 to 2450 rpm, feed rate between 0.09 to 0.4 mm/rev and cutting depth between 0.6 to 2.5 mm were employed. Some data have been constructed to illustrate the main effects of machining parameters on the surface roughness.

In Figure2- 47-a, the depth of cut of 1.3 mm and spindle speed of 1700 rpm were adjusted. It can be seen that the roughness increased with increasing feed rate. With feed rate of 0.21 mm/rev and spindle speed of 1700 rpm, the increase in cutting depth increased the roughness (Figure2- 47-b). With adjusting the feed rate at 0.21 mm/rev and the cutting depth at 1.3 mm, the surface roughness increased with increasing cutting speed (Figure2- 47-c). Surface roughness at the same feed rate becomes higher when a smaller nose radius is used (Figure2- 47-d).

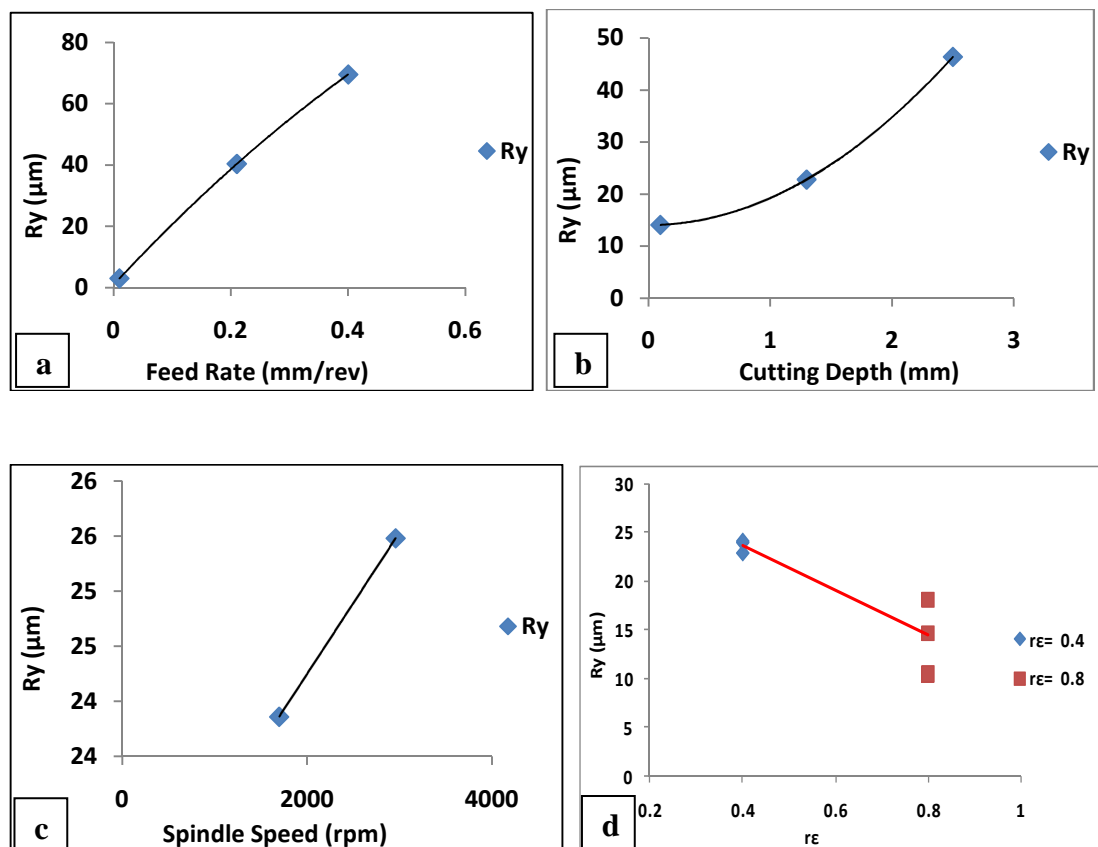


Figure2- 47: a) Influence of feed rate on surface roughness; b) Influence of depth of cut on surface roughness; c) Influence of cutting speed on surface roughness; d) Effect of nose radius on surface roughness( feed rate = 0.21 mm/rev., cutting depth= 1.3 mm, cutting speed = 1700 rpm).

Michael et al. [91] examined how the surface of a bainitic steels is affected by hard turning. They used different machining parameters (feed rate of 0.1 mm/rev, cut of depth of 0.1 mm and cutting speed from 50 to 999 mm/min) and then evaluated the surface in terms of residual stress, surface roughness and microstructure analysis. For the theoretical calculation of  $R_t$  they used the following formula

$$R_t \approx \frac{f^2}{8r_\epsilon} \quad (2-50)$$

where  $R_t$  is the surface roughness from top to bottom,  $f$  the feed rate, and  $r_\epsilon$  the tool nose radius. The effect of cutting speed on roughness can be seen in Figure 2-48, at a speed of 170 m/min a minimum  $R_t$  value was found.

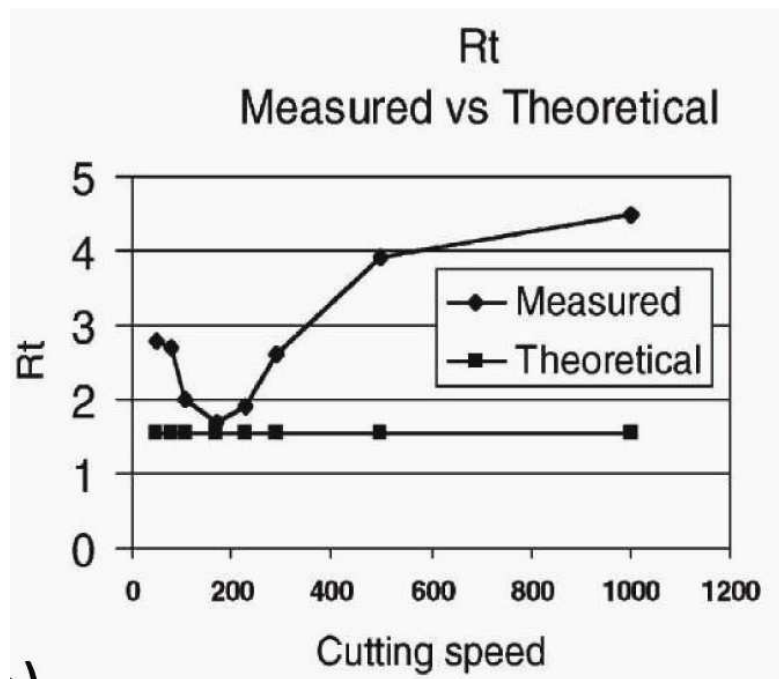


Figure 2-48: Surface roughness at cutting speeds from 50 to 999 m/min [91]

Ataollah et al. [92] studied the relationship between surface integrity, turning process parameters and fatigue behaviour of 34CrNiMo6. They produced fatigue samples using five different feed rates (from 0.05 to 0.4 mm/rev) with inserts differing in nose radius  $r_\epsilon$  (0.2 to 0.8 mm) (Figure 2-45). The depth of cut of 0.5 mm and cutting speed of 80 m/min were adjusted. From Figure 2-49, surface roughness at the same feed rate becomes higher when a smaller nose radius is used.

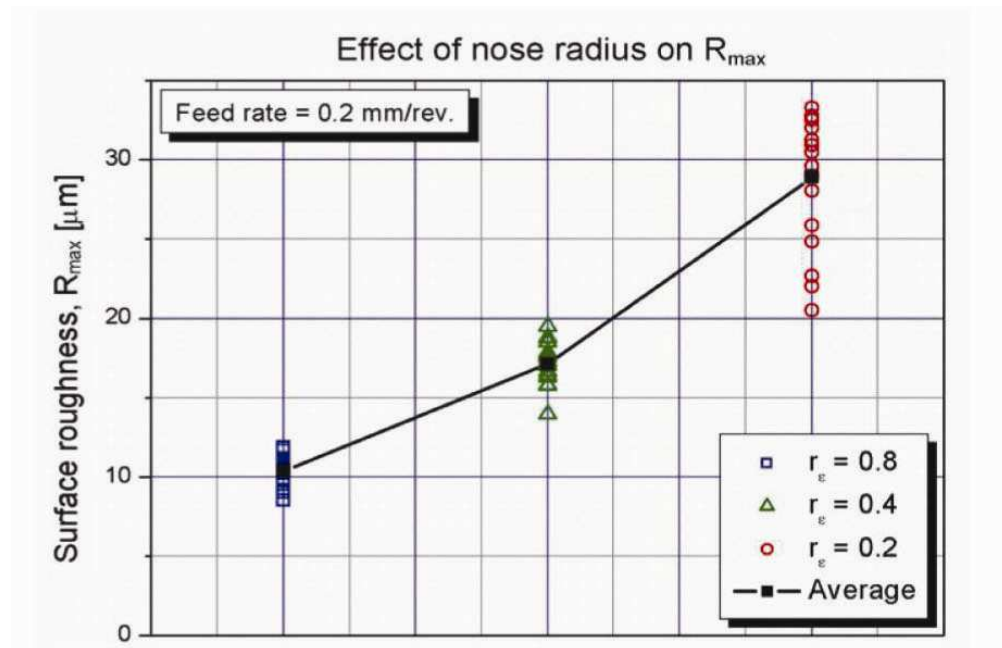


Figure 2-49: Effect of nose radius on  $R_{max}$ , feed rate = 0.2 mm/rev [92].

W. Bouziz et al. [93] investigated the influence of machining on surface characteristics in two different materials a carbon steel (CS) and duplex stainless steels (DSS). The chemical composition of carbon steel (in wt.%) was: 0.35 C, 0.5 Mn, 0.15Si, 0.035S, 0.03P and the chemical composition of duplex stainless steel (in wt.%) was: 0.02 C, 0.49 Mn, 0.62 Si, 24.66 Cr, 2.81 Mo, 7.43 Ni, 0.16 N and 2.52 Cu. Different cutting speed (160 to 440 m/min.), feed rate (0.05 to 0.2 mm/rev.) and cut of depth of 0.5 mm were employed to produce the workpiece. Surface roughness and residual stresses were analyzed. Figure 2-50 shows the evolution of the roughness with feed and cutting speed. It can be seen that in the CS samples the roughness increased with increasing feed rate. The increase in cutting speed decreased the roughness for both materials.

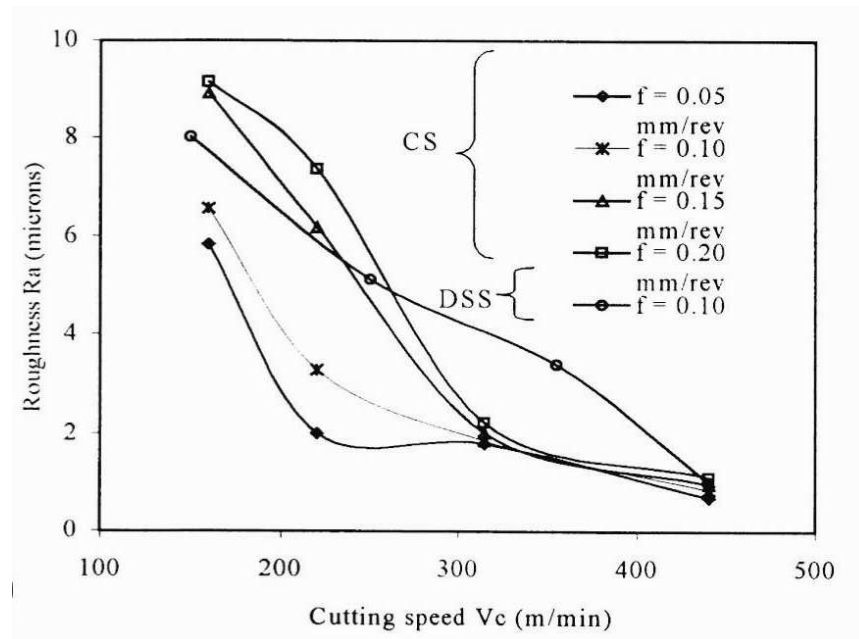


Figure 2-50: Roughness evolution with feed and cutting speed [93].

Karina et al. [94] studied the influence of machining parameters of turned surface of AISI 4140 steel (Chromium-molybdenum steel) on fatigue strength. They produced cylindrical fatigue samples with different machining conditions by changing the final cutting conditions feed rate (0.12 to 0.25 mm/rev), cut of depth (0.4 to 2 mm), cutting speed (15 to 100 m/min)). Figure 2-51(a-c) show the effect of machining parameters on the surface roughness. The surface roughness decreased with increasing depth of cut (Figure 2-51-a). An increase of feed rate led to increased surface roughness (Figure 2-51-b). The surface roughness decreased with increasing cutting speed initially rapidly, then more slowly (Figure 2-51-c

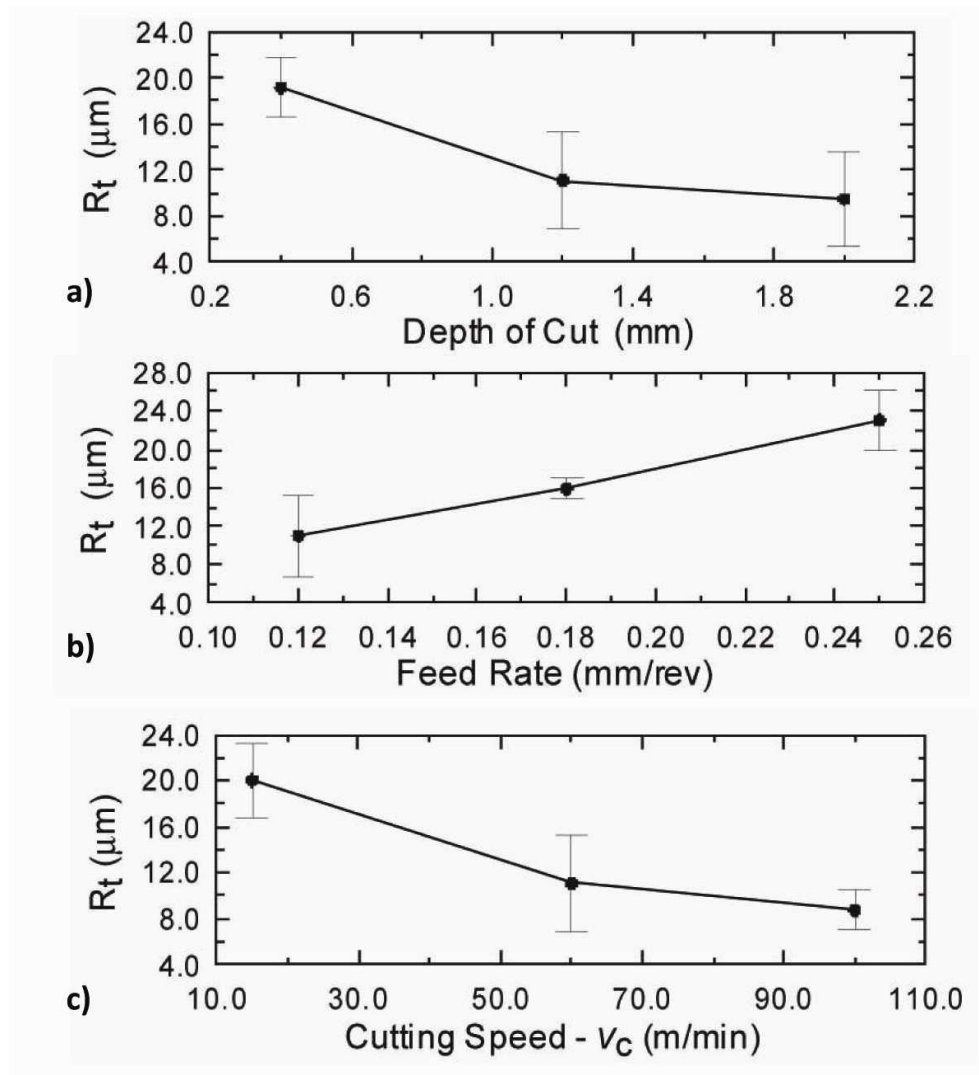


Figure 2-51: a) Influence of depth of cut on surface roughness parameters; b) Influence of feed rate on surface roughness parameters; c) Influence of cutting speed on surface roughness parameters [94].

In summary, the austenitic stainless steels, carbon steel and AISI 4140, surface roughness increases as feed rate increase. As the cutting speed increases the surface roughness increase in austenitic stainless steel and bainitic steel. While it decrease with cutting speed in AISI 4140, carbon steel and duplex steel. The surface roughness in austenitic stainless steels increases with cutting depth. An increase of the nose radius of the inserts caused a decrease of the surface roughness in machining of austenitic stainless steel and 34Cr Ni Mo

### 2.5.3.2. Effects of Machining on Residual Stress

Michael et al. [91], used different machining parameters ( feed rate of 0.1 mm/rev, cut of depth of 0.1 mm and cutting speed from 50 to 999 mm/min) and then evaluated the surface in terms of residual stress in bainitic steels. They found that the cutting speed clearly affects the amount of residual stress. As shown in Figure 2-52, the maximum residual stress (-775 MPa around 10  $\mu\text{m}$  below the surface) was generated at a cutting speed of 230 m/min.

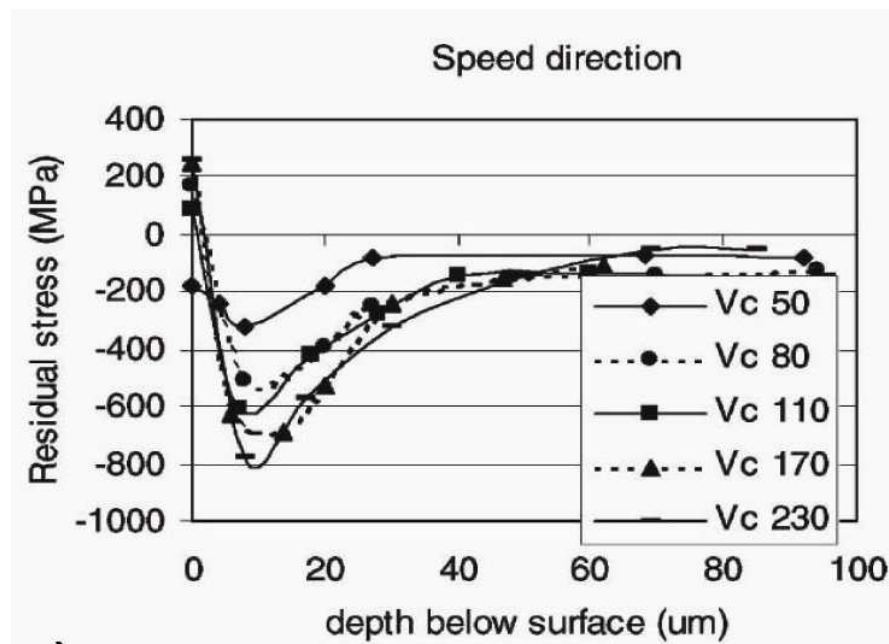


Figure 2-52:a) Residual stress at cutting speeds from 50 to 230 m/min [91].

Ataollah et al. [92] studied the relationship between surface integrity, turning process parameters and fatigue behaviour of 34CrNiMo6. The same machining parameters were used as discussed in the effect of machining on surface roughness in section (2.5.3.1). The residual stress tends to become more compressive as feed rate increases (Figure 2-53-a, b). An increase of the nose radius of the inserts caused a decrease of the compressive residual stresses.

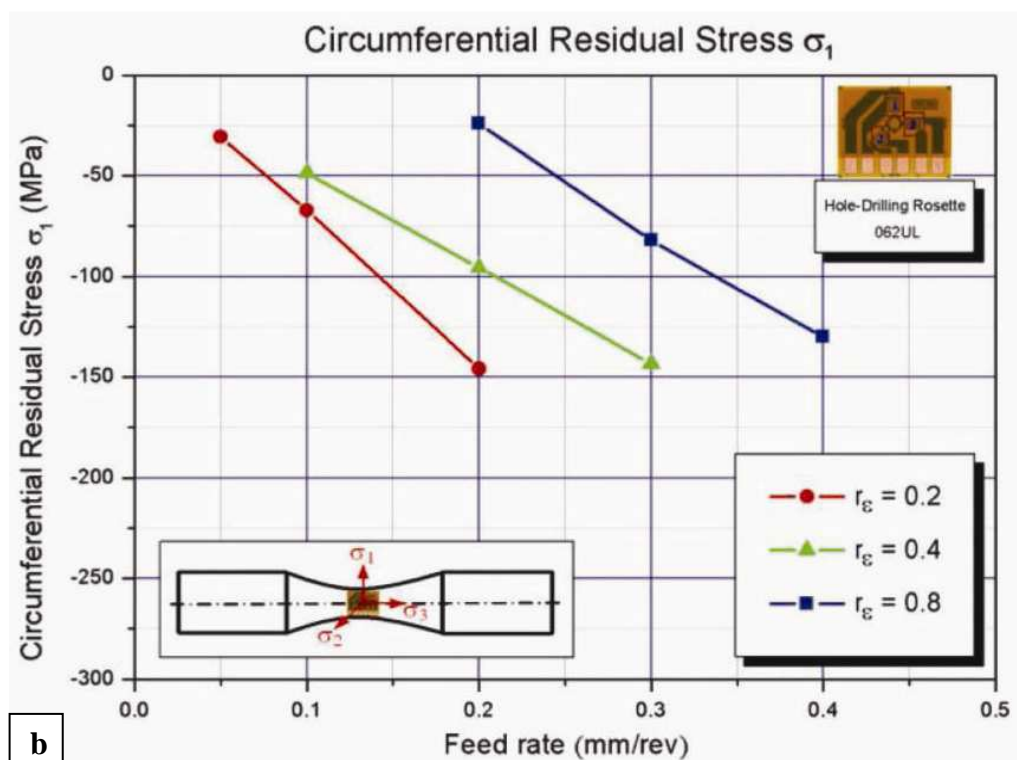
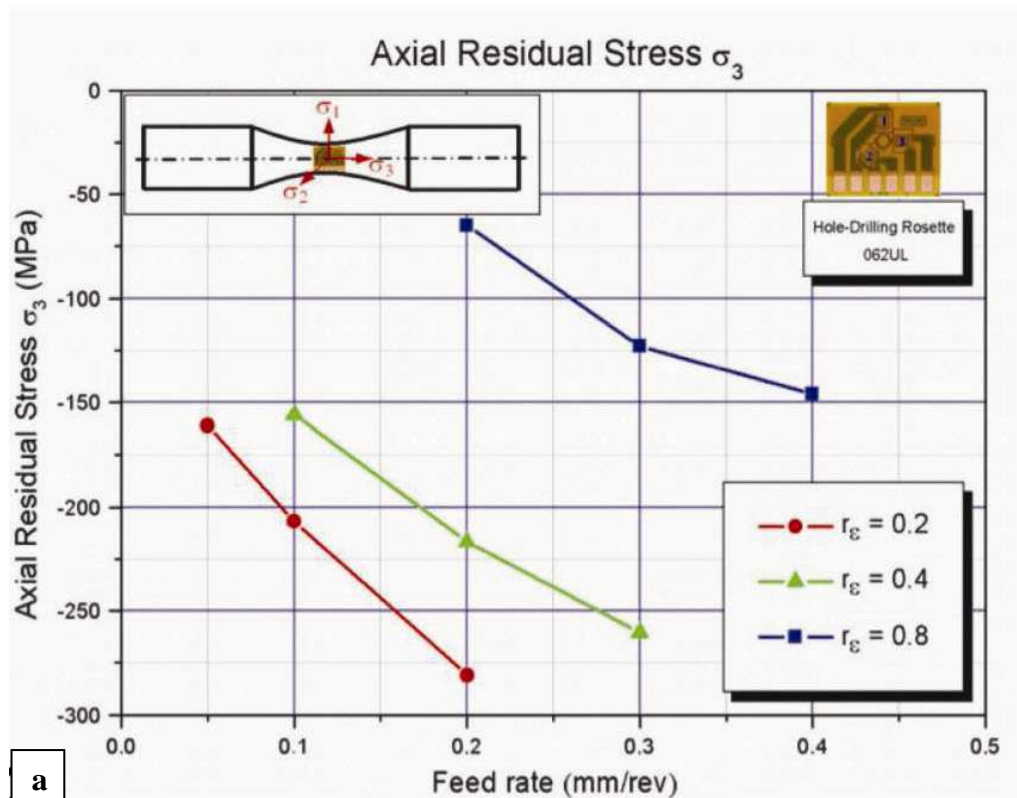


Figure 2-53: b) Axial residual stress  $\sigma_3$  versus feed rate; c) Circumferential residual stress  $\sigma_1$  versus feed rate [89].



W. Bouzid et al. [93] investigated the influence of machining on surface characteristics in a carbon steel (machining parameters mentioned in section 2.5.3.1). Residual stresses were analyzed. Figure 2-54-a, b show the effect of feed and the cutting speed on residual stress profile in parallel direction of feed and perpendicular direction of feed, respectively. In the parallel direction, as feed and cutting speed increased, the residual stress reached a higher level, and decreased gradually with depth until becoming stable at close to zero. In the perpendicular direction, the residual stress was compressive and decreased in magnitude with depth. The affected depth for both directions was similar.

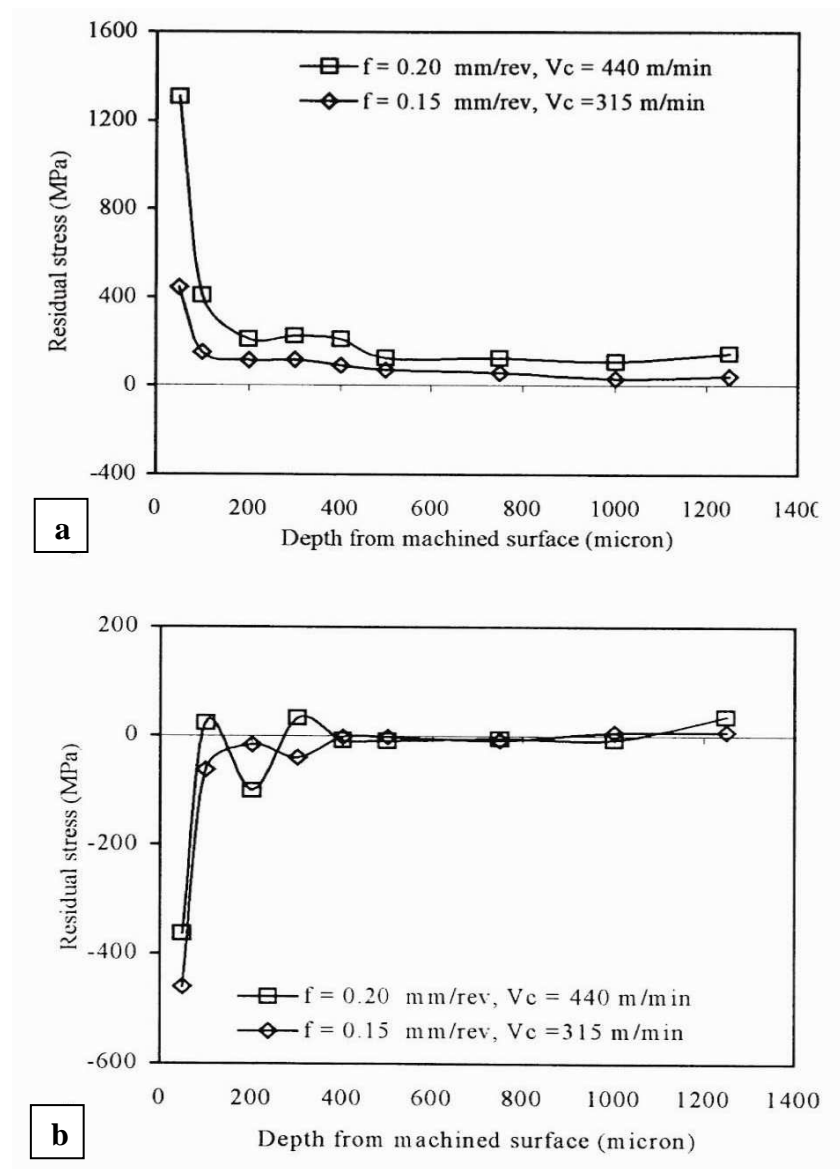


Figure 2-54: a) Parallel residual stress evolution for the carbon steel material; b) Perpendicular residual stress evolution for the carbon steel material [93].

Austenitic stainless steels are considered difficult to machine because of their low thermal conductivity and high mechanical and microstructural sensitivity to the strain and stress rate. They are prone to work-hardening, which induces mechanical changes on the machined surface [10].

From Kuroda et al [90] some data have been constructed to illustrate the main effects of machining parameters on the surface residual stress.

In Figure 2-55-a, the depth of cut of 1.3 mm and spindle speed of 1700 rpm were adjusted. It can be seen that the residual stress increased with increasing feed rate. With feed rate of 0.21 mm/rev and spindle speed of 1700 rpm, the increase in cutting depth decreased the residual stress (Figure 2-55-b). With adjustments of the feed rate at 0.21 mm/rev and the cutting depth at 1.3 mm, the surface residual stress decreased with increasing cutting speed (Figure 2-55-c). An increase of the nose radius of the inserts caused a decrease of the compressive residual stresses (Figure 2-55-d).

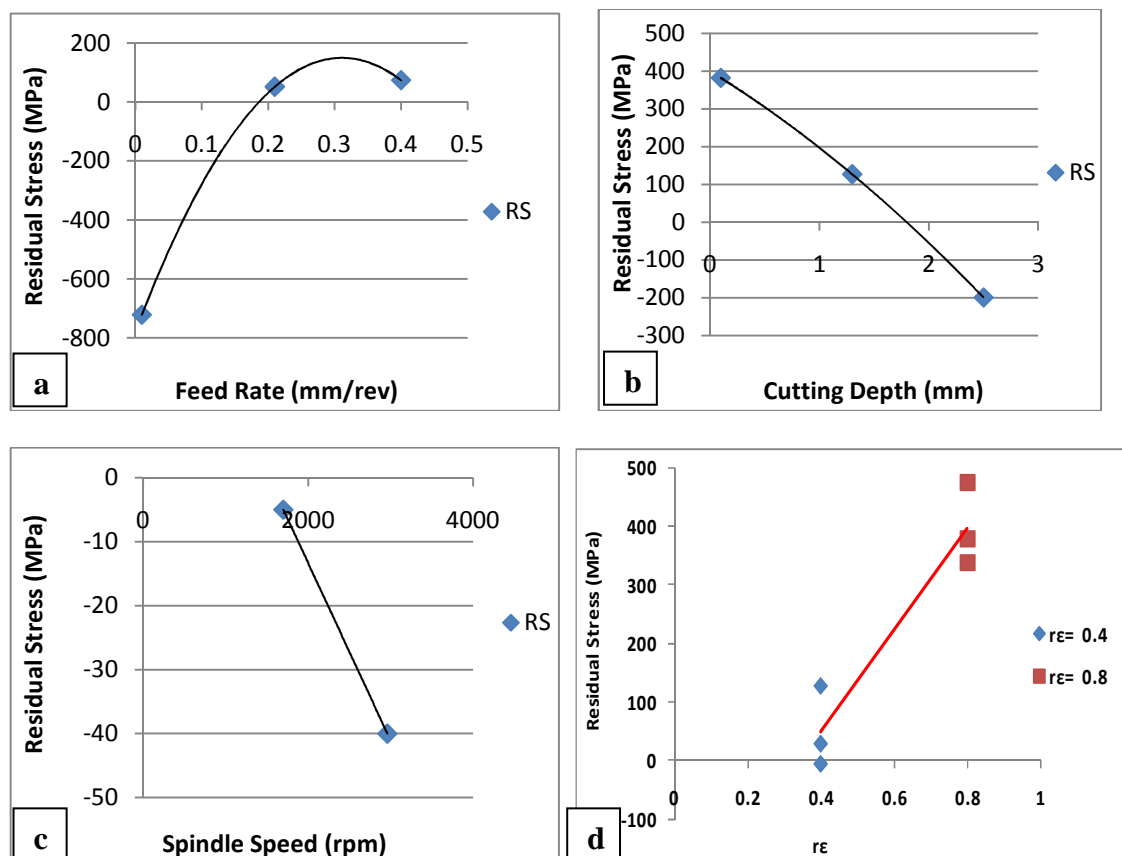


Figure 2-55: a) Influence of feed rate on residual stress; b) Influence of depth of cut on residual stress; c) Influence of cutting speed on residual stress; d) Effect of nose radius on surface stress (feed rate = 0.21 mm/rev., cutting depth = 1.3 mm, cutting speed = 1700 rpm).

Shapiro [95] studied the effect of residual stress and surface condition on the stress corrosion cracking of austenitic stainless steels. Cylindrical type 316Ti samples of approximately 20mm in length and 6.35mm in diameter were machined using a lathe with different combinations of machining parameters. Feed rates between 0.10 to 0.32 mm/rev and cutting depth between 0.6 to 1.9 mm were employed.

In Figure 2-56, the tensile residual stresses generally increase with the tool feed rate in both directions (i.e. Axial and circumferential direction). Also, the axial stresses tend to increase with cut depth and the circumferential stress decrease.

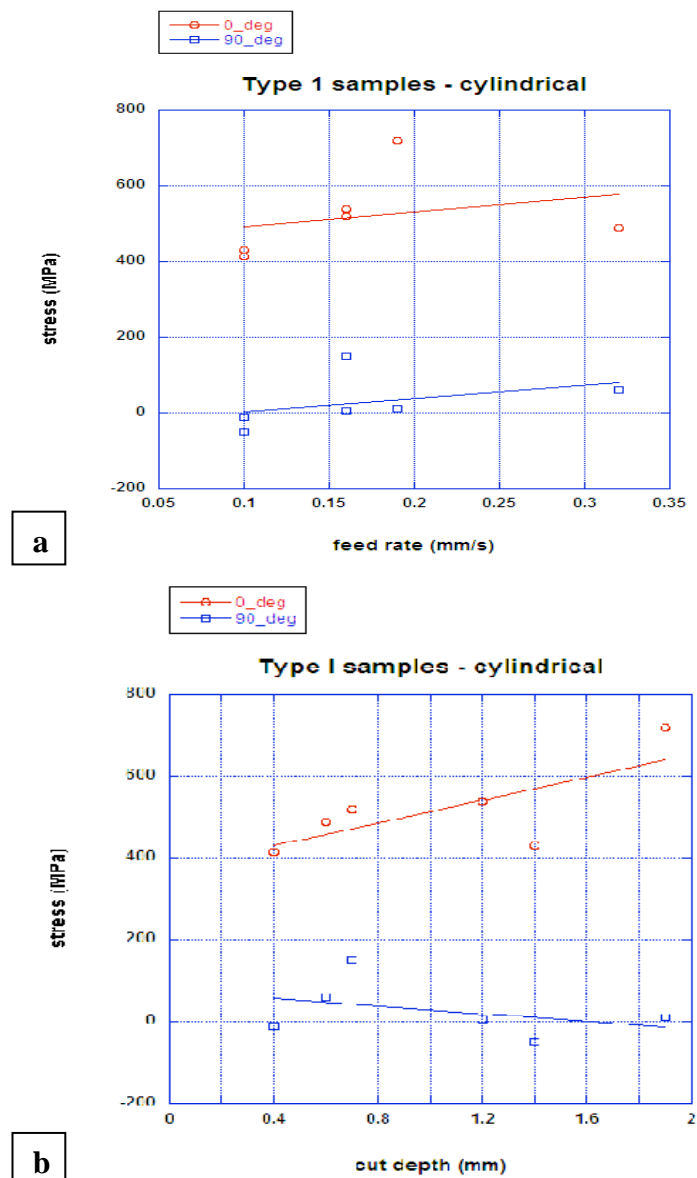


Figure 2-56: a) variation in residual stress with machining feed rate, b) variation in residual stress with machining cut depth [95].

J.C.Outerro et al. [96] studied the effect of machining parameters (cutting speed, feed rate and depth of cut) on the residual stress induced in turning of AISI 316L steel. Figure 2-57-a shows the influence of the cutting speed on residual stresses. At constant feed rate (0.2 mm/rev.) a depth cut at 2 mm and different cutting speeds (between 75 and 125 m/min), the circumferential residual stresses decrease by about 150 MPa where cutting speed increase from 75 to 125 m/min. The longitudinal residual stresses do not change significantly with the cutting speed where they have its mean value around (-500 MPa).

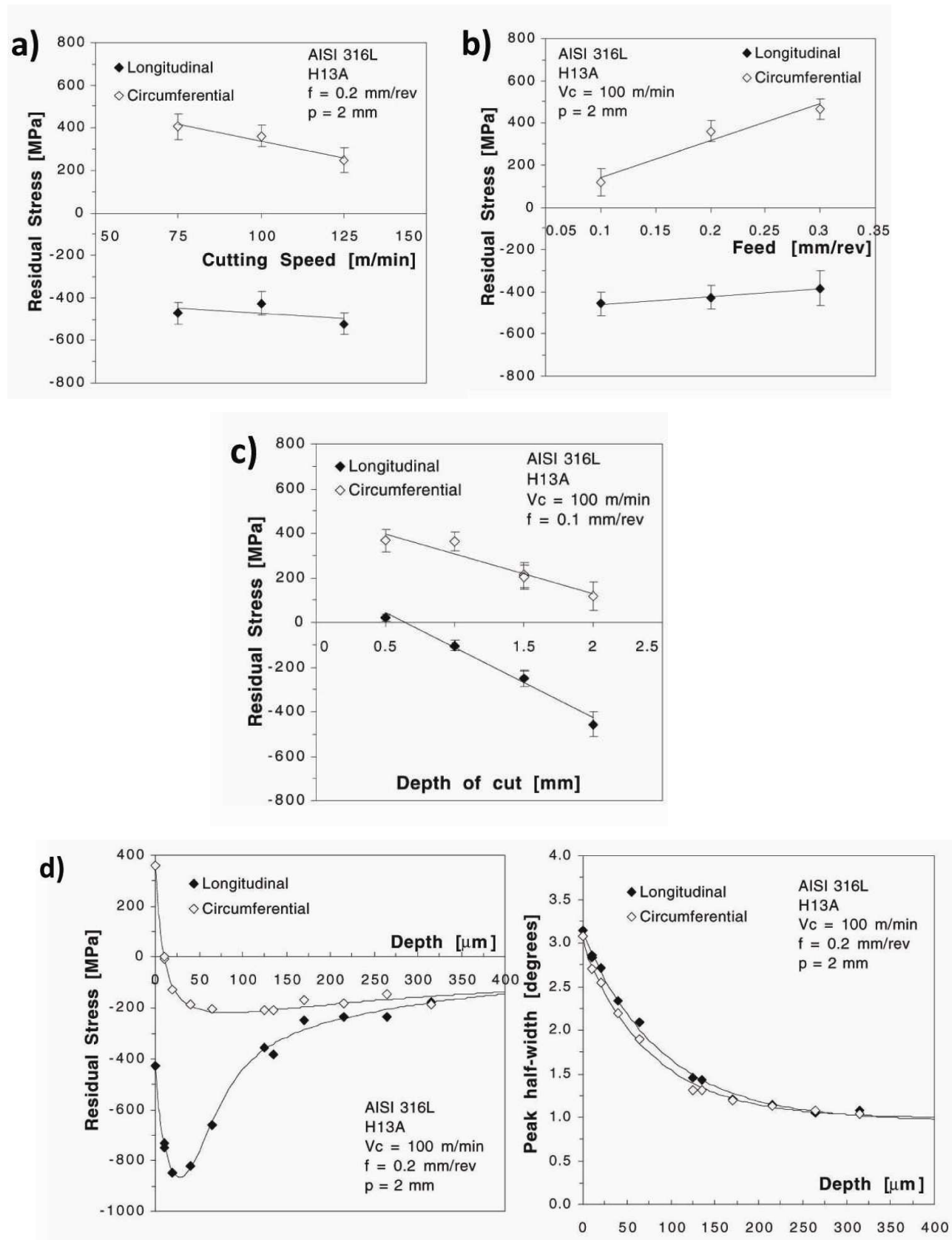


Figure 2-57: a) Evolution of the superficial residual stresses with the cutting speed; b) with the feed; c) with the depth of cut; d) Typical shape of residual stress and peak half-width profile for the AISI 316L steel [96].

The effect of feed rate was analyzed by using a constant speed (100 m/min.) and depth of cut of 2 mm. From Figure 2-57-b it can be seen that, the circumferential residual stress increased by about 300 MPa where the feed increased from 0.1 to 0.3 mm/rev. While the longitudinal residual stress does not change significantly staying around -425 MPa. The effect of the depth of cut was analyzed at a constant cutting speed (100 m/min.) and the feed of 0.1 mm/rev. As shown in Figure 2-57-c both circumferential and longitudinal residual stresses decreased when the depth of cut increases from 0.5 to 2 mm. Figure 2-57-d shows the residual stress profile in circumferential and longitudinal directions. In the circumferential direction, the tensile stress was of the order of about (+350 MPa) at the surface, decreasing to about (-200 MPa) over a distance of 90  $\mu\text{m}$ , while the compressive residual stresses of about (-450 MPa) were found in the longitudinal direction. The profile of residual stresses for both directions changes continuously with depth down to a certain maximum value in the compressive region and then gradually decreases until it becomes stable at the level of residual stress before machining. Figure 2-57-d, shows the peak half-width with depth profile. It can be seen that, the values of the longitudinal and circumferential peak half-width for each depth are identical. This shows that the workhardened layer thickness is about 250  $\mu\text{m}$ . Jang et al. [97] in their study of surface residual stresses in machining austenitic stainless steel AISI 304 by conventional turning as a function of machining speed, feed rate, depth of cut, and tool geometry. At different feed rate (0.084 to 0.132 mm/rev.) a depth cut (0.508 to 1.016 mm) and different cutting speeds (between 180 and 580 m/min), they found identical trends of residual stress with machining parameters for those of J.C.Outerro [96] for 316L. They found that the surface residual stresses in the circumferential direction are tensile and compressive residual stress on the longitudinal direction.

M'Saoubi et al. [98] in their study of residual stresses induced by orthogonal cutting in AISI 316L steels. Different cutting speeds (75 to 400 m/min.), feed rate (0.1 to 0.3 mm/rev.) and cuts of depth of 4 and 6 mm were employed to produce the workpiece.

They found that the thickness of the tensile layer decreased with cutting speed, but increased for high feed rate values. It was found that high tensile residual stresses (close to + 1000 MPa) on the machined surface and these stresses decrease at a high rate in the depth direction, becoming zero at a distance of 100–200  $\mu\text{m}$  from the surface.

In summary, the residual stress left by machining depends on the type of material being machined and on machining parameters. In austenitic stainless steel and carbon steel,

the surface residual stress increases as feed rate increases but decreases in 34Cr Ni Mo. In the machining of austenitic stainless steel, as the cutting speed and cutting depth increases the surface residual stress decrease. The surface residual stress increases with nose radius in the machining of austenitic stainless steel and 34Cr Ni Mo.

In austenitic stainless steels, It was found that high tensile residual stresses exist on the machined surface and these stresses decrease at a high rate in the depth direction, becoming zero at a distance of 100–200  $\mu\text{m}$  from the surface.

#### 2.5.3.3. *Effects of Machining on Fatigue Resistance*

Ataollah et al. [92] studied the relationship between surface integrity, turning process parameters and fatigue behaviour of 34CrNiMo6. Same machining parameters were used as discussed in the effect of machining on surface roughness section (2.5.3.1). The residual stress tends to become more compressive as feed rate increases. An increase of the nose radius of the inserts caused a decrease of the compressive residual stresses (Figure 2-53). As a result of this increase of compressive residual stress, the fatigue life increased. The benefit, however, was minimal in the LCF regime and increased as the HCF regime is approached as seen in Figure 2-58.

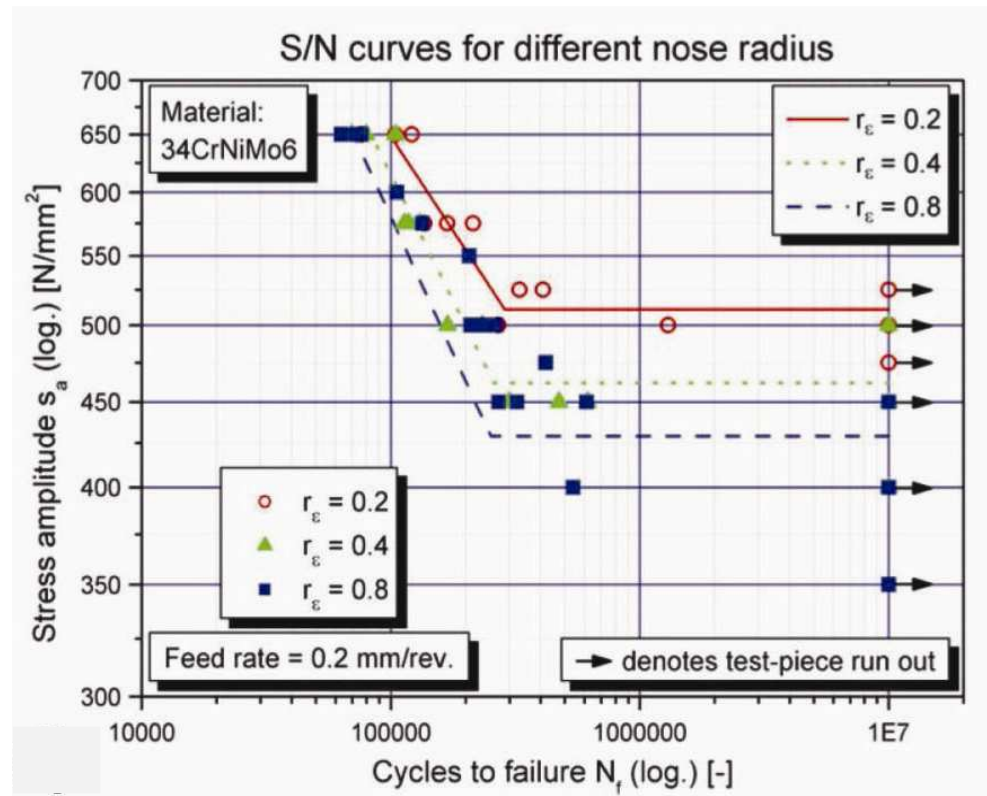


Figure 2-58: Fatigue life of turned specimens with different nose radius[92].

Hiroyuki et al. [99], investigated the effect on fatigue life of residual stress and surface hardness resulting from different cutting conditions of 0.45% C steel. Different feed rates (0.05 to 0.4 mm/rev), cutting speed of 100 m/min, cut of depth of 0.2 mm and nose radius (0.2 and 0.8 mm) were employed to produce fatigue samples. The rotating bending fatigue test was performed on the test specimens machined.

Figure 2-59 shows fatigue life against the surface hardness and the residual stress. Each plotted point shows the central value of one combination of the cutting conditions. As a general trend, the fatigue life is short in region A where the axial residual stress is tensile and the surface hardness is not high (about 250 HV). On the other hand, the fatigue life around the region B is very long. In this region, the axial residual stress is around zero and the surface hardness is over 290 HV. Comparing the region C and A, where the region C shows higher compressive residual stress but the surface hardness is almost same as region A, the region C apparently shows a higher fatigue life than the region A.

They showed that it possible to give higher fatigue life of the machined components comparing with the virgin material if compressive residual stress and high hardness within surface layer can be induced by machining.



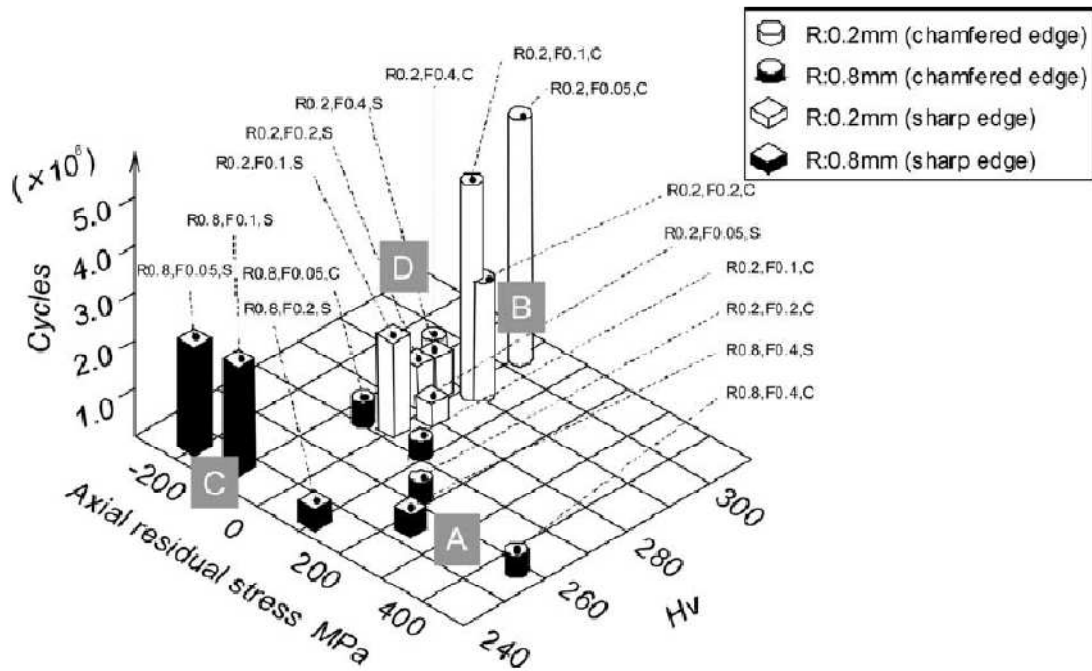


Figure 2-59: Interaction of axial residual stress and hardness on fatigue life [99].

Karina et al. [94] studied the influence of machining parameters of a turned surface of AISI 4140 steel on fatigue strength. They produced cylindrical fatigue samples with different machining conditions by changing the final cutting conditions (machining parameters mentioned in section (2.5.3.1)). Fatigue tests (high cycle fatigue) were carried out on a rotating bending fatigue test machine. In some samples, residual stress was eliminated by heat treatment. As shown in Figure 2-60, the fatigue limit decreased almost linearly with increasing surface roughness.

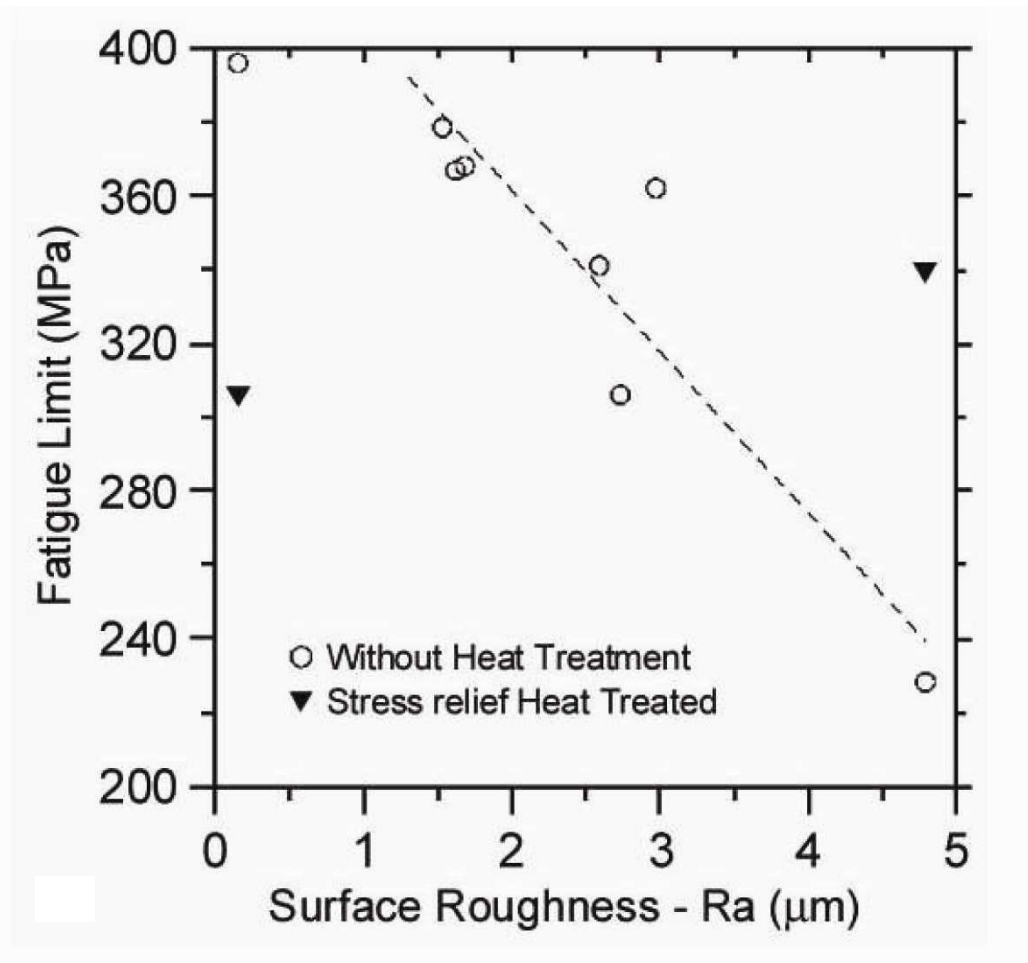


Figure 2-60: Influence of surface roughness on fatigue limits of all analyzed specimens [94].

In summary, the fatigue life in structures is dependent on the surface quality. Crack initiation and propagation can be attributed to surface integrity produced by machining. Surface roughness, residual stress and microstructure are proposed as parameters to describe surface integrity. These parameters can vary separately according to the machining conditions. Machining parameters such as, Cutting speed, feed rate, tool geometry have a large impact on surface integrity. So, there is a relationship between surface integrity, machining parameters and fatigue life.

#### 2.5.4. *Effect of Machining on near surface Microstructure of Austenitic stainless steels.*

Machining operations produce effects that are similar to those of shot peening or rolling treatments on the resulting properties of the near-surface material, but with additional more or less pronounced thermal effects [88].

Several studies have demonstrated the effects of mechanical surface treatments on microstructure.

Stamm et al. [100], investigated the effect of laser surface treatment on high cycle fatigue of AISI 316L stainless steel. The fatigue experiments were performed under stress control in air at room temperature. They found moderate tensile stresses instead of high compressive stresses in the surface and the surface was roughened by the laser melting but, the change of the grain morphology to a fine dendritic cellular structure in the melted surface layer led to improved fatigue life. This was attributed to the fact that the growth of microstructurally small cracks may be suppressed or even stopped because grain boundaries are effective obstacles for crack growth.

The surface microstructures of peened and deep rolled type 304 austenitic stainless steel exhibited a complex near surface microstructure, consisting of nanocrystalline regions, deformation bands and strain induced martensitic twin lamellae with high dislocation densities in the austenitic matrix as shown in Figure 2-61 [37].

Figure 2-62 shows a dark field TEM-image of the direct surface regions of shot peened AISI 304. The dark regions are fcc-grains; the bright regions are bcc-grains. It can be seen that the observed nanocrystalline surface layer consists of martensitic bcc- $\alpha$ -grains and fcc austenitic grains.

The quantity and depth of martensite varied with surface processing, and extended throughout the plastically strained region (Figure 2-63). The smaller the grain size, the more  $\alpha$ -martensite was detected.

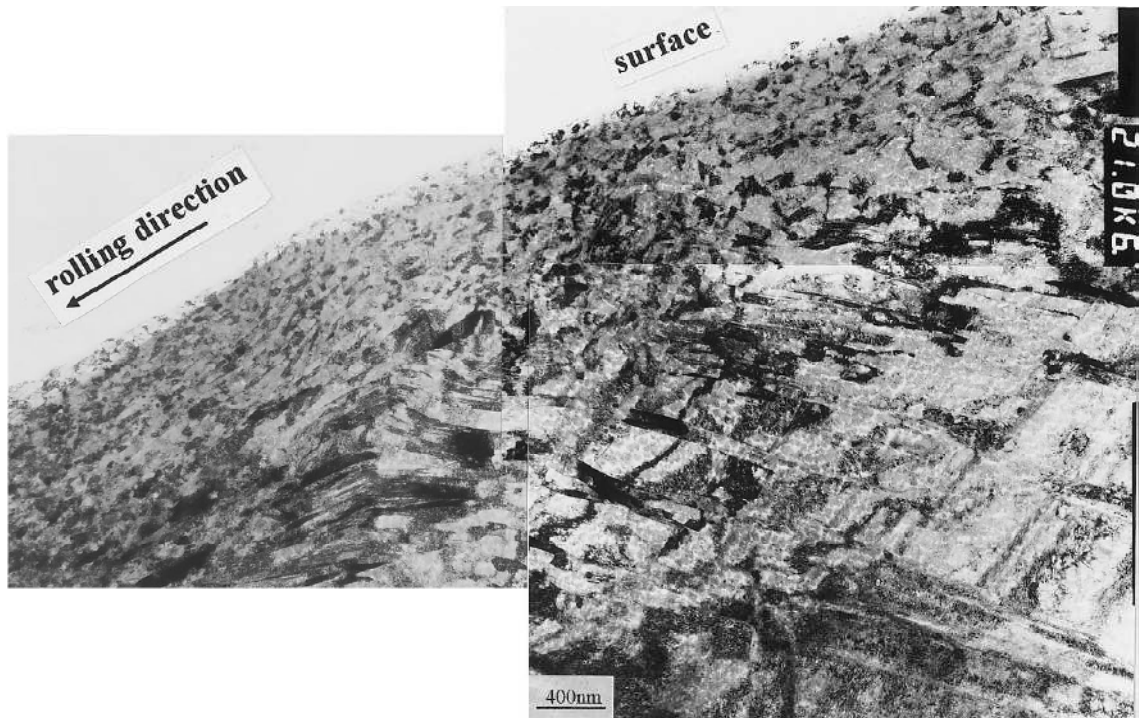


Figure 2-61: TEM-cross-section of the direct surface regions of deep rolled AISI 304 (scale bar is 400 nm) [37].

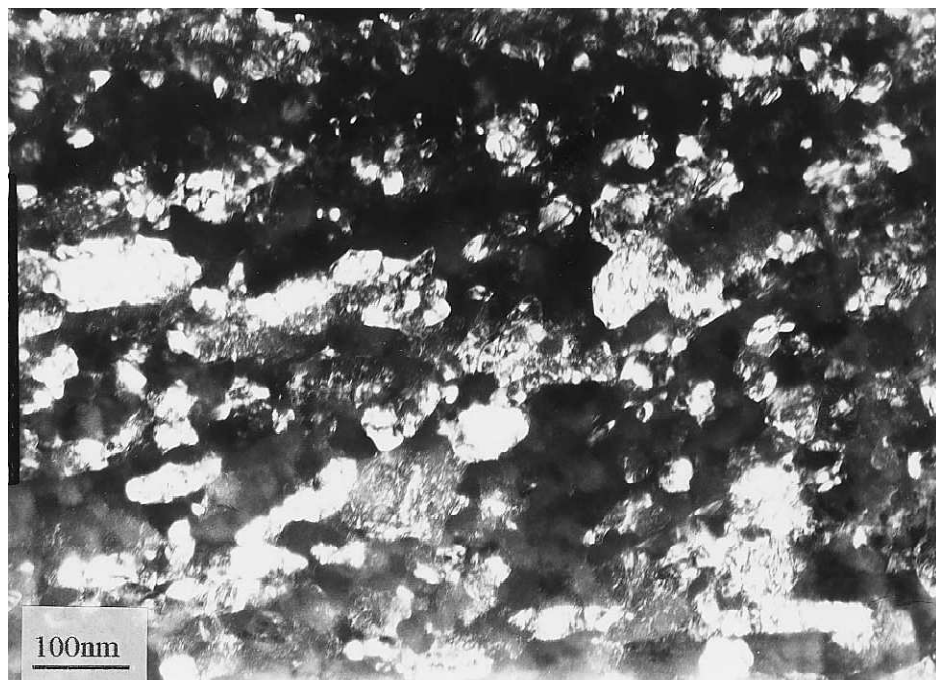


Figure 2-62: Dark field TEM of the direct surface regions of shot peened of AISI 304, showing nanocrystalline fcc-bcc layer [37].

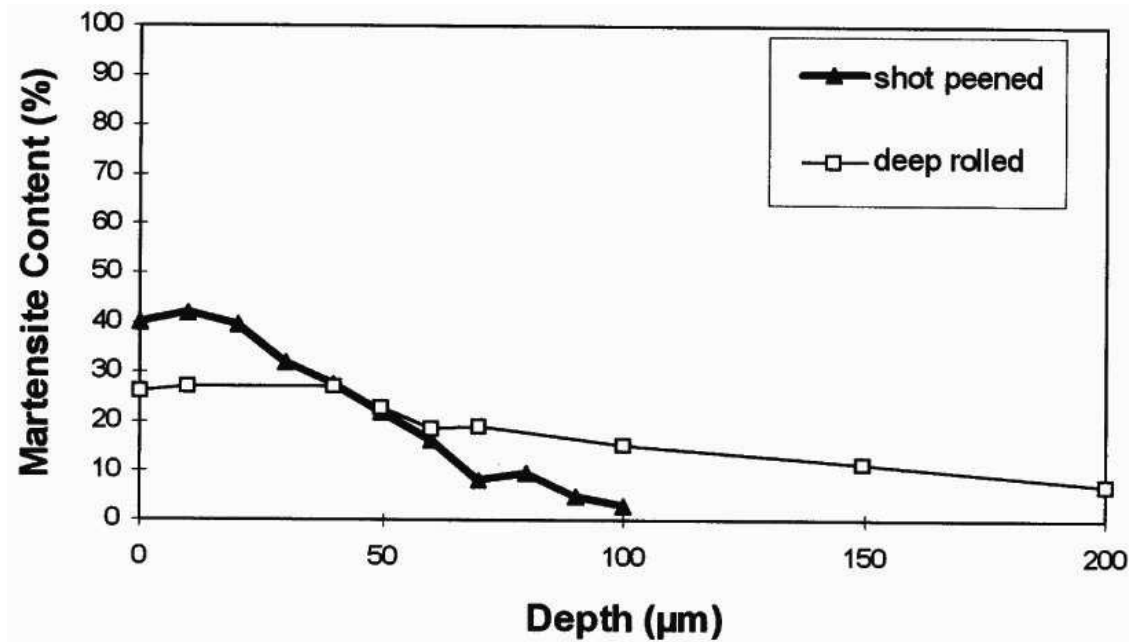


Figure 2-63: Variation of martensite content with depth below the surface for peened and deep rolled 304 [37].

H.W. Zhang et al. [101] investigated the formation of a nanostructured surface layer on an AISI 304 stainless steel by means of the surface mechanical attrition treatment (SMAT). The basic principle of SMAT is the generation of plastic deformation in the top surface layer of a bulk material by means of repeated multidirectional impacts of flying balls on the sample surface as shown in Figure 2-64 [102].

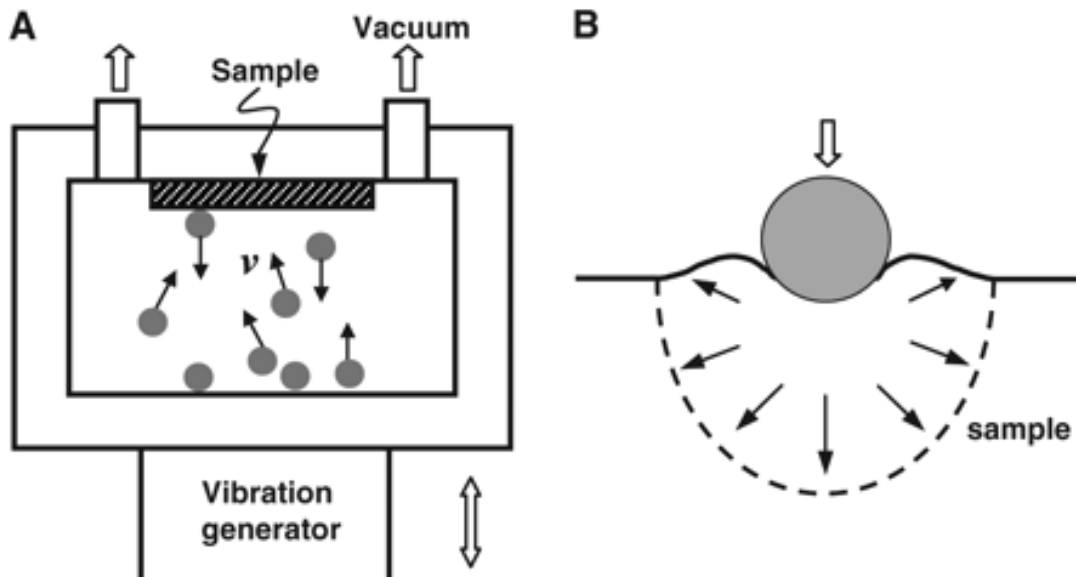
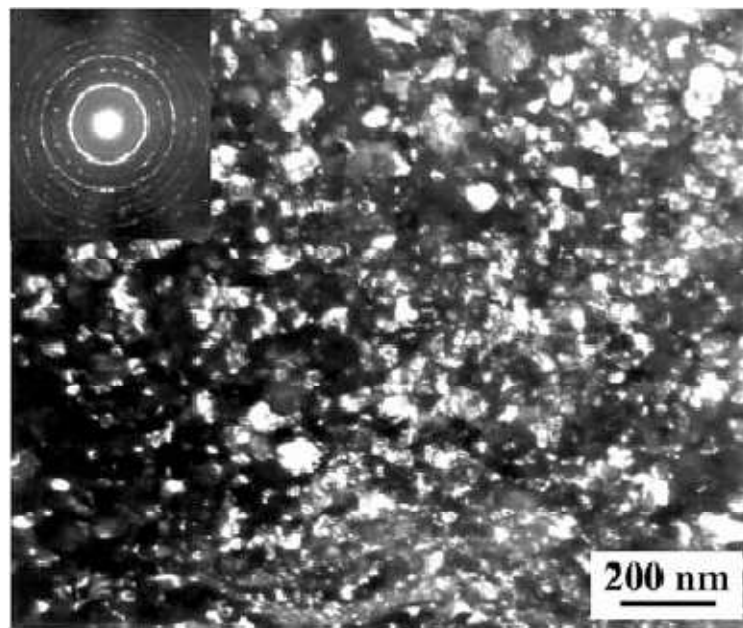


Figure 2-64: Schematic illustrations of (A) the SMAT technique and (B) the localized plastic deformation zone induced by the vibrating [102].

X-ray diffraction (XRD), scanning electron microscopy (SEM) and transmission electron microscopy (TEM) were used to characterise the microstructure of the surface layer of the SMATed sample. They found that the grain refinement process in the surface layer involves formation of planar dislocation arrays and twins in deformed grains, twin–twin intersections leading to grain subdivision and a martensite transformation as well, and formation of randomly orientated refined crystallites. Figure 2-65 shows typical plane-view TEM observations of the top surface layer from the treated surface. The microstructure of the top surface layer is characterized by uniformly distributed nanometerscale grains. The corresponding selected-area electron diffraction (SAED) pattern shows that these grains are martensites with random orientations, and no austenite is detected.

They concluded that the formation of nanocrystallites in the top surface layer may be attributed to the much larger strain and strain rate, as well as the multidirectional repetitive loading.



*Figure 2-65: Typical plane-view TEM observations of the top surface of SMATed AISI 304 stainless steel [101].*

# Chapter 3

## *Experimental Techniques and Methods*

*In this chapter the experimental work details and the different techniques and equipment that have been employed in experiments are introduced.*

### **3.1. Introduction**

The N-R model was implemented to predict the fatigue behaviour of the specimens with various controlled surface conditions, obtained by machining. In order to implement the N-R model, various surface/microstructure properties of the fatigue specimens such as surface roughness, hardness, the residual stress profile and the intrinsic fatigue limit are required.

Also, to study the microstructural damage associated with fatigue in run-out ( $>10^7$  cycles), the surfaces and near surface microstructures were characterised by scanning electron microscopy (SEM), transmission electron microscopy (TEM), X-ray diffraction and electron back-scatter diffraction (EBSD). The fatigue limits were determined using a rotating-bending machine by means of the staircase method.

### **3.2. Materials and Specimen Preparation**

The materials used were austenitic stainless steels (AISI 304L/AISI 316L) rod, both supplied in a “cold drawn” condition. The materials were supplied in the form of a round bar 10 mm in diameter. The chemical composition analysis was carried by Bureau Veritas UK Ltd<sup>1</sup>. Using the Inductively coupled Plasma-Optical Emission Spectrometer (ICP- OES) technique [103].

### **3.3. Mechanical Properties**

The baseline tensile properties for both materials were assessed using an MTS Alliance RT/100 extensometer with a 100kN load cell. The strain rate was set to 0.02 mm/s. The samples were designed in accordance with the ASTM E-8-04 standard test method for

---

<sup>1</sup>Bureau Veritas UK Ltd, Acrewood Way, St Albans, Hertfordshire AL4 0JY, United Kingdom.

tension testing of metallic materials [104]; a gauge diameter of 5 mm, a gauge length of 30 mm (Figure 3- 1).

Three samples were tested for each material. All mechanical tests were performed in air and at ambient conditions.

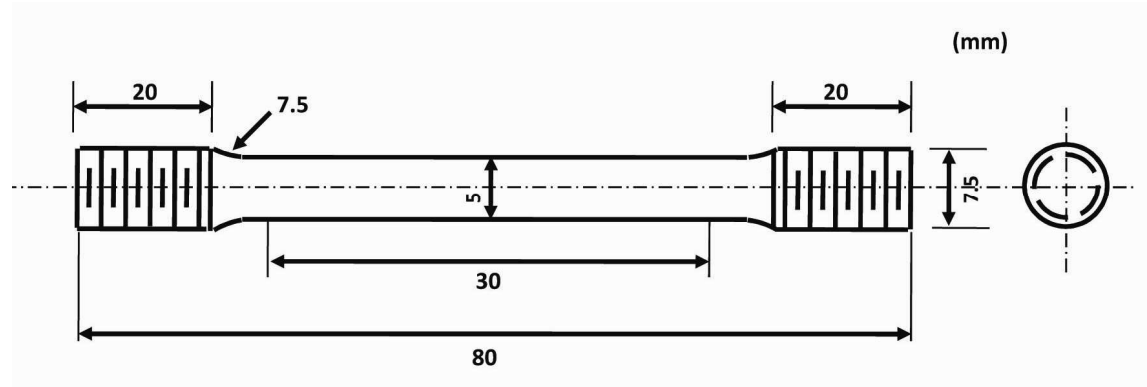


Figure 3- 1: Sketch of a tensile test specimen.

#### 3.4. Metallographic Specimen Preparation

The microstructure of the as-received specimens of both materials (AISI 304L and AISI 316L) were characterized using optical microscopy (Olympus BH2-UMA). Standard metallographic preparation techniques were employed to reveal microstructures of both materials. Metallographic transverse sections and longitudinal sections of both materials (Figure 3- 2) were prepared for metallographic investigation using a diamond impregnated saw (Struers Accutom-5, thickness of 0.5  $\mu\text{m}$ , cutting speed of 3000 Rev./min. feed rate of 0.025 mm/s). The specimens were embedded in Bakelite-type compression mounting resin. These specimens were subjected to several successive steps of grinding and polishing. They were mechanically ground using finer grades of SiC paper, i.e., 240, 400, 600, 800 and 1200 grit, with water as lubricant. The specimens were fine polished with 6, 1 and 1/4 $\mu\text{m}$  diamond pastes (Buehler) using oil as lubricant. Finally, they polished with a colloidal silica liquid to get a mirror-like surface finish without scratches.

The ground and polished samples were etched using electrochemical etching (a solution of 10% of oxalic acid at 5.0V for 30-60s at room temperature) and observed using optical microscopy.



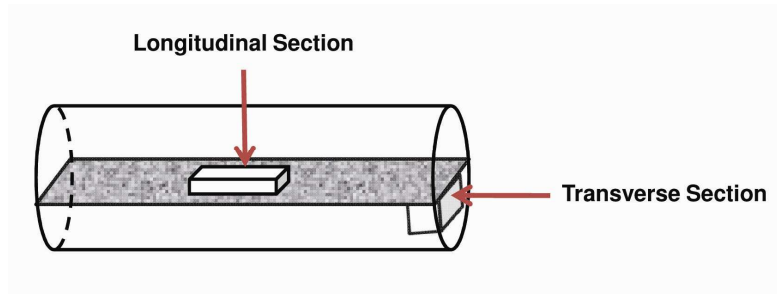


Figure 3- 2: Schematic view of sectioning of as-received material.

### 3.5. Measurement of Grain Size of As-Received Materials

Grain sizes for both materials were measured using the Linear Intercept method for both materials [105]. Three micrographs were obtained from section perpendicular to the surface, parallel to the specimen longitudinal axis using optical microscope (Olympus BH2-UMA). The optical microscope is interfaced with a LEICA DC200 frame grabber and equipped with an Olympus MS-Plane lens. In each micrograph, 10 lines were used to determine the intercepts. The specimens were etched using electrochemical etching (a solution of 50% of  $\text{HNO}_3$  and 50% of  $\text{H}_2\text{O}$  at 1V for 60s at room temperature) to reveal grain size. This etchant was used because it shows the grain boundaries of austenitic stainless steels. Subsequently, the grain size measurements become easier than for samples etched with 10% of oxalic acid.

### 3.6. Preliminary Sample Preparation and Selection of Machining Parameters

In order to produce fatigue specimens with different surface conditions, a set of specimens as shown in Figure 3- 3 (represent the diameter and the gauge length of fatigue samples) were produced. The final sample geometry was 6.35 mm diameter and 20 mm length. This is the same diameter as the gauge section of the fatigue specimens which were used in this project. The purpose of preparing this kind of specimen instead of fatigue samples was to limit the consumption of the supplied materials.

Thirty six cylindrical specimens of AISI 304L as shown in Figure 3- 3 were prepared using a numerically controlled lathe (A Harrison alpha-T). The tool was a “WWT DNMG” insert, 0.4 mm tip radius. Three specimens for each condition were produced as shown in Table 3- 1. Tool wear can be significant in austenitic stainless steels owing to their high work hardening capacity and low thermal conductivity [106, 107]. So, the tool tip was replaced for every specimen prior to the final cut in order to minimize wear effects (each cutting tool has 4 tips). A normal coolant flow was used at all times.

In order to obtain very different residual stress distributions and different roughness, four groups of specimens were produced with different final cutting conditions (AISI 304L). Three final cutting conditions (spindle speed, feed rate and cutting depth) of the lathe were employed to produce three specimens for each condition. The final cutting conditions were changed for each group till the desired residual stress, surface roughness and uniform machining marks were obtained. These cutting conditions were used based on the response surface model, which was developed in the previous work [90]. This model was employed to select machining conditions to design fatigue specimens with controlled combination of roughness and surface residual stress.



*Figure 3- 3: Configuration of cylindrical specimen used in this Project.*

Table 3- 1: Cutting conditions for cylindrical specimens.

Groups	Sample 1 Code	Sample 2 Code	Sample 3 Code	Spindle Speed (r/mm)	Feed Rate (mm/r)	Cutting Depth (mm)
Group 1	A 1-1	A 2-1	A 3-1	2500	0.25	0.1
	B 1-1	B 2-1	B 3-1	2500	0.1	2.5
	C 1-1	C 2-1	C 3-1	2500	0.25	1.65
Group 2	A 1-2	A 2-2	A 3-2	1500	0.25	0.1
	B 1-2	B 2-2	B 3-2	1500	0.1	2.5
	C 1-2	C 2-2	C 3-2	1500	0.25	1.8
Group 3	A 1-3	A 2-3	A 3-3	1700	0.25	0.1
	B 1-3	B 2-3	B 3-3	1700	0.1	2.5
	C 1-3	C 2-3	C 3-3	1700	0.25	1.8
Group 4	A 1-4	A 2-4	A 3-4	1500	0.25	0.4
	B 1-4	B 2-4	B 3-4	1500	0.1	2
	C 1-4	C 2-4	C 3-4	1500	0.1	0.4

### 3.7. Fatigue Specimens Preparation

The cutting conditions parameters of group 4 were selected to produce fatigue samples for this research because of the good quality of produced surfaces (i.e. uniformity of machining marks) of group 4 (Table 3- 1) and to ensure keeping the cutting conditions quite close to that used in previous work [4, 108] for comparison purpose.

The geometry of fatigue specimens is given in Figure 3- 4. These were prepared by a using numerically controlled lathe (A Harrison alpha-T). The tool was a “WWT DNMG” insert, 0.4 mm tip radius. Two different conditions of surface roughness and surface residual stress were produced, by changing the final cutting conditions (spindle speed, feed rate and cutting depth) of the lathe, the cutting conditions of which are listed in Table 3- 2. These conditions were selected from the response surface [90] to obtain residual stresses that were either close to zero (fine machined-F) or tensile (rough machined-R).

To produce an annealed condition for fine and rough machining conditions (i.e. stress free), sets of fatigue specimens were annealed at 900°C for 10 minutes in argon atmosphere. Other specimen sets were similarly annealed and then electrochemically polished to remove approximately 150 µm from the diameter (i.e. stress free and roughness free). Figure 3- 5 shows fatigue samples in different conditions.

The spindle speed (1500 rev. /min) and cut depth (0.4 mm) were the same for both conditions, with a feed rate of 0.25 mm/rev. for the rough machined condition-A (Low

cutting depth) and 0.1 mm/rev. for the fine machined condition-C. Six conditions were prepared to assess the fatigue limit as shown in Table 3- 3.

Table 3- 2: Cutting conditions for fatigue specimens.

Cutting Condition	Condition Code	Spindle Speed (r/mm)	Feed Rate (mm/r)	Cutting Depth (mm)
Close to Zero Stress (Fine)	F	1500	0.1	0.4
Tensile Stress (Rough)	R	1500	0.25	0.4

Table 3- 3: Fatigue specimen conditions for AISI 304L and AISI 316L (RS: residual stress).  
Note, conditions 3 and 6 were prepared by electropolishing a fine machined specimen (C).

No.	Condition	Effect
1	Fine Machined (C)	RS + Roughness
2	Fine Machined (C) & Annealed	Roughness
3	Electropolished (Annealed)	-
4	Rough Machined (A)	RS + Roughness
5	Rough Machined (A) & Annealed	Roughness
6	Electropolished (Not Annealed)	-

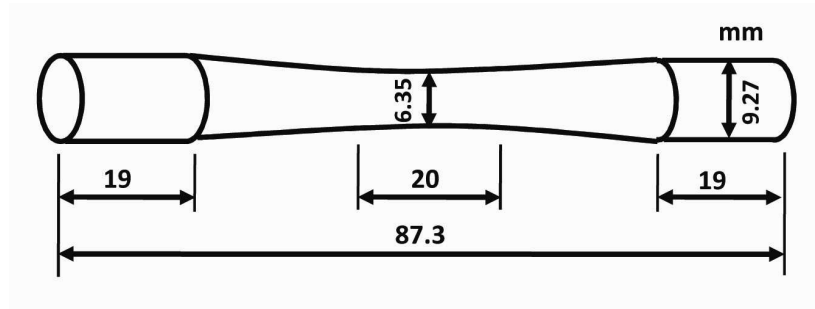


Figure 3- 4: geometry of fatigue specimens.

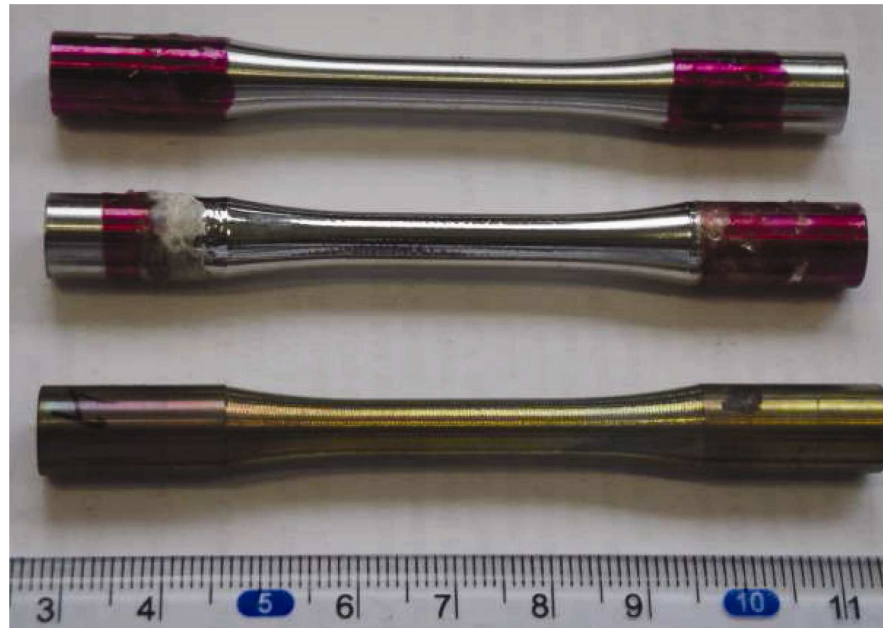


Figure 3- 5: As-Machined, As-Electropolished and Annealed Samples.

### 3.8. Annealing Following Machining

In order to obtain the fatigue limit in the absence of residual stress and study the effect of roughness, sets of specimens were annealed. For both materials the preliminary samples and fatigue samples were annealed by the same procedure to eliminate the residual stress induced by machining. The samples were placed on a ceramic boat individually. This was placed into tube furnace under an argon gas flow at 900°C for 10 minutes. The temperature was measured by connecting a thermocouple to the sample.

### 3.9. Electropolishing Following Annealing

In order to obtain the intrinsic fatigue limit in the absence of residual stress and surface roughness, sets of samples were electropolished after annealing. The electropolishing was performed in a solution of 8% perchloric acid ( $\text{HClO}_4$ ) and 92% acetic acid ( $\text{CH}_3\text{COOH}$ ) at room temperature under a voltage tension of 45 V. Figure 3- 6 shows the set up of the electropolishing. The cathode was stainless steel type AISI 304 sheet. Due to the cylindrical shape of the specimens, this sheet was folded in a tube shape to ensure uniform material removal from the specimens. The specimens were connected with approximate 60 mm length and 2 mm diameter stainless steel wire using spot welding. This wire was used to facilitate the handling of the specimen inside the electrolyte. This wire covered with lacomit to prevent material removal from the wire itself. The specimens were connected to the positive pole (anode). The specimen's

diameter was measured before and after the electropolishing process using a micrometer. The same electropolishing procedure was used to remove material in order to obtain the depth profile for measurement of residual stresses.

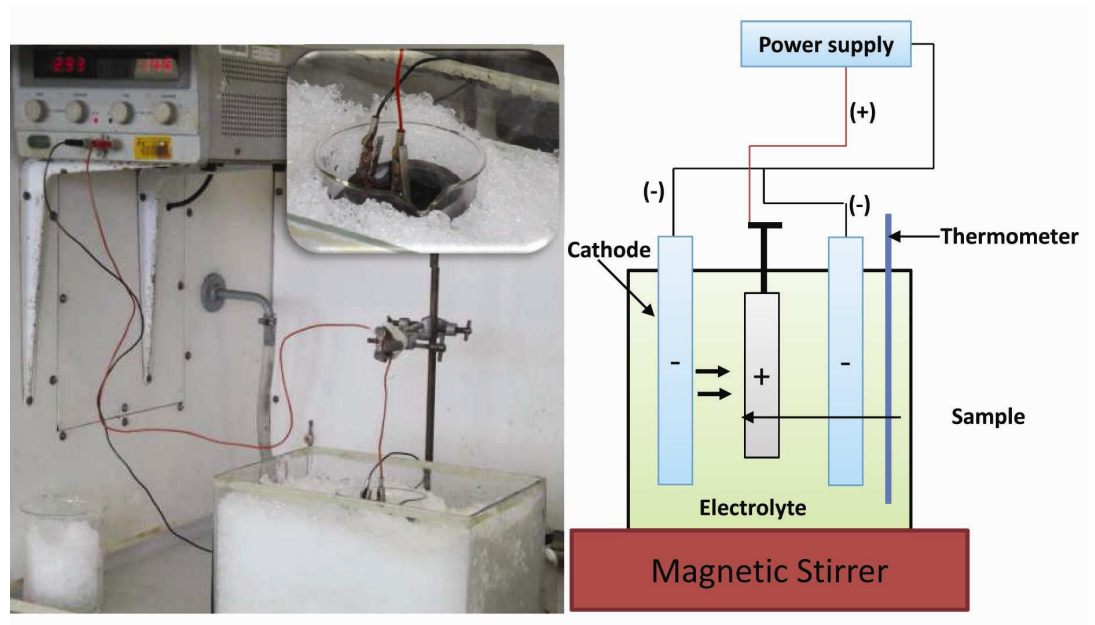


Figure 3- 6: Schematic image and photo of the electro-polishing cell.

### 3.10. Fatigue Limit Determination

The fatigue tests for both materials were performed using a R.R Moore rotating-bending machine at room temperature in air (Figure 3- 7). Fatigue limits were identified using the staircase method with 20 specimens, employing a step-width of 2 MPa. The fatigue endurance limit was set at  $10^7$  cycles.

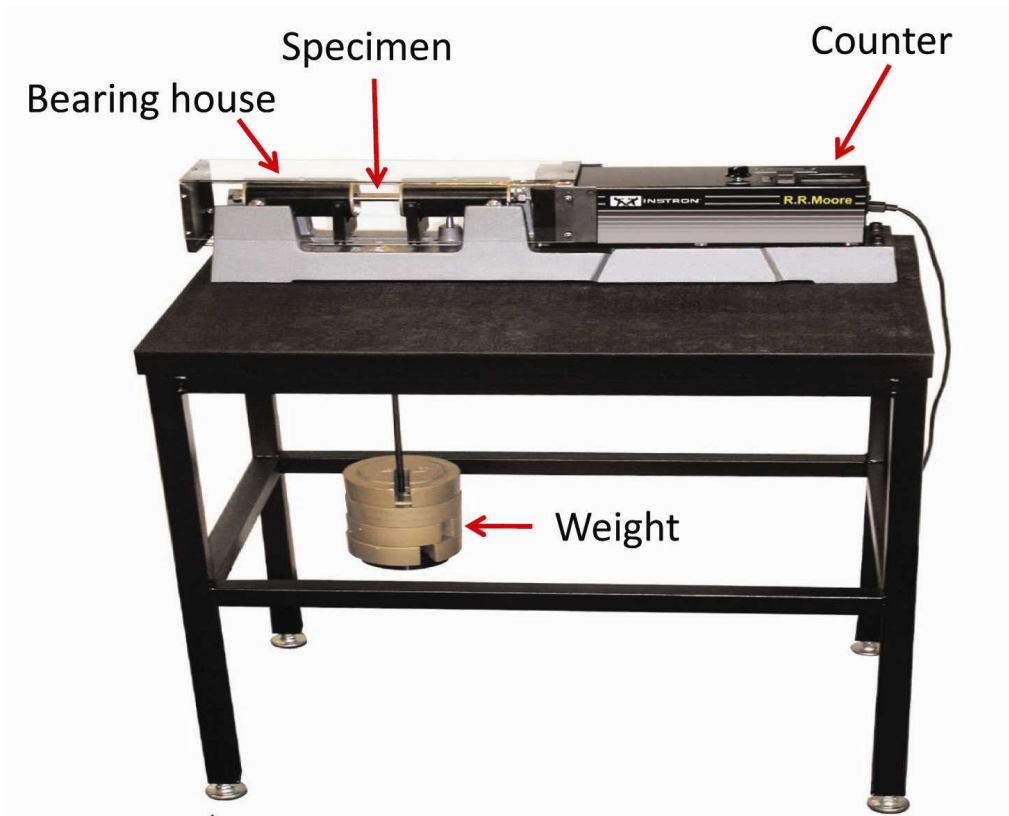


Figure 3- 7: R.R Moore rotating-bending machine [109].

### 3.11. Calculation of Applied Load

In Model R.R. Moore High speed (Rotating Beam Fatigue Testing Machine), the stress in the specimen is calculated from the following formula.

$$S = \frac{16 WL}{\pi D^3} \quad (3-1)$$

Where:

$S$  = Extreme fiber Stress (MPa).

$W$  = Total load on specimen (Kg).

$L$  = Moment arm (distance from end support to load point) (mm).

$D$  = Minimum diameter of specimen (mm).

Since  $L$  is fixed at 4 in (101.6 mm), the value of  $W$  for the desired value of  $S$  can readily be determined for any diameter specimen. The chart in Appendix was prepared to give a loading factor for each value of  $D$ . To obtain the required load using the chart, the factor which corresponds to the diameter of the specimen at the desired stress expressed in thousand per square inch. Before applying the load, allowance must be made for the effective weight of the bearing housings, loading harness and weight pan,

which amounts to 10 lbs (5 Kg). E.g. to produce a stress of 28,530 lbs per square inch in a 0.306 in diameter specimen, the reading opposite 0.306 on the chart is the factor of 1.4065. 1.4065 times 28.53 equals 40.13 lbs. Subtract the effective weight to obtain the actual weight that must be applied, 40.13 minus 10.0 equals 30.13 lbs [109].

### **3.12. Staircase Method Procedure**

The staircase method procedure is as follows [11]. An initial guess of the fatigue limit, a stress step size (2 MPa) and an endurance limit ( $10^7$ ) are selected. The first specimen is tested at a stress level equal to the estimated mean value of the fatigue limit. If failure occurs before  $10^7$  cycles, the next specimen is tested at one increment below the first stress level (2 MPa). If there is no failure at the first stress level, then the next test is at the stress one increment above the first level (2 MPa). This procedure is continued for all the test specimens to be tested, the stress level for each test being dependent on the previous result. The analysis of staircase method has been employed as discussed in chapter two (2.2.8.4).

### **3.13. X-ray Diffraction Technique to assess martensitic phase**

X-ray diffraction (XRD) is a versatile, non-destructive technique that reveals information about the chemical composition and crystallographic structure of materials. By determining the lattice spacing (d-spacing) in a sample it is possible to extract crystallographic information.

Briefly, the sample is illuminated with x-rays of a fixed wave-length and the x-rays are scattered in the sample and a detector is used to collect the scattered x-ray intensity. Measurements are performed by determining the intensity and the 2-theta diffraction angle in a diffraction pattern. The 2-theta ( $2\theta$ ) angle can then be converted to d-spacing between the crystal planes by Bragg's law ( $\lambda=2d\sin\theta$ ). The intensity (I) is measured to discriminate the various d-spacings and the results are used to identify possible structure matches.

The presence of martensitic phase in fatigue samples before fatigue test and after fatigue test was measured for both materials using X-ray diffraction with Co  $K\alpha$  radiation at 40 kV and 40 mA. An X-pert-1 diffractometer was used with step scan mode to cover the angular  $2\theta$  range from  $40^\circ$  to  $140^\circ$ . The  $2\theta$  step size was  $0.05^\circ$  with a collecting time of 10s at each step.



### 3.14. X-ray Diffraction Technique to measure Residual Stress

The residual stress was measured by the  $\sin^2\psi$  method [110]. The X-ray diffraction technique has been used to quantify the residual stresses by means of a machine 'PROTO' associated with 'XRDWin' software. The X-ray source was a  $K\alpha$  ray of Mn (20 kV, 4 mA,  $\lambda = 0.21$  nm, plane  $\langle 311 \rangle_{hkl}$ ,  $2\theta = 156^\circ$ , 1mm collimator).

Figure 3- 8 shows a schematic diagram of the different angles and rotations used in residual stress measurements, and a sketch of the two detector arrangement of the Proto system [110].

Depth profiles of residual stress were obtained using successive electropolishing at intervals of approximately  $30\mu\text{m}$ . The Young's modulus and Poisson's ratio employed were 193 GPa and 0.29, respectively. No correction was carried out to account for the material removal of surface layers, as the effect was calculated to be less than 7 % [111] Residual stress measurements were obtained from at least three independent specimens for each condition and for both materials.

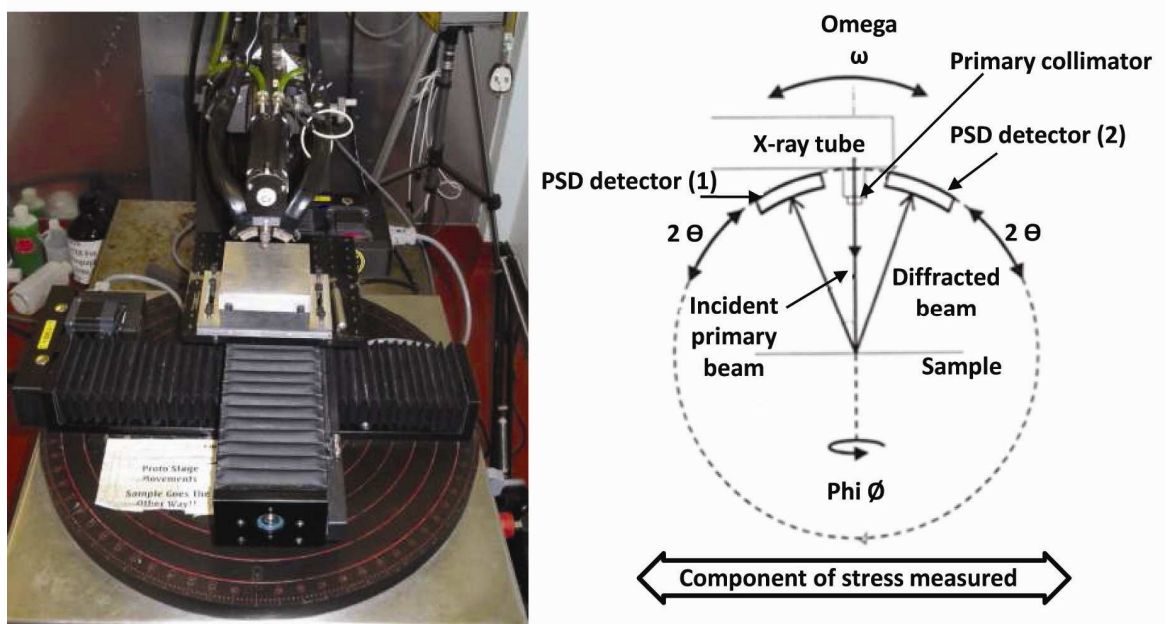


Figure 3- 8: X-Ray diffractometer (proto i-XRD) [110].

### 3.15. Full Width at Half the Maximum Peak (FWHM) of Machined Surface

Simultaneously, XRD technique can measure the broadening of X-ray diffraction peaks to quantify the degree of cold work in the material.

The degree of plastic strain in the crystal lattice can be expressed qualitatively by its effect on the width of X-Ray diffraction peaks [112]. This arises from the distortion of lattice planes by dislocations, giving rise to a spread of diffraction conditions for a given set of crystal planes. X-ray diffraction data for the peak was analysed for the (311) diffraction plane to obtain the peak width as a function of depth below the machined surface. To enable measurements at the exposed surface, Material was removed by successive electropolishing as mentioned in section 3.9.

### **3.16. Surface Roughness**

#### **3.16.1. Stylus Profilometry**

Preliminary surface roughness measurements were performed using a Taylor-Hobson Talysurf 50 stylus profilometer. This system assesses surface roughness line profiles with a maximum traverse distance of 50 mm. Measurements are based on inductive signal detection with a cantilever pick-up arm. The pick-up arm contains a preloaded needle with a conical diamond tip with a radius of 1.5 to 2.5  $\mu\text{m}$ , giving a height resolution of 16 nm within a height range of 1 mm. In roughness measurement, this needle is dragged across the sample surface; the resultant vertical motion of the stylus compresses a piezoelectric element, which generates a linear voltage response.

For every machining condition three samples were measured. The measurement was repeated four times for each sample at different locations. Surface roughness profiles ( $R_y$  and  $S$ ) of each machined specimens were characterised. Where  $R_y$  and  $S$  are the largest peak to valley height and the mean spacing of adjacent local peaks, respectively.

#### **3.16.2. Optical profilometry**

Optical profilometry is a non-contact technique for the measurement of surface topography. Its benefits as compared to traditional non-optical techniques (e.g. stylus profilometry) it is a non-contacting, real-time measurement of surface topography, and in addition operates in two dimensions to provide a visualisation of the surface. It can measure surface heights and valleys to sub-micrometre accuracy over very small (several square microns) and relatively large (several square millimetres) areas. Peak-to-valley values were given, as were  $R_a$  and  $R_q$  values.

### 3.17. Surface Hardness

The Vickers hardness of machined specimens was measured using an Instron indentation instrument (Wilson model Tukan 2100), with an applied load and load time of 500 g and 10 s, respectively. The measurements were repeated 10 times for each sample, and the averages and standards deviation were evaluated. Due to the geometry of the cylindrical specimens and the difficulty to fix it under the indenter, the specimens were embedded in cold mounting resin to ensure the stability of specimen under the indenter as shown in Figure 3- 9.



Figure 3- 9: Fixing of microhardness specimens.

### 3.18. Nano-Indentation

Nano-Indentation testing has been developed to study the mechanical properties of very small volumes of material. Hardness (H) and elastic modulus (E) are the properties most frequently measured by Nano-Indentation tester.

The nano-indenter performs indentation test by driving a diamond indenter into the specimen surface and dynamically collecting the applied force and displacement data. Hardness and elastic modulus data are produced and then exported as excel spreadsheets. The MTS Nano-Indenter XP was used in this study to measure the hardness near to the surface of the machined samples before and after fatigue test.

The gauge length of the specimen was extracted from the fatigue sample and then Ni plated. Secondly, from this gauge length, the section perpendicular to the surface, parallel to the specimen longitudinal axis was embedded in Bakelite-type compression

mounting resin. Finally, the specimens were prepared using the standard metallographic preparation techniques as mentioned in section (3.4). The indentation depth and the distance between the indentations were 500 nm and 30  $\mu\text{m}$ , respectively.

### **3.19. Electron Microscopy for Fracture surfaces and Fatigue Cracks**

In order to characterise the deformation which takes place sub-surfaces after machining and fatigue testing, fatigued and un-fatigued samples (as machined) were studied using Scanning Electron Microscopy (SEM), Electron Backscatter Diffraction (EBSD), and Transmission Electron Microscopy (TEM).

### **3.20. Scanning Electron Microscopy (SEM)**

Scanning electron microscopy (SEM) is the most widely-used technique for studying the surface characteristics of materials. A highly-focused, scanning (primary) electron beam with an energy of 0.5 - 30 keV hits the surface of the specimen and produces many low energy secondary electrons. SEM operates in two primary imaging modes, namely, secondary mode and backscattered mode. The secondary electrons resulting from the interaction of the specimen with the electron beam provide topographic information regarding the morphological characteristics of the specimen. The secondary electrons can be used in the study of fracture surfaces, grain sizes, mechanical damage assessment, microcracks and contamination location. The backscattered electron is used to obtain information about the atomic number contrast (i.e. relative phase distribution).

The fracture surfaces of fatigued specimens and arrested cracks nuclei on the surface of run-out ( $>10^7$  cycles) fatigue tests were observed using a Philips XL30 Scanning Electron Microscope (SEM) which is equipped with field emission gun (FEG-SEM). Secondary electron mode and Backscattered mode were employed. The machine was operated at an accelerating voltage ranging between 15 kV and 20 kV and spot size of 3-4.

#### **3.20.1. Electron Backscatter Diffraction (EBSD)**

EBSD can be used to measure the crystal orientation, measure grain boundary misorientation, discriminate between different materials, and provide information about local crystalline perfection.

The technique is based on the use of diffraction patterns from bulk samples in the scanning electron microscope (SEM). Figure 3- 10 shows the configuration of a typical EBSD system. The electron beam hits the specimen surface at a small angle as, the specimen tilted to a relatively high angle (typically 70°) thus achieving a large fraction of electrons diffracted (backscattered) by the lattice planes in the specimen [113]. Pattern comprised of a number of Kikuchi bands forms on a phosphor screen attached to a highly sensitive camera as a result of the diffracted electrons. As shown in Figure 3- 11, each band consists of a couple of parallel Kikuchi lines.

Backscattered electrons that satisfy Bragg's diffraction condition ( $\lambda=2d\sin\theta$ ) for a given plane emanate in diffraction cones from both the front and back surface of each family of lattice planes (only the diffraction on one plane was shown here) [114]. The intersection of these cones with the phosphor screen form Kikuchi lines.

The Kikuchi lines appear as straight lines on the screen. Each Kikuchi band represents the trace of the family of crystal lattice planes from which it is formed. From the angles between the bands and from their width the Miller indices of these lattice planes can be determined. Finally, from indexed bands the crystal orientation and phase can be calculated automatically by EBSD software.

In this research, the microstructures close to the surface, from metallographic sections perpendicular to the surface parallel to the specimen longitudinal axis, were studied using High-resolution electron backscatter diffraction (EBSD) mapping in a Philips XL30 field emission gun-scanning electron microscope (FEG-SEM) equipped with an HKL Nordlys II detector and Channel 5 software. The sample was tilted to 70° and then focusing on the interesting region, the pattern was acquired using the Channel 5 Flamenco HKL software. The map was acquired using the beam scanning mode in the acceleration voltage of 20kV, with spot size of 3-4, 100  $\mu\text{m}$  aperture and working distance of 20 mm. The acquisition time was set to 60 ms per point, with a step size of 0.5  $\mu\text{m}$ . University of Manchester software (V-map) was employed for display and analyse the data obtained from EBSD [115, 116].

The specimens were prepared using the standard metallographic preparation techniques as mentioned in section (3.4). In order to obtain a good quality in the EBSD patterns and avoid any residual deformation or stress in the surface layers due to mechanical polishing, electropolishing was applied. The electropolishing was performed in a

solution 8% perchloric acid ( $\text{HClO}_4$ ) and 92% acetic acid ( $\text{CH}_3\text{COOH}$ ) at room temperature under a voltage tension of 45 V for 60 s.

The Euler map shows grain orientations, where the colour is derived from the relative orientations of the crystal axes. Non-indexed points (i.e. where it was not possible to determine grain orientation from the back scattered electron pattern) appear as green. Maps can also be obtained which describe qualitatively the degree of contrast in the backscatter diffraction map. The band contrast is affected by plastic deformation [113, 117], and this provides a qualitative view of the distribution of plastic strain.

Small angle grain boundaries are indicated by white lines in Euler maps. The dark contrast beneath the surface shown in Band contrast maps corresponds to the region in Euler maps where a density of small angle grain boundary is higher than the internal region.

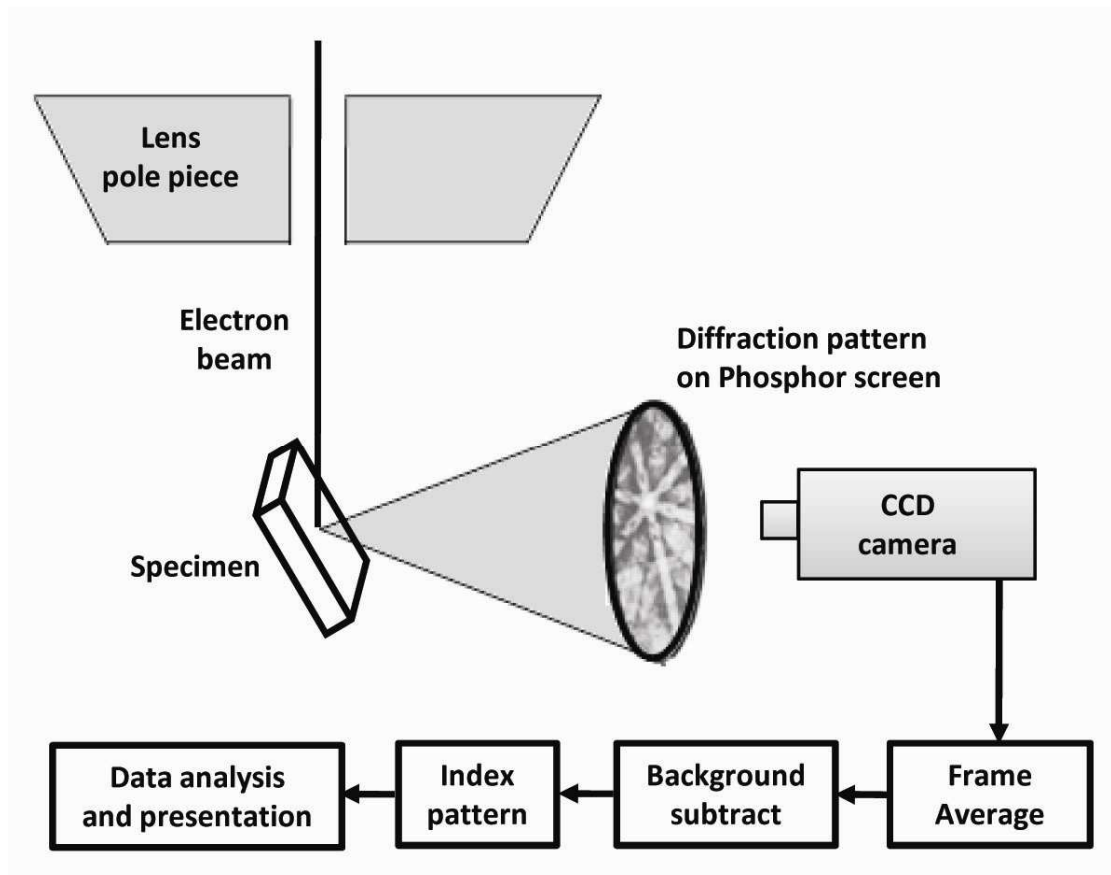


Figure 3- 10: Schematic of the components of an EBSD system [113].

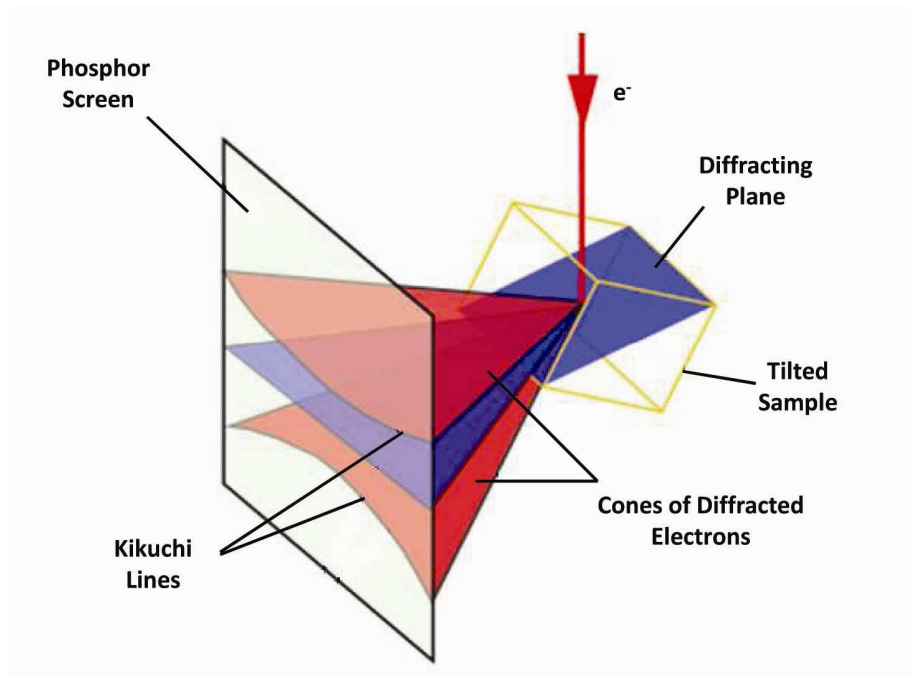


Figure 3- 11: The formation of the Kikuchi diffraction pattern [114].

### 3.20.2. Transmission Electron Microscopy (TEM)

Transmission electron microscopy (TEM) has become the most powerful tool for characterization of materials. The TEM consists of an electron gun and assembly of lenses all enclosed in an evacuated column. The working principle of TEM is shown schematically in Figure 3- 12. The electrons are emitted from the top of the microscope (electron gun) and travel through vacuum in the column of the microscope. A high-resolution CM-200 FEG-TEM was employed in the current study.

To focus the electrons into a very fine beam, electromagnetic lenses are used. When the electron beam hit the specimen some of the electrons are scattered and disappear from the beam. A diffraction pattern (DP) will be created on the back focal plane as results of un-scattered electrons come out from the exit surface of the specimen. A selected aperture will be inserted above the specimen permitting only electrons that pass through it to hit the specimen. The operation by using a selected aperture is known as selected-area diffraction (SAD). The SAD diffraction pattern contains a bright central spot and scattered electrons. The TEM can use either the central spot or the scattered electrons to form an image. These techniques are called bright-field (BF) imaging and a dark-field (DF) imaging. In order to create the BF and DF image, an aperture is inserted in the back focal plane of the objective lens. The aperture is adjusted to select only the centre

spot or diffracted electrons. If the direct electrons are used, then the image is a BF image; if the diffracted electrons are used, it is a DF image [118].

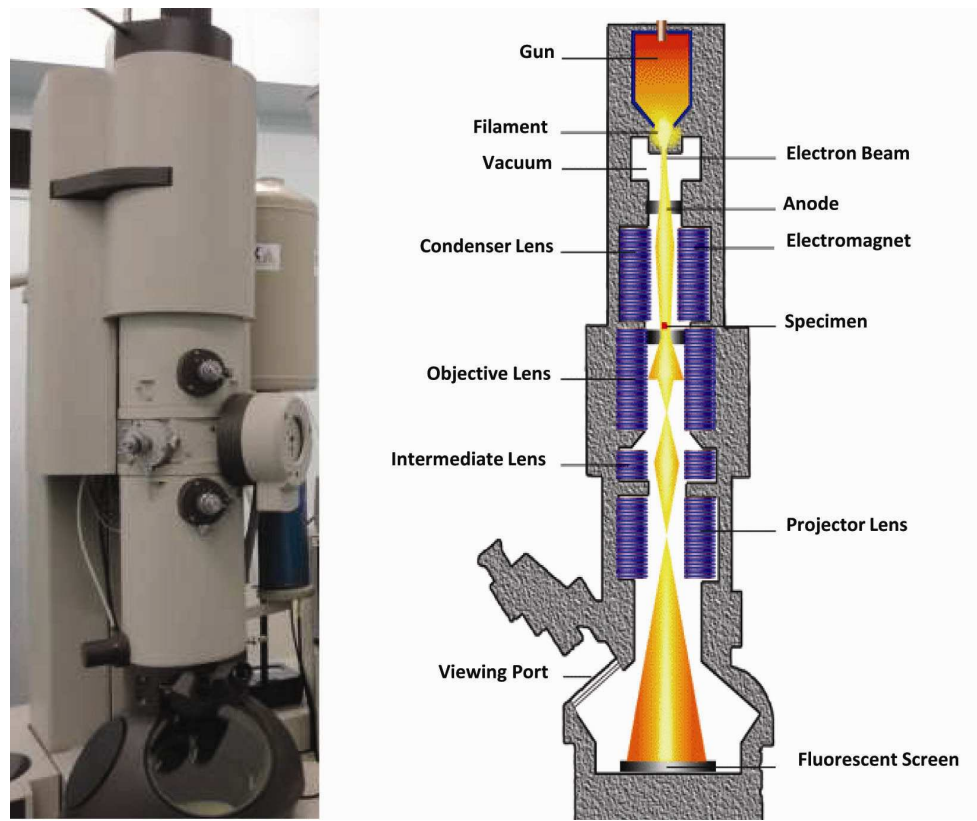


Figure 3- 12: An Overview of the TEM.

### 3.20.3. Sample preparation for TEM using Focused Ion Beam (FIB)

In order to obtain TEM samples at selected surface regions of fatigued samples, the TEM sample was prepared by FIB, using an FEI Dual Beam system. It is not easy to thin such selected areas by using traditional methods of specimens preparation, such as a twin-jet technique. Figure 3- 13 and Figure 3- 14 show four stages of FIB preparation process to prepare TEM samples for fine machined-1 and electropolished-3 samples. The first step is marking the exact area of interest (by cross positioning) and defining the dimension of the lamella (length; 10-15  $\mu\text{m}$  and height: 5-7  $\mu\text{m}$ ). As in Figure 3- 13-b, to allow the lamella to be thinned to the final thickness without damage, platinum protective layer was deposited on the surface (thickness: 1.5  $\mu\text{m}$ ). A staircase was formed through FIB milling on both side of the lamella using Ga<sup>+</sup> source at 30 KV and a current of 3000 pA. Low Ga<sup>+</sup> current of 100 pA was applied to perform the final thinning of the lamella (< 100 nm) (Figure 3- 13-c). Finally, the lamella was disconnected by FIB from the matrix, lifted out (Figure 3- 13-d) and placed on a TEM grid that fits in a TEM specimen-holder for analysis Figure 3- 13-f).



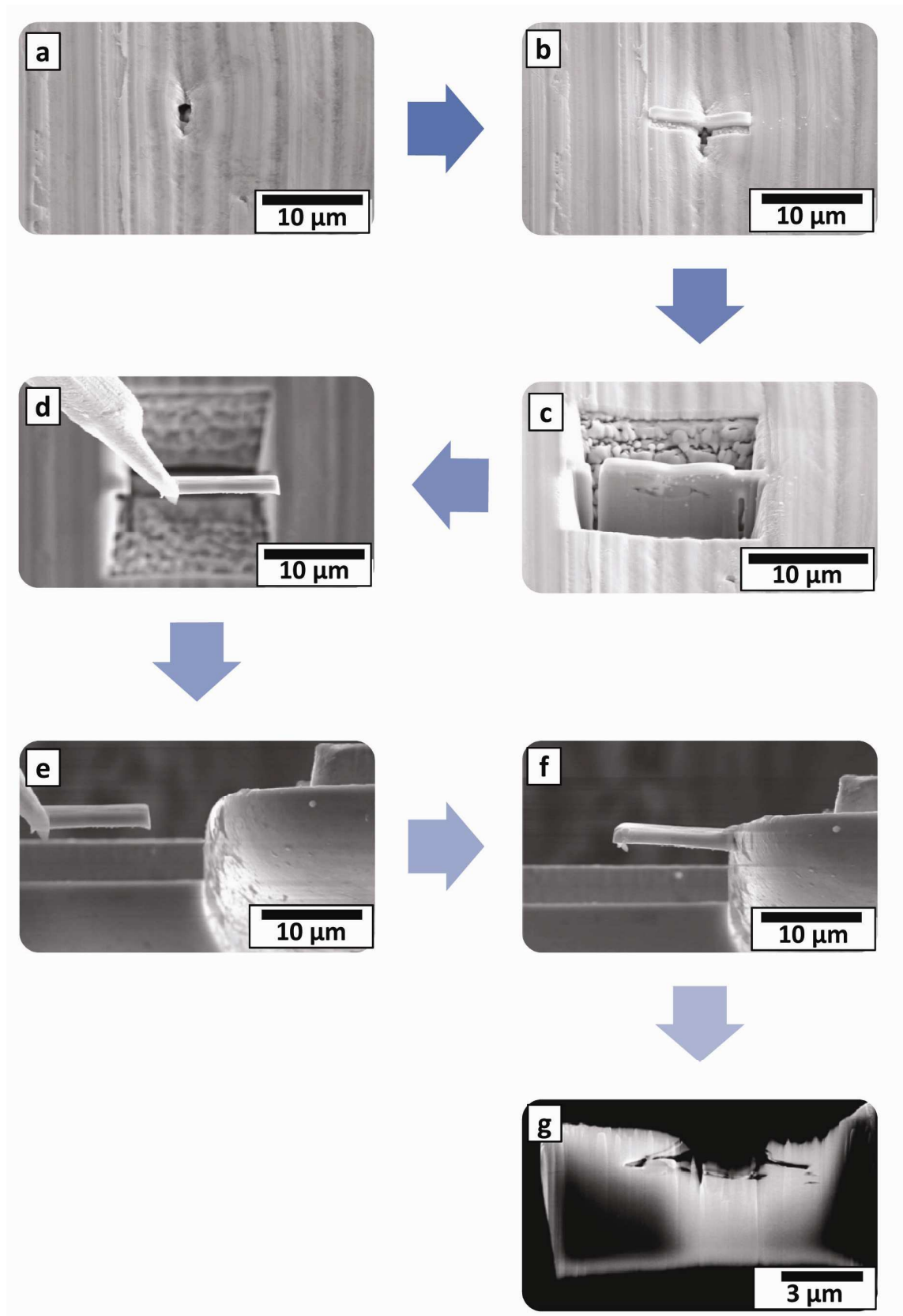


Figure 3- 13: Lift-out TEM sample preparation. a) Area of interest on the sample surface; b) Platinum protective layer over the interest area; c) U-shaped profile of the sample before left out; d) Lift out of the sample; e) Connecting the TEM sample to the grid; f) TEM sample fixed on the grid before thinning; g) Final shape of the sample after thinning.

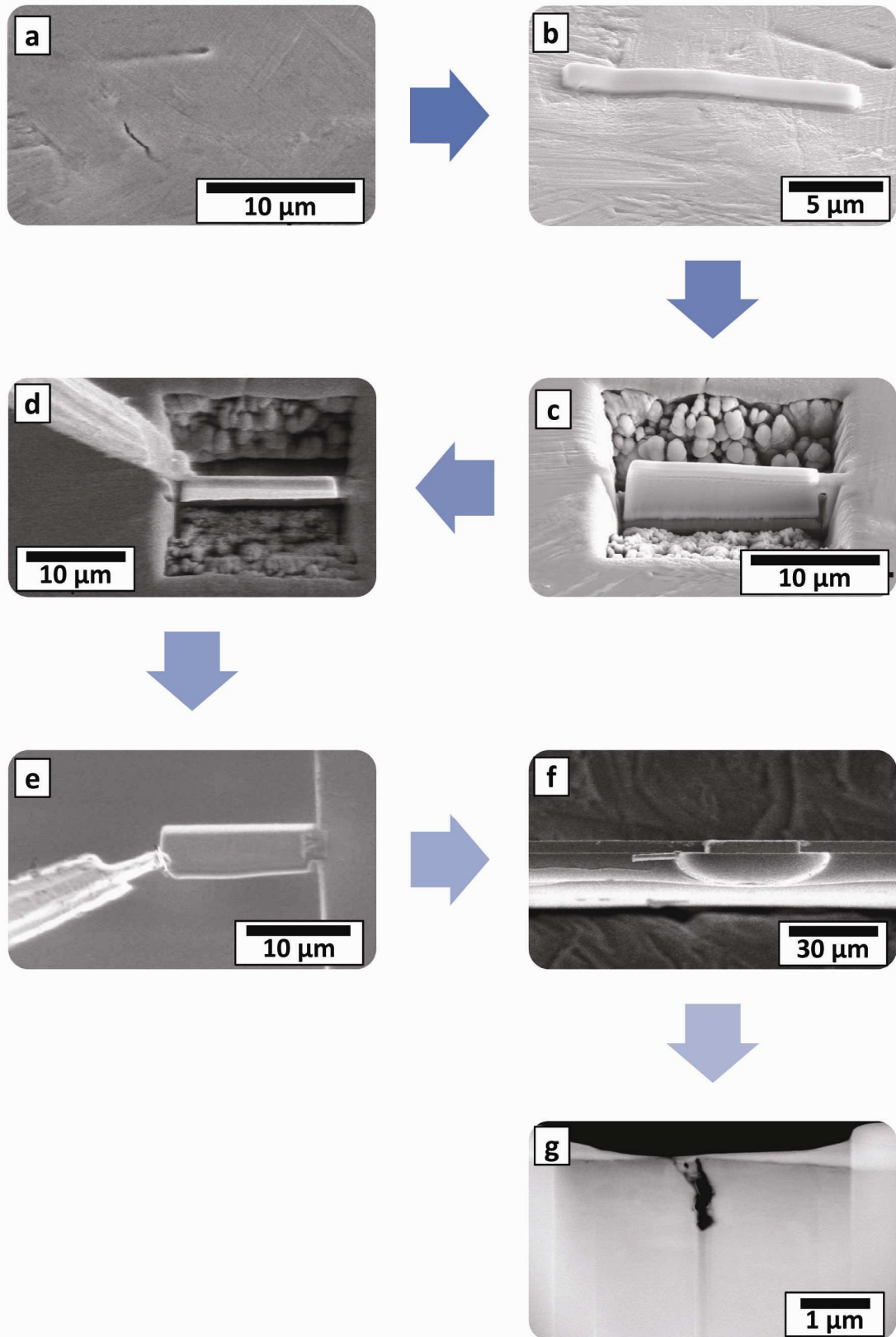


Figure 3- 14: Lift-out TEM sample preparation. a) Area of interest on the sample surface; b) Platinum protective layer over the interest area; c) U-shaped profile of the sample before left out; d) Lift out of the sample; e) Connecting the TEM sample to the grid; f) TEM sample fixed on the grid before thinning; g) Final shape of the sample after thinning.

### 3.21. Ni Plating of specimens

In order to preserve the edges of the section for metallographic preparation and to allow EBSD analysis within a few  $\mu\text{m}$  of the edge of the section, the surfaces of run-out specimens were nickel plated prior to sectioning.

The gauge length part (20 mm) was cut from run-out specimen. The specimens were connected with approximate 60 mm length and 2 mm diameter stainless steel wire using spot welding. In order to ensure that the Ni plated parts were clean and that the Ni plating layer attached properly to this part, these parts were cleaned with acetone and then immersed in  $\text{HCl} + \text{H}_2\text{O}$  (1:1) for 2-5 min before immersing in the Ni-bath solution. As shown in Figure 3- 15 a cable is attached to the stainless steel wire, and the other end of the wire is attached to the negative of a power supplier (the cable is black in this picture). The red cable is connected to the positive power supplier; the other end of the red cable is connected to a plate made of pure nickel. The electrolyte temperature was kept between 40 – 60 °C. The composition of Ni bath is shown in Table 3- 4.

Table 3- 4: Composition of Nickel Bath.

Materials	Quantity
$\text{NiSO}_4$	225 g
$\text{NiCl}_2$	50 g
$\text{H}_3\text{BO}_3$	33 g
$\text{Na}_2\text{SO}_4$	40 g

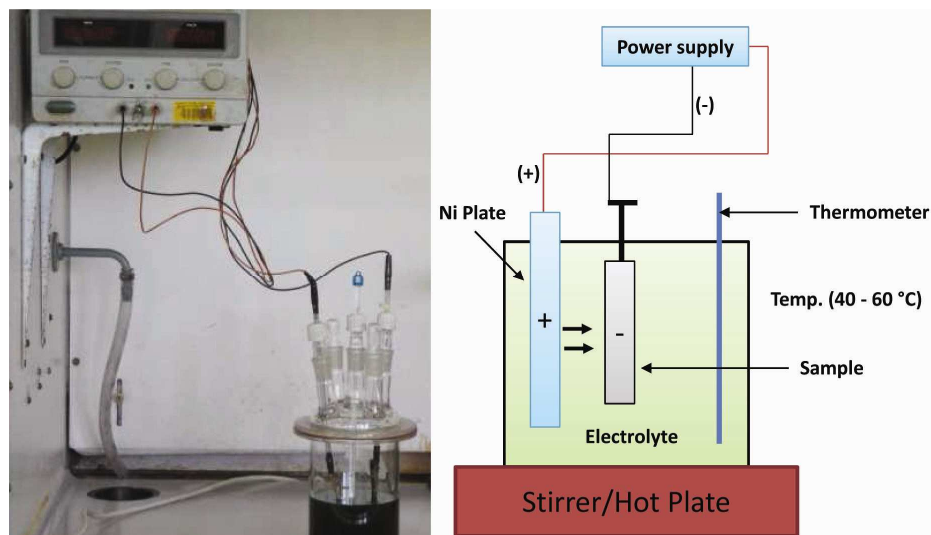


Figure 3- 15: Schematic image and photo of the Electroplating setup.

# Chapter 4

## Results

### 4.1. Materials and Specimen Preparation

#### 4.1.1. Materials

The materials used were austenitic stainless steel (AISI 304L/AISI 316L) rods. Their measured chemical compositions are given in Table 4- 1. Table 4- 2 lists the mechanical properties of the as-received material.

Table 4- 1: Chemical composition of the stainless steels employed, and comparable higher carbon steels (wt %).

Material	C	P	S	Si	Mn	Cr	Ni	Mo	Fe
AISI 304L	0.022	0.040	0.028	0.33	1.24	17.65	8.33	0.37	Bal.
ASTM 304*	0.03	0.045	0.03	1.00	2.00	18-20	8-12	-	Bal.
AISI 316L	0.022	0.042	0.027	0.38	1.57	17.25	10.85	2.07	Bal.
ASTM 316*	0.03	0.045	0.03	1.00	2.00	16-18	10-14	2.00-3.00	Bal.

\*: [119]

Table 4- 2: Mechanical properties of as-received materials. ( $R_{p0.2\%}$  = Yield strength at 0.2% strain / UTS = Ultimate Tensile Strength).

Materials	As Received Condition	$R_{p0.2\%}$ [MPa]	UTS [MPa]
AISI 304L	Cold Drawn	433 -435	707 -711
AISI 316L	Cold Drawn	425 - 445	614 - 621

Table 4- 3 compares values of  $M_s$ ,  $M_d$  of AISI 304L with AISI 316L. The values were calculated using Eq. 2-3 and Eq. 2-4 and the nominal compositions from Table 4- 1.

Table 4- 3: Values of  $M_s$  and  $M_d$  values for AISI 304L and AISI 316L.

Materials	$M_s$ (°C)	$M_d$ (30/50) (°C)
AISI 304 L	-34.3	39
AISI 316 L	-183.5	-63

Figure 4- 1 shows the microstructure of AISI 304L and AISI 316L in the as received condition, observed by optical microscopy. The microstructures are typical of austenitic stainless steel. The microstructure consists of equiaxed austenite grains and annealing

twins. The microstructure also shows slip bands resulting from cold working. Figure 4-2 shows the microstructure of AISI 304L as received, revealed by EBSD.

Annealing at 900°C for 10 minutes show significant effect on the grain size near to the machined surface as shown in Figure 4-3, but not elsewhere.

#### 4.1.2. Grain Size

The grain sizes of AISI 304L and AISI 316L (as-received) were characterised by optical microscopy. The average grain sizes of AISI 304L and AISI 316L, to be used in the microstructure based fatigue model, were  $54 \pm 6 \mu\text{m}$  and  $57 \pm 7 \mu\text{m}$ , respectively. It can be seen that the grain size for both materials are nearly identical in all directions. The ASTM grain size (GS [ASTM]) of the two materials is 7.

Table 4- 4: Grain sizes of as-received and as-annealed materials.

Material	Condition	Grain Size ( $\mu\text{m}$ )			
		Longitudinal Section		Transverse Section	
		Parallel to the specimen longitudinal axis	Perpendicular to the specimen longitudinal axis	Parallel to the specimen longitudinal axis	Perpendicular to the specimen longitudinal axis
AISI 304L	As-Received	$65 \pm 7$	$54 \pm 6$	$46 \pm 4$	$57 \pm 7$
AISI 316L	As-Received	$71 \pm 8$	$57 \pm 7$	$50 \pm 5$	$54 \pm 7$



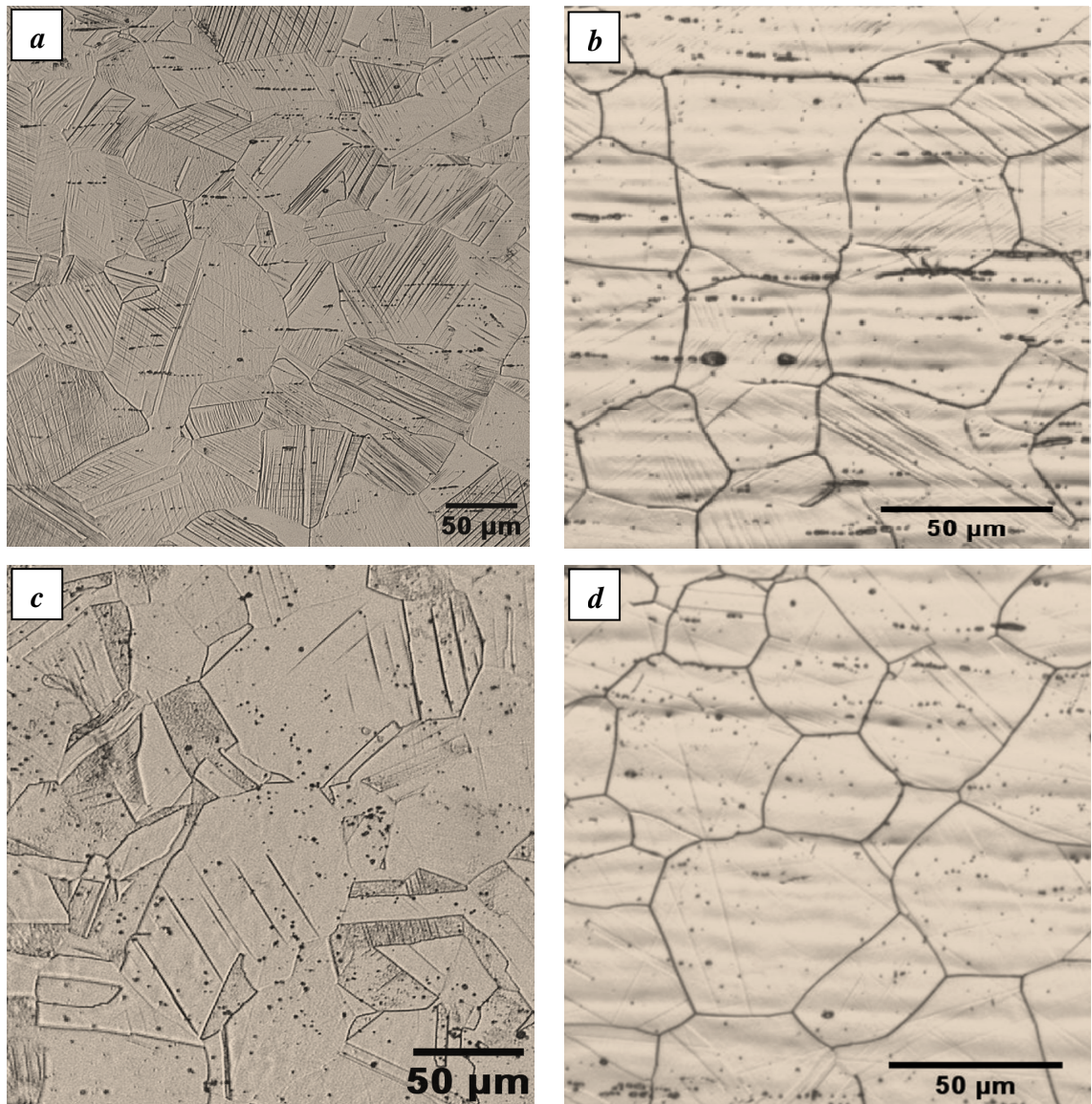


Figure 4- 1: the microstructure of AISI 304L and AISI 316L as received, observed by optical microscopy; a) AISI 304L As-Received (Etched with Oxalic Acid), b) AISI 304L As-Received (Etched with 50% of HNO<sub>3</sub> and 50% of H<sub>2</sub>O), c) AISI 316L As-Received (Etched with Oxalic Acid), d) AISI 316L As-Received (Etched with 50% of HNO<sub>3</sub> and 50% of H<sub>2</sub>O).



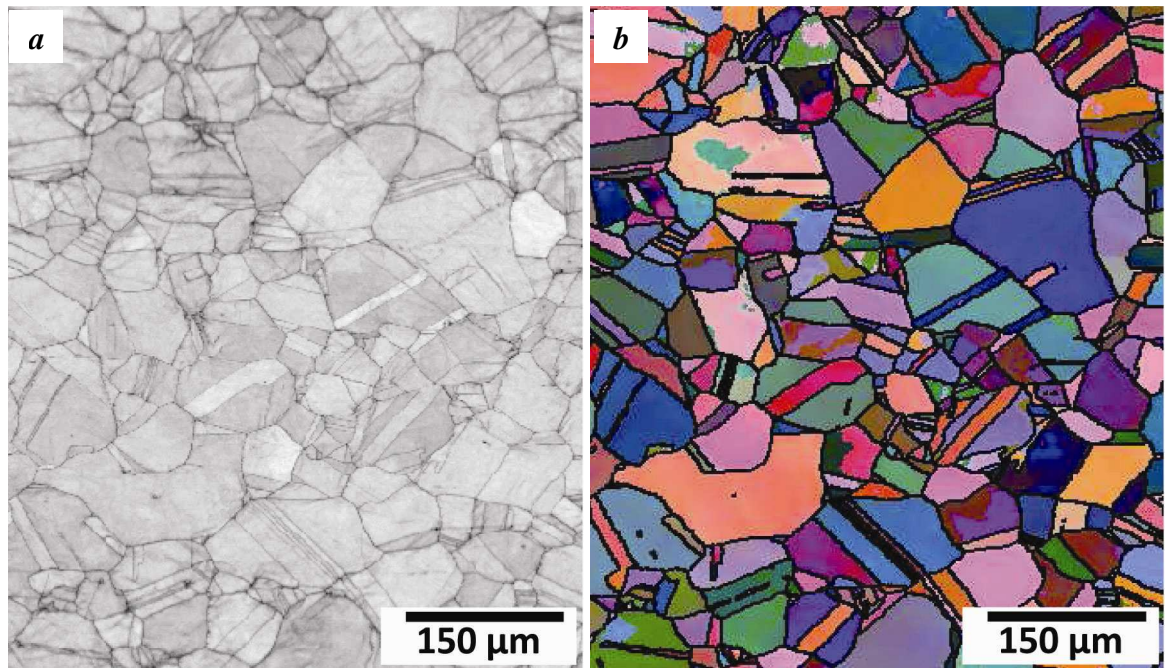


Figure 4- 2: EBSD microstructure map of the as-received microstructure of AISI304L; a) band contrast map; b) Euler map.

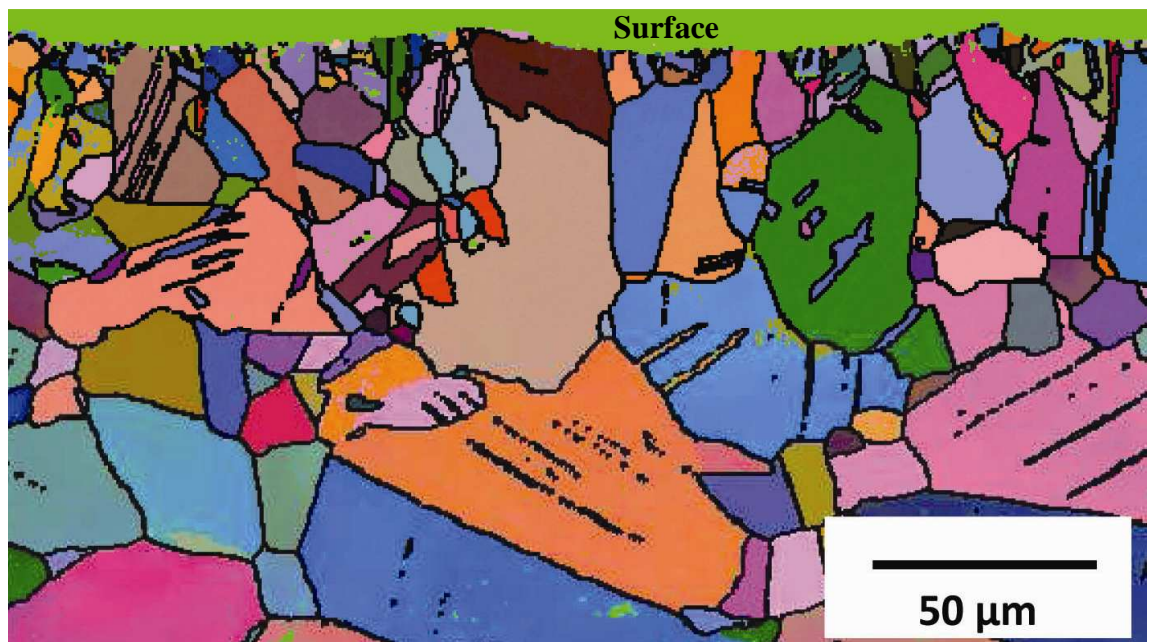


Figure 4- 3: EBSD microstructure map of fine machined and annealed sample of AISI304L.

### 4.1.3. Specimen Preparation

#### 4.1.3.1. Selection of Machining Parameters

Figure 4- 4 and Figure 4- 5 were constructed using equation. 4-1 and equation 4-2 to illustrate the main effects of machining parameters (spindle speed, feed rate and cutting depth) on the axial residual stress (MPa) and surface roughness  $R_y$  ( $\mu\text{m}$ ).

These equations (4-1) and (4-2) describe the response surface model which was developed in previous work [90]. Where X, Y and Z are the variables of the spindle speed (rev./min.), the feed rate (mm/rev.) and cutting depth (mm), respectively.

$$R_y = -1.03 - 1.90 \times 10^{-3} X + 57.2Y + 5.45Z - 2.48 \times 10^{-6} X^2 + 149Y^2 - 0.239Z^2 + 0.0235 XY + 4.06 \times 10^{-3} XZ - 11.3YZ \quad (4-1)$$

$$RS = -715 + 0.365X + 5370Y - 218Z - 6.65 \times 10^{-5} X^2 - 9960Y^2 + 27.4Z^2 - 0.0618XY - 0.0594XZ + 177YZ \quad (4-2)$$

In both figures, three conditions are labelled; A, which represents **Rough condition I** (Low cutting depth, high feed rate), B, which represents **Rough condition II** (Large cutting depth, low feed rate) and C, which represents the **Fine condition** (low cutting depth, low feed rate). These figures show the effects of feed rate and cutting depth on the roughness  $R_y$  ( $\mu\text{m}$ ) and residual stress (MPa). This response surface was then used to identify combinations of feed rate and cutting depth that gave significant and controlled variations in roughness and residual stress.



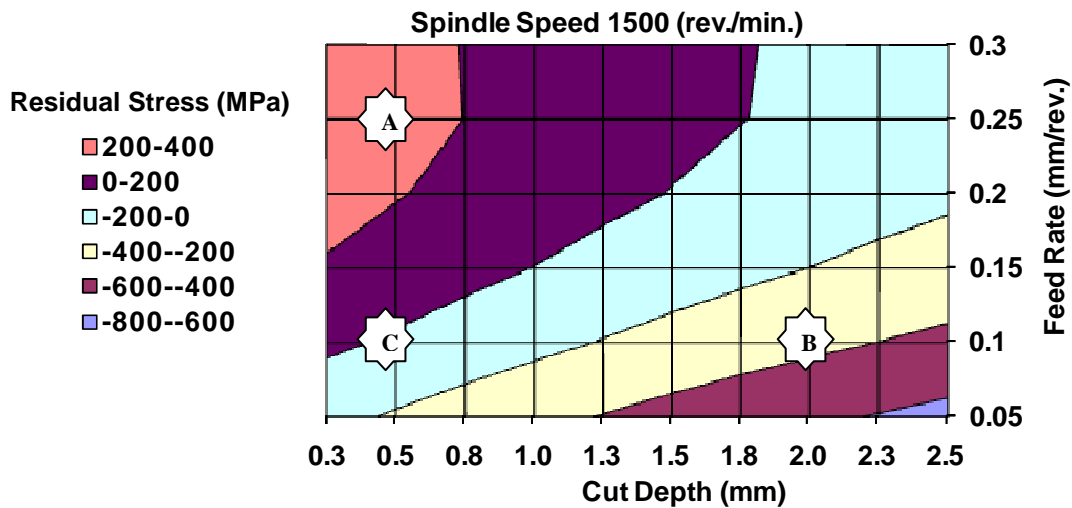


Figure 4- 4: Effect of machining parameter on residual stress.

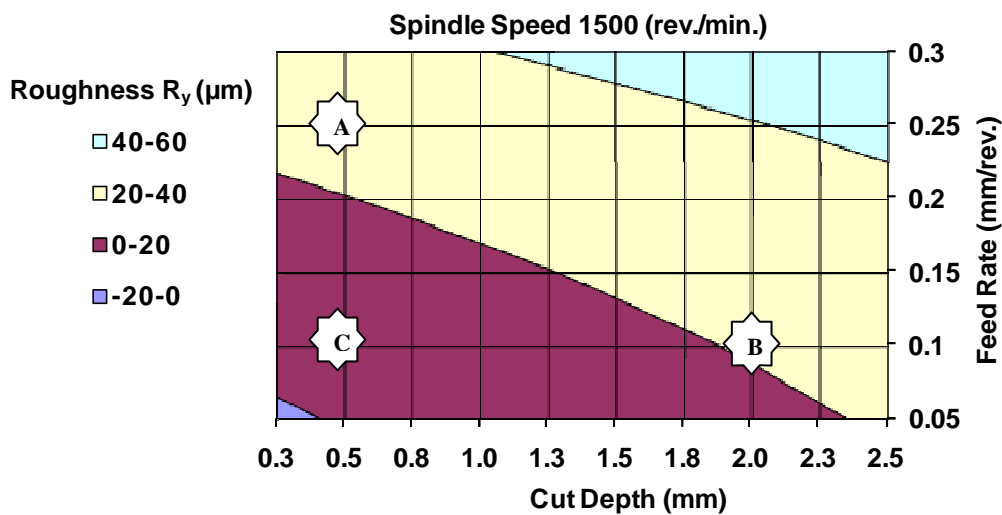


Figure 4- 5: Effect of machining parameter on roughness  $R_y$ .

## 4.2. Surface Characterisation

### 4.2.1. Surface Roughness using Stylus Profilometry

The averages and standards deviation of  $R_y$  and  $S$  were evaluated (Table 4- 5). Where  $R_y$  and  $S$  are the largest peak to valley height and the mean spacing of adjacent local peaks, respectively.

As described in section (3.6), four groups of specimens were produced with different final cutting conditions (AISI 304L) in order to obtain very different residual stress distributions and different roughness. These groups can be seen in Table 4- 5.

Table 4- 5: Roughness measurements of machined specimens with different machining conditions.

Materials	Groups	Sample Code	Spindle Speed (r/mm)	Feed Rate (mm/r)	Cutting Depth (mm)	R <sub>y</sub> (μm)	S (μm)
AISI 304L	Group 1	A	2500	0.25	0.1	21 ± 1	249 ± 02
		B	2500	0.1	2.5	09 ± 04	95 ± 05
		C	2500	0.25	1.65	27 ± 03	232 ± 33
	Group 2	A	1500	0.25	0.1	23 ± 01	243 ± 07
		B	1500	0.1	2.5	12 ± 02	82 ± 02
		C	1500	0.25	1.8	29 ± 01	243 ± 03
	Group 3	A	1700	0.25	0.1	25 ± 02	248 ± 07
		B	1700	0.1	2.5	09 ± 01	50 ± 01
		C	1700	0.25	1.8	27 ± 01	75 ± 10
	Group 4	A	1500	0.25	0.4	23 ± 2	249 ± 1
		B	1500	0.1	2	8 ± 2	64 ± 1.4
		C	1500	0.1	0.4	7 ± 1	58 ± 1.3
AISI 316L	Group 4	A	1500	0.25	0.4	23 ± 1	249 ± 2
		B	1500	0.1	2	9 ± 1	58 ± 3
		C	1500	0.1	0.4	8 ± 1	60 ± 2

#### 4.2.2. Surface Roughness using Optical profilometry

The optical profilometry data obtained in this project was used to supplement that obtained from stylus profilometry.

The high peak-to-valley and the spacing of adjacent local peaks were summarized in Table 4- 6. Figure 4- 6 and Figure 4- 7 are examples of optical profilometry data for fine machined (C) sample and rough machined (A) sample. Some variation between the two measurement types in the magnitude of the data was expected. This is because the sensitivities of the two techniques and their accuracies will not be the same. As stylus profilometry works by the dragging of a needle across the sample's surface, the radius of its tip and the tip sharpness will determine the equipment's sensitivity to deviations in the detection of small (in relation to the size of the stylus tip) asperities.

Table 4- 6: Roughness measurements of machined specimens by stylus profilometry and optical profilometry.

Conditions	Stylus profilometry		Optical profilometry			
	R <sub>y</sub> (μm)	S (μm)	R <sub>y</sub> (μm)		S (μm)	
			Min.	Max.	Min.	Max.
Fine Machined (C)	08 ± 1	60 ± 2	3	3.98	98.12	100
Rough Machined (A)	23 ± 1	249 ± 2	23	24.8	236	250

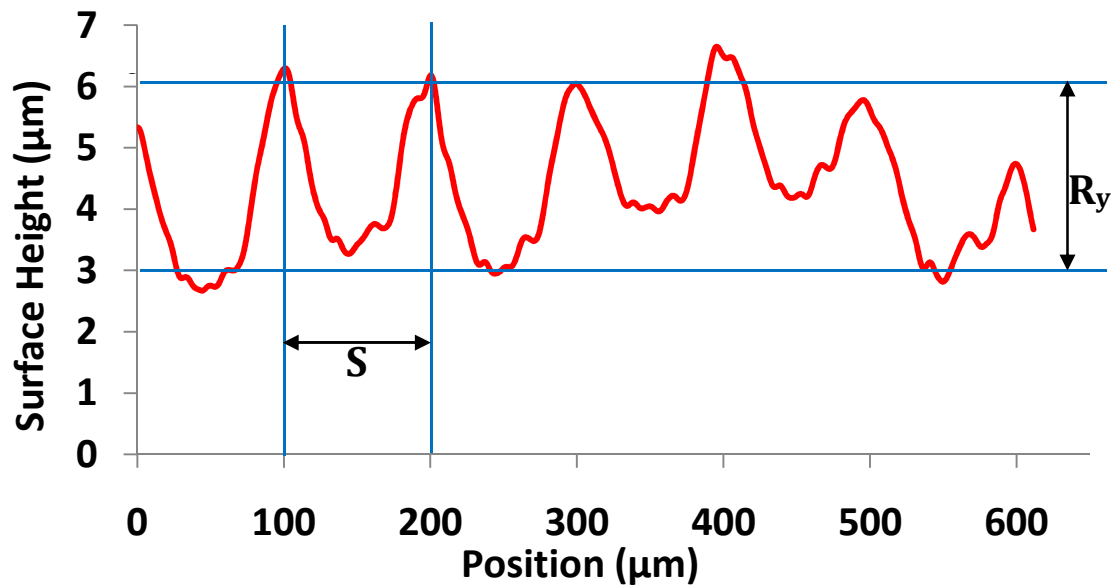


Figure 4- 6: Line segment profile of fine condition-C (Optical profilometry data).  $S$ : the spacing of adjacent local peaks;  $R_y$ : the high peak-to-valley.

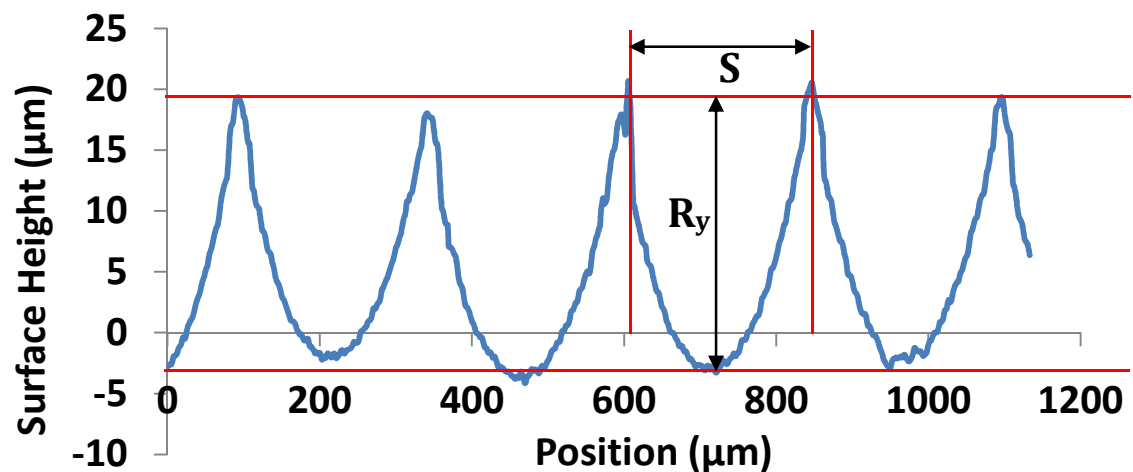


Figure 4- 7: Line segment profile of Rough condition-A (Low cutting depth, high feed rate), (Optical profilometry data).  $S$ : the spacing of adjacent local peaks;  $R_y$ : the high peak-to-valley.

#### 4.2.3. Hardness

Figure 4- 8 shows the effects of electropolishing and annealing on machined specimens for both materials. From this figure it can be seen that the variations between the machined samples are not significant. However, electropolishing and annealing at 900°C for 10 minutes significantly reduces the hardness by 35%. The values of surface hardness for both materials in different conditions are tabulated in Table 4- 7.

In AISI 304L, similar hardness levels were found for all machining conditions and these were also reduced significantly by annealing. The lowest hardness was measured after

electro-polishing the annealed microstructure. Comparable results can be seen in AISI 316L, but the lowest hardness was measured in fine annealed sample.

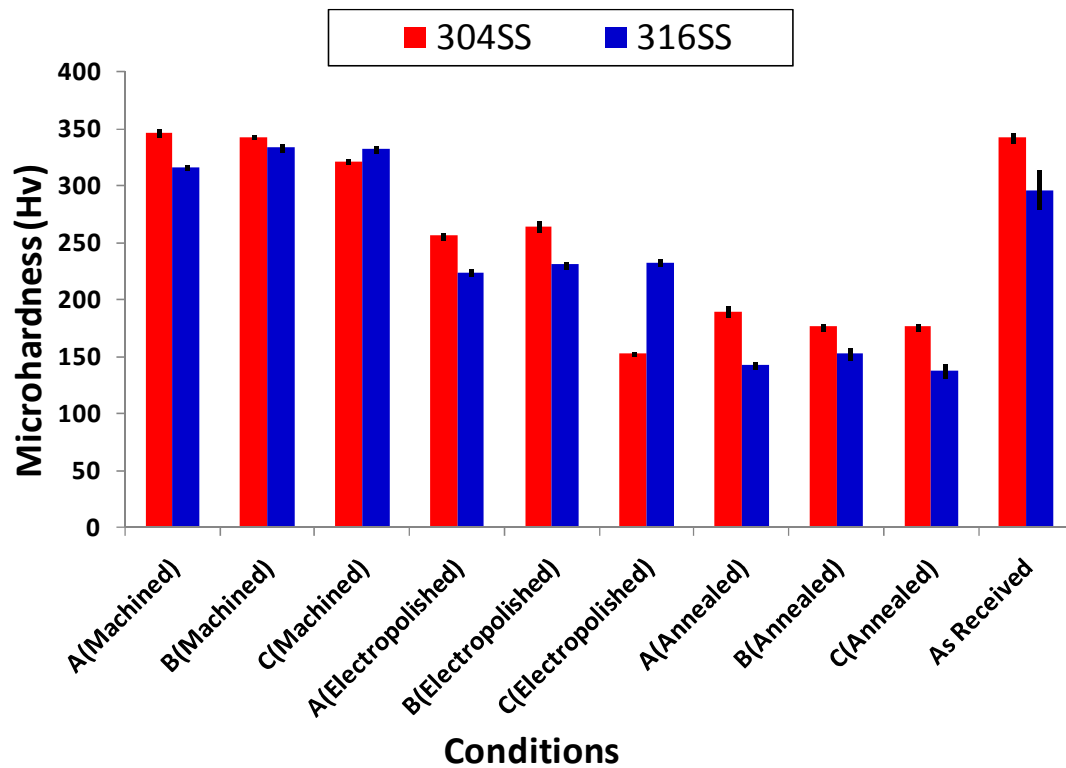


Figure 4- 8: Comparison of the surface hardness (Vickers) of the machined, electropolished, Annealed and as received (AISI 304L/AISI 316L).

Table 4- 7: Surface hardness (Vickers) of the machined, electropolished, Annealed (AISI 304L/AISI 316L).

Sample Codes	AISI 304L			AISI 316L		
	Machined	Annealed & Electropolished	Annealed	Machined	Annealed & Electropolished	Annealed
<b>A</b>	347 ± 4	256 ± 3	189 ± 5	315 ± 3	224 ± 2	142 ± 3
<b>B</b>	343 ± 2	264 ± 5	176 ± 3	333 ± 3	231 ± 3	152 ± 6
<b>C</b>	321 ± 2	152 ± 2	176 ± 3	332 ± 3	233 ± 3	138 ± 7

#### 4.2.4. Residual Stress

Figure 4- 9 shows the depth profiles of the axial and circumferential stresses for the machined samples for AISI 304L. The error bars are the standard deviation of measurements (9 measurements). Tensile stress of the order of ( $261 \pm 60$  MPa) was measured at the surface in the Rough condition –A (Low cutting depth), decreasing to ( $-281 \pm 35$  MPa) over a distance of  $120 \mu\text{m}$ . Compressive stress of the order of ( $-165 \pm 38$  MPa) was at the surface in Rough condition –B (Large cutting depth), increasing in

magnitude to  $(-485 \pm 45 \text{ MPa})$  over a distance of  $90 \mu\text{m}$ . In fine machined-C, the surface stress is about  $(14 \pm 35 \text{ MPa})$  decreasing to  $(-300 \pm 34 \text{ MPa})$  over a distance of  $90 \mu\text{m}$ . In AISI 316L (Figure 4- 11), tensile stress of the order of  $(302 \pm 95 \text{ MPa})$  at the surface in Rough condition–A (Low cutting depth), decreasing to  $(-252 \pm 94 \text{ MPa})$  over a distance of  $150 \mu\text{m}$ . Compression stress of the order of  $(-306 \pm 27 \text{ MPa})$  at the surface in Rough (Large cutting depth) condition, decreasing to  $(-412 \pm 23 \text{ MPa})$  over a distance of  $60\mu\text{m}$ . In fine machined-C, the stress is about  $(8 \pm 47 \text{ MPa})$  decreasing to  $(-257 \pm 41 \text{ MPa})$  over a distance of  $90\mu\text{m}$ .

It can be seen for AISI 304L and AISI 316L that the axial stresses vary significantly between machined specimens within a surface layer of approximately  $100 \mu\text{m}$ . Further than this, the differences are less significant. There are no significant residual stresses beyond a distance of approximately  $300 \mu\text{m}$  from the surface. In all conditions, the level of residual stresses in the both directions changes continuously with depth down to a maximum value in the compressive region and then gradually decreases stabilizing at the level close to zero. The circumferential residual stresses are tensile at the surface, but show similar trends to the axial stresses.

Figure 4- 10 and Figure 4- 12 for AISI 304L and AISI 316L respectively, show the axial and circumferential depth profiles for the machined and annealed conditions of machined specimens for both materials. As can be seen from these graphs, annealing at  $900^\circ\text{C}$  for 10 minutes effectively eliminates the machining induced residual stresses.

These results for the surface stresses are in good agreement with those predicted by the response surface [90]. For both steels, the expected surface stresses, predicted using the response surface for these machining conditions were  $280 \text{ MPa}$  and  $0 \text{ MPa}$ , respectively. In AISI 304L, the rough machined surface has significant tensile residual stress  $(261 \pm 60 \text{ MPa})$  in comparison to the fine machined surface  $(14 \pm 35 \text{ MPa})$ . A similar pattern emerges in AISI 316L, where the rough machined surface has tensile residual stress  $(302 \pm 95 \text{ MPa})$  in comparison to the essentially stress-free fine machined surface  $(8 \pm 47 \text{ MPa})$ .

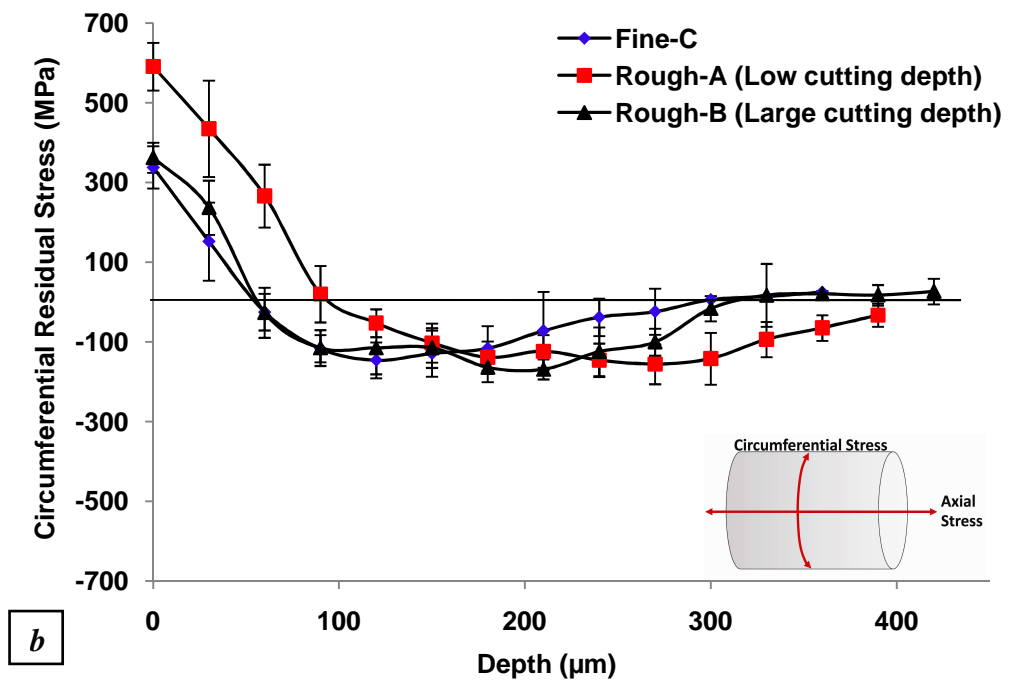
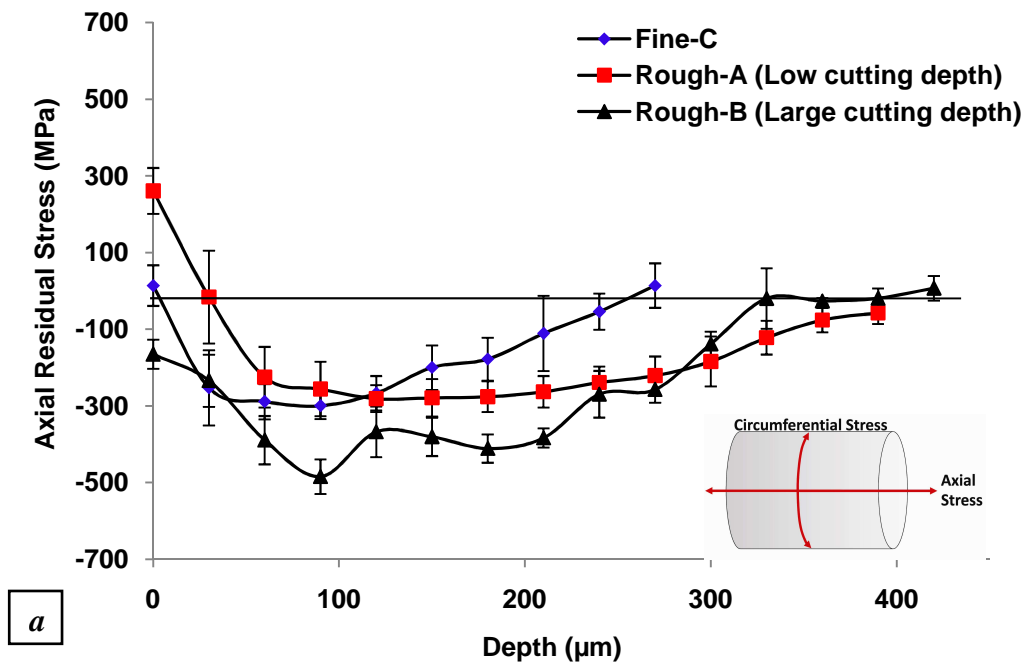


Figure 4- 9: Residual Stress of AISI 304L; a) Depth profiles of axial residual stress, b) Depth profiles of circumferential residual stress.

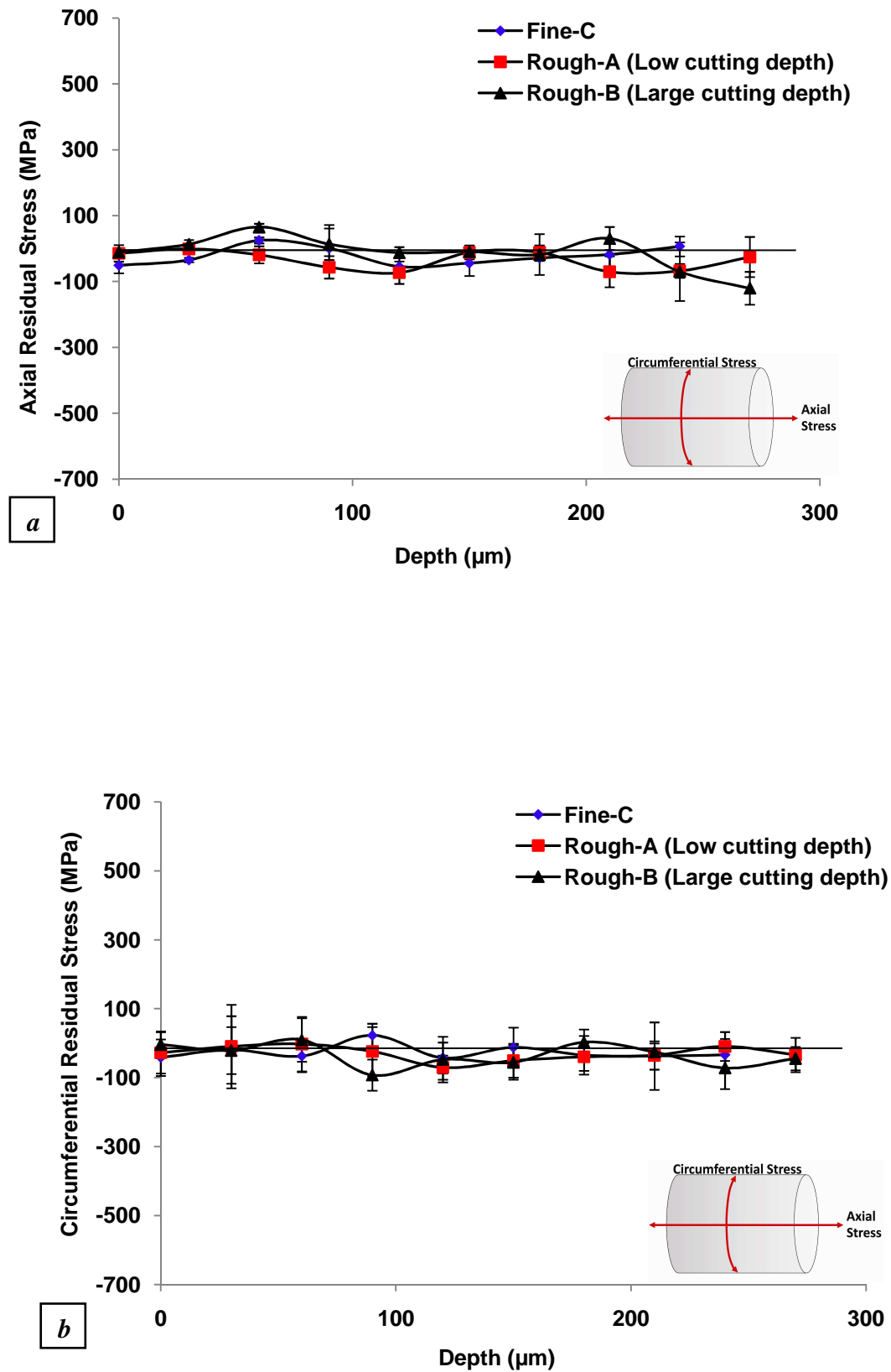


Figure 4- 10: Effect of annealing on the depth profiles (AISI 304L); a) axial residual stress, b) circumferential residual stress.

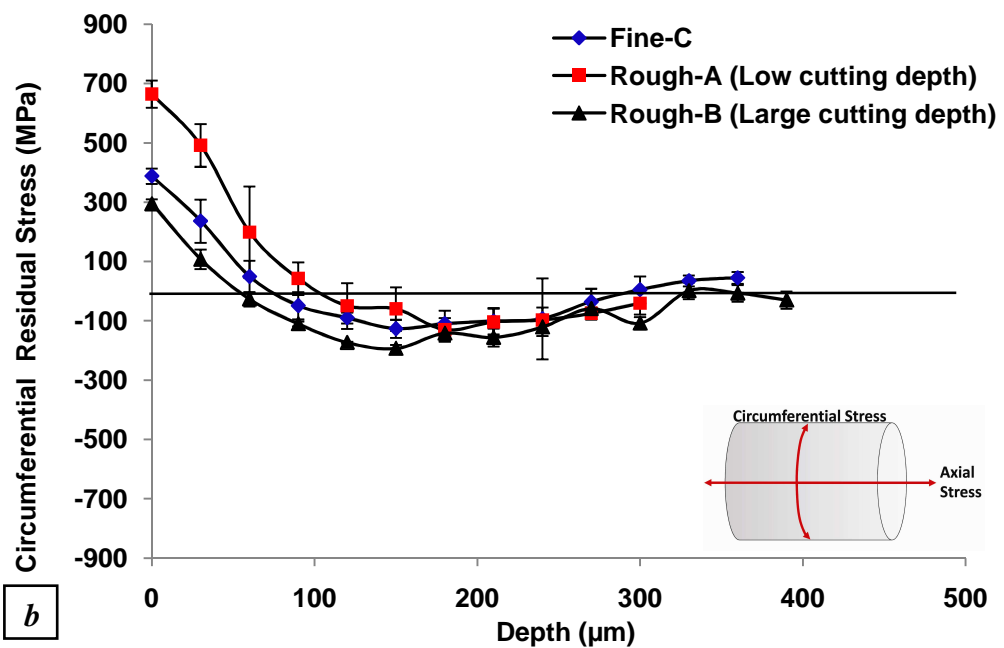
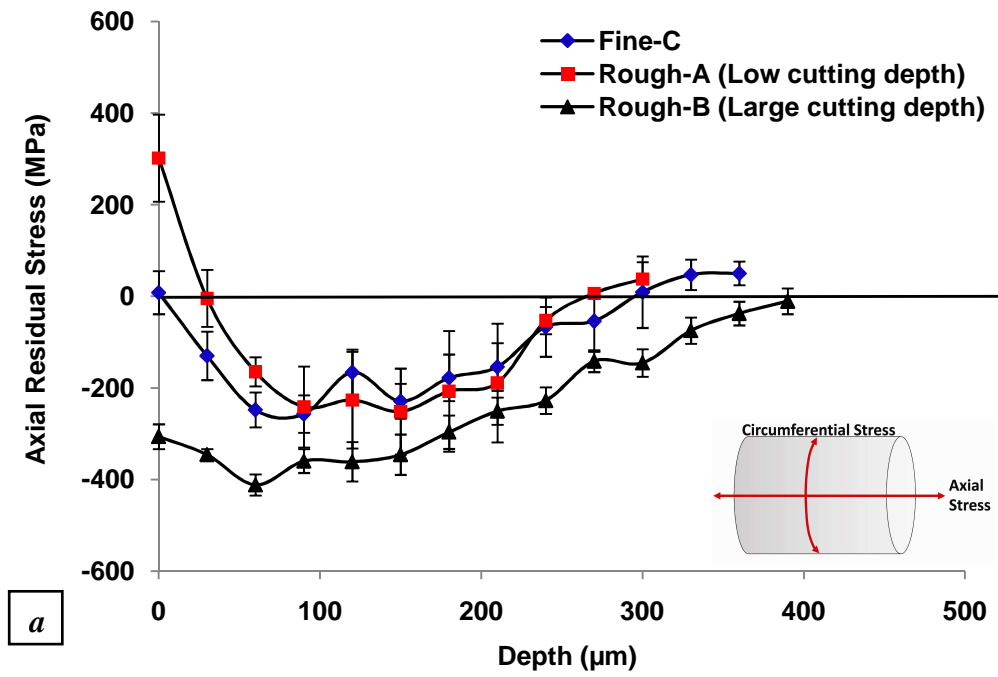


Figure 4- 11: Residual Stress of AISI 316L; a) Depth profiles of axial residual stress, b) Depth profiles of circumferential residual stress.



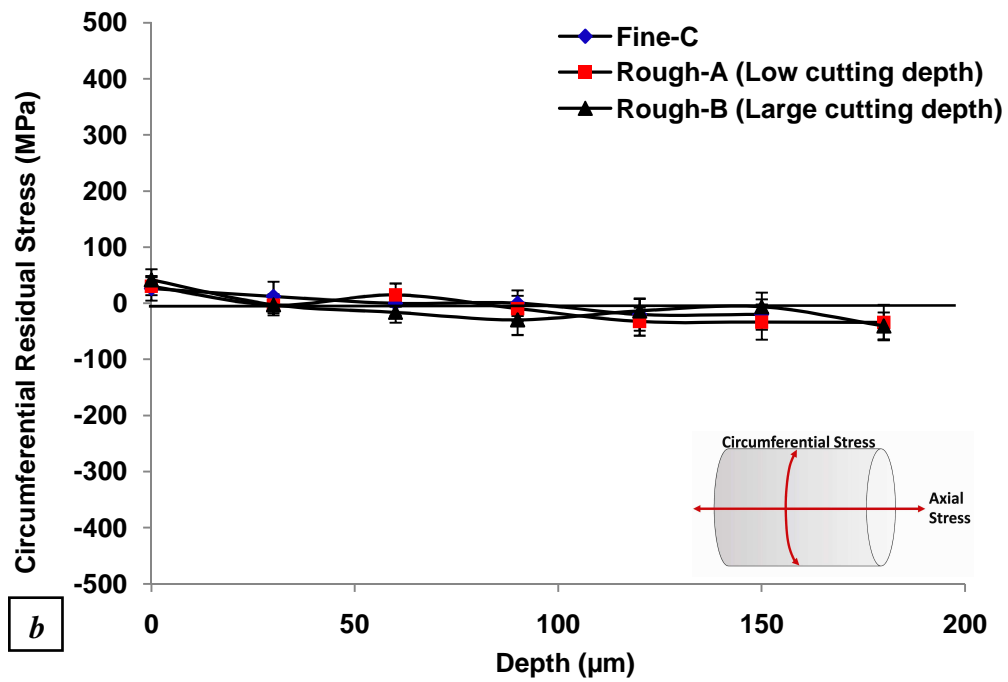
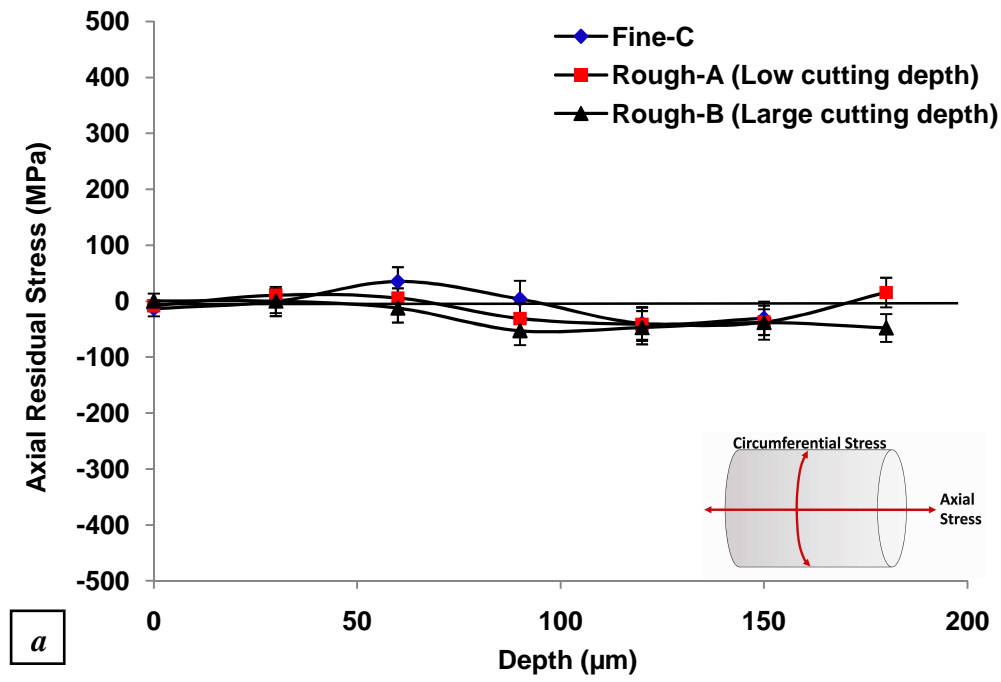


Figure 4- 12: Effect of annealing on the depth profiles (AISI 316L); a) axial residual stress, b) circumferential residual stress.

#### 4.2.5. *Plastic Strain*

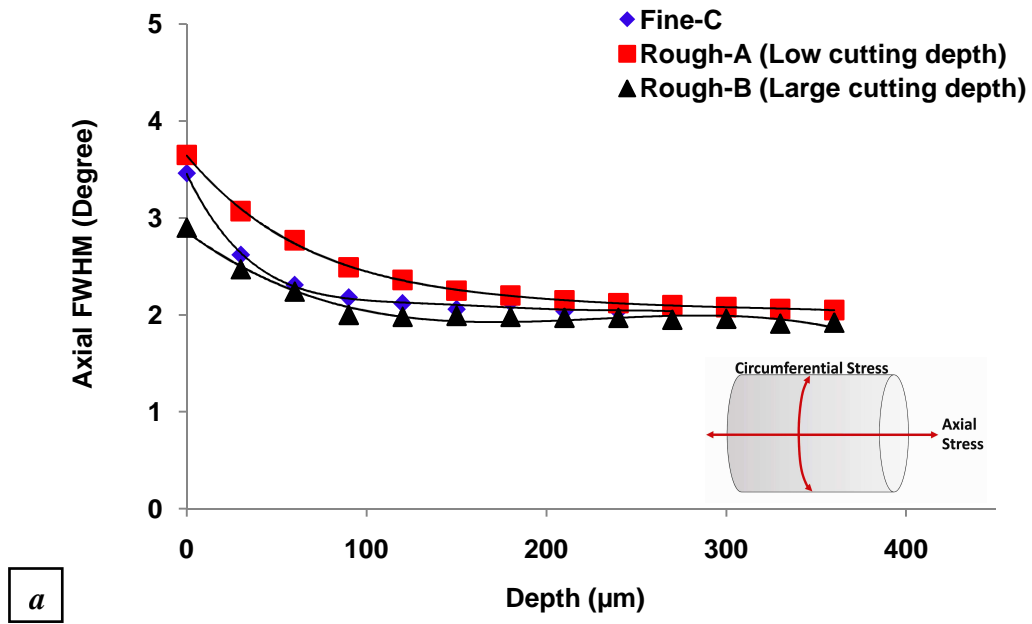
Figure 4- 13 for AISI 304L shows the evolution with depth of the peak half-width. As seen, the values of the longitudinal and circumferential peak half-width for each depth are almost identical.

The peak half-width reaches its maximum around 3.65, 3, 3.5 degree at the machined surface for rough condition-A (Low cutting depth), rough condition-B (Large cutting depth) and fine condition-C, respectively. It decreases gradually in depth and then stabilizes at the peak half-width value found in the work material before machining (around 2).

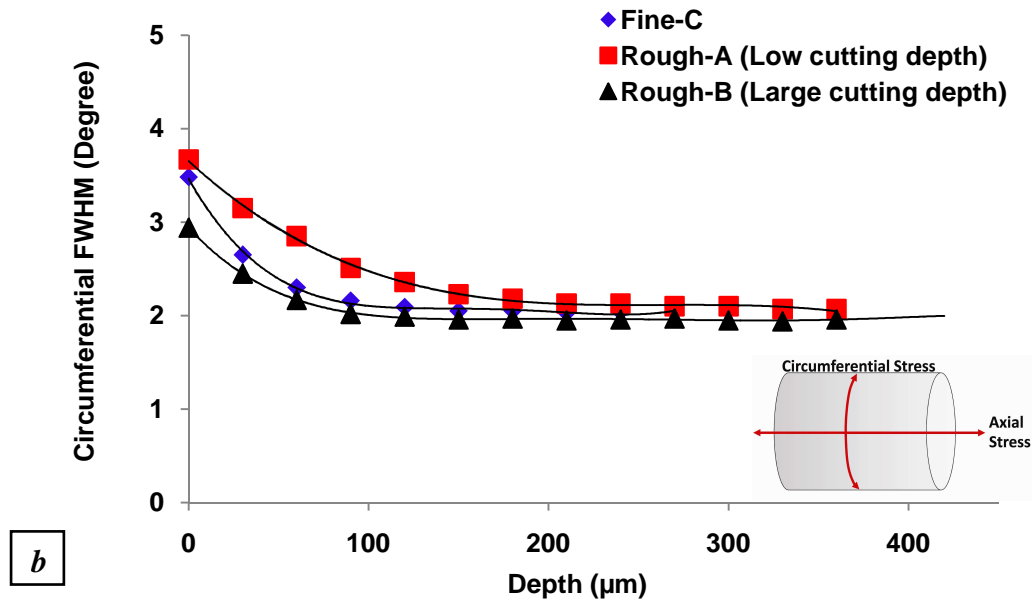
Figure 4- 14 for AISI 316L shows the in-depth evolution of the peak half-width. As seen, the values of the longitudinal and circumferential peak half-width for each depth are almost identical to that observed in AISI 304L.

The peak half-width reaches its maximum around 4.15, 3.66, 3.5 degree at the machined surface for rough condition-A (Low cutting depth), rough condition-B (Large cutting depth) and fine condition-C, respectively. It decreases gradually in depth and then stabilizes at the peak half-width value found in the work material before machining (around 2).

The depth at which the peak half-width stabilizes corresponds to the thickness of the work-hardening layer due to machining. For the all machining conditions, this layer was found to be around 200  $\mu\text{m}$ .



a



b

Figure 4- 13: Variation of diffraction peak width (FWHM) with depth below surface (AISI 304L); a) axial residual stress, b) circumferential residual stress.

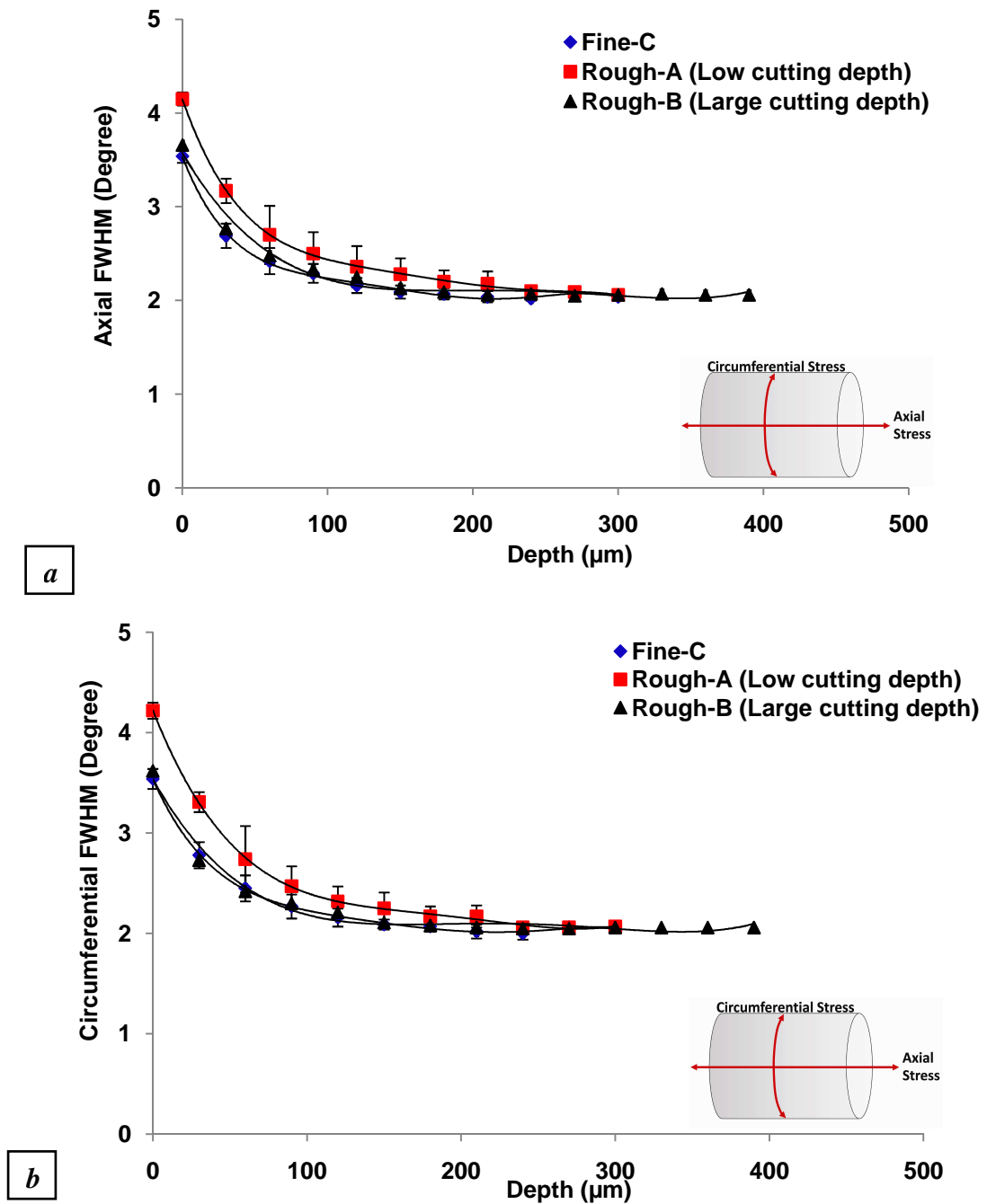


Figure 4- 14: Variation of diffraction peak width (FWHM) with depth below surface (AISI 316L); a) axial residual stress, b) circumferential residual stress.

#### 4.2.6. Surfaces of Machined Specimens before Fatigue Test

Figure 4- 15 shows the surfaces of three conditions before fatigue test. It can be seen from the photographs that there are no observable cracks as a result of machining on the surfaces for all conditions. Machining marks can be seen for fine and rough conditions. Figure 4- 15 shows the surface of electropolished specimen with smooth surface.

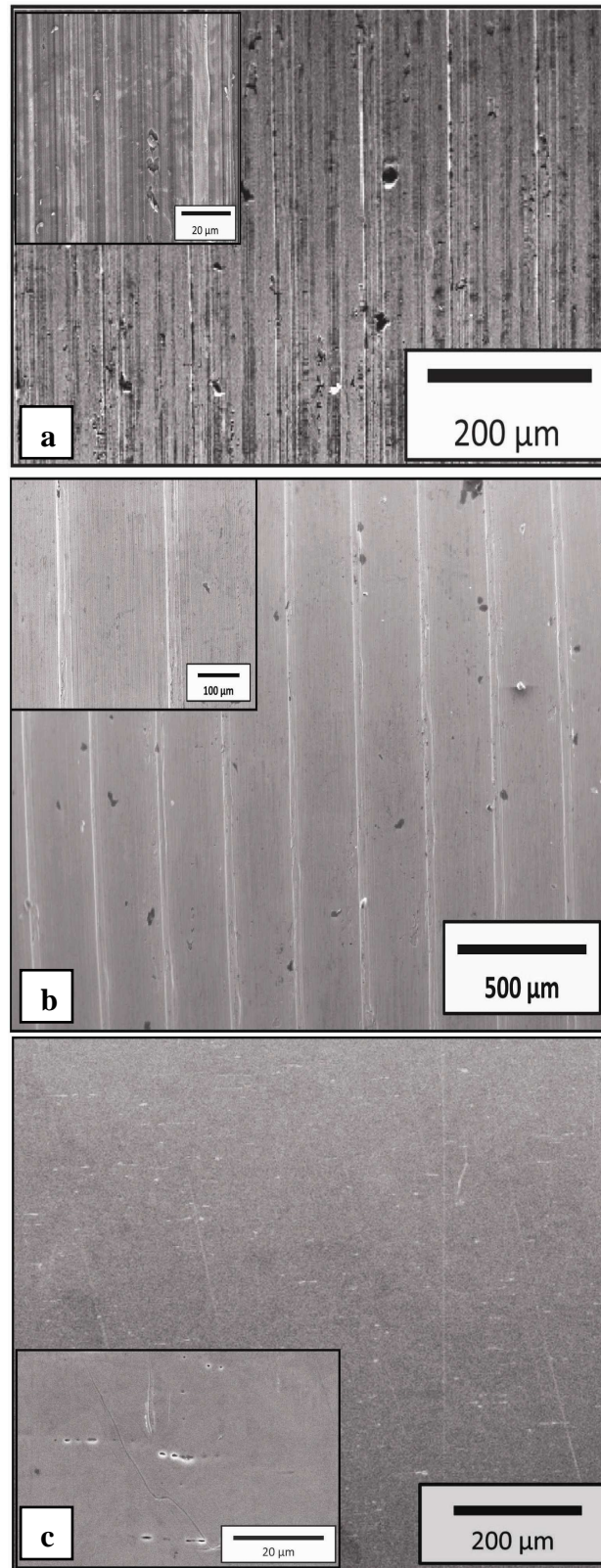


Figure 4- 15: Machined surfaces before fatigue test of AISI 304L; a) Fine machined (C); b) Rough Machined (A); c) Electropolished (annealed).

### 4.3. *Fatigue Limit*

The individual fatigue test results of AISI 304L/ AISI 316L obtained by the staircase method are listed in the following figures (Figure 4- 16 to Figure 4- 18). Table 4- 8 shows the fatigue limits evaluated from the data for both materials. The descriptions and numerical identifiers (1 through to 6) of the surface conditions identified in this table will be used throughout the thesis.

#### 4.3.1. *Fatigue Limit of AISI 304L*

From the data in Table 4- 8, it can be seen that there was a 15% and 3% difference between the fatigue limits of the rough machined (4) and fine machined (1) specimen, respectively and the intrinsic fatigue limit (electropolished (3) specimen).

The difference between the fatigue limits of the fine machined (2) annealed specimen and the intrinsic fatigue limit (electropolished (3) specimen) is about 2% and similar fatigue limits for the rough machined (5) annealed specimen and the intrinsic fatigue limit (electropolished (3) specimen).

#### 4.3.2. *Fatigue Limit of AISI 316L*

From the data in Table 4- 8 for AISI 316, it can be seen that there was a 4% and 5% difference between the fatigue limits of the rough machined (4) and fine machined (1) specimen, respectively and the intrinsic fatigue limit (electropolished (3) specimen).

The difference between the fatigue limits of the rough machined & annealed (5) specimen and the intrinsic fatigue limit (electropolished (3) specimen) is about 11% and 2% difference between the fatigue limits of the fine machined & annealed (2) specimen and the intrinsic fatigue limit (electropolished (3) specimen).

In general for both materials, it can be seen that the electropolished (6) and electropolished/annealed (3) samples have the same fatigue limit. This fatigue limit is higher in the AISI 304L than the AISI 316L. The fine machined (1) samples have a higher fatigue limit than the electropolished (6), where as the rough machined (4) have a lower fatigue limit. The fine machined & annealed (2) samples are also higher than the electropolished (6), with a larger effect in the AISI 304L. The rough machined & annealed (5) samples, compared to the electropolished (3) are similar for the AISI 304L and lower for the AISI 316L.

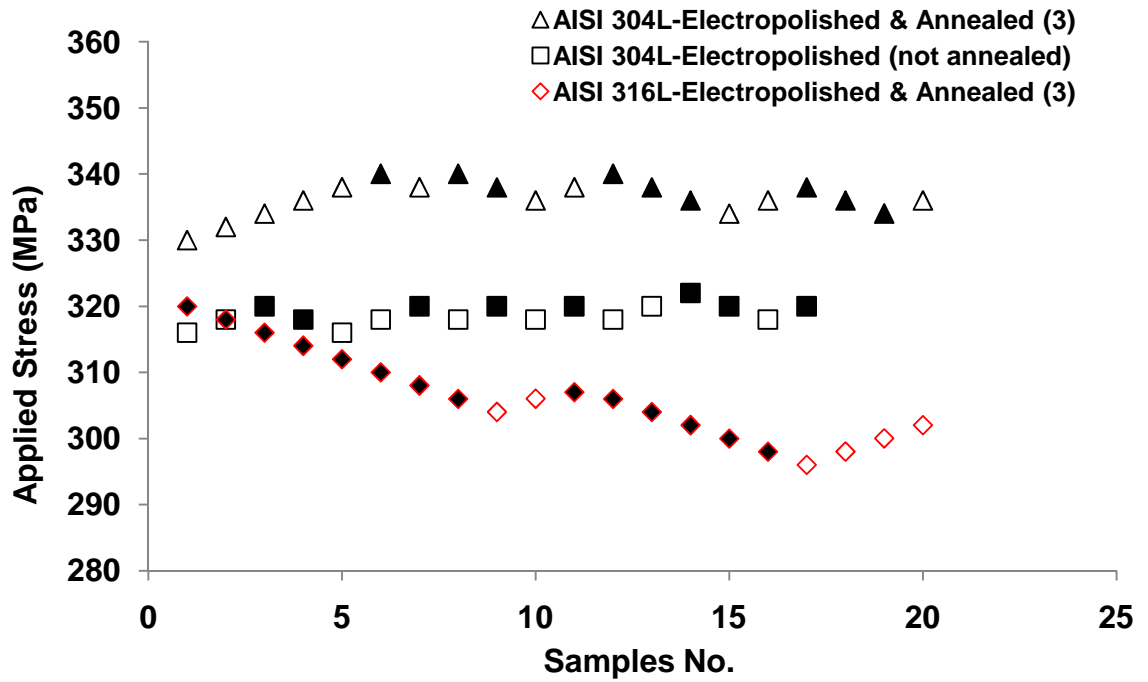


Figure 4- 16: Fatigue data of AISI 304L/AISI 316L (electropolished & annealed (3), electropolished (not annealed) specimens). Open symbols are run-outs and closed symbols are failures.

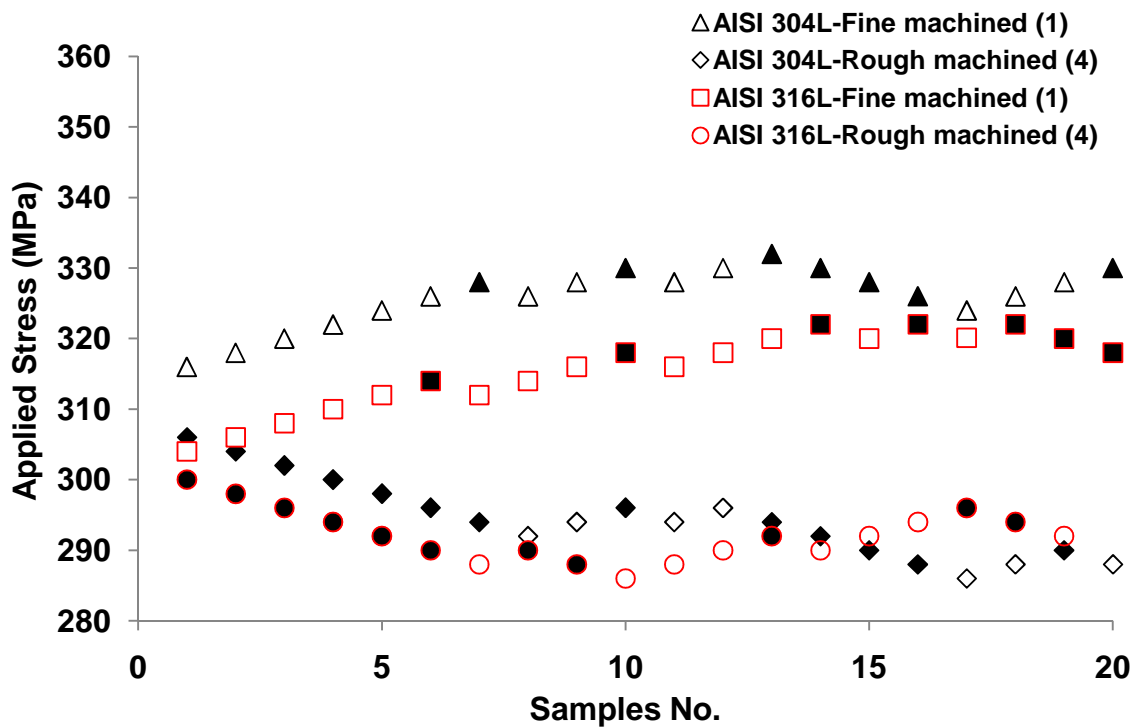


Figure 4- 17: Fatigue data of AISI 304L/AISI 316L (fine machined (1), rough machined (4) specimens). Open symbols are run-outs and closed symbols are failures.

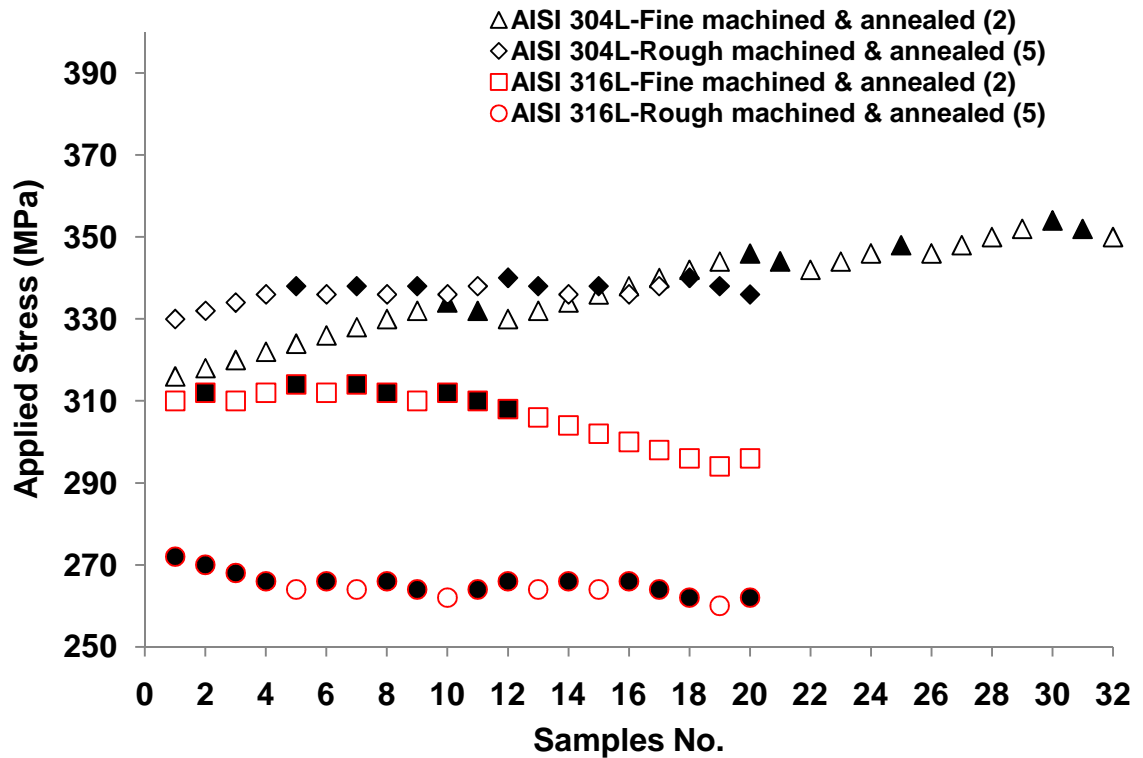


Figure 4- 18: Fatigue data of AISI 304L/AISI 316L (fine machined & annealed, rough machined & annealed specimens). Open symbols are run-outs and closed symbols are failures.

Table 4- 8: Fatigue limits obtained by staircase method ( $\pm$  one standard deviation), (RS: residual stress).

No.	Condition	Fatigue Limit (MPa)	
		AISI 304	AISI 316
1	Fine Machined (C)	$327\pm 8$	$318\pm 3$
2	Fine Machined (C) & Annealed	$343\pm 18$	$307\pm 20$
3	Electropolished (Annealed)	$337\pm 2$	$302\pm 5$
4	Rough Machined (A)	$291\pm 3$	$291\pm 2$
5	Rough Machined (A) & Annealed	$337\pm 1$	$264\pm 1$
6	Electropolished (Not Annealed)	319	$304\pm 3$

#### 4.4. Surface Characterization of run-out specimens

Small numbers of small cracks were observed on the surface of fine machined (1) and rough machined (4) after fatigue testing as shown in Figure 4- 19-b and Figure 4- 19-c. Most of these cracks were located perpendicular to the stress direction and located in the root of machining marks. In electropolished (3) specimen of AISI 304L which had been fatigued at 336 MPa, persistent slip bands (PSBs) are observed to emerge on the surface in a few grains. Small cracks were observed along these PSBs and inclined at approximately  $45^\circ$  to the stress axis (Figure 4- 19-a). Black holes in this photograph are



pits due to the electropolishing. For the AISI 304L material the kind of cracks were not observed before the fatigue test as shown in Figure 4- 15.

Figure 4- 20-a shows persistent slip bands (PSBs) on the surface of electropolished (3) specimen and fatigued at 304 MPa for AISI 316L. Also, some cracks were observed along the PSBs and were inclined at approximately  $45^\circ$  to the stress axis. A few surface cracks can be observed in fine machined condition (1) perpendicular to the stress axis and located in the root of the machining marks as shown in Figure 4- 20-b.

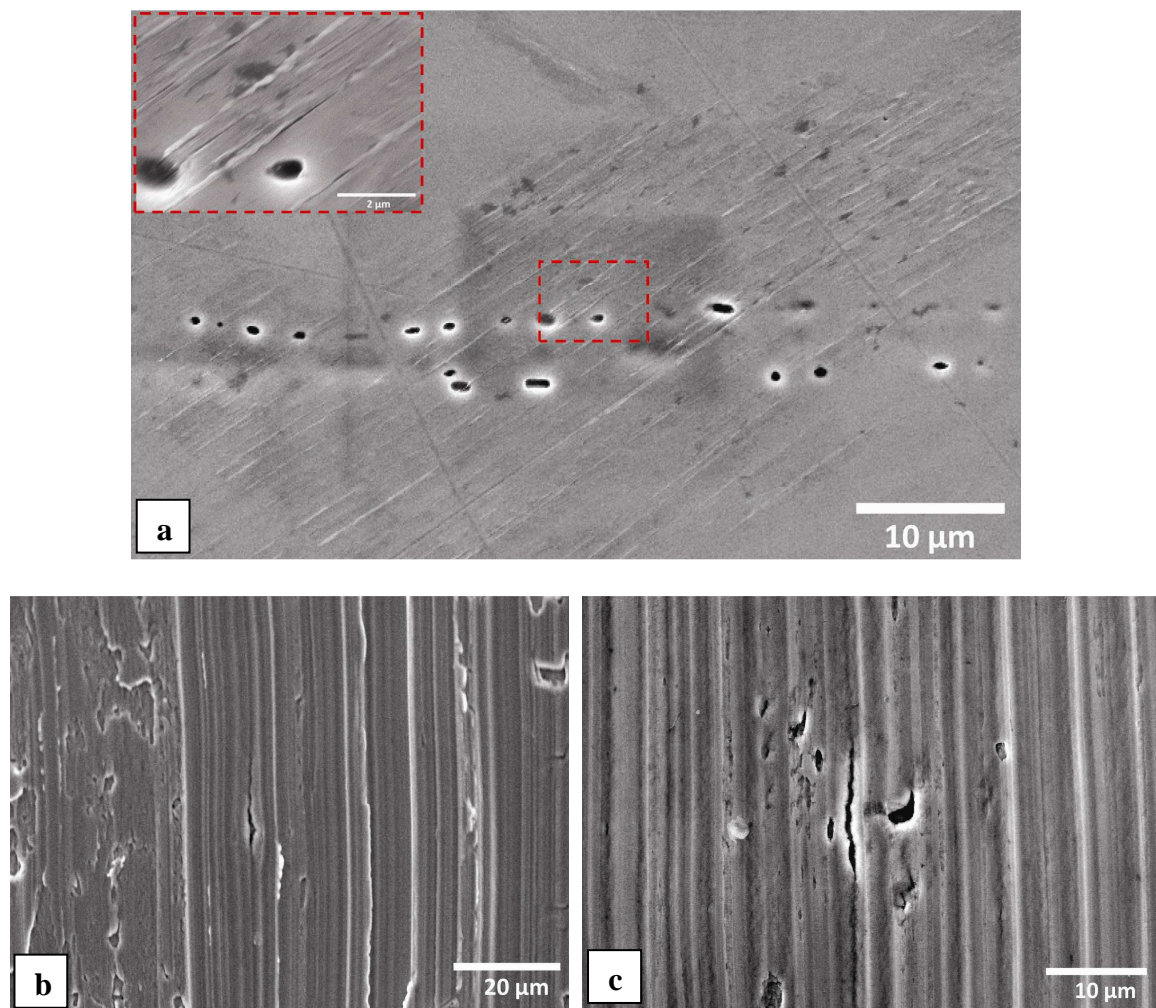


Figure 4- 19: Surface cracks in run-out fatigued samples for AISI 304L: a) Electropolished (3) (336 MPa); b) Fine machined(1) run-out fatigued samples (328 MPa); c) Rough machined(4) run-out fatigued samples (294 MPa).( $\leftrightarrow$  stress axis).

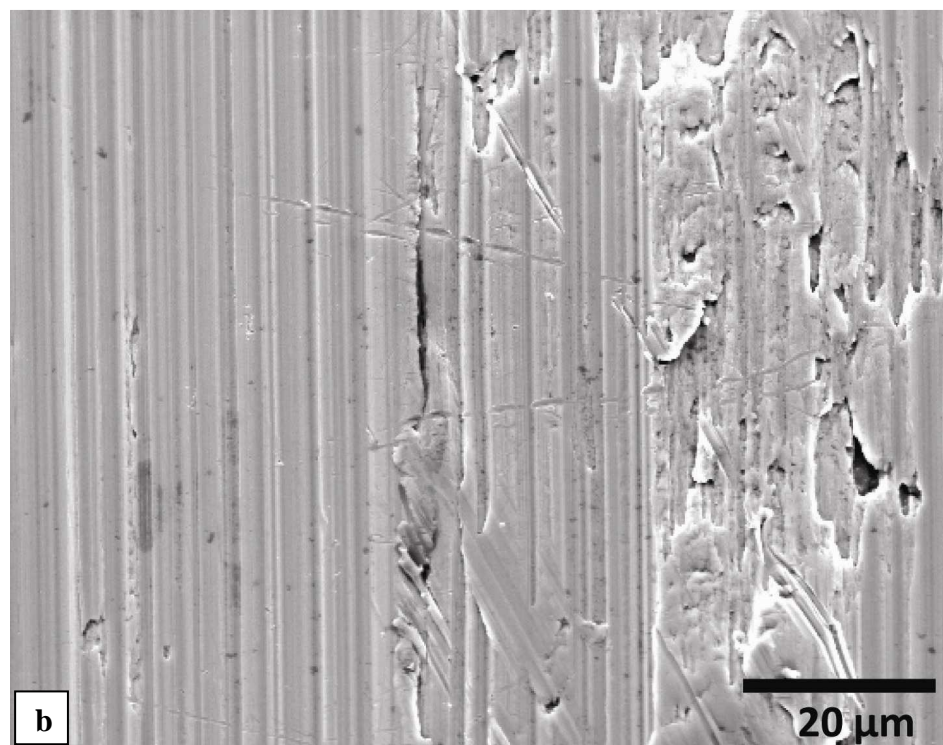
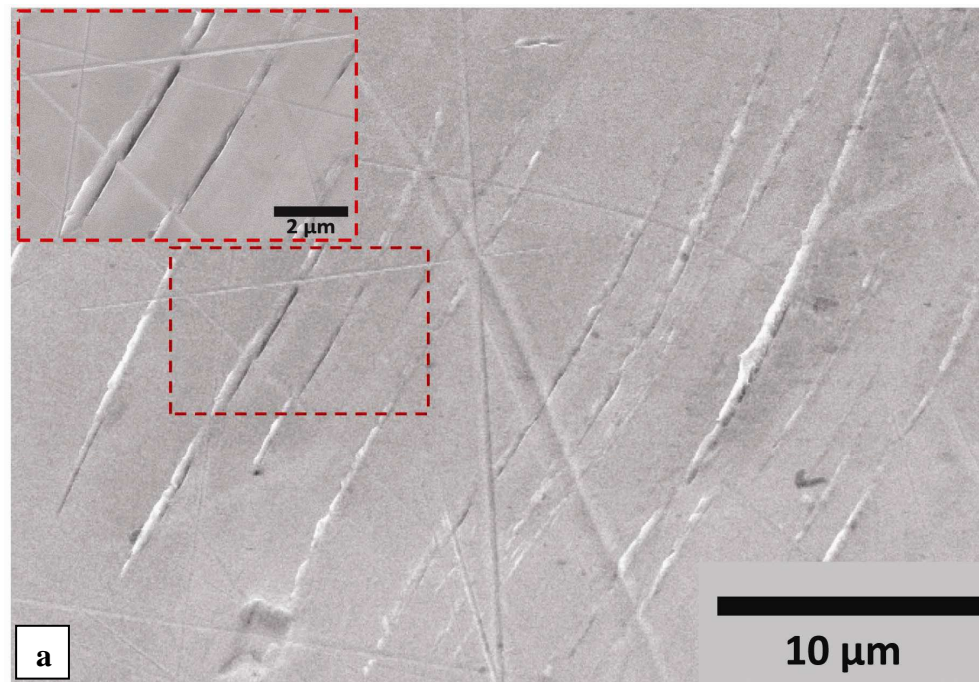


Figure 4- 20: Surface cracks in run-out fatigued samples for AISI 316L: a) Electropolished (3) run-out fatigued samples (304 MPa); b) Fine machined (1) run-out fatigued samples (320MPa) ( $\leftrightarrow$  stress direction).

#### 4.5. *Fracture Morphology in failed specimens*

Investigations were carried out on fracture surfaces for fine machined (1), rough machined (4), and annealed & electropolished (3) specimens for both material AISI 304L and AISI 316L as shown in Figure 4- 21 to Figure 4- 24. Examination of the fracture surface of these specimens was performed: (a) at low magnification to identify the fatigue and final fracture (overload) regions and (b) at higher magnifications to identify regions of crack initiation and early crack growth in the fatigue region, and also to identify the fracture features in the overload region.

As can be observed, in both materials for machined samples, the fracture of the specimen is dominated by the propagation of a single crack nucleated at the root of the machining marks (Figure 4- 21-a and d), which leads to a ductile fracture zone on the opposite side of the specimen.

In electropolished (3) specimen (336 MPa), on the surface around the origin zone (Figure 4- 22-d) shows the plastic deformation and formation of slip bands at the crack initiation site.

At higher magnifications, striations were observed in the fatigue fracture region (Figure 4- 21-d, Figure 4- 22-b). The regions of transgranular fracture show fatigue striations accompanied by local secondary cracks in electropolished (3) (Figure 4- 22-b).

The overload region (Figure 4- 21-c) comprised of microscopic voids of a variety of sizes and shallow dimples indicating the highly ductile nature of the failure process.

Similar fracture surface features were observed for AISI 316L. Also, in this material, the fracture of the specimen is dominated by the propagation of a single crack nucleated at the root of the machining marks (Figure 4- 23-a and d). In Figure 4- 23-f and Figure 4- 24-b, striations were observed in the fatigue fracture region.

The overload region contained of microscopic voids of a variety of sizes and dimples indicating the highly ductile nature of the final failure as can be seen in Figure 4- 23-b.

Figure 4- 24-d shows plastic deformation and formation of slip bands on the surface around the origin zone in electropolished (3) specimen (298 MPa).



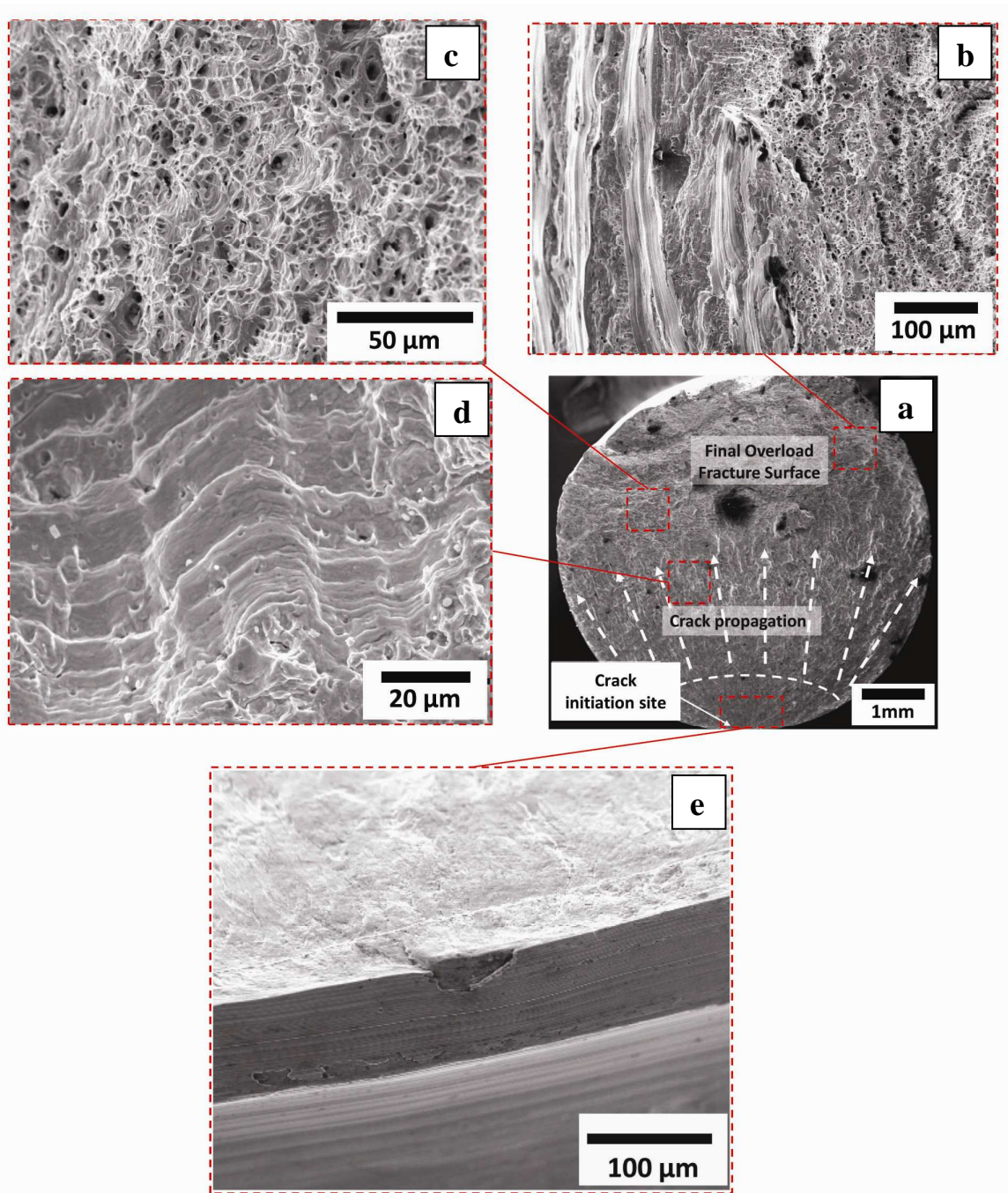


Figure 4- 21: a) Fracture surfaces of AISI 304L, fine machined (1) and fatigue tested at 330 MPa; b) Final fast fracture region; c) Dimples; d) striations; e) Crack origin.

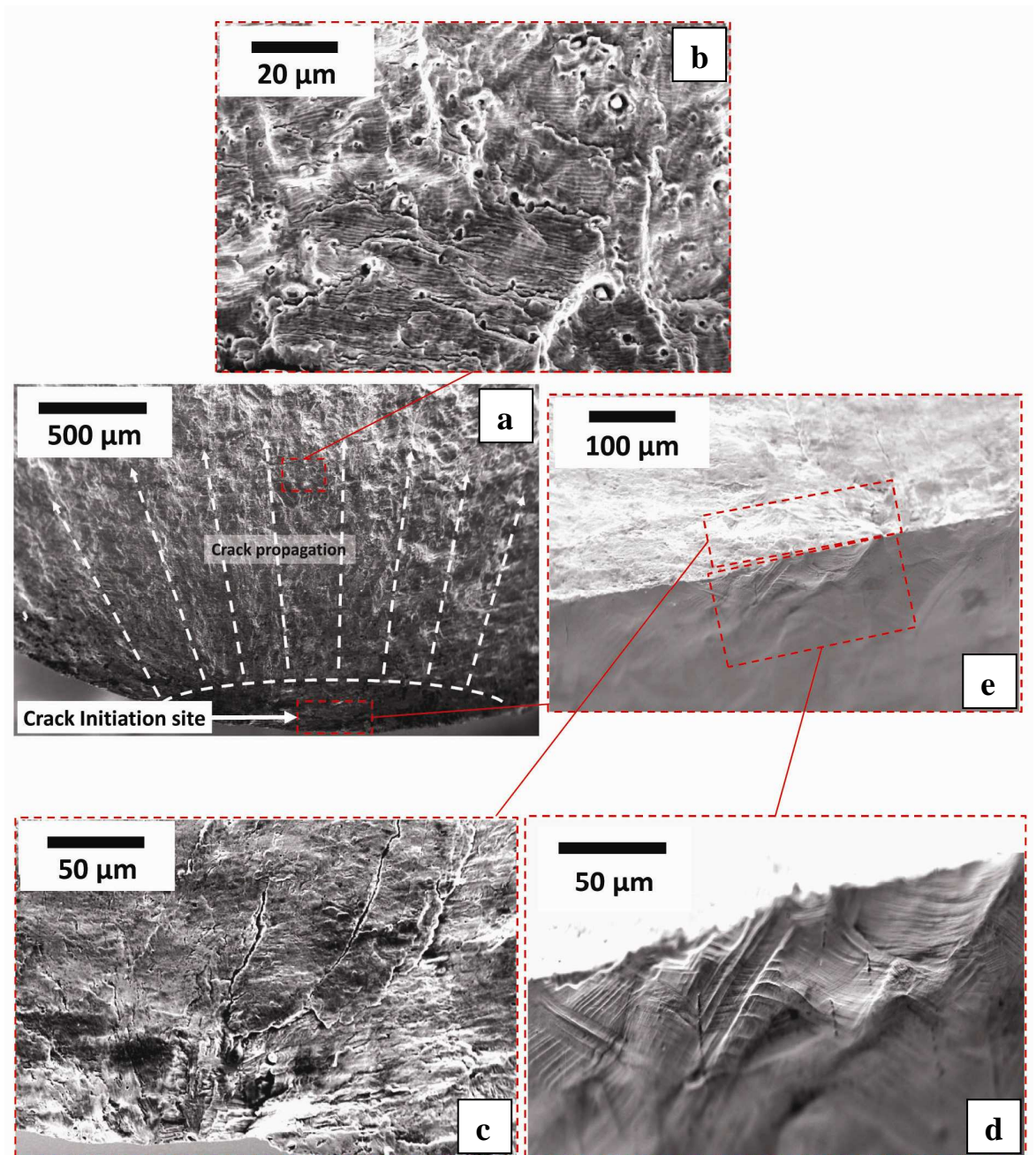


Figure 4- 22: a) Fracture surfaces of AISI 304L, Electropolished (3) and fatigue tested at 336 MP.; b) Striations; c) Crack origin from the top; d) Lateral view of crack origin; e) Crack origin zone.



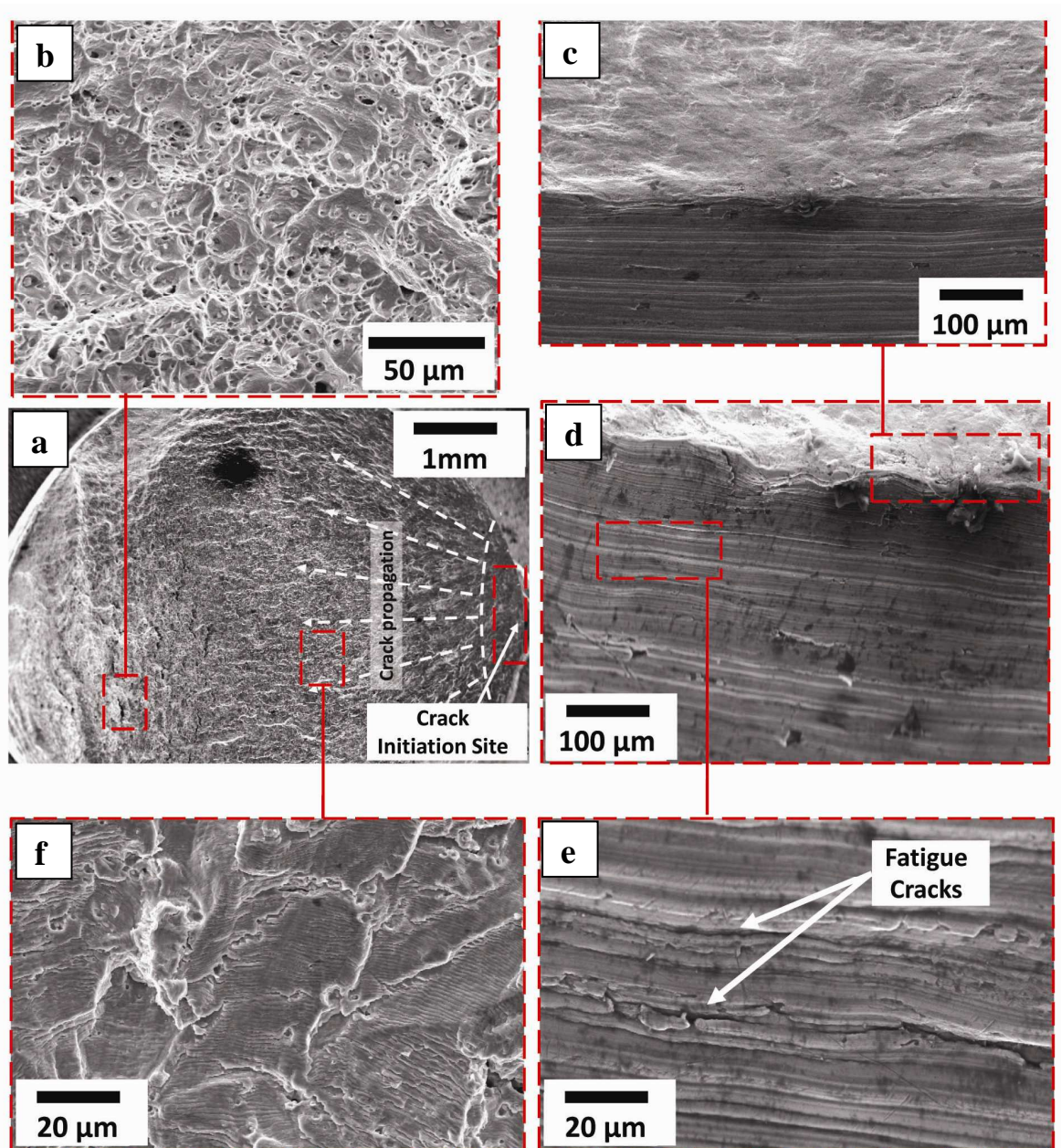


Figure 4- 23: a) Fracture surfaces of AISI 316L, fine machined (1) and fatigue tested at 322 MPa. ; b) Dimples; c) Crack origin zone; d) Lateral view of crack origin; e) Lateral view of crack origin zone show fatigue cracks; f) striations.

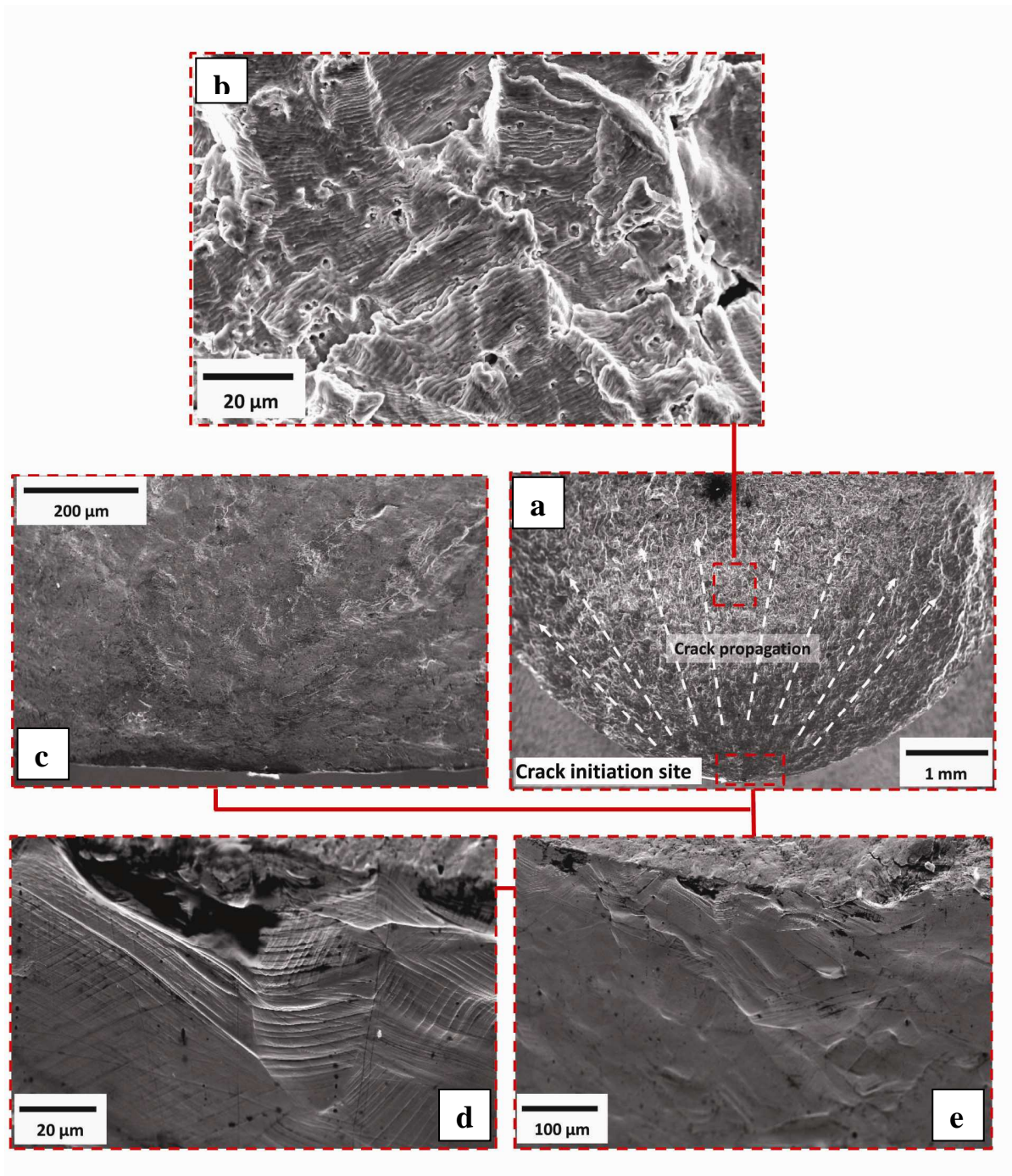


Figure 4- 24: a) Fracture surfaces of AISI 316L, Electropolished (3) and fatigue tested at 298 MPa; b) striations.; c) Top view of crack origin zone; d and e) Lateral view of crack origin zone.

#### 4.6. EBSD of near surface of fatigued run-out specimens

Metallographic cross sections of fatigued run-out samples, parallel to the specimen longitudinal axis were examined by SEM and EBSD. Two types of maps taken with EBSD are shown in Figure 4- 25 to Figure 4- 34. These are band contrast maps and



Euler maps. Maps were obtained for both material AISI 304L and AISI 316L before and after fatigue testing (run-out specimens).

#### **4.6.1. EBSD of AISI 304L**

##### *4.6.1.1. Machined Samples*

In this case, the dark contrast in the Band contrast maps represent strained regions, therefore the dark lines indicated by the arrow in Figure 4- 26-a are judged to be slip lines or slip bands. Many slip bands and small angle grain boundaries were observed near the surface in the rough machined samples, although the strained region seemed to be deeper and greater in intensity compared with fine machined samples.

Before fatigue testing, the observations (Figure 4- 25-a) show that there is little observable plastic strain in the fine machined (C) samples, evident only as slip bands that penetrate to a depth of approximately 30  $\mu\text{m}$ . The rough machined (A) samples show a greater degree of plastic strain close to the surface in depth below the surface of approximately 40  $\mu\text{m}$  below the surface (Figure 4- 26).

After fatigue testing close to the fatigue limit for  $10^7$  cycles, there is an apparent increase in the intensity of plastic strain observed by EBSD in the fine machined (1) samples (Figure 4- 25), but no significant increase in depth. For the rough machined (4) samples, there is no significant change in the depth of the plastic strain region, but very little increase in the intensity of plastic strain (Figure 4- 26-c).

The intensity of band contrast was highest close the machined surfaces and this was not noticeably affected by fatigue cycling.



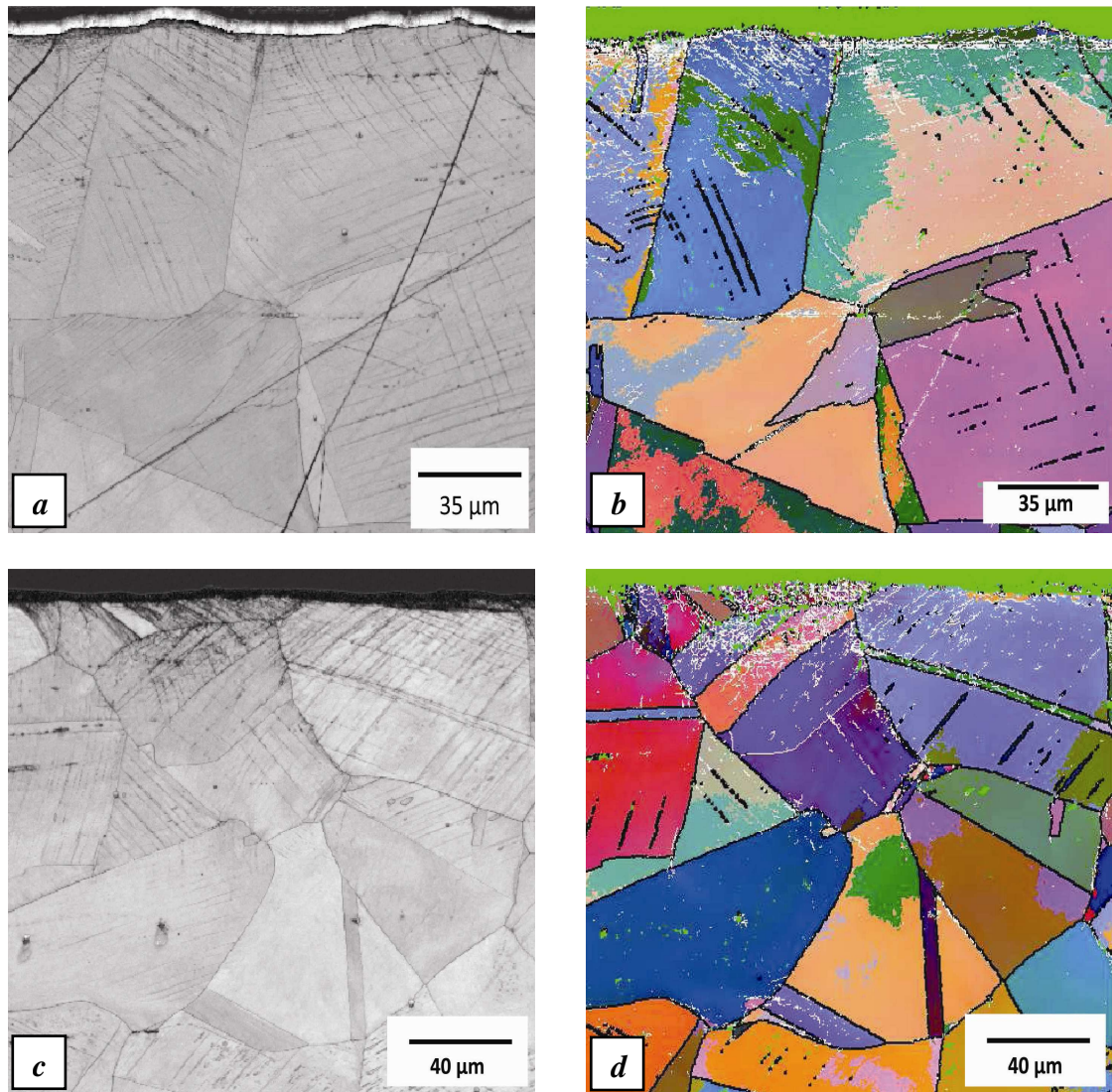


Figure 4- 25: AISI 304L a) Band contrast map of fine machined(C) specimens **before** fatigue test; b) Euler map of fine machined (C) specimens **before** fatigue test; c) Band contrast map of fine machined(1) specimens **after** fatigue test (328 MPa); d) Euler map of fine machined (1) specimens **after** fatigue test. Small angle grain boundaries are indicated by the white lines in (b and d).

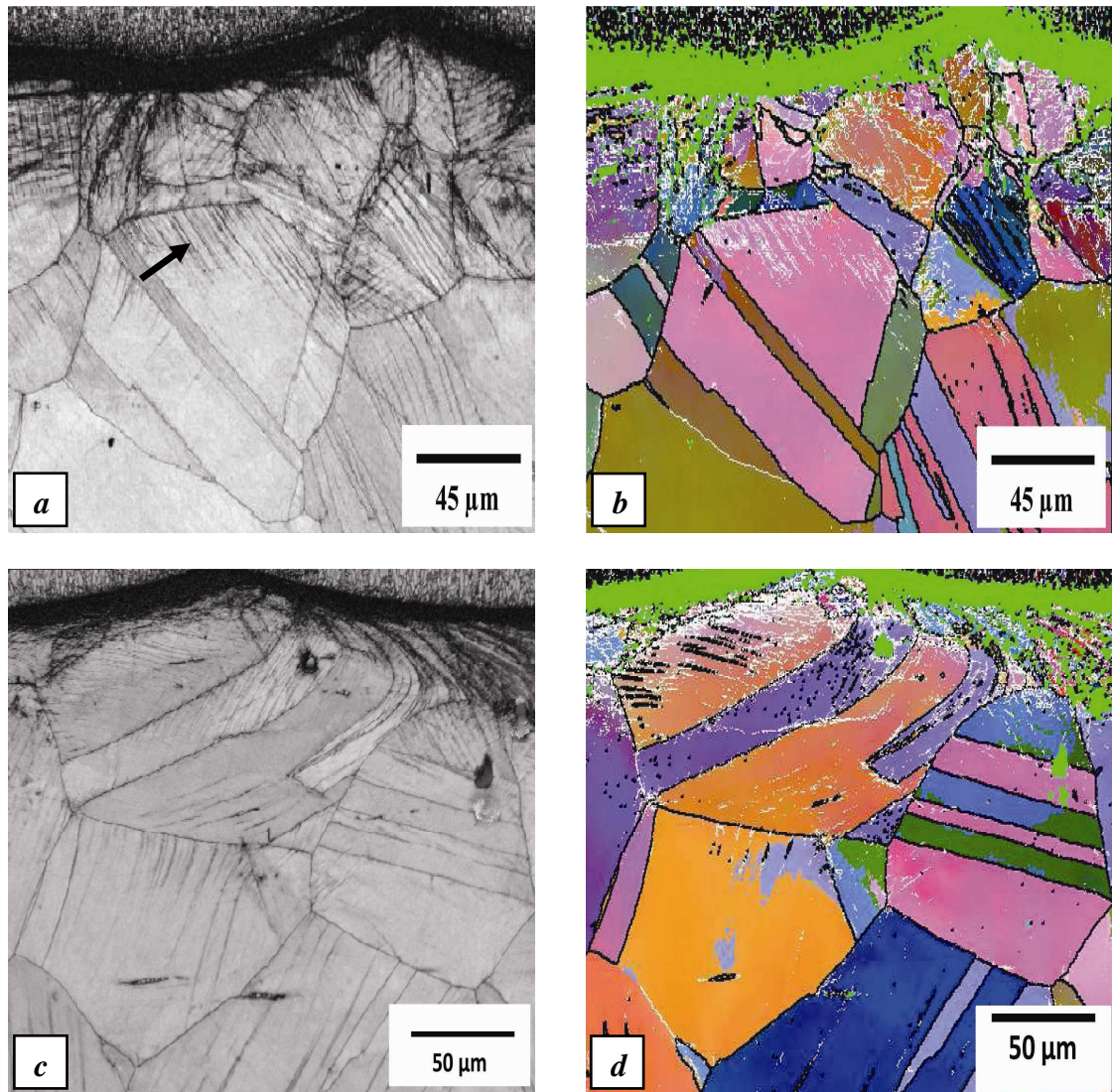


Figure 4- 26: AISI 304L a) Band contrast map of rough machined (A) specimens **before** fatigue test; b) Euler map of rough machined (A) specimens **before** fatigue test; c) Band contrast map of rough machined (4) specimens **after** fatigue test (286 MPa); d) Euler map of rough machined (4) specimens **after** fatigue test.

#### 4.6.1.2. Electropolished Samples

In electropolished (3) specimens, fatigue to run-out appeared to cause a slight increase in the density of slip bands revealed by the band contrast maps (Figure 4- 27-c). Slip bands were evident, prior to fatigue testing, in the bulk microstructure both before and after annealing. The density of these slip bands was reduced in the annealed samples.



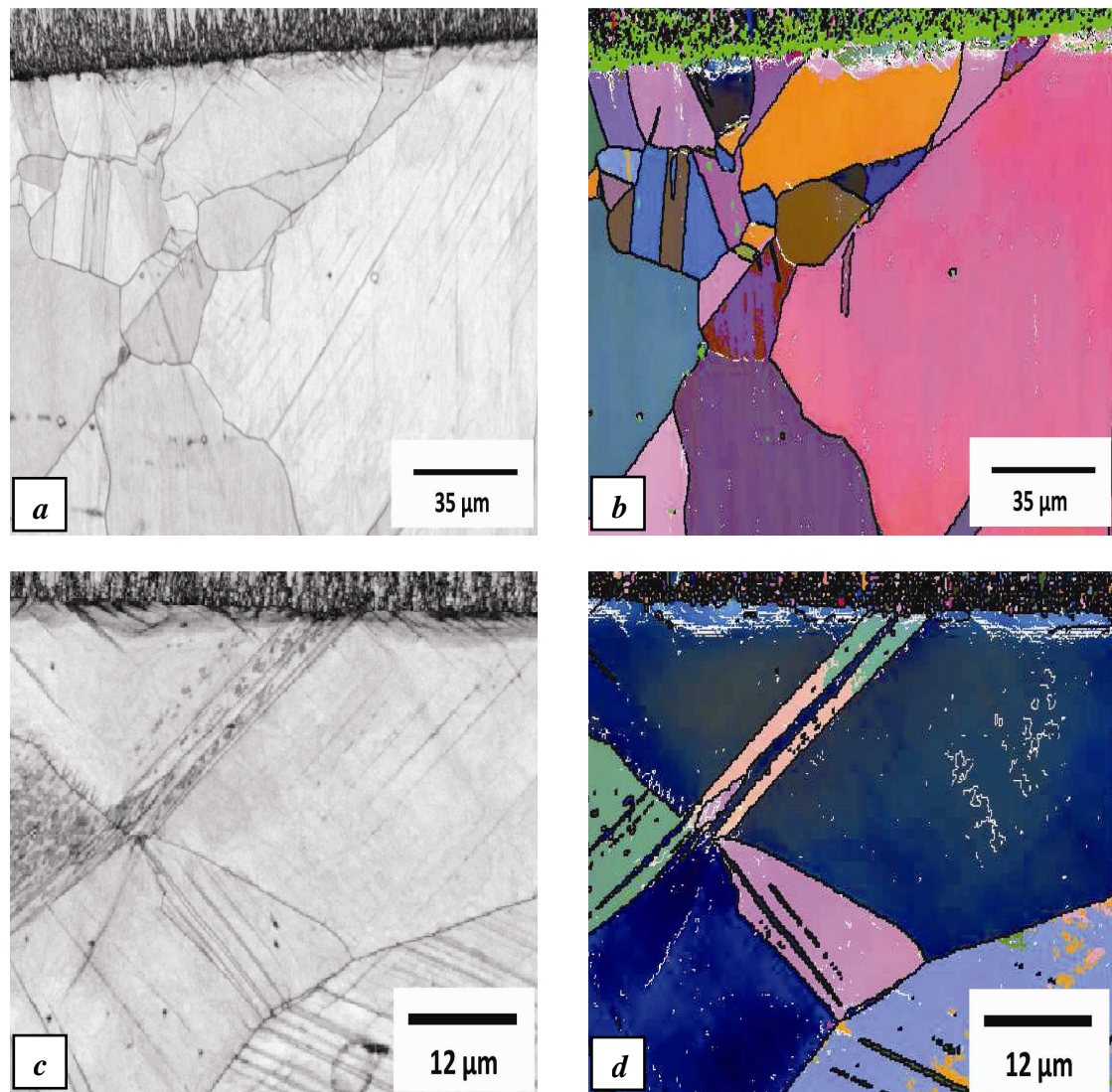


Figure 4- 27: AISI 304L a) Band contrast map of electropolished (annealed) specimens **before** fatigue test; b) Euler map of electropolished (annealed) specimens **before** fatigue test; c) Band contrast map of electropolished (3) specimens **after** fatigue test (338 MPa); d) Euler map of electropolished (3) specimens **after** fatigue test.

#### 4.6.1.3. Annealed Samples

Annealing at 900°C for 10 minutes had a significant effect on the grain size near the machined surface as shown in Figure 4- 28 and Figure 4- 29. Fine grain size (about 3 μm) was observed within a depth of about 30 μm and 40 μm from the surface in fine machined & annealed (2) and rough machined & annealed (5) specimens, respectively.

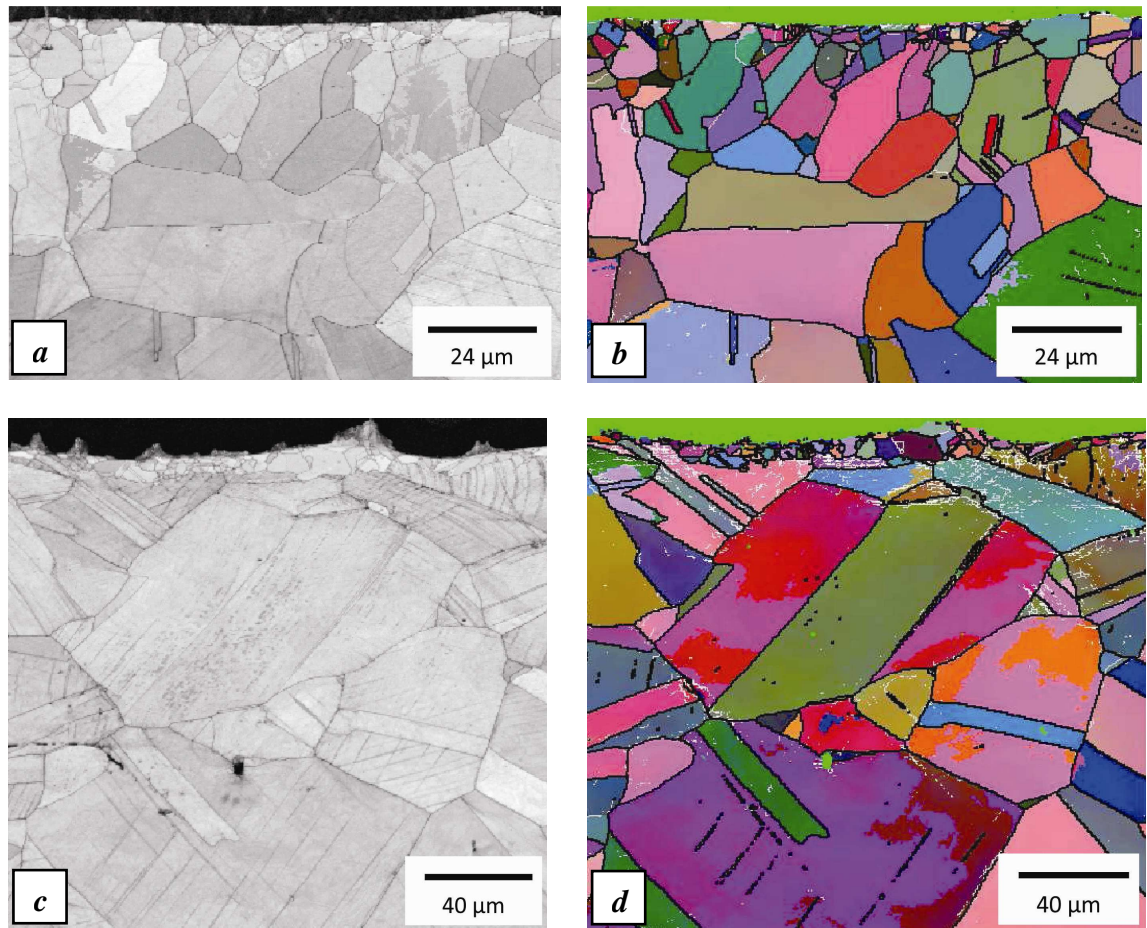


Figure 4- 28: Figure 4- 26: AISI 304L a) Band contrast map of fine machined & annealed(C) specimens **before** fatigue test; b) Euler map of fine machined & annealed(C) specimens **before** fatigue test; c) Band contrast map of fine machined & annealed(2) specimens **after** fatigue test (352 MPa); d) Euler map of fine machined & annealed(2) specimens **after** fatigue test.



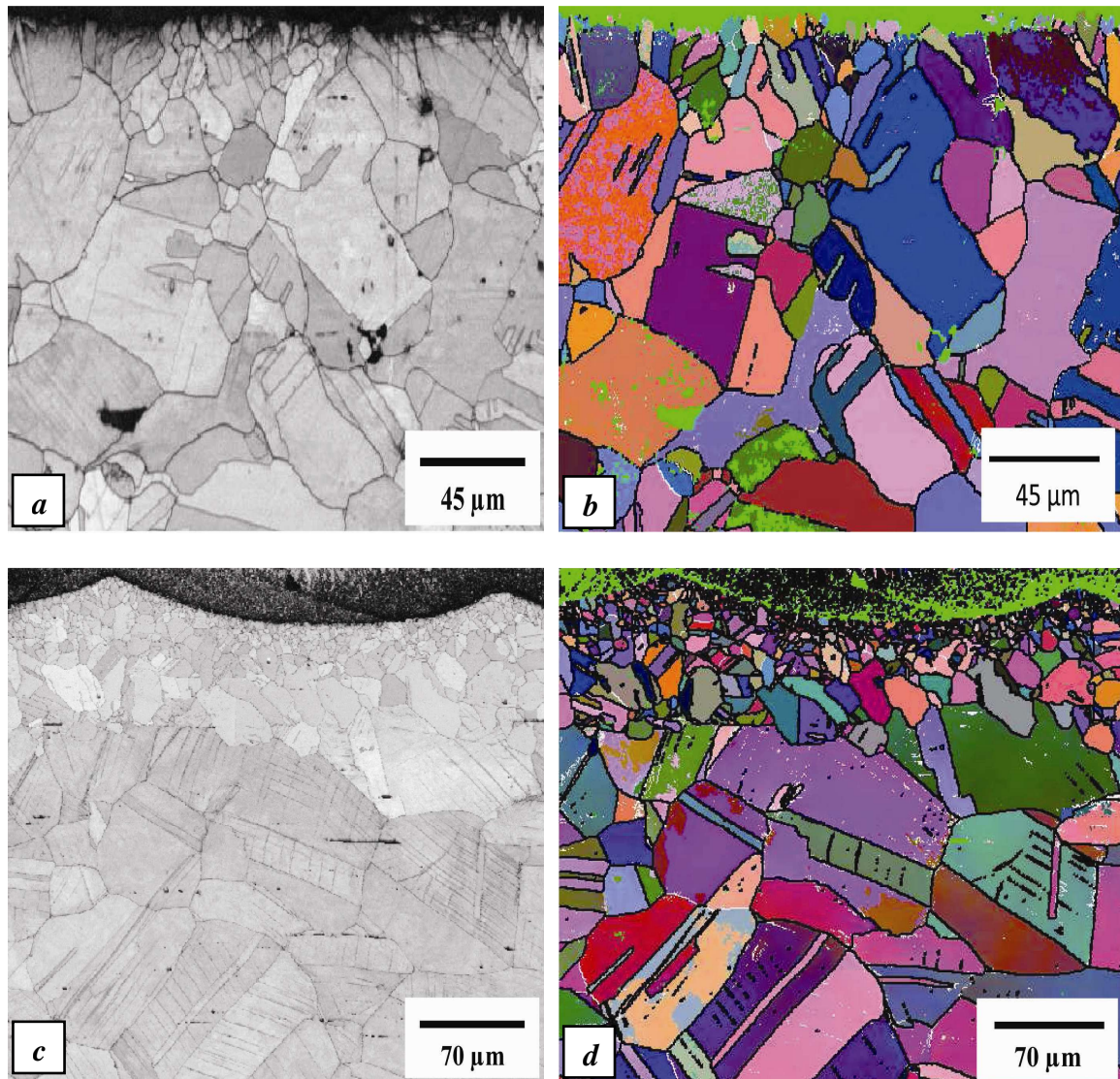


Figure 4- 29: AISI 304L a) Band contrast map of rough machined & annealed (A) specimens **before** fatigue test; b) Euler map of rough machined & annealed (A) specimens **before** fatigue test; c) Band contrast map of rough machined & annealed (5) specimens **after** fatigue test (338 MPa); d) Euler map of rough machined & annealed (5) specimens **after** fatigue test.

#### 4.6.2. EBSD of AISI 316L

##### 4.6.2.1. Machined Samples

In AISI 316L, it can be seen that the deformed microstructure before and after the fatigue test is similar to that in AISI 304L. Run-out samples show that there is an apparent increase in the intensity of plastic strain observed by EBSD in the fine machined (1) samples (Figure 4- 30-c), but no significant increase in the depth of the strained region. For the rough machined (4) samples, there is no significant change in the depth of the plastic strain region, but very little increase in the intensity of plastic strain (Figure 4- 31-c).

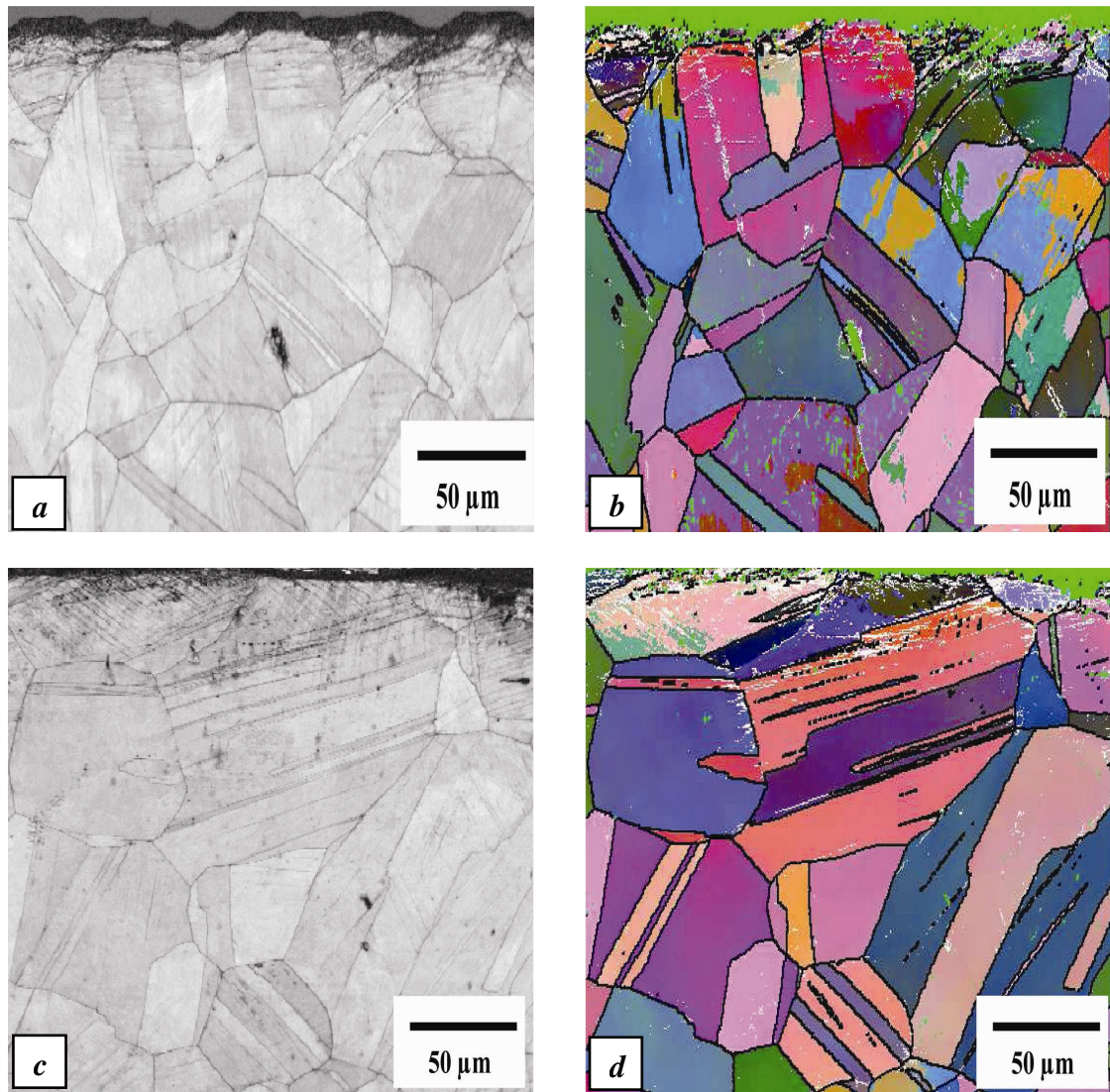


Figure 4- 30: AISI 316L a) Band contrast map of fine machined (C) specimens **before** fatigue test; b) Euler map of fine machined (C) specimens **before** fatigue test; c) Band contrast map of fine machined (I) specimens **after** fatigue test (304 MPa); d) Euler map of fine machined (I) specimens **after** fatigue test.



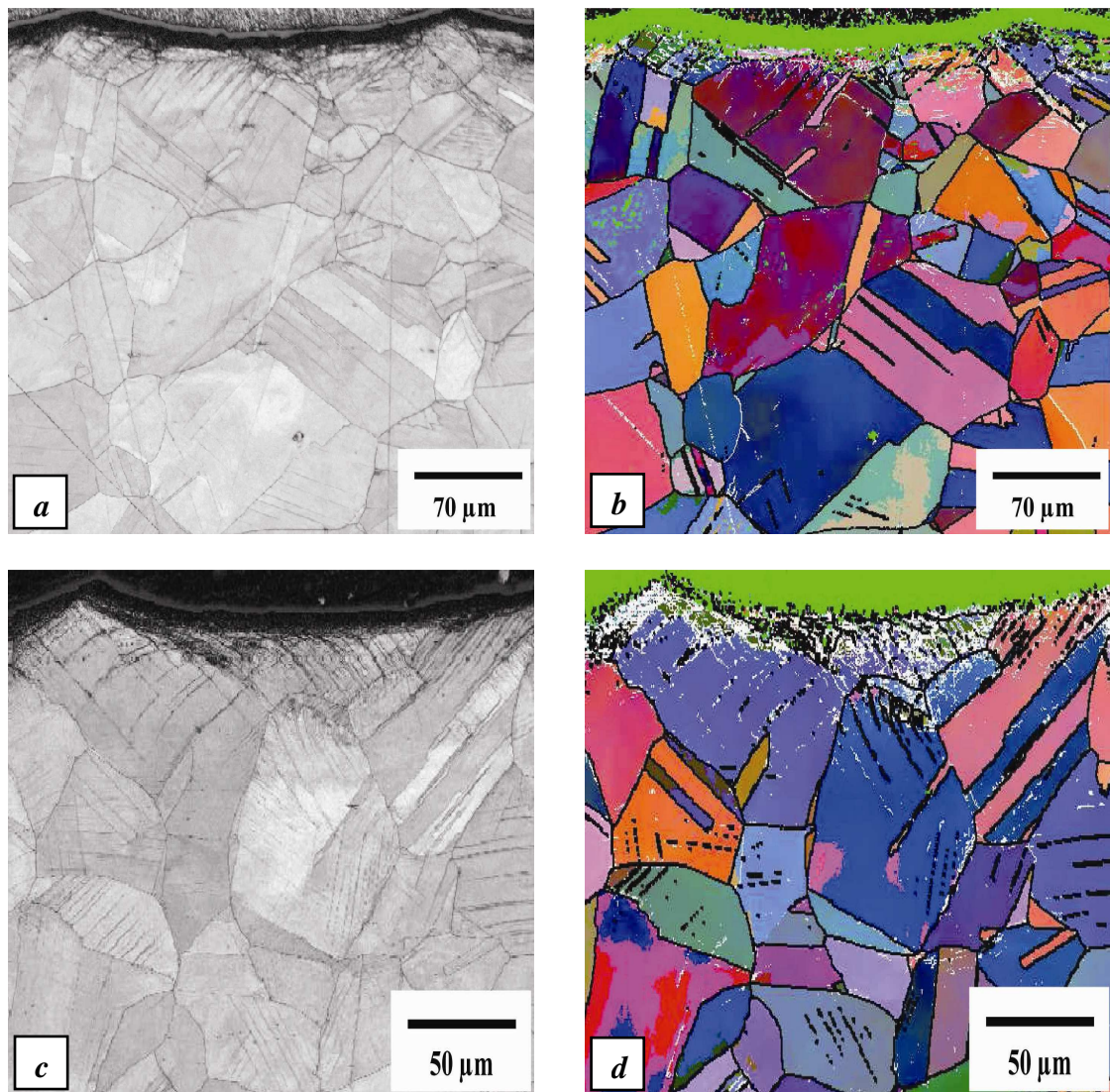


Figure 4- 31: AISI 316L a) Band contrast map of rough machined (A) specimens **before** fatigue test; b) Euler map of rough machined (A) specimens **before** fatigue test; c) Band contrast map of rough machined (4) specimens **after** fatigue test (290 MPa); d) Euler map of rough machined (4) specimens **after** fatigue test.

#### 4.6.2.2. Electropolished Samples

It can be seen that in the electropolished (3) specimens, fatigued to run-out, the density of slip bands increases as shown in Figure 4- 32. Slip bands can be seen prior to fatigue testing, in the bulk microstructure.

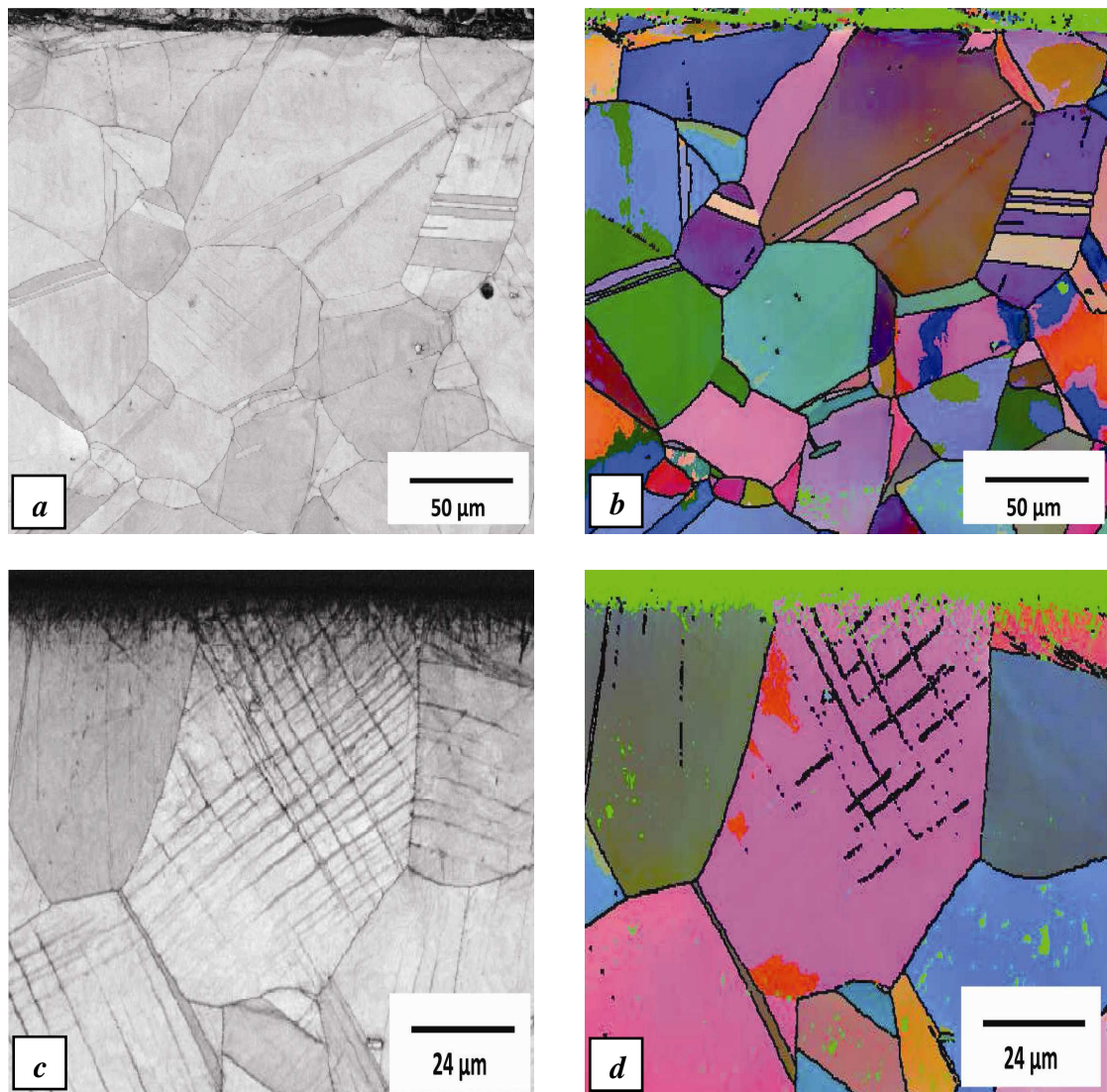


Figure 4- 32: AISI 316L a) Band contrast map of electropolished specimens **before** fatigue test; b) Euler map of electropolished specimens **before** fatigue test; c) Band contrast map of electropolished (3) specimens **after** fatigue test (306 MPa); d) Euler map of electropolished (3) specimens **after** fatigue test.

#### 4.6.2.3. Annealed Samples

The effect of annealing (at 900°C for 10 minutes) on the grain size near the machined surface was observed as shown in Figure 4- 33 and Figure 4- 34. Fine grain size (about 3 μm) can be seen within a depth of about 10 μm and 50 μm from the surface in fine machined & annealed (2) and rough machined & annealed (5) specimens, respectively.



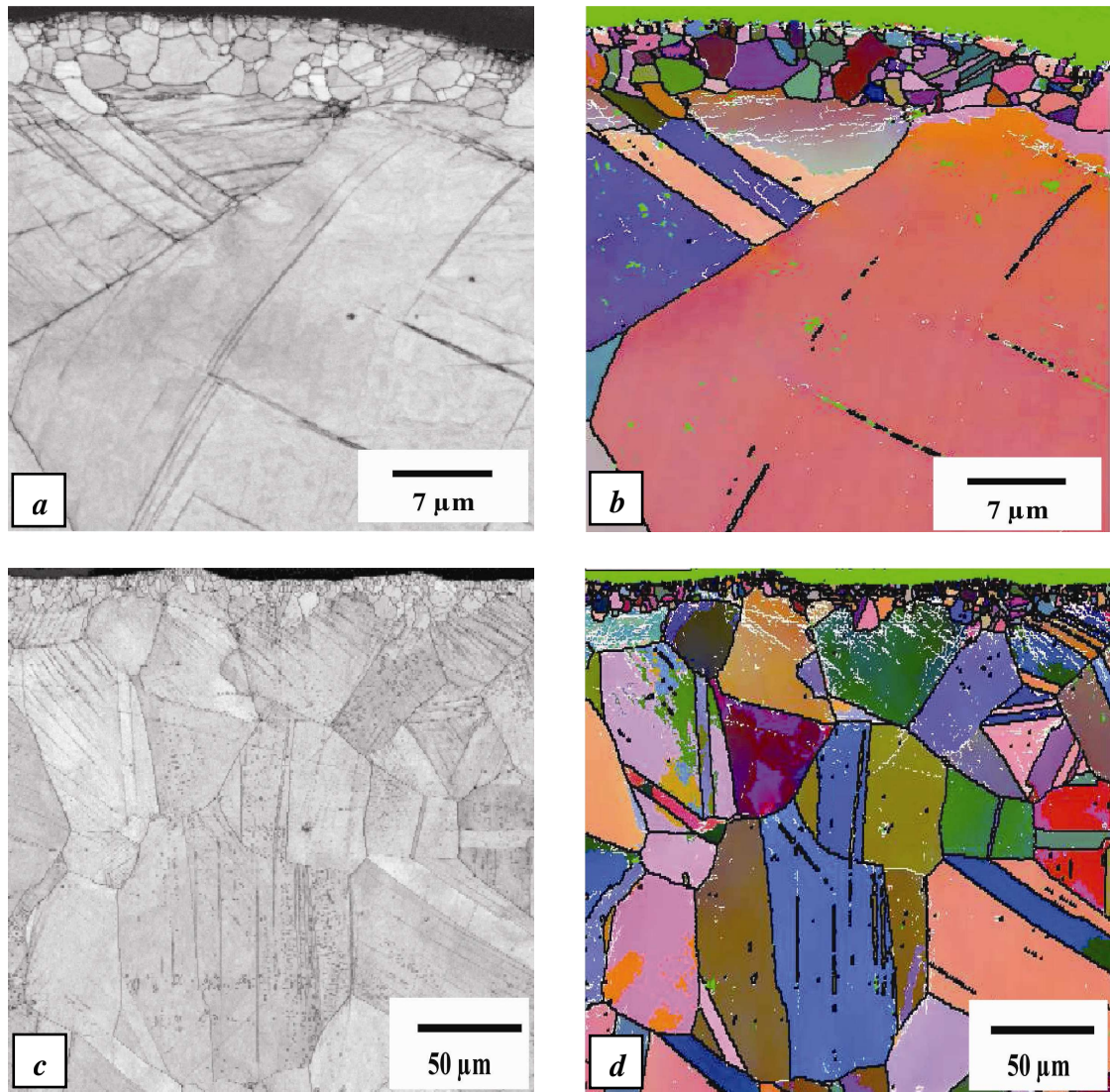


Figure 4- 33: AISI 316L a) Band contrast map of fine annealed specimens **before** fatigue test; b) Euler map of fine annealed specimens **before** fatigue test; c) Band contrast map of fine machined & annealed (2) specimens **after** fatigue test (294 MPa); d) Euler map of fine machined & annealed (2) specimens **after** fatigue test.

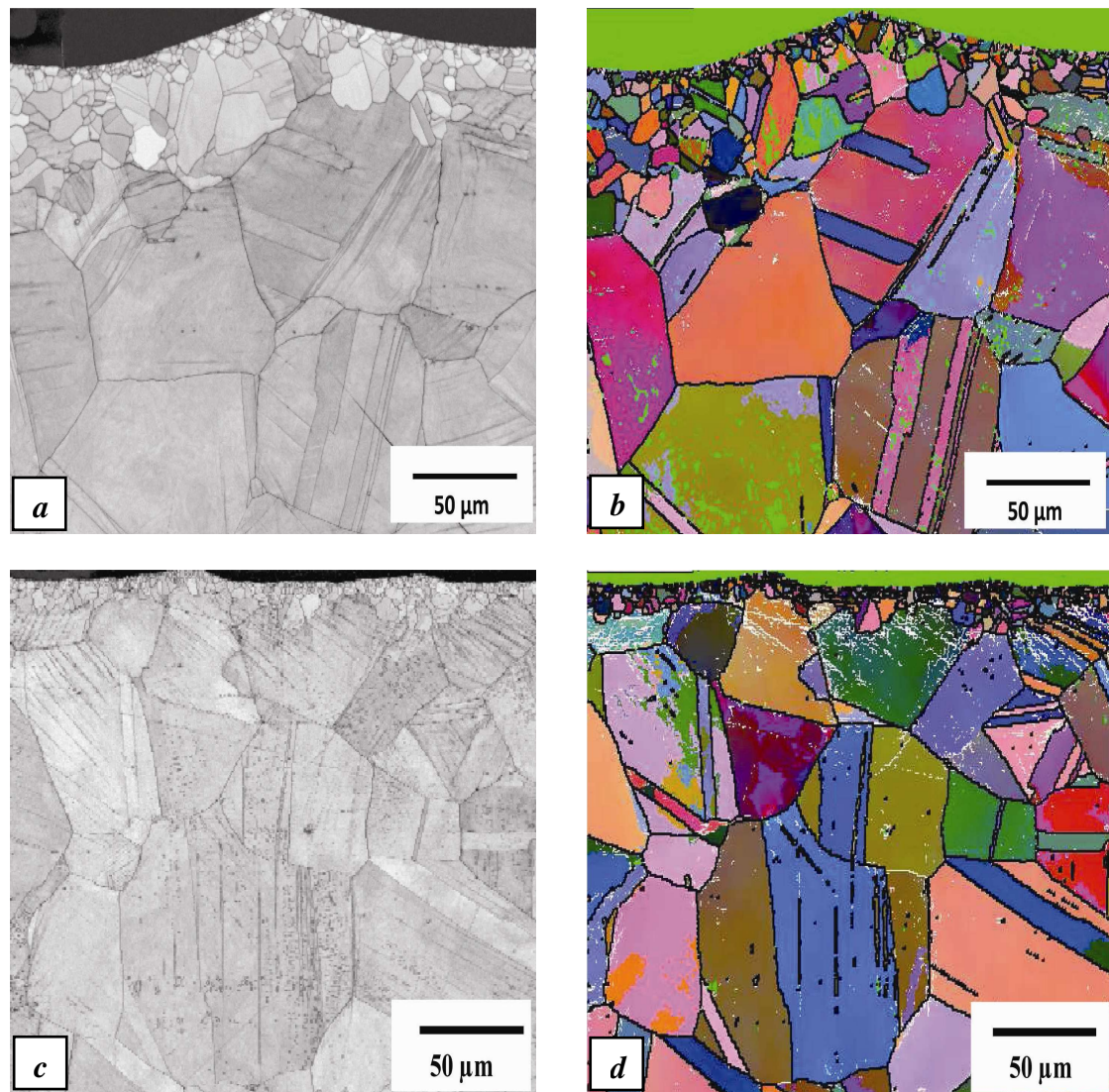


Figure 4- 34: AISI 316L a) Band contrast map of rough annealed specimens *before* fatigue test; b) Euler map of rough annealed specimens *before* fatigue test; c) Band contrast map of rough machined & annealed(5) specimens *after* fatigue test (264 MPa); d) Euler map of rough machined & annealed(5) specimens *after* fatigue test.

#### 4.7. Microstructural Damage Characterisation

##### 4.7.1. Metallography of Stable Cracks

Metallographic observations of longitudinal sections from run out ( $10^7$  cycles) specimens were taken from the sections perpendicular to the surface, parallel to the specimen longitudinal axis for both materials.

##### 4.7.1.1. Stable Cracks in AISI 304L

Figure 4- 35 shows small numbers of crack-like features in all cases of AISI 304L. These tended to be quite linear in the electropolished (3) and fine machined condition



(1), but features with a more irregular profile were observed on the rough machined (4) surfaces. These cracks are all significantly smaller than the average grain size of the bulk of the microstructure ( $\sim 54 \mu\text{m}$ ).

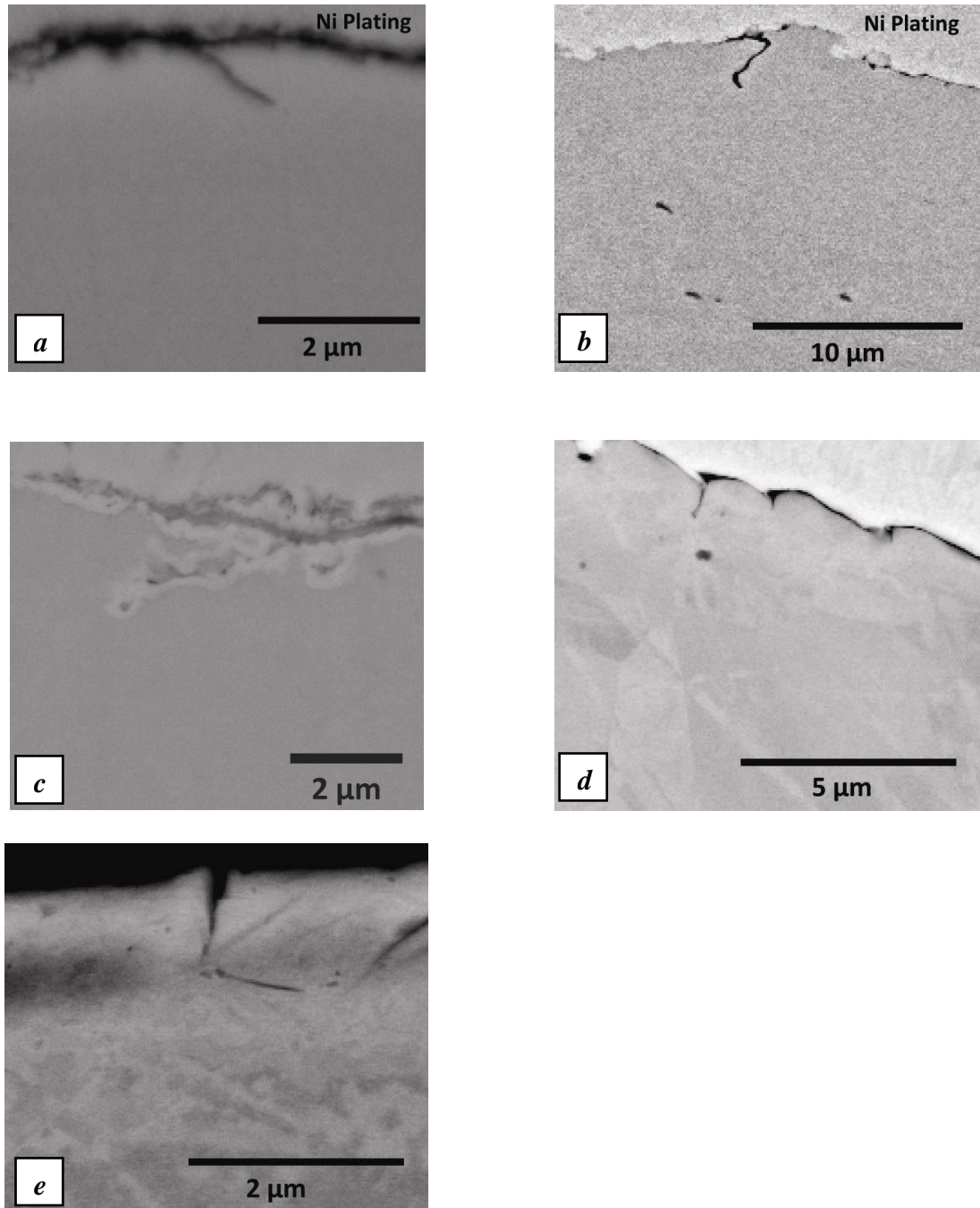


Figure 4- 35: Crack-like features in fatigued (run-out) specimens of AISI 304L: a) Fine machined (1) sample (tested at 324 MPa); b) Rough machined (4) sample (tested at 288 MPa); c) Fine machined & Annealed (2) sample (tested at 350 MPa); d) Rough machined & Annealed (5) sample (tested at 336 MPa); e) Electropolished (3) sample (tested at 338 MPa) ( $\leftrightarrow$  stress axis).

#### 4.7.1.2. *Stable Cracks in AISI 316L*

The metallographic observations of longitudinal sections from run out ( $10^7$  cycles) specimens of AISI 316L are shown in Figure 4- 36. It can be seen that the crack-like features in all cases are essentially identical to those observed in the AISI 304L. The electropolished samples clearly show stable fatigue crack nuclei (Figure 4- 36-e). The irregular surface features observed in the rough machined (4) samples are associated with defects introduced by machining.

Features with a more irregular profile were observed on fine machined conditions (1) and the rough machined surfaces. The cracks in the electropolished (3) samples observed to be inclined at approximately  $45^\circ$  to the stress axis.

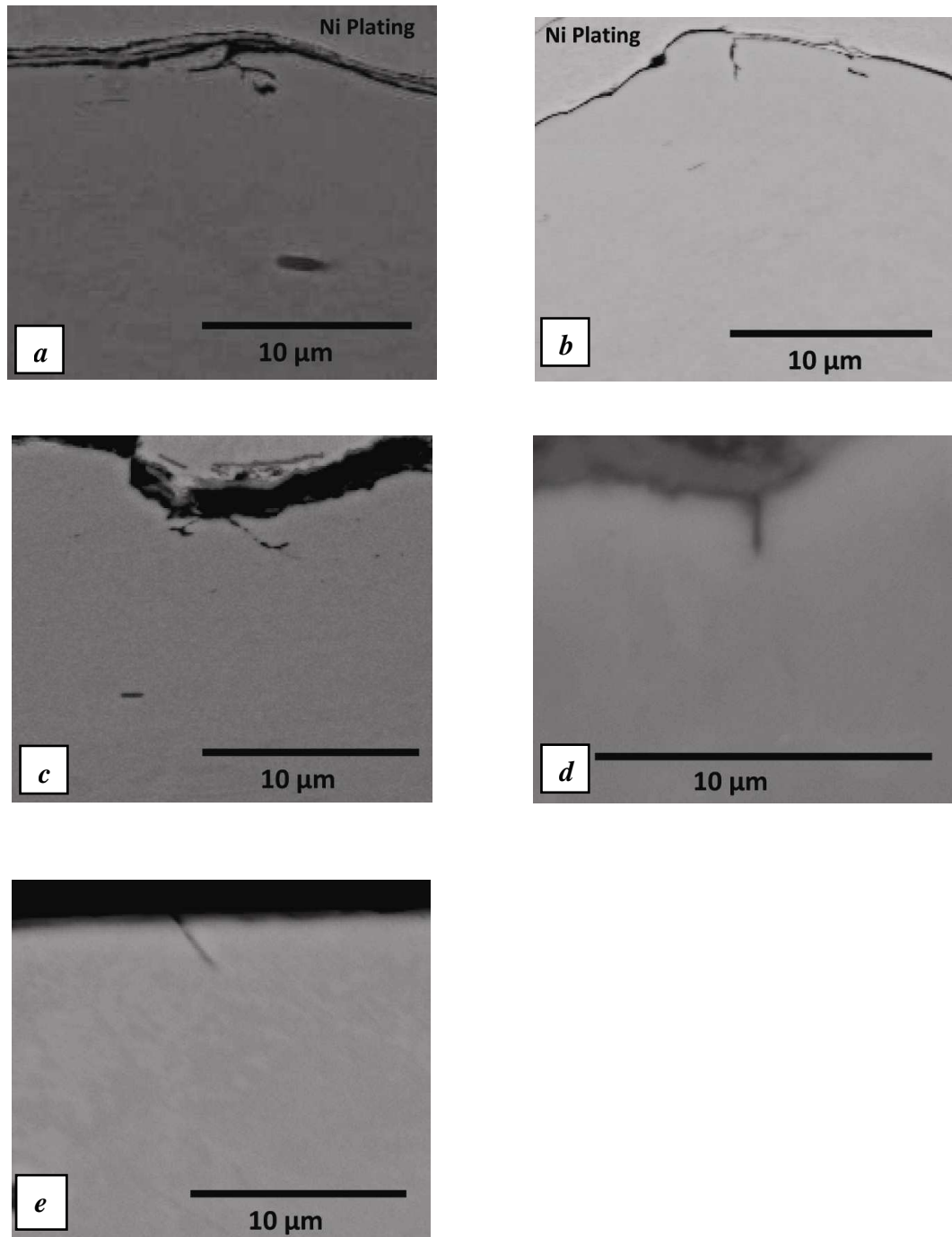


Figure 4- 36: Crack-like features in fatigued (run-out) specimens of AISI 316: a) Fine machined (1) sample (tested at 316 MPa); b) Rough machined (4) sample (tested at 292 MPa); c) Fine machined & Annealed (2) sample (tested at 310 MPa); d) Rough machined & Annealed (5) sample (tested at 260 MPa); e) Electropolished (3) sample (tested at 298 MPa), ( $\leftrightarrow$  stress axis).

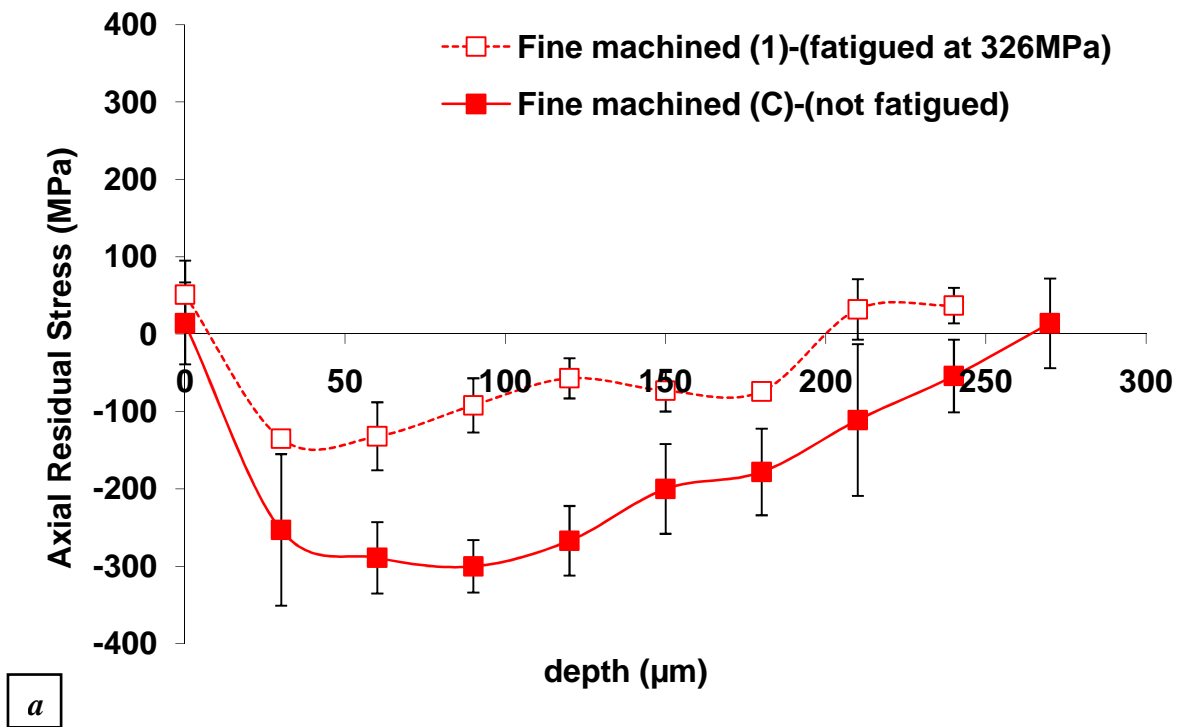
#### 4.8. *Characterisation of Surface Damage after fatigue using X-Ray Diffraction*

##### 4.8.1. *AISI 304L*

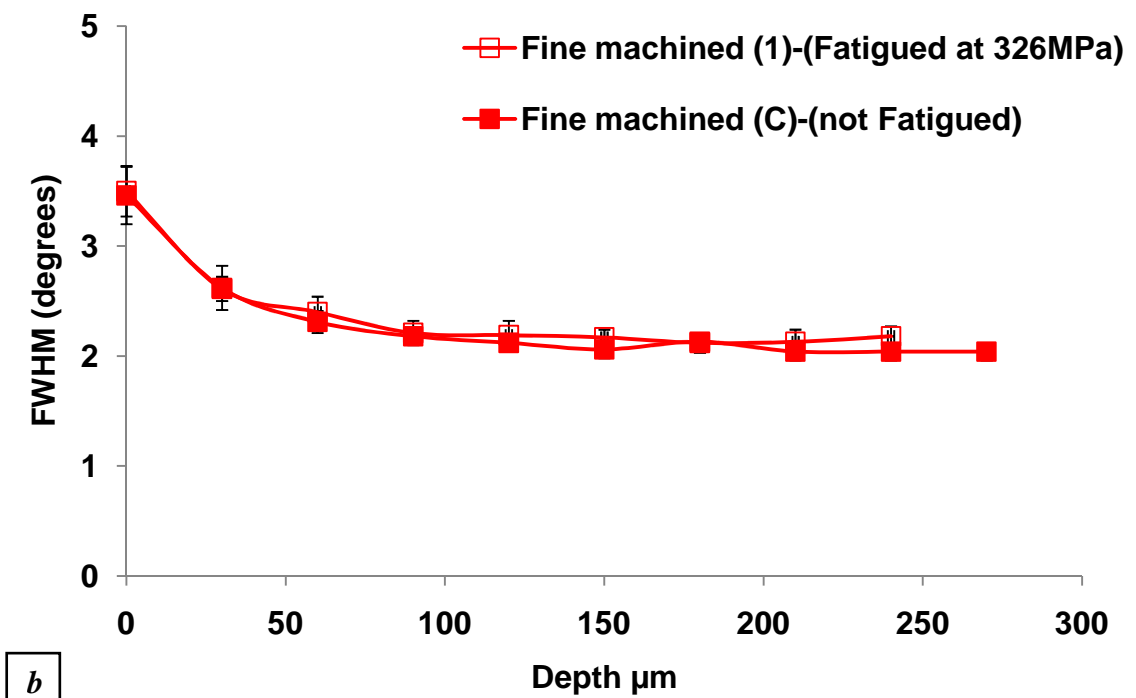
Corresponding data for residual stress and the full width at half the maximum peak (FWHM), which are a measure of the degree of work hardening, are shown in Figure 4- 37-a and Figure 4- 38-a for fine condition (1) and rough condition (4), respectively after fatigue.

In fine machined (1) sample, it is apparent that there is a marked relaxation of residual stress occurs after fatigue test below the surface Figure 4- 37-a. The residual stress at the surface has a slight relaxation while the maximum compressive stress level is significantly reduced. A similar relaxation occurs in rough machined (4) sample after fatigue, but the reduction in the residual stress level is far less Figure 4- 38-a.

Figure 4- 37-b and Figure 4- 38-b shows the full width at half the maximum peak FWHM of fine machined (1) and rough machined (4) samples after fatigue test for AISI 304L. As can be seen from these graphs, the FWHM distributions for both conditions (fine and rough) remain quite stable. These results indicate that the presence of the work hardened layer, appear to be relatively unaffected by fatigue.



a



b

Figure 4- 37: a) Depth profiles of axial residual stress for AISI 304L fine machined before and after fatigue; b) FWHM profile with depth below surface for AISI 304L fine machined before and after fatigue.

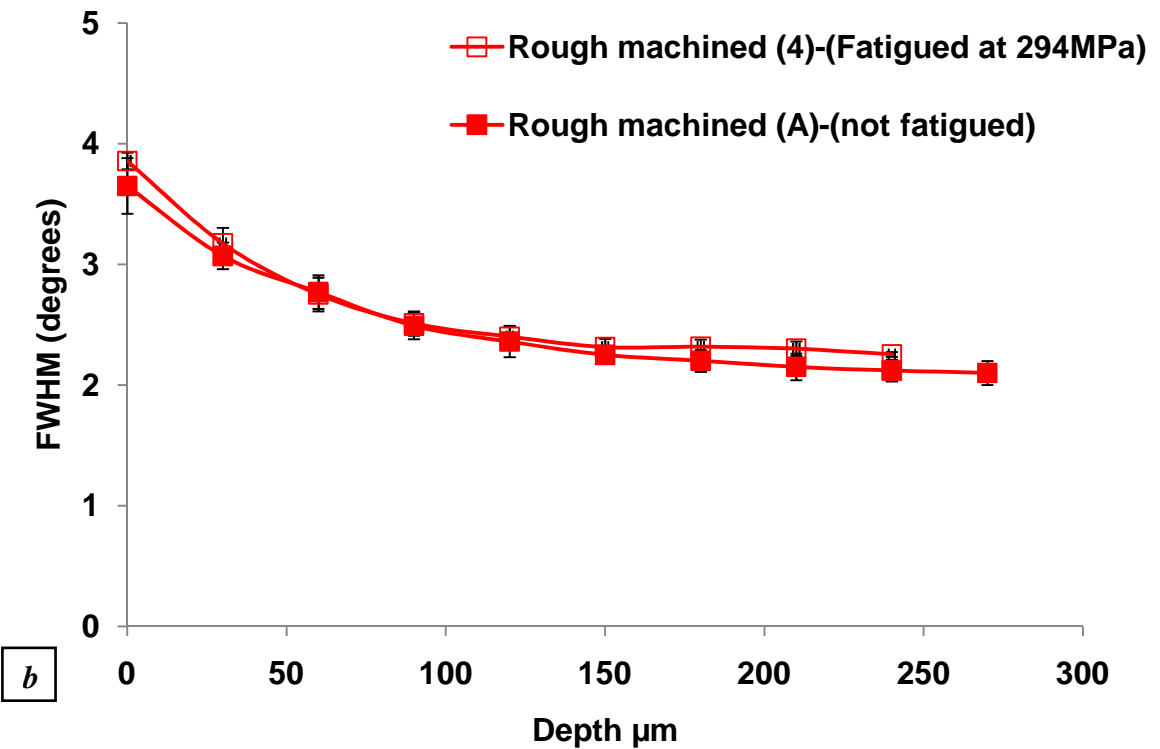
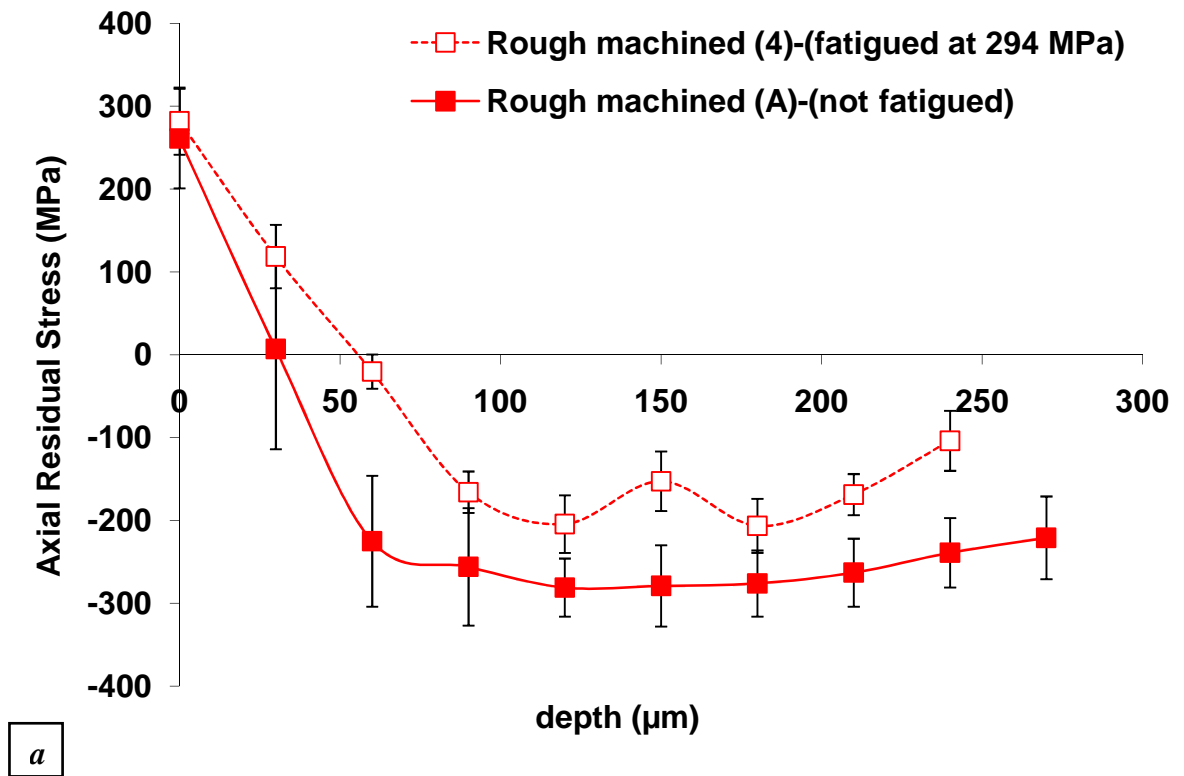


Figure 4- 38: a) Depth profiles of axial residual stress for AISI 304L rough machined before and after fatigue; b) FWHM profile with depth below surface for AISI 304L rough machined before and after fatigue.



**4.8.2. AISI 316L**

It is apparent from Figure 4- 39-a and Figure 4- 40-a for fine condition (1) and rough condition (4), respectively after fatigue that there is a relaxation in subsurface stresses but no significant relaxation in the surface stresses

The full width at half the maximum peak FWHM of fine condition (1) and rough condition (4) samples after fatigue test shows that the distributions remain slightly stable (Figure 4- 39-b and Figure 4- 40-b). The effect of fatigue on residual stress distribution and FWHM distribution in AISI 316L is similar to that in AISI 304L.

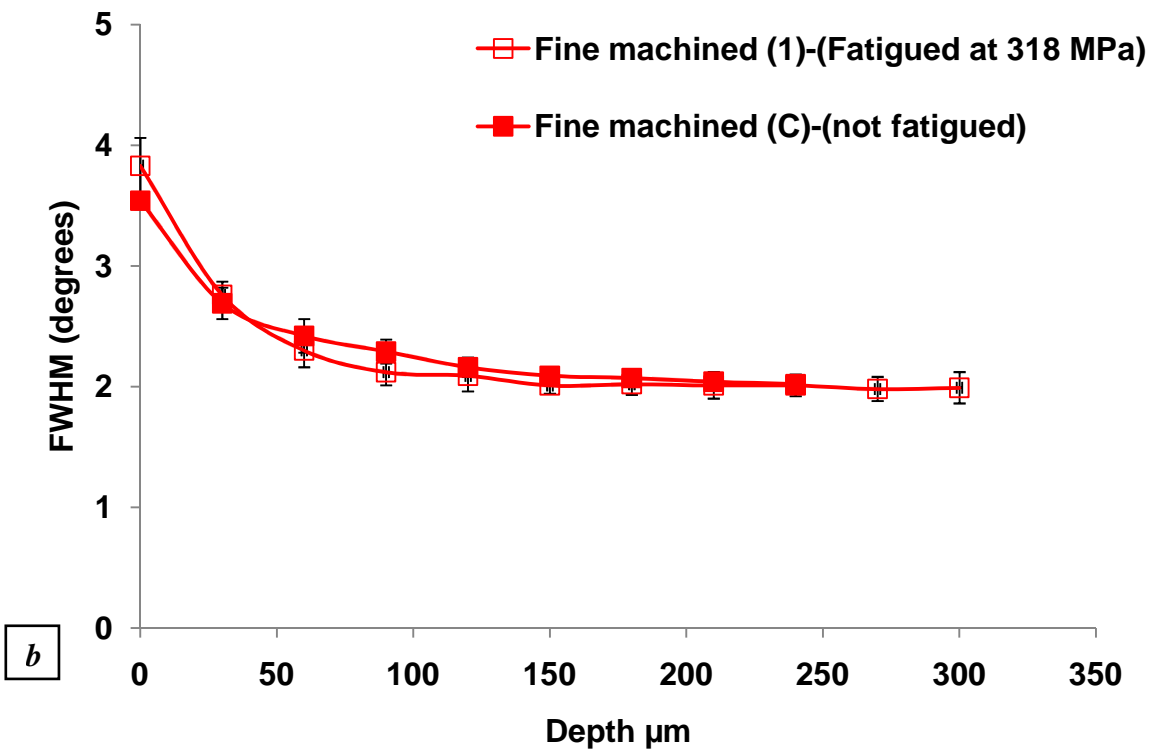
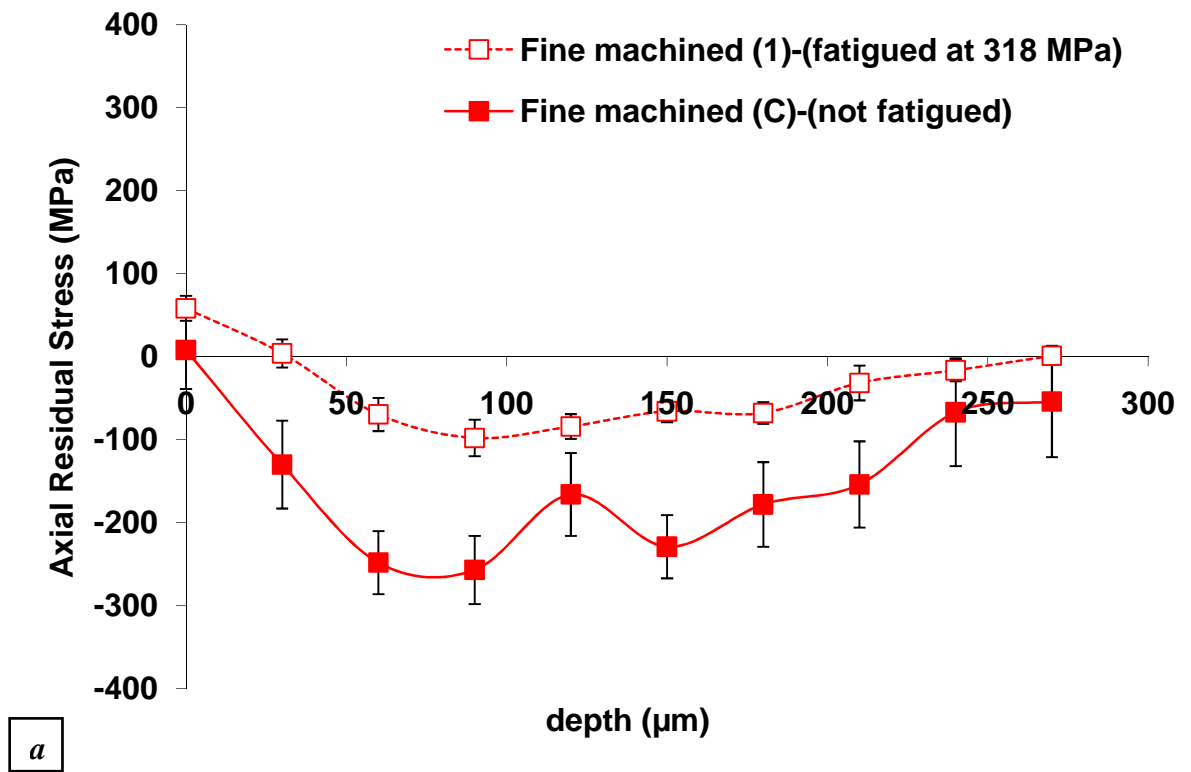


Figure 4- 39: a) Depth profiles of axial residual stress for AISI 316L fine machined before and after fatigue; b) FWHM profile with depth below surface for AISI 316L fine machined before and after fatigue.

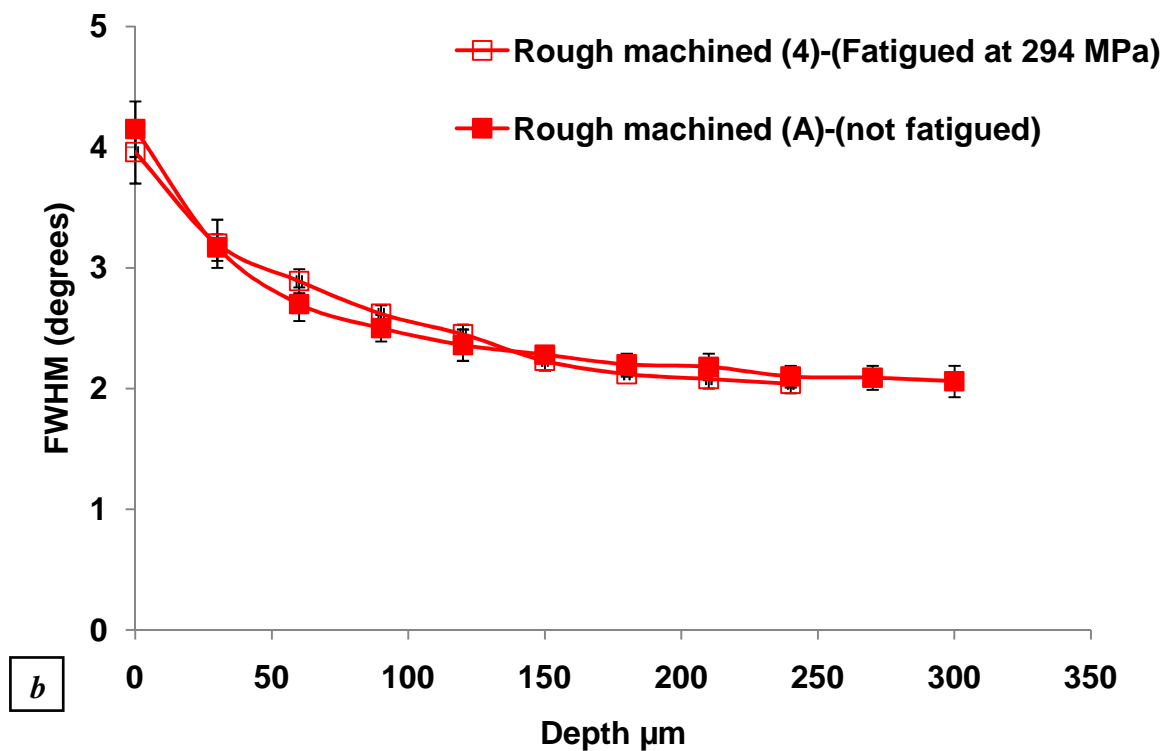
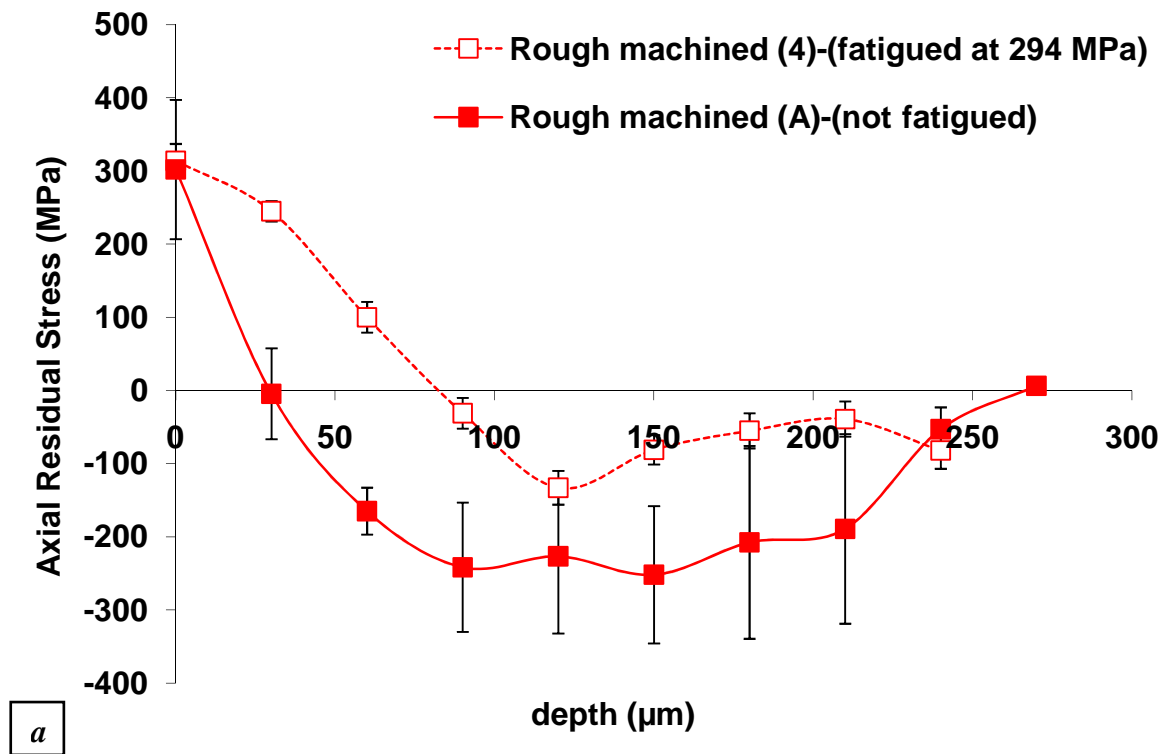


Figure 4- 40: a) Depth profiles of axial residual stress for AISI 316L rough machined before and after fatigue; b) FWHM profile with depth below surface for AISI 316L rough machined before and after fatigue.

#### 4.9. *Characterisation of Surface Damage after fatigue using Nano-indentation*

Figure 4- 41 and Figure 4- 42 show nano-hardness depth profiles of fine and rough samples in the fatigued and un-fatigued conditions for AISI 304L and AISI 316L, respectively.

##### **4.9.1. Nano-indentation of AISI 304L**

In fine machined (1), hardness decreases from the surface to the level of hardness changes continuously with depth down (depth of approximately 50  $\mu\text{m}$ ) and then remains stable. A similar trend can be seen after fatigue testing with a slight increase in the hardness at the surface, which then returns to the same level of hardness at the same depth (Figure 4- 41-a).

In rough machined (4), hardness profile before fatigue show that there is a gradual decreases from the surface to depth of approximately 50  $\mu\text{m}$  and then remains stable. A similar trend can be seen after fatigue testing with slightly lower hardness at the surface, but the stabilizing of hardness can takes place at a depth of approximately 70  $\mu\text{m}$  (Figure 4- 41-b)-.

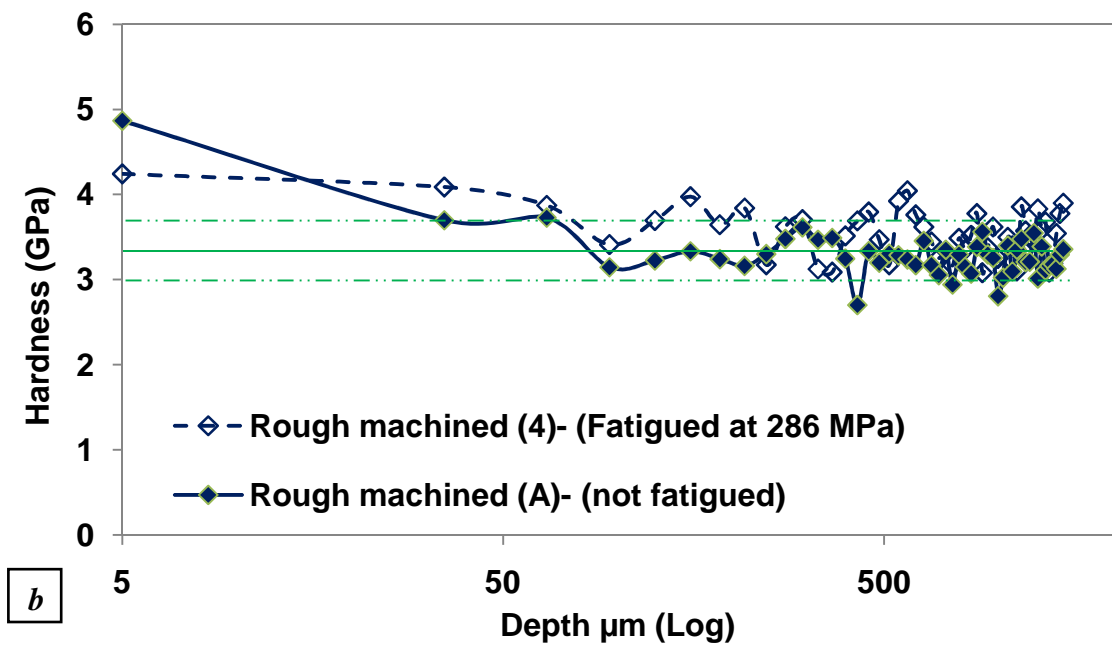
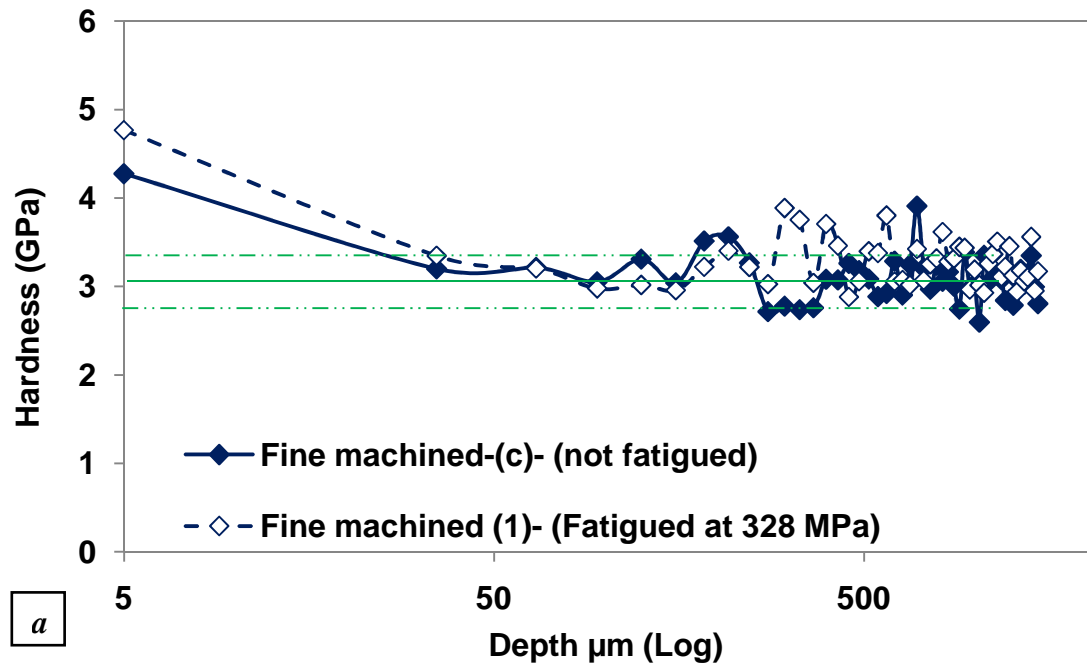


Figure 4- 41: Subsurface nanohardness profile of (AISI 304L); a) fine machined before and after fatigue test; b) rough machined before and after fatigue test.

#### **4.9.2. Nano-indentation of AISI 316L**

In the fine machined (1), the hardness decreases from the surface. The level of hardness changes continuously with depth (to a depth of approximately 50  $\mu\text{m}$ ) and then remains stable. After fatigue testing, the hardness at the surface does not change significantly and follows the similar trend of hardness as in the sample before fatigue (Figure 4- 42-a).

In the rough machined (4), the hardness profile before fatigue shows that there is a gradual decrease from the surface to a depth of approximately 50  $\mu\text{m}$  and it then remains stable. A similar trend can be seen after fatigue testing with a slightly lower hardness at the surface, which decreases until remaining stable beyond a depth of approximately 50  $\mu\text{m}$ . (Figure 4- 42-b).

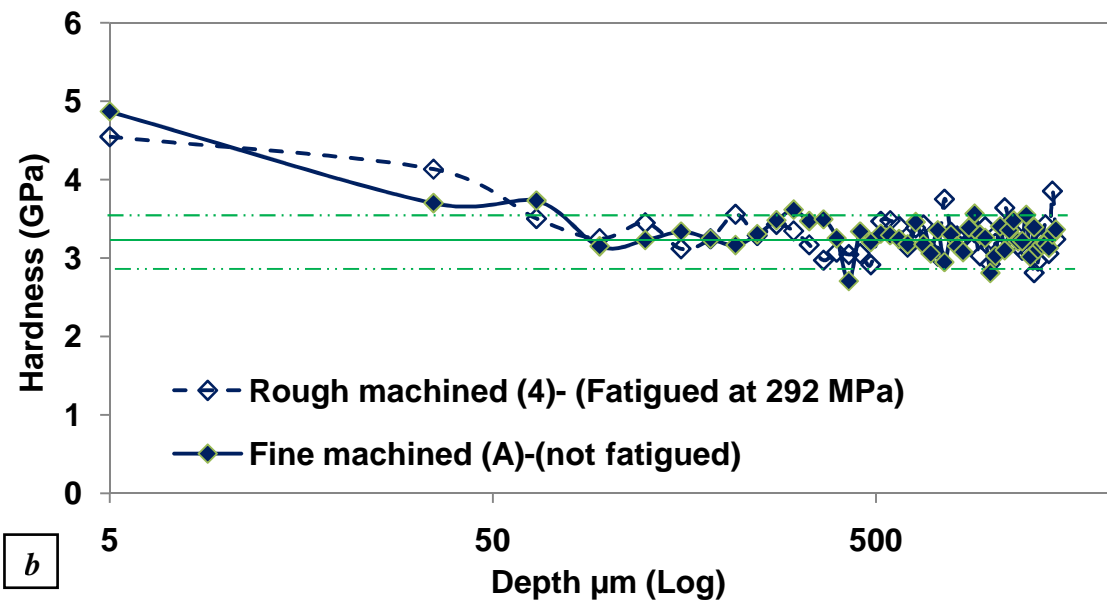
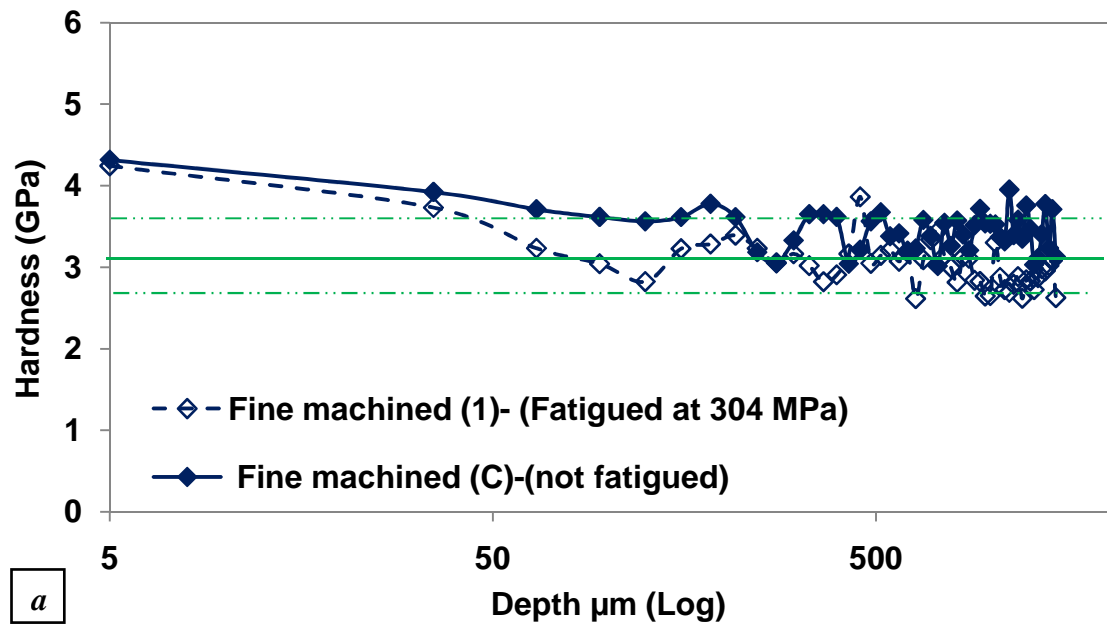


Figure 4- 42: Subsurface nanohardness profile of (AISI 316L): a) fine machined before and after fatigue test; b) rough machined before and after fatigue test.

#### 4.10. *X-Ray Diffraction for fatigue samples before and after fatigue test*

##### 4.10.1. *AISI 304L*

The XRD patterns of fine machined (1) and rough machined (4) specimens show the existence of FCC austenite phase and a small amount of BCC phase after fatigue testing and no BCC peak before fatigue. This can be seen in Figure 4- 43 and Figure 4- 44. The XRD patterns of electropolished (3) samples fatigued at 334 MPa, show FCC austenite phase and BCC phase (Figure 4- 45). The FCC austenite phase and BCC phase can also be seen in fine machined & annealed (2) samples and rough machined & annealed (5) samples after fatigue testing at 342 MPa and 336 MPa, respectively, (Figure 4- 46 and Figure 4- 47).

The results show that there is a body-centered cubic (BCC) phase developed, which may be either ferrite or martensite. The presence of martensite will be confirmed by Transition Electron Microscope (TEM) study in section 4.12.2.

Table 4- 9 shows the ratios between the FCC (austenite) peak and BCC peak (inside the dotted rectangle in the x-ray diffraction patterns). It can be seen that there is more BCC phase in the machined samples. Figure 4- 48 shows the comparison between the broadening in BCC peaks for fine machined (1), rough machined (4) and electropolished (3) samples. It can be seen that the machined conditions show broadening in the BCC peak compared to electropolished BCC peak.



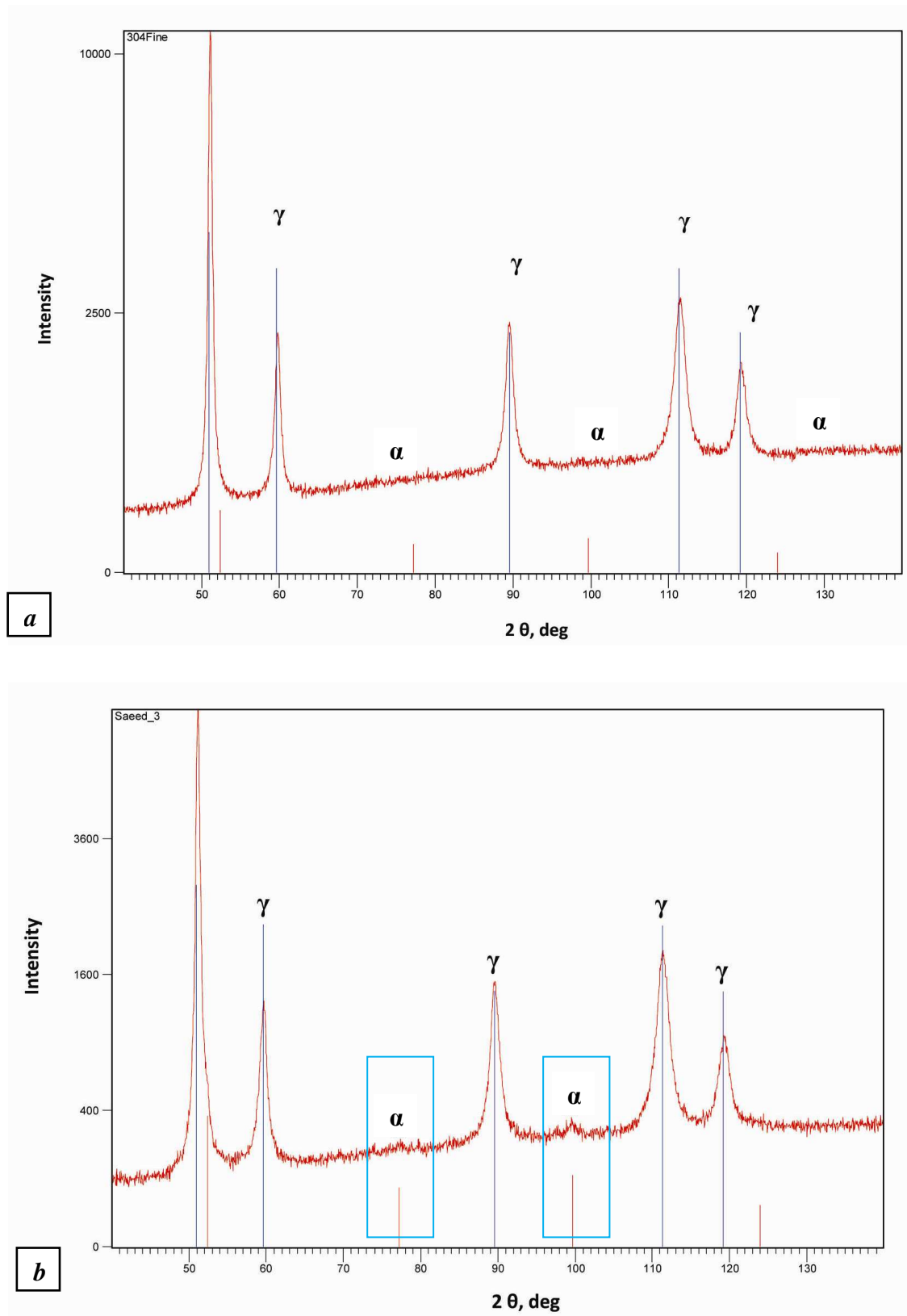


Figure 4- 43: X-ray spectrum of AISI 304L a) Fine machined (C) (not fatigued); b) Fine machined (I) fatigued (run-out) at 324 MPa.

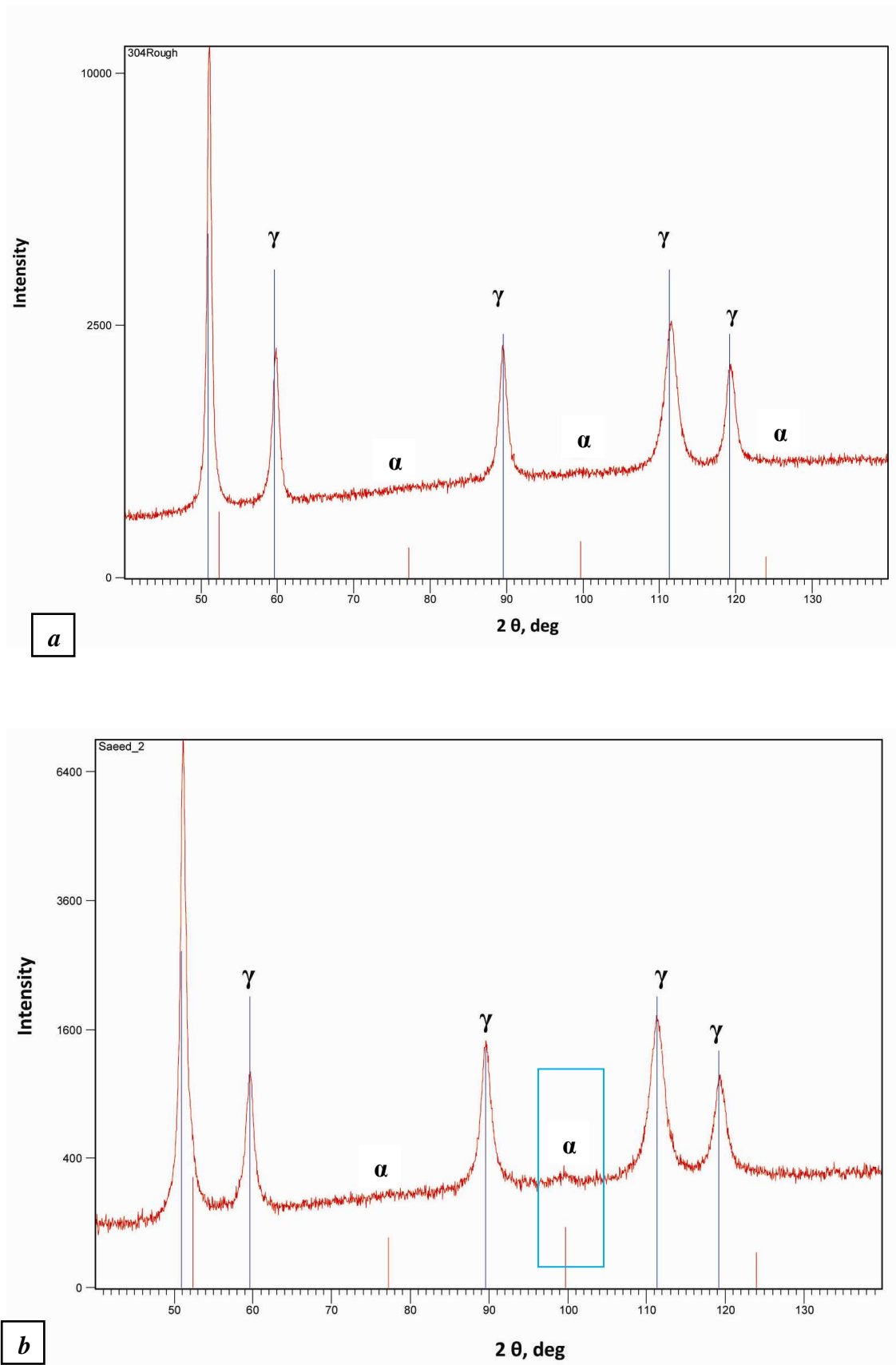


Figure 4- 44: X-ray pattern of AISI 304L a) Rough machined (A) ( not fatigued); b) Rough machined ( 4) fatigue test (run-out) at 292 MPa.

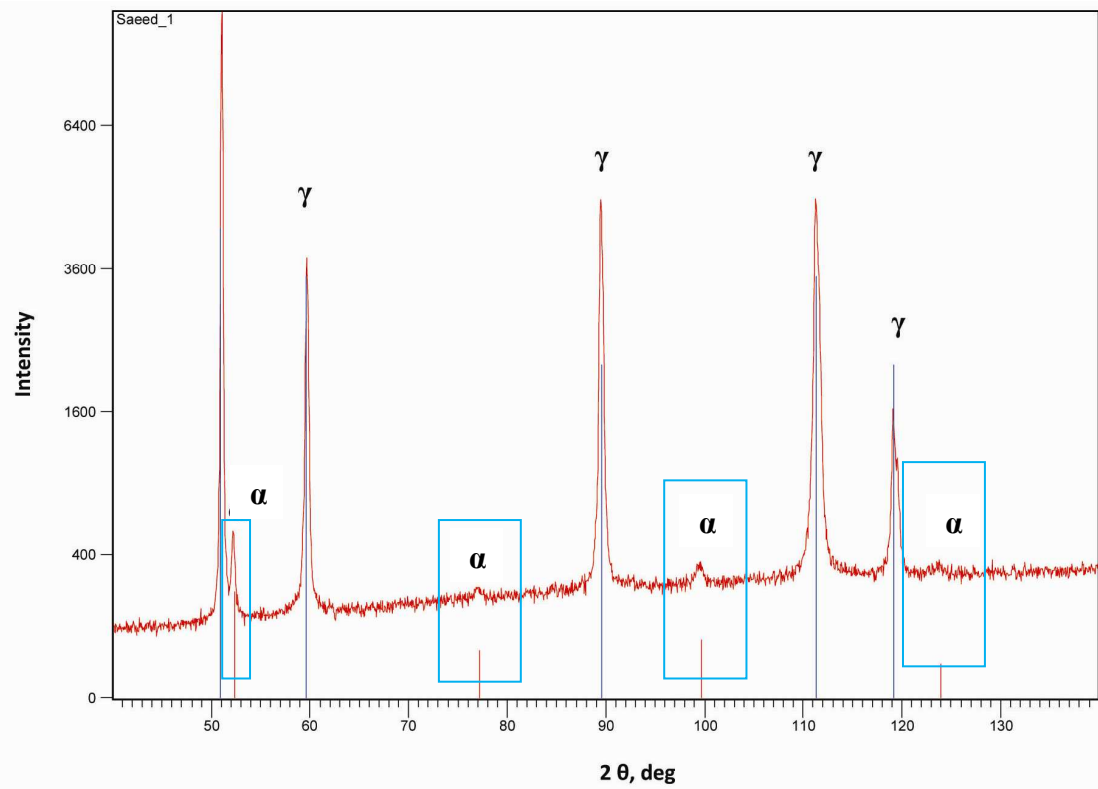


Figure 4- 45: X-ray pattern of AISI 304L run-out Electropolished (3) tested at at 336 MPa.

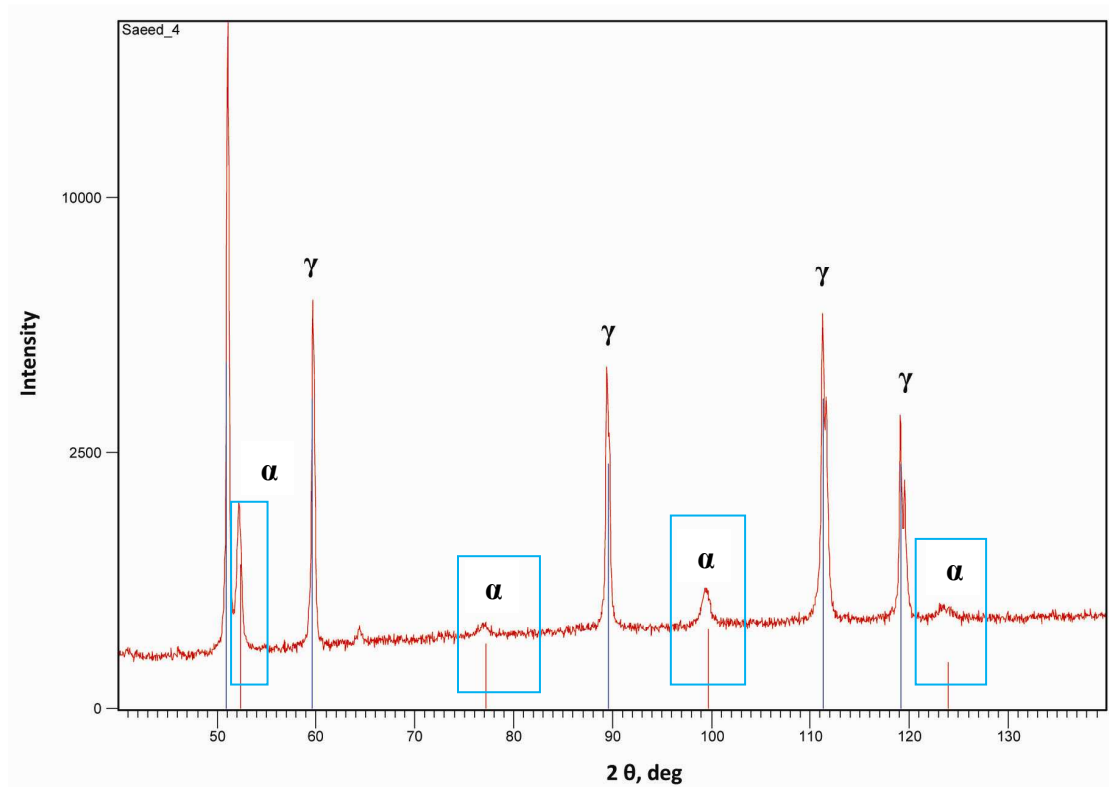


Figure 4- 46: X-ray spectrum of AISI 304L a) Fine machined & annealed (2) fatigue test (run-out) at 342 MPa.

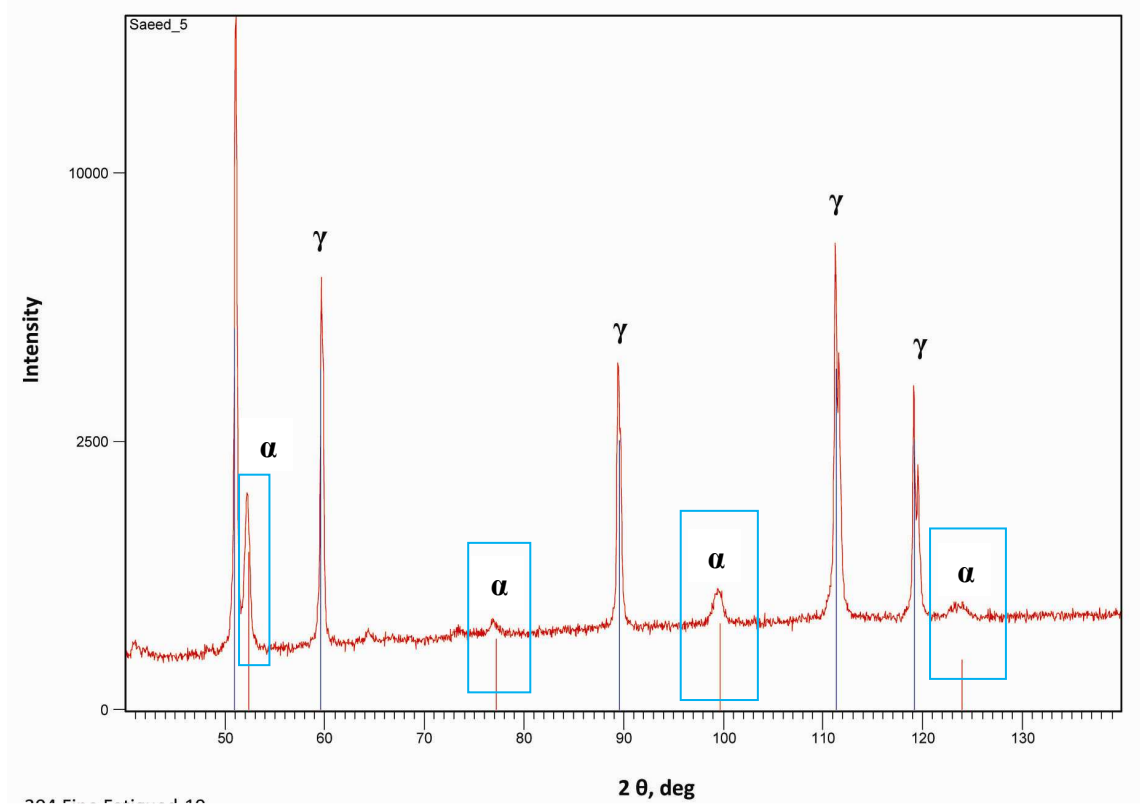


Figure 4- 47: X-ray spectrum of AISI 304L a) Rough machined & annealed (5) fatigue test (run-out) at 336 MPa.

Table 4- 9: Ratios between BCC peaks and austenite peaks for run-out samples.

Conditions	$\alpha$ (Intensity)	$\gamma$ (Intensity)	Ratio
Fine machined (1)	89	1258	0.071
Fine machined & Annealed (2)	278	4178	0.067
Electropolished (3)	88	4570	0.019
Rough machined (4)	83	1220	0.068
Rough machined & Annealed (5)	236	3877	0.061

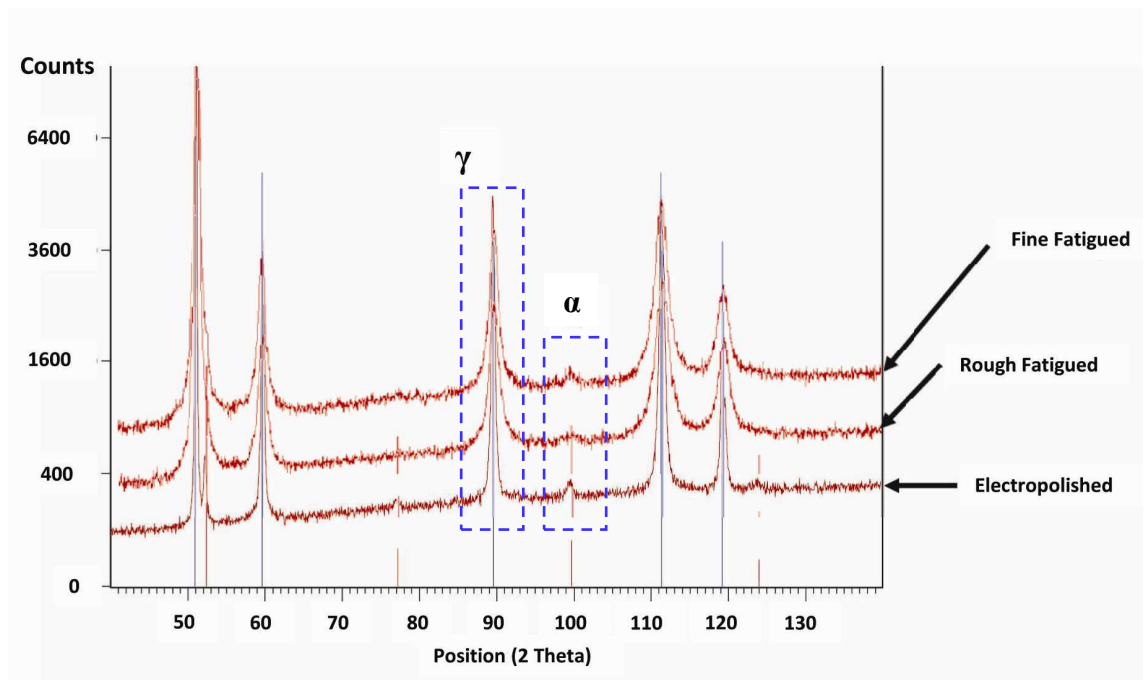


Figure 4- 48: X-ray diffraction patterns of AISI 304L for fine machined (1), rough machined (4) and electropolished (3) fatigued specimens (the vertical axis represents the intensity for electropolished specimen).

#### 4.10.2. AISI 316L

The XRD patterns of fine machined (1) and rough machined (4) fatigued specimens show only FCC austenite phases after fatigue test and no BCC peaks (Figure 4- 49 and Figure 4- 50). Electropolished (3) samples fatigued at 300 MPa, show FCC austenite phase and no BCC phase peaks can be observed (Figure 4- 51). So, the XRD patterns of AISI 316L, shows that there is no BCC peaks before and after fatigue testing in AISI 316L.

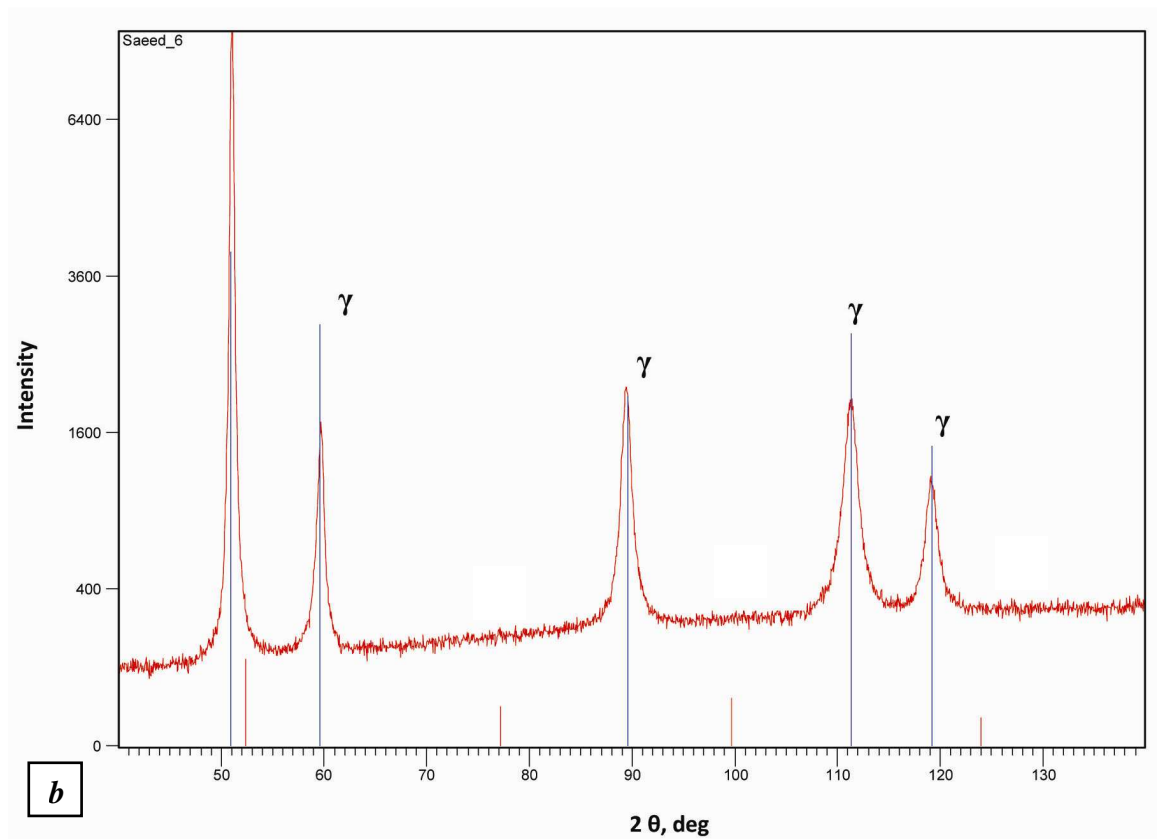
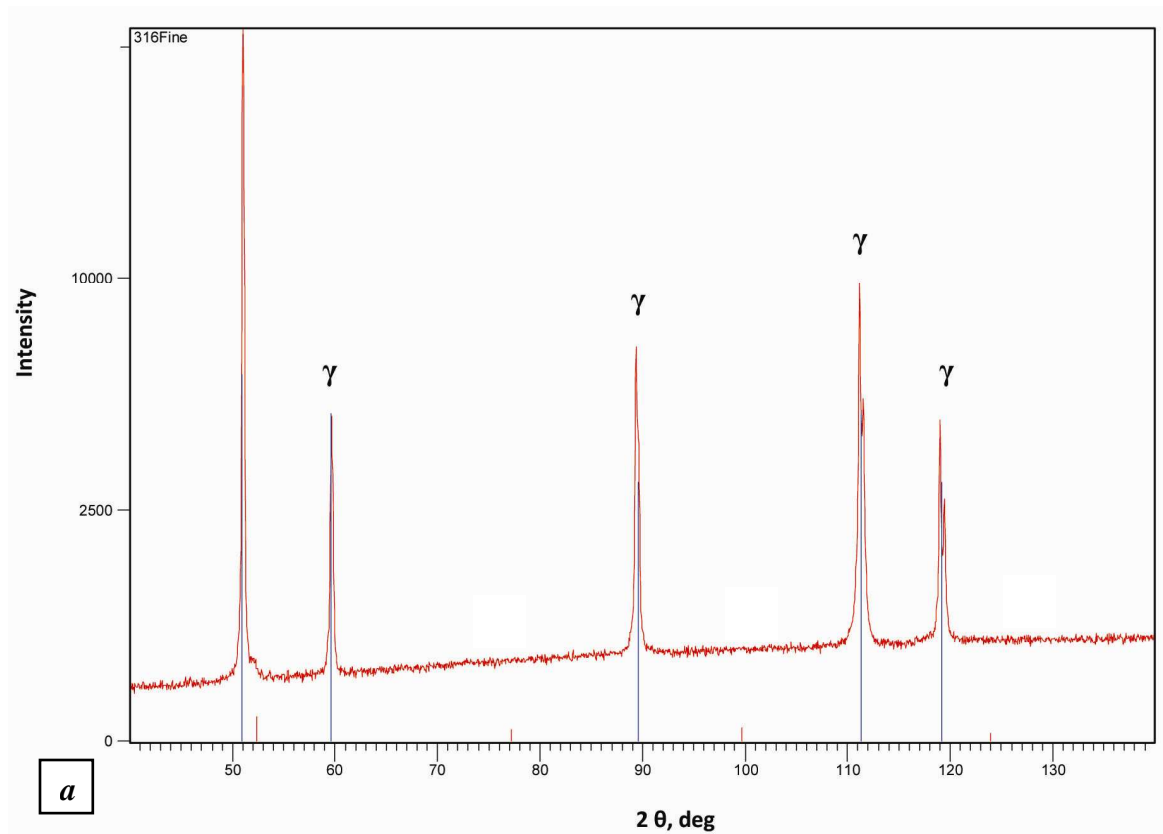


Figure 4- 49: X-ray pattern of AISI 316 a) Fine machined (C) (not fatigued); b) Fine machined (1) fatigued (run-out) at 320 MPa.

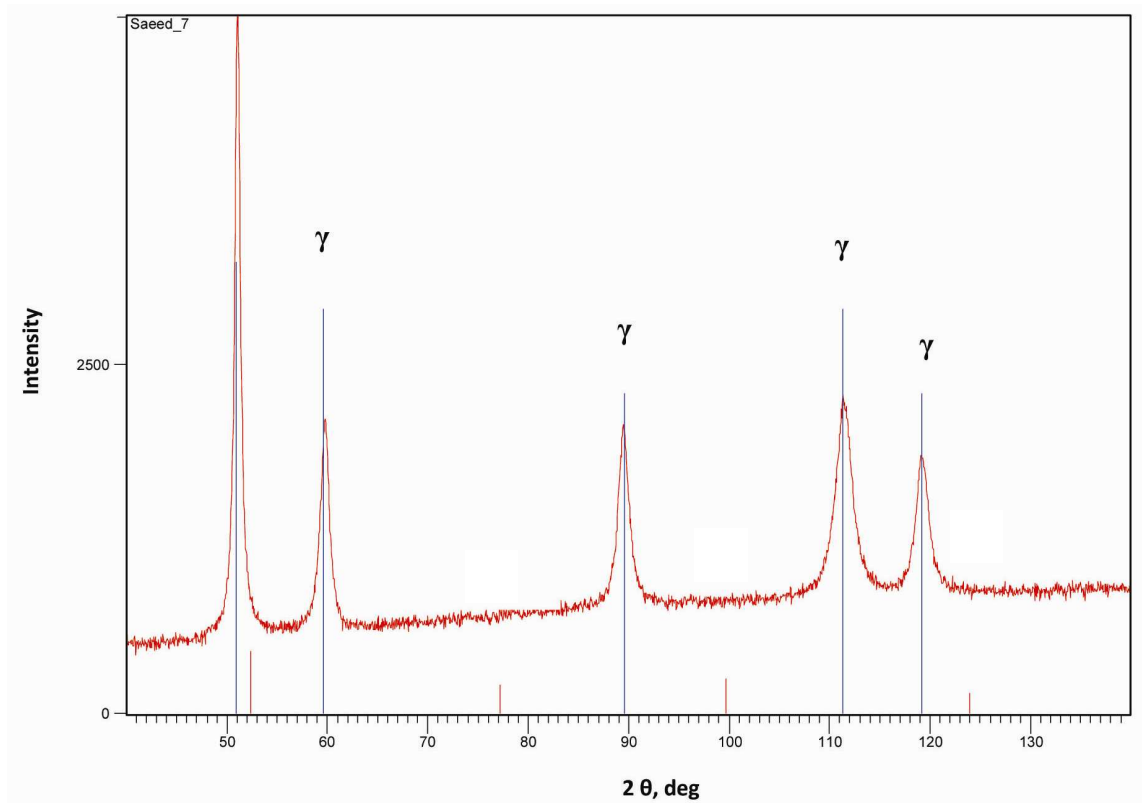


Figure 4- 50: X-ray pattern of AISI 316, Rough machined (4) fatigued (run-out) at 286 MPa.

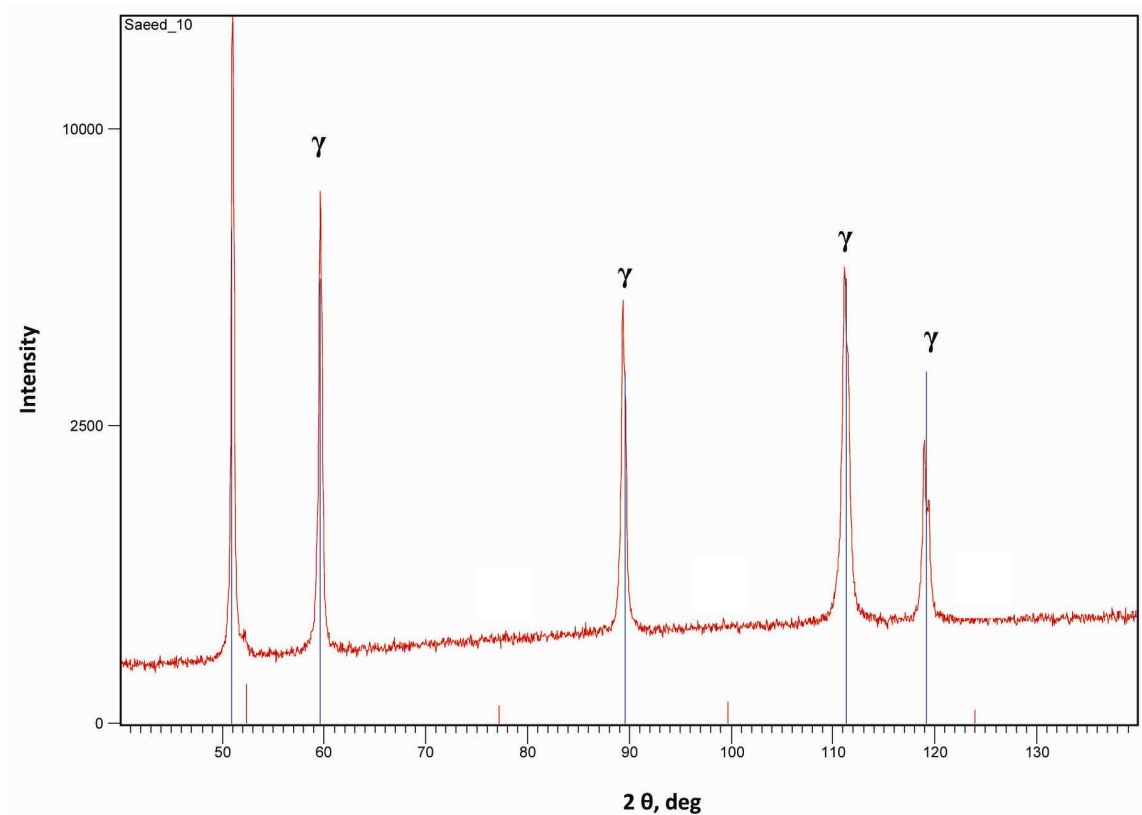


Figure 4- 51: X-ray pattern of AISI 316 Electropolished (3) and fatigued (run-out) at 300 MPa.

#### 4.11. *Interactions of Cracks with Microstructure*

Both austenitic AISI 304L and AISI 316L stainless steels showed that they have lamellar features in the microstructure (Figure 4- 55-a and Figure 4- 56-a). The cracks are observed to interact with these.

##### **4.11.1. Interactions of Cracks with Microstructure of AISI 304L**

In AISI 304L, Figure 4- 52-a and Figure 4- 53-a show these lamellar features as red lines in the electropolished (3) specimen and rough machined (4) specimen, respectively. Their misorientation profile (Figure 4- 52-b-c and Figure 4- 53-b-c), with misorientation of  $60^\circ$ , and their habit plane (indicated by their trace) is that of coherent twins.

In a distance of about 8 mm from the fracture surface of rough machined & annealed (5) specimen which broke at 340 MPa (Figure 4- 55), the observed crack propagates through the near surface microstructure and then meets a coherent twin. This forces the crack to deflect before continuing propagation. Figure 4- 55 show the misorientation of these features (twins) and their habit plane (indicated by their trace).

##### **4.11.2. Interactions of Cracks with Microstructure of AISI 316L**

In AISI 316L, Figure 4- 54-a (grain G2) shows similar features in rough machined & annealed specimen which had failed after testing at a stress amplitude of 262 MPa (the position of this crack is located at a distance about 6 mm from the fracture surface). As shown in Figure 4- 54 c, d and e, their misorientation profiles and their habit plane (indicated by their trace) shows that they are coherent twins[120].

In a typical run-out of Electropolished (3) specimens at 306 MPa, it is clear that the short cracks are arrested at similar features (Figure 4- 56). Figure 4- 56-c and d shows that their misorientation profiles and their habit plane (indicated by their trace) shows that they are coherent twins



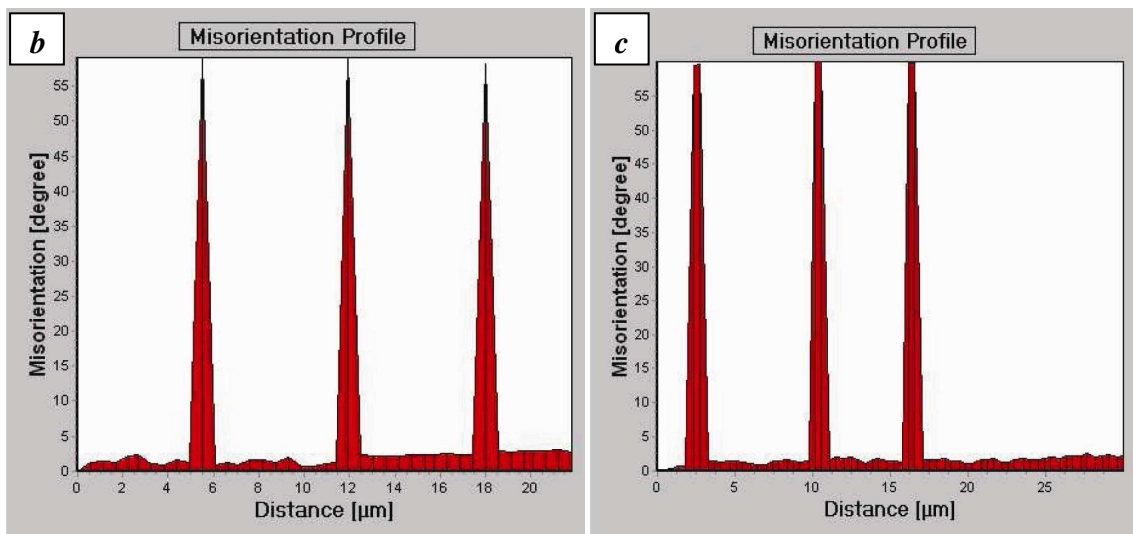
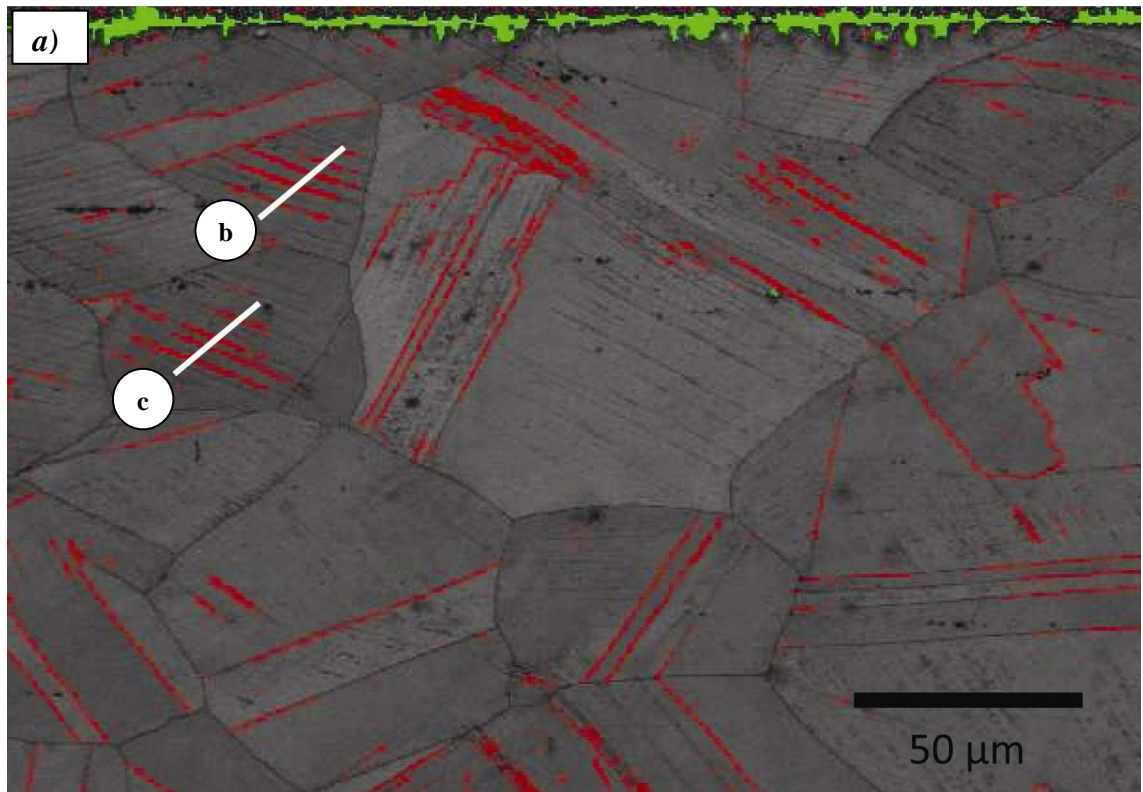


Figure 4- 52: a) Band contrast map of AISI 304L Electropolished (3) specimen (fatigued test at 338 MP); b) and c) the misorientation profile of twins in a), (white line represent the location of the misorientation profile).

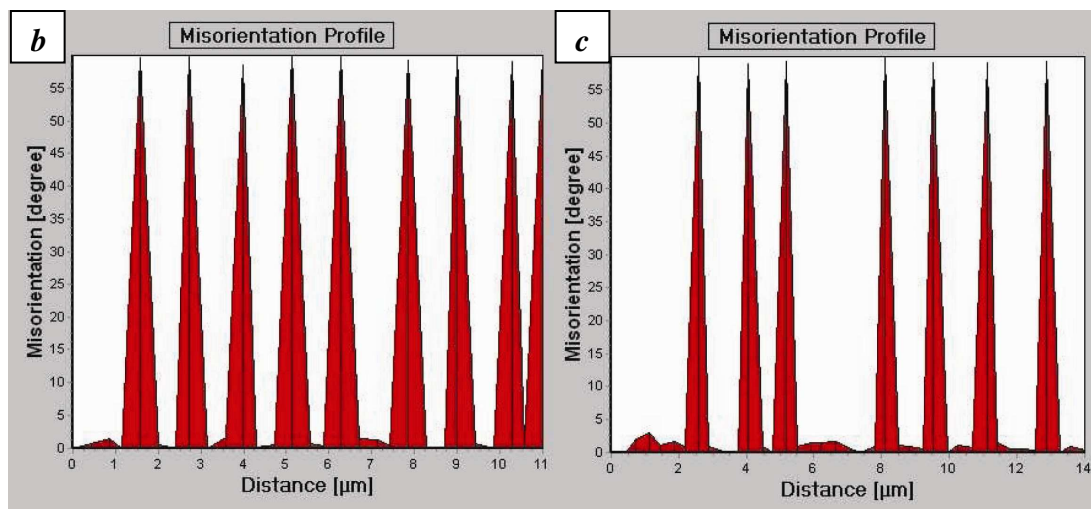
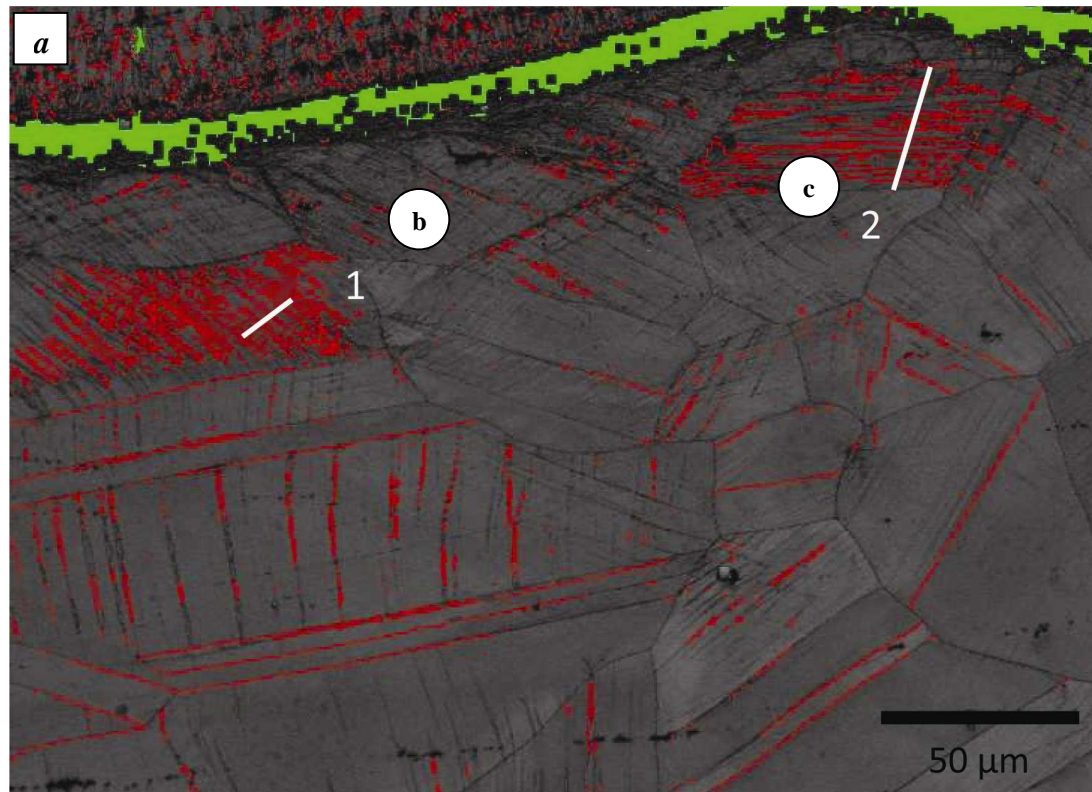


Figure 4- 53: a) Band contrast map of AISI304L rough machined (4) specimen (fatigued test at 288 MP); b) and c) the misorientation profile of twins in a), (, white line represent the location of the misorientation profile).

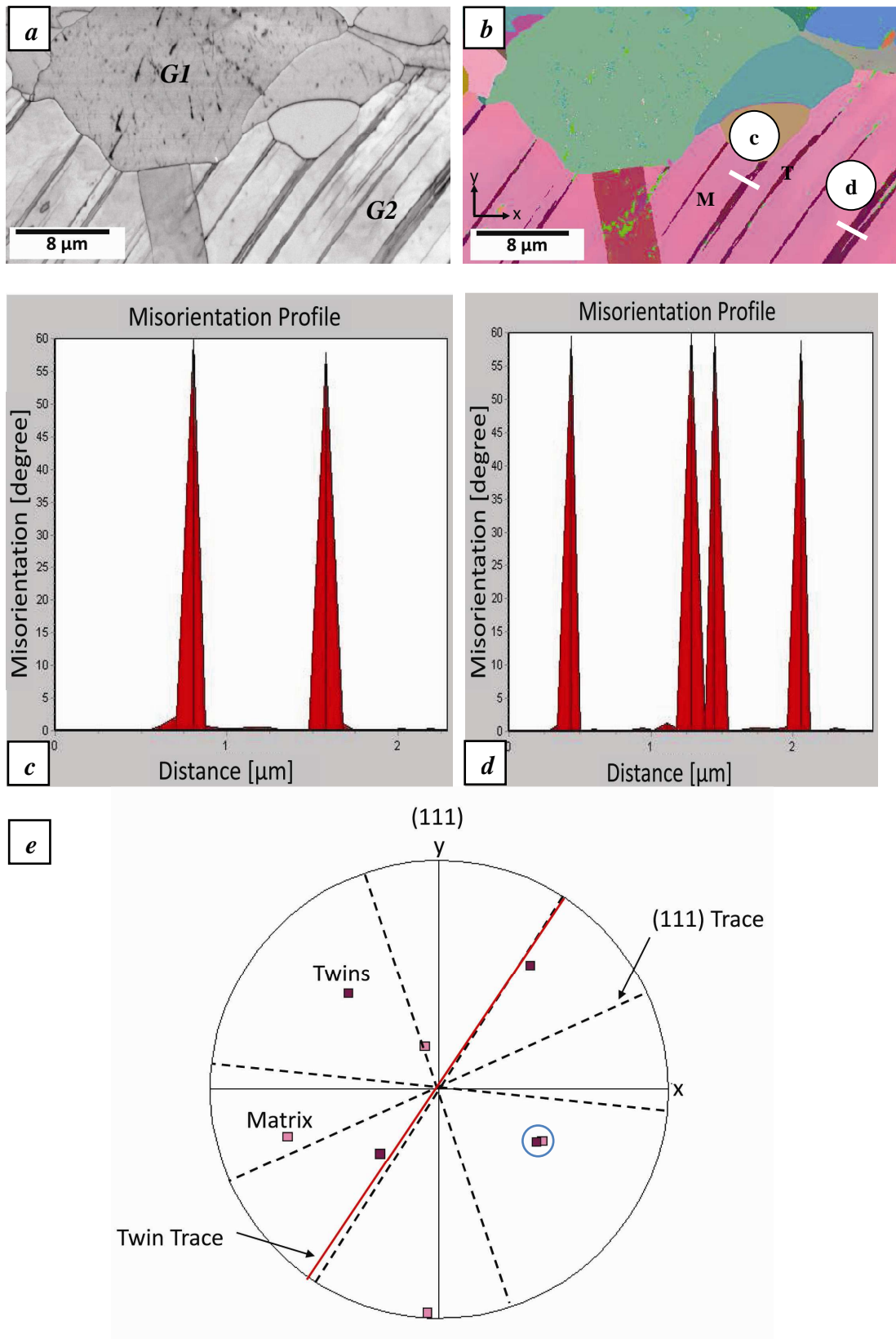


Figure 4- 54: EBSD of Crack features in rough annealed specimen which broke at 262 MPa (position of this crack is located at a distance about 6 mm from the fracture surface) in AISI 316L: a) Band contrast map; b) Euler map (M: Matrix and T: Twin). c) and d) the misorientation profile of twins in a), ( white line represent the location of the misorientation profile.), e)  $\{111\}$  pole figure shows the orientations of the lamellar features and matrix in b).



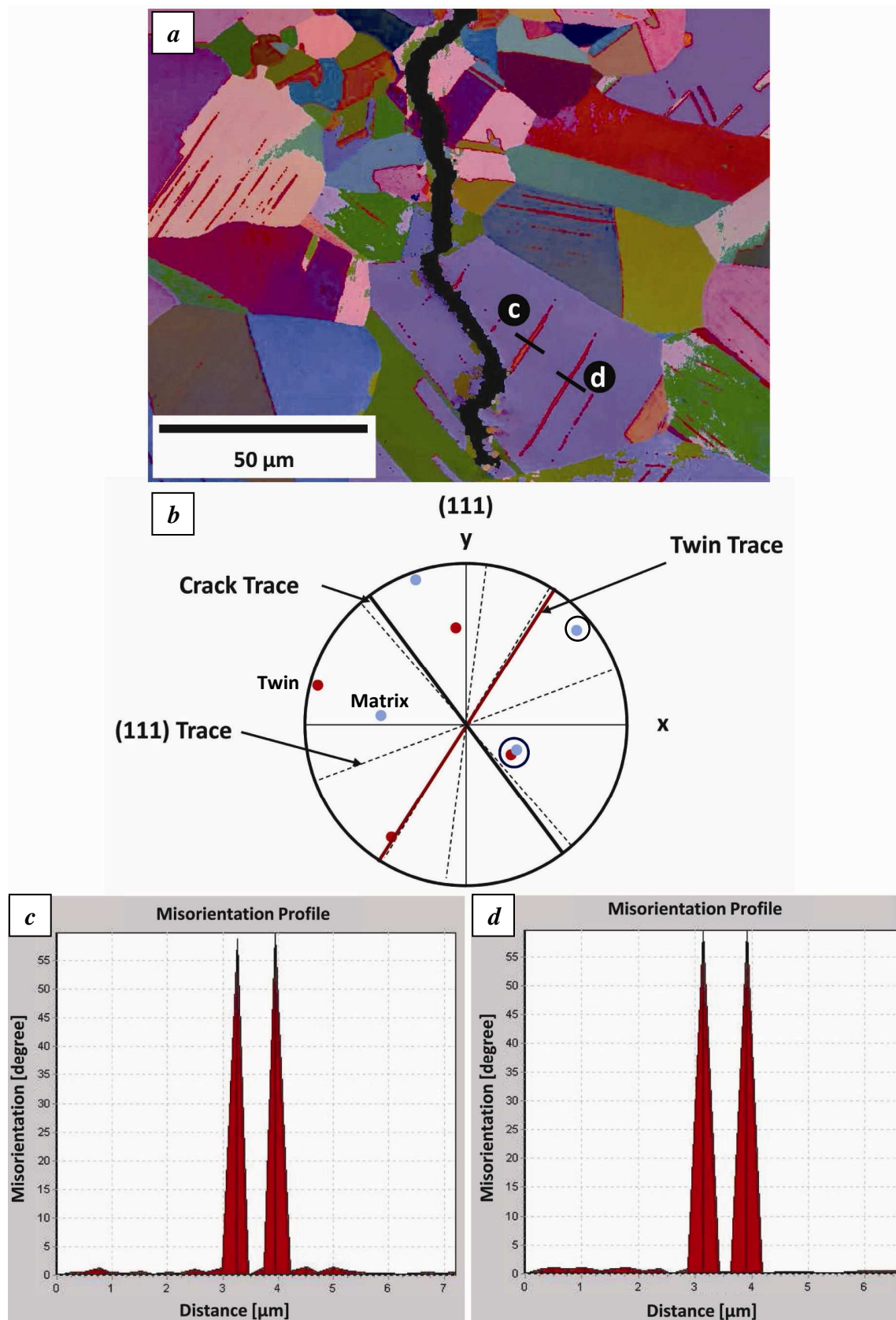


Figure 4- 55: a) Arrested cracks by twins in fatigued specimen AISI 304L(Rough machined & annealed specimen fatigued at 340 MPa) Euler map of the crack; b)  $\{111\}$  pole figure shows the orientations of the lamellar features and matrix in a; c and d) the misorientation profile of twins in a).

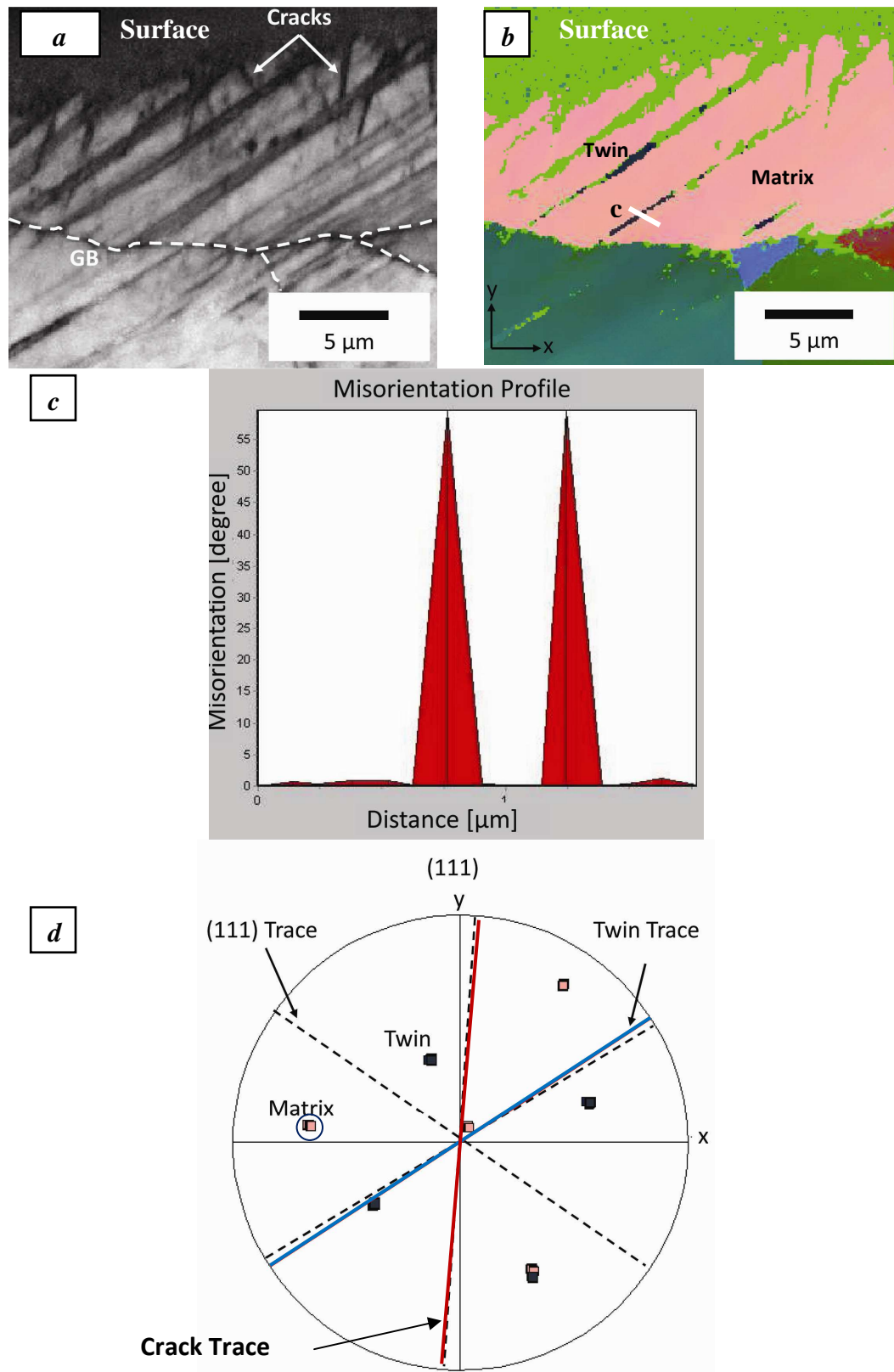


Figure 4- 56: In AISI 316L; a) Arrested cracks by twins [GB: Grain Boundary] in fatigued specimen (Electropolished (3) specimen fatigued at 306 MPa); b) Euler map of a. c) the misorientation profile of twins in a), ( white line represent the location of the misorientation profile.). d)  $\{111\}$  pole figure shows the orientations of the lamellar features and matrix in b).

#### 4.12. *Characterisation of Surface Damage after fatigue using TEM*

It is not easy to prepare TEM samples from the near surface regions by using traditional methods of specimen preparation, such as a twin-jet polishing technique. So, the FIB or focussed ion beam, milling technique was used to prepare samples. Due to lack of availability of FIB to prepare samples for all conditions before and after fatigue for both materials, only two samples were prepared from AISI 304L. One from a fine machined (1) sample and the other from an electropolished (3) sample containing short cracks.

##### 4.12.1. *Fine machined sample*

In order to study the deformed microstructure at the surface of machined samples, TEM cross-sections of the near surface regions of run-out fine machined (1) sample of AISI 304L (fatigued at 326 MPa) was prepared using the FIB technique as shown in Figure 3- 13.

Figure 4- 57-a shows the location of the selected area on the surface of the run-out fine machined (1) sample and the final shape of the TEM sample. The top side in Figure 4- 57- b shows the surface of this sample with a defect which may have been induced by machining. The TEM images were taken from the top side on the right and left of this defect close to the surface. Figure 4- 58-a and b show the bright field image of the near surface region of this sample. As can be seen, the direct surface exhibits nanocrystalline regions. The regions closest to the surface exhibit smaller grains than the deeper regions. There are similarities between the microstructure close to the surface in this sample and those described by Altenberger [37] on the effect of deep rolling and shot peening in type 304 austenitic stainless steel.

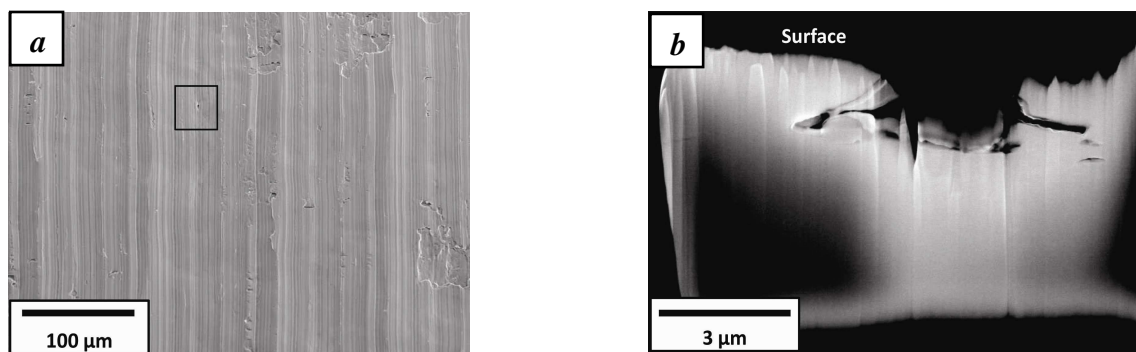


Figure 4- 57: a) The position selected to extract TEM sample from the surface of run-out fine machined-1 sample of AISI 304L (fatigued at 336 MPa); b) Final shape of TEM sample fixed on TEM grid after thinning using FIB.

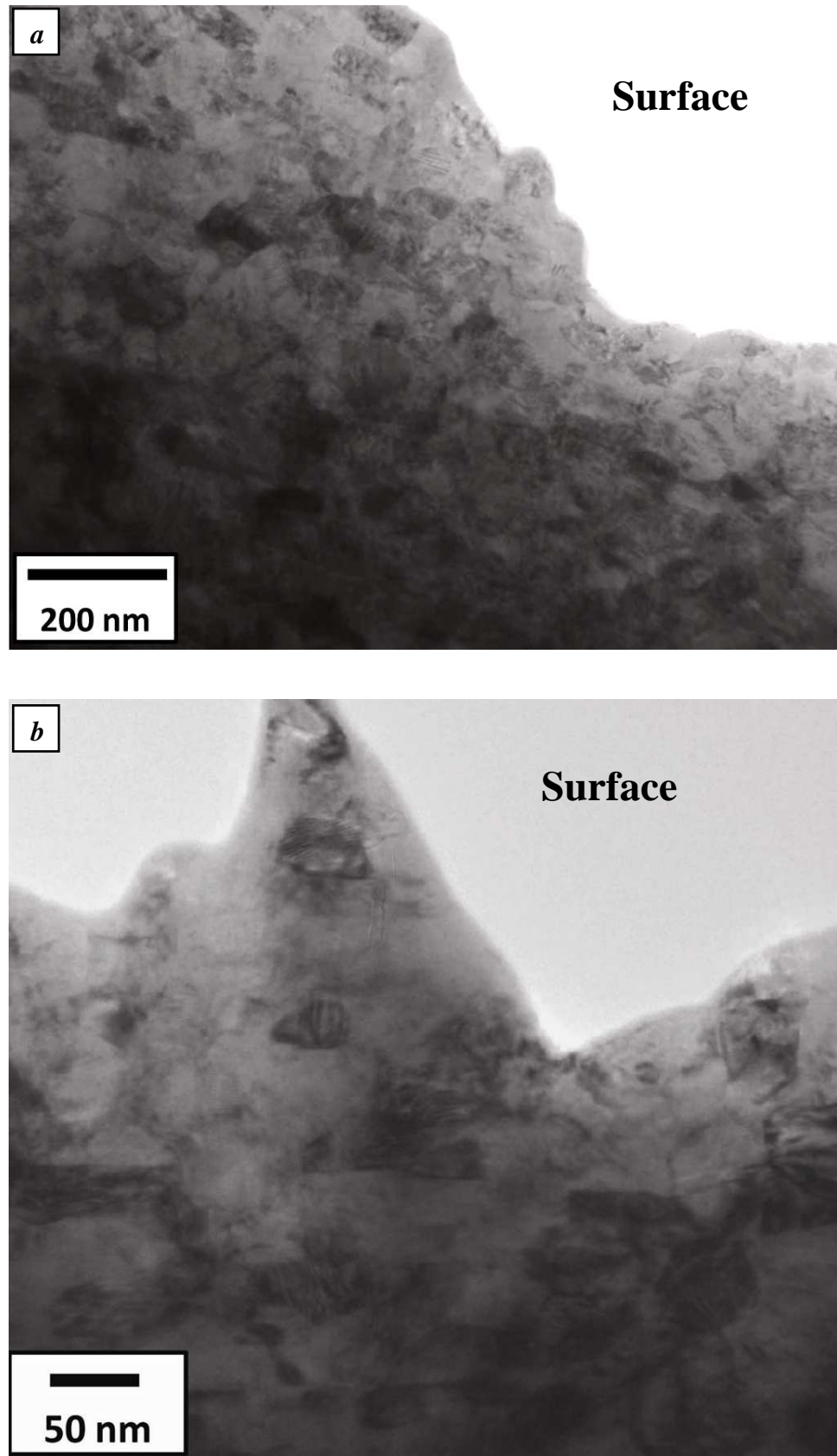


Figure 4- 58: a,b) A bright field image from different regions near the surface, illustrating the deformed microstructure and nanocrystalline regions of run-out fine machined-1 sample of AISI 304L (fatigued at 336 MPa).



#### 4.12.2. Electropolished Sample

In order to study the deformed microstructure at the surface of an electropolished sample and the interaction of the crack with this microstructure, a TEM cross-section of the near surface region of a run-out electropolished (3) sample of AISI 304L (fatigued at 336 MPa) containing a crack was prepared using the FIB technique as shown in Figure 3- 14.

Figure 4- 59-a shows the location of selected area on the surface of run-out electropolished (3) sample of AISI 304L and the final shape of TEM sample.

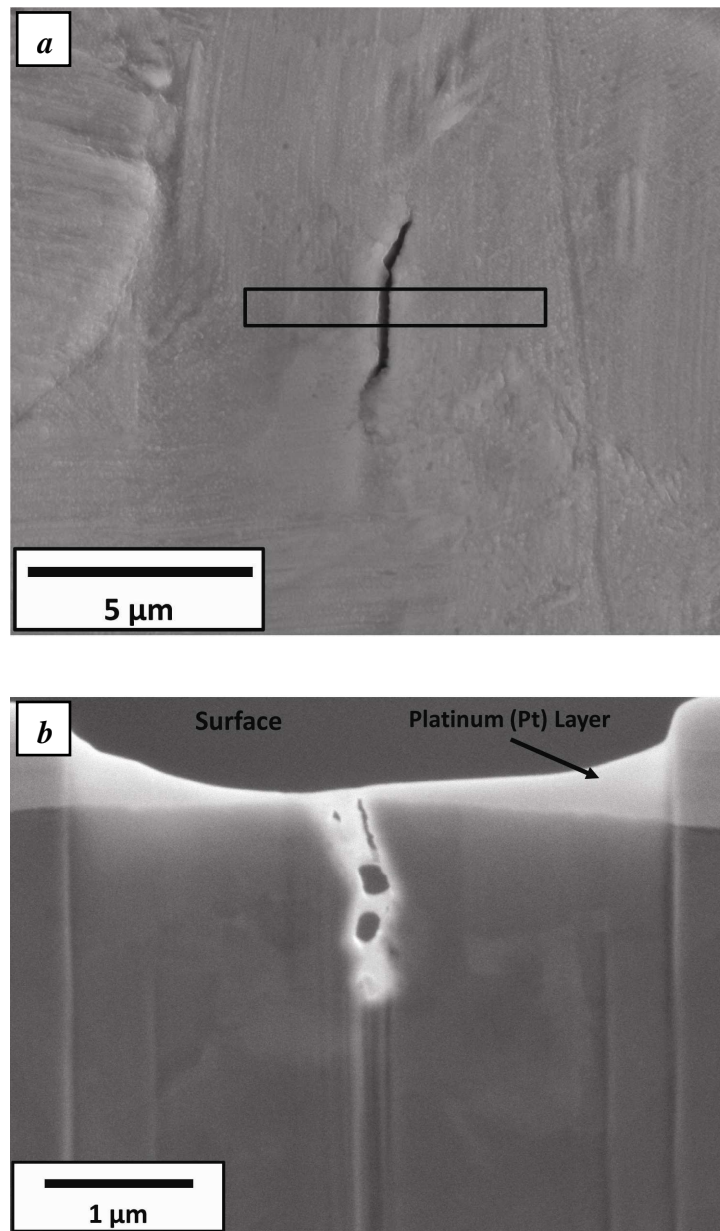


Figure 4- 59: a) The position selected to extract TEM sample from the surface of run-out fine machined-1 sample of AISI 304L (fatigued at 336 MPa); b) Final shape of TEM sample fixed on TEM grid after thinning using FIB (white layer is Platinum (Pt)).



Some materials were observed inside the crack. So, the Energy Dispersive X-Ray (EDX) analysis was carried out to identify these materials, at the bottom of the crack (b), surface layer (a) and at the matrix (c) as shown in Figure 4- 61-a. The EDX analysis indicates that this material is Platinum (Pt) as result of FIB preparation (Figure 4- 61-c and d). A Cu peak can be seen in the spectrums. The Cu peak may be detected from the Copper (Cu) ring used to fix the sample on the TEM holder.

Figure 4- 60 shows the deformed microstructure at the surface of the cross-section of the direct or near surface regions of run-out electropolished specimen of AISI 304L (fatigued at 336 MPa) including the short crack. The crack length is approximately 2  $\mu\text{m}$ . An inhomogeneous dislocation arrangement of high density near the surface and around the crack (dark regions around the crack tip) can be seen.

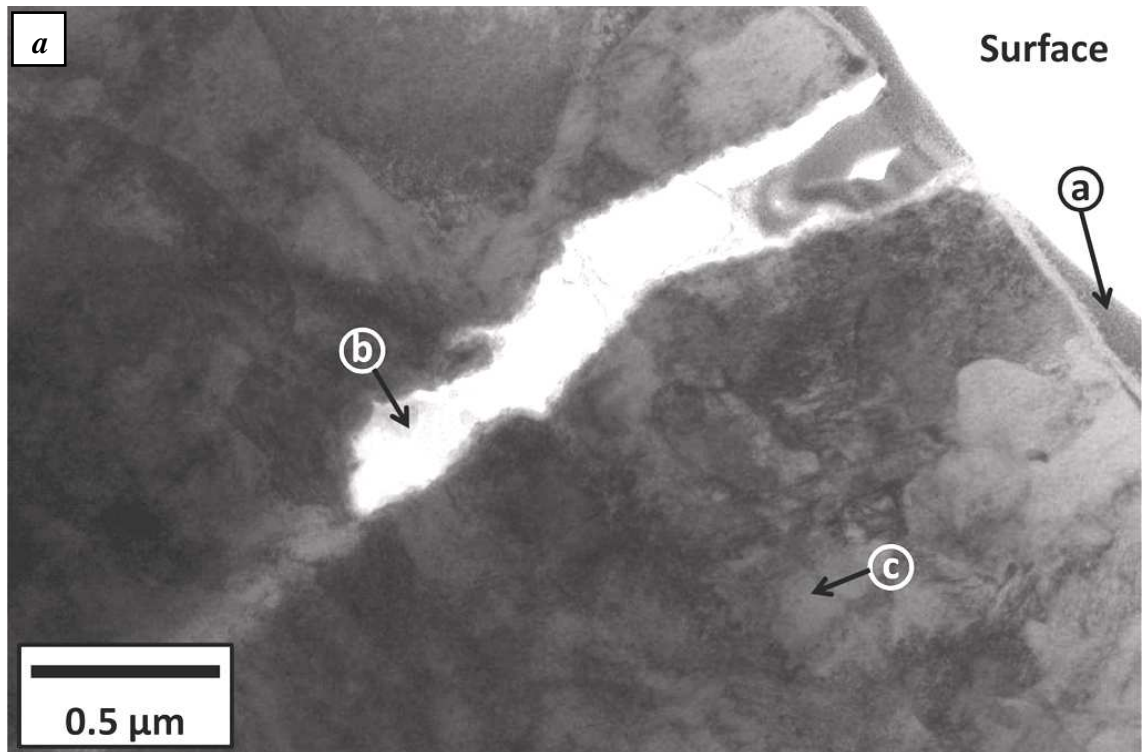


Figure 4- 60: A bright field image near the surface, illustrating the deformed microstructure and fatigue crack of run-out electropolished specimen of AISI 304L (fatigued at 336 MPa). a,b,c represent Pt layer on the surface of the sample, the material filled the crack (bottom of the crack), the matrix, respectively.

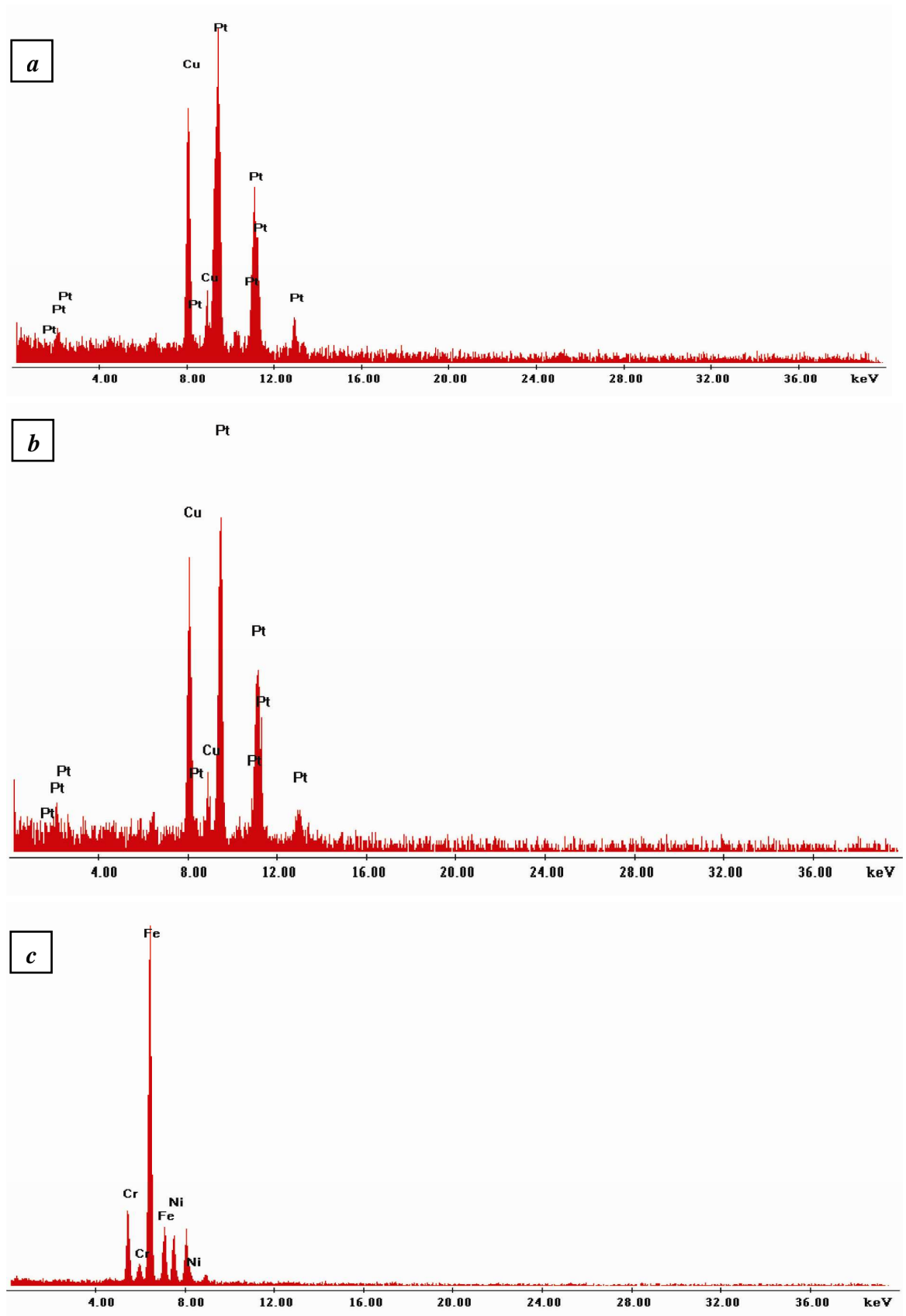


Figure 4- 61: a) EDX analysis of Pt layer on the surface, b) EDX analysis of the material filled the crack (bottom of the crack), c) EDX analysis of the matrix.

Figure 4- 62 shows a TEM observation around the crack tip. The corresponding selected-area electron diffraction (SAED) pattern ‘(b)’ indicated that both martensite and austenite are detected in this region. Figure 4- 62-c shows the corresponding indexed diagram of austenite at zone axis of [011]. To index the martensite spots the distance (r) between the direct beam spot and a diffraction spot was measured. Based on the known information from the austenite spots the camera constant  $\lambda L$  can be calculated using equation (4-3). The d-spacing for  $(200)_\gamma$  in Figure 4- 62-b was obtained from the Powder Diffraction Standard (PDF) card for austenite and the distance (r) between the spot of  $(200)_\gamma$  to the beam spot was then measured. Using this camera constant and by measuring the distance between the interest spot and the beam spot, the d-spacing can be calculated using eq. (4-3) and matched it with the d-spacing for all possible planes in PDF card.

$$r_{hkl} = \frac{\lambda L}{d_{hkl}} \quad (4-3)$$

The dark field images (Figure 4- 62-d and e) are obtained from the diffraction spots of martensite and the austenite unit cells, respectively, as indicated in the SAED pattern (b). Spot  $(1\bar{1}1)_\gamma$  was used to obtain the dark field image (d) and spot  $(110)_\alpha$  to obtain (e).

Figure 4- 62-d shows that the crack tip interacts with the edge of martensite packet (white area).

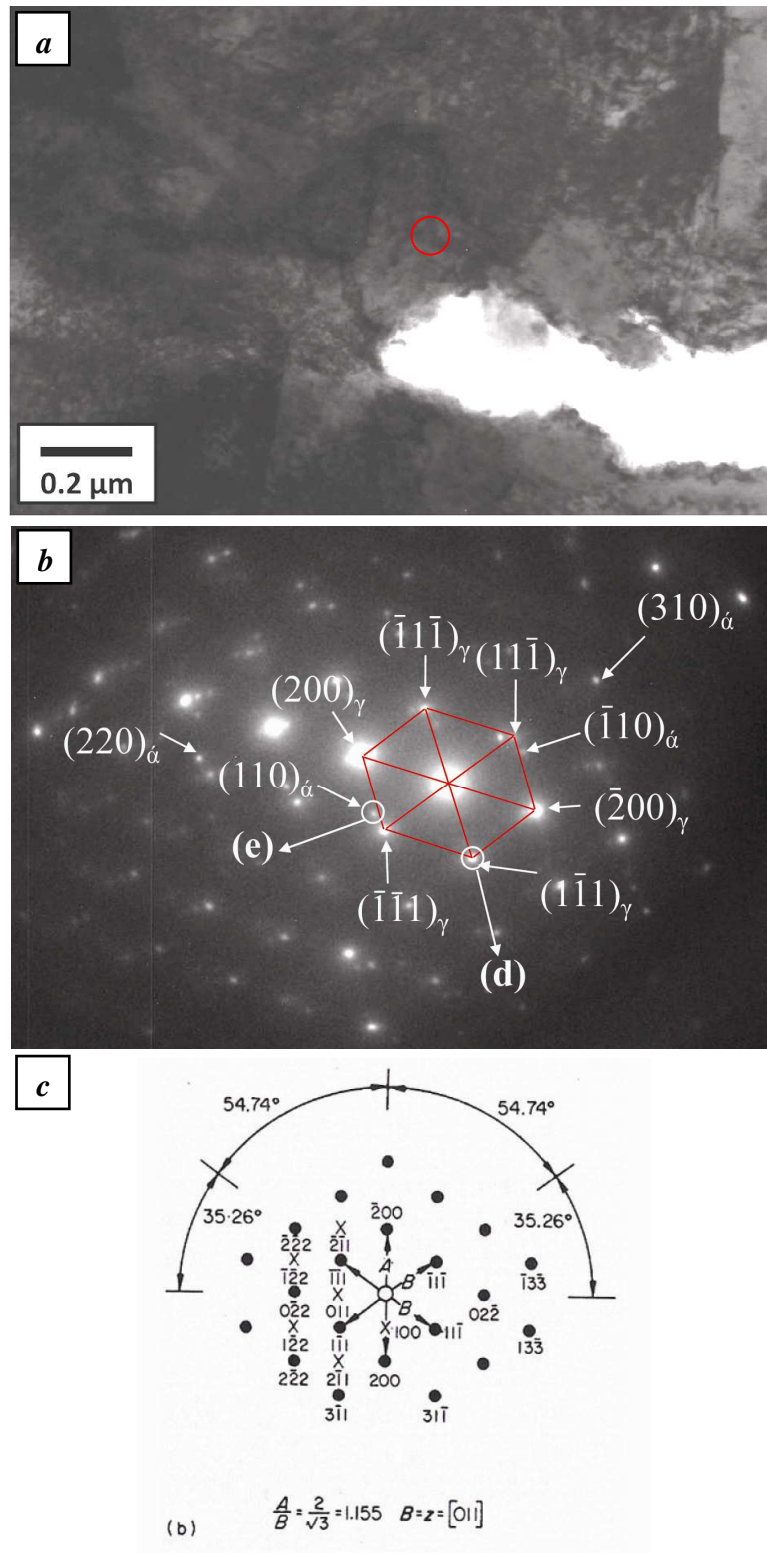


Figure 4-62: (a), (b) and (c), see the caption in next page.

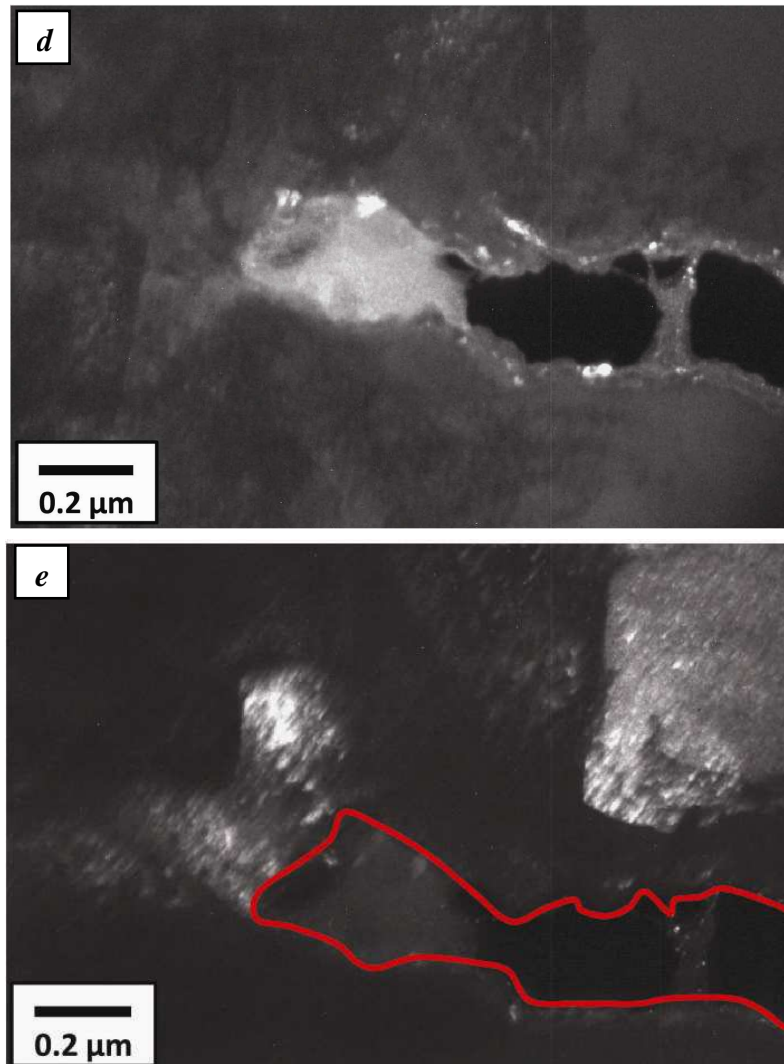


Figure 4- 62: The cross-sectional TEM observations of run-out electropolished specimen of AISI 304 (fatigued at 336 MPa), a) bright field, b) SAED patterns, C) Indexed diagram for FCC crystal structure and (d and e) dark field images.

# Chapter 5

## Discussion

### 5.1. Materials and Microstructures

The chemical composition of both materials, as shown in Table 4- 1, shows agreement with the corresponding standard specifications.

Table 4- 3 compares values of  $M_s$ ,  $M_d$  for AISI 304L with AISI 316L. Both can describe the tendency for martensite formation in the two materials. Both values for  $M_s$  are in the sub-zero scale.  $M_d$  values, the temperature at which 50% of austenite is transformed to martensite with 30% of deformation, suggest that the formation of martensite at room temperature for AISI 304L is expected.

Steels that present higher values of  $M_d$ , for example AISI 304L, are more susceptible to form induced martensite when deformed at room temperature. Steels like AISI 316L, that present low values for temperature  $M_d$ , generally do not present strong martensite formation when deformed at room temperature[14].

The microstructures are typical of austenitic stainless steel. The microstructure consists of equiaxed austenite grains and annealing twins. The presence of slip bands in both materials can be seen in Figure 4- 1 (a and c). The slip bands are therefore related to either introduced or remaining plastic strain resulting from pre-cold working.

**Summary:** The two stainless steel materials used in this project are representative for commercial-grade AISI 304L and AISI 316L stainless steels. The metallographic investigation and the mechanical property showed the presence of the slip bands which may resulting from pre-cold working.

### 5.2. Selection of Machining Parameters

These results for the surface stresses are in good agreement with those predicted by the response surface [90]. In AISI 304L, the rough machined-A surface has significant tensile residual stress ( $261 \pm 60$  MPa) in comparison to the fine machined-C surface ( $14 \pm 35$  MPa). The expected surface stresses, predicted using the response surface for these machining conditions were 280 MPa and 0 MPa, respectively. A similar pattern emerges in AISI 316L, where the rough machined-A surface has tensile residual stress ( $302 \pm 95$  MPa) in comparison to the essentially stress-free fine machined-C surface ( $8 \pm 47$  MPa). The predicted surface stresses, using the response surface for these machining conditions were 280 MPa and 0 MPa, respectively.

The measurements demonstrate that the response surface is a quite robust tool for estimating the effects of machining on the surface residual stress.

### 5.3. Observed Fatigue Limit and Surface Residual Stress

The results of observed fatigue limits (Table 4- 8) for both materials show that the range of surface roughness developed by machining has no significant effect on fatigue limits.

The fatigue data obtained from three type 304 austenitic stainless steels with different microstructures (i.e. this work and [36]) are shown in Figure 5- 1-a, as a function of the surface residual stress. In Figure 5- 1-b, the same data are shown in terms of the difference from the intrinsic fatigue limit, which is measured relative to the electropolished samples. The fine grain size microstructure had a grain size of  $\sim 8\mu\text{m}$  and a bulk hardness in the annealed, electropolished condition of 275 Hv; the coarse grain size microstructure had a grain size of  $\sim 40\mu\text{m}$  and a bulk hardness of 200 Hv. The hardness of these alloys in the electropolished and annealed conditions differ, and this has a significant effect in their relative fatigue limits. These data show that the surface residual stress in type 304 is a dominant factor in determining the effects of machining on the fatigue limit, for microstructures that had intrinsic fatigue limits between approximately 300 MPa and 385 MPa. The fatigue limit of the type 316 shows much less sensitivity to the surface stress.

The surface residual stress is found to be the dominant factor controlling this reduction in fatigue resistance, with no measurable effects of surface roughness nor surface cold work.

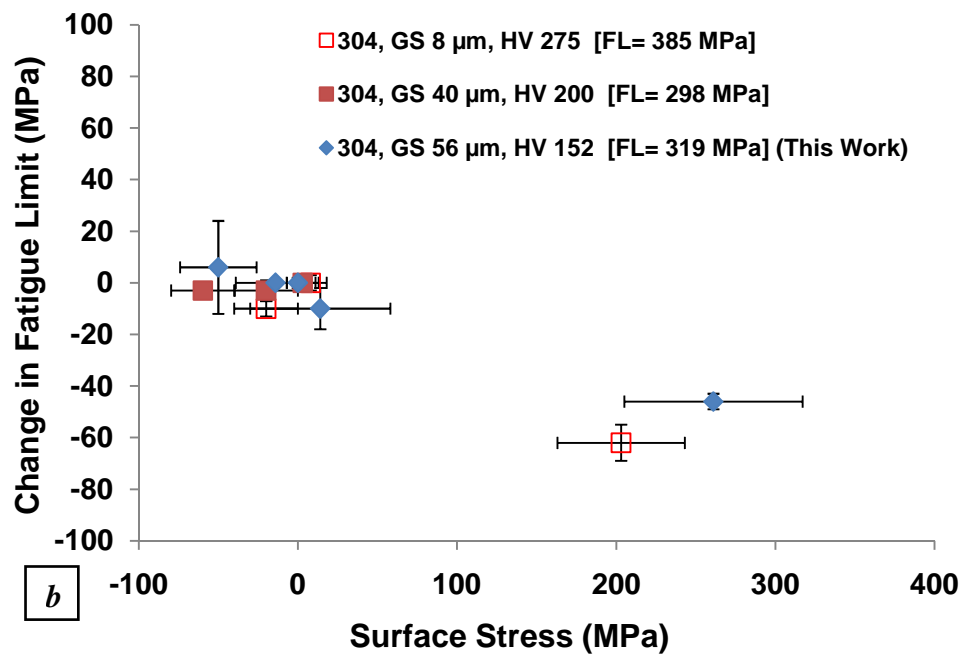
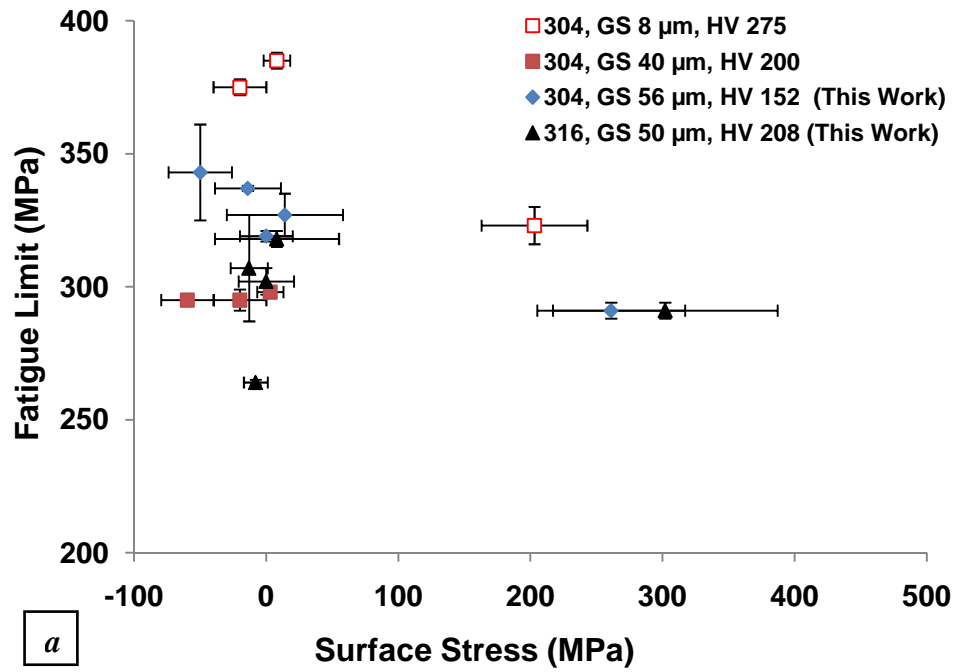


Figure 5-1: (a) and (b), see the caption in next page.



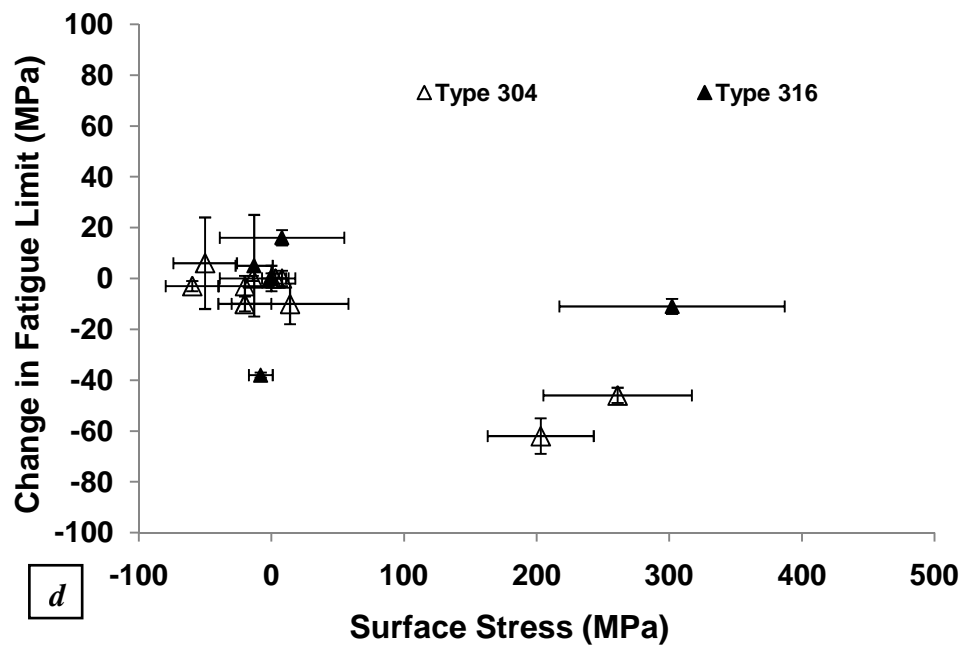
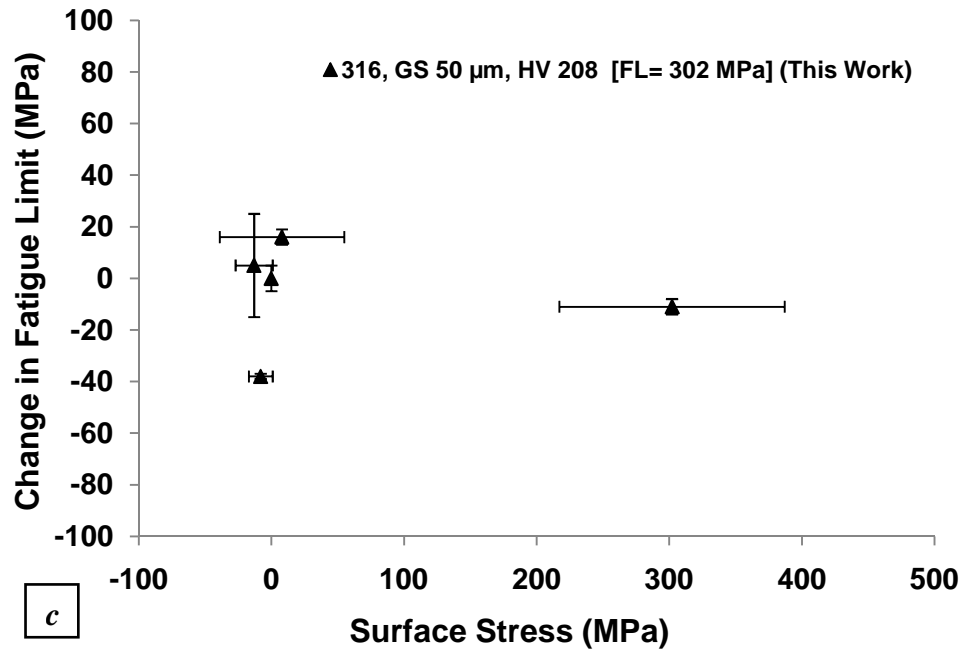


Figure 5- 1: The effect of surface residual stress on the fatigue limit , a) measured fatigue limit as a function of the surface residual stress; b) change in fatigue limit relative to the intrinsic fatigue limit for electropolished samples (type 304); c) change in fatigue limit relative to the intrinsic fatigue limit for electropolished samples (type 316); d) change in fatigue limit relative to the intrinsic fatigue limit for electropolished samples (type 304/type 316). Gs: Grain Size; Hv: Hardness; FL: Fatigue Limit of electropolished and annealed.

**Summary:**

- ❖ The data show that the surface residual stress is the most significant parameter that determines the effects of surface preparation on the fatigue limit of type 304 austenitic stainless steel.
- ❖ The fatigue limit of the type 316 shows much less sensitivity to the surface stress.
- ❖ The range of surface roughness developed by machining has no significant effect.

**5.4. Near Surface and Microstructure of AISI 304L**

Figure 4- 25-a shows typical observations for fine-C non-fatigued specimens. It shows that there is very little observable plastic strain in this sample, evident only as slip bands that penetrate a depth of approximately 40  $\mu\text{m}$ . The rough machined-A specimens (non-fatigued) show a greater degree of plastic strain close to the surface, but this also extends to comparable depth below the surface as shown in Figure 4- 26-a.

The electropolished samples show the effect of fatigue testing on the intrinsic microstructure. It can show a small degree of plastic strain after fatigue close to the surface which penetrates a depth of approximately 10  $\mu\text{m}$  as demonstrated in Figure 4- 27-c.

Fatigue at stresses close to the fatigue endurance limit (run-out samples) in austenitic stainless steels causes the development of a plastically strained microstructure by increasing the density of slip bands, but with no significant increase in depth. This is apparent from the small, but observable, effect of fatigue on the diffraction peak width in Figure 4- 37-b and Figure 4- 38-b for fine-C and rough-A machined samples respectively. There is no consistency in the depths at which the effects are observed using X-ray diffraction and EBSD. X-ray diffraction showed that the plastic strain extended from the surface to the bulk with greater depth (in the range of 150 to 200  $\mu\text{m}$ ). This could be attributed to a lower sensitivity of EBSD to plastic strain compared to X-ray diffraction.

It can be found from the X-ray diffraction (XRD) profiles of Figure 4- 43 to Figure 4- 47 for AISI 304L that the machined samples have austenite phase, while the as-fatigued surfaces are composed of the austenite phase and the bcc phase. Clearly, martensite

transformation took place in the surface layer during fatigue testing and this can be confirmed by the presence of martensite in electropolished sample after fatigue. None was observed before fatigue.

TEM confirmed that both martensite and austenite are detected in electropolished (3) samples (Figure 4- 62-e). The present findings are consistent with other work [36] which found that martensite can be formed in the near surface region after machining and also after fatigue in type 304 austenitic stainless steels.

TEM observations of run-out fine machined (1) show that the surface region is nanocrystalline. These findings are consistent with those observations of the effects of deep rolling and shot peening on the near surface microstructure in the type 304 austenitic stainless steel [37].

TEM and X-ray diffraction (XRD) findings show the formation of strain induced martensite with fatigue cycling in AISI 304L. Also, the deformed microstructure of this material contained coherent twins, as shown by EBSD. These twins can be seen in Figure 4- 52 and Figure 4- 53 for electropolished (3) and rough machined (4) samples. Their misorientation profile shows that they are twins.

### **5.5. Surface Cracks and Fracture Surface in AISI 304L**

A few surface cracks can be seen on the surface of all conditions in run-out specimens. Examples are shown in Figure 4- 19 for AISI 304L. In electropolished run-out specimen (tested at 336 MPa), the microcracks were found along slip bands as shown in Figure 4- 19-a. These were inclined at approximately  $45^\circ$  to the stress axis. In fine machined (1) and rough machined (4) run-out specimens, the surface cracks were found to be in the root of the machining marks and perpendicular to the stress axis as depicted in Figure 4- 19-b&c. From the fractographs in Figure 4- 21-a, it is seen that the crack initiated at the surface and propagated inward, leaving a distinct region of crack propagation (radial marks).

The white arrows indicate the direction of crack propagation. The crack initiation site (origin) and the area where the crack started to propagate along the matrix can be identified by the convergence of the radial marks. They point back to the location of the original fatigue crack. In all fractured specimens, the fracture process was dominated by the propagation of a single crack.

At higher magnifications, striations were observed in the fatigue fracture region, while the overload region showed dimple-type of fracture (Figure 4- 21-c). It can be seen that, the fatigue cracks preferentially initiated at the root of machining marks as shown in Figure 4- 21e.

In broken electropolished specimen (336 MPa), the origin zone (Figure 4- 22-d) shows the plastic deformation and formation of slip bands at the crack initiation site. This can be seen as well in Figure 4- 19-a at the surface of electropolished run-out specimen.

### **5.6. Near Surface and Microstructure of AISI 316L**

Fine machined -C non-fatigued specimens in Figure 4- 30 a show that there is very little observable plastic strain as slip bands that penetrate a depth of approximately 30  $\mu\text{m}$ . Run-out fine machined (1) samples show that fatigue to run-out appeared to cause a slight increase in the density of slip bands as shown in Figure 4- 30-c. The rough machined-A specimens (non-fatigued) show a greater degree of plastic strain close to the surface, but this also extends to similar depth below the surface (Figure 4- 31-c)

The electropolished samples show the effect of fatigue testing in the absence of the prior effect of machining. These samples demonstrate a small degree of plastic strain after fatigue close to the surface, which penetrates to a depth of approximately 40  $\mu\text{m}$  (Figure 4- 32-c)

Plastically strained microstructure developed in austenitic stainless steels. This is shown by the slight increase in the density of slip bands as a result of fatigue at the high stresses close to the fatigue endurance limit (run-out samples). This can be seen from the small, but observable, effect of fatigue on the diffraction peak width in Figure 4- 39-b and Figure 4- 40-b for fine machined -C and rough machined-A samples respectively. The plastic strain extended from the surface to the bulk with greater depth, in the range of 150 to 200  $\mu\text{m}$ .

As shown in Figure 4- 49 to Figure 4- 51, x-ray diffraction (XRD) profiles show all samples before and after fatigue test consist of austenite peaks and no bcc peaks were observed.

EBSA showed that coherent twins can be observed in this microstructure. Coherent twins can be seen in run-out electropolished (3) specimen fatigued at 306 MPa as shown in Figure 4- 56.

### 5.7. *Surface Cracks and Fracture Surface in AISI 316L*

All conditions show few surface cracks on the surface of in run-out specimens. An example is shown in Figure 4- 20. This electropolished (3) run-out specimen (tested at 304 MPa) demonstrates microcracks along slip bands, as shown in Figure 4- 20-a. These were inclined at approximately 45° to the stress axis.

Fracture surfaces of this material (Figure 4- 23 to Figure 4- 24) show that the crack initiated at the surface and propagated inward, leaving a distinct region of crack propagation (radial marks).

The white arrows indicate the direction of crack propagation. The crack initiation site (origin) and the area where the crack started to propagate along the matrix can be identified by the convergence of the radial marks. They point back to the location of the original fatigue crack. In all fractured specimens, the fracture process was dominated by the propagation of a single crack.

At higher magnifications, striations were observed in the fatigue fracture region, while the overload region showed dimple-type of fracture.

In broken electropolished (3) specimen (298 MPa), the origin zone (Figure 4- 24-d) shows the plastic deformation and formation of slip bands at the crack initiation site.

#### **Summary:**

- ❖ The surface cracks were found to be in the root of the machining marks and perpendicular to the stress axis.
- ❖ TEM, X-ray diffraction (XRD) and EBSD findings show the formation of strain induced martensite with fatigue cycling in AISI 304L and none observed in AISI 316L.
- ❖ The fracture process in all fractured specimens; was dominated by the propagation of a single crack.
- ❖ Identical features of fracture surfaces were found for both materials.

### 5.8. Analysis of the crack path

To use an argument based on the Schmid factor to explain the change in crack direction and why the cracks arrest at twins, the Schmid factor of all of the slip systems should be calculated for the matrix and the twins.

The orientation of each single point on the sample surface is described in three Euler angles ( $\phi_1$ ,  $\Phi$ ,  $\phi_2$ ) obtained from EBSD measurement. The Euler angles can be transformed into a  $3 \times 3$  orientation matrix which links the components of a vector measured in the crystal coordinate system (e.g., the  $[100]/[010]/[001]$  system in a cubic structure) with the components of the vector described in the sample coordinate system (e.g., the Cartesian coordinate system, X-Y-Z, with X aligned with the loading axis) [121].

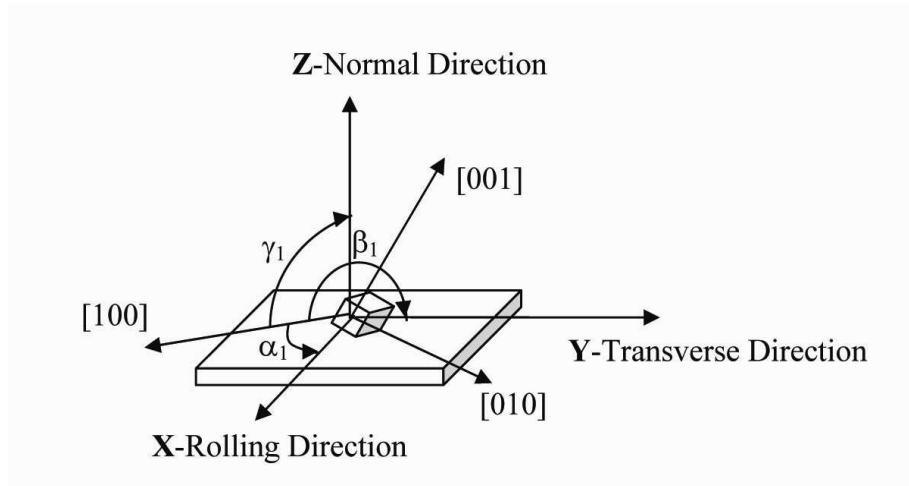


Figure 5- 2: Relationship between the specimen coordinate system XYZ (or RD, TD, ND for a rolled product) and the crystal coordinate system  $[100]$ ,  $[010]$ ,  $[001]$  [121].

Once the specimen and crystal coordinate systems are specified as in Figure 5- 2, we have,

$$C_c = g C_s \quad (5-1)$$

where  $C_c$  and  $C_s$  are the crystal and specimen coordinate systems respectively and  $g$  is the orientation matrix,

$$\begin{pmatrix} \cos\alpha_1 & \cos\beta_1 & \cos\gamma_1 \\ \cos\alpha_2 & \cos\beta_2 & \cos\gamma_2 \\ \cos\alpha_3 & \cos\beta_3 & \cos\gamma_3 \end{pmatrix} = \begin{pmatrix} g_{11} & g_{12} & g_{13} \\ g_{21} & g_{22} & g_{23} \\ g_{31} & g_{32} & g_{33} \end{pmatrix} \quad (5-2)$$

The first row of the matrix is given by the cosines of the angles between the first crystal axis,  $[100]$  and three specimen axes X, Y and Z in turn. These three angles,  $\alpha_1$ ,  $\beta_1$ ,  $\gamma_1$ ,

are labelled on Figure 5- 2. The other two rows are related to the other two crystal axis and can be calculated similarly. The elements of the orientation matrix in terms of the Euler angles are given by

$$\begin{aligned}
 g_{11} &= \cos \varphi_1 \cos \varphi_2 - \sin \varphi_1 \sin \varphi_2 \cos \Phi \\
 g_{12} &= \sin \varphi_1 \cos \varphi_2 + \cos \varphi_1 \sin \varphi_2 \cos \Phi \\
 g_{13} &= \sin \varphi_2 \sin \Phi \\
 g_{21} &= -\cos \varphi_1 \sin \varphi_2 - \sin \varphi_1 \cos \varphi_2 \cos \Phi \\
 g_{22} &= -\sin \varphi_1 \sin \varphi_2 + \cos \varphi_1 \cos \varphi_2 \cos \Phi \\
 g_{23} &= \cos \varphi_2 \sin \Phi \\
 g_{31} &= \sin \varphi_1 \sin \Phi \\
 g_{32} &= -\cos \varphi_1 \sin \Phi \\
 g_{33} &= \cos \Phi
 \end{aligned} \tag{5-3}$$

These nine elements of the orientation matrix can be directly calculated from the raw data that are collected by electron backscattered diffraction (EBSD).

#### **5.8.1. The Crack Path in AISI 304L**

From Figure 5- 3 the crack changed its direction as it met the twin. To achieve the active slip planes, the Schmid factor for all 12 systems in both grain (G1) and twin (T) were calculated and shown in Table 5- 2 and Table 5- 3 respectively.

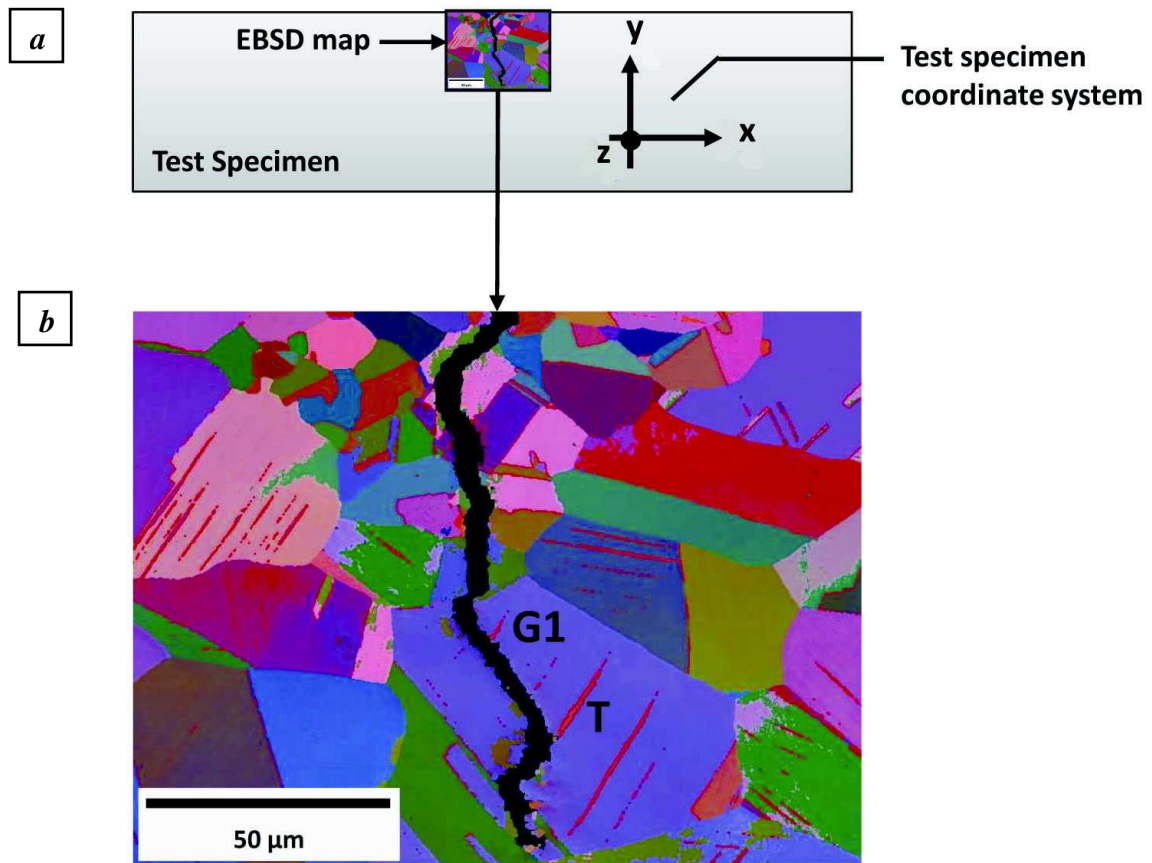


Figure 5- 3: a) Test sample section showing the region of the EBSD map; b) the corresponding map showing the interaction between the crack and the twin (T) in grain (G1).

EBSD was performed in the area around the crack using SEM XL30 from which the data was analysed using V-map software [122]. The information obtained was stored in the form of Euler angles, and unit orientation vectors given with respect to the coordinate system shown in Figure 5- 2. The orientation data are given for grain 1 and the twin in Table 5- 1.

Table 5- 1: Orientation data for grain (G1) and the twin (T).

Grain	$\varphi_1$	$\Phi$	$\varphi_2$	$g_{11}$	$g_{12}$	$g_{13}$	$g_{21}$	$g_{22}$	$g_{23}$	$g_{31}$	$g_{32}$	$g_{33}$
Grain 1	173.11	36.2	77.71	-0.757	-0.288	0.586	-0.306	0.949	0.071	0.577	0.126	0.807
Twin	274.55	31.32	20.8	-0.908	0.417	-0.041	0.376	0.768	-0.518	0.185	0.486	0.854
				y			x			z		
				Loading axis						Surface normal		

The orientation matrix for each grain that maps a vector in the test sample coordinate system, shown in Figure 5- 2, to that in the crystal system can be obtained from the orientation vectors in Table 5- 1 as follows:



Assuming purely bending in the test sample, simply for the purposes of determining Schmid factors, the loading direction,  $L = (010)$  is axial and the twelve Schmid factors for each grain may be determined from Equation 5-4:

$$s^\alpha = (gl \cdot n^\alpha)(gl \cdot s^\alpha) \quad (5-4)$$

where  $n^\alpha$  and  $s^\alpha$  are the fcc unit normal to the slip planes,  $\{111\}$  in fcc crystals, and unit slip directions along  $\langle 110 \rangle$  respectively, in which  $\alpha = 1, \dots, 12$ .

Table 5- 2: The Schmid factors of all possible slip planes in grain-1. (highlighted row represent the slip system with highest Schmid factor).

System	(hkl)	[uvw]	$\phi$	$\lambda$	Schmid Factor	ABS* (Schmid)
1	(111)	$[\bar{1}10]$	65.7	27.5	0.37	0.37
2	( $\bar{1}11$ )	[101]	40	99.6	-0.13	0.13
3	( $1\bar{1}1$ )	$[10\bar{1}]$	133.1	105.5	0.18	0.18
4	( $\bar{1}\bar{1}1$ )	[101]	109.3	95.8	0.03	0.03
5	(111)	$[\bar{1}01]$	65.7	74.5	0.11	0.11
6	( $\bar{1}11$ )	$[0\bar{1}1]$	40.1	128.4	-0.48	0.48
7	( $1\bar{1}1$ )	[110]	133.1	62.9	-0.31	0.31
8	( $\bar{1}\bar{1}1$ )	[011]	109.3	43.9	-0.24	0.24
9	(111)	$[0\bar{1}1]$	65.7	128.5	-0.26	0.26
10	( $\bar{1}11$ )	[110]	40.1	62.9	0.35	0.35
11	( $1\bar{1}1$ )	[011]	133.1	43.9	-0.42	0.42
12	( $\bar{1}\bar{1}1$ )	$[1\bar{1}0]$	109.3	152.5	0.29	0.29

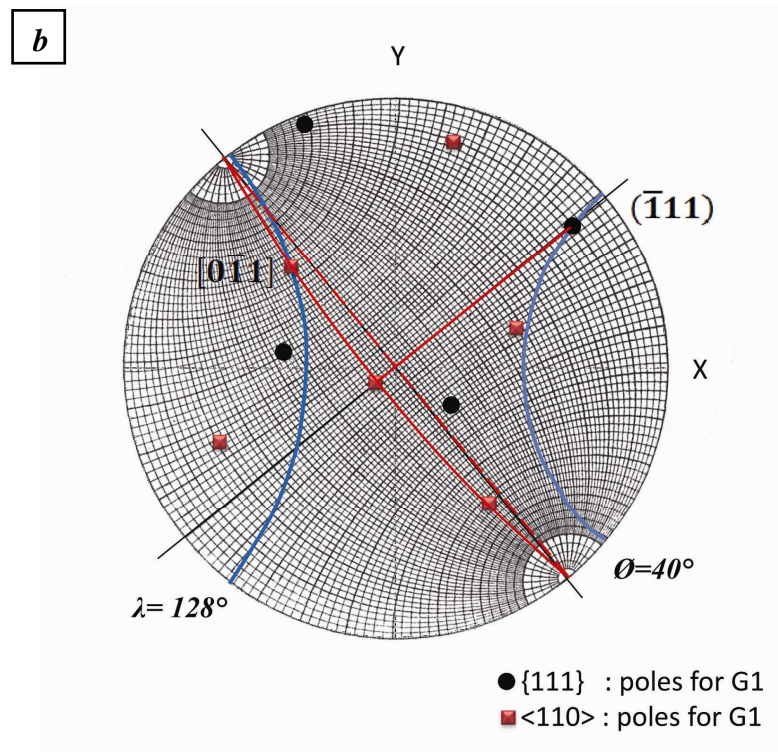
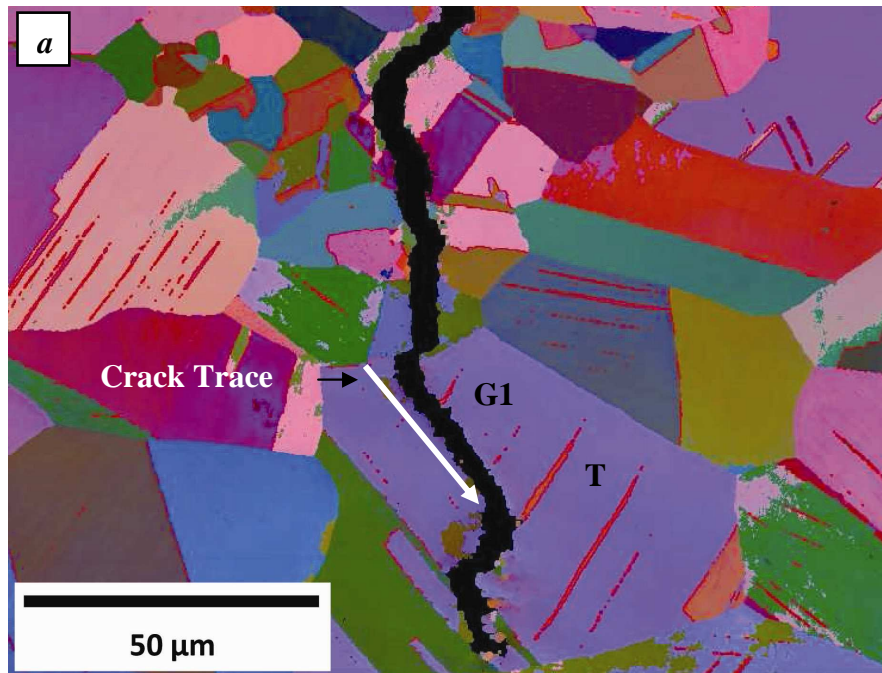
\* Absolute value.

Table 5- 3: The Schmid factors of all possible slip planes in the twin. (highlighted row represent the slip system with highest Schmid factor).

System	(hkl)	[uvw]	$\phi$	$\lambda$	Schmid Factor	ABS* (Schmid)
1	(111)	$[\bar{1}10]$	113.5	102.1	0.08	0.08
2	( $\bar{1}11$ )	[101]	83.3	87.8	0	0
3	( $1\bar{1}1$ )	$[10\bar{1}]$	62.6	132.1	-0.31	0.31
4	( $\bar{1}\bar{1}1$ )	[101]	12.7	87.8	0.04	0.04
5	(111)	$[\bar{1}01]$	113.5	47.9	-0.27	0.27
6	( $\bar{1}11$ )	$[0\bar{1}1]$	83.3	28.4	0.10	0.10
7	( $1\bar{1}1$ )	[110]	62.6	147.3	-0.39	0.39
8	( $\bar{1}\bar{1}1$ )	[011]	12.7	99.9	-0.17	0.17
9	(111)	$[0\bar{1}1]$	113.5	28.4	-0.35	0.35
10	( $\bar{1}11$ )	[110]	83.3	147.3	-0.01	0.01
11	( $1\bar{1}1$ )	[011]	62.6	99.9	-0.08	0.08
12	( $\bar{1}\bar{1}1$ )	$[1\bar{1}0]$	12.7	77.9	0.21	0.21

\* Absolute value.

According to the analysis based on the calculated results in Table 5- 2 and Table 5- 3, slip systems of  $(\bar{1}11)/[0\bar{1}1]$  and  $(1\bar{1}1)/[110]$  should operate most readily in grain (G1) and the twin (T), respectively.



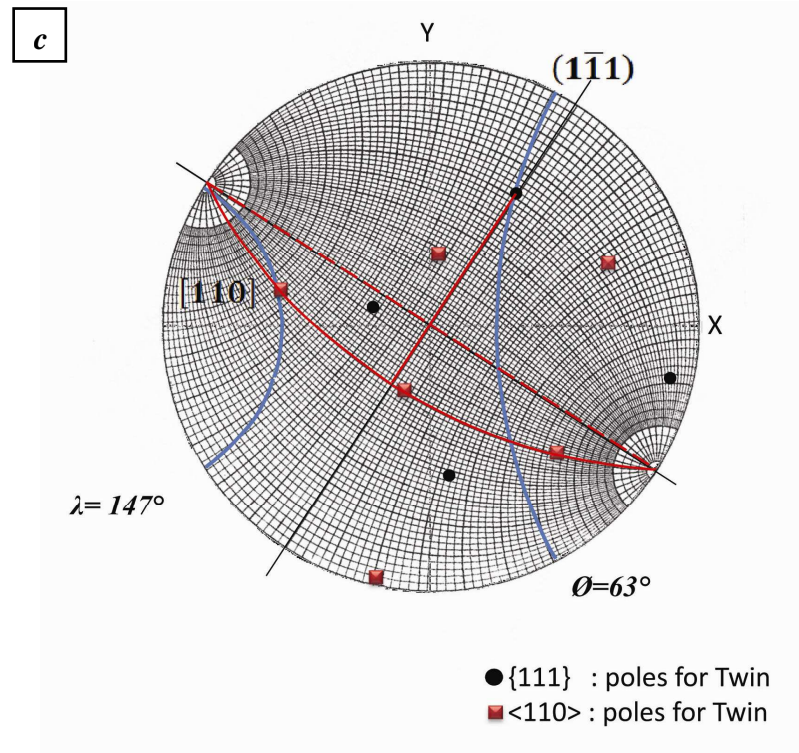


Figure 5- 4: a) the corresponding map showing the interaction between the crack and the twin, b) stereographic projection  $\{111\}$  pole figure for grain surrounding the arrested crack with the plane system of the highest Schmid factor trace, c) stereographic projection  $\{111\}$  pole figure for the twin with the plane system of the highest Schmid factor trace.

As shown in Figure 5- 4, the highest Schmid factor planes from Table 5- 2 and Table 5- 3 are presented on pole figure (represented by  $\emptyset$ ,  $\lambda$  using (blue lines) Wulff net). Where  $\emptyset$ ,  $\lambda$  are angle between the stress axis and the normal to the slip plane and angle between the stress axis and the slip direction, respectively.  $\{111\}$  and  $\{110\}$  pole figures for grain 1 and the twin were obtained using V-Map software. The solid black circles represent the pole figure of  $\{111\}$  and the red square represent pole figure  $\{110\}$ . As shown in the figures the Wulff net was used to measure the angle of 90 degrees to get the great circle (red circle in the figures) of the slip plane to match the highest Schmid factor.

It can be seen in Figure 5- 4-b, that the crack trace matches well with the calculated ones of the  $(\bar{1}11)/[0\bar{1}1]$  plane system in grain 1 in which the calculated Schmid factor was highest, indicating that this slip plane was likely to be the crack plane.

Figure 5- 4-c shows that no match between the crack trace and the calculated ones of the  $(1\bar{1}1)/[110]$  plane system in the twin. The crack does not propagate in the twin, but seems to continue propagation along the twin interface instead.

When there are two possible cracking planes in two adjacent grains (I and II), as shown in Figure 5- 5, the orientation relationship between the two cracking planes contains two components with respect to the crack propagation direction. One is the tilt component, as shown in Figure 5- 5(a), and the other is the twist component as in Figure 5- 5(b). The boundaries could have both components. In the case of Figure 5- 5(a), the crack easily propagates across the boundary. However, in the case of Figure 5- 5(b), crack propagation across the boundary is thought to be difficult. A propagating crack in grain I meets the cracking plane in grain II at one point, so a successive crack in grain II can be initiated at this point, or a crack in grain I goes around and propagates into grain II through another neighbouring grain having a low twist component [123]. The twist angle has a more profound influence on fracture resistance than the tilt angle as shown by Zhai et al in a study on fatigue crack propagation in the Al–Li alloy 8090 [53].

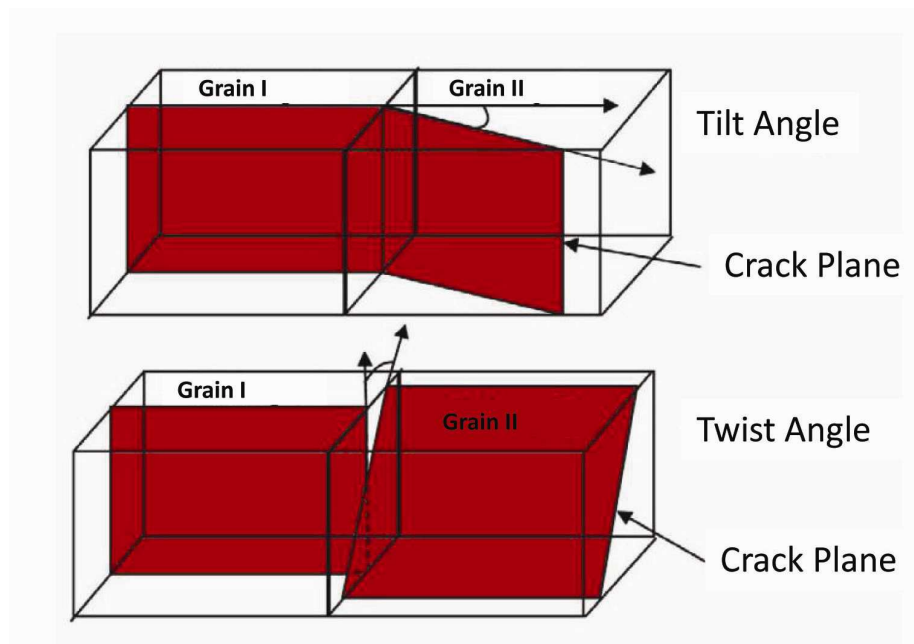


Figure 5- 5: Schematic describing the crack plane misorientation across a grain boundary in terms of the tilt angle (a), and the twist angle (b.) [123].





### 5.8.2. The Crack Path in AISI 316

Figure 5- 7 shows the crack is arrested by twins. To determine the active slip planes, the Schmid factor for all 12 systems in both matrix and twins were calculated and shown in Table 5- 5 and Table 5- 6, respectively.

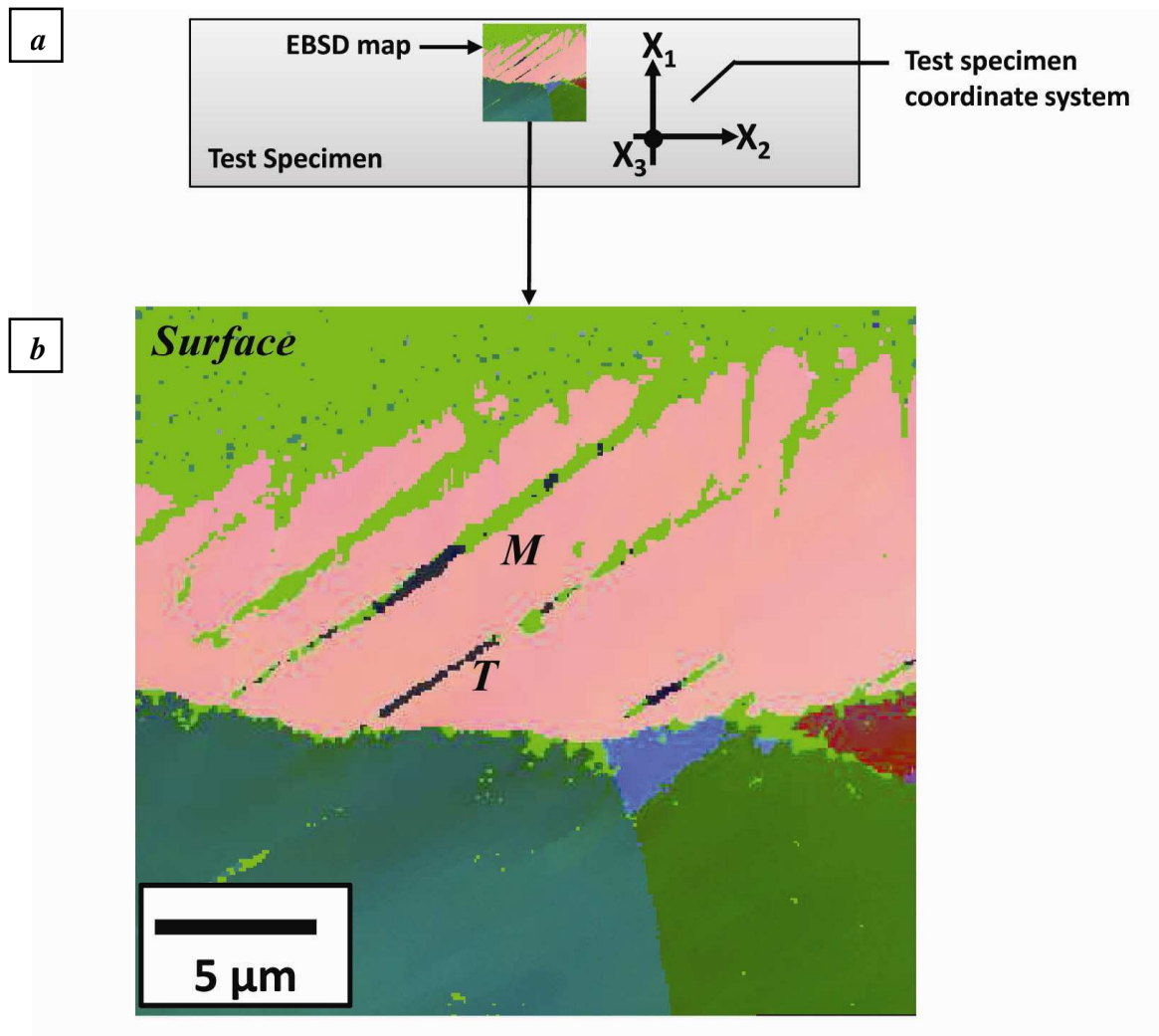


Figure 5- 7: a) Test sample section showing the region of the EBSD map; b) the corresponding map showing the interaction between the cracks and the twins.

Table 5- 4: Orientation data for the matrix and the twin.

Grain	$\varphi_1$	$\Phi$	$\varphi_2$	$g_{11}$	$g_{12}$	$g_{13}$	$g_{21}$	$g_{22}$	$g_{23}$	$g_{31}$	$g_{32}$	$g_{33}$
Grain 1	326.27	47.25	45.38	0.012	0.792	-0.611	0.852	-0.327	-0.408	0.523	0.516	0.679
Twin	51.12	14.04	19.18	0.935	0.319	-0.152	0.345	-0.92	0.189	0.08	0.229	0.97
				y			x			z		
							Loading axis			Surface normal		

Table 5- 5: The Schmid factors of all possible slip planes in the matrix. (highlighted row represent the slip system with highest Schmid factor).

System	(hkl)	[uvw]	$\phi$	$\lambda$	Schmid Factor	ABS* (Schmid)
1	(111)	$[\bar{1}10]$	89.3	143.4	- 0.01	0.01
2	( $\bar{1}11$ )	[101]	158.7	76.1	- 0.22	0.22
3	( $1\bar{1}1$ )	$[10\bar{1}]$	67.7	23.5	0.32	0.32
4	( $\bar{1}\bar{1}1$ )	[101]	124.4	67.7	- 0.22	0.22
5	(111)	$[\bar{1}01]$	89.3	156.5	- 0.01	0.01
6	( $\bar{1}11$ )	$[0\bar{1}1]$	158.8	96.5	0.11	0.11
7	( $1\bar{1}1$ )	[110]	67.7	69.3	0.13	0.13
8	( $\bar{1}\bar{1}1$ )	[011]	124.4	124.3	0.32	0.32
9	(111)	$[0\bar{1}1]$	89.3	96.5	0	0
10	( $\bar{1}11$ )	[110]	158.8	69.3	0.33	0.33
11	( $1\bar{1}1$ )	[011]	67.7	124.3	- 0.21	0.21
12	( $\bar{1}\bar{1}1$ )	$[\bar{1}\bar{1}0]$	124.4	36.6	- 0.32	0.32

\* Absolute value.

Table 5- 6: The Schmid factors of all possible slip planes in the twin. (highlighted row represent the slip system with highest Schmid factor).

System	(hkl)	[uvw]	$\phi$	$\lambda$	Schmid Factor	ABS* (Schmid)
1	(111)	$[\bar{1}10]$	102.7	153.4	0.19	0.19
2	( $\bar{1}11$ )	[101]	128.4	67.7	- 0.24	0.24
3	( $1\bar{1}1$ )	$[10\bar{1}]$	32.9	83.6	0.09	0.09
4	( $\bar{1}\bar{1}1$ )	[101]	63.9	67.7	0.17	0.17
5	(111)	$[\bar{1}01]$	102.7	96.4	0.02	0.02
6	( $\bar{1}11$ )	$[0\bar{1}1]$	128.4	38.5	- 0.49	0.49
7	( $1\bar{1}1$ )	[110]	32.9	113.8	- 0.34	0.34
8	( $\bar{1}\bar{1}1$ )	[011]	63.9	120.9	- 0.23	0.23
9	(111)	$[0\bar{1}1]$	102.7	38.5	- 0.17	0.17
10	( $\bar{1}11$ )	[110]	128.4	113.8	0.25	0.25
11	( $1\bar{1}1$ )	[011]	32.9	120.9	- 0.43	0.43
12	( $\bar{1}\bar{1}1$ )	$[\bar{1}\bar{1}0]$	63.9	26.6	0.39	0.39

\* Absolute value.

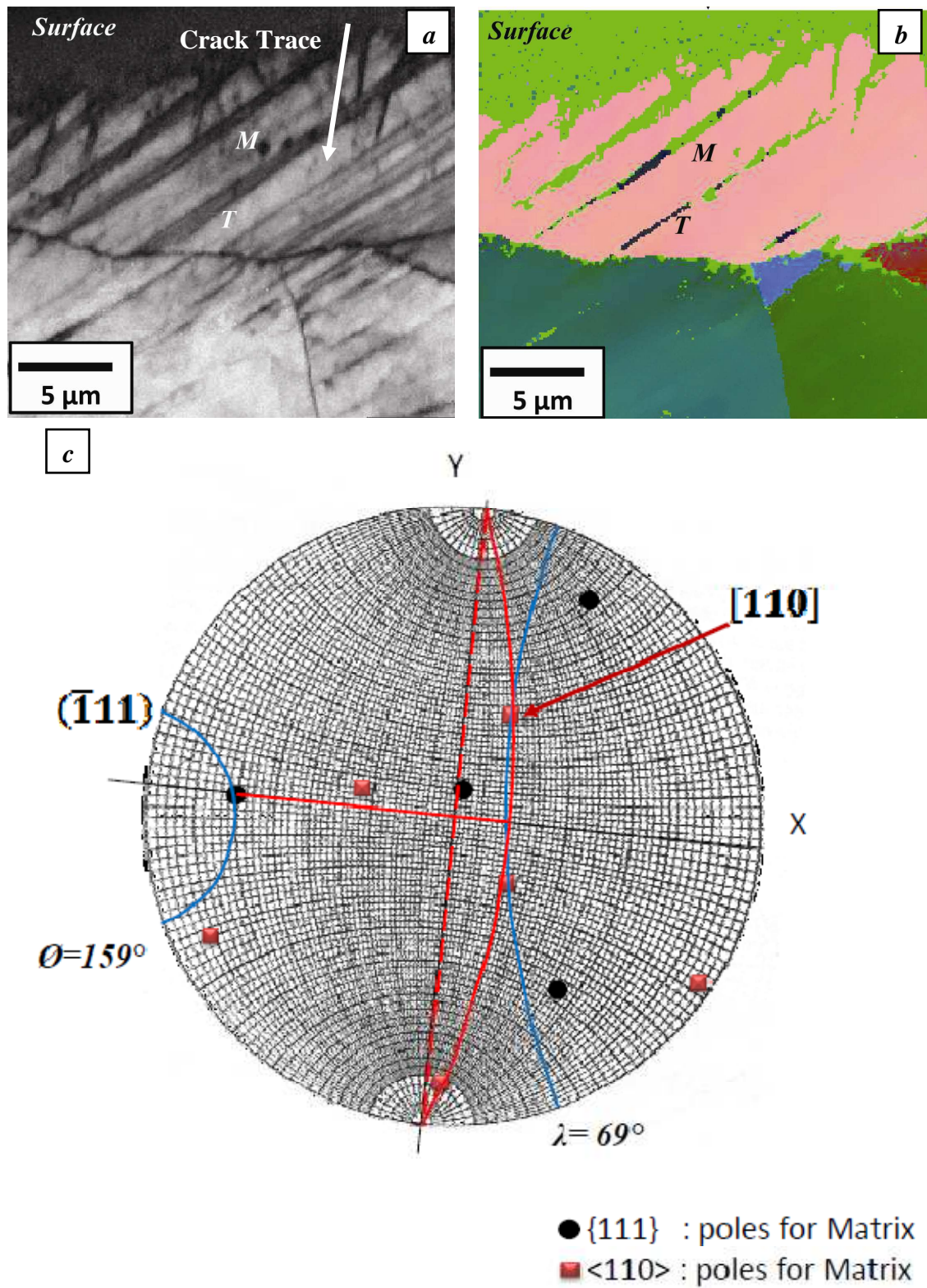


Figure 5-8: (a), (b) and (c), see the caption in next page.



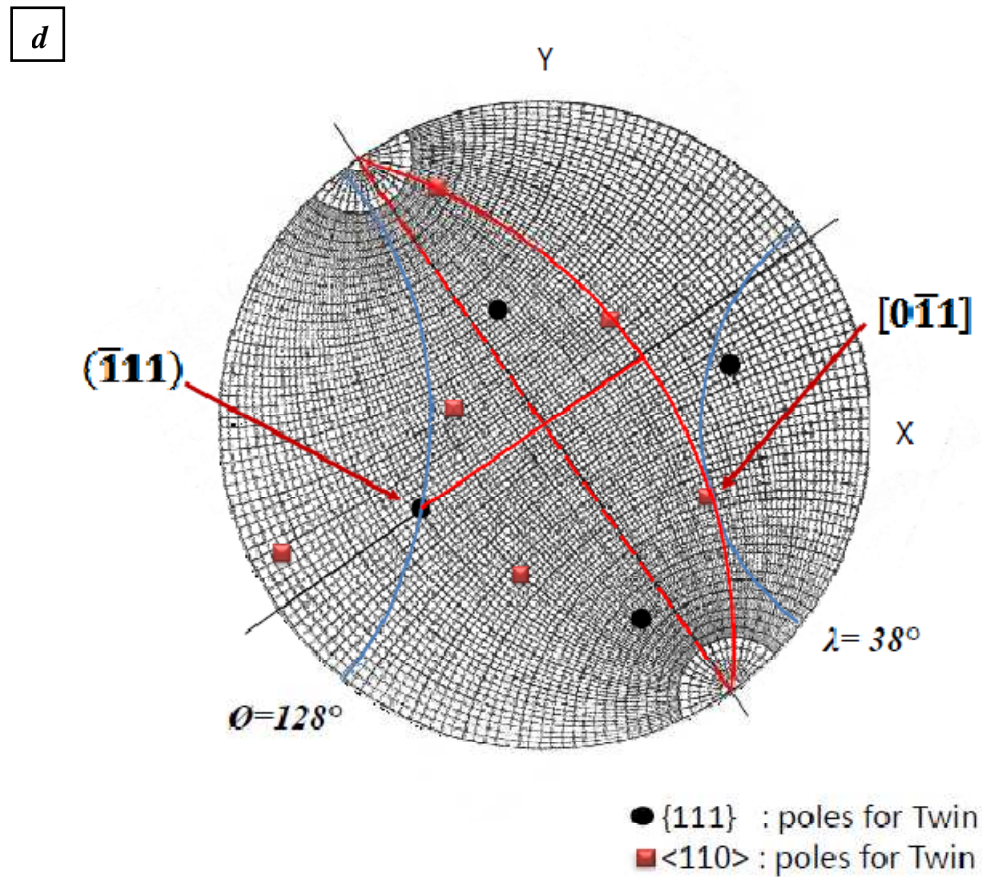


Figure 5- 8: a,b) the corresponding map showing the interaction between the crack and the twin, c) stereographic projection {111} pole figure for grain surrounding the arrested crack with the plane system of the highest Schmid factor trace, d) stereographic projection {111} pole figure for the twin with the plane system of the highest Schmid factor trace.

As shown in Figure 5- 8-c and d, the highest Schmid factor planes from Table 5- 5 and Table 5- 6 are presented on pole figure (represented by  $\emptyset$ ,  $\lambda$  using (blue lines) Wulff net). Where  $\emptyset$ ,  $\lambda$  are angle between the stress axis and the normal to the slip plane and angle between the stress axis and the slip direction, respectively. Pole figure {111} and {110} for matrix and the twin were obtained using V-Map software. The solid black circles represent the pole figure of {111} and the red square represent pole figure {110}. As shown in the figures the Wulff net used to measure the angle of 90 degrees to get the great circle (red circle in the figures) of the slip plane match the highest Schmid factor.

It can be seen in Figure 5- 8-c, that the crack trace matches well with the calculated ones of the  $(\bar{1}11)/[110]$  slip plane system in the matrix in which the calculated Schmid factor was highest, indicating that this slip plane was likely to be the crack plane.

Figure 5- 8-d shows that no match between the crack trace and the calculated ones of the  $(\bar{1}11)/[0\bar{1}1]$  slip plane system in the twin.

The pole figure of  $\{111\}$  for the matrix and the twin (T) were shown in Figure 5- 9. Sold black circles represent pole figure of  $\{111\}$  for the matrix and the open black circles for the twin (T).

The crack trace used to measure the angle between the crack pole and the active slip plane  $(\bar{1}11)/[0\bar{1}1]$  pole in the twin. As shown in Figure 5- 9 the twist angle is the angle between the poles of the crack and the pole of the active slip plane in the twin. The tilt angle is the angle between the normal to the crack trace and the normal to the active slip plane. These angles were measured using Wulff net. The twist angle is about  $40^\circ \pm 2^\circ$  and the tilt is about  $40^\circ \pm 2^\circ$ . Propagation from the matrix to the twin (T) was predicted to be difficult because the tilt angle and twist angle values seems to be large. So, this is show that the crack cannot continue along the same plane as it meets the twin.

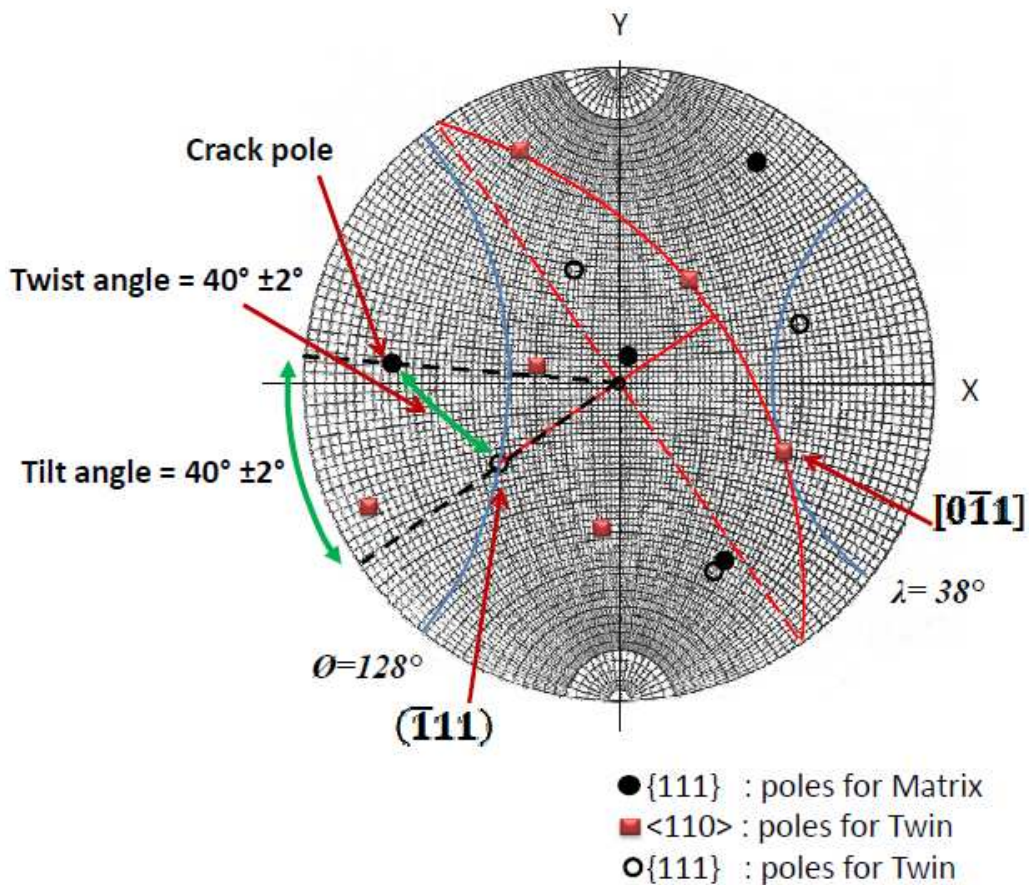


Figure 5- 9: Determination of cracked plane and angles of twist and tilt components; (a)  $\{111\}$  pole figure (Sold black circles represent pole figure of  $\{111\}$  for matrix and the open black circles for the twin).

### 5.8.3. The Crack Path in AISI 304L (Interaction with Martensite)

In Figure 5- 10 (a,b and c) the line x-y shows the relative orientations of the bright field/dark field and diffraction pattern images. The orientation in dark field image in c) is different to that in a) and b) due to the change of the magnification. This image was also recorded in a different session in the microscope.

The austenite planes identified by the diffraction spots in the diffraction pattern (Figure 5- 10-b) have been represented on a pole figure (Figure 5- 11). The traces of austenite  $\{111\}$  planes have also been identified on the same pole figure using the standard stereogram of the cubic system to index their relationships. The traces of the crack, from Figure 5- 10-a (Crack-A and crack-B) have been represented on the pole figure, and are compared with the traces of austenite  $\{111\}$  planes. The objective was to check whether or not they were consistent. This would be expected if the crack was propagating along slip planes, as observed in the EBSD analysis of the AISI 316L stainless steel. However, it can be seen that the crack traces don't match any of the austenite  $\{111\}$  slip planes traces (Figure 5- 11). Hence that the crack did not propagate on the austenite  $\{111\}$  slip planes.

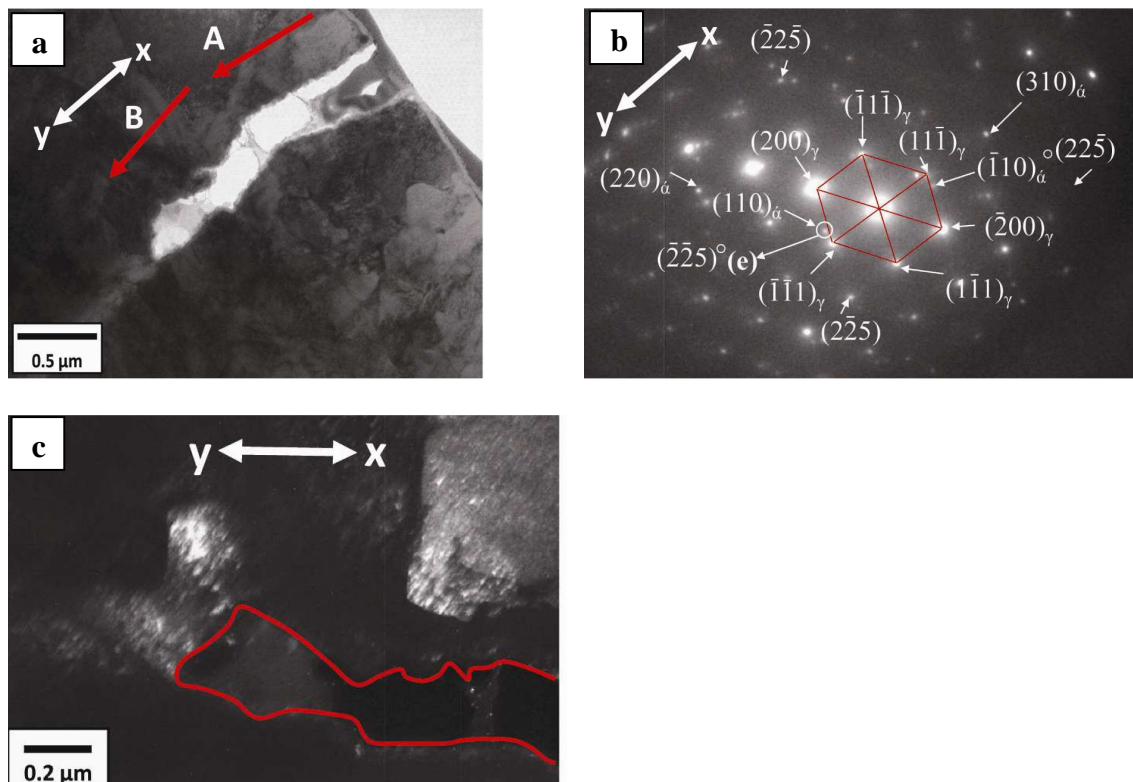


Figure 5- 10: a) bright field image of the crack in AISI304L as electropolished sample; b) Diffraction pattern; c) Dark field image, which shows the crack arrested at a martensite packet interface. The  $(110)$  martensite diffraction spot used is circled in (b) and labelled.





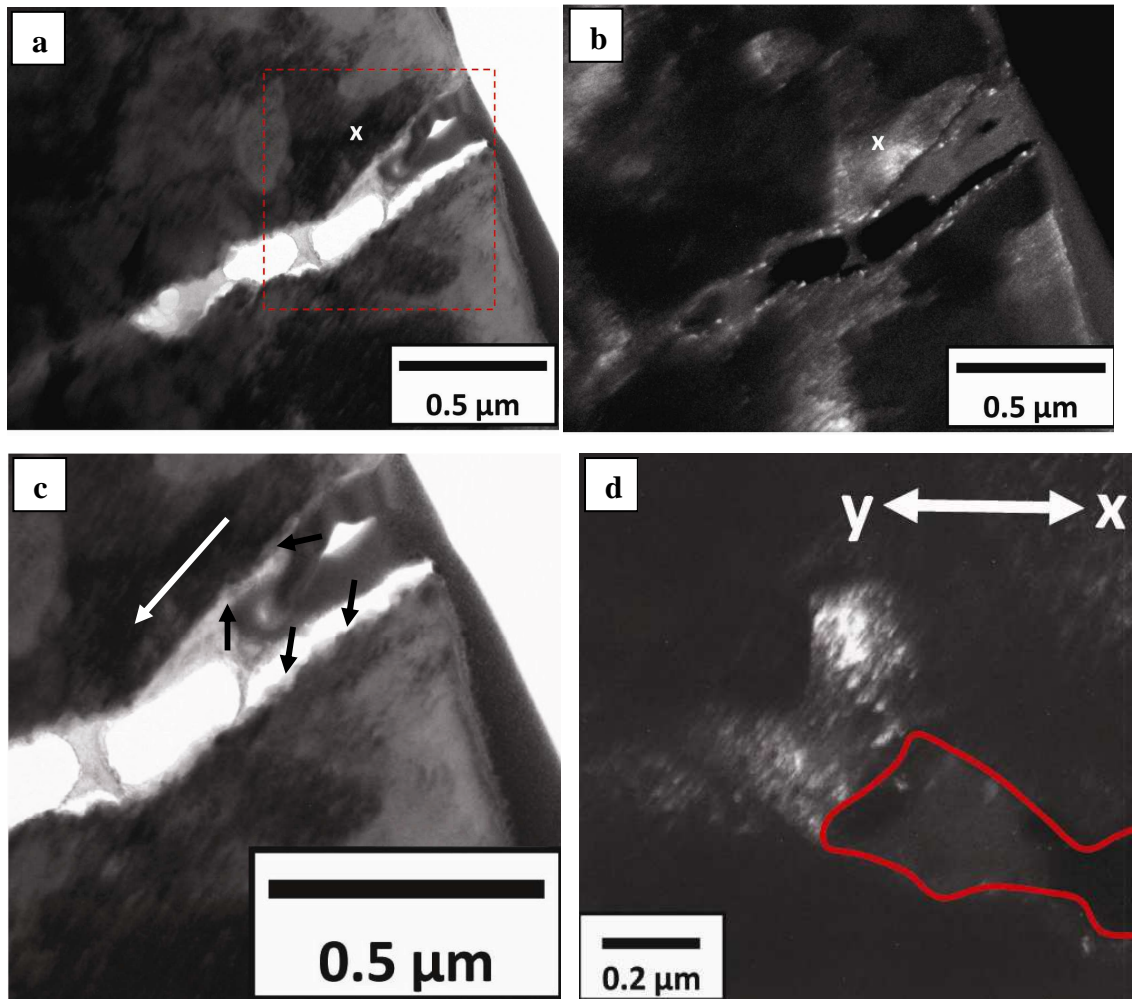


Figure 5- 12: Crack interaction with martensite in AISI304L as electropolished sample; a) Bright field image; b) Dark field image; c) Zoom in of the martensite region in a); d) Zoom in of the crack tip show the martensite stop the crack.

**Summary:**

- ❖ Schmid factors of all of the slip systems in the grains the crack propagate through were calculated. Based on the highest Schmid factor for each grain the active slip planes were indicated.
- ❖ In AISI 304L, the crack trace matches the active slip system in grain 1 and then propagate along the twin interface but not in the twin.
- ❖ In AISI 316L, the crack trace matches the active slip system in the matrix and cannot propagate along the same plane as it meets the twin.
- ❖ The crack in electropolished sample of AISI 304L propagates along the interface of the martensite laths. This crack impeded when it reached a martensite packet of different orientation.

### 5.9. Reproducibility of N-R model

Before applying the model in this project, a graph was plotted using the N-R model to understand the basic characteristics of the model and to implement the necessary surface coding to develop and apply the model. The implementation of the model was tested against literature applications of the model.

#### 5.9.1. N-R model for fatigue crack growth in shot-peened Aluminium

N-R model was used to model the fatigue crack growth in shot-peened components of Al 2024-T351. Two types of specimen are considered: un-peened and shot-peened aluminium specimens. The fatigue limits of the un-peened and peened specimens were measured to be 220 and 270 MPa, respectively [74]. In the shot-peened specimen, the closure stress profile was estimated from the residual stress distribution Figure 5- 13 and the closure stress is ignored for the un-peened specimen. The predicted threshold stress profile obtained by substituting the above experimental data using Eq. (5-5) is shown in Figure 5- 14. The predicted profile of the threshold stress in Figure 5- 14 is almost the same as reported in [74] as shown in Figure 5- 15.

$$\sigma_{Li} = \left( \sigma_1^i + \frac{m^i \sigma_{FL}}{m^i \sqrt{i}} \right) \quad (5-5)$$

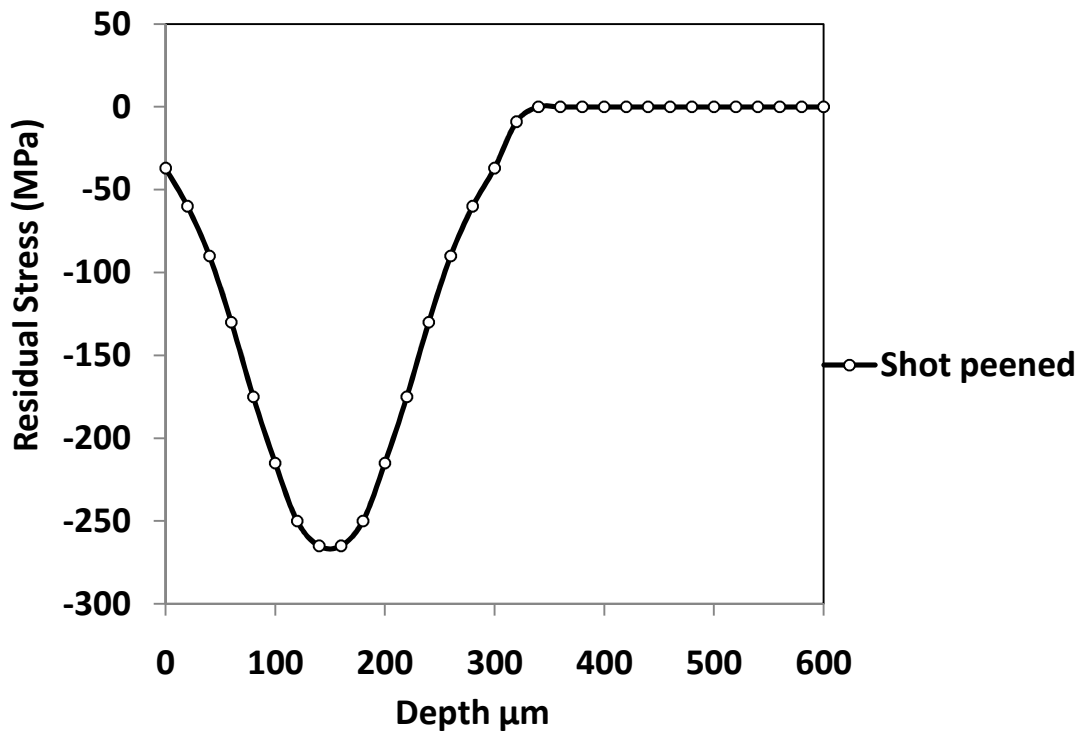


Figure 5- 13: Residual stress profile used in the implementation of the model [74].

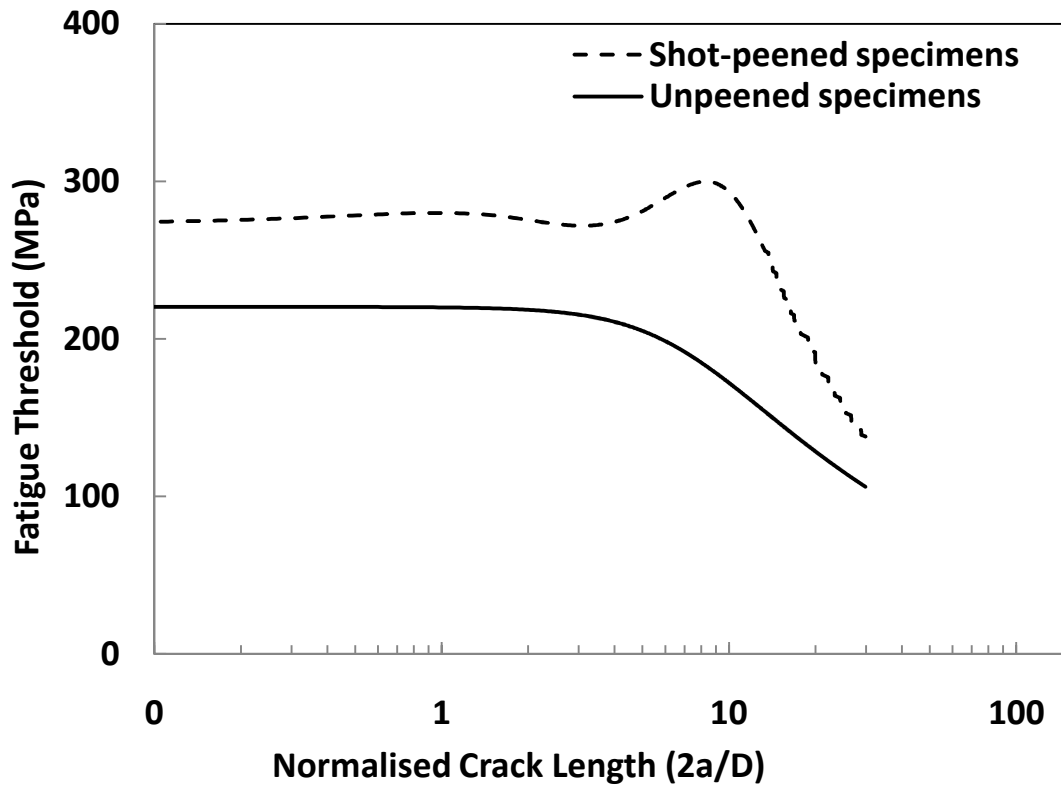


Figure 5- 14: Threshold stress profile using N-R model for unpeened and shot peened specimens to check the model used in this work.

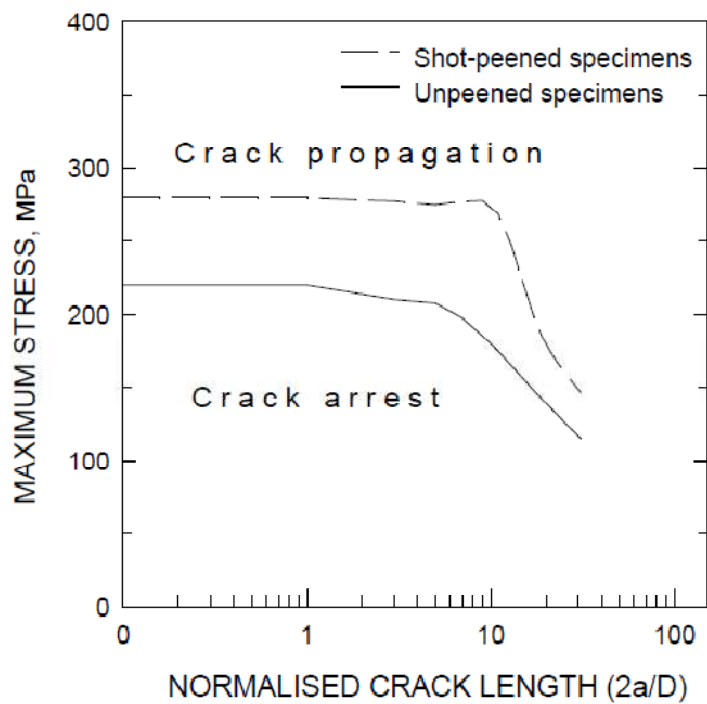


Figure 5- 15: Kitagawa-Takahashi type diagram for unpeened and shot peened specimens of AL 2024-T351, four-point bending,  $R=0.1$ ,  $D$ =grain diameter [74].

### 5.9.2. N-R Model to predict notches effect on Fatigue Crack Growth in Mild Steel

Kitagawa-type diagram reported in [78, 79] was successfully reproduced using the N-R model. Eq. (5-6) was used to reproduce the diagram. The geometric characteristics of the material are summarized in Table 5- 7. Table 5- 8 shows the data of notched specimens.  $\alpha$  and  $\beta$  are the depth and the width of notches, respectively.

$$\sigma_{Li} = Z_i \left( \sigma_1^i + \frac{m^i \sigma_{FL}}{m^1 \sqrt{i}} \right) \quad (5-6)$$

Table 5- 7: characteristics of mild steel 0.22% C used to reproduce the Kitagawa diagram [78].

Material	R	$\sigma_{FL}$ (MPa)	D( $\mu$ m)
Mild steel 0.22% C	-1	202	30

Table 5- 8: Data of notched specimens of mild steel 0.22% C [78].

Conditions	$\alpha$ (mm)	$\rho$ (mm)	$\beta$ (mm)[ $\beta = \sqrt{\rho\alpha}$ ]
A	5.08	0.10	0.71
B	5.08	0.25	1.13

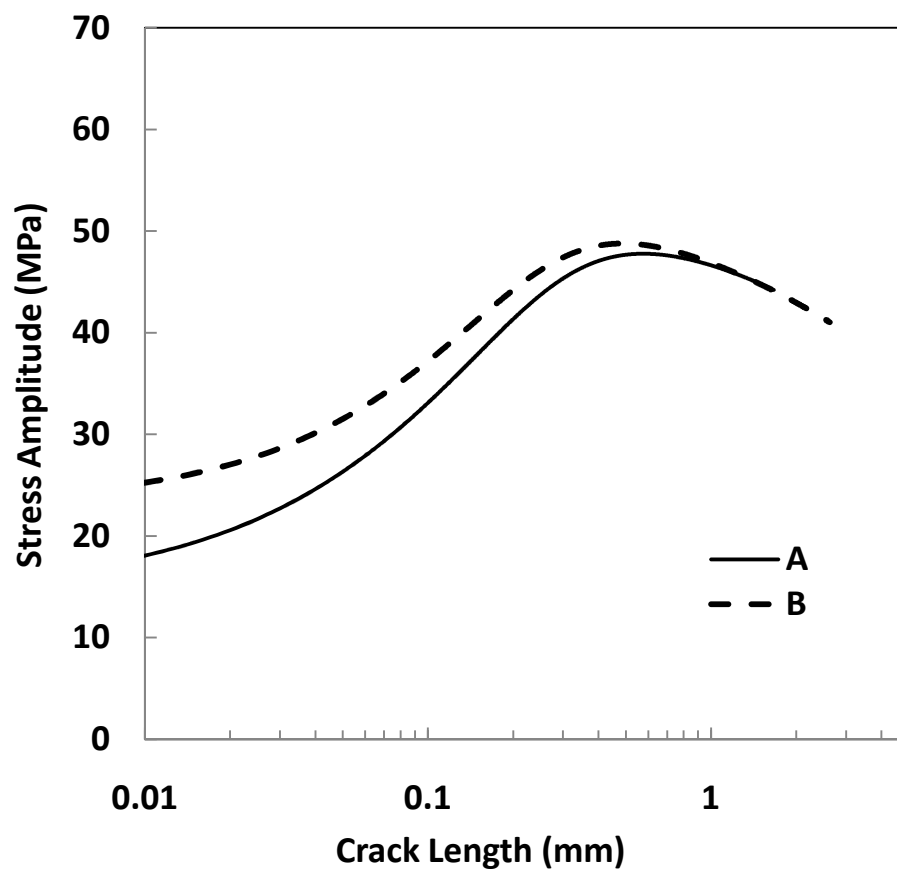


Figure 5- 16: Threshold stress as a function of the crack length for different notches size to check the model used in this work.



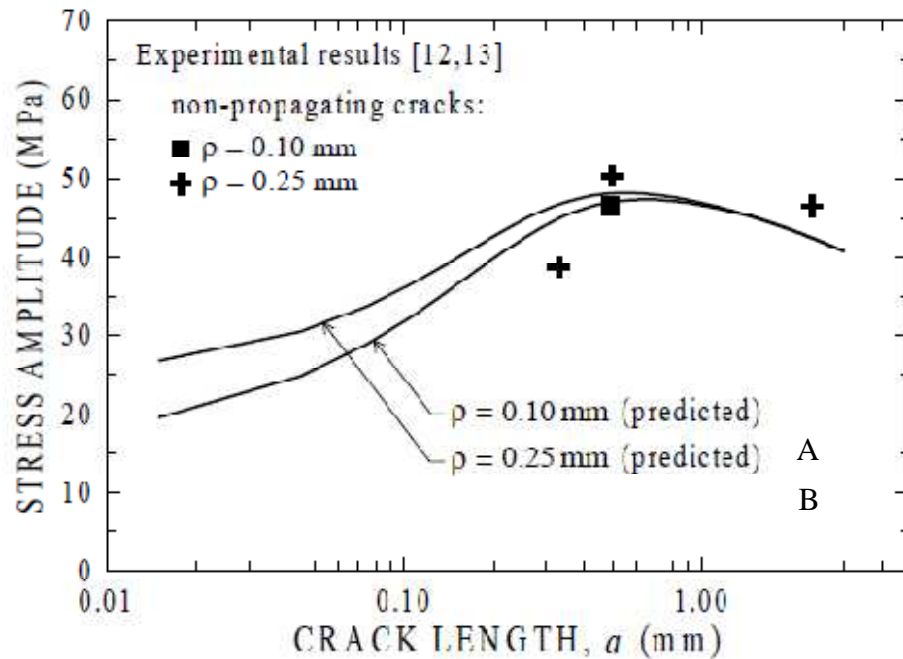


Figure 5- 17: Threshold stress as a function of the crack length for different notches size reported in [78].

The predicted profile of the threshold stress in Figure 5- 16 is almost the same as reported in [78] (Figure 5- 17).

**Summary:**

Reproductions of the published data demonstrates that the N-R model has been successfully implemented in this work.

**5.10. Fatigue Limit Prediction for Machined Surfaces**

The measured surface and microstructure parameters (barrier spacing,  $D$ , (i.e. grain size), residual stresses, experimental intrinsic fatigue limits,  $\sigma_{FL}$ , surface roughness and hardness,  $H_v$ ) were used to calculate the fatigue crack propagation threshold stress for each condition, using the implementation of the Navarro-Rios (N-R) short fatigue crack model (Eq.5-5). The surface hardness is used to derive the threshold for long fatigue cracks (Eq. 2-46) and hence the variation of grain orientation factor,  $m^i/m^l$ , with crack size relative to the number of grains,  $i$ . The roughness data collected by Stylus Profilometry were used to implement the N-R model. These data were used because the differences between them and the optical profilometry data were small and the

measurements were carried out for three samples from each condition and four times at different locations. The residual stress profiles for fine machined(C) and rough machined (A) (Figure 5- 18-a and Figure 5- 19-a) were converted into closure stress profiles Figure 5- 18-b and Figure 5- 19-b) by integration using Eq. (2-39). The integration was approximated by Simpson's method. Residual stresses were neglected for the annealed samples in the model predictions.

Table 5- 9, presents the key microstructure parameters required to implement the N-R fatigue model.

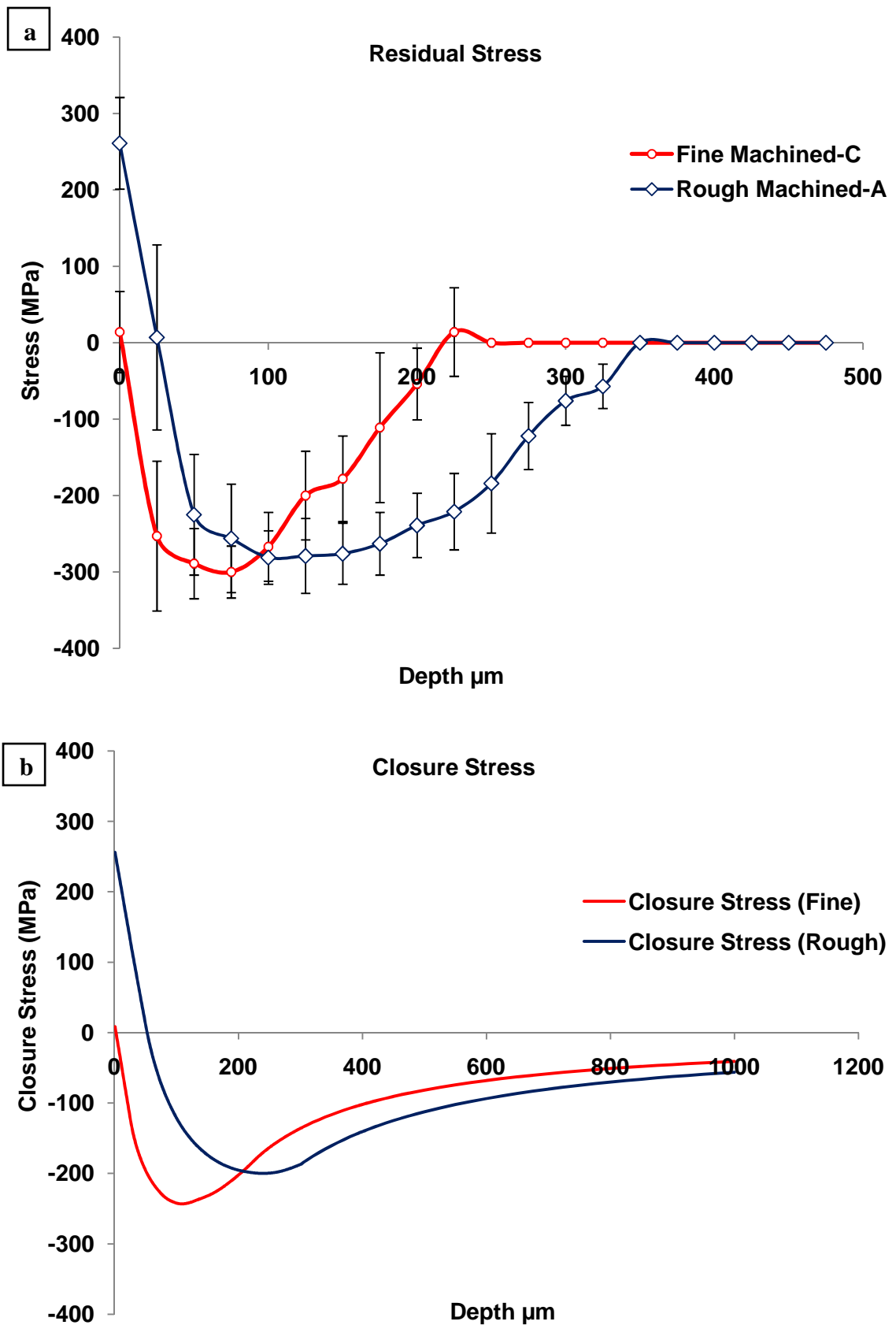


Figure 5- 18: AISI 304L, a) Residual stress of fine and rough conditions; b) Estimated closure stress of fine and rough conditions.

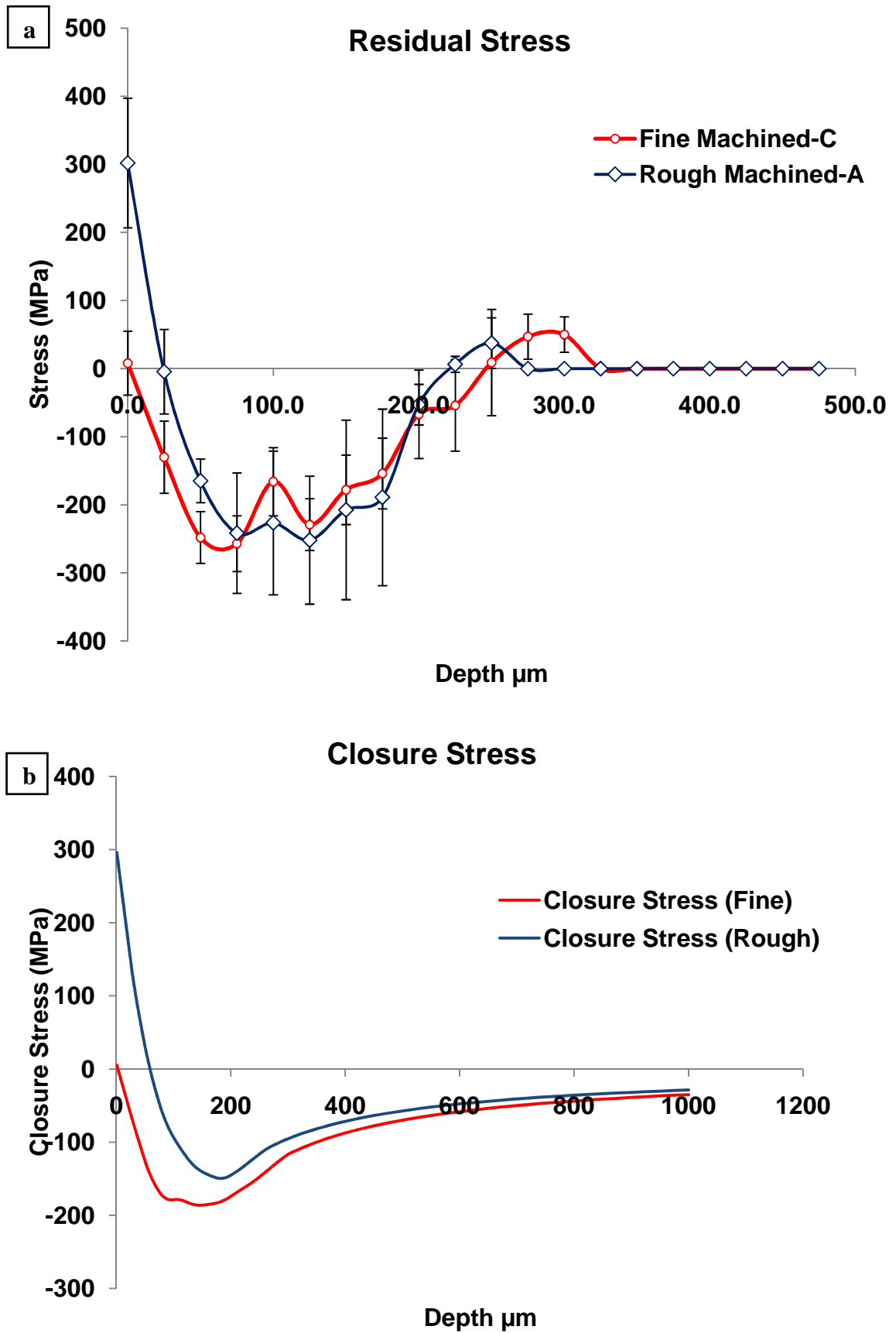


Figure 5- 19: AISI 316L, a) Residual stress of fine and rough conditions; b) Estimated closure stress of fine and rough conditions.

Table 5- 9: Parameters of machined surfaces ( $\pm$  one standard deviation).

Surface/Microstructure Parameters			
<b>AISI 304L</b>	Roughness, $R_y$ ( $\mu\text{m}$ ) (Maximum peak to valley height)	Fine Machined-1	$7 \pm 1$
		Rough Machined-4	$23 \pm 2$
	Roughness, $S$ ( $\mu\text{m}$ ) (Average peak spacing)	Fine Machined-1	$58 \pm 1.3$
		Rough Machined-4	$249 \pm 1$
	Microhardness, $H_v$	Fine Machined-1	$321 \pm 2$
		Rough Machined-4	$347 \pm 6$
		Electropolished-3	$152 \pm 2$
$D$ (Grain Size $\mu\text{m}$ )		$54 \pm 6$	
Intrinsic Fatigue Limit, $\sigma_{FL}$ (MPa)		$337 \pm 2$	
<b>AISI 316L</b>	Roughness, $R_y$ ( $\mu\text{m}$ ) (Maximum peak to valley height)	Fine Machined-1	$8 \pm 2$
		Rough Machined-4	$23 \pm 2$
	Roughness, $S$ ( $\mu\text{m}$ ) (Average peak spacing)	Fine Machined-1	$60 \pm 2$
		Rough Machined-4	$249 \pm 2$
	Microhardness, $H_v$	Fine Machined-1	$332 \pm 3$
		Rough Machined-4	$315 \pm 3$
		Electropolished-3	$233 \pm 3$
$D$ (Grain Size $\mu\text{m}$ )		$57 \pm 7$	
Intrinsic Fatigue Limit, $\sigma_{FL}$ (MPa)		$302 \pm 5$	

An important aspect of the model is the assumption that the austenite grain boundaries act as barriers to crack propagation. The grain size is assumed to be the average barrier spacing. The N-R short crack model is most sensitive to factors with a similar length scale to the barrier spacing. This causes the compressive residual stress peak from machining to have a significant effect on crack propagation, as well as the stress concentration from the surface roughness.

The peak threshold value for each condition is the minimum stress amplitude for unstable crack propagation, which is the fatigue limit (Figure 5- 20 and Figure 5- 21). In the model (Figure 5- 20 and Figure 5- 21), the crack length at stress amplitude below the fatigue limit represents the maximum expected arrested crack length.

As shown in Figure 5- 20, the model shows that the tensile surface stress in the rough machined (4) condition encourages the propagation of short crack nuclei. Afterward, the crack propagation arrested at a depth equal to the depth of the compressive stress peak to give stable crack nuclei.

From the model predictions, it can be seen that the fatigue limits for both fine machined (1) and rough machined (4) samples are higher than the intrinsic fatigue limits of the

electropolished (3) samples. This is due to the effect of the compressive stress peak, which dominates the predicted behaviour.

Compared with the electropolished (3) condition, the fatigue limit of the fine machined & annealed (2) samples, which have low roughness, does not significantly reduce, while, the stress concentration arising from the rough machined (4) surface tends to reduce the fatigue limit, and to encourage stable crack nuclei below the fatigue limit. Subsequently, the implementation of the N-R model to austenitic stainless steels suggests that there should be significant effects of the surface roughness and residual stresses arising from machining. The model predictions for AISI 316L are similar to that predicted for AISI 304L as it can be seen in Figure 5- 21.

By comparing the fatigue limits obtained by fatigue tests with the model predictions, it can be seen that there is no agreement between them for both materials (Figure 5- 22). It can be seen that the observed fatigue data are insensitive to the surface roughness and the sub-surface compressive residual stress peak, contrary to the predictions. These results are consistent with previous observations in austenitic stainless steels studied by M. Kuroda [4, 108].

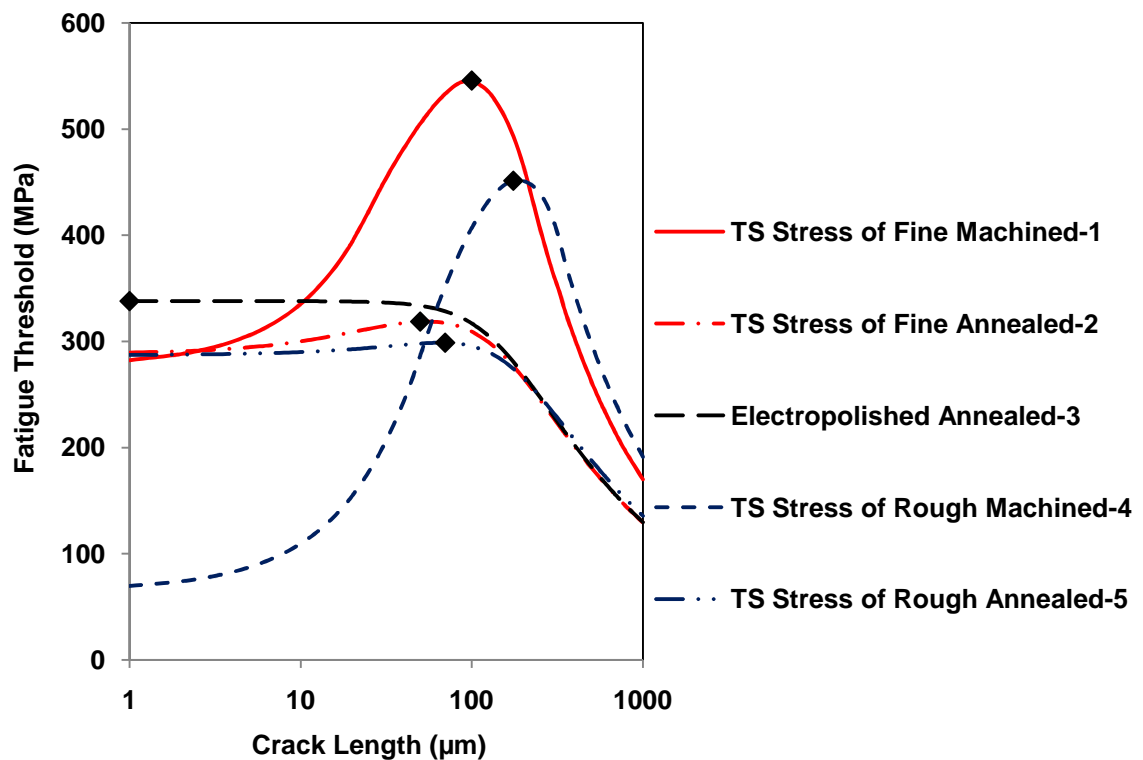


Figure 5- 20: AISI 304L, a) Threshold stress profiles predicted for; as machined specimens, annealed specimens and electropolished specimens (TS: Threshold stress).

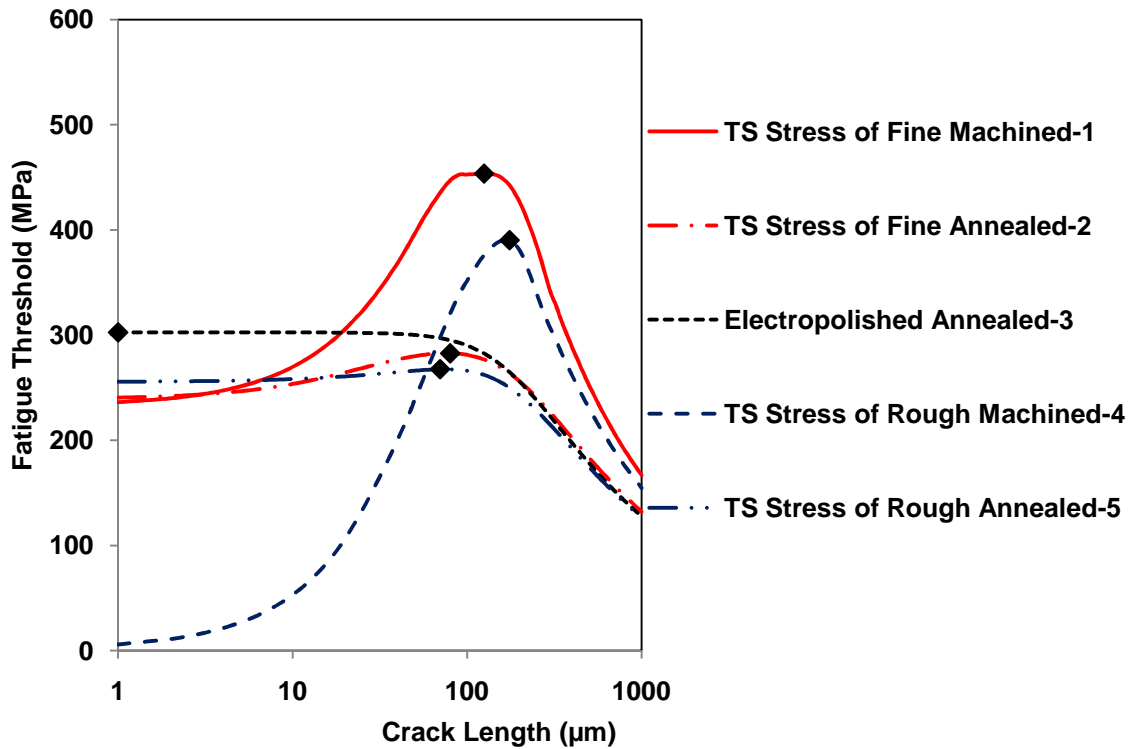


Figure 5- 21: AISI 316L, a) Threshold stress profiles predicted for; as machined specimens, annealed specimens and electropolished specimens (TS: Threshold stress).

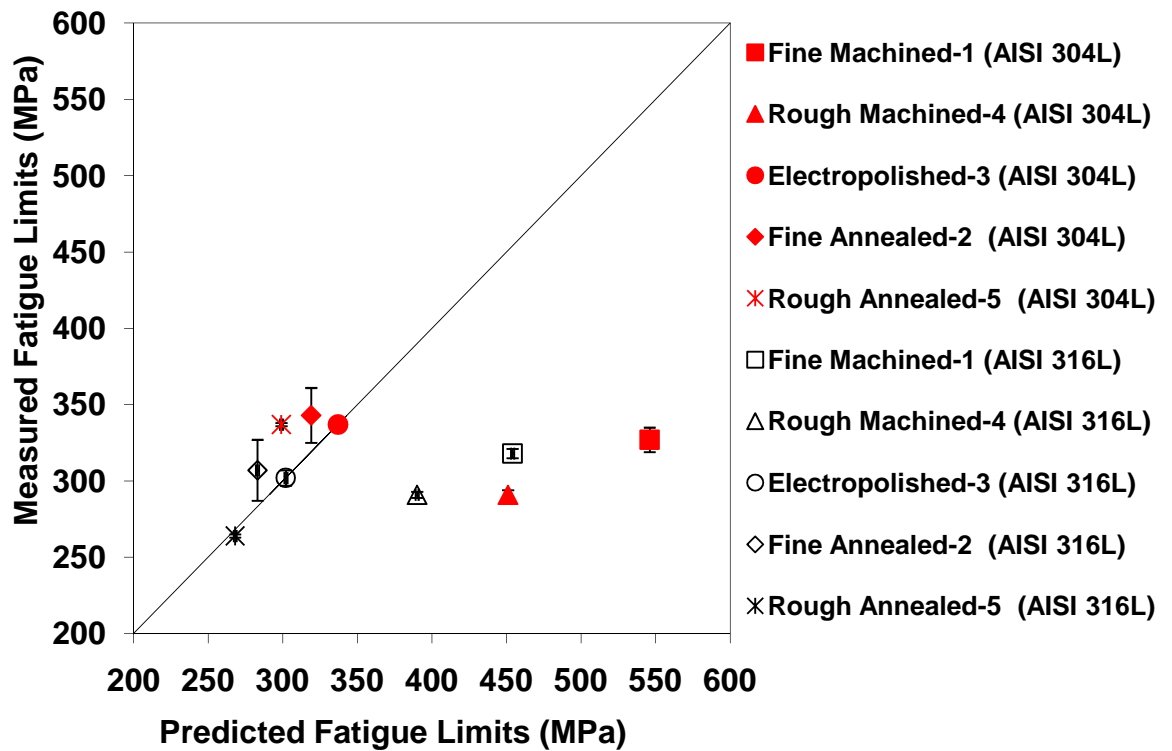


Figure 5- 22: Predicted fatigue limit in comparison with the measured fatigue limit (N-R Model) for all conditions for AISI 304L and AISI 316L.

**Summary:**

It can be seen that the implementation of the N-R model to austenitic stainless steels suggests that there should be significant effects of the surface roughness and residual stresses arising from machining. This is contrary to the experimental observations.

**5.11. Validity of the N-R Model for austenitic stainless steels**

It can be seen that there is no agreement between the predictions of the N-R model and the experimental measurements of the fatigue limit as shown above. From the predictions, it can be found that the model significantly over-predicts the effect of roughness on the fatigue limit. This is apparent by comparing the predicted fatigue limit of the annealed rough machined samples with the electropolished sample.

The effect of closure stress on the fatigue process can be seen by comparing the closure stress profile (Figure 5- 18-b) and the threshold stress profile (Figure 5- 20 and Figure 5- 21). The crack is predicted to propagate over the depth and to be arrested at a similar position of the compressive residual stress peak (~ 100  $\mu\text{m}$  and 200  $\mu\text{m}$  for fine machined (1) and rough machined (4), respectively).

The depth of the observed cracks in run-out samples was less than the depth of plastic strain zone developed close to the surface by fatigue as shown by EBSD (Figure 4- 25 to Figure 4- 27 for AISI 304L and Figure 4- 30 to Figure 4- 32 for AISI 316L). Also, the depth of these cracks was less than the depth of the plastically strained zone which developed by machining as supported by X-ray diffraction (Figure 4- 13-a and Figure 4- 14-a). So, it can be found that the cracks were found within a plastically strained region at the surface.

The maximum depth of observed cracks was approximately 5  $\mu\text{m}$  and the position of the compressive residual stress peak for fine machined (1) and rough machined (4) conditions was approximately 100  $\mu\text{m}$  and 200  $\mu\text{m}$ , respectively. So, the depth of cracking has no relation to the position of the compressive residual stress peak.

From all indications mentioned above, the observed short fatigue cracks were found to be arrested in cyclically plastic strained microstructure, which differs from the original bulk microstructure of the material and also from the near surface microstructure that is developed during surface preparation. The electropolished samples can demonstrate the



cyclically plastic strained microstructure where there is no significant effect of prior plastic strain from machining.

The reason of development of this cyclically plastic strained microstructure near to the surface of the test specimen may be attributed to the low yield strength of austenitic stainless steel and a high intrinsic fatigue limit (i.e. large plastic strain range required to develop a fatigue crack) [4].

In this analysis, the barrier spacing employed to implement the N-R model was the austenite grain size ( $\sim 56 \mu\text{m}$  for both materials) and the depth of plastic strain zone is smaller than the grain size. This implies that there are microstructural barriers in the cyclically plastic strained microstructure close to the surface, which may be more significant to crack propagation than the austenite grain boundaries. It has previously been proposed [125] that slip bands can act as barriers to fatigue cracks.

The degree of plastic strain in the near surface region increases as shown by the EBSD analysis (Figure 4- 25 to Figure 4- 29). The x-ray analyses show the formation of strain induced martensite with fatigue cycling in AISI 304L (Figure 4- 43 to Figure 4- 47). This is supported by TEM observations (Figure 4- 62). This is consistent with literature observations for the effect of cyclic plastic strain amplitude on martensite volume fraction in unstable stainless steels [37, 126].

The cyclically strained microstructure at the surface is cold worked as a result of martensite formation. Neutron diffraction studies of martensite in austenitic steels showed that the  $\alpha$  martensite acts as a strengthening phase as it supports a higher stress than the austenite under external loading [127].

In AISI 304L, martensite packet was observed to impede crack propagation as shown in Figure 4- 62-e. It can be seen that the crack tip stopped at the edge of martensite packet. So, the crack can follow the martensite laths as discussed in section 5.8.3 and arresting at those packet boundaries. Also, twins were observed to arrest fatigue cracks as shown in Figure 4- 55. In this material a martensite packet arrested the crack at depths less than about  $5\mu\text{m}$  from the surface.

In AISI 316L, martensite was not detected in the deformed microstructure as supported by x-ray analyses (Figure 4- 49 to Figure 4- 51). Twins were observed to arrest fatigue cracks in this material as shown in Figure 4- 56. These twins were observed at a depth similar to the depth of martensite packet in AISI 304L (about  $5\mu\text{m}$ ) from the surface.

It can be seen from Figure 4- 56 that the crack in AISI 316L lies on plane {111}. In AISI 316L the cracking is stage I and it is shear. The crack plane in AISI 304L could be controlled by microstructure rather than by the crystal slip plane orientations. The crack plane in AISI 304L might be a stage II crack (growth under opening and closing mode).

This shows that there is a difference between AISI 304L and AISI 316. So, perhaps this is the cause of the different behaviour in the sensitivity to the surface stress.

**Summary:**

- ❖ The cracks were found within a plastically strained region at the surface. The depth of cracking has no relation to the position of the compressive residual stress peak. The observed short fatigue cracks were found to be arrested in cyclically plastic strained microstructure.
- ❖ The microstructure of both materials shows that there are microstructural barriers in the cyclically plastic strained microstructure close to the surface, which may be more significant to crack propagation than the austenite grain boundaries.
- ❖ In AISI 304L, martensite packet was observed to impede crack propagation.
- ❖ In AISI 316L, no martensite was detected and twins were observed to arrest fatigue crack.

## 5.12. Development of N-R Model for the Fatigue Limit of Austenitic Stainless Steels

### 5.12.1. Refined Barrier Spacing

As shown before using austenite grain size ( $\sim 56 \mu\text{m}$ ) as the barrier spacing leads the N-R model to predict significant differences in the fatigue limit between the machining conditions; but this does not agree with the experimental observations. As discussed before, the near surface microstructure show some evidence such as plastically strained region size (smaller than the grain size) and observed crack length ( $\sim 1 \mu\text{m}$ ) that indicate that there are barrier spacings significantly smaller than the employed austenite grain size.

In AISI 304, Figure 5- 23 and Figure 5- 24 show the fatigue thresholds for fine machined (1), rough machined (4) conditions and electropolished (3) condition with refined barrier spacing ( $\sim 0.5 \mu\text{m}$  similar to the observed martensite packet width observed in run-out electropolished (3) as in Figure 4- 62-e).

By comparing threshold stress curve after refined barrier spacing in Figure 5- 23 with threshold stress curve before in Figure 5- 20, it can be seen that in fine machined (1) condition, the prediction gives a fatigue limit that is 12% lower than the observed one by changing the barrier spacing from grain size diameter to small barrier spacing ( $0.5 \mu\text{m}$ ) and the depth to which arrested cracks may develop is decreased to a magnitude that is consistent with the experimental observations. In rough machined (4) condition, the fatigue limit decreased to a fatigue limit lower than the observed one by 64% and the depth to which arrested cracks may develop decreased to length is consistent with the observed one.

In AISI 316, Figure 5- 23 and Figure 5- 24 also demonstrate the fatigue thresholds for fine machined (1), rough machined (4) conditions and electropolished (3) condition with refined barrier spacing ( $\sim 3 \mu\text{m}$ ) similar to the observed twins spacing observed in run-out electropolished (3) as it can be seen in Figure 4- 56.

Fine machined (1) condition, demonstrates a fatigue limit lower than the observed one by 16% and the depth of arrested cracks is consistent with the experimental observations. Rough machined (4) condition show a fatigue limit lower than that

observed by 54% and the depth to which arrested cracks may develop decreased to length close to the observed one.

Electropolished (3) samples for both materials show that the depth of arrested crack is more consistent with the experimental observations.

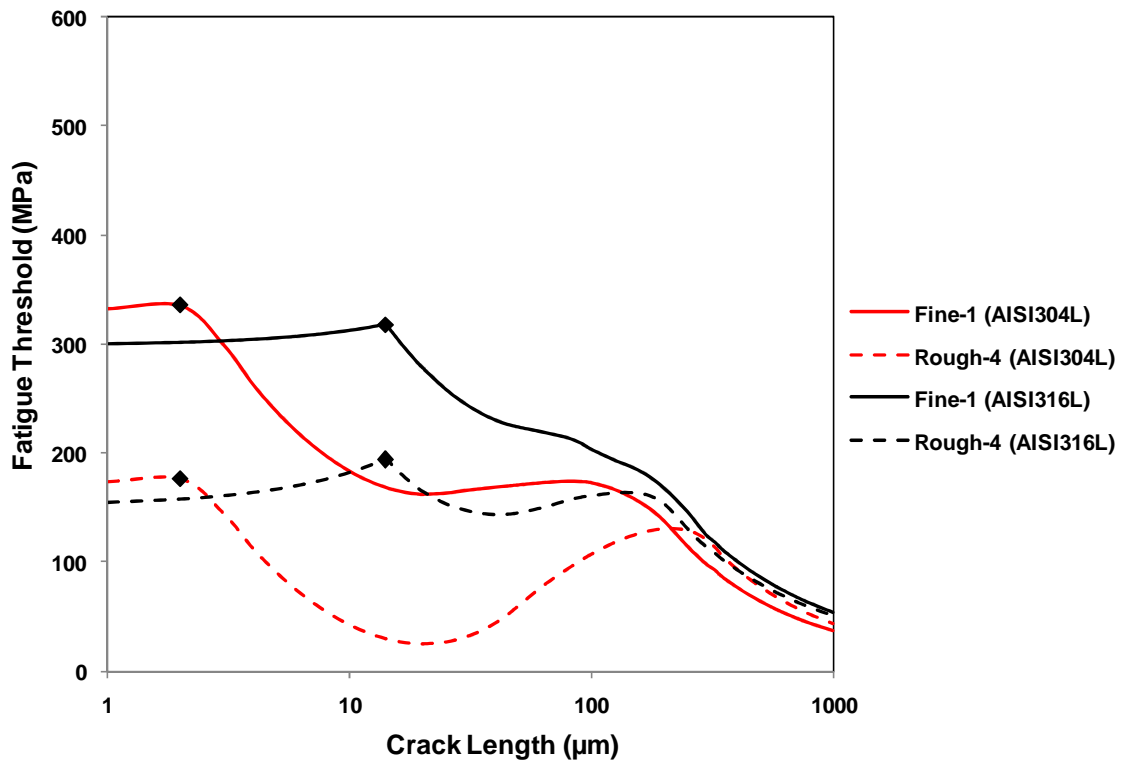


Figure 5- 23: Effect of refined barrier spacing ( $0.5 \mu\text{m}$  for AISI 304L and  $3 \mu\text{m}$  for AISI 316L) on the threshold stress in machined samples for AISI 304L and AISI 316L.

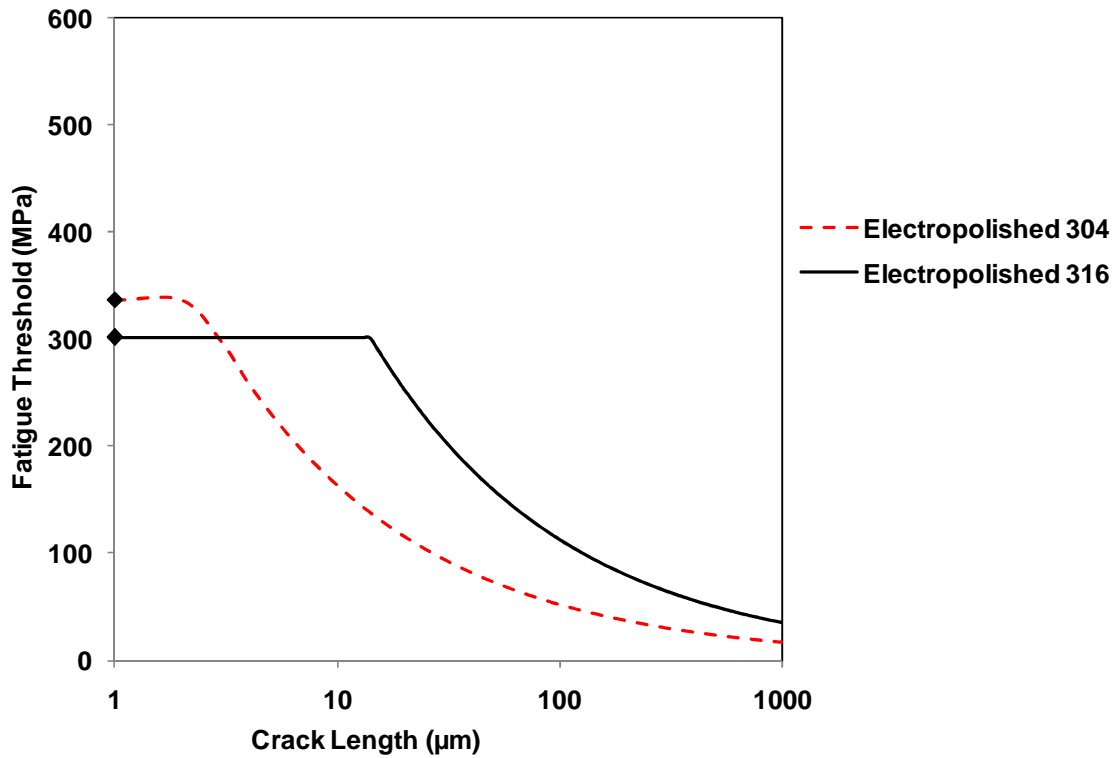


Figure 5- 24: Effect of refined barrier spacing ( $0.5 \mu\text{m}$  for AISI 304L and  $3 \mu\text{m}$  for AISI 316L) on the threshold stress in electropolished annealed-3 samples for AISI 304L and AISI 316L.

### 5.12.2. Surface Roughness Effect

The experimental observations of austenitic stainless steels show that no significant effect for the surface roughness on fatigue limit. This can be attributed to the fact that in plastically strained region, the small barrier spacing, relative to the notch dimensions, may arrest the crack before the action of surface roughness becomes effective [3]. So, in austenitic stainless steels, the surface roughness effect may be neglected and removed from the N-R model.

In order to see the effect of neglecting the surface roughness, the model (Equation 5-6) for austenitic stainless steels can be written as:

$$\sigma_{Li} = \left( \sigma_1^i + \frac{m^i \sigma_{FL}}{m^1 \sqrt{i}} \right) \quad (5-7)$$

In AISI 304L, it can be seen that in fine machined (1) condition, the prediction gives a fatigue limit that is 2% higher than the observed one and the depth of arrested cracks is more consistent with the experimental observations. Rough machined (4) condition shows a fatigue limit lower than the observed by 49% and show similar depth of arrested cracks to the observed crack length.

AISI 316L shows that the fatigue limit in fine machined (1) condition is similar to that observed and the crack arrest at depth is close to the observed values. Also, the depth of arrested crack in rough machined (4) condition in this material is close to the observed length and the fatigue limit became lower than the observed value by 40%.

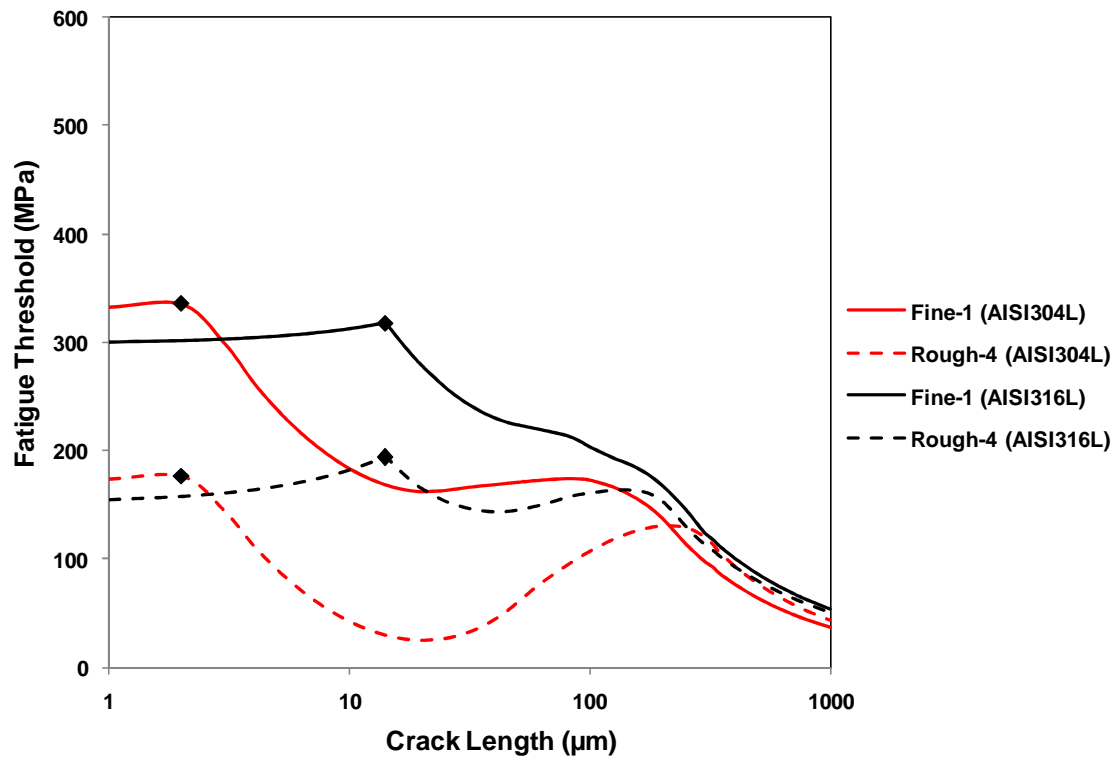


Figure 5- 25: Effect of neglecting surface roughness effect on the threshold stress in machined samples for AISI 304L and AISI 316L.

### 5.12.3. Relaxation of Residual stress

Kuroda et al. [3] measured the surface residual stresses and concluded that there was no relaxation. However, in this investigation the subsurface stresses were also measured. In AISI 304L, Figure 4- 37-a and Figure 4- 38-a, can show the profile depth of the axial stress of pre- and post-fatigue samples (tested at 326 and 294 MPa) for fine machined (1) and rough machined (4) samples, respectively. In AISI 316L, Figure 4- 39-a and Figure 4- 40-a show the profile depth of the axial stress of pre- and post-fatigue samples (tested at 318 and 294 MPa) for fine machined (1) and rough machined (4) samples, respectively. It can be seen that all stresses changed on average by approximately 50 % in the subsurface region after fatigue testing. This clearly shows that there is a relaxation in subsurface but the surface stresses are not significantly affected. This is consistent with Kuroda et al's observation, but shows their conclusion to be incorrect.

Figure 5- 26 and Figure 5- 27 demonstrate the profile depth of the closure stress of pre- and post-fatigue samples for fine machined (1) and rough machined (4) conditions for AISI 304L and AISI 316L, respectively. In order to simulate the effect of the redistribution of stress after fatigue on the model predictions, the stress relaxation after fatigue was converted to closure stress and used in the N-R model with a refined barrier spacing and neglecting of the surface roughness effect. The effect on the threshold for both conditions presented is shown in Figure 5- 28.

For both materials, in the fine machined condition, it can be seen that the predicted fatigue limit disagrees with the observed fatigue limit, although the depth to which arrested cracks may develop is decreased to a magnitude that is consistent with the experimental observations. Also, the effect of compressive stress peak was reduced. In the rough machined condition, the prediction for rough machined (4) condition gives a fatigue limit that is 77% lower than the observed one in AISI 304L and a very small fatigue limit for AISI 316L. Also, the depth to which arrested cracks may develop does not agree with the observed crack length.

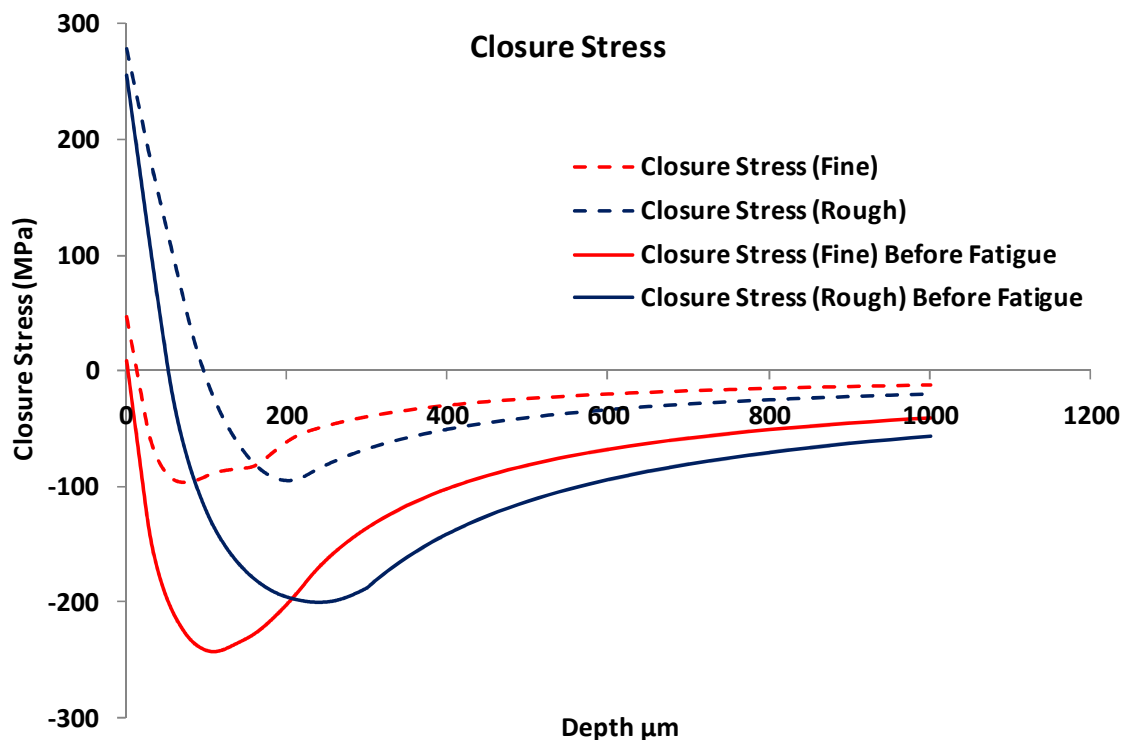


Figure 5- 26: Closure stress profiles of the fine-1 and rough-4 machined samples for AISI 304L before and after fatigue test.

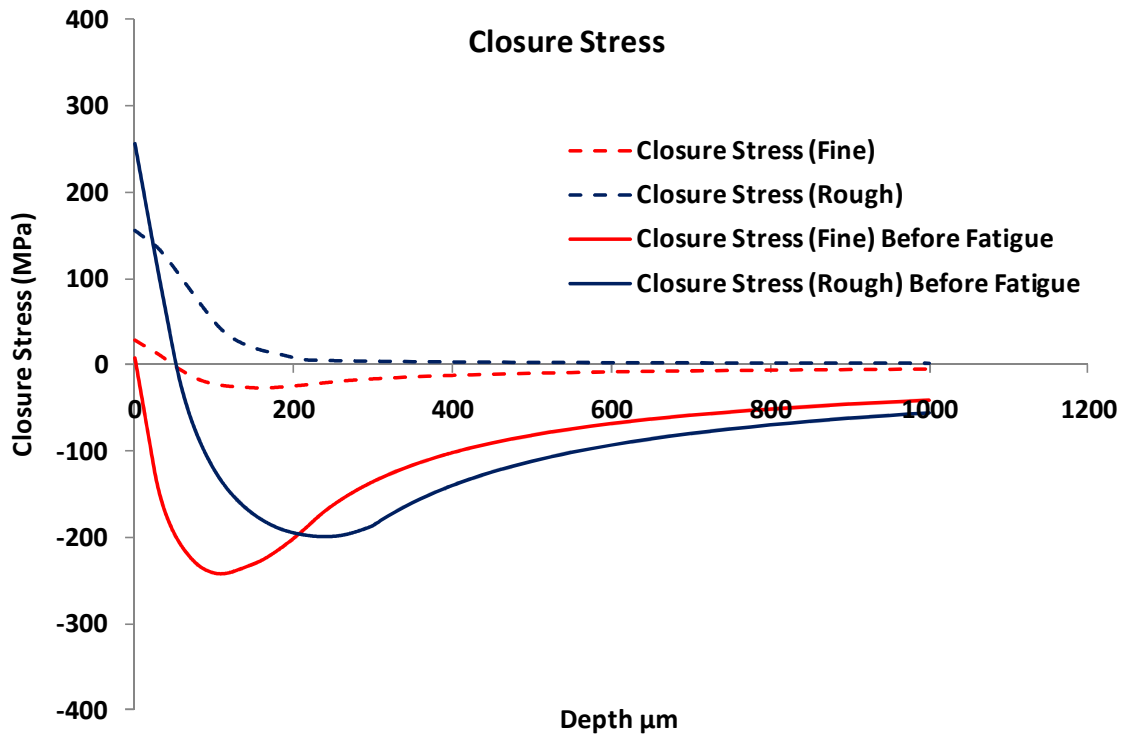


Figure 5- 27: Closure stress profiles of the fine and rough machined samples for AISI 316L before and after fatigue test.

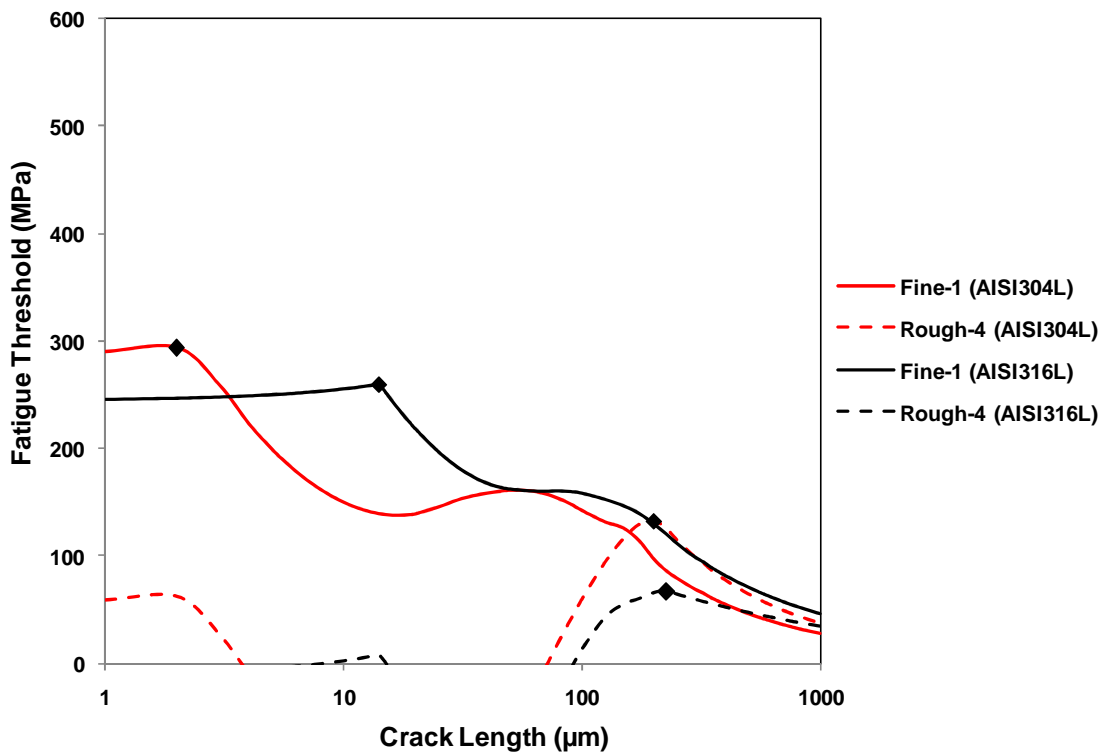


Figure 5- 28: Effect of stress relaxation using measured residual stresses after fatigue test on the threshold stress in machined samples for AISI 304L and AISI 316L.



After fatigue testing all stresses changed below the specimen surface. Figure 5- 29 and Figure 5- 30 for AISI 304L and AISI 316L, respectively, show the ratio between the stresses before and after fatigue test for both conditions. This data suggest that the stresses for fine and rough conditions were relaxed by relaxation factor of about 0.5. It can be seen from Figure 5- 29-a and Figure 5- 30-a that the certainty in this ratio is increased dramatically as we approach the surface. A similar magnitude of relaxation was observed over the majority of the stress profile. So, it was assumed that in the absence of more accurate measurements that same factor occurs in the near surface region where the stress gradient is steeper. Based on this, a more simple model that assumes that there is a constant relaxation factor was implemented as shown in Figure 5- 31. This is in contrast to the model used in (section 5.12.1 and 5.12.2), in which the measured residual stresses, as a function of position, were used to calculate the closure stress profile.

In AISI 304L, the predicted fatigue limit and crack length in fine machined (1) condition show good agreement with the observed results (within 2%). While, the rough machined (4) condition shows that the crack length agree with the observed but the fatigue limit is now less than the observed fatigue limit by about 49%.

In 316L, fine machined (1) condition show that the predicted fatigue limit agrees with the observed fatigue limit by 100%, and the crack length show good agreement with the observed results. While, the rough machined (4) condition shows that the crack length agree with the observed but the prediction gives a fatigue limit that is 40% lower than the observed one. By comparing the fatigue limits obtained by fatigue tests with the model predictions, it can be seen that there are agreements in fine machined (1) condition and no agreement in the rough machined (4) condition for both materials (Figure 5- 32).

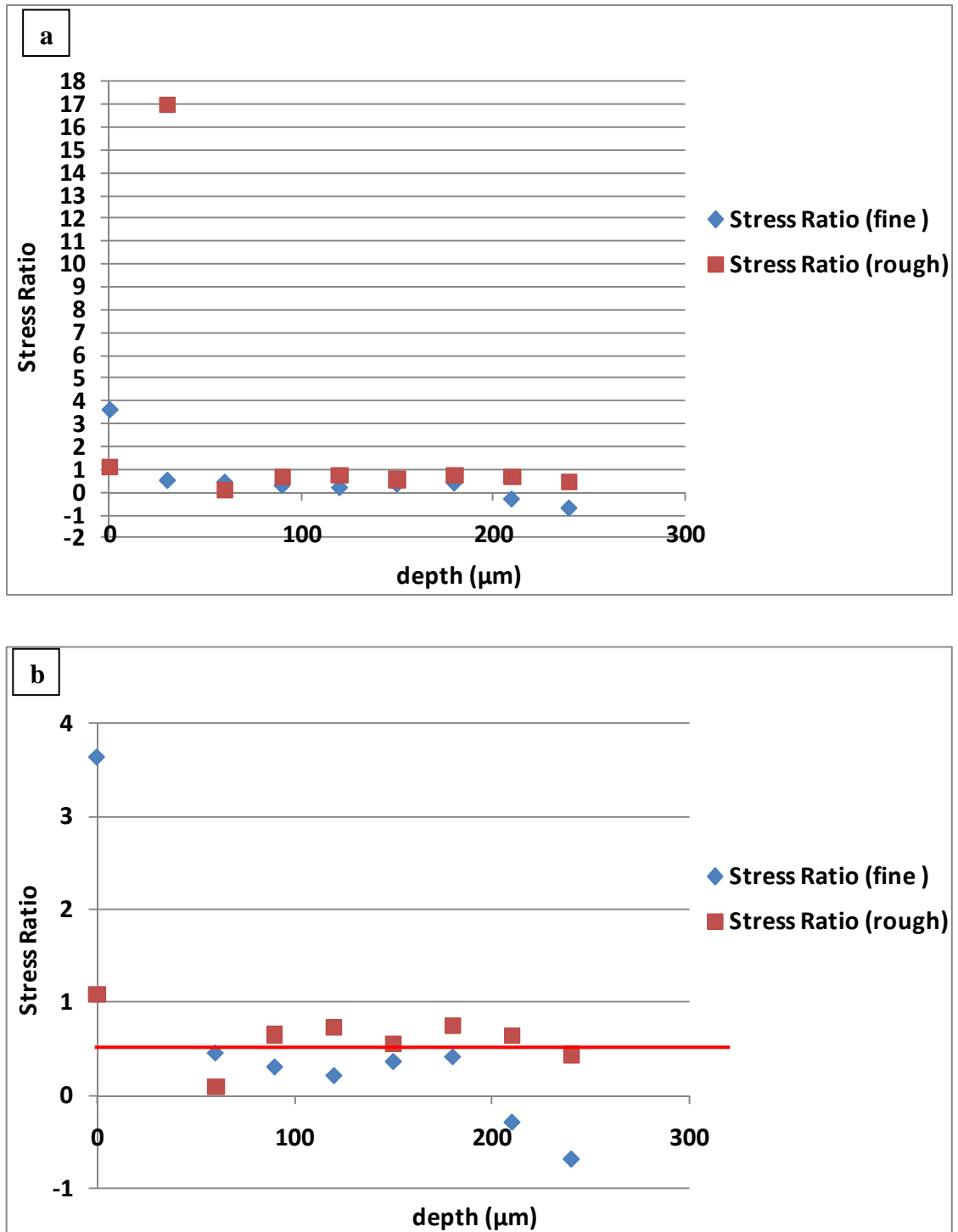


Figure 5- 29: Stress ratio between the residual stress before and after fatigue test for AISI 304L.

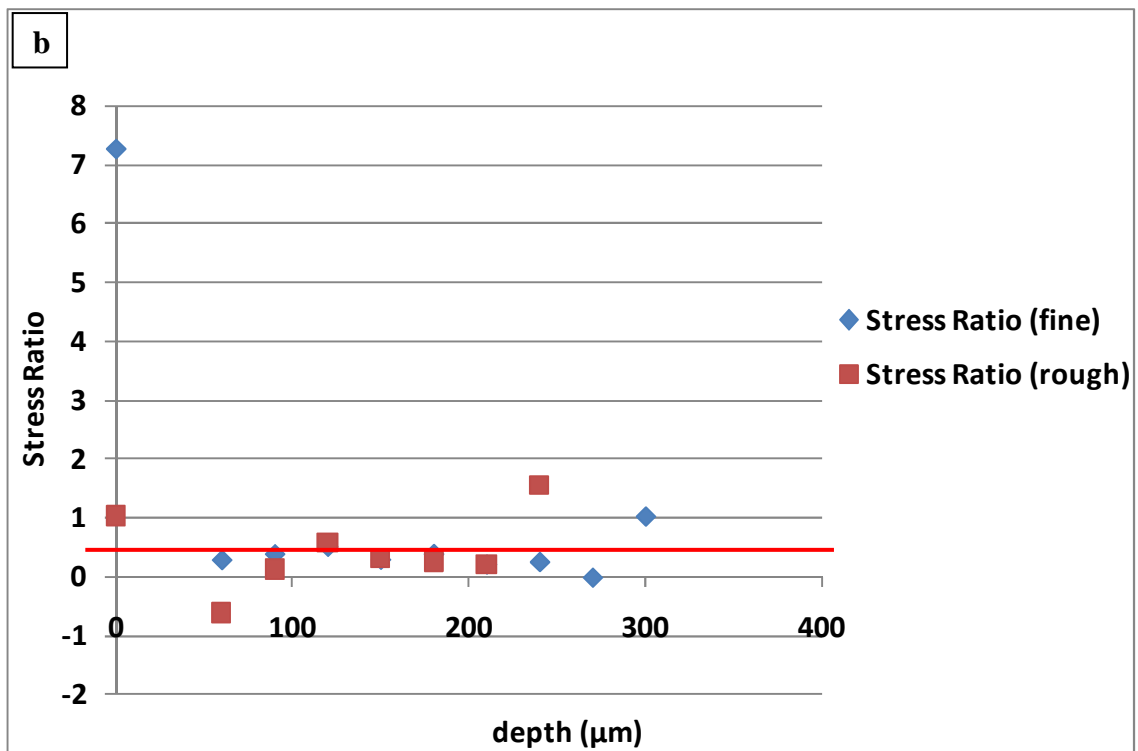
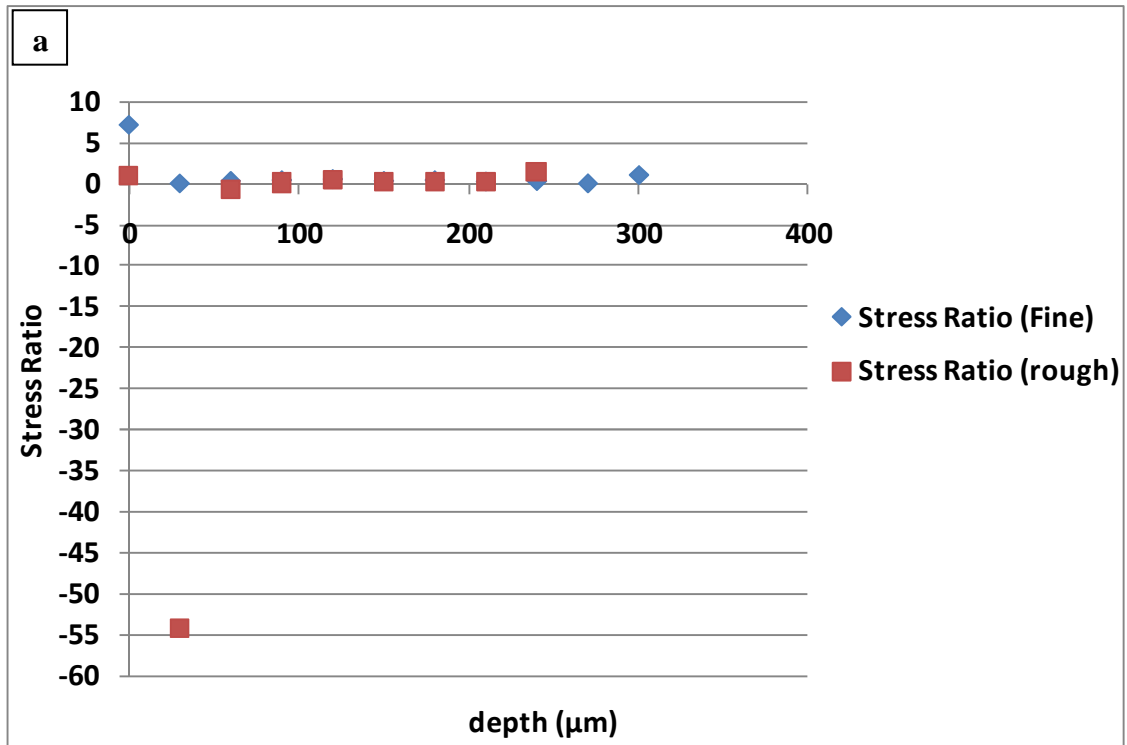


Figure 5- 30: Stress ratio between the residual stress before and after fatigue test for AISI 316L.

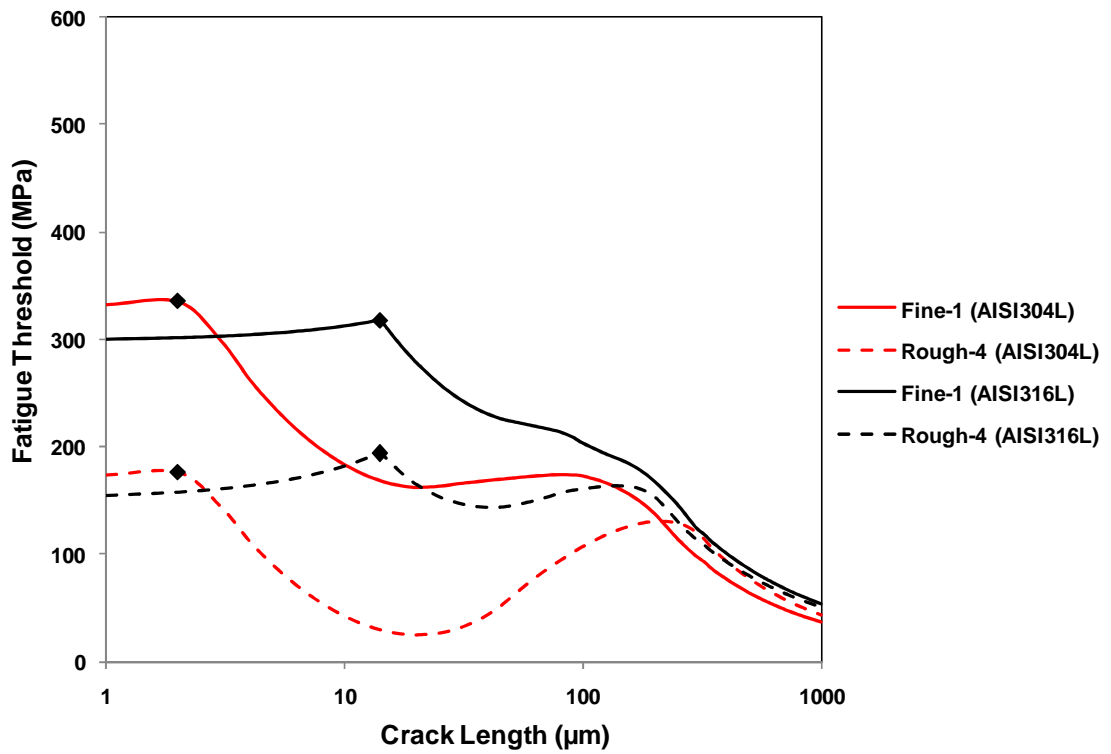


Figure 5- 31: Effect of residual stress relaxation on the threshold stress in machined samples for AISI 304L and AISI 316L using relaxation factor of 0.5.

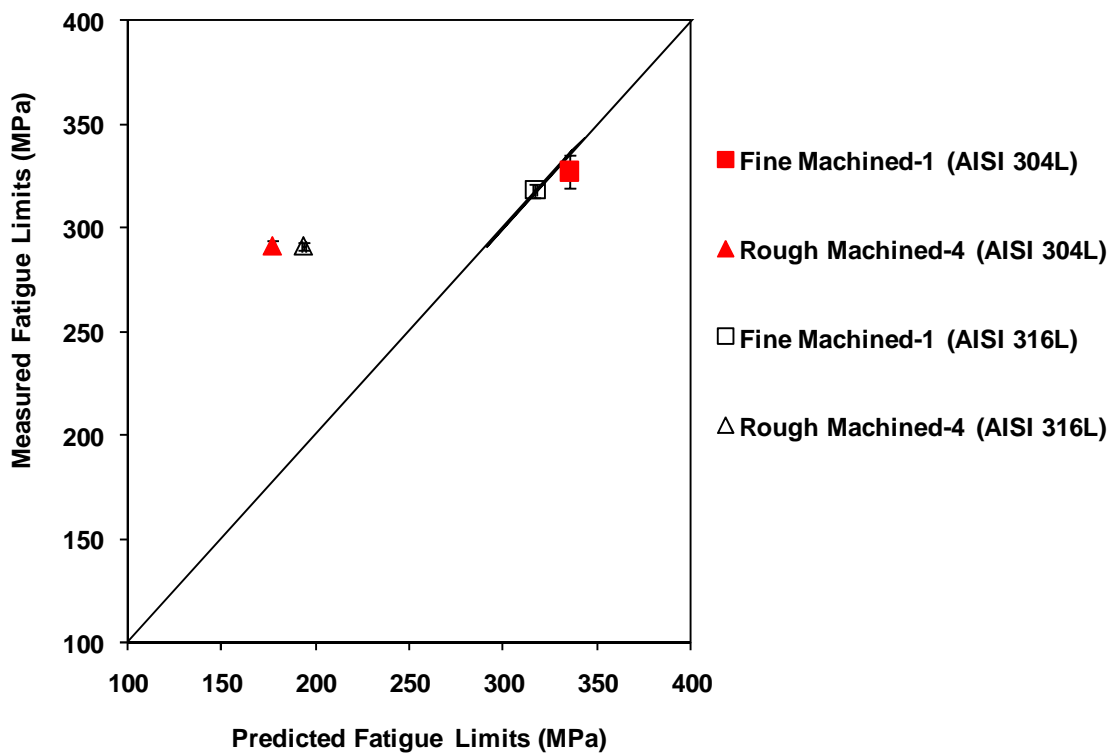


Figure 5- 32: Predicted fatigue limit in comparison with the measured fatigue limit (new model) for machining conditions for AISI 304L and AISI 316L.

#### 5.12.4. Other Factors

The fatigue loading (fatigue cycling) creates a refined microstructure where new interfaces appear that interfere with crack propagation. The N-R model is based on spacing and strength of those interfaces. Due to the lack of data of the strength of those interfaces, the model assumes the most important thing is the spacing.

Also, as a result of the lack of the data that show what the prior cold work does to the strength, the model assumes that the fine and rough machined have similar spacing of the martensite and similar strength of the martensite in AISI 304L. In AISI 316L, the model assumes that the fine and rough machined materials have similar spacing of the deformation twins and similar strength of deformation.

In AISI 304L, the fatigue resistance is affected by the prior deformation of the microstructure, cyclic deformation and the tendency to form martensite. This effect could be different between fine and rough conditions.

The implications of X-Ray diffraction data show that there is more martensite in machined condition as shown in Table 4- 9 by comparing the ratios between austenite peak and martensite peak (inside the dotted rectangle in the x-ray diffraction patterns). Qualitatively, X-Ray diffraction shows that the grain size of those martensite laths in the machined condition appears to be smaller than that in the electropolished as it can be seen from the broadening in the martensite peak compared to the electropolished martensite peak as shown in Figure 4- 48. The peak broadening increases as grain size decreases [112].

So, if this is the case, in modelling the propagation of fatigue crack in such microstructure, the fatigue cracks should follow the martensite laths and arrest at those packet boundaries. To pass across those boundaries, the crack will initiate slip in the next packet. The lath width will act as a barrier to these dislocations movement. The lath width could affect the strength of this barrier. Subsequently, it will be reasonable to postulate the intrinsic fatigue resistance of the martensite in the machined and fatigued microstructure is higher than the intrinsic fatigue resistance of martensite formed in the electropolished microstructure by fatigue.

K. Spencer et al. [127-129] studied the strengthening that results from the formation of strain-induced martensite in austenitic stainless steel (304L and 316L). They reported

that the size of the  $\alpha$  laths was typically  $\leq 500$  nm and the martensite acts as a reinforcing phase as it supports a higher stress than the austenite under external loading. The data reported in the literature can be used to estimate the sensitivity of the model to those parameters. So, in AISI 304L, relaxation factor of 0.5, barrier spacing of  $0.5 \mu\text{m}$  ( $0.5 \mu\text{m}$  similar to the observed martensite packet size) and the intrinsic fatigue limit increased by 2% and 30% for fine machined (1) and rough machined (4) condition, respectively, were used to simulate the sensitivity of the model to these parameters. The agreement with the measured fatigue limits by increasing the intrinsic fatigue resistance by 3% and 30% is good for both conditions (Figure 5- 33).

In AISI 316L, relaxation factor of 0.5, barrier spacing of  $0.5 \mu\text{m}$  and the intrinsic fatigue resistance increased by 3% and 30% for fine and rough condition, respectively, were used to simulate the sensitivity of the model to these parameters. By increasing the intrinsic fatigue resistance by 2% and 30% the predicted fatigue limit and crack length show consistency with the observed data for both conditions in this material (Figure 5- 33).

By comparing the fatigue limits obtained by fatigue tests with the model predictions, it can be seen that there are good agreements in fine machined (1) condition and rough machined (4) condition for both materials (Figure 5- 34).

This postulation shows how much the resistance would have to be increased to get agreement with the observed results for both materials. The required changes, of 2% and 30% increase in intrinsic fatigue resistance for fine and rough condition, respectively is not large, and may be reasonable.

These changes are consistent (in relative magnitude) with what might be expected if the machining affected the martensite lath spacing more in rough machining than in fine machining. So, it is recommended that TEM observations should be made to measure the effect of machining condition on lath spacing for all machining conditions before and after fatigue testing.

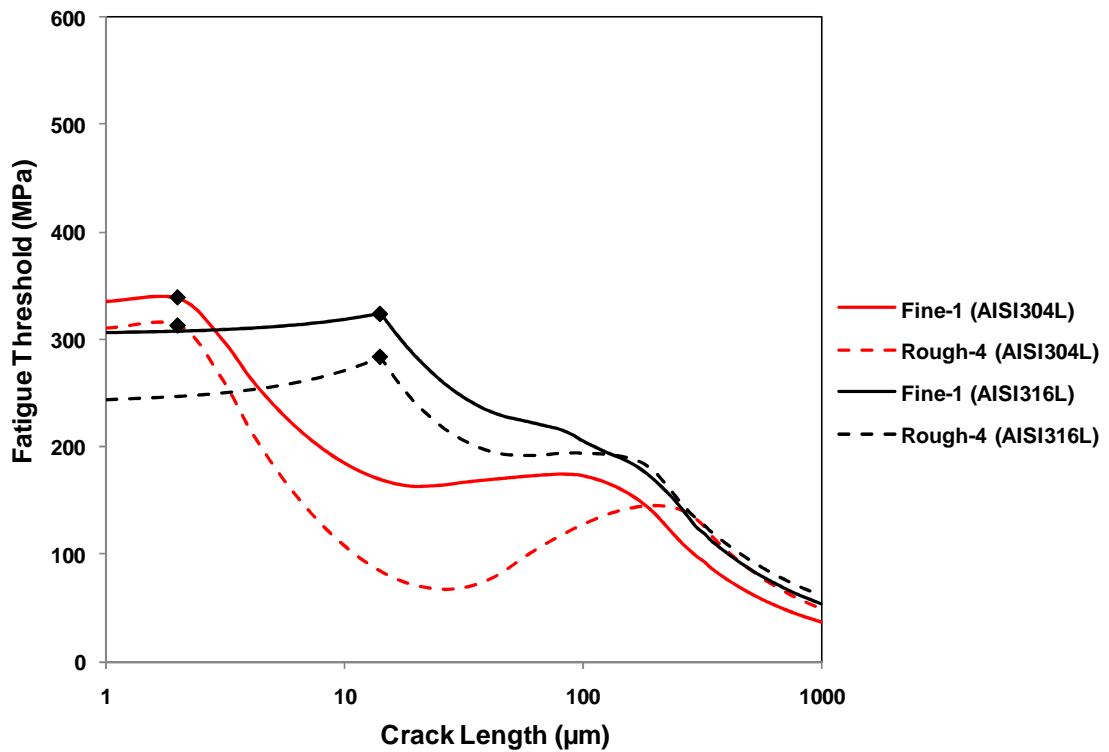


Figure 5- 33: Effect of residual stress relaxation for machining conditions using relaxation factor of 0.5, intrinsic fatigue limit (increased by 5% for fine-1 machined and by 30% for rough-4 machined condition), refined barrier spacing (0.5 µm).

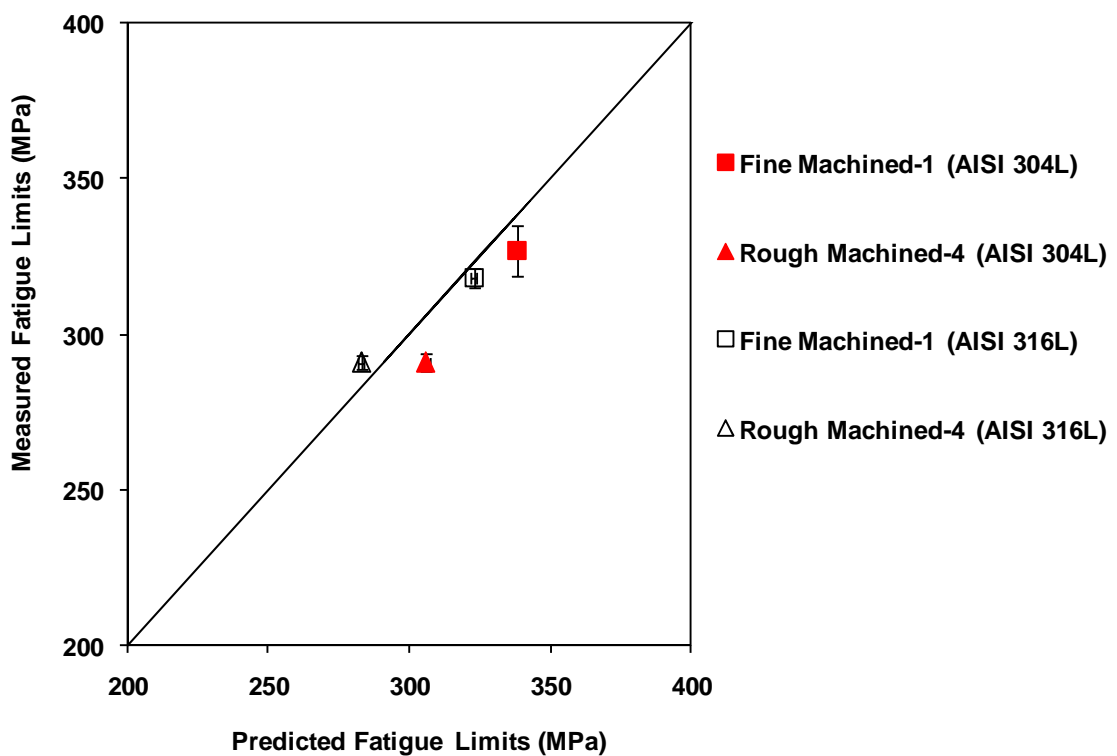


Figure 5- 34: Predicted fatigue limit in comparison with the measured fatigue limit (new model) for machining conditions for AISI 304L and AISI 316L.

**Summary:**

A development of the N-R model, which takes into account the effect of parameters which were neglected in the N-R model for austenitic stainless steels such as martensite laths spacing (different between fine and rough machining) and deformation twins spacing (different between fine and rough machining) and changes in intrinsic fatigue resistance can predict the behaviour observed.

**5.13. Annealed Microstructure**

Annealing at 900°C for 10 minutes had a significant effect on the grain size near the machined surface in AISI 304L as shown in Figure 4- 28 and Figure 4- 29 and in AISI 316L as shown in Figure 4- 33 and Figure 4- 34.

In AISI 304L, fine grain size (~3 µm) was observed within a depth of about 30 µm and 40 µm from the surface in fine machined & annealed (2) and rough machined & annealed (5) specimens, respectively.

In AISI 316L, similar fine grain size (~3 µm) was observed within a depth of about 10 µm and 50 µm from the surface in fine machined & annealed (2) and rough machined & annealed (5) specimens, respectively.

In AISI 304L, as shown in Table 4- 8, the fatigue limit of the fine machined & annealed (2) was 2% higher than the intrinsic fatigue limit (3). Similar fatigue limits can be seen in rough machined & annealed (5) and the intrinsic fatigue limit (3).

AISI 304L show that there is no effect of surface roughness on the fatigue limit as discussed earlier. Also, the grain size near the surface in annealed samples is about 3 µm. By employing these data in the model (i.e. ignoring the surface roughness and use of the observed grain size after annealing as barrier spacing) it can be seen that the prediction of fatigue limits for both conditions are in good agreement with the observations (Figure 5- 35). By changing the barrier spacing to a size similar to the martensite packets size (0.5 µm), the model shows good agreement for both fatigue limits and the arrested crack depth with the experimental observations (Figure 5- 36). This shows the presence of martensite, which is associated with the small grain size at the surface produced as result of annealing in these specimens after fatigue. The tendency for martensite formation at surfaces is reported to be sensitive to grain size. For



instance, coarse grains (of the order of 60 $\mu$ m) adjacent to a free surface in 304 austenitic stainless steel have been shown to develop less martensite when strained, in comparison to finer grain size [130]. The martensite act as a strengthening phase as reported from neutron diffraction studies of martensite in austenitic steels [127].

This is supported by the implications of X-ray diffraction patterns of fine machined & annealed (2) and rough machined & annealed (5) where both conditions have more martensite than the electropolished specimen by comparing the ratios between austenite peak and martensite peak as shown in Table 4- 9.

In AISI 316, it can be seen from the data in Table 4- 8 that the fatigue limit in fine machined & annealed (2) is lower than the intrinsic fatigue limit (electropolished-3) by 5%. Rough machined & annealed (5) shows a lower fatigue limit (about 13% lower than the intrinsic fatigue limit). This could be attributed to the presence of the cracks that machining produced on the surface. So, the initiation should be easier. Also, the recrystallization at the surface due to the annealing may resist the twinning.

By using these data (i.e. ignoring the surface roughness and the observed grain size near the surface was employed as barrier spacing) in the model, the predictions of fatigue limit and the arrested crack depth show good agreement with the experimental observations for fine machined & annealed (2). The prediction for rough machined & annealed (5) shows higher fatigue limit (about 13% higher than the experimental observation) as shown in Figure 5- 35. By comparing the fatigue limits obtained by fatigue tests with the model predictions, it can be seen that there are good agreements in fine machined & annealed (2) and rough machined & annealed (5) for AISI 304L (Figure 5- 37).

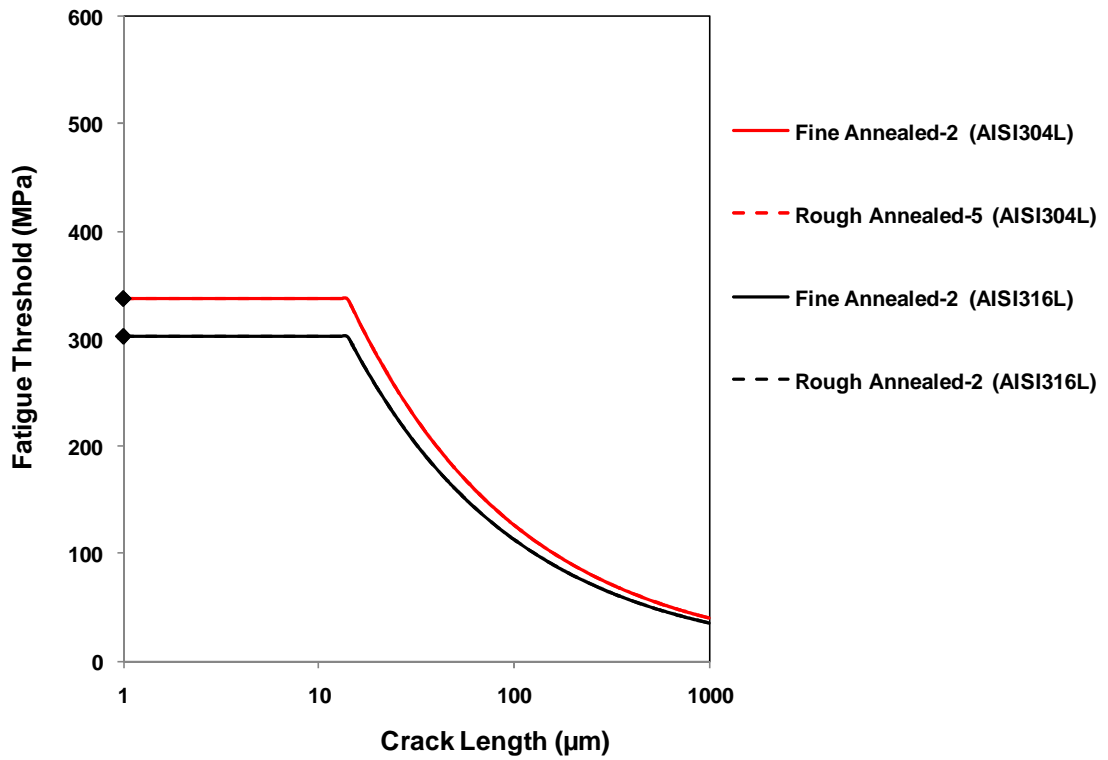


Figure 5- 35: Effect of annealed microstructure on the threshold stress in AISI 304L and AISI 316L (neglecting surface roughness effect and using barrier spacing of observed grain size ( $3 \mu\text{m}$ )).

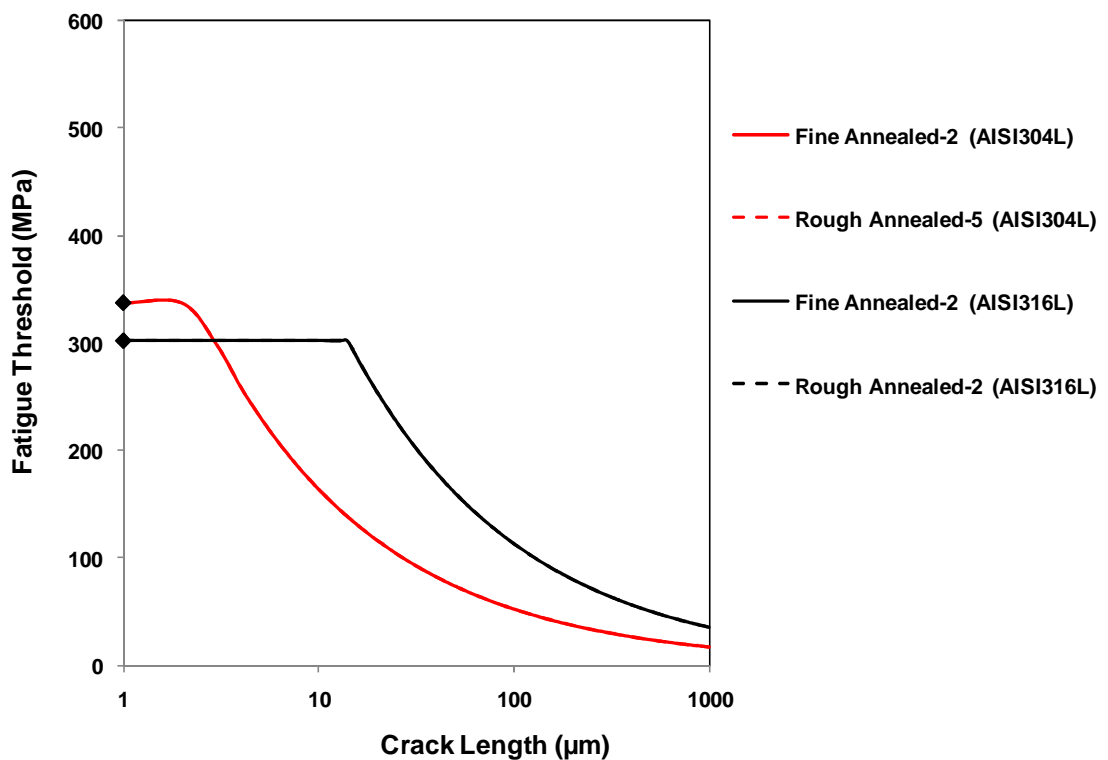


Figure 5- 36: Effect of annealed microstructure on the threshold stress in AISI 304L and AISI 316L (neglecting surface roughness effect and using barrier spacing of observed martensite packet size ( $0.5 \mu\text{m}$ ) for AISI 304L and observed twin spacing ( $3 \mu\text{m}$ ) for AISI 316L).

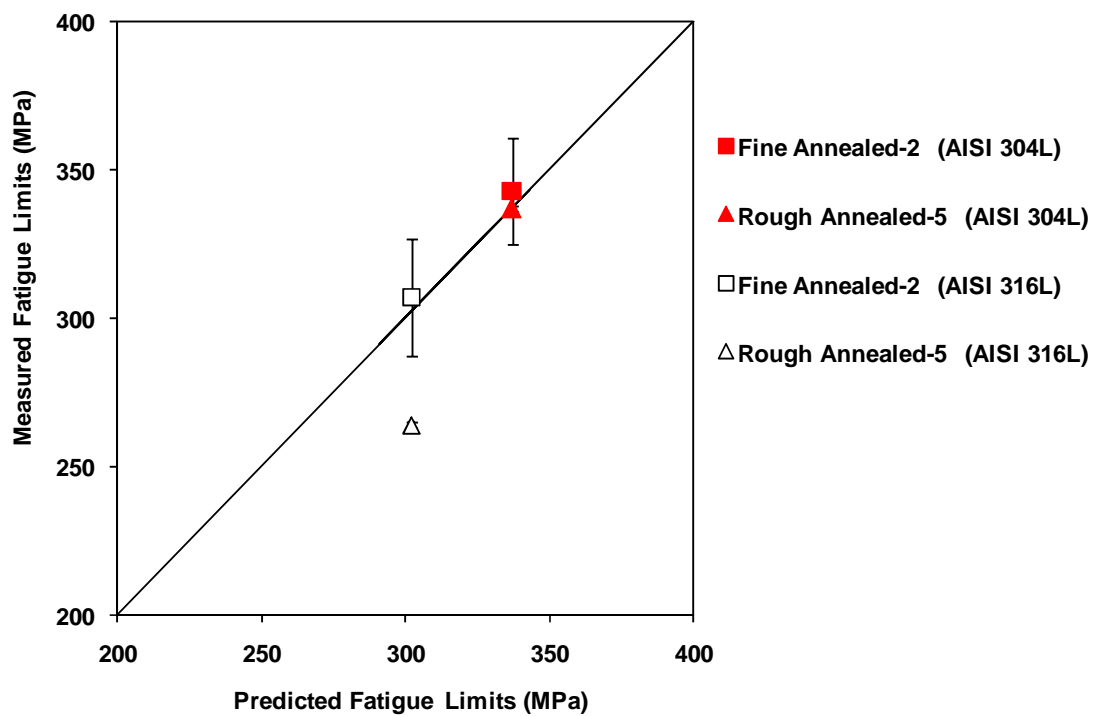


Figure 5- 37: Predicted fatigue limit in comparison with the measured fatigue limit (new model) for annealed microstructure for AISI 304L and AISI 316L.

**Summary:**

Annealed microstructures for AISI 304L show good agreement with the simple model for both machining conditions. In AISI 316L, only fine machined & annealed (2) condition show good agreement with the model but the rough machined & annealed (5) show disagreement.

# Chapter 6

## *Conclusion and Further Work*

### **6.1. Summary of experimental work**

In order to design fatigue specimens of austenitic stainless steels with controlled surface characteristics, for the purpose of investigating the effects of machining-induced residual stresses and roughness on fatigue behaviour, thirty six cylindrical specimens (6.35 mm diameter and 20 mm length) of AISI 304L/AISI 316L were prepared using a numerically controlled lathe. Three final cutting conditions (spindle speed, feed rate and cutting depth) of the lathe were employed to produce three specimens for each condition. The final cutting conditions were selected, based on the response surface model, which was developed in the previous work to obtain the desired residual stress and surface roughness.

The selected conditions were examined in detail, to establish the residual stress profile with depth and the effects of annealing and electropolishing. The data obtained were used to select the fine and rough machining parameters used to prepare fatigue specimens.

Surface roughnesses of the cylindrical samples were obtained by use of a Talysurf stylus profilometer. Additionally, surface roughness of a set of four cylindrical specimens was assessed by optical profilometry. The hardness was measured using an Instron indentation instrument.

The residual stresses were characterised by means of residual strain measurement using an x-ray diffractometer (Proto iXRD); the residual stresses were calculated by the XRD's software. Residual stress measurements were obtained in two directions; at axial direction and circumferential direction. Depth profiles of residual stress were obtained using successive electropolishing at intervals of approximately 30 $\mu$ m.

Two sets of fatigue specimens were prepared by a numerically controlled lathe (fine and rough condition) for AISI 304L and AISI 316L. These sets of fatigue samples were sorted into six conditions for both materials. Namely, fine machined (1), fine machined

& annealed (2), electropolished annealed (3), electropolished (not annealed), rough machined (4), rough machined & annealed (5).

For both materials, sets of fatigue specimens (fine and rough machined specimens) were annealed at 900°C for 10 minutes under an argon gas flow. Other specimen sets (fine machined specimens) were similarly annealed and then electrochemically polished to remove approximately 150 µm from the diameter.

The fatigue limits for each condition were determined using a rotating-bending machine by means of the staircase method. After fatigue testing, the surfaces and near surface microstructures were characterised by scanning electron microscope (SEM), electron backscatter diffraction (EBSD), transition electron microscope (TEM), hardness testing and X-ray diffraction for residual stress measurement.

## **6.2. Summary of research Observations**

A summary of the most significant research results, and their significance, are presented here.

### **6.2.1. Surface and Microstructure Characterisation**

- ❖ The axial stresses vary significantly between machined specimens within a surface layer of approximately 100 µm further than this, the differences are less significant, and there are no significant residual stresses beyond a distance of approximately 300 µm from the surface. The circumferential residual stresses are tensile at the surface for all machined specimens, but show similar trends to the axial stresses for both materials.
- ❖ Rough machining on a lathe, using a high feed rate, introduced significant tensile residual stress at the machined surface whereas fine machining gave a negligible stress. Both rough and fine machining cause significant sub-surface compressive residual stresses. The residual stresses were completely relieved at 900°C for 10min.
- ❖ The full width at half the maximum peak (FWHM) obtained by X-ray diffraction showed that measurable peak broadening occurs within less than approximately 200 µm, 100 µm and 100 µm of the surface in tensile stress, compressive stress

and zero stress specimens, respectively. This is indicated that the machining in austenitic stainless steels causes the development of a plastically strained microstructure by increasing the density of slip bands.

- ❖ The surface microhardness is not significantly affected by variation in machining parameters. This surface hardened layer was removed by electropolishing or annealing at 900°C. Annealing had significant effect on the grains in the vicinity of the surface, causing grain refinement, relative to the bulk microstructure.
- ❖ The XRD patterns of fine machined (1) and rough machined (4) specimens show the existence of FCC austenite phase and no martensite after machining.

### 6.2.2. *Fatigue Test -Results*

- ❖ Surface residual stress is the most significant parameter which determines the effects of surface preparation on the fatigue limit of type AISI 304L austenitic stainless steel. The fatigue limit of the AISI 316L shows much less sensitivity to the surface stress. Tensile stress close to the surface reduces the fatigue limit.
- ❖ The range of surface roughness developed by machining has no significant effect. After fatigue testing there is a relaxation in subsurface stresses but the surface stresses are not significantly affected.
- ❖ The surface cracks were found to be in the root of the machining marks and perpendicular to the stress axis. The fracture process in all fractured specimens; was dominated by the propagation of a single crack.
- ❖ In both materials, the depth of the observed cracks in run-out samples was less than the depth of plastic strain zone developed close to the surface by fatigue as shown by EBSD.
- ❖ For both materials, the depth of these cracks was less than the depth of the plastically strained zone which developed by machining as supported by X-ray diffraction. For both materials, the depth of cracking has no relation to the position of the compressive residual stress peak.

- ❖ TEM and X-ray diffraction (XRD) findings show the formation of strain induced martensite with fatigue cycling in AISI 304L whereas none are observed in AISI 316L. EBSD shows that twins, developed by fatigue, were observed in both materials.

### ***6.2.3. Short Fatigue Crack Model of Austenitic Stainless Steels***

- ❖ The N-R model for short fatigue crack propagation has been implemented for austenitic stainless steels (AISI 304L and AISI 316L).
- ❖ The fatigue limits predicted by the fatigue model were compared with the results of the fatigue tests obtained by staircase method. There is no agreement between the prediction and observations.
- ❖ A development of the N-R model, which takes into account the effect of parameters that were neglected in the N-R model such as martensite lath spacing and deformation twins spacing, can predict the observed effects of surface machining on the fatigue limit.

### 6.3. Conclusions

From the research observations in this thesis the following conclusions can be drawn:

- i The surface residual stress is the most significant parameter that determines the effects of surface preparation on the fatigue limit of type 304 austenitic stainless steel. While, in AISI 316 L the fatigue limit shows much less sensitivity to the surface stress. There is a relaxation in subsurface stresses but no significant relaxation in the surface stresses. Tensile stress close to the surface reduces the fatigue limit
- ii No martensite was observed after machining in both materials. Fatigue cycling produces martensite in AISI 304L, whereas none was observed in AISI 316L. In AISI 304L, martensite packets, developed by fatigue, were observed to arrest the crack nuclei in run-out ( $>10^7$  cycles) fatigue tests.
- iii Twins, developed by fatigue, were observed in both materials. In AISI 316L, crack nuclei in run-out ( $>10^7$  cycles) fatigue tests were observed to arrest at twins, developed by fatigue due to the large value of twist and tilt angles between the crack and the active slip planes in the twin.
- iv The effects of surface machining on the fatigue limit in AISI 304L can be predicted if some parameters such as martensite lath spacing and deformation twin spacing and change in intrinsic fatigue resistance taking into the account in the development of the N-R model. Using these parameters to develop the N-R model not work in AISI 316L.

### 6.4. Further Work

The following would be essential to provide enough characterisations of short fatigue crack in fatigue austenitic stainless steels with various controlled surface conditions, obtained by machining and also to develop successful models to predict the effect of the surface finish on the fatigue limit.

Further investigations of the effects of surface preparation on fatigue by producing another machining condition (compressive residual stress) using the response surface model should confirm whether the model predictions are valid for a wide range of



surface conditions. Full characterisation of surface and microstructure of this condition before and after fatigue testing should be carried out.

SEM should be used to observe the fracture surfaces of fatigued specimens and arrested cracks nuclei on the surface of run-out ( $>10^7$  cycles) fatigue tests and EBSD should be used to study the microstructure close to the surface and observe the crack interaction with the deformed microstructure.

In this work the majority of the EBSD analyses were performed with indexing of the backscatter diffraction patterns using face-centre cubic (fcc) parameters. In order to check the availability of martensite phase, both fcc and body centred cubic (bcc) parameters should be set during the data collection.

The microstructures that are developed in AISI 304L by machining and high cycle fatigue deformation creates a refined microstructure where new interfaces appear which interfere with crack propagation. The N-R model is based on spacing and strength of those interfaces. Due to the lack of data on the strength of those interfaces, the model assumes the only important thing is the spacing.

The parameters that have not been measured in this work such as martensite laths spacing in AISI 304L (different between fine and rough machining) and deformation twins spacing for both materials (different between fine and rough machining) could make the model work more successfully.

This would require characterisation by transmission electron microscopy (TEM). This work would increase confidence in the understanding of the mechanism and provide the information which could make the model work successfully. So, intensive TEM study for all surface conditions after machining and after fatigue test should be carried out. This can be done by preparing TEM samples from the surface using FIB technique for electropolished sample, fine machined samples and rough machined samples (before and after fatigue test).

If the model works successfully then the effect of surface machining on the fatigue limit of austenitic stainless steels can be estimated using the intrinsic fatigue limit for annealed/electropolished samples and the measured surface residual stress or the estimated residual stress using a response surface empirical model.

## References

1. Karlsson, *Stainless Steels Past, Present and Future*. 2004.
2. H. K. D. H. Bhadeshia; R. W. K. Honeycombe, *Steels Microstructure and Properties*. Second ed. 2003.
3. M. Kuroda.; T. J Marrow; A. H. Sherry. *Effect of surface finish on the fatigue limit in austenitic stainless steels*. in *16th European Conference on Fracture*. 2006. Turino: Springer.
4. M. Kuroda.; T. J Marrow, *Modelling the effects of surface finish on fatigue limit in austenitic stainless steels*. *Fatigue Fract Engng Mater Struct* 2008. **31**: p. 1–19.
5. K. J. Miller, *The behaviour of short fatigue cracks and their initiation part II - a general summary* *Fatigue Fract Engng Mater Struct*, 1987. **10** p. 93-113.
6. K. J. Miller, *The short crack problem*. *Fatigue Engng Mater Struct*, 1982. **5** p. 223-232.
7. Hussain. K. and De Los Rios, E.R., *Short fatigue crack behaviour and analytical models: a review*. *Eng Fract Mech*, 1997. **58** p. 327-354.
8. Masatoshi Kuroda, T.J.M., *Preparation of Fatigue specimens With Controlled Surface Characteristics*. 2006.
9. Béla Leffler, *Stainless steels and their properties*. 2005.
10. P. Marshal, *Austenitic Stainless Steels, Microstructure and Mechanical Properties*. 1984.
11. B.S, *British Standard*. BSCN 10088-1. 2005.
12. Mars G. Fontana, *Corrosion Engineering*. Third ed. 1986.
13. Materials, A.t.Z.o., *Stainless Steel - Mechanical Properties*. <http://www.azom.com/details.asp?ArticleID=1181>, 2002.
14. Hamilton F. G., S.S., Pedro d. L., Ricardo P., Válder N., Paulo M., Sérgio S. M., *Deformation Induced Martensite in an AISI 301LN Stainless Steel: Characterization and Influence on Pitting Corrosion Resistance*. *Materials Research*, 2007. **10**(4): p. 359-366.
15. Nishida., S.-I., *Failure Analysis in Engineering Applications*. 1992.
16. R.Stephens; A. Fatemi, R.R.S.H.O.F., *Metal Fatigue in Engineering*. Second ed. 2001.
17. J. Shigley; M. Charles; B. Richard, *Mechanical Engineering Design*. 2004.
18. S. Suresh, *Fatigue of Materials*. Second ed. 2001.
19. William D. Callister, J., *Materials Science and Engineering an Introduction*. Third ed. 1994.
20. Yung; Li; Lee; P. Jwo; H. Richard; B. Mark, *Fatigue Testing and Analysis theory and Practice 2005: Ed. Elsevier Inc*.
21. J. Polak; P. Liskutin, *Nucleation and short crack growth in fatigued polycrystalline copper* *Fatigue Fract. Engng Muter. Struct.* , 1990. **13**(2): p. 119-133.
22. U. Krupp, *Fatigue Crack Propagation in Metals and Alloys: Microstructural Aspects and Modelling Concepts*. 2007.
23. J. Polak; A. Vasek; K. Obrtlík, *Fatigue damage in two step loading of 316L Steel. Part I: Evolution of persistent slip bands*. *Fatigue Fract. Eng. Mater. Struct.*, 1996. **19**: p. 147–155.
24. J. Polak; J. Man; K. Obrtlík, *Atomic force microscopy study of the early fatigue damage*. *Mater. Sci. Forum*, 2005. **482**: p. 45–50.
25. J. Polak; J. Man; K. Obrtlík, *AFM evidence of surface relief formation and models of fatigue crack nucleation*. *Int. J. Fatigue*, 2003. **25**: p. 1027–1036.

26. J. Polaka; J. Mana; T. Vystavel; M. Petrenec, *The shape of extrusions and intrusions and initiation of stage I fatigue cracks. Materials Science and Engineering A*, 2009. **A 517**: p. 204–211.
27. J. Man; K. Obrtlík; C. Blochwitz; J. Polak, *Atomic force microscopy of surface relief topography in individual grains of fatigued 316L austenitic stainless steel. Acta Mater*, 2002. **50**: p. 3767–3780.
28. J. Man; K. Obrtlík; J. Polak, *Study of surface relief evolution in fatigued 316L austenitic stainless steel by AFM. Mater. Sci. Eng. A*, 2003. **351**: p. 123–132.
29. J. Man; M. Petrenec; K. Obrtlík; J. Polak, *AFM and TEM study of cyclic slip localization in fatigued ferritic X10CrAl24 stainless steel. Acta Mater.*, 2004. **52**: p. 5551–5561.
30. P. Villechaise; L. Sabatier; J. C. Girard, *On slip band features and crack initiation in fatigued 316L austenitic stainless steel. Part I: Analysis by electron backscattered diffraction and atomic force microscopy. Mater. Sci. Eng. A*, 2002. **323**: p. 377–385.
31. J. Lankford, *The growth of small fatigue cracks in 7075-T6 Aluminium. Fatigue Engng Mater Struct*, 1982. **5**: p. 233.
32. H.T. Pang; P.A.S. Reed, *Effects of Microstructure on room temperature fatigue crack initiation and short crack Propagation in Udimet 720Li Ni-Base Superalloy. International Journal of Fatigue*, 2008. **30**((10-11)): p. 2009-2020.
33. S. Andrews; H. Sehitoglu, *A computer model for fatigue crack growth from rough surfaces. Int. J. Fatigue*, 2000. **22**: p. 619.
34. F. Bahram; B. George; G. James, *Fatigue and fracture mechanics of high risk parts 1997*.
35. W. M. Wolfgang, *Planning and Evaluation of Fatigue Tests. ASM Handbook*, 1996. **19, Fatigue And Fracture**.
36. T.J. Marrow, M.K., *Surface Preparation Effects on Fatigue. Report to MoD*, 2006. **Final Report**.
37. I. Altenberger; B. U. Scholtes; H. Martin; H. Oettel, *Cyclic deformation and near surface microstructures of shot peened or deep rolled austenitic stainless steel AISI 304. Material Science and Engineering A*, 1999. **264**: p. 1-16.
38. M. Topic a, R.B.T., C. Allen *The fatigue behaviour of metastable (AISI-304) austenitic stainless steel wires. International Journal of Fatigue*, 2007. **29**: p. 656-665.
39. C. Müller-Bollenhagen, M.Z., H.-J. Christ, *Very high cycle fatigue behaviour of austenitic stainless steel and the effect of strain-induced martensite. International Journal of Fatigue*, 2009. **xx**: p. xxx-xxx.
40. K. Masaki; Y. Ochi; T. Matsumura, *Initiation and propagation behaviour of fatigue cracks in hard shot pened type 316L steel in high cycle fatigue. Fatigue fract. Engng. Mater. Struct. , 2004. 27: p. 1137-1145.*
41. Duyi Ye , S.M., Noburo Nagashima, Naoyuki Suzuki,, *The low-cycle fatigue, deformation and final fracture behaviour of an austenitic stainless steel. Materials Science and Engineering A 2006. 415: p. 104–117.*
42. S. Ganesh; S. Raman; K. A. Padmanabhan, *Effect of prior cold work on the roomtemperature low-cycle fatigue behaviour of AISI 304LN stainless steel. Int. J. Fatigue ,1996. 18, No. 2: p. 71-79.*
43. S. Pearson, *Initiation of Fatigue Cracks in Commercial Aluminium Alloys and The Subsequent Propagation of Very Short Cracks. . Engineering Fracture Mechanics*, 1975. **7**: p. 235-247.
44. J. Stolarz, *Multicracking in low cycle fatigue: A surface phenomenon Mater. Sci. Eng. A*, 1997. **A234-236**: p. 861.

45. C. Kaynak; A. Ankara; T. J. Baker, *Effects of short cracks on fatigue life calculations. int. J. Fatigue*, 1996. **18**(1): p. 25-31.
46. S. Suresh; R. O. Ritchie, *Propagation of short fatigue cracks. International Metals Reviews*, 1984. **29**: p. 445.
47. F. Ellyin, *Fatigue damage, Crack growth and Life prediction*. 1997.
48. A. F. Blom; A. Hedlund; W. Zhao; A. Fathulla; B. Weiss; R. Stickler, *Short fatigue crack growth in Al2024 and Al 7475. Proc. The behaviour of short fatigue cracks. Miller, K.J.; de Los Rios, E.R. (Eds.), ESIS, London (1986) 37.*
49. A. Navarro; E. R. de los Rios, *Short and long fatigue crack growth: A unified model. Philosophical Magazine A*, 1988. **57**: p. 15.
50. U. Krupp; W. Floer; J. Lei; Y. M. Hu; H. Christ; A. Schick; C. Fritzen, *Mechanisms of short fatigue crack initiation and propagation in  $\beta$ -Ti alloy. Philosophical Magazine A*, 2002. **82**: p. 3321.
51. S. Zaefferer; J. Kuo; Z. Zhao; M. Winning; D. Raabe, *The influence of the grain boundary misorientation on the plastic deformation of aluminum bicrystals. Acta Mater*, 2003. **51**: p. 4719.
52. T. Zhai; X. P. Jiang; J. X. Li; M. D. Garratt; G. H. Bray, *The grain boundary geometry for optimum resistance to growth of short fatigue cracks in high strength Al alloys. International Journal of Fatigue*, 2005. **27**: p. 1202.
53. T. Zhai; A. J. Wilkinson; J. W. Martin, *A crystallographic mechanism for fatigue crack propagation through grain boundaries Acta Materialia* 2000. **48**: p. 4917.
54. K. Tokaji; T. Ogawa. *The growth behaviour of microstructurally small fatigue cracks in metals in Proc. short fatigue cracks, ESIS 1, K.J. Miller, E.R. de Los Rios (Eds), Mechanical Engineering Publications. 1992. London.*
55. A. Turnbull; E. R. de los Rios, *The effect of grain size on fatigue crack growth in an aluminium magnesium alloy Fatigue Engng Mater Struct*, 1995. **18**: p. 1355.
56. K. Tokaji; T. Ogawa; K. Ohya, *The effect of grain size on small fatigue crack growth in pure titanium. Fatigue*, 1994. **16**: p. 571-578.
57. Y. Zhong; F. Xiao; J. Zhang; Y. Shan; W. Wang; K. Yang, *In situ TEM study of the effect of M/A films at grain boundaries on crack propagation in an ultra-fine acicular ferrite pipeline steel. Acta Mater.*, 2006. **54**: p. 435.
58. N. Y. Tang, *In situ fracture experiment on a duplex stainless steel Mater. Sci. Eng. A*, 1989. **117**: p. 157-165.
59. D. Taylor, *Fatigue thresholds: their applicability to engineering situations Int J Fatigue*, 1988. **10**: p. 67-79.
60. C. H. Wang; K. J. Miller, *Short fatigue crack growth under mean stress, uniaxial loading. Fatigue Fract. Engng Mater. Struct.*, 1993. **16**: p. 181-198.
61. Y. Nakai; K. Ohji, *Predictions of growth rate and closure of short fatigue cracks. In: ESIS 13 (Edited by K J Miller and E R de los Rios), Mechanical Engineering Publications, London, 1992: p. 169-189.*
62. K. J. Miller. *Initiation and growth rates of short fatigue cracks. in Eshelby Memorial Conference. 1984. Fundamentals of Deformation & Fracture Cambridge University Press, 1984. p. 477-500.*
63. Hussain. K, D.L.R., E.R. and A Navarro, *A two-stage micromechanics model for short fatigue cracks Eng Fract Mech*, 1993. **44** p. 425-436.
64. E. R. De los Rios; H. J. Mohamed; K. J. Miller, *A micro-mechanics analysis for short fatigue crack growth. Fatigue Fract Engng Mater Struct*, 1985. **8**: p. 49-63.
65. E. R. De los Rios; P. Mercier; B. M. El-Sehily, *Short crack growth behaviour under variable amplitude loading of shot peened surface. Fatigue Fract. Engng Mater. Struct.*, 1996. **19**: p. 175-184.

66. H. Kitagawa; S. Takahashi. *Applicability of fracture mechanics to very small cracks or the cracks in the early stage.* in *Proceedings 2nd International Conference on Mechanical Behaviour of Materials.* 1976. Boston, 627-631.
67. K. Tanaka; T. Mura, *A Dislocation Model for Fatigue Crack Initiation.* *Journal of Applied Mechanics* 1981. **48**(97-103).
68. S. Taira; K. Tanaka; Y. Nakai, *A Model of Crack Tip Slip Band Blocked by Grain Boundary.* *MECH. RES. COMM.*, 1978. **5**: p. 375-381.
69. K. Tanaka; A. Akiniwa; Y. Nakai; R. P. Wei, *Modelling of Small Fatigue Crack Growth Interacting with Grain boundary.* *Engineering Fracture Mechanics* 1986. **24**, **No. 6**: p. 803-819.
70. L. Grabowski; J. E. KING, *Modelling short crack growth behaviour in nickel base superalloys.* *Fatigue Fract. Engng Mater. Struct.* , 1992. **15**, **No. 6** p. 595-606.
71. B. A. Bilby; A. H. Cottrell; K. H. Swinden, *The spread of plastic yield from a notch.* . *Proc. R. Soc. Lond. A, Math Phys. Sci.* , 1963. **272**: p. 304-314.
72. A. Navarro; E. R. de los Rios, *A microstructurally short fatigue crack growth equation.* *Fatigue Fract. Engng Mater. Struct.*, 1988. **11**: p. 383-396.
73. A. Navarro; E. R. de los Rios, *Fatigue crack growth modeling by successive blocking of dislocations.* *Proc. R. Soc. Lond. A, Math Phys. Sci.*, 1992. **437**: p. 375-390.
74. E. R. De los Rios; M. Trull; A. Levers, *Modeling fatigue crack growth in shot-peened components of Al 2024-T351.* *Fatigue Fract. Engng Mater. Struct.* , 2000. **23**: p. 709-716.
75. S. Curtis; E.R. de los Rios, C.A.R., A. Levers. , *Analysis of the effects of controlled shot peening on fatigue damage of high strength aluminium alloys.* *International Journal of Fatigue* 2003. **25**: p. 59-66.
76. C. A. Rodopoulos; S.A. Curtis; E.R. de los Rios; J. SolisRomero, *Optimisation of the fatigue resistance of 2024-T351 aluminium alloys by controlled shot peening-methodology, results and analysis.* . *International Journal of Fatigue* . 2004. **26**: p. 849-856.
77. C. Vallellano; M. R. Mariscal; A. Navarro; J. Dominguez, *A micromechanical approach to fatigue in small notches.* *Fatigue Fract. Engng Mater. Struct.*, 2005. **28**: p. 1035-1045.
78. C. Vallellano; A. Navarro; J. Dominguez, *Fatigue crack growth threshold conditions at notches part II: generalization and application to experimental results* *Fatigue Fract. Engng Mater. Struct.* , 2000. **23**: p. 123-128.
79. C. Vallellano; A. Navarro; J. Dominguez, *Fatigue crack growth threshold conditions at notches part I: theory.* *Fatigue Fract. Engng Mater. Struct.*, 2000. **23**: p. 113-121.
80. Curtis S., E.R.d.l.R., C.A. Rodopoulos, A. Levers. , *Analysis of the effects of controlled shot peening on fatigue damage of high strength aluminium alloys.* *International Journal of Fatigue* 2003. **25**: p. 59-66.
81. C. Vallellano; A. Navarro; F. Garcia; J. Dominguez, *On the estimation of microstructural effects in the near-threshold fatigue of small cracks.* *The Journal of Strain Analysis for Engineering Design*, 2008. **43**, **Number 5** p. 337-347.
82. Curtis S., S., J., De los Rios, E. R., Rodopoulos, C. A. and Levers, A., *Predicting the interfaces between fatigue crack growth regimes in 7150-T651 aluminium alloy using the fatigue damage map.* *Mater. Sci. Eng. A*, 2003. **344**: p. 79-85.
83. Y. Murakami; M. Endo. *Effects of hardness and crack geometries on  $\Delta K_{th}$  of small cracks emanating from small defects.* in *EGF Pub.1* (Edited by K J Miller

- and E R de los Rios), *Mechanical Engineering Publications*, London, 1986 :P. 275-293.
84. O. Tugrul; K. Tsu; E. Hsu, *Effects of cutting edge geometry, workpiece hardness, feed rate and cutting speed on surface roughness and forces in finish turning of hardened AISI H13 steel* *Int J. Adv. Manuf. Technol.*, 2005. **25**: p. 262–269.
  85. D. Patrik; G. Fredrik; J. Michael, *The influence of rake angle, cutting feed and cutting depth on residual stresses in hard turning*. *Journal of Materials Processing Technology* 2004. **147** p. 181–184.
  86. R. G. Bruce; W. K. Dalton; J. E. Neely; R. R. Kibbe, *Modern Materials and Manufacturing Processes*. Third ed. 2004.
  87. John R. Walker, *Machining Fundamentals*. 2004: The Goodheart-Willcox Company, Inc.
  88. *Mechanical Surface Treatment*. *Encyclopedia of Materials: Science and Technology*. 2001. 5253-5262.
  89. Tugrul Ozel, T.-K.H., Erol Zeren., *Effects of cutting edge geometry, workpiece hardness, feed rate and cutting speed on surface roughness and forces in finish turning of hardened AISI H13 steel*. *Int J Adv Manuf Technol.*, 2005. **25**: p. 262-269.
  90. Kuroda M., T.J., *Marrow Preparation of Fatigue specimens With Controlled Surface Characteristics*. *Journal of Materials Processing Technology* 2006.**203**, 1-3, p. 396-403.
  91. J. Michael; D. Patrik; G. Fredrik, *Cutting speed influence on surface integrity of hard turned bainite steel*. *Journal of Materials Processing Technology* 2002. **128**: p. 318–323.
  92. J. Ataollah; R. Ulfried; J. Wilfried, *The effect of machining on the surface integrity and fatigue life*. *Int. J. Fatigue*, 2008. **30**: p. 2050–2055.
  93. W. Bouzid Sai, N.B., Salah L., *Influence of machining by finishing milling on surface characteristics*. *International Journal of Machine Tools & Manufacture* 2001. **41** p. 443–450.
  94. S. Karina; F. Wisley; S. Ernani, *Influence of Machining Parameters on Fatigue Endurance Limit of AISI 4140 Steel*. *J. Braz. Soc. Mech. Sci. & Eng.*, 2008. **30 no.1**
  95. K. N. Shapiro, *the effect of residual stress and surface condition on the stress corrosion cracking of austenitic stainless steels*, in *School of Materials*. 2008, *The University of Manchester: Manchester*.
  96. J. C. Outeiro; A. M. Dias; J. L. Lebrun; V. P. Astakhov, *Machining residual stress in AISI 316L steel and their correlation with the cutting parameters*. *Machining Science and Technology*, 2002. **6**(2): p. 251-270.
  97. D.Y. Jang a, T.R.W., K.J. Kozaczek, CR. Hubbard, O.B. Cavin., *Surface residual stresses in machined austenitic stainless steel*. *Wear*, 1996. **194**: p. 168-173.
  98. Saoubi M., R.O., J.C.; Changeux, B.; Lebrun, J.L.; Dias, A.M., *Residual stress analysis in orthogonal machining of standard and resulfurized AISI 316L steels*. *J. Mater. Process. Technol.*, 1999. **96 (1-3)**: p. 225–233.
  99. Sasahara Hiroyuki, *The effect on fatigue life of residual stress and surface hardness resulting from different cutting conditions of 0.45%C steel*. *International Journal of Machine Tools & Manufacture*, 2005. **45**: p. 131–136.
  100. H. Stamm; U. Holzwardth; D. J. Boermanf; Dos Santoms; A. Olchini; R. Zausch, *Effect of laser surface treatment on high cycle fatigue of AISI 316L stainless steel fatigue fract Engng Mater Struct.*, 1996. **19**(8): p. 985-995.

101. H.W. Zhang; Z.K. Heib; G. Liu; J. Lu; K. Lu, Formation of nanostructured surface layer on AISI 304 stainless steel by means of surface mechanical attrition treatment *Acta Mater*, 2003. **51**: p. 1871–1881.
102. W. P. Tong, N.R.T., Z. B. Wang, J. Lu, K. Lu Nitriding Iron at Lower Temperatures *Science*, 2003. **299**: p. 686 - 688.
103. Jack Cazes, *Analytical Instrumentation Handbook*. Third ed. 2005.
104. ASTM, *Standard Test Methods for Tension Testing of Metallic Materials*. ASTM International, 2004.
105. R.L. Higginson, C.M.S., *Worked Examples in Quantitative Metallography* 2003.
106. Z. Tekiner; S. Yesilyurt, Investigation of the cutting parameters depending on process sound during turning of AISI 304 austenitic stainless steel. *Mater. Des.*, 2004. **25**: p. 507–513.
107. I. Korkut; M. Kasap; I. Ciftci; U. Seker, Determination of optimum cutting parameters during machining of AISI 304 austenitic stainless steel. *Mater. Des.*, 2004. **25**: p. 303–305
108. M. Kuroda.; T. J Marrow, Analyses of the effects of surface finish on fatigue limit in austenitic stainless steels by mechanistic modelling. 2006.
109. Model R.R. Moor High Speed Rotating Beam Fatigue Testing Machine (Operating Instructions).
110. M. E. Fitzpatrick; A. T. Fry; P. Holdway; F. A. Kandil; J. Shackleton; L. Suominen, Determination of Residual Stresses by X-ray Diffraction. *Measurement Good Practice Guide No. 52*. 2002.
111. M G Moore, W.P.E., Mathematical correction for stress in removed layers in X-ray diffraction residual stress analysis., *SAE Trans*, 1958. **66** p. 340-345.
112. B. D. Cullity; S.R. Stock, *Elements of X-Ray Diffraction*. Third Edition ed. 2001.
113. F. J. Humphreys, Review Grain and subgrain characterisation by electron backscatter diffraction. *Journal of Material Science*, 2001. **36**: p. 3833 – 3854.
114. J. Adam; Schwartz; Mukul Kumar; L. Brent, *Electron Backscatter diffraction in Materials Science*. 2000.
115. Humphreys, F.J., *Vmap Manual - Orientation Mapping and Quantitative Metallography by EBSD*. Manchester Materials Science Centre, 2001.
116. F. J. Humphreys; I. Brough, High-Resolution Electron Backscatter Diffraction with a Field Emission Gun Scanning Electron Microscope. *Journal of Microscopy*, 1999. **195**: p. 16-19.
117. R. M. Saoubi; L. Ryde, Application of the EBSD technique for the characterisation of deformation zones in metal cutting. *Materials Science and Engineering A* , 2005. **405**: p. 339–349.
118. D. Scott, E.G., *Analytical Characterization of Aluminum, steel, and Superalloys*. 2006.
119. ASTM, *Annual Book of ASTM Standards*. Vol. 01.03. 2005: ASTM. 184-191.
120. Robert E.; Reed-Hill; R. Abbaschian, *Physical Metallurgy Principles*., Third ed.
121. V. Randle and O. Engler, *Introduction to Texture Analysis: Macrotexture, Microtexture and Orientation Mapping*. 2000.
122. F. J. Humphreys; I. Brough, *Vmap Manual - Orientation Mapping and Quantitative Metallography by EBSD*. Manchester Materials Science Centre, 2001.
123. K. Sharvan; W.A Curtin, Crack interaction with microstructure. *September 2007*. **10**(9).
124. E. Robert; R. Abbaschian, *Physical Metallurgy Principles*. Third ed.

125. J.P. Lucas, W.W.G., *Proposed criterion for fatigue threshold: dislocation substructure. Fatigue of Engineering Materials and Structures*, 1983. **6**: p. 271-280.
126. I. Nikitin; I. Altenberger, *Comparison of the fatigue behavior and residual stress stability of laser-shock peened and deep rolled austenitic stainless steel AISI 304 in the temperature range 25–600 °C. Materials Science and Engineering A* 2007. **465** p. 176–182.
127. K. Spencer, J.D.E., K. T. Conlon, M. Veron, Y. Brechet., *Strengthening via the formation of strain-induced martensite in stainless steels. Machining Science and Engineering A*, 2004. **387-389**: p. 873-881.
128. K. Spencer; M. Veron; K. Yu-Zhang; J. D. Embury, *The strain induced martensite transformation in austenitic stainless steels Part 1 – Influence of temperature and strain history. Materials Science and Technology* 2009. **25**(1).
129. K. Spencer; K. T. Conlon; Y. Bre´chet; J. D. Embury, *The strain induced martensite transformation in austenitic stainless steels Part 2 – Effect of internal stresses on mechanical response. Materials Science and Technology* 2009. **25**(1).
130. Amar K. De, D.C.M., Martin C. Mataya, John G. Speer, David K. Matlok, *Quantitive measurment of deformation-induced martensite in 304 stainless steel by X-ray diffraction. Scripta Materialia*, 2004. **50**: p. 1445-1449.



**Appendix-A***Table A- 1: Fatigue test data of AISI 304L Fine machined (1).*

Sample No.	Minimum Diameter mm	Applied Stress MPa	Fatigue Life Cycle
1	6.285	316	1.00E+07
2	6.442	318	1.00E+07
3	6.25	320	1.00E+07
4	6.382	322	1.00E+07
5	6.295	324	1.00E+07
6	6.362	326	1.00E+07
7	6.333	328	1.26E+06
8	6.355	326	1.00E+07
9	6.265	328	1.00E+07
10	6.29	330	4.49E+05
11	6.295	328	1.00E+07
12	6.38	330	1.00E+07
13	6.353	332	7.39E+05
14	6.325	330	5.39E+05
15	6.416	328	6.61E+05
16	6.39	326	3.55E+05
17	6.392	324	1.00E+07
18	6.414	326	1.00E+07
19	6.425	328	1.00E+07
20	6.427	330	7.73E+05

Table A- 2: Fatigue test data of AISI 304L Fine machined &amp; annealed (2).

Sample No.	Minimum Diameter mm	Applied Stress MPa	Fatigue Life Cycles
1	6.425	316	1.00E+07
2	6.285	318	1.00E+07
3	6.335	320	1.00E+07
4	6.400	322	1.00E+07
5	6.360	324	1.00E+07
6	6.400	326	1.00E+07
7	6.443	328	1.00E+07
8	6.312	330	1.00E+07
9	6.335	332	1.00E+07
10	6.307	334	1.03E+06
11	6.316	332	1.59E+06
12	6.295	330	1.00E+07
13	6.260	332	1.00E+07
14	6.277	334	1.00E+07
15	6.330	336	1.00E+07
16	6.277	338	1.00E+07
17	6.444	340	1.00E+07
18	6.380	342	1.00E+07
19	6.570	344	1.00E+07
20	6.257	346	3.90E+05
21	6.470	344	5.88E+05
22	6.480	342	1.00E+07
23	6.360	344	1.00E+07
24	6.350	346	1.00E+07
25	6.408	348	5.13E+04
26	6.514	346	1.00E+07
27	6.300	348	1.00E+07
28	6.255	350	1.00E+07
29	6.295	352	1.00E+07
30	6.295	354	6.04E+05
31	6.290	352	7.43E+05
32	6.310	350	1.00E+07

Table A- 3: Fatigue test data of AISI 304L Fine machined &amp; annealed Electropolished(3).

Sample No.	Minimum Diameter mm	Applied Stress MPa	Fatigue Life Cycles
1	6.240	330	1.00E+07
2	6.180	332	1.00E+07
3	6.150	334	1.00E+07
4	6.080	336	1.00E+07
5	6.145	338	1.00E+07
6	6.208	340	3.01E+04
7	6.190	338	1.00E+07
8	6.225	340	1.09E+05
9	6.140	338	6.88E+04
10	6.130	336	1.00E+07
11	6.120	338	1.00E+07
12	6.112	340	2.41E+04
13	6.263	338	4.15E+04
14	6.250	336	1.61E+04
15	6.425	334	1.00E+07
16	6.380	336	1.00E+07
17	6.283	338	4.09E+06
18	6.396	336	1.82E+06
19	6.345	334	3.16E+06
20	6.135	336	1.00E+07

Table A- 4: Fatigue test data of AISI 304L Fine machined &amp; Electropolished(6).

Sample No.	Minimum Diameter mm	Applied Stress MPa	Fatigue Life Cycles
1	5.750	316	1.00E+07
2	5.950	318	1.00E+07
3	5.860	320	1.94E+06
4	5.830	318	3.63E+05
5	5.850	316	1.00E+07
6	5.970	318	1.00E+07
7	5.850	320	9.34E+05
8	5.900	318	1.00E+07
9	5.780	320	9.66E+05
10	5.990	318	1.00E+07
11	6.000	320	5.96E+05
12	5.950	318	1.00E+07
13	6.050	320	1.00E+07
14	6.050	322	4.38E+04
15	5.860	320	2.55E+05
16	6.145	318	1.00E+07
17	6.060	320	3.77E+05

Table A- 5: Fatigue test data of AISI 304L rough machined (4).

Sample No.	Minimum Diameter mm	Applied Stress MPa	Fatigue Life Cycles
1	6.37	306	4.79E+05
2	6.325	304	4.64E+05
3	6.375	302	4.99E+05
4	6.396	300	5.88E+05
5	6.332	298	5.90E+05
6	6.382	296	7.36E+05
7	6.365	294	7.94E+05
8	6.372	292	1.00E+07
9	6.38	294	1.00E+07
10	6.367	296	2.07E+06
11	6.366	294	1.00E+07
12	6.366	296	4.67E+05
13	6.476	294	6.28E+05
14	6.41	292	5.34E+05
15	6.364	290	6.35E+05
16	6.382	288	1.02E+06
17	6.332	286	1.00E+07
18	6.324	288	1.00E+07
19	6.405	290	1.49E+06
20	6.376	288	1.00E+07

Table A- 6: Fatigue test data of AISI 304L rough machined &amp; annealed (5).

Sample No.	Minimum Diameter mm	Applied Stress MPa	Fatigue Life Cycles
1	6.390	330	1.00E+07
2	6.325	332	1.00E+07
3	6.350	334	1.00E+07
4	6.450	336	1.00E+07
5	6.404	338	1.58E+05
6	6.375	336	1.00E+07
7	6.385	338	8.58E+04
8	6.345	336	1.00E+07
9	6.305	338	4.79E+04
10	6.445	336	1.00E+07
11	6.380	338	1.00E+07
12	6.350	340	8.52E+04
13	6.383	338	1.04E+05
14	6.370	336	1.00E+07
15	6.330	338	4.76E+05
16	6.365	336	1.00E+07
17	6.390	338	1.00E+07
18	6.420	340	7.39E+04
19	6.385	338	1.05E+05
20	6.335	336	2.92E+04

Table A- 7: Fatigue test data of AISI 316L Fine machined (1).

Sample No.	Minimum Diameter mm	Applied Stress MPa	Fatigue Life Cycles
1	6.312	304	1.00E+07
2	6.35	306	1.00E+07
3	6.343	308	1.00E+07
4	6.362	310	1.00E+07
5	6.362	312	1.00E+07
6	6.335	314	5.22E+05
7	6.34	312	1.00E+07
8	6.361	314	1.00E+07
9	6.38	316	1.00E+07
10	6.335	318	5.01E+05
11	6.37	316	1.00E+07
12	6.375	318	1.00E+07
13	6.325	320	1.00E+07
14	6.38	322	8.47E+05
15	6.35	320	1.00E+07
16	6.33	322	3.43E+05
17	6.35	320	1.00E+07
18	6.35	322	1.75E+06
19	6.37	320	9.74E+05
20	6.35	318	1.39E+06

Table A- 8: Fatigue test data of AISI 316L Fine machined &amp; annealed (2).

Sample No.	Minimum Diameter mm	Applied Stress MPa	Fatigue Life Cycles
1	6.343	310	1.00E+07
2	6.350	312	1.48E+06
3	6.390	310	1.00E+07
4	6.365	312	1.00E+07
5	6.360	314	1.67E+05
6	6.385	312	1.00E+07
7	6.410	314	1.36E+06
8	6.380	312	6.86E+05
9	6.382	310	1.00E+07
10	6.370	312	2.01E+05
11	6.375	310	9.34E+05
12	6.315	308	5.42E+05
13	6.350	306	9.80E+05
14	6.353	304	1.33E+06
15	6.341	302	1.32E+06
16	6.344	300	2.57E+06
17	6.382	298	1.25E+06
18	6.380	296	1.45E+06
19	6.337	294	1.00E+07
20	6.376	296	1.00E+07

Table A- 9: Fatigue test data of AISI 316L Fine machined &amp; annealed Electropolished (3).

Sample No.	Minimum Diameter mm	Applied Stress MPa	Fatigue Life Cycles
1	6.290	320	7.59E+05
2	6.250	318	1.13E+06
3	6.300	316	8.93E+05
4	6.260	314	1.08E+06
5	6.305	312	1.89E+06
6	6.320	310	1.35E+06
7	6.280	308	1.03E+06
8	6.335	306	1.44E+06
9	6.315	304	1.00E+07
10	6.313	306	1.00E+07
11	6.225	307	1.27E+06
12	6.246	306	1.33E+06
13	6.303	304	9.85E+05
14	6.284	302	1.07E+06
15	6.290	300	1.23E+06
16	6.290	298	2.10E+06
17	6.255	296	1.00E+07
18	6.255	298	1.00E+07
19	6.275	300	1.00E+07
20	6.300	302	1.00E+07

Table A- 10: Fatigue test data of AISI 316L rough machined (4).

Sample No.	Minimum Diameter mm	Applied Stress MPa	Fatigue Life Cycles
1	6.545	300	4.73E+05
2	6.56	298	9.92E+05
3	6.525	296	5.54E+04
4	6.475	294	7.32E+05
5	6.52	292	5.59E+05
6	6.52	290	5.82E+05
7	6.504	288	1.00E+07
8	6.52	290	6.01E+05
9	6.52	288	5.06E+05
10	6.53	286	1.00E+07
11	6.38	288	1.00E+07
12	6.54	290	1.00E+07
13	6.518	292	7.30E+05
14	6.53	290	1.00E+07
15	6.52	292	1.00E+07
16	6.524	294	1.00E+07
17	6.515	296	7.15E+05
18	6.53	294	1.29E+06
19	6.34	292	1.00E+07

Table A- 11: Fatigue test data of AISI 316L rough machined &amp; annealed (5).

Sample No.	Minimum Diameter mm	Applied Stress MPa	Fatigue Life Cycles
1	6.460	272	5.09E+05
2	6.470	270	3.98E+05
3	6.488	268	5.98E+05
4	6.447	266	4.39E+05
5	6.473	264	1.00E+07
6	6.411	266	8.65E+05
7	6.494	264	1.00E+07
8	6.400	266	3.98E+05
9	6.411	264	5.68E+05
10	6.458	262	1.00E+07
11	6.470	264	8.97E+05
12	6.470	266	1.30E+06
13	6.446	264	1.00E+07
14	6.443	266	9.04E+05
15	6.440	264	1.00E+07
16	6.470	266	2.93E+06
17	6.430	264	7.11E+05
18	6.460	262	2.57E+06
19	6.460	260	1.00E+07
20	6.455	262	4.23E+06

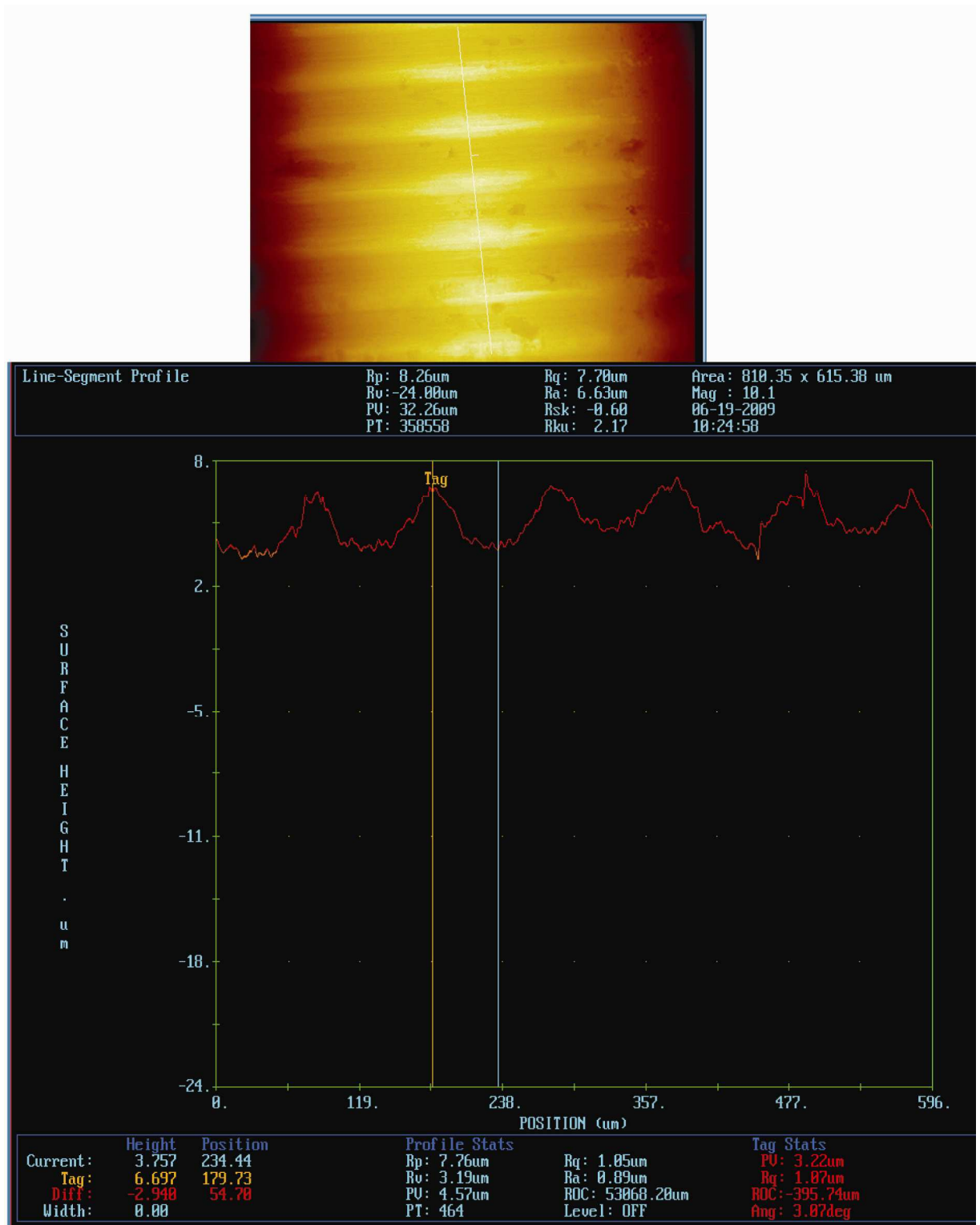


Figure A- 1: Surface map and line profile for fine sample show the high peak-to-valley.



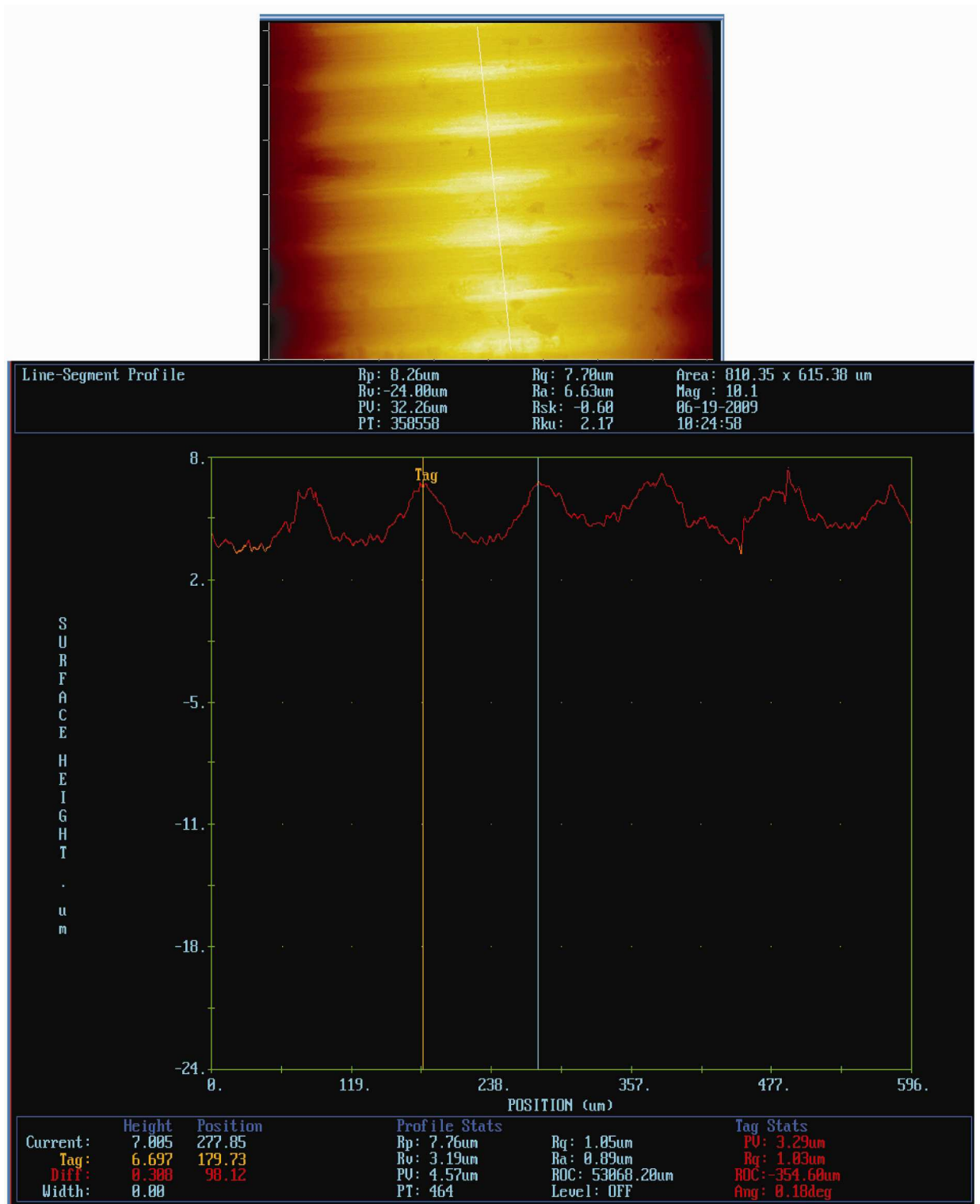


Figure A- 2: Surface map and line profile for fine sample show the spacing of adjacent local peaks.

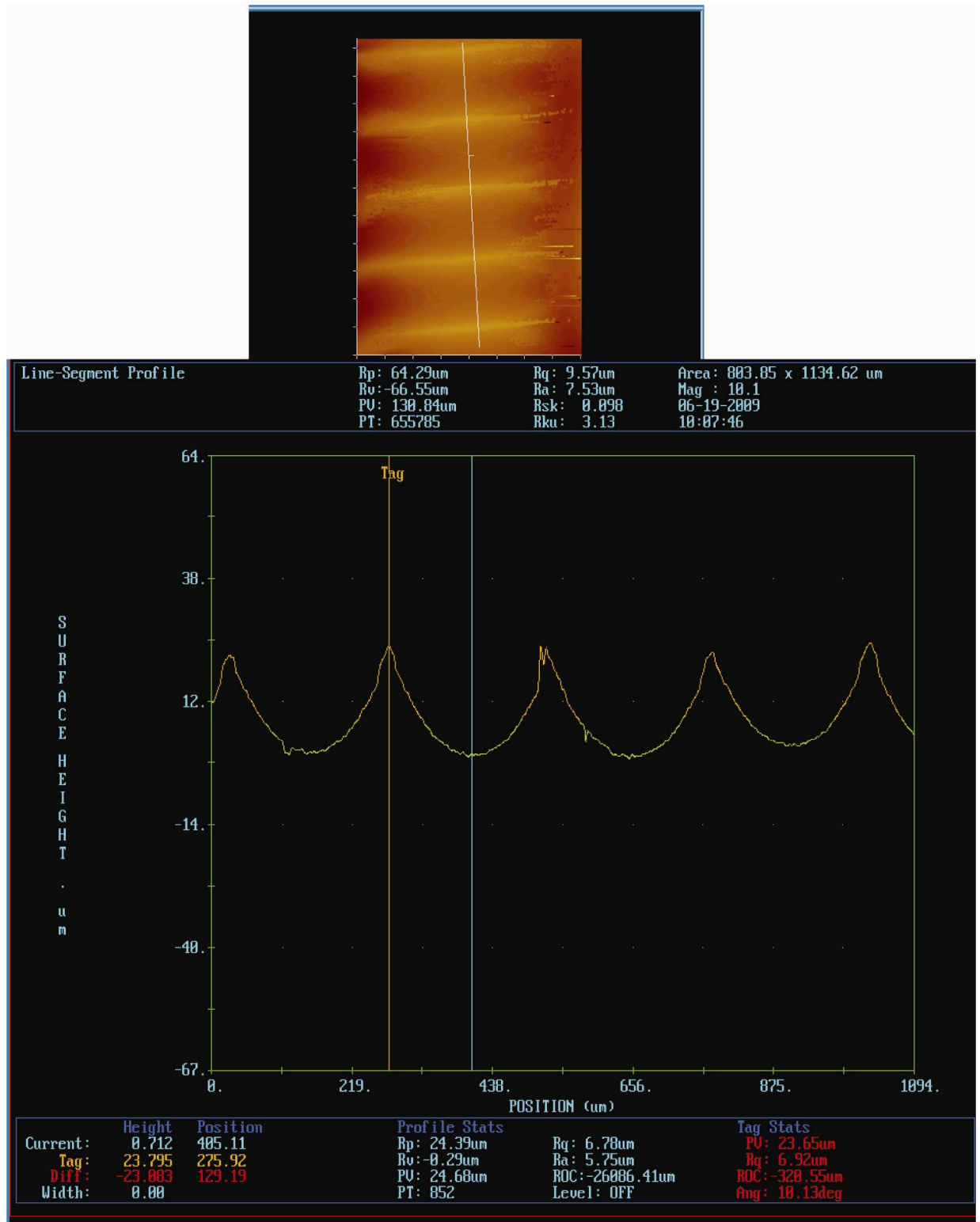


Figure A- 3: Surface map and line profile for rough sample show the high peak-to-valley.

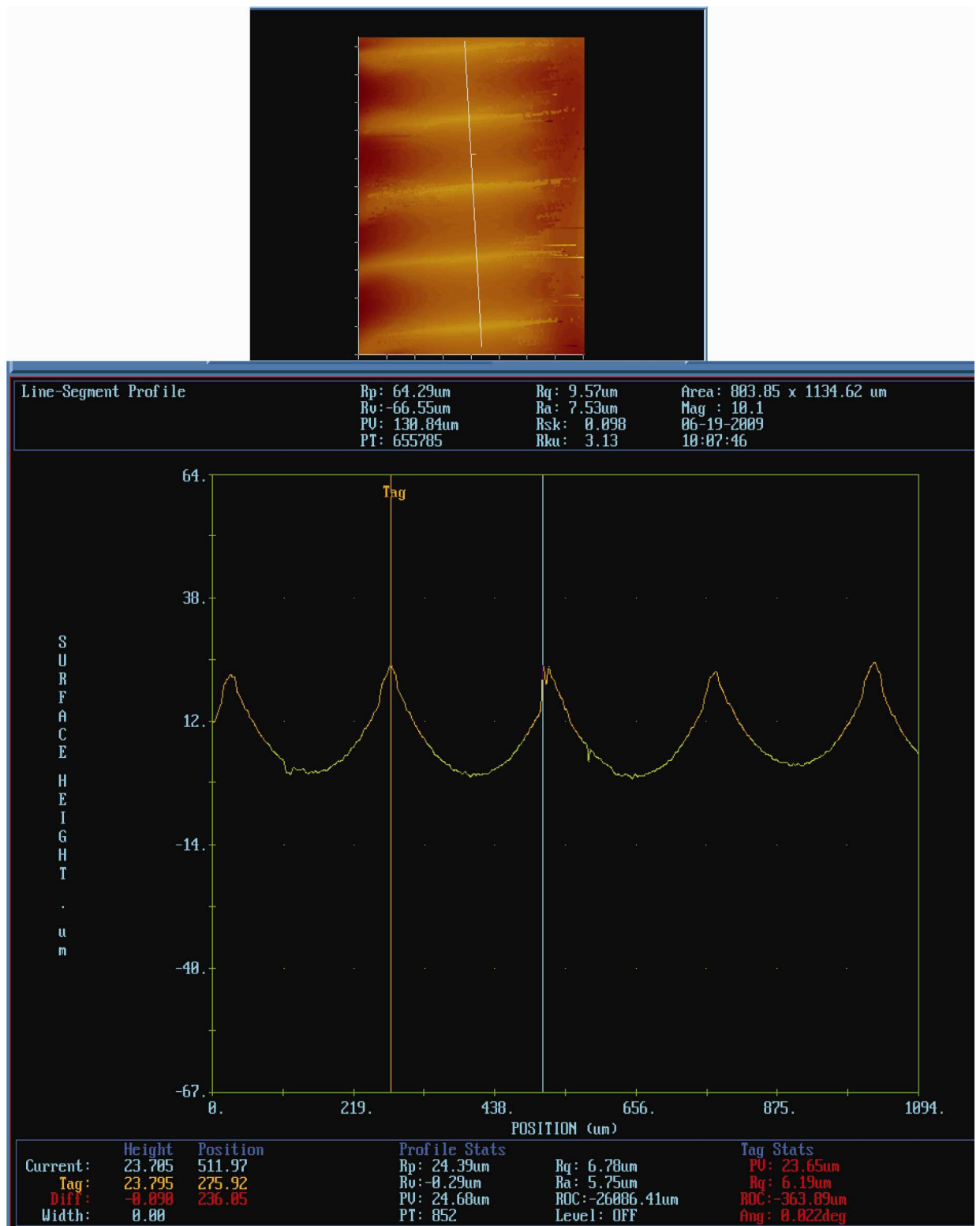



Figure A- 4: Surface map and line profile for rough sample show the spacing of adjacent local peaks.

Bureau Veritas UK Ltd  
 Acrewood Way, St Albans, Hertfordshire AL4 0JY  
 United Kingdom  
 Telephone: + 44 (0) 1727 816702 Fax: + 44 (0) 1727 816700



**BUREAU  
VERITAS**

TEST REPORT

The University of Manchester  
 School of Materials Corrosion, Corrosion and Protection Centre  
 The Mill  
 Sackville Street  
 Manchester M60 1QD

Your Ref      ELM456854  
 Our Ref      01368334  
 Date      04.12.08

**COMPONENTS FOR CHEMICAL ANALYSIS**

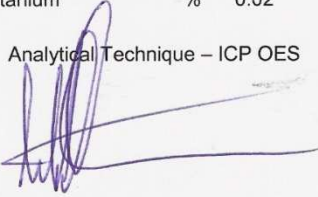
**Certificate Number      M8655**

Date of Receipt      28.11.08      Date of Test      04.12.08

Description      Stainless Steel 304 as received      Stainless Steel 316 as received

Carbon	%	0.022	0.022
Silicon	%	0.33	0.38
Manganese	%	1.24	1.57
Phosphorus	%	0.040	0.042
Sulphur	%	0.028	0.027
Nickel	%	8.33	10.85
Chromium	%	17.65	17.25
Molybdenum	%	0.37	2.07
Niobium	%	<0.02	0.02
Titanium	%	0.02	<0.02

Analytical Technique – ICP OES



S Rowbotham BEng (Hons) CEng MIMMM  
 Senior Materials Consultant

**End of Report**

This Test Report may not be reproduced other than in full, except with the prior written approval of the issuing laboratory  
 Bureau Veritas UK Ltd. Registered in England No. 1758622 Registered Office: 2nd Floor, Tower Bridge Court, 224-226 Tower Bridge Road, London SE1 2TX

Figure A- 5: Chemical composition analysis for AISI 304L/ AISI 316L.



000058-02-0604-EN  
Operating Instructions

Model R.R. Moore High Speed  
Rotating Beam Fatigue Testing Machine

Table 5. The R.R. Moore loading factor chart.

Dia.	Factor	Dia.	Factor	Dia.	Factor	Dia.	Factor	Dia.	Factor	Dia.	Factor	Dia.	Factor	Dia.	Factor
0.050	0.0061	0.100	0.0491	0.150	0.1657	0.200	0.3927	0.250	0.7670	0.300	1.3254	0.350	2.1046	0.400	3.1416
0.051	0.0065	0.101	0.0506	0.151	0.1690	0.201	0.3986	0.251	0.7762	0.301	1.3387	0.351	2.1227	0.401	3.1652
0.052	0.0069	0.102	0.0521	0.152	0.1723	0.202	0.4046	0.252	0.7855	0.302	1.3521	0.352	2.1409	0.402	3.1890
0.053	0.0073	0.103	0.0536	0.153	0.1758	0.203	0.4106	0.253	0.7949	0.303	1.3655	0.353	2.1592	0.403	3.2128
0.054	0.0077	0.104	0.0552	0.154	0.1793	0.204	0.4167	0.254	0.8044	0.304	1.3791	0.354	2.1776	0.404	3.2368
0.055	0.0082	0.105	0.0568	0.155	0.1828	0.205	0.4228	0.255	0.8139	0.305	1.3928	0.355	2.1961	0.405	3.2609
0.056	0.0086	0.106	0.0585	0.156	0.1864	0.206	0.4291	0.256	0.8235	0.306	1.4065	0.356	2.2147	0.406	3.2851
0.057	0.0090	0.107	0.0601	0.157	0.1899	0.207	0.4354	0.257	0.8332	0.307	1.4203	0.357	2.2334	0.407	3.3094
0.058	0.0096	0.108	0.0618	0.158	0.1936	0.208	0.4417	0.258	0.8430	0.308	1.4342	0.358	2.2523	0.408	3.3339
0.059	0.0101	0.109	0.0636	0.159	0.1973	0.209	0.4481	0.259	0.8528	0.309	1.4482	0.359	2.2712	0.409	3.3585
0.060	0.0106	0.110	0.0653	0.160	0.2010	0.210	0.4546	0.260	0.8628	0.310	1.4624	0.360	2.2902	0.410	3.3832
0.061	0.0111	0.111	0.0671	0.161	0.2048	0.211	0.4611	0.261	0.8728	0.311	1.4766	0.361	2.3094	0.411	3.4079
0.062	0.0117	0.112	0.0689	0.162	0.2087	0.212	0.4677	0.262	0.8828	0.312	1.4908	0.362	2.3286	0.412	3.4329
0.063	0.0123	0.113	0.0708	0.163	0.2126	0.213	0.4744	0.263	0.8930	0.313	1.5052	0.363	2.3479	0.413	3.4579
0.064	0.0129	0.114	0.0727	0.164	0.2165	0.214	0.4811	0.264	0.9032	0.314	1.5197	0.364	2.3674	0.414	3.4831
0.065	0.0135	0.115	0.0747	0.165	0.2205	0.215	0.4878	0.265	0.9135	0.315	1.5343	0.365	2.3869	0.415	3.5084
0.066	0.0141	0.116	0.0766	0.166	0.2245	0.216	0.4947	0.266	0.9239	0.316	1.5489	0.366	2.4066	0.416	3.5339
0.067	0.0148	0.117	0.0786	0.167	0.2286	0.217	0.5016	0.267	0.9343	0.317	1.5637	0.367	2.4264	0.417	3.5594
0.068	0.0154	0.118	0.0807	0.168	0.2328	0.218	0.5086	0.268	0.9449	0.318	1.5785	0.368	2.4463	0.418	3.5851
0.069	0.0161	0.119	0.0827	0.169	0.2369	0.219	0.5156	0.269	0.9555	0.319	1.5935	0.369	2.4663	0.419	3.6109
0.070	0.0168	0.120	0.0848	0.170	0.2412	0.220	0.5227	0.270	0.9662	0.320	1.6085	0.370	2.4864	0.420	3.6368
0.071	0.0176	0.121	0.0869	0.171	0.2455	0.221	0.5298	0.271	0.9769	0.321	1.6236	0.371	2.5066	0.421	3.6628
0.072	0.0183	0.122	0.0891	0.172	0.2498	0.222	0.5371	0.272	0.9878	0.322	1.6388	0.372	2.5270	0.422	3.6889
0.073	0.0191	0.123	0.0913	0.173	0.2542	0.223	0.5443	0.273	0.9988	0.323	1.6541	0.373	2.5474	0.423	3.7153
0.074	0.0199	0.124	0.0936	0.174	0.2586	0.224	0.5517	0.274	1.0100	0.324	1.6696	0.374	2.5679	0.424	3.7417
0.075	0.0207	0.125	0.0959	0.175	0.2631	0.225	0.5591	0.275	1.0209	0.325	1.6851	0.375	2.5886	0.425	3.7682
0.076	0.0215	0.126	0.0982	0.176	0.2676	0.226	0.5666	0.276	1.0320	0.326	1.7006	0.376	2.6093	0.426	3.7949
0.077	0.0224	0.127	0.1005	0.177	0.2722	0.227	0.5742	0.277	1.0432	0.327	1.7163	0.377	2.6303	0.427	3.8217
0.078	0.0233	0.128	0.1029	0.178	0.2768	0.228	0.5818	0.278	1.0546	0.328	1.7321	0.378	2.6512	0.428	3.8486
0.079	0.0242	0.129	0.1054	0.179	0.2815	0.229	0.5895	0.279	1.0661	0.329	1.7481	0.379	2.6723	0.429	3.8756
0.080	0.0251	0.125	0.0959	0.180	0.2863	0.230	0.5972	0.280	1.0776	0.330	1.7641	0.380	2.6935	0.430	3.9028
0.081	0.0261	0.126	0.0982	0.181	0.2911	0.231	0.6051	0.281	1.0891	0.331	1.7801	0.381	2.7148	0.431	3.9301
0.082	0.0271	0.127	0.1005	0.182	0.2959	0.232	0.6129	0.282	1.1008	0.332	1.7963	0.382	2.7363	0.432	3.9575
0.083	0.0281	0.128	0.1029	0.183	0.3008	0.233	0.6209	0.283	1.1126	0.333	1.8126	0.383	2.7578	0.433	3.9850
0.084	0.0291	0.129	0.1054	0.184	0.3058	0.234	0.6289	0.284	1.1244	0.334	1.8289	0.384	2.7795	0.434	4.0127
0.085	0.0301	0.135	0.1208	0.185	0.3108	0.235	0.6370	0.285	1.1363	0.335	1.8454	0.385	2.8012	0.435	4.0405
0.086	0.0312	0.136	0.1235	0.186	0.3158	0.236	0.6452	0.286	1.1484	0.336	1.8620	0.386	2.8231	0.436	4.0685
0.087	0.0323	0.137	0.1262	0.187	0.3210	0.237	0.6535	0.287	1.1619	0.337	1.8787	0.387	2.8451	0.437	4.0965
0.088	0.0335	0.138	0.1288	0.188	0.3262	0.238	0.6617	0.288	1.1726	0.338	1.8955	0.388	2.8672	0.438	4.1247
0.089	0.0346	0.139	0.1318	0.189	0.3314	0.239	0.6701	0.289	1.1849	0.339	1.9123	0.389	2.8895	0.439	4.1530
0.090	0.0358	0.140	0.1347	0.190	0.3367	0.240	0.6786	0.290	1.1972	0.340	1.9293	0.390	2.9118	0.440	4.1815
0.091	0.0370	0.141	0.1376	0.191	0.3420	0.241	0.6871	0.291	1.2096	0.341	1.9464	0.391	2.9342	0.441	4.2100
0.092	0.0382	0.142	0.1406	0.192	0.3474	0.242	0.6957	0.292	1.2221	0.342	1.9635	0.392	2.9568	0.442	4.2387
0.093	0.0395	0.143	0.1435	0.193	0.3529	0.243	0.7043	0.293	1.2347	0.343	1.9809	0.393	2.9795	0.443	4.2676
0.094	0.0408	0.144	0.1466	0.194	0.3584	0.244	0.7131	0.294	1.2474	0.344	1.9982	0.394	3.0023	0.444	4.2965
0.095	0.0421	0.145	0.1497	0.195	0.3639	0.245	0.7219	0.295	1.2602	0.345	2.0157	0.395	3.0251	0.445	4.3256
0.096	0.0434	0.146	0.1528	0.196	0.3696	0.246	0.7308	0.296	1.2730	0.346	2.0333	0.396	3.0482	0.446	4.3648
0.097	0.0448	0.147	0.1559	0.197	0.3753	0.247	0.7397	0.297	1.2860	0.347	2.0510	0.397	3.0714	0.447	4.3842
0.098	0.0462	0.148	0.1594	0.198	0.3810	0.248	0.7487	0.298	1.2991	0.348	2.0687	0.398	3.0946	0.448	4.4137
0.099	0.0476	0.149	0.1624	0.199	0.3868	0.249	0.7578	0.299	1.3122	0.349	2.0866	0.399	3.1181	0.449	4.4433

**Note:**

The Loading Factor Chart (Table 5) is in English units. When a metric weight set is used with the machine, be sure to convert the dimension values to English units before using the chart.

Figure A- 6: Chemical composition analysis for AISI 304L/ AISI 316L.

## ***Appendix-B***

### **The Author**

***Place of birth:*** Khamis Mushayt, Saudi Arabia.

***Year of Birth:*** Sep. 7 1975

#### ***Education:***

- The University of Manchester, Manchester. UK.  
2006- Current, PhD candidate (School of Materials)
- The University of Sheffield, Sheffield. UK.  
2003 - 2004 M.A. (Master of Metallurgy)
- King Fahd University of Petroleum and Minerals, Dhahran, Saudi Arabia.  
1996 - 2001 B.A. (Applied Mechanical Engineering)

#### ***Employment:***

2001 – Current, Lab. Engineer, Research and Technology Centre, Saudi Basic Industries Corporation (SABIC), Jubail, Saudi Arabia.

1998 – 1999, trainee engineer in gas turbine maintenance, Saudi Consolidated Electric Company. Abha, Saudi Arabia.

#### ***Selected publications:***

**S. Al-Shahrani, and T.J. Marrow:** Effect of Surface Finish on Fatigue of Stainless Steels, 12th International Conference on Fracture (ICF 12), Ottawa, Canada, 2009.

**S. Al-Shahrani, and T.J. Marrow:** Effect of Surface Finish on Fatigue Limit in AISI 316L Austenitic Stainless Steels, The 3rd Saudi International Conference, Surrey, UK, 2009.

**S. Al-Shahrani, and T.J. Marrow:** Influence of Twins on Short Fatigue Cracks in Type 316 Stainless Steel, Materials Structures & Micromechanics of Fracture (MSMF6), in Brno, Czech Republic, 2010. (**Accepted**)

Saeed Al-Shahrani